SCHOLARLY PUBLICATIONS

A CURRENT AWARENESS BULLETIN
OF RESEARCH OUTPUT

@DTU

(58th Edition)

OCTOBER, 2017

BY: CENTRAL LIBRARY

DELHI TECHNOLOGICAL UNIVERSITY
(FORMERLY *DELHI COLLEGE OF ENGINEERING)*
GOVT. OF N.C.T. OF DELHI
SHAHBAD DAULATPUR, MAIN BAWANA ROAD
DELHI 110042

PREFACE

This is the **Fifty eight** Issue of Current Awareness Bulletin started by Delhi Technological University, Central Library. The aim of the bulletin is to compile, preserve and disseminate information published by the faculty, students and alumni for mutual benefits. The bulletin also aims to propagate the intellectual contribution of Delhi Technological University (DTU) as a whole to the academia.

The bulletin contains information resources available in the internet in the form of articles, reports, presentations published in international journals, websites, etc. by the faculty and students of DTU. The publications of faculty and student which are not covered in this bulletin may be because of the reason that the full text either was not accessible or could not be searched by the search engine used by the library for this purpose.

The learned faculty and students are requested to provide their uncovered publications to the library either through email or in CD, etc to make the bulletin more comprehensive.

This issue contains the information published during **October, 2017**. The arrangement of the contents is alphabetical. The full text of the article which is either subscribed by the university or available in the web is provided in this bulletin.

Central Library

CONTENTS

1. A Case Study on Techniques for Improving Weak and CompressibleClay Soil under a High Earth Embankment, ***6.Shanko Ayele Abera***, Civil, DTU

2. American Sign Language Recognition System Using Image Processing Method, ***6.Amit Kumar Gautam*** and Ajay Kaushik, Electronics and Communication, DTU

3. Biomolecules mediated targeting of vascular endothelial growth factor in neuronal dysfunction: An in Silico approach, ***6.Niraj Kumar Jha*** and ***3.Pravir Kumar***, Biotechnology. DTU

4. Blind image deblurring via gradient orientation-based clustered coupled sparse dictionaries, Kuldeep Singh, ***3.Dinesh Kumar Vishwakarma*** and Gurjit Singh Walia, Electronics and Communication, DTU

5. Charlier–Szász–Durrmeyer type positive linear operators, ***3.Naokant Deo*** and ***6.Minakshi Dhamija,*** Applied Mathematics, DTU

6. Computational modeling of small molecule inhibitors of mitochondrial fusion, Vinod Scaria, Salma Jamal and ***3.Yasha Hasija***, Biotechnology, DTU

7. Dynamics of a Delayed Prey-Predator Model Using Modified Holling Tanner Functional Response With Migration, ***6.Charu Arora*** and ***3.Vivek Kumar***, Applied Mathematics, DTU

8. Effective sensitization of Eu3+ and energy transfer in Sm3+/Eu3+ co-doped ZPBT glasses for CuPc based solar cell and w-LEDs applications, ***6.Kaushal Jha*** and ***3.M. Jayasimhadri***, Applied Physics, DTU

9. Effecton Surface Properties OF Mild SteelDuring Dry Turning& Wet Turning On Lathe, ***3.Ravi Butola***, Jitendrakumar, ***8.Vaibhavkhanna***, ***6.ParveshAli*** and ***8.Vishesh Khanna***, Mechanical, Production & Industrial and Automobile, DTU

10. Estimation of Asiaticoside by Using RP-HPLC and FAME Analysis of Medicinally Important Plant Centella asiatica, ***7.Arpita Roy***, ***7.Koyel Kundu***, ***6.Gaurav Saxena*** and ***3.Navneeta Bharadvaja***, Biotechnology, DTU

11. ESTIMATION OF WEIGHTING DISTRIBUTION USING FUZZY MEMBERSHIPS AND WAVELET TRANSFORMATION WITH PSO OPTIMIZATION IN SATELLITE IMAGE ENHACEMENT, Nitin Sharma and ***3.Om Prakash Verma***, Electronics and Communication, DTU

12. Experimental investigation on friction stir welding of copper alloys, ***3.R.S. Mishra*** and ***3.V Jeganathan***, Mechanical, Production & Industrial and Automobiles, DTU

13. Filters Modified ComplementarySplit-Ring Resonator Geometries with Face to Face Orientations in Substrate Integrated Waveguide for Applications as Band Pass, Jigyasa Sharma, Dhirendra Kumar, and ***3.Asok De***, Electronics and Communication, DTU

14. FlavorDB: a database of flavor molecules, Neelansh Garg, Apuroop Sethupathy, Rudraksh Tuwani, Rakhi NK, ***6.Shubham Dokania***, Arvind Iyer, Ayushi Gupta, Shubhra Agrawal, ***6.Navjot Singh,*** Shubham Shukla, Kriti Kathuria, Rahul Badhwar, Rakesh Kanji, Anupam Jain, Avneet Kaur, Rashmi Nagpal and Ganesh Bagler, DTU

15. Friction stir processing of magnesium alloys used in automobile and aerospace applications, ***3.R.S. Mishra*** and ***6.Sumit Jain***, Mech, Prod & Indus and Automo, DTU

16. Generalized input impedance modelling of TLnetwork-based HFDPS for validating frequencydependent criteria for power-signal integrity, ***8.1.Ankit Gupta***, ***8.1.Nikhil Kumar*** and Sudip K Mazumder, Electrical, DTU

17. Hybrid Abrasive Flow Machining for Nano Finishing - A Review, ***6.Parvesh Ali***, ***6.Sachin Dhull***, ***3.R.S.Walia***, ***3.Q.Murtaza*** and ***3.Mohit Tyagi,*** DTU

18. Hybrid Control of High Efficient Resonant Converter for Renewable Energy System, H. M. Suryawanshi, Snehal P. Pachpor, T.Ajmal , ***7.1.Girish G***. Talapur, Shelas Sathyan, M. S. Ballal, V. B. Borghate and M. R. Ramteke, Electrical, DTU

19. KDR Mutation: A High-Frequency Rare Mutation and its Correlation with other Somatic Mutations in Indian Colorectal Cancer Patients, Mayank Jauhri, ***6.Vani Gupta***, Yogender Shokeen, Sachin Minhas, Sunita Bhalla and Shyam Aggarwal, Biotechnology, DTU

20. Manganese(III) mediated synthesis of A2B Mn(III) corroles: A new general and green synthetic approach and characterization, ***6.Omprakash Yadav***, ***6.Atul Varshney*** and ***3.Anil Kumar***, Applied Chemistry, DTU

21. MEASURING THE IMPACT OF GREEN HUMAN RESOURCE FACTORS ON ENVIRONMENTAL PERFORMANCE USING STRUCTURE EQUATION MODELING, ***3.Anu Singh Lather*** and ***3.Shikha Goyal.*** DTU

22. Parameters affecting target detection in VNIR and SWIR range, Deepti Yadav, M.K. Arora, ***3.K.C. Tiwari*** and J.K. Ghosh, Civil, DTU

23. Probing Charge-Transfer and Short-Lived Triplet States of a Biosensitive Molecule, 2,6-ANS: Transient Absorption and Time-Resolved Spectroscopy, ***3.Mohan Singh Mehata***, Yang Yang and Keli Han, Applied Physics, DTU

24. Quantifying phase separation in terms of magnetoresistive hysteresis loops in strongly phase-separated manganite thin films, ***6.Sandeep Singh***, ***3.Pawan Kumar Tyagi*** and H. K. Singh, Applied Physics, DTU

25. SECOND HANKEL DETERMINANT FOR CERTAIN CLASS CLOSE TO CONVEX FUNCTIONS, ***6.Kanika Khatter*** and ***3.S.Sivaprasad Kumar***, Applied Mathematics, DTU

26. Silver Nanoparticles Synthesis from a Pharmaceutically Important Medicinal Plant Plumbago Zeylanica, ***6.Arpita roy*** and ***3.Navneeta Bharadvaja***, Biotechnology, DTU

27. Spectroscopic Studies of single Near Ultraviolet pumped Tb3+ doped Lithium Lead Alumino Borate Glasses for Green Lasers and Tricolour w-LEDs, ***6.Nisha Deopa*** and ***3.A. S. Rao***, Applied Physics, DTU

28. Sportsmen's energy package Cordyceps sinensis: Medicinal importance and responsible phytochemical constituents, Yogesh Chandra Joshi, Mukesh Chandra Joshi, ***6.Vivek Chopra***, Rakesh Kumar Joshi, Rajni Kant Sharma and Vikrant Kumar, Biotechnology, DTU

29. STUDY OF MICROSTRUCTURE AND PHASE OF PLASMA SPRAYED HIGH MOLYBDENUM COMPOSITE COATING, ***3.Shailesh Mani Pandey***, ***3.R.S.Walia*** and ***3.Qasim Murtaza***, Mechanical, DTU

30. Supplementary Material Identification of a novel class of BRD4 inhibitors by computational screening and binding simulations, Bryce K. Allen, ***3.Saurabh Mehta***, Stuart W.J. Ember, Jin-Yi Zhu, Ernst Schönbrunn, Nagi G. Ayad and Stephan C. Schürer, Applied Chemistry, DTU

31. Thermodynamic (Energy-Exergy) analysis of combined cycle gas turbine power plant (CCGT) for improving its thermal performances, ***3.R.S Mishra*** and ***6.Amit Singh***, Mechanical, Production & Industrial and Automobile, DTU

32. Thermodynamic (energy-exergy) analysis of pre-cooled linde system, ***3.R. S. Mishra*** and ***6.Devendra Kumar***, Mechanical, Production & Industrial and Automobiles, DTU

33. Thermodynamic performance analysis of claude cryogenic system, ***3.R. S. Mishra*** and ***6.Devendra Kumar***, Mechanical, Production & Industrial and Automobiles, DTU

34. Uptake of Heavy Metals from Industrial Wastewater Using In Vitro Plant Cultures, ***6.Nupur Jauhari***, ***6.Sanjay Menon***, Neelam Sharma and ***3.Navneeta Bharadvaja,*** Biotechnology, DTU

35. Utility of thermodynamic (exergy-exergy) analysis in cryogenic systems for liquefaction of gases: A Review, ***3.R.S Mishra*** & ***6.Devendra Kumar***, Mechanical, Production & Industrial and Automobile, DTU

1. *Chancellor*

2. *Pro Vice Chancellor*	***2.1.*** *Ex Pro Vice Chancellor*
3. *Faculty*	***3.1.*** *Ex Faculty*
4. *Teaching-cum-Research Fellow*	***4.1.****Asst. Librarian*
5. *Alumni*	
6. *Research Scholar*	***6.1.*** *Ex Research Scholar*
7. *PG Scholar*	***7.1.*** *Ex PG Scholar*
8. *Undergraduate Student*	***8.1.*** *Ex Undergraduate Student*

6th International Conference on Emerging Trends in Engineering, Technology, Science and Management
(IETE,Bengaluru) Institution of Electronics and Telecommunication Engineers, Ganganagar, Bengaluru, Karnataka, India (ICETETSM-17)
07th October 2017, www.conferenceworld.in ISBN: 978-93-86171-70-2

A Case Study on Techniques for Improving Weak and CompressibleClay Soil under a High Earth Embankment

Mr. Shanko Ayele Abera,

[1](M.Sc.), Dilla University, College of Engineering and Technology,
Department of Construction Technology and Management, Dilla, Ethiopia
Ph.D. Scholar @ Delhi Technological University, Department of Civil Engineering, Delhi, (India)

ABSTRACT.

This paper investigates the suitability of three soil improvement techniques for the construction of a high earth embankment on thick weak and highly compressible clay soil. The eastern approach embankment of Hidase Bridge on the River Nile linking Gonder and Gojam was chosen as a case study and a comprehensive site investigation program was carried out to determine the properties the subsurface soils. The study results showed that unless the subsurface soils have been improved they may fail or undergo excessively large settlements due to the embankment construction. Three ground improvement techniques based on the principles of the "staged construction method, SCM", "vertical sand drain, VSD" and "sand compaction piles, SCP" of embankment foundation soil treatment are discussed and evaluated.

Embankment design options based on applications of the above methods have been proposed for foundation treatment to adequately support embankment loads. A method performance evaluation based on the improvement of soil properties achieved; the time required for construction and compared estimated costs criteria was made to assess the effectiveness and expected overall performance. Adoption of any of the soil improvement techniques considered depends mainly on the most critical and decisive factor governing the embankment design. Based on the overall performance for the embankment case studied, the sand drains are considered as the most appropriate improvement method followed by the sand compaction piles technique whereas the staged construction method showed the poorest overall performance.

I.INTRODUCTION

The design and construction of high embankments placed on weak and compressible soils i.e. low shear strength and excessively large settlements pose several problems with respect to their safety and stability. This has lead to the development of ground improvement techniques for overcoming such instability problems. The main geotechnical aspects that should normally be considered for such soil conditions include the settlement and bearing capacity of foundation soils and the stability of embankment. The soil settlement typically consists of three components; immediate, primary and secondary. The primary settlement is due to compression of the soil resulting from the gradual escape of water from the voids of loaded soil and accounts for the majority of the total settlement.

The stability of an embankment built on highly compressible soils can be evaluated by determining the soil shear strength of the embankment and foundation soil strata using the Terzaghi's bearing capacity. Foundation

ISBN: 978-93-86171-70-2

soils can provide adequate support for overlying embankments if the imposed stresses do not exceed their shear strength. Overstressing the embankment or foundation soil may result in embankment slope failures. In Ethiopia, most the approach road embankments leading major bridge projects built across River Nile or its main tributaries must be constructed at relatively large heights on weak alluvial deposits that need to be improved. Various ground improving methods such as the surcharge loading, stone columns, wick drains, sand compaction piles and geo-synthetic reinforcement, have been used in various countries to accelerate settlement and enhance embankment stability issues associated with embankment construction on weak soils. This study investigates the suitability of three soil improvement techniques for the design of a high approach embankment on thick weak and compressible clay soil deposits. Embankment design solutions based on the principles of the "staged construction method, SCM", "vertical sand drain, VSD" and "sand compaction piles, SCP" techniques for the treatment of the natural weak foundations soils are discussed and evaluated in this paper.

Description of the case study

considered the embankment site chosen for study was the location of the eastern abutment of Hidase Bridge built across River Nile to link Gojam and Gonder in Amhara State, Ethiopia. The embankment is of the rolled earth type with a maximum height of 12.0m. 30m top width and 78m bottom width with 1:2 (vertical: horizontal) side slopes. A site investigation program comprised of borehole drilling, cone penetration tests (CPT) soundings and laboratory tests was carried out to determine the required properties the subsurface soils. Typical soil profiles, SPT and CPT plots with depth of the investigated embankment site are illustrated in figures 1 and 2.

Depth (m)	Soil Types and groups
0-3	Silty Clay, CL
3-4	Clayey silt, ML
4-5	Silty clay, CL
5- 6	Clayey silty sand, SM
6-9	Silty sand, SP
9-13	Fine sand with little gravel, SP
13-14	weathered Sandstone

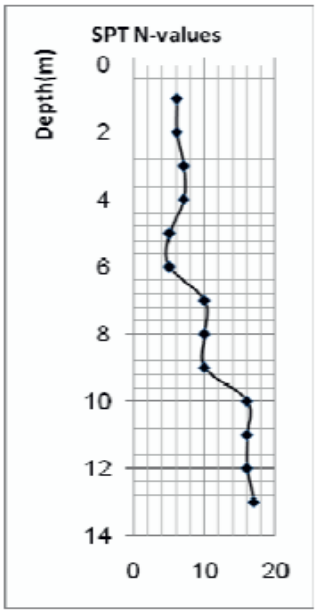

Fig. 1 Typical profiles of soil types and SPT results

ISBN: 978-93-86171-70-2

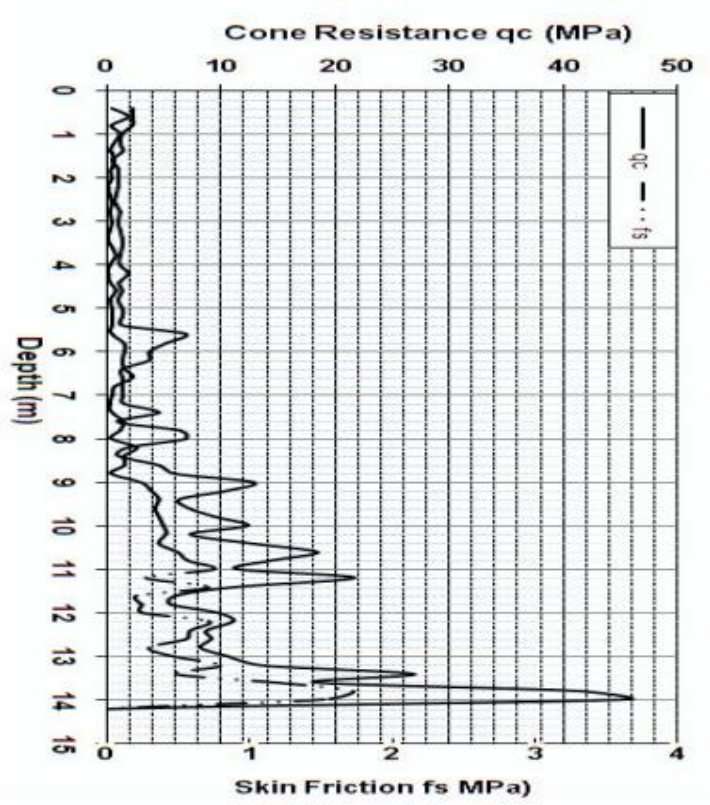

Fig. 2 Typical CPT profile in study site

As may be noted in these figures, the soil profile comprised of a soft silty clay soil layer ranging in depth from 1.0m to 6.0m, underlain by a very loose to medium dense poorly graded fine to medium coarse silty sand or sandy silts extending to a depth of 14.0m. These alluvial deposits rest directly on the highly weathered sandstone formation. The natural moisture content varied from 26% to 42% with most values between 28 and 32%. The natural dry density ranged between 11.0 and 14.5kN/m3. The total settlement of clay soil was computed from the results of consolidation tests performed on representative undisturbed soil samples and a value of 874mm was obtained for the profile representing the worst subsurface conditions. The settlement component due to primary consolidation was found to constitute from 75 to 90% of the total computed soil settlements with an average value of 690mm. The coefficient of consolidation cv was estimated using the rate of settlement and was found to vary from 4.3 to 5.2m2/year. Based on these values, the time required to reach 90% of the total settlement was found to vary considerably from 1.2 to 9.5 years. The results obtained from the SPT, CPT and UCS laboratory tests were used to estimate the shear strength parameters and the bearing capacity of the embankment foundation soils. The undrained cohesion of the clay layer was in the range of 45 to 55kPa with an average value of 50kPa. The allowable bearing capacity of the clay soil layer was estimated to be 150 to 170kPa. Based on analysis of the investigation results it was obvious that the subsurface soil conditions prevailing at study site will not be capable to support the loads imposed by the high embankment adequately. Therefore, the upper weak and highly compressible clay soil stratum should be treated before embankment construction using ground improvement techniques. Various ground improvement techniques are currently available and have successfully been applied to increase shear strength and reduce compressibility

ISBN: 978-93-86171-70-2

characteristics of weak and compressible soils. Choice of any of them depends among several factors on the geological formation of the soil, soil characteristics, cost and experience. The analytical study undertaken to investigate the effectiveness and suitability of three selected techniques for improving of the embankment foundation soils is described in the following section.

II. IMPROVEMENT METHODS CONSIDERED FOR WEAK CLAY SOILS TREATMENT

2.1. Staged construction method (SCM)

The low strength and compressible nature of the subsoil clay strata warrant special precaution to be taken in order to avoid failure during to construction in case a single stage construction option is adopted. Construction over soft clays can only be done in single stage safely for high embankments with very flat slopes or having berms on slopes which renders it to be uneconomical with respect to land and earthwork. Such a problem may be overcome by applying the stage construction method. This technique is mainly employed as a means of gradually increasing the shear strength of soft clay soils which would otherwise be inadequate to carry the embankment load safely. Consideration is given to the advantage of shear strength increase in of sub-soil strata due to consolidation by surcharge of embankment loading. The principle of the stage construction method is shown in figure 3 below.

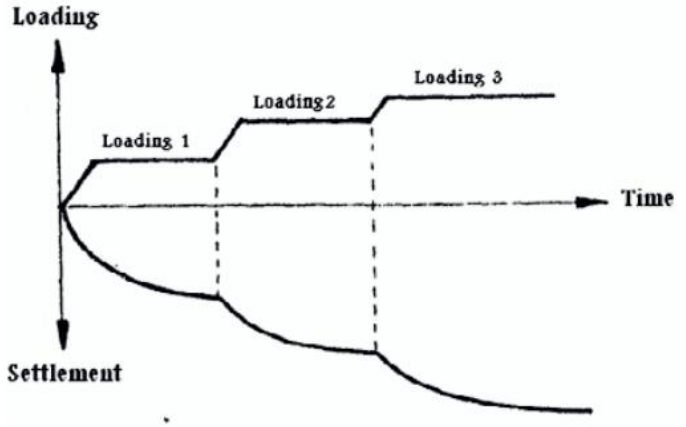

Fig. 3 Principle of staged construction method

To investigate the possibility of applying this method for improving the foundation soils under the embankment considered, the following fill material and subsoil parameters and assumptions were made:

- Embankment fill material having saturated unit weight of 20kN/m3, angle of internal friction of φ = 35˚ and cohesion c = 0.
- Compressible cohesive soil layer of average thickness 5m, submerged unit weight γ_{sub} 7kN/m3, average cohesion of subsoil cu of 50kN/m2, angle of shearing resistance φ of 6˚ and average coefficient of consolidation Cv = 4.80m2/year.

The staged construction design procedure described by the Ministry of Railways in India [1] was followed to achieve a 90% degree of the primary consolidation through construction of the embankment in three successive phases with 6 months waiting times after the first and the second stages. An intermediate drain path (i.e.

ISBN: 978-93-86171-70-2

between single and double drainage conditions) was assumed as the bottom layer is semi-impervious. The factor of safety (FS) for embankment stability is correlated to D/H (clay layer thickness to embankment height ratio) for different φ (friction angle of the fill) and a stability N number given by ($cu/\gamma H$). The stability of the 12m high embankment was analysed assuming construction gradually in 6.0m, 4.5m and 1.5m in the 1st, 2nd and 3rd stages respectively using the design charts developed by Sanglerat et al [2]. A minimum FS value of 1.20 is required for embankment stability according to this design method. Evaluation of the degree of improvement attained in the clay foundation stratum using staged construction method showed that:

I. Allowing 6 months waiting period after the 1st loading stage produced an increase in the undrained shear strength of about 9% and a consolidation degree of 35% in the clay layer. The factor of safety for embankment stability was found to be 2.18 (> 1.20).

II. Allowing 6 months waiting time after the 2ndloading stage resulted in an increase of about 20% in the undrained shear strength and gave a consolidation degree of about 50% and 35% after the 1st and 2nd construction stages respectively due to the added embankment height of 4.5m. The embankment factor of safety for embankment stability was found to be 1.49.

2.2. Vertical sand drains (VSD)

The use of vertical sand drains in soft clay accelerate the primary consolidation of clay since they bring about rapid dissipation of excess pore water pressure under embankment loading. Vertical drains are normally used where preloading alone will not be efficient. The installation of sand drains into relatively thick clay strata increases the rate of consolidation of the clay under the load by shortening the drainage path. The advantages of this method include; (a) The increased rate of gain in shear strength of clay enables the load to be applied more rapidly than would otherwise have been possible (b) The increasing rate of consolidation of the clay results in a reduction of the time required for the primary consolidation settlement; thus the structures or embankments can be put to use earlier than it would be possible otherwise The design of any sand drain project involves the determination of drain spacing which will give the required degree of consolidation in specified period of time. Such drains are usually installed in triangular or square grid pattern with spacing ranging from 1 m to 4 m. The spacing is generally fixed depending upon the loading conditions of embankment and soft subsoil characteristics. The depth of treatment is often taken as the full depth of soft or impermeable soils. Barron [3] proposed a solution for radial consolidation by based on Terzaghi's three dimensional consolidation equations whereby the overall drainage is the summation of the vertical and radial drainages. The design of sand drains can be done knowing the coefficient of consolidation, preloading time period, target degree of consolidation and drain diameter. An analytical method of sand drains design based on the above solution was applied using the data and information gathered for the subsurface soils and the embankment at the study site considered. Drains with 0.20 to 0.40m diameters arranged in square and triangular grid patterns were assumed to achieve a target consolidation degree of 90% after waiting (loading) time durations of 6, 8 and 10 months. Double drainage was assumed in the analysis considering that the drains are extended to reach the pervious sand layer underlying the compressible soil. A summary of the sand drain design options expressed in terms of the required spacing (m) is given in Table 1 for assumed drain diameters, construction time durations and piles arrangement patterns.

ISBN: 978-93-86171-70-2

Table 1 Summary of vertical sand drain design options for foundation soil improvement

Waiting Time		6 Months		8 Months		10 Months	
Grid pattern		Sq.	Tr.	Sq.	Tr.	Sq.	Tr.
drains diam. (m)	0.20	2.6	2.8	-	-	3.6	3.9
	0.25	-	-	3.2	3.4	-	-
	0.30	2.8	3.0	-	-	3.9	4.2
	0.35	-	-	3.3	3.5	-	-
	0.40	-	-	3.6	3.8	-	-

Based on the data in Table 1, the most feasible design options for all drain diameters would be those of the triangular grid patterns having diameter/spacing of 0.20m/2.8m for 6 months, 0.25m/3.0m for 8 months and 0.30m/4.0m for 10 months waiting times. The sand drain design option with 0.20m diameter and 2.80m spacing represents the most viable since it requires the shortest waiting time duration. A graphical solution published by Terrasol and cited by Kirmani [4] was also used for the case study under consideration to compare with the analytical sand drain design of. For the same drain diameters, the graphical method gave more conservative design (i.e. closer drain spacing) than those obtained in the analytical method by 25% to 33% for the square and triangular grid patterns respectively.

2.3. Sand compaction piles (SCP)

The sand compaction piles (SCP) is a forced replacement improvement technique in a soft soil which has been developed and applied in Japan since 1966 [5] to improve stability and/or reduce compressibility of cohesive soils. Sand is fed through a casing pipe into the ground and compacted either by vibration, dynamic impact or static excitation to construct a compacted sand pile. Figure 4 shows the principle of the SCP improvement method in which the replacement ratio asis defined in terms of the soil void ratio as:

$a_s = \Delta e/((1+e_0)$ ---------- (1)

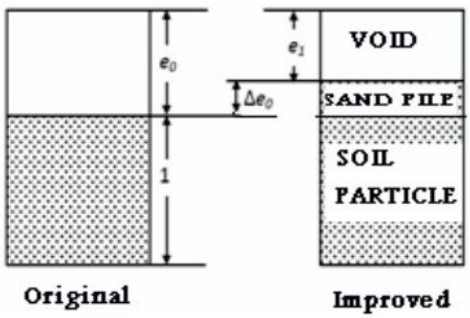

Fig. 4 Principle sand compaction piles method

ISBN: 978-93-86171-70-2

Sand amounting to a change in void ratio Δe from original value e_0 to final value e1 is introduced into the original ground of volume represented by $(1+e_0)$. A sand compaction piles (SCP) design method based on "area replacement ratio" concept [5] was applied to improve the strength and compressibility properties of the cohesive soil prevailing at the study site. In this method, the area replacement ratio (a_s) is defined as the ratio of the granular pile area (A_s) over the whole area of the equivalent cylindrical unit within the cell (A_s+A_c), where $A_s$is the horizontal area of a granular pile and A_c is the horizontal area of the clayey ground surrounding the piles. The as value can be calculated for given diameter and spacing of sand piles using different equations for the square and triangular arrangement patterns. For sand piles of 1.0m diameter with 2.0 and 2.5m spacing, the corresponding as values will be 0.197 and 0.126 for the square pattern and 0.227 and 0.145 for the triangular pattern of sand piles spaced at 2.0m and 2.5m respectively. The bearing capacity of ground improved by the SCP method is often evaluated using the Terzaghi's theory. The bearing capacity values of uniform clay (qas) and uniform sand (qas) are first calculated individually then the bearing capacity of SCP improved ground (qa) is calculated by the weighted average of the bearing capacities of all piles using the replacement area ratio, as according to:

$q_a = [a_s * q_{as} + (1-a_s) * q_{ac}$ ----------(2)

The bearing capacities of clay ground (qac) and pile sand soils (qas) are given by:

$qac = (c*Nc/FS)$ ---------- (3)

$qas = (0.5* \beta *\gamma_s*N\gamma/FS)$ ---------- (4)

Where c is the clay soil cohesion, Nc and Nγ are the bearing capacity factors, β is the foundation width, γ_s is the sand soil unit weight and FS is the factor of safety against shear failure. The input data soil required for applying this method were derived and used for the computations of the allowable bearing capacity of the SCP improved soil strata. A summary of the allowable bearing capacities for pile sand materials with various values of internal friction angle is presented in Table 2.

Table 2 Estimated allowable bearing capacity of improved foundation soil (kN/m^2)

Sand soil properties		Triangular pattern at spacing of		Square pattern at spacing of	
φ	Nγ	2.0m	2.5m	2.0m	2.5m
33	35	199	196	193	191
34	41	213	207	205	200
35	48	228	219	219	211
36	57	249	235	235	224

The reduction in the primary consolidation settlement of improved ground may be calculated by multiplying the final consolidation settlement of the original ground before improvement by a reduction facto, β related to the stress ratio (n) the area

replacement ratio (as) as follows:

$\beta = (1+ (n-a_s))-1$ ---------- (5)

ISBN: 978-93-86171-70-2

A stress ratio n value of 5 was assumed for computing the settlement reduction factor β for soils treated with sand piles of 1.0m diameter and different spacing and arrangement patterns in the considered case study using the above equation and a summary the values obtained is given in Table 3.

Table 3 Values of settlement reduction factor (β)

Pile grid pattern	Triangular		Square	
Sand pile pacing (m)	2	2.5	2	2.5
Area replacement ratio (a_s)	0.227	0.145	0.197	0.126
Settlement reduction factor (β)	0.524	0.632	0.560	0.665

Based on evaluation of the results given in Tables 2 and 3 for the treated clay soils it is obvious that the most appropriate design is to use 1.0m diameter sand

piles distributed in a triangular pattern at spacing of 2.0m and the sand piles should be compacted to achieve a minimum internal friction angle of 34˚.

III. COMPARISON AND GENERAL EVALUATION OF SOIL IMPROVEMENT METHODS

3.1.Effectiveness of soil improvement methods

Based on the findings of this study an assessment of the success and effectiveness of the ground improvement techniques to attain an acceptable embankment design was made for the case study under consideration. The discussion is focused on the main ground improvement design issues which include settlement reduction, gain in shear strength, shortening of construction time and cost effectiveness.

3.2.Reduction of consolidation settlement

As stated in section 2, excessively large total settlements are anticipated to take place in the compressible soils due to the placement of the high embankment if they have not been improved. A very long time (42 months) would be required to reach 90% settlement in untreated foundation soils. The magnitudes and rate of estimated settlements computed in this study were considered unacceptable and therefore measures should be taken to expedite this process. In practice, it is generally desirable that the compressible soils underlying bridge abutments reach 90% consolidation within a year. In the staged construction method, the degree of settlement achieved in the clay soil layer before the application of the 3rd stage loading was about 85% which is approaching 90% value normally targeted in the application of soil improvement techniques. Similarly, installation of sand drain prior to embankment construction is expected to result in a 90% degree of the primary consolidation settlement. On the other hand, reinforcing the embankment foundation soils by sand compaction piles is expected to produce only 48% reduction in the anticipated primary consolidation settlement of the untreated soils.

ISBN: 978-93-86171-70-2

3.3.Gain in soil shear strength

The natural upper cohesive soil in the investigated site has low shear strength and an estimated allowable bearing capacity of 150 to 170kPa which is much lower than the pressures expected to be imposed by embankment weight (~220kPa). Construction of a high embankment on such soils necessitates using gentle side slopes and/or berms in the embankment section which involves very large volumes of fill and considerable delays in the construction time schedule which renders the project to be not feasible. The gain in the bearing capacity of the clay soil due to the staged construction method was estimated to be about 20% of the untreated clay soil after the 2nd construction phase. Application of the sand drain design is expected to produce an improvement of about 40% in the bearing capacity of the treated cohesive foundation soil. It is expected that the shear strength and thus the allowable bearing capacity of the clay soil will be increased by 35% as a result of improvement by the sand compaction piles method.

3.4.Time required for construction

As previously stated, a very long time (3.5 years) would be required to reach 90% degree of consolidation if the embankment is constructed in a single stage on the unimproved foundation soils. Using staged construction method, the embankment construction can be accomplished in about 1.25 to 1.50 years including material filling and waiting time after the two main construction phases. In the sand drain method, assuming that 4.5 months would be required for sand drains installation and fill material placement then the approximate duration needed for embankment construction will be between 10.5 and 14.5 months. The time required for soil improvement by the SCP technique is dependent on availability of the appropriate plant and experienced contractor who can execute the works. In case such facilities and requirements are secured, then the construction could be completed within a time much shorter than that required for sand drain method. For comparison, this time was estimated to be about 8 months.

3.5.Rough comparison of improvement method costs

Cost effectiveness is essential for selecting the most suitable embankment foundation soils treatment method. The total cost of the project considered in this study is governed by many factors such as the size of the job, costs of construction materials, machinery and plants and work force. It will be extremely difficult to estimate the overall cost for the application of improvement techniques to be considered in the specific case studied.

In this study, only a rough costing comparison was assumed for each of the improvement methods considered to evaluate their performance. Staged construction does not require importing foreign construction material or using expensive plants (such as drilling rigs and heavy compaction machines) as opposed to the other two methods and therefore it will the most cost effective method.

Generally, the types of materials and equipment used for installation of sand drain and sand piles resemble each other but may considerably differ in the amounts and quality of replacement sand material used and the sizes and technical specifications of plant required. Considering these differences, an assumption was made herein such that the costs of the sand drain and sand compaction methods exceed that of the staged construction method by 25 and 50% respectively.

ISBN: 978-93-86171-70-2

3.6.General evaluation of soil improvement method performance

A simple analysis approach was adopted for the evaluation of the three improvement methods with respect to their effectiveness and expected embankment performance based on the design options proposed for subsurface soil treatment. The following criteria were used for the ranking the expected overall performance of the three improvement techniques:

- The degree of improvement in soil properties of treated soil (namely the reduction in total settlement and gain in the shear strength).
- The time required for construction, and
- Comparisons of embankment construction cost

Each of the above criteria may be evaluated and expressed in terms of ranking indices (R1 to R4) reflecting the discrepancy from the best (most desirable) result scored by a given design method. For example, the best performance for the settlement reduction criterion obtained in the sand drain method (90%) is taken as a datum for computing absolute deviations (in percentage) of the reductions in the other two methods and so forth. An overall ranking index (R), defined as the sum of single indices shall be used to quantitatively evaluate the performance of each method. According to this evaluation criterion, the lower the ranking index the better would be the performance of the method and vice versa. A summary of the overall performance data pertaining to the improvement methods ranking according to the above criteria is given in Table 4.

Table 4 Ranking of the soil improvement methods

Design method and Evaluation criteria		SCM	VSD	SCP
Settlement reductions	%	85	90	48
	R1	6	0	47
Shear strength gains	%	20	40	35
	R2	50	0	13
Construction times	years	1.38	0.88	0.67
	R3	106	31	0
Comparable costs	%	100	125	150
	R4	0	25	50
Overall Ranking	R	162	56	110
	Final rank	3	1	2

Based on the evaluation comparison data given in Table 4, it may be noted that:

i. None of the soil improvement techniques proved to perform consistently with respect to the evaluation criteria set in this analysis. Significant overall performance differences were indicated by various methods. The overall ranking indices (R) values ranged from 56 for the method ranked as the best (sand drains) to 162 for the staged construction rated as of the poorest performance with an intermediate ranking index of 110 for the sand compaction piles method. Thus, the sand drain method is considered to be of the highest overall performance followed by the sand compaction piles whereas staged construction techniques is rated as of the lowest overall performance.

ISBN: 978-93-86171-70-2

ii. If the degree of improvements related to the settlement and shear strength properties of the treated foundation soils is the governing embankment design criteria, then the sand drain method will also come first followed by the staged construction and sand compaction piles methods in the second and third places respectively.

iii. In case the embankment construction time will be the sole decisive factor, as was the actual situation for this project, then the SCP technique would be the preferred soil improvement technique followed by the sand drain and the staged construction as the second and third methods respectively.

iv. On the other hand, if there are constraints on the budget allocated for project finance, then the staged construction method is considered as the most economical soil improvement design for this project. The sand drain or sand compaction pile methods may be adopted if more funds could be secured before commencement of construction works.

IV. CONCLUSIONS

This study investigates the suitability of staged construction, sand drains and sand compaction piles soil improvement methods for the design of a 12m high earth embankment on weak and compressible alluvial clay deposits Based on the subsurface soil conditions at study site, either of the following design options may be used to improve the characteristics of highly compressible embankment foundation soils:

I. To build the embankment in three construction stages with 6 months waiting time after first and second stages, or

II. To install vertical sand drains of 0.2m diameter spaced at 2.8m in triangular grid pattern through the upper soft clay soils and extended down to pervious strata, or

III. To use 1.0m diameter sand compaction piles arranged at 2.0m spacing in a triangular grid pattern.

The study results showed that the above design options produced satisfactory improvements in treated foundation soils with respect to stability and the future performance of embankment. An evaluation of the above techniques was made with respect to their expected performances when applied for embankment construction at the study site. The evaluation was based on the degree of soil improvement achieved by each method; the time required for construction and rough comparisons of estimated improvement costs.

Depending on the most critical and/or decisive design/construction factor the most appropriate soil improvement technique may be adopted as discussed in this paper. For the case study under consideration, the sand drain ground improvement method is considered to be the most appropriate based on the overall performance followed by the sand compaction piles technique whereas the staged construction method was rated in the third place.

REFERENCES

[1.] R. A. Barron, “Consolidation of fine grained soils by drain wells”, TRANSACTIONS, ASCE, Vol. 113, p718 (1948)

ISBN: 978-93-86171-70-2

[2.] "Guidelines on soft soils – Stage construction method," Guideline No. GE: G-5, Geotechnical Engineering Directorate, Research Design and Standards Organisation, Ministry of Railway, Manak Nagar, India (2005)

[3.] M. Kitazume, "The sand compaction pile method"Taylor and Francis Publishers, 246p, (2005)

[4.] G. Sanglerat, G. Olivari and B. Cambou, "Practical problems in soil mechanics and foundation engineering, 1", Elsevier, Amsterdam (1985)

[5.] A.K.M.Zein,"Study of Various Techniques for improving Weak and Comprehenssible clay soil under a High Earth Embankment"(2013)

[6.] S. M. H. Kirmani, "Consolidation of soil for foundation by using sand drains" IEP-SAC Journal, Riyadh, Saudi Arabia (2004-2005)

ResearchGate

See discussions, stats, and author profiles for this publication at: https://www.researchgate.net/publication/319432033

Biomolecules mediated targeting of vascular endothelial growth factor in neuronal dysfunction: An in Silico approach

Article *in* Asian Journal of Pharmaceutical and Clinical Research · September 2017

DOI: 10.22159/ajpcr.2017.v10i9.19466

CITATIONS
0

READS
17

2 authors:

Niraj Kumar Jha
Delhi Technological University
12 PUBLICATIONS **57** CITATIONS
SEE PROFILE

Pravir Kumar
Delhi Technological University
61 PUBLICATIONS **1,064** CITATIONS
SEE PROFILE

Some of the authors of this publication are also working on these related projects:

To dissect the role of post-mitotic cell division and activation of apoptotic pathway in aged neurons and muscles View project

To elucidate the mechanism of HSPs action together with CHIP in attenuation of toxic Aβ peptide View project

All content following this page was uploaded by Pravir Kumar on 25 September 2017.

The user has requested enhancement of the downloaded file.

ASIAN JOURNAL OF PHARMACEUTICAL AND CLINICAL RESEARCH

INNOVARE ACADEMIC SCIENCES
Knowledge to Innovation

Vol 10, Issue 9, 2017

Online - 2455-3891
Print - 0974-2441

Research Article

BIOMOLECULES MEDIATED TARGETING OF VASCULAR ENDOTHELIAL GROWTH FACTOR IN NEURONAL DYSFUNCTION: AN *IN SILICO* APPROACH

NIRAJ KUMAR JHA[1], PRAVIR KUMAR[2]*

[1]Department of Biotechnology, Molecular Neuroscience and Functional Genomics Laboratory, Delhi Technological University (Formerly DCE), New Delhi - 110 042, India. [2]Department of Biotechnology, Delhi Technological University (Formerly Delhi College of Engineering), New Delhi - 110 042, India. Email: pravirkumar@dce.edu

Received: 01 May 2017, Revised and Accepted: 20 May 2017

ABSTRACT

Objective: Neurodegenerative diseases are a debilitating age-related disorder manifested by memory loss, impaired motor activity, and loss of muscle tone due to the accumulation of toxic metabolites in the brain. Despite the knowledge of factors causing neurodegenerative disorders, it remains irreversible and incurable. Growing evidence have currently advocated the physiological and pathological contribution of hypoxia-induced vascular endothelial growth factor (VEGF) in neuronal loss. The objective of this research report highlights biomolecules mediated targeting of VEGF activity based on *in silico* approaches that could establish a potential therapeutic window for the treatment of different abnormalities associated with impaired VEGF.

Methods: We employed various *in silico* methods such as drug-likeness parameters, namely, Lipinski filter analysis, Pock Drug tool for active site prediction, AUTODOCK 4.2.1, and LigPlot1.4.5 for molecular docking studies.

Results: Three-dimensional structure of VEGF was generated and Ramachandran plot obtained for quality assessment. RAMPAGE displayed 99.5% of residues in the most favored regions, 0.5% residues in additionally allowed, and no residues in disallowed regions in VEGF, showing that stereochemical quality of protein structure is good. Further, initial screenings of the molecules were done based on Lipinski's rule of five. Finally, we have found Naringenin to be most effective among three biomolecules in modulating VEGF activity based on minimum inhibition constant, Ki, and highest negative free energy of binding with the maximum interacting surface area during docking studies.

Conclusion: The present study outlines the novel potential of biomolecules in regulating VEGF activity for the treatment of different abnormalities associated with impaired VEGF.

Keywords: Hypoxia, Vascular endothelial growth factor, Biomolecules, Active site prediction, Molecular docking.

© 2017 The Authors. Published by Innovare Academic Sciences Pvt Ltd. This is an open access article under the CC BY license (http://creativecommons.org/licenses/by/4. 0/) DOI: http://dx.doi.org/10.22159/ajpcr.2017.v10i9.19466

INTRODUCTION

Neurodegenerative diseases are pathological conditions that have an insidious onset and chronic progression. Different models have been established to study these diseases to understand their underlying mechanisms and to investigate new therapeutic strategies [1]. Several downstream signaling molecules are reported to trigger under hypoxia. Vascular endothelial growth factor (VEGF) is one of them, which is responsible for the formation of new blood vessels (angiogenesis) and lead to the supply of nutrients and oxygen for normal homeostasis [2]. Moreover, the crucial role of VEGF in the brain is not restricted only to controlling vessel growth: But it has direct effects on different types of neural cells including neural stem cells. Conversely, altered expression of this molecule has been implicated in virtually every type of angiogenic disorder, including those associated with cancer, ischemia, and inflammation [3]. Moreover, studies have also revealed the pathological implication of VEGF in the progression of neurodegenerative disorders (NDDs) including, Alzheimer's disease, Huntington disease, and amyotrophic lateral sclerosis. Recent genetic studies have revealed that reduced VEGF levels cause neurodegeneneration through impairing neural tissue perfusion [4]. Importantly, implementation of different biomolecules may helpful in regulating the altered levels of VEGF in cells. The growing evidence for an etiologic role of VEGF in neurodegeneration provides an underlying principle for considering the therapeutic potential of VEGF for NDDs, which are mostly not curable. In this framework, we have introduced different biomolecules (naringenin, quercetin, and sesamol) for targeting VEGF. These biomolecules have chemoprotective, anti-inflammatory, neuroprotective, and anti-aging property. For this purpose, we have performed *in silico* based structural and functional analysis of these molecules for revealing its therapeutic importance against neuronal loss through modulating the impaired expression of VEGF. The objective of this study is to explore neuroprotective action of these biomolecules in regulating the altered level of VEGF to attenuate the toxicity associated with toxic proteins in neuronal death.

METHODS

Visualization and quality assessment of three-dimensional (3D)-structure of VEGF

3D-structure of VEGF (ID: 1QTY) was generated using protein data bank (PDB), structural evaluation, and stereochemical analysis was performed using RAMPAGE (http://www.mordred.bioc.cam.ac.uk/~rapper/rampage.php). Errat server was used to find the accuracy of the structure and visualization of determined structures was performed using University of California, San Francisco Chimera.

Active site prediction

The active sites of VEGF were predicted using the Pock Drug tool (http://pockdrug.rpbs.univ-paris-diderot.fr/cgi-bin/index.py?page=home). The PDB structure of VEGF was uploaded and active sites were predicted using f-pocket estimation and setting ligand proximity threshold at 5.5.

Ligand optimization

Reported ligand molecules along with their physical and chemical properties were retrieved from PubChem Compound Database (http://

www.pubchem.ncbi.nlm.nih.gov/). PubChem is a composite database that is backed up by three primary databases, i.e., polycarbonate compounds (PC) substance, PC compund, and PC BioAssay. PubChem provides biological activity and chemical information of small molecules. PC substance contains information about the substances; PC compound contains information about chemical compounds, and PC BioAssay provides information about Bioassays. Three compounds (naringenin, quercetin, and sesamol) were selected. SDF files of ligands were converted in PDB file with the help of Open Babel tool that could be used for docking study. Visualization of molecular structure of compounds was done using PyMOL.

Lipinski filter analysis of screened drugs

An online tool Lipinski filter (http://www.scfbio-iitd.res.in/software/drugdesign/lipinski.jsp) was used to retrieve the information about drug-likeness properties of biomolecules with the help of Lipinski rule of five. Lipinski rule helps differentiate drug and non-drug such as properties of molecules. It is used to identify the possibility of success or failure due to drug-likeness for molecules fulfiling with two or more of the following rules: (a) Molecular mass should be <500 Da, (b) high lipophilicity (expressed as log p<5), (c) <5 hydrogen bond donors, (d) <10 hydrogen bond acceptors, and (e) molar refractivity should be between 40 and 130.

Preparation of protein and ligand molecules

Preparation of protein involves the addition of polar hydrogen atoms, neutralization of charge, and removal of any miscellaneous structures from the protein molecule by AUTODOCK 4.2.1 whereas ligand preparation involves the neutralization of charge.

Molecular docking studies

Prepared and optimized structures of ligands and protein were ultimately used for molecular docking using AUTODOCK 4.2.1 for predicting the possible protein-ligand interactions and the results that include the understanding of the association that involves H-bonding, and hydrophobic interactions were analyzed using LIGPLOT1.4.5, a program to generate schematic diagrams of protein-ligand interactions.

RESULTS

3D-structure visualization and quality assessment

3D-structure of VEGF was generated and visualized using UCSF Chimera (Fig. 1a). Even though, there were no steric clashes in the structure generated, it was assessed for geometric and energy aspects. Ramachandran plot was used to check the reliability of predicted 3D-structure of VEGF. RAMPAGE checks the stereochemical quality of a protein structure by analyzing residue-by-residue geometry and overall structural geometry. Ramachandran plot was obtained for VEGF for quality assessment. RAMPAGE displayed 99.5% of residues in the most favored regions, 0.5% residues in additionally allowed, and no residues in disallowed regions in VEGF (Fig. 1b). Errat server was used to determine the accuracy of the model. Result of Errat showed 95.694% accurate structure for VEGF.

Active site prediction

Of top 10 pockets, VEGF had best pocket at P4 with a drug ability score of 0.95 and 0.01 standard deviation (Table 1). The volume of given pocket was 1338.57 cubic angstroms and fourteen residues were involved in interaction at this site.

Lipinski filter analysis of screened drugs

Further, the screening of ligand molecules was done on the basis of Lipinski's rule of five. Lipinski filter analysis revealed that all the compounds selected possessed drug likeness and can be used for docking purposes (Fig. 2).

Molecular docking of VEGF with biomolecules

Biomolecules bound to VEGF at P4 pocket and same residues as predicted were involved in the interaction. The estimated free energy of binding for VEGF and naringenin was - 7.56 kcal/mol and total intermolecular energy was - 9.05 kcal/mol. Similarly, the estimated free energy of binding for VEGF and quercetin was - 7.10 kcal/mol and total intermolecular energy was - 8.89 kcal/mol. Likewise, the estimated free energy of binding for VEGF and sesamol was - 5.09 kcal/mol and total intermolecular energy was - 5.39 kcal/mol. Molecular docking pattern of VEGF with screened molecules (naringenin, quercetin, and sesamol) have been identified and depicted in Fig. 3. On the basis of docking analysis, interacting compounds with minimum binding constant and highest negative free energy of binding are most effective. Docking calculation of VEGF with these molecules has been presented in Table 2.

Binding site of VEGF with selected compounds along with its reported Inhibitory active site

Binding site residues of VEGF interacting with naringenin, quercetin, and sesamol were found to be the same as the residues involved in their respective catalytic sites. Interacting residues of VEGF with naringenin, quercetin, and sesamol along with their identified catalytic sites have

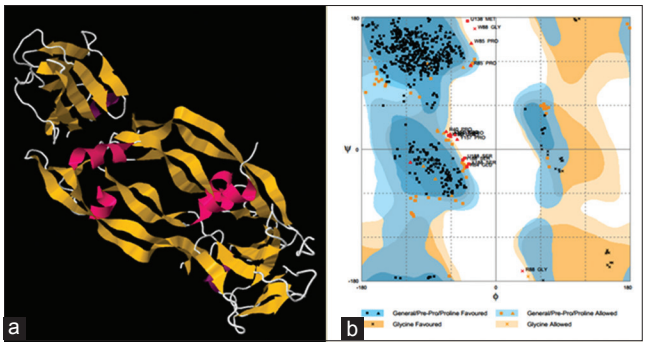

Fig. 1: (a) Three-dimensional-structure and (b) Ramachandran plot of vascular endothelial growth factor protein

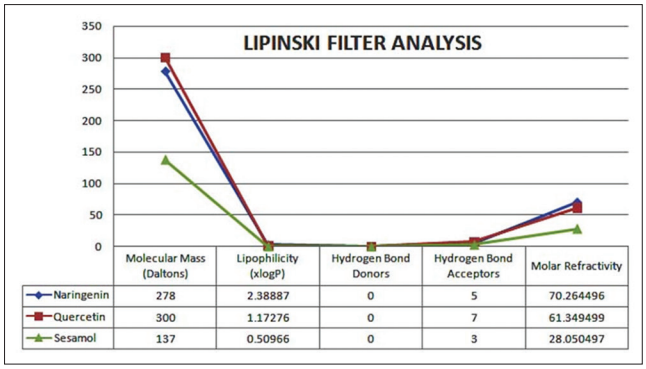

Fig. 2: Differentiation of drugs on the basis of Lipinski rule of five by Lipinski filter

Table 1: Active sites of vascular endothelial growth factor

Pockets	Vol. Hull*	Hydroph. Kyte*	Polar Res.*	Aromatic Res.*	Otyr atom	Nb. Res.*	Drugg Prob*	Standard Deviation
P 0	2205.45	-0.58	0.67	0.2	0.0	30.0	0.63	0.09
P 1	2500.5	-0.67	0.66	0.19	0.0	32.0	0.59	0.08
P 16	452.91	0.83	0.43	0.0	0.0	14.0	0.93	0.02
P 18	744.97	0.56	0.5	0.14	0.0	14.0	0.94	0.01
P 19	455.66	0.83	0.43	0.0	0.0	14.0	0.93	0.02
P 2	1622.2	-0.86	0.68	0.24	0.0	25.0	0.49	0.12
P 3	1819.24	-0.87	0.69	0.21	0.03	29.0	0.53	0.03
P 4	1338.57	0.34	0.62	0.19	0.04	21.0	0.95	0.01
P 5	1159.82	-0.3	0.67	0.24	0.04	21.0	0.83	0.02
P 6	1368.17	-1.2	0.75	0.06	0.0	16.0	0.14	0.02

been show in Table 3 and their two-dimensional and 3D pattern of interaction is presented in Fig. 4.

DISCUSSION

Neurodegeneration is an umbrella term for a range of conditions which primarily affect the neurons in the human brain [5]. Despite the knowledge of various factors which contribute in the occurrence and progression of NDDs, the exact cause and cure remains elusive. Abnormal expression of VEGF protein in terminally differentiated neurons is a recently known phenomenon which has been shown to drive neurodegeneration followed by apoptosis [6]. Free-radical injury of microvessels under hypoxia causes neuroinflammation and oligemia which thereafter leads to Aβ accumulation through vascular damage and the activation of proangiogenic factors including, hypoxia-inducible factor-1α, and VEGF-1 [7]. Further, invading macrophages and monocytes also causes neuronal damage through activation of VEGF-1 [8]. Similarly, low VEGF levels not only impair spinal cord perfusion and cause chronic ischemia of motoneurons but also deprive these cells of vital VEGF-dependent survival and neuroprotective signals.

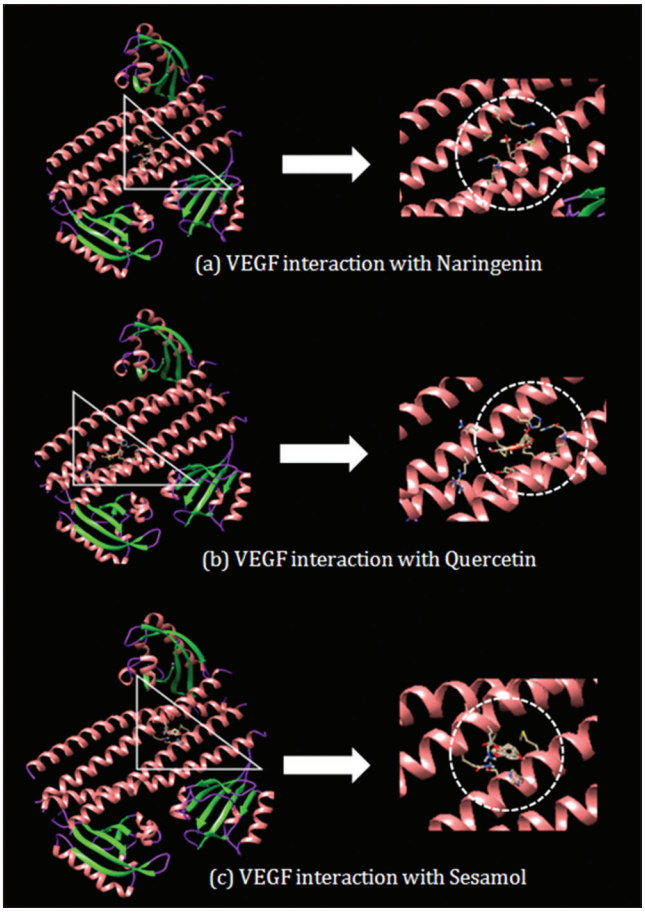

Fig. 3: Binding of vascular endothelial growth factor with selected compounds

Both phenomenons result in progressive degeneration of motoneurons, associated with muscle weakness, paralysis, and death [9]. Thus, it seems imperative to design therapeutic strategies aimed at attenuating the altered level of VEGF to inhibit the cascade of neurodegeneration.

Flavonoids have been advocated to exert human health benefits by antioxidant and anti-inflammatory mechanisms [10]. Naringenin reportedly prevent oxidative stress and nuclear factor kappa B (NF-κB)-mediated inflammatory brain damage in the rat model of focal cerebral injury. Further, prophylactic treatment with naringenin ameliorated functional outcomes and abrogated the ischemic brain injury by suppressing NF-κB-mediated neuroinflammation [11]. Similarly, a significant raise in neuronal survivability was observed with quercetin treatment in rats administered 6-OHDA. Both naringenin and quercetin also reversed the effect of hypobaric hypoxia and elicit neuroprotective response by reducing VEGF level in the murine model [12]. Further, sesamol pre-treatment restored oxidative defense possibly by its free radical scavenging lighted the neuroprotective effect of sesamol against 3-NP-induced neuronal damage [13]. Taken together, all these data provide convincing evidence of using VEGF interaction bioflavonoids such as naringenin and quercetin in attenuating the level of VEGF and in turn, inhibit the cascade of neuronal death.

RAMPAGE displayed 99.5% of residues in the most favored regions, 0.5% residues in additionally allowed and no residues in disallowed regions in VEGF, showing that stereochemical quality of protein structure is good. Result of Errat showed 95.694% accurate structure for VEGF. Lipinski filter analysis of all the compounds revealed that these compounds could act such as a drug and have drug-like property as these compounds meet the criteria of Lipinski Rule of five. Finally, molecular docking studies indicated that all these compounds can bind to and modulate the level of VEGF and possibly, halt or inhibit toxic proteins induced neuronal death in NDDs. Docking study revealed that all three compounds are interacting at the reported active binding site and binding atomic coordination was compared with the template complex coordination and found that docked drug coordination was similar with the known coordination. Amino acid residues of VEGF involved in interaction with naringenin, quercetin, and sesamol were found to be the same as the residues involved in binding with earlier used inhibitors. These observations clearly indicate that we can efficiently determine active site coordinates to investigate the effect of inhibitors on the functional active site of protein. In this result, the most effective compound was found to be naringenin as showing minimum inhibition constant, Ki, and lowest free energy of binding with maximum interacting surface area [14-17]. These findings can be further validated through *in vitro* and *in vivo* studies in neurodegeneration. Overall, although further work is required, these studies advocate the pivotal role of VEGF in NDDs and provide adequate grounds for estimating the potential therapeutic effectiveness of VEGF in their management.

CONCLUSION

The results of our study provide novel potential of biomolecules such as naringenin, quercetin, and sesamol in regulating VEGF expression in the brain, which has wider implications in the progression as well as protection against NDDs. Moreover, of these three biomolecules naringenin is showing better interaction with VEGF based on their minimum binding constant and highest negative free energy.

Table 2: Docking calculation of compounds with VEGF

Compound name	Estimated free energy of binding (kcal/mol)	Estimated binding constant (μM)	Estimated intermolecular energy (kcal/mol)	vdW+Hbond+desolv energy (kcal/mol)	Electrostatic energy (kcal/mol)	Estimated internal energy (kcal/mol)	Torsional free energy (kcal/mol)
Naringenin	−7.56	1.74	−9.05	−9.03	−0.02	+9.69	+1.19
Quercetin	−7.10	6.21	−8.89	−8.73	−0.16	+9.49	+1.79
Sesamol	−5.09	186.16	−5.39	−5.33	−0.06	+0.33	+0.30

VEGF: Vascular endothelial growth factor

Table 3: VEGF known inhibitory site and selected compounds interacting residues

Compounds	Interacting residues
Reported active site	PHE^{375}, VAL^{376}, ASP^{377}, HIS^{378}, ARG^{379}, VAL^{381}, ALA^{382}, GLY^{385}, GLN^{387}, PRO^{388}, GLN^{389}, GLU^{390}, LEU^{392}, LYS^{432} and ASN^{433} of chain A. GLN^{434}, MET^{605}, THR^{606}, GLU^{608}, GLN^{609}, LYS^{610}, LYS^{612}, GLU^{613}, and GLU^{616} of chain B. MET^{598}, HIS^{601}, SER^{602}, MET^{605}, THR^{606}, LEU^{607}, GLU^{608}, GNL^{609}, THR^{611}, LYS^{612}, GLU^{613}, ILE^{614}, ASP^{615} and GLU^{616} of chain C. ARG^{594}, MET^{598}, HIS^{601}, SER^{602}, MET^{605}, THR^{606}, GLN^{609}, LYS^{612} and GLU^{613} of chain F. SER^{241}, LYS^{242}, ASP^{259}, ARG^{260}, THR^{262}, GLU^{263}, LEU^{264}, ILE^{265}, GLY^{266}, HIS^{268}, PRO^{269}, GLU^{270}, ALA^{311}, LYS^{312}, HIS^{313}, GLY^{314}, GLY^{315}, TYR^{316}, VAL^{317}, TRP^{318}, VAL^{343}, and LEU^{344} of Chain G
Naringenin	MET^{605}, THR^{606}, GLU^{608}, and GLN^{609} residues of chain C and MET^{605}, THR^{606}, and GLN^{609} residues of chain F
Quercetin	GLN^{609}, LYS^{612}, GLU^{613}, and GLU^{616} residues of chain C and ARG^{594}, MET^{598}, HIS^{601}, and SER^{602} residues of chain F
Sesamol	MET^{598}, HIS^{601}, and SER^{602} residues of chain C and GLN^{609}, LYS^{612}, and GLU^{613} residues of chain F

VEGF: Vascular endothelial growth factor

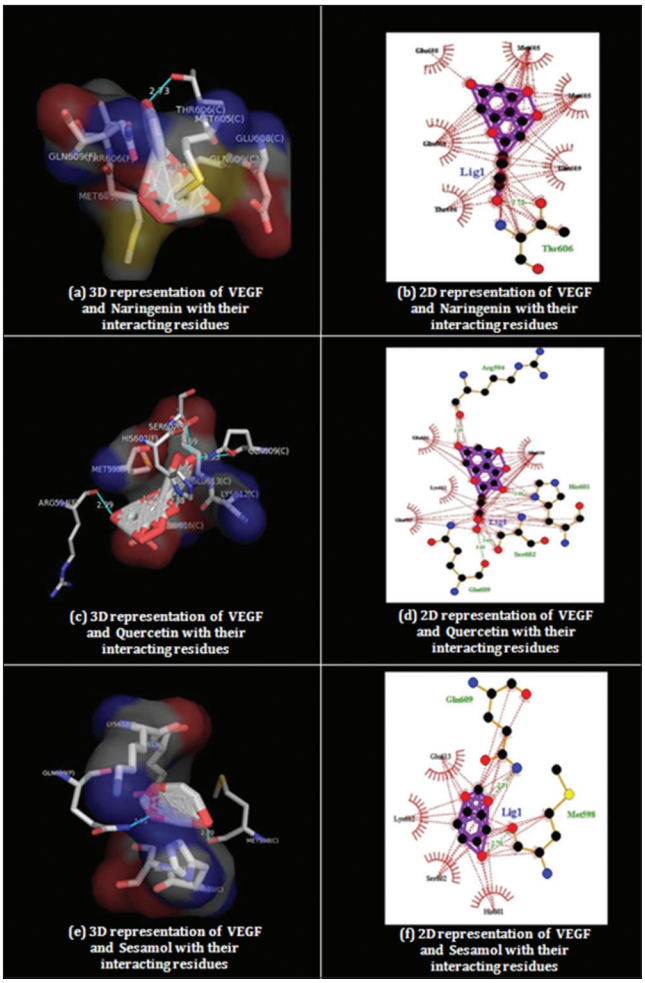

Fig. 4: Three-dimensional- and two-dimensional-representation of vascular endothelial growth factor and ligand interaction

ACKNOWLEDGMENT

The authors would like to thank senior management of Delhi Technological University for their encouragement and support. The authors would also like to thank Technical Education Quality Improvement Program-II for providing Fellowship to NKJ.

REFERENCES

1. Schlachetzki JC, Saliba SW, Oliveira AC. Studying neurodegenerative diseases in culture models. Rev Bras Psiquiatr 2013;35 Suppl 2:S92-100.
2. Hohman TJ, Bell SP, Jefferson AL; Alzheimer's Disease Neuroimaging Initiative. The role of vascular endothelial growth factor in neurodegeneration and cognitive decline: Exploring interactions with biomarkers of Alzheimer disease. JAMA Neurol 2015;72:520-9.
3. Storkebaum E, Carmeliet P. VEGF: A critical player in neurodegeneration. J Clin Invest 2004;113(1):14-8.
4. Lange C, Storkebaum E, de Almodóvar CR, Dewerchin M, Carmeliet P. Vascular endothelial growth factor: A neurovascular target in neurological diseases. Nat Rev Neurol 2016;12(8):439-54.
5. Schneider SA, Dusek P, Hardy J, Westenberger A, Jankovic J, Bhatia KP. Genetics and pathophysiology of neurodegeneration with brain iron accumulation (NBIA). Curr Neuropharmacol 2013;11(1):59-79.
6. Wyss-Coray T, Rogers J. Inflammation in Alzheimer disease-a brief review of the basic science and clinical literature. Cold Spring Harb Perspect Med 2012;2(1):a006346.
7. Vagnucci AH Jr, Li WW. Alzheimer's disease and angiogenesis. Lancet 2003;361(9357):605-8.
8. Dalton HJ, Armaiz-Pena GN, Gonzalez-Villasana V, Lopez-Berestein G, Bar-Eli M, Sood AK. Monocyte subpopulations in angiogenesis. Cancer Res 2014;74(5):1287-93.
9. Pandey KB, Rizvi SI. Plant polyphenols as dietary antioxidants in human health and disease. Oxid Med Cell Longev 2009;2(5):270-8.
10. Raza SS, Khan MM, Ahmad A, Ashafaq M, Islam F, Wagner AP, *et al.* Neuroprotective effect of naringenin is mediated through suppression of NF-?B signaling pathway in experimental stroke. Neuroscience 2013;230:157-71.
11. Haleagrahara N, Siew CJ, Mitra NK, Kumari M. Neuroprotective effect of bioflavonoid quercetin in 6-hydroxydopamine-induced oxidative stress biomarkers in the rat striatum. Neurosci Lett 2011;500(2):139-43.
12. Sarkar A, Angeline MS, Anand K, Ambasta RK, Kumar P. Naringenin and quercetin reverse the effect of hypobaric hypoxia and elicit neuroprotective response in the murine model. Brain Res 2012;1481:59-70.
13. Kumar P, Kalonia H, Kumar A. Protective effect of sesamol against 3-nitropropionic acid-induced cognitive dysfunction and altered glutathione redox balance in rats. Basic Clin Pharmacol Toxicol 2010;107(1):577-82.
14. Maida E, Se BB, Divakar S, Geetha G. Ligand based pharmacophore modeling, virtual screening and molecular docking studies to design novel pancreatic lipase inhibitors. Int J Pharm Pharm Sci 2017;9(4):48-64.
15. Rigoberto VG, Rodolfo AV, Vera LP. Chemical compounds and biological activity of an extract from *Bougainvillea x buttiana* (Var. Rose) holttum and standl. Int J Pharm Pharm Sci 2017;9(3):42-6.
16. Dharani RS, Ranjitha R, Sripathi R, Muhammad KS, Ravi S. Docking studies in target proteins involved in antibacterial action mechanisms: Alkaloids isolated from scutellariagenus. Asian J Pharm Clin Res 2016;9(5):121-5.
17. Manjula J, Maheswari R. Biological and docking studies of novel aroylhydrazones. Int J Pharm Pharm Sci 2017;9(5):81-5.

View publication stats

Pattern Anal Applic
DOI 10.1007/s10044-017-0652-5

THEORETICAL ADVANCES

Blind image deblurring via gradient orientation-based clustered coupled sparse dictionaries

Kuldeep Singh[1] · Dinesh Kumar Vishwakarma[2] · Gurjit Singh Walia[3]

Received: 23 January 2017 / Accepted: 22 September 2017
© Springer-Verlag London Ltd. 2017

Abstract In this paper, we proposed a novel sparse representation-based blind image deblurring algorithm, which exploits the benefits of coupled sparse dictionary, and patch gradient orientation-based sparsifying sub-dictionary learning. We jointly trained coupled dictionaries for blurred and clear image patches to take advantages of the similarity of sparse representation in the blurred and clear image patch pair with respect to their corresponding dictionaries. The first step of the algorithm is to estimate blur kernel from the test image itself which is utilized in generating blur image training set from the clear image training set. Instead of learning a large coupled dictionary, we have proposed to cluster the patches having similar geometric structures and learn smaller sub-dictionaries for each group to improve the effectiveness of sparse modeling of the information in an image. While reconstructing the image, the sparse representation of a blurred image patch is applied to the blur-free dictionary to generate a blur-free image patch. For choosing a sub-dictionary which best describes a particular patch, minimum residue error criterion is formulated. An iterative error compensation mechanism is carried out to enhance the deblurring performance and to compensate for sparse approximation. The performance of proposed deblurring method is evaluated in terms of PSNR, SSIM, ISNR, and visual quality results. The simulation results demonstrate that the proposed method achieves very competitive deblurring performance as compared to other complementary blind deblurring methods.

Keywords Image deblurring · Gradient orientation · Coupled dictionary · Sparse representation

1 Introduction

The need for the image quality improvement is vital because of factors including limited hardware capabilities of image capturing devices, uneven lighting conditions, and noisy environment. Image quality improvement techniques can be advantageous in improving the recognition accuracy of various tasks of computer vision system [1]. The key techniques for quality improvement in an image include denoising [2], contrast enhancement [3], super-resolution [4], deblurring [5], and so forth. Image deblurring among these techniques is one of the most complex problems. Image deblurring is an ill-posed inverse problem caused due to relative motion between the scene and the image acquisition device. The aim of deblurring process is to restore a high-quality image from its degraded version. A typical image deblurring process can be mathematically modeled as

$$Y = \boldsymbol{\psi} \otimes X + \boldsymbol{\eta} \tag{1}$$

where Y is the observed blurred image, X is the latent sharp image to be restored, ψ is the spatial-invariant blur kernel, $\otimes$ is the convolution operator, and η is the additive white noise usually assumed to be following Gaussian distribution.

The image deblurring problem can be classified into two categories: First non-blind image deblurring problem where the blur kernel is known, and second blind image deblurring problem where negligible or no information is available

✉ Kuldeep Singh
kuldeep.er@gmail.com

[1] Central Research Lab, Bharat Electronics Ltd, Ghaziabad, India

[2] Department of Electronics and Communication, Delhi Technological University, Delhi, India

[3] SAG, Defense Research and Development Organization, Ministry of Defense, Delhi, India

Published online: 05 October 2017

about the blur kernel. Blind image deblurring is a complex problem and vast amount of research has been conducted in this field. The focus of this paper is to study one specific approach "sparse representation-based image deblurring." The deblurring problem for handling motion-induced image blur is attempted in this paper. Recent advancements [2, 4, 6–8] in sparse representation-based image processing have made these methods very effective tools for solving the ill-posed image restoration problem.

In this paper, we propose a novel sparse representation-based image deblurring algorithm, which exploits the benefits of coupled sparse dictionary, and learning patch orientation-based sparsifying sub-dictionaries. By jointly training coupled dictionaries for blurred and deblurred image patches, we can utilize the similarity of sparse representation between the blurred and deblurred image patch pair with respect to their corresponding dictionaries. The division of larger dictionary into smaller sub-dictionaries based on gradient orientation angles of the patches improves the performance of sparse coding of the image. The sparsity measure over such a coupled dictionary is used as a regularization constraint to recover a clear image patch from corresponding blurred image patch. This idea is inspired from earlier research on ridge orientation-based dictionaries for fingerprint super-resolution [9] and denoising [10]. The proposed method has following significant contributions:

(a) Novel methodology for division of larger dictionary into sub-dictionaries based on dominant orientation to improve the effectiveness of sparse modeling of image patches.
(b) Proposal of sub-dictionary for flat patches to improve the reconstruction of clear patch where dominant orientation is not present.
(c) Novel methodology for adaptive selection of best suitable sub-dictionary while reconstruction of blurred patch based on minimum residue error criterion.
(d) Proposal of iterative error compensation mechanism to eliminate discrepancy due noise or inaccuracy in sparse representation of image.

The rest of this paper is organized as follows: Sect. 2 discusses the state-of-the art. Section 3 describes the proposed deblurring algorithm. In Sect. 4, experimental results evaluating the performance of proposed deblurring method and comparison with other existing algorithms are presented. Finally, conclusions are drawn in Sect. 5.

2 Related methods

Blind image deblurring has always been an area of interest for computer vision researchers, and tremendous research has been conducted in the past. The popular traditional approaches for blind image deblurring perform simultaneous estimation of kernel and the latent image by exploiting a prior knowledge. Fergus et al. [11] introduced a two-step deblurring approach, which first estimates the blur kernel, and using the estimated kernel, latent image is estimated by applying standard de-convolution algorithm. In this paper, we have focused on solution of ill-posed blind image deblurring problem using sparse representation. The popular sparse representation-based deblurring methods are surveyed, and the analysis is presented next. Shan et al. [12] proposed a unified probabilistic model utilizing sparse priors for estimating blur kernel and latent image simultaneously. Zhang and Zhang [13] proposed "intermediate-language" based incremental, iterative sparse deblurring approach. Cai et al. [14] introduced deblurring as a joint optimization problem, which simultaneously maximizes the sparsity of the blur kernel and the sparsity of the clear image using curvelets system for kernels and framelet system for images. Hu et al. [15] proposed an iterative method which utilizes sparsity constraints to restore the latent image, estimates the kernel, and updates the sparse dictionary directly from a single image. Zhang et al. [16] devised a method that exploits the sparsity prior of natural images to help alleviating the ill-posed inverse blind deblurring problem. Lau et al. [17] devised a direct sparse deblurring algorithm that explicitly takes into account the "sparse" natural statistics of the image as a regularizer and performs deblurring without solving an ill-conditioned problem. Sometimes this approach is also referred to as "analysis by synthesis." Liu et al. [18] introduced a sparse representation regularization framework, which reformulate the variational problem as a linear equality constrained problem and then minimized its augmented Lagrangian function.

The structural mapping which exists between clear and blurred image has not been extracted properly in the past in the process of image deblurring. In this paper, the structural mapping is exploited by jointly training coupled dictionary for blurred and clear image, where the atoms in blurred dictionary will have one-to-one mapping with corresponding clear dictionary. By jointly training coupled dictionaries, we can enforce the similarity of sparse representations between the blurred and deblurred image pair with respect to their own dictionaries and accomplish the task of extracting structural mapping between blurred and clear image.

3 Proposed method

The proposed deblurring method undergoes three main steps: Kernel estimation, clustered coupled dictionary learning, and sparse deblurring. Each step is explained in detail in the following sections.

3.1 Kernel estimation

The problem of blind deblurring involves estimation of both latent sharp image X and blur kernel ψ from given noisy version Y. The blind deblurring problem can be formulated as:

$$\left\{\hat{X}, \hat{\psi}\right\} = \arg\min_{X,\psi} \|\psi \otimes X - Y\|_2^2 + \phi(X) + \theta(\psi) \tag{2}$$

where $\phi(X)$ and $\theta(\psi)$ are regularization term on expected sharp image and possible blur kernel, respectively. The optimization problem in (2) can be solved using iterative alternating optimization where kernel and image estimation task is taken up alternatively. In the model (2) keeping the latent image estimate fix and optimizing the blur kernel estimate reduces the minimization problem to following form

$$\hat{\psi} = \min_{\psi} \|\psi \otimes \hat{X} - Y\|_2^2 + \gamma\|\psi\|_2^2 \tag{3}$$

Here $\hat{X}$ is the latent image estimate and Y is the blurred image. We initialize $\hat{X} = Y$ and ψ as Gaussian kernel. This is a least square problem with Tikhonov regularization [19], which leads to a closed form solution for ψ.

$$\hat{\psi} = F^{-1}\left(\frac{F\left(\hat{X}\right)^{*}.F(Y)}{F\left(\hat{X}\right)^{*}.F\left(\hat{X}\right) + \gamma I}\right) \tag{4}$$

where $F()$ and $F()^{-1}$ represent Fourier transform and inverse Fourier transform, respectively. "*" denotes complex conjugacy and "." denotes component-wise multiplication. I represents the identity matrix of the same size as that of the image. γ is a weight for the Tikhonov regularization and taken as $\gamma = 5$ as per [20]. The kernel estimate $\hat{\psi}$ is in optical transfer function form, and it is thus converted into a point spread function. Given the kernel estimate $\hat{\psi}$ the estimate of latent image can be updated by solving below optimization problem.

$$\hat{X} = \min_{X} \|\hat{\psi} \otimes X - Y\|_2^2 + \rho\|\nabla X\|_2^2 \tag{5}$$

The regularization term $\|\nabla X\|_2^2$ ensures that the estimated latent image has smooth gradients. ρ is small constant, and we have taken $\rho = 0.05$. The optimization problem in (5) can be solved efficiently with fast Fourier transform (FFT) as [20] by using (6)

$$\hat{X}_{\text{new}} = F^{-1}\left(\frac{F(\hat{\psi})^{*}.F(Y) + \rho F\left(\hat{X}_{old}\right)}{F(\hat{\psi})^{*}.F(\hat{\psi}) + \rho I}\right) \tag{6}$$

$\hat{X}_{\text{new}}$ refers to the new estimate of $\hat{X}$ for next iteration while $\hat{X}_{\text{old}}$ refers to the previous estimate of $\hat{X}$ which is utilized to obtain the new estimate of $\hat{X}$. $F(\hat{\psi})$ refers to the kernel estimate in optical transfer function form. The above-mentioned procedure is repeated iteratively to estimate the kernel $\psi = \hat{\psi}$. The difference between successive kernel estimates is monitored, and if the difference is not significant then the iterative process can be stopped.

3.2 Clustered coupled dictionary learning

In the coupled dictionary learning step, a pair of dictionaries one for blurred and the other for deblurred patches is jointly learned. By jointly training two dictionaries for blurred and deblurred image patches, we can exploit the similarity of sparse representation between the blurred and deblurred image patch pair with respect to their corresponding dictionaries. Hence, sparse coefficients of blurred image patch can be directly applied with the deblurred image patch dictionary to create a deblurred image patch. This implies that the sparse coefficients that encode the clear image with the atoms from the clear dictionary are the same as the sparse coefficients that encode the blurred image with atoms from the blurred dictionary. To start with the dictionary learning process, a set of natural latent (clean) images $\{X_j\}$ is assembled. The corresponding blurred image set $\{Y_j\}$ is constructed by blurring $\{X_j\}$ with the estimated kernel formed in the above step. The dictionary learning process starts with extraction of uniform patches of size $\sqrt{p} \times \sqrt{p}$ with an overlapping of two pixels between adjacent patches to avoid artifacts at near patch boundaries. Once the patches are extracted from both the training sets, the next step involves clustering of these patches based on gradient orientation. The method of clustering is explained in the below section.

3.2.1 Gradient orientation-based patch clustering

The self-similarity among image patches can be utilized to divide larger sparse dictionary into smaller sub-dictionaries for improving the effectiveness of sparse modeling of information in an image, thus improving the results of sparse representation-based super-resolution [9] and denoising [10]. The self-similarity among patches is rendered through similar gradient orientation angle. The extracted patches from training images consist of both smooth and rough patches, and the categorization is done based on a variance threshold. The classification of rough patches into dominant and non-dominant orientation patches is based on the dominant measure computed by performing singular value decomposition (SVD) on gradient vector of each patch [21]. The summary of classification of the image patches is depicted in Fig. 1.

The mathematical procedure for patch classification is explained below:

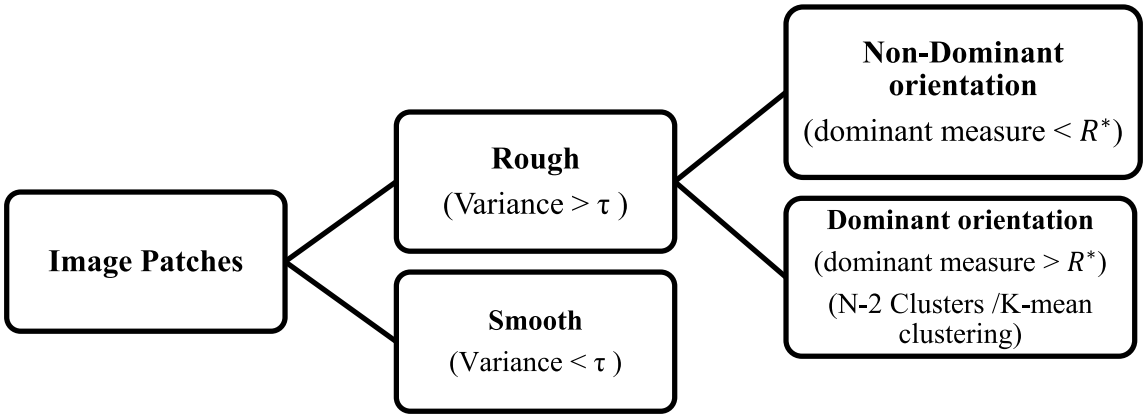

Fig. 1 Classification of image patches

Step 1 Extract patches of size $\sqrt{p} \times \sqrt{p}$ with an overlapping of two pixels between adjacent patches from both the training sets $\{Y_j\}$ and $\{X_j\}$

Step 2 Compute the local estimate of gradient at every *i*th pixelcorr

$$\nabla y(x,y)_i = \left\{ \frac{\partial I(x,y)}{\partial x}, \frac{\partial I(x,y)}{\partial y} \right\} \tag{7}$$

where x and y are spatial coordinates in the image patch.

Step 3 Estimate the gradient map $G \in R^{p\times 2}$ of the patch

$$G = \left\{ \nabla y(x,y)_1, \nabla y(x,y)_2, \ldots, \nabla y(x,y)_p \right\}^{\mathrm{T}} \tag{8}$$

Step 4 Calculate the singular value decomposition (SVD) of the gradient map

$$G = USV^{\mathrm{T}} \tag{9}$$

Here $U \in R^{p\times p}$ represents each vector's contribution to the corresponding singular vector; $S \in R^{p\times 2}$ represents the energy in the dominant directions; and $V \in R^{2\times 2}$ represents an orientation, in which the columns v_1 and v_2 represent the dominant and subdominant orientation of the gradient field, respectively.

Step 5 Compute the dominant measure R

$$R = \frac{S_1 - S_2}{S_1 + S_2}; \quad \begin{pmatrix} \text{Non-Dominant if } R \le R^* \\ \text{Dominant if } R > R^* \end{pmatrix} \tag{10}$$

Here S_1 and S_2 are singular values representing the energy value in the dominant direction. A thresholding operation based on significance level threshold R^* is applied to classify the patches further into dominant and non-dominant orientation patches. The dominant measure of a patch lower than the significance level threshold, R^*, signifies that the singular values are remarkably different and there is a strong possibility that the patch contains pure white noise [21].

Step 6 The gradient orientation of a given patch can be computed as

$$O(x,y) = \frac{1}{2} \arctan\left(\frac{G_{rs}}{G_{rr}}\right) \tag{11}$$

Here G_{rr} and G_{rs} are block horizontal and vertical gradients, respectively, and are defined as:

$$G_{rs} = \sum_{u=i-\left(\frac{w}{2}\right)}^{i+\left(\frac{w}{2}\right)} \sum_{v=j-\left(\frac{w}{2}\right)}^{j+\left(\frac{w}{2}\right)} 2G_r(x,y)G_s(x,y) \tag{12}$$

$$G_{rr} = \sum_{u=i-\left(\frac{w}{2}\right)}^{i+\left(\frac{w}{2}\right)} \sum_{v=j-\left(\frac{w}{2}\right)}^{j+\left(\frac{w}{2}\right)} \left(G_r^2(x,y) - G_s^2(x,y)\right) \tag{13}$$

Here G_r and G_s are horizontal gradient value and vertical gradient value, respectively.

Step 7 Clustering of the dominant orientation patches based on gradient angles is done using K-means clustering algorithm, which is a popular unsupervised classification technique

The above-mentioned patch classification process results in N clusters (classes Ω_n): one for smooth, one for non-dominant orientation patches, and $N-2$ clusters for the image patches having different orientation angles.

3.2.2 *Coupled dictionary learning*

The dictionary learning approach for faster processing involves learning of patch-sized atoms instead of image-sized atoms. The dictionary "φ" is a collection of atoms, build by jointly optimizing the sparse dictionary and the coefficients. The coupled dictionary signifies that we learn a set of dictionary each for blurred and clear image training set simultaneously by concatenating them with proper normalization. The

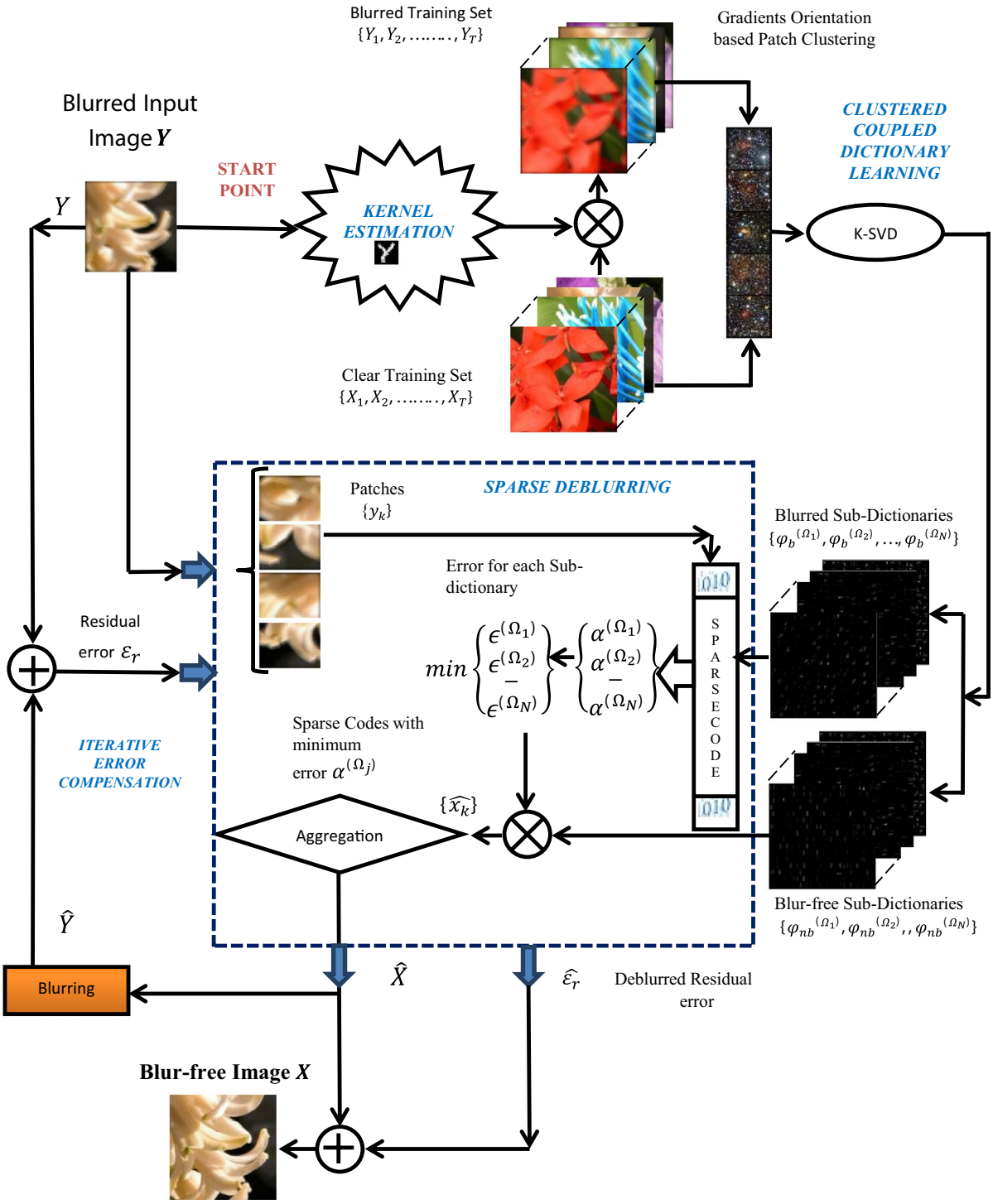

Fig. 2 Depiction of workflow diagram of proposed algorithm

optimization problem for training sub-dictionaries for each cluster of patches involves solving the below equation

$$\left\{\hat{\alpha}_{\Omega_n}, \varphi^{(\Omega_n)}\right\} = \underset{\alpha,\varphi}{\operatorname{argmin}} \sum_{k\in\Omega_n} \left(\|\varphi^{(\Omega_n)}\alpha_{\Omega_n} - I\|_2^2 + \beta\|\alpha_{\Omega_n}\|_0\right) \tag{14}$$

Here $n = 1, 2, 3, \ldots N$ is the index for sub-dictionaries trained and for couple dictionary, $\varphi = \left\{\varphi_{\mathrm{b}}\varphi_{\mathrm{nb}}\right\}^{\mathrm{T}}$ φ_{b} and φ_{nb} are blurred and clear image dictionaries, respectively, and $I = \left\{\left\{y_i\right\}, \left\{x_i\right\}\right\}^{\mathrm{T}}$ is a matrix containing image patches sampled from blurred and clear image training sets, respectively. In the proposed method for constructing sub-dictionaries,

K-SVD [2, 7] method of dictionary learning is chosen due to its noise rejection capability and simplicity. The dictionary learning step yields N coupled sub-dictionaries, i.e., $\left\{\varphi^{(\Omega_1)}, \varphi^{(\Omega_2)}, \ldots, \varphi^{(\Omega_N)}\right\}$. The smooth and non-dominant clusters have less number of patches; hence, lesser number of atoms are learned for the sub-dictionaries corresponding to these clusters.

3.3 Sparse deblurring

The sparse deblurring step involves two fundamental steps: sparse coefficient calculation and error compensation.

3.3.1 Sparse coefficient calculation

In this step, sparse coding of individual blurred patches is performed in terms of each blurred sub-dictionary. The sparse coefficient matrix $\left\{\varphi_{\mathrm{b}}^{(\Omega_1)}, \varphi_{\mathrm{b}}^{(\Omega_2)}, \ldots, \varphi_{\mathrm{b}}^{(\Omega_N)}\right\}$ is formed for each blurred patch corresponding to the set of sub-dictionaries. For this task, the sparse coding problem can be formulated as

$$\hat{\alpha}^{(\Omega_n)} = \underset{\alpha}{\operatorname{argmin}} \|y_k - \varphi_{\mathrm{b}}^{(\Omega_n)}\alpha\|_2^2 + \beta\|\alpha\|_1 \tag{15}$$

Orthogonal matching pursuit (OMP) algorithm provides efficient solution to this optimization problem. For the recovery of the deblurred patch, a residue error $\varepsilon^{(\Omega_n)}$ corresponding to each sub-dictionary for a particular blurred patch is estimated.

$$\left\{\varepsilon^{(\Omega_n)}\right\} = \|y_k - \varphi_{\mathrm{b}}^{(\Omega_n)}\hat{\alpha}^{(\Omega_n)}\|_2 \tag{16}$$

The deblurred image patch is recovered using sparse coefficients corresponding to the sub-dictionary which have the least residue error. The deblurred patch can be restored as

$$\hat{x}_k = \varphi_{\mathrm{nb}}^{(\Omega_n)}\hat{\alpha}^{(\Omega_n)} \tag{17}$$

The final deblurred image is computed by aggregation of all the estimated deblurred patches$\{x_k\}$.

3.3.2 Iterative error compensation

An iterative error compensation mechanism is enforced to compensate the error due to sparse approximation in the deblurring process. Suppose Y is original blurred image and $\hat{X}$ is restored deblurred image, now the blurred version of $\hat{X}$ is calculated using the estimated kernel ψ, i.e., $\hat{Y} = \psi \otimes \hat{X}$. The residual error can be defined as $\varepsilon_r = Y - \hat{Y} = Y - \psi \otimes \hat{X}$. This blurred residual error is subjected to proposed deblurring algorithm to estimate the deblurred counterpart $\hat{\varepsilon}_r$, i.e., $\varepsilon_r = \psi \otimes \hat{\varepsilon}_r$. The final estimate of latent image is calculated as $X = \hat{X} + \hat{\varepsilon}_r$. Based on the above step-wise description, the procedure of proposed blind image deblurring approach can be summarized as Algorithm 1.

Algorithm 1: Blind image deblurring using gradient orientation-based clustered coupled dictionaries

Input: Blurred image Y, training set of clear images $\{X_1, X_2, \ldots, X_T\}$

Output: The blur-free image X.

Step 1: Estimate kernel $\boldsymbol{\psi}$ by iterating through Eq. (4) and (6) using Tikhonov regularization.

Step 2: Generate blurred training set $\{Y_1, Y_2, \ldots, Y_T\}$ by convolving the estimated kernel $\boldsymbol{\psi}$ with clear training set images.

Step 3: Extract patches of size $\sqrt{p} \times \sqrt{p}$ from both training set images and perform gradient orientation-based clustering of patches using Eqs. (7–13).

Step 4: Train N coupled sub-dictionaries $\left\{\varphi^{(\Omega_1)}, \varphi^{(\Omega_2)}, \ldots, \varphi^{(\Omega_N)}\right\}$ using Eq. (14).

Step 5: Extract patches $\{y_k\}$ from input blurred image Y. Perform sparse coding and calculate error $\varepsilon^{(\Omega_n)}$ corresponding to each blurred sub-dictionary as per Eq. (16) for each patch.

Step 6: Choose sparse coefficient corresponding to sub-dictionary having least error and recover blur-free patches $\{\hat{x}_k\}$ using Eq. (17).

Step 7: Perform aggregation of blur-free patches $\{\hat{x}_k\}$ to obtain $\hat{X}$.

Step 8: Blur $\hat{X}$ to obtain $\hat{Y}$ and calculate residual error $\varepsilon_r = Y - \hat{Y} = Y - \boldsymbol{\psi} \otimes \hat{X}$.

Step 9: Apply same deblurring algorithm step (5–7) on ε_r and obtain clear residual error $\hat{\varepsilon}_r$.

Step 10: Obtain final blur-free image $X = \hat{X} + \hat{\varepsilon}_r$.

The theoretical discussion of all the three steps, i.e., Kernel estimation, clustered coupled dictionary learning, and sparse deblurring of proposed algorithm, is discussed above. For better understanding of the various steps involved in the proposed method, a graphical overview is presented in Fig. 2.

4 Simulation results

An evaluation methodology consisting of two experiments is devised to demonstrate the performance comparison. The first experiment involves performance evaluation of the proposed deblurring algorithm in comparison with Fergus et al. [11], Shan et al. [12], and Hu et al. [15] methods in terms of image quality measures. The second experiment involves performance evaluation based on visual quality of the image. For experimentation, we have chosen two types of images, i.e., natural images and flower images; however, the algorithm is not limited to any specific type of images. The proposed algorithm can be applied to any type of images for that the training set for dictionary learning should be chosen from similar kind of images. Two separate pair of coupled sub-dictionaries each for natural and flower images are constructed. In the

dictionary learning process of flower images, we have used approximately 150 natural flower images and approximately 35,000 image patches of size 5×5 pixels were taken with an overlapping of two pixels between adjacent patches to maintain the continuity. Similarly, for natural images we have used 100 images and approximately 25,000 patches are extracted. The validation of proposed algorithm is conducted on seven flower images and two natural images. For experimentation, the values of the thresholds τ and R^* are set to be 50 and 0.175 empirically. The variance and dominant measure thresholds can be empirically adjusted as per requirement of different data sets. The total number of sub-dictionaries learned here are seven, i.e., $N = 7$ including one each for smooth and non-dominant group and five for dominant orientation group. However, the number of sub-dictionaries can be made adaptive to the number of patches clustered in each group. Practically it has been observed that considering higher numbers of clusters results into very few patches in some sub-groups does not lead to significant improvement in deblurring results.

4.1 Comparison of quality measures

The performance of proposed deblurring method is evaluated in terms of popular image quality measures, i.e., peak signal-to-noise ratio (PSNR), improvement in signal-to-noise ratio (ISNR) and Structural Similarity Index (SSIM). Although there are other image quality assessment methods, the quality measurement index based on PSNR and ISNR is widely adopted in image quality assessment. In order to measure the visual quality of the recovered image more appropriately, SSIM measure is used. The PSNR, ISNR, and SSIM are defined as:

$$\mathrm{PSNR} = 10 \times \log \frac{255^2}{\mathrm{MSE}}; \quad \mathrm{MSE} = \frac{1}{MN} \sum_{x=0}^{M-1} \sum_{y=0}^{N-1} \left[A(x,y) - B(x,y)\right]^2 \tag{18}$$

$$\mathrm{ISNR} = 10 \times \log \frac{\sum_{x,y} (C(x,y) - A(x,y))^2}{\sum_{x,y} (B(x,y) - A(x,y))^2} \tag{19}$$

$$\mathrm{SSIM}(a,b) = \frac{\left(2\mu_a\mu_b + c_1\right)\left(2\sigma_{ab} + c_2\right)}{\left(\mu_a^2 + \mu_b^2 + c_1\right)\left(\sigma_a^2 + \sigma_b^2 + c_2\right)} \tag{20}$$

Here, (x, y) is the index of a pixel in the image. A, B, and C are latent image, output image of deblurring algorithm, and blurred image, respectively. μ_a and μ_b are the mean values of input and output images, $_{\rho a}$ and ρ_b are the standard deviations, σ_{ab} is the covariance, $c_1 = \left(K_1 L\right)^2$ and $c_2 = \left(K_2 L\right)^2$,with L being the maximum pixel value, $K_1 = 0.01$ and $K_2 = 0.03$ [22].

Table 1 The PSNR comparison

Image/method	Fergus et al.	Hu et al.	Shan et al.	Proposed method
Flower1	20.9724	18.1310	18.2157	**21.1765**
Flower2	19.5118	18.1292	21.6273	**22.1072**
Flower3	18.3796	15.7814	16.3001	**19.8587**
Flower4	24.9328	21.2387	23.7943	**26.3513**
Flower5	17.1729	13.7493	20.6785	**20.8929**
Flower6	23.4379	19.6449	22.1069	**23.8983**
Flower7	26.0961	19.282	18.3428	**26.9773**
Lena	19.077	22.734	**26.131**	26.0425
Barbara	19.6910	19.2430	23.6239	**23.8602**

Table 2 The ISNR comparison

Image/method	Fergus et al.	Hu et al.	Shan et al.	Proposed method
Flower1	0.1962	0.1551	−0.2992	**0.2309**
Flower2	0.1448	−0.4100	0.0480	**0.1649**
Flower3	−1.1897	−2.2940	1.1794	**1.9352**
Flower4	−1.6012	−0.2751	−0.1279	**−0.0912**
Flower5	−1.7803	−1.6269	**1.2512**	1.1667
Flower6	−0.5760	−0.6821	**0.1910**	0.1729
Flower7	−13,569	−1.3279	0.7380	**0.8901**
Lena	−1.4934	0.4421	**0.6949**	0.6725
Barbara	−0.6377	−0.1572	0.1964	**0.6382**

The PSNR performance comparison results are depicted in Table 1. Best results are highlighted in bold. The PSNR results reveal that the proposed method outperforms other methods and obtains the highest PSNR values for all the test images except "*Lena*" image. Higher PSNR value signifies that the quality of reconstruction using proposed deblurring method is better than the other methods.

ISNR measure quantifies the amount of improvement in the reconstruction process. Higher values of ISNR signify that the deblurring process has improved the PSNR; hence, the quality of the image is enhanced. Table 2 summarizes the comparison result based on ISNR measure, best values are depicted in bold.

From the SSIM performance comparison results shown in Table 3, it is evident that the proposed deblurring methods have the best SSIM results highlighted in bold for almost all the test images. Better results in terms of SSIM index show that more details and edges are retained by the proposed method during deblurring process which is very crucial in measuring image quality. The visual results shown in Figs. 3, 4, and 5 also support the SSIM performance.

Table 3 The SSIM comparison

Image/method	Fergus et al.	Hu et al.	Shan et al.	Proposed method
Flower1	0.5433	0.4013	0.4389	**0.5577**
Flower2	0.6405	0.5792	0.7039	**0.7164**
Flower3	0.4560	0.3150	0.5122	**0.5492**
Flower4	0.7011	0.5645	0.7371	**0.7490**
Flower5	0.7763	0.7700	0.5109	**0.7922**
Flower6	0.3462	0.2226	0.4884	**0.5574**
Flower7	0.7214	0.7126	0.7610	**0.7705**
Lena	0.5365	0.7991	**0.8172**	0.8061
Barbara	0.4841	0.5886	0.6269	**0.6547**

4.2 Visual quality comparison

To validate the deblurring performance of any algorithm, the visual quality inspection is very much crucial. The visual quality comparison of proposed algorithm with other deblurring algorithms, i.e., Fergus et al. [11], Hu et al. [15], and Shan et al. [12], on flower images is illustrated in Fig. 3. The visual quality results of "Lena" and "Barbara" images are presented in Figs. 4 and 5, respectively.

From visual results in Fig. 3, it is clearly noticeable that Hu et al. results have noise residuals and artifacts, and Fergus et al. method has failed in removing blur from the images. The results of Shan et al. method are satisfactory and are effective in reconstructing smooth image areas; however, it fails to recover fine image edges. The visual quality results of "Lena" and "Barbara" in Figs. 4 and 5,

Fig. 3 Visual quality comparison **(a)** blurred, **b** Fergus et al., **c** Hu et al., **d** Shan et al., and **e** proposed method

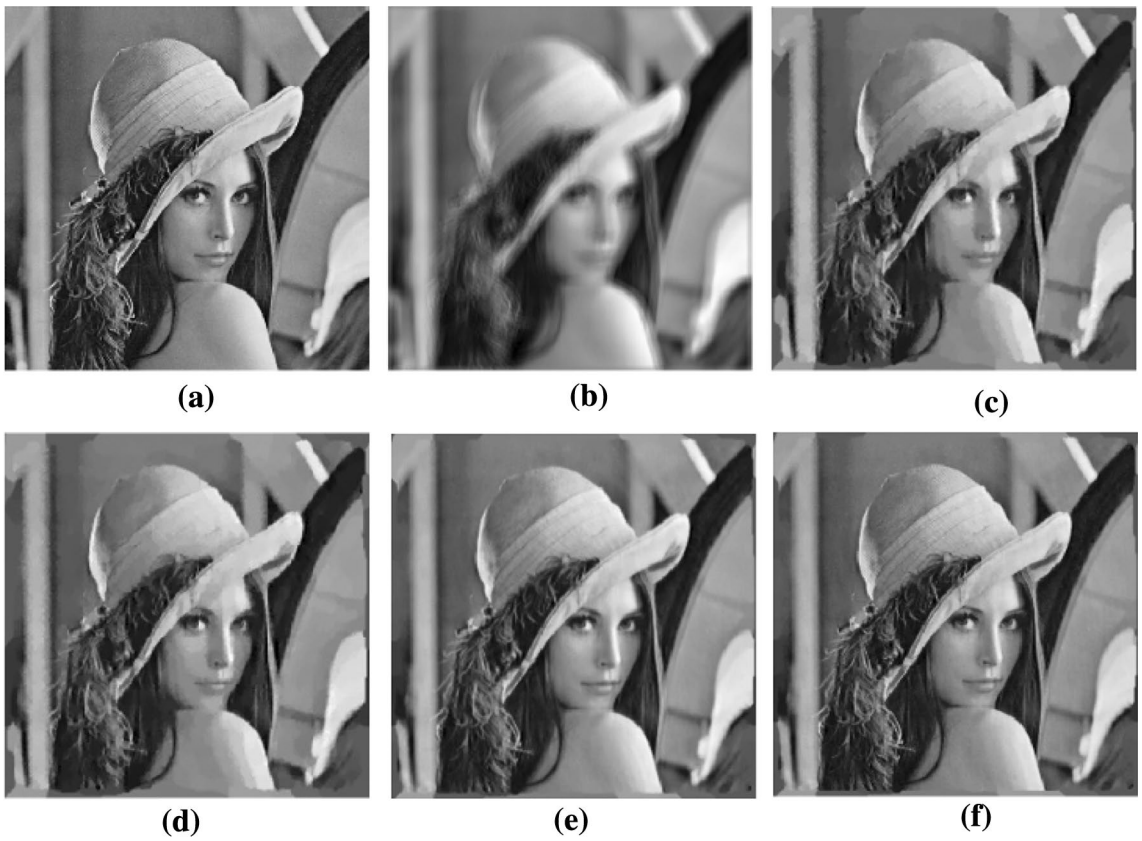

Fig. 4 Visual quality comparison **a** latent, **b** blurred, **c** Fergus et al., **d** Hu et al., **e** Shan et al., and **f** proposed

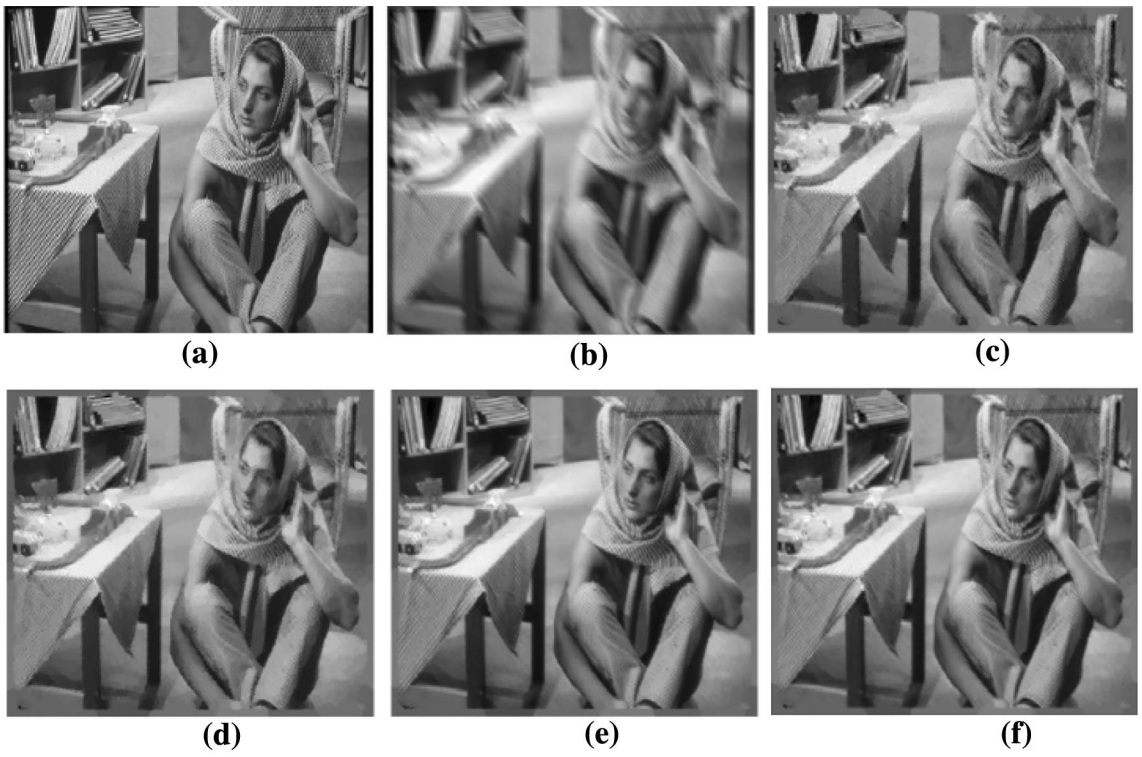

Fig. 5 Visual quality comparison **a** latent, **b** blurred, **c** Fergus et al., **d** Hu et al., **e** Shan et al., and **f** proposed

respectively, depict that our method recovers sharp images effectively in both smooth and textured areas and avoid ringing artifacts. The analysis of visual results reveals that the proposed method not only removes the blurring effects and noise, but also leads to better visual quality.

The specific reasons behind the better performance of proposed deblurring method are summarized below:

- Utilization of structural mapping which lies between blurred and clear image in the process of coupled dictionary learning.
- Learning separate sub-dictionaries for smooth and textured patches in the image has driven excellent deblurring results for both smooth and areas having dominant orientation.
- The sparse coding solution do not demand exact equality between the blurred patch and corresponding clear patch reconstructed using Eq. (15). Due to this sparse approximation, the reconstructed clear image may not satisfy the constraint in Eq. (1). To eliminate the discrepancy due to sparse approximation, an iterative error compensation mechanism is enforced in the proposed method.

5 Conclusion

In this paper, we have proposed a novel sparse representation-based blind image deblurring algorithm. The basic idea behind the proposed approach is to learn smaller sub-dictionaries from the patches clustered based on dominant orientation instead of learning a single large dictionary. The reason behind better deblurring performance of the proposed method is the effectiveness of sub-dictionaries, since every subgroup consists of geometrically similar patches thus helping in better sparse modeling of information. The novelty of paper lies in exploiting the similarity of sparse representation between the blurred and deblurred image patch pair by jointly training two dictionaries for blurred and deblurred image patches. Experimental results show that the proposed method outperforms other deblurring algorithms.

References

1. Vishwakarma DK, Singh K (2016) Human activity recognition based on spatial distribution of gradients at sub-levels of average energy silhouette images. IEEE Trans Cogn Dev Syst PP(99):1
2. Elad M, Aharon M (2006) Image denoising via sparse and redundant representations over learned dictionaries. IEEE Trans Image Process 15(12):3736–3745
3. Singh K, Vishwakarma DK, Walia GS, Kapoor R (2016) Contrast enhancement via texture region based histogram equalization. J Mod Opt 63(15):1444–1450
4. Yang J, Wright J, Huang T, Ma Y (2010) Image super-resolution via sparse representation. IEEE Trans Image Process 19(11):2861–2873
5. Ben-Ezra M, Nayar S (2004) Motion-based motion deblurring. IEEE Trans Pattern Anal Mach Intell 26(6):689–698
6. Donoho D (2006) Compressed sensing. IEEE Trans Inf Theory 52(4):1289–1306
7. Aharon M, Elad M, Bruckstein A (2006) K-SVD: an algorithm for designing overcomplete dictionaries for sparse representation. IEEE Trans Signal Process 54(11):4311–4322
8. Dong W, Zhang L, Shi G, Wu X (2011) Image deblurring and super-resolution by adaptive sparse domain selection and adaptive regularization. IEEE Trans Image Process 20(7):1838–1857
9. Singh K, Gupta A, Kapoor R (2015) Fingerprint image super-resolution via ridge orientation-based clustered coupled sparse dictionaries. J Electron Imaging 24(4):043015-1–043015-10
10. Singh K, Kapoor R, Nayar R (2015) Fingerprint denoising using ridge orientation based clustered dictionaries. Neurocomputing 167:418–423
11. Fergus R, Singh B, Hertzmann A, Roweis S, Freeman W (2006) Removing camera shake from a single photograph. In: SIGGRAPH
12. Shan Q, Jia J, Agarwala A (2008) High-quality motion deblurring from a single image. ACM Trans Graph 27(3):1–10
13. Zhang H, Zhang Y (2009) Sparse representation based iterative incremental image deblurring. In: IEEE international conference on image processing
14. Cai J, Ji H, Liu C, Shen Z (2009) Blind motion deblurring from a single image using sparse approximationty. In: IEEE conference on computer vision and pattern recognition
15. Hu Z, Huang J, Yang M (2010) Single image deblurring with adaptive dictionary learning. In: IEEE international conference on image processing
16. Zhang H, Yang J, Zhang Y, Huang T (2011) Sparse representation based blind image deblurring. In: IEEE international conference on multimedia and expo
17. Lou Y, Bertozzi A, Soatto S (2011) Direct sparse deblurring. J Math Imaging Vis 39(1):1–12
18. Liu Q, Liang D, Song Y, Luo J, Zhu Y, Li W (2013) Augmented Lagrangian-based sparse representation method with dictionary updating for image deblurring. SIAM J Imaging Sci 6(3):1689–1718
19. Tikhonov AN, Arsenin VY (1979) Solutions of ill-posed problems. SIAM Rev 21(2):266–267
20. Cho S, Lee S (2009) Fast motion deblurring. ACM Trans Graph 28(5):1–8
21. Feng X, Milanfar P (2002) Multiscale principal components analysis for image local orientation estimation. In: Asilomar conference on signals, systems and computers
22. Wang Z, Bovik A, Sheikh H, Simoncelli E (2004) Image quality assessment: from error visibility to structural similarity. IEEE Trans Image Process 13(4):600–612

Afr. Mat.
DOI 10.1007/s13370-017-0537-1

Charlier–Szász–Durrmeyer type positive linear operators

Naokant Deo[1] · **Minakshi Dhamija**[1]

Received: 28 March 2016 / Accepted: 12 October 2017
© African Mathematical Union and Springer-Verlag GmbH Deutschland 2017

Abstract In the present paper, we study modified Szász–Durrmeyer positive linear operators involving Charlier polynomials, one of the discrete orthogonal polynomials which are generalization of Szász Durrmeyer operators. Also, King type modification of these operators is given. We obtain uniform convergence of our operators with the help of Korovkin theorem, asymptotic formula and the order of approximation by using classical modulus of continuity.

Keywords Szász–Durrmeyer operators · Charlier polynomials · Modulus of continuity

Mathematics Subject Classification 41A25 · 41A36

1 Introduction

In the year 1950, for $f \in C[0, \infty)$, Szász [11] introduced the well-known Szász operators on half axis as:

$$S_n(f; x) = \sum_{k=0}^{\infty} e^{-nx} \frac{(nx)^k}{k!} f\left(\frac{k}{n}\right), \quad x \in [0, \infty). \tag{1.1}$$

Jakimovski and Leviatan [6] introduced a Favard–Szász type operators by using Appell polynomials. Later, Ciupa [1] studied the following Durrmeyer type integral modification of these operators:

$$P_n(f; x) = \frac{n^{\lambda+k+1}}{\Gamma(\lambda+k+1)} \frac{e^{-nx}}{g(1)} \sum_{k=0}^{\infty} p_k(nx) \int_0^{\infty} e^{-nt} t^{\lambda+k} f(t) dt, \quad x \in [0, \infty), \tag{1.2}$$

✉ Minakshi Dhamija
minakshidhamija11@gmail.com

Naokant Deo
naokantdeo@dce.ac.in

[1] Department of Applied Mathematics, Delhi Technological University (Formerly Delhi College of Engineering), Bawana Road, Delhi 110042, India

Published online: 23 October 2017

where $p_k(x) \geq 0$ is Appell polynomial defined as:

$$g(u)e^{ux} = \sum_{k=0}^{\infty} p_k(x)u^k$$

and $g(z) = \sum_{n=0}^{\infty} a_n z^n$ is an analytic function in the disk $|z| < R(R > 1)$ and $g(1) \neq 0$.

Ismail [5] defined the generating function of Poisson–Charlier polynomials $C_k(u; a)$ by

$$\sum_{k=0}^{\infty} C_k(u; a)\frac{t^k}{k!} = e^t\left(1 - \frac{t}{a}\right)^u, \quad |t| < a, \tag{1.3}$$

where

$$C_k(u; a) = \sum_{r=0}^{k} \binom{k}{r} (-u)_r \left(\frac{1}{a}\right)^r$$

and $(\alpha)_k$ is the Pochhammer's symbol given as:

$$(\alpha)_0 = 1, (\alpha)_k = \frac{\Gamma(\alpha + k)}{\Gamma(\alpha)} = \alpha(\alpha + 1)...(\alpha + k - 1), \quad k = 1, 2, ...$$

These Poisson–Charlier polynomials are positive for $a > 0$ and $u \leq a$.

Recently, Varma and Taşdelen [15] introduced positive linear operators involving Charlier polynomials, one of the discrete orthogonal polynomials which were generalization of Szász operators:

$$L_n(f; x, a) = e^{-1}\left(1 - \frac{1}{a}\right)^{(a-1)nx} \sum_{k=0}^{\infty} \frac{C_k(-(a-1)nx; a)}{k!} f\left(\frac{k}{n}\right), \quad a > 1, \tag{1.4}$$

and they derive some direct results concerning uniform convergence and degree of approximation by using classical modulus of continuity.

Motivated from [1,15], for $f \in C[0, \infty)$, we consider Durrmeyer type Charlier–Szász positive linear operators

$$V_n(f; x, a) := e^{-1}\left(1 - \frac{1}{a}\right)^{(a-1)nx} \sum_{k=0}^{\infty} \frac{C_k(-(a-1)nx; a)}{k!} \frac{n^{\lambda+k+1}}{\Gamma(\lambda + k + 1)}$$
$$\times \int_0^{\infty} e^{-nt} t^{\lambda+k} f(t)dt, \tag{1.5}$$

where $a > 1, \lambda \geq 0, \ x \in [0, \infty)$ and Γ is gamma function. As $a \to \infty$ and $\lambda = 0$, we obtain again Szász–Durrmeyer operators introduced by Mazhar and Totik [8]. Work done by various researchers for Durrmeyer operators as well as operators associated with some polynomial can be seen in [2,3,9,10,12–14,16].

The aim of this paper is to present the above Durrmeyer variant i.e. operators (1.5) alongwith its King type modification, studying in each case uniform convergence, asymptotic formula and degree of approximation by using modulus of continuity. In the last section we give only the definition and moments of king type modification of operators (1.4) and we let an open gate for further research.

2 Auxiliary results and degree of approximation

In this section, first we give some basic definitions and lemmas. With the help of well-known Korovkin theorem, we state our main theorem and then calculate the rate of convergence by classical modulus of continuity, second modulus of continuity and Peetre's K-functional.

Definition 2.1 For $\delta > 0$ and $f \in \tilde{C}[0,\infty)$, the modulus of continuity $\omega(f;\delta)$ of the function f is defined by

$$\omega(f;\delta) := \sup_{\substack{x,y\in[0,\infty)\\ |x-y|\le\delta}} |f(x)-f(y)|, \tag{2.1}$$

where $\tilde{C}[0,\infty)$ is the space of uniformly continuous functions on $[0,\infty)$. Then, for any $\delta > 0$ and each $x \in [0,\infty)$, it is well known that one can write

$$|f(x)-f(y)| \leqslant \omega(f;\delta)\left(\frac{|x-y|}{\delta}+1\right). \tag{2.2}$$

Definition 2.2 For $f \in \tilde{C}_B[0,\infty)$, the second modulus of continuity of 'f' is defined by

$$\omega_2(f;\delta) := \sup_{0<t\le\delta} \|f(x+2t)-2f(x+t)+f(x)\|_{\tilde{C}_B}, \tag{2.3}$$

where $\tilde{C}_B[0,\infty)$ is the class of real valued bounded and uniformly continuous functions defined on $[0,\infty)$ and $\|f\|_{\tilde{C}_B} = \sup_{x\in[0,\infty)} |f(x)|$.

Definition 2.3 Peetre's K-functional for the function $f \in \tilde{C}_B[0,\infty)$ is defined by

$$K(f;\delta) := \inf_{g\in\tilde{C}_B^2[0,\infty)} \left\{\|f-g\|_{\tilde{C}_B} + \delta\|g\|_{\tilde{C}_B^2}\right\}, \tag{2.4}$$

where

$$\tilde{C}_B^2[0,\infty) = \left\{g \in \tilde{C}_B[0,\infty) : g', g'' \in \tilde{C}_B[0,\infty)\right\}$$

and norm $\|g\|_{\tilde{C}_B^2} := \|g\|_{\tilde{C}_B} + \|g'\|_{\tilde{C}_B} + \|g''\|_{\tilde{C}_B}$. From the above definitions, we can conclude the following inequality:

$$K(f;\delta) \le M\left\{\omega_2\left(f;\sqrt{\delta}\right) + \min(1,\delta)\|f\|_{\tilde{C}_B}\right\}, \quad \forall \delta > 0 \tag{2.5}$$

The constant M does not depend upon f and δ.

Let us define the class H as follows:

$$H := \left\{f : x \in [0,\infty), \frac{f(x)}{1+x^2} \text{ is convergent as } x \to \infty\right\}.$$

Lemma 2.4 [15] *The operators given by* (1.4) *satisfy the following equalities:*

$$L_n(1;x,a) = 1,$$
$$L_n(t;x,a) = x + \frac{1}{n},$$
$$L_n\left(t^2;x,a\right) = x^2 + \frac{x}{n}\left(3+\frac{1}{a-1}\right) + \frac{2}{n^2},$$

where $x \ge 0$.

Lemma 2.5 *The operators V_n satisfy the following equalities*

$$V_n(1;x,a) = 1, \tag{2.6}$$

$$V_n(t;x,a) = x + \frac{(\lambda+2)}{n}, \tag{2.7}$$

$$V_n\left(t^2;x,a\right) = x^2 + \frac{x}{n}\left\{\frac{1}{a-1} + 2(\lambda+3)\right\} + \frac{1}{n^2}\left\{\lambda^2+5\lambda+7\right\}. \tag{2.8}$$

Proof We can easily obtain above three assertions with the help of Charlier polynomials (1.3). □

Remark 2.6 For $V_n(f;x,a)$ operators, verify that

$$V_n(t-x;x,a) = \frac{(\lambda+2)}{n}$$

and

$$V_n\left((t-x)^2;x,a\right) = \frac{x}{n}\left(\frac{2a-1}{a-1}\right) + \frac{1}{n^2}(\lambda^2+5\lambda+7).$$

Proof Using Lemma 2.5 and linearity of operators $V_n(f;x,a)$, it is easy to prove the above result. □

Lemma 2.7 [4] *Let $g \in C^2[0,b]$ and for $n \geq 1$, $\{L_n(g;x)\}$ be a sequence of positive linear operators with the property $L_n(1;x) = 1$. Then*

$$|L_n(g;x) - g(x)| \leq \left\|g'\right\| \sqrt{L_n\left((t-x)^2;x\right)} + \frac{1}{2}\left\|g''\right\| L_n\left((t-x)^2;x\right). \tag{2.9}$$

Lemma 2.8 [17] *For $f \in C[a,b]$ and $h \in (0, \frac{b-a}{2})$, let f_h be the second order Steklov function attached to the function f. Then we have the following inequalities:*

$$\|f_h - f\| \leq \frac{3}{4}\omega_2(f;h), \tag{2.10}$$

$$\left\|f_h''\right\| \leq \frac{3}{2h^2}\omega_2(f;h). \tag{2.11}$$

Theorem 2.9 *Let $f \in C[0,\infty) \bigcap H$, then we have*

$$\lim_{n\to\infty} V_n(f;x,a) = f(x)$$

uniformly on each compact subset of $[0,\infty)$.

Proof By using Lemma 2.5, we have

$$\lim_{n\to\infty} V_n\left(t^i;x,a\right) = x^i, \quad i = 0,1,2$$

uniformly on each compact subset of $[0,\infty)$.
Hence, by applying well known Korovkin theorem, we obtain the desired results. □

We establish the asymptotic behavior of operators (1.5) by giving a Voronovskaja type theorem.

Theorem 2.10 *Let f be a bounded and integrable function on $[0,\infty)$. If there exists first and second derivative of the function f at a fixed point $x \in [0,\infty)$, then*

$$\lim_{n\to\infty} n\left(V_n\left(f;x,a\right)-f\left(x\right)\right)=\left(\lambda+2\right)f'\left(x\right)+\frac{1}{2}x\left(\frac{2a-1}{a-1}\right)f''(x).$$

Proof Using Taylor's expansion formula of function f, it follows

$$f(t)=f(x)+(t-x)f'(x)+\frac{1}{2!}(t-x)^2f''(x)+\varepsilon(t,x)(t-x)^2,$$

where $\varepsilon(t,x):=\varepsilon(t-x)$ is a bounded function and $lim_{t\to x}\varepsilon(t,x)=0$. Taking into account the linearity of modified Szász Durrmeyer operators and then apply the operators V_n on both sides of above equation, we get

$$\begin{aligned}V_n\left(f;x,a\right)-f(x)=V_n\left(t-x;x,a\right)f'(x)+\frac{1}{2}V_n\left((t-x)^2;x,a\right)f''(x)\\+V_n\left(\varepsilon(t,x)\cdot(t-x)^2;x,a\right).\end{aligned}$$

Therefore using Remark 2.6, we get

$$\begin{aligned}\lim_{n\to\infty} n\left(V_n\left(f;x,a\right)-f\left(x\right)\right)=\left(\lambda+2\right)f'\left(x\right)+\frac{1}{2}x\left(\frac{2a-1}{a-1}\right)f''(x)\\+\lim_{n\to\infty} n\left(V_n\left(\varepsilon(t,x)\cdot(t-x)^2;x,a\right)\right).\end{aligned}\tag{2.12}$$

We estimate the last term on the right hand side of the above equality, applying the Cauchy–Schwarz inequality, such that

$$V_n\left(\varepsilon(t,x)\cdot(t-x)^2;x,a\right)\le\sqrt{V_n\left(\varepsilon^2(t,x);x,a\right)}\sqrt{V_n\left((t-x)^4;x,a\right)}.\tag{2.13}$$

Because $\varepsilon^2(x,x)=0$ and $\varepsilon^2(\cdot,x)\in C[0,\infty)\bigcap H$, using the convergence from Theorem 2.9, we get

$$\lim_{n\to\infty} V_n\left(\varepsilon^2(t,x);x,a\right)=\varepsilon^2(x,x)=0.\tag{2.14}$$

Therefore, from (2.13) and (2.14) yields

$$\lim_{n\to\infty} n\left(V_n\left(\varepsilon(t,x)\cdot(e_1-x)^2;x,a\right)\right)=0$$

and using (2.12) we obtain the asymptotic behavior of operators (1.5). □

Now, we find the rate of convergence by following theorems:

Theorem 2.11 *Let $f\in\tilde{C}[0,\infty)\bigcap H$, then the operators V_n satisfy:*

$$\left|V_n\left(f;x,a\right)-f(x)\right|\le 2\omega\left(f;\sqrt{\gamma_n\left(x\right)}\right),$$

where

$$\gamma_n(x)=V_n\left((t-x)^2;x,a\right)=\frac{x}{n}\left(\frac{2a-1}{a-1}\right)+\frac{1}{n^2}(\lambda^2+5\lambda+7).\tag{2.15}$$

Proof By using Lemma 2.5 and property of modulus of continuity, we have

$$|V_n(f;x,a)-f(x)| \le e^{-1}\left(1-\frac{1}{a}\right)^{(a-1)nx}\sum_{k=0}^{\infty}\frac{C_k(-(a-1)nx;a)}{k!} \times \frac{n^{\lambda+k+1}}{\Gamma(\lambda+k+1)}\int_0^{\infty} e^{-nt}t^{\lambda+k}|f(t)-f(x)|\,dt$$

$$\le \left\{1+\frac{1}{\delta}e^{-1}\left(1-\frac{1}{a}\right)^{(a-1)nx}\sum_{k=0}^{\infty}\frac{C_k(-(a-1)nx;a)}{k!} \times \frac{n^{\lambda+k+1}}{\Gamma(\lambda+k+1)}\int_0^{\infty} e^{-nt}t^{\lambda+k}|t-x|\,dt\right\}\omega(f;\delta).$$

Now applying Cauchy–Schwarz inequality for the integral, we get

$$|V_n(f;x,a)-f(x)| \le \left\{1+\frac{1}{\delta}e^{-1}\left(1-\frac{1}{a}\right)^{(a-1)nx}\sum_{k=0}^{\infty}\frac{C_k(-(a-1)nx;a)}{k!} \times \frac{n^{\lambda+k+1}}{\Gamma(\lambda+k+1)}\left(\int_0^{\infty} e^{-nt}t^{\lambda+k}dt\right)^{1/2}\left(\int_0^{\infty} e^{-nt}t^{\lambda+k}(t-x)^2dt\right)^{1/2}\right\}\omega(f;\delta).$$

Once again using Cauchy–Schwarz inequality for sum, we obtain

$$|V_n(f;x,a)-f(x)| \le \left\{1+\frac{1}{\delta}\left(e^{-1}\left(1-\frac{1}{a}\right)^{(a-1)nx}\sum_{k=0}^{\infty}\frac{C_k(-(a-1)nx;a)}{k!} \times \frac{n^{\lambda+k+1}}{\Gamma(\lambda+k+1)}\int_0^{\infty} e^{-nt}t^{\lambda+k}dt\right)^{1/2} \times \left(e^{-1}\left(1-\frac{1}{a}\right)^{(a-1)nx}\sum_{k=0}^{\infty}\frac{C_k(-(a-1)nx;a)}{k!} \times \frac{n^{\lambda+k+1}}{\Gamma(\lambda+k+1)}\int_0^{\infty} e^{-nt}t^{\lambda+k}(t-x)^2dt\right)^{1/2}\right\}\omega(f;\delta)$$

$$= \left\{1+\frac{1}{\delta}(V_n(1;x,a))^{1/2}\left(V_n\left((t-x)^2;x,a\right)\right)^{1/2}\right\}\omega(f;\delta).$$

Choose $\delta=\sqrt{\gamma_n(x)}$ and using Lemma 2.5, we have

$$|V_n(f;x,a)-f(x)| \le 2\omega\left(f;\sqrt{\gamma_n(x)}\right),$$

which is the desired result. □

Theorem 2.12 *If $f \in \tilde{C}_B^2[0,\infty)$ then we have*

$$|V_n(f;x,a)-f(x)| \le \frac{1}{n}\mu(x)\|f\|_{\tilde{C}_B^2},$$

where

$$\mu(x) = \frac{2a-1}{2(a-1)}x + \frac{1}{2}\left(\lambda^2 + 7\lambda + 11\right).$$

Proof By Taylor's formula

$$f(t) = f(x) + f'(x)(t-x) + f''(\eta)\frac{(t-x)^2}{2}, \quad \eta \in (x,t).$$

The linearity property of the operators V_n and (2.6) gives that

$$V_n(f;x,a) - f(x) = f'(x)\,V_n((t-x);x,a) + \frac{f''(\eta)}{2}V_n\left((t-x)^2;x,a\right).$$

Using Lemma 2.5 in above result, we have

$$\begin{aligned}
|V_n(f;x,a) - f(x)| &\leq \left(\frac{\lambda+2}{n}\right)\|f'\|_{\tilde{C}_B} \\
&\quad + \frac{1}{2}\left[\frac{x}{n}\left(\frac{2a-1}{a-1}\right) + \frac{1}{n^2}\left(\lambda^2+5\lambda+7\right)\right]\|f''\|_{\tilde{C}_B} \\
&\leq \frac{1}{n}\left[\frac{1}{2}\left(\frac{2a-1}{a-1}\right)x + \left(\lambda^2+6\lambda+9\right)\right]\|f\|_{\tilde{C}_B^2} \\
&= \frac{1}{n}\mu(x)\,\|f\|_{\tilde{C}_B^2},
\end{aligned}$$

which is required result. □

Theorem 2.13 *Let* $f \in \tilde{C}_B[0,\infty)$*, then*

$$|V_n(f;x,a) - f(x)| \leq 2M\left(\omega_2(f,h) + \min\left(1,h^2\right)\right)\|f\|_{\tilde{C}_B},$$

where

$$h := \sqrt{\frac{\mu(x)}{2n}}.$$

Proof Let $g \in \tilde{C}_B^2[0,\infty)$ then by using Theorem 2.12, we have

$$\begin{aligned}
|V_n(f;x,a) - f(x)| &\leq |V_n(f-g;x,a)| \\
&\quad + |V_n(g;x,a) - g(x)| + |g(x) - f(x)| \\
&\leq 2\left[\|f-g\|_{\tilde{C}_B} + \frac{1}{2n}\left\{\frac{1}{2}\left(\frac{2a-1}{a-1}\right)x\right.\right. \\
&\quad \left.\left. + \left(\lambda^2+6\lambda+9\right)\right\}\|g\|_{\tilde{C}_B^2}\right].
\end{aligned}$$

Since L.H.S of above inequality does not depend upon g, so by choosing $h := \sqrt{\frac{\mu(x)}{2n}}$, we get

$$|V_n(f;x,a) - f(x)| \leq 2K\left(f,h^2\right).$$

Now, using the relation between Peetre's K-functional and second modulus of continuity, we get desired result. □

3 King type modification

In this section, we discuss better convergence rates by King type operators. King [7] studied an interesting class of Bernstein operators which preserves e_0 and e_2. For $f \in C[0,1]$

$$(B_n f)(x) = \sum_{k=0}^{n} \binom{n}{k} r_n^k(x)\,(1-r_n(x))^{n-k} f\left(\frac{k}{n}\right), \quad x \in [0,1],$$

where $\{r_n(x)\}$ is a sequence of continuous functions on $[0,1]$ with $0 \leqslant r_n(x) \leqslant 1$. For $r_n(x) = x$, $n \in \mathbb{N}$; operators B_n become classical Bernstein operators.

Using this King's idea, now we assume that $\{s_n\}$ be a sequence of continuous functions on $[0,\infty)$ such that after replacing $s_n(x)$ by x in $V_n(f;x,a)$, we get modified Durrmeyer type Charlier–Szász positive linear operators:

$$\hat{V}_n(f;x,a) := e^{-1}\left(1-\frac{1}{a}\right)^{(a-1)ns_n(x)} \sum_{k=0}^{\infty} \frac{C_k(-(a-1)ns_n(x);a)}{k!} \frac{n^{\lambda+k+1}}{\Gamma(\lambda+k+1)} \times \int_0^{\infty} e^{-nt} t^{\lambda+k} f(t)dt, \tag{3.1}$$

where $s_n(x) = \frac{nx-\lambda-2}{n}$, $a > 1$ and $x \geq 0$.

Next, we give basic lemmas for moments which are helpful to present main theorems on the same line as in case of operators (1.5).

Lemma 3.1 *The operators $\hat{V}_n(f;x,a)$ satisfy following equalities:*

$$\hat{V}_n(1;x,a) = 1,$$
$$\hat{V}_n(t;x,a) = x,$$
$$\hat{V}_n\left(t^2;x,a\right) = x^2 + \frac{x}{n}\left(\frac{2a-1}{a-1}\right) - \frac{1}{n^2}\left\{\frac{(4a-3)\lambda+(a+1)}{a-1}\right\}.$$

Proof It is very easy to prove above equalities by using Lemma 2.5. □

Remark 3.2 For $\hat{V}_n(f;x,a)$ operators, verify that

$$\hat{V}_n\left((t-x)^2;x,a\right) = \frac{x}{n}\left(\frac{2a-1}{a-1}\right) - \frac{1}{n^2}\left\{\frac{(4a-3)\lambda+(a+1)}{a-1}\right\}.$$

Proof Using Lemma 3.1 and linearity of operators $\hat{V}_n(f;x,a)$, it is easy to prove the above result. □

Theorem 3.3 *Let $f \in C[0,\infty) \bigcap H$, then*

$$\lim_{n\to\infty} \hat{V}_n(f;x,a) = f(x),$$

uniformly on each compact subset of $[0,\infty)$.

Proof By using Lemma 3.1, we have

$$\lim_{n\to\infty} \hat{V}_n\left(t^i;x,a\right) = x^i, \quad i = 0,1,2$$

uniformly on each compact subset of $[0,\infty)$.

Hence, by applying Korovkin theorem, we get the desired result. □

Theorem 3.4 *Let f be a bounded and integrable function on $[0,\infty)$ having first and second derivative of the function f at a fixed point $x \in [0,\infty)$, then*

$$\lim_{n\to\infty} n\left(\hat{V}_n(f;x,a) - f(x)\right) = \frac{1}{2}x\left(\frac{2a-1}{a-1}\right)f''(x).$$

Theorem 3.5 *Let $f \in \tilde{C}[0,\infty)\bigcap H$, then the operators $\hat{V}_n$ satisfy:*

$$\left|\hat{V}_n(f;x,a) - f(x)\right| \le 2\omega\left(f;\sqrt{\alpha_n(x)}\right),$$

where

$$\alpha_n(x) = \frac{x}{n}\left(\frac{2a-1}{a-1}\right) - \frac{1}{n^2}\left\{\frac{(4a-3)\lambda + (a+1)}{a-1}\right\}. \tag{3.2}$$

Theorem 3.6 *If $f \in \tilde{C}_B^2[0,\infty)$ then we have*

$$\left|\hat{V}_n(f;x,a) - f(x)\right| \le \frac{1}{n}\beta(x)\|f\|_{\tilde{C}_B^2},$$

where

$$\beta(x) = \frac{2a-1}{2(a-1)}x + \frac{1}{2}\left\{\frac{(4a-3)\lambda + (a+1)}{a-1}\right\}.$$

Theorem 3.7 *Let $f \in \tilde{C}_B[0,\infty)$, then*

$$\left|\hat{V}_n(f;x,a) - f(x)\right| \le 2M\left(\omega_2(f,h) + \min\left(1,h^2\right)\right)\|f\|_{\tilde{C}_B},$$

where

$$h := \sqrt{\frac{\beta(x)}{2n}}.$$

Remark 3.8 Now we claim that the error estimation obtained in (3.2) is better than (2.15) for $f \in \tilde{C}[0,\infty)\bigcap H$, $a > 1$, $\lambda \ge 0$, $x \in [0,\infty)$, and $n \in N$. To prove this claim we must show that $\alpha_n(x) \le \gamma_n(x)$.

Now

$$\begin{aligned}\alpha_n(x) \le \gamma_n(x) &\Leftrightarrow \frac{x}{n}\left(\frac{2a-1}{a-1}\right) - \frac{1}{n^2}\left\{\frac{(4a-3)\lambda + (a+1)}{a-1}\right\}\\ &\le \frac{x}{n}\left(\frac{2a-1}{a-1}\right) + \frac{1}{n^2}(\lambda^2 + 5\lambda + 7)\\ &\Leftrightarrow \lambda^2 + \left(\frac{9a-8}{a-1}\right)\lambda + \frac{8a-6}{a-1} \ge 0,\end{aligned}$$

which is true as $\lambda \ge 0$, $a > 1$.

Remark 3.9 Now we define a King type modification of L_n operators and give basic lemma for this operator:

$$\hat{L}_n(f;x,a) = e^{-1}\left(1 - \frac{1}{a}\right)^{(a-1)nr_n(x)}\sum_{k=0}^{\infty}\frac{C_k(-(a-1)nr_n(x);a)}{k!}f\left(\frac{k}{n}\right),$$

where $r_n(x) = \frac{nx-1}{n}$, $a > 1$ and $x \ge 0$.

Lemma 3.10 *The operators* $\hat{L}_n(f;x,a)$ *satisfy following equalities:*

$$\hat{L}_n(1;x,a) = 1,$$
$$\hat{L}_n(t;x,a) = x,$$
$$\hat{L}_n\left(t^2;x,a\right) = x^2 + \frac{x}{n}\left(\frac{a}{a-1}\right) - \frac{1}{n^2}\left\{\frac{1}{a-1}\right\}.$$

Acknowledgements The authors are extremely thankful to the referee for valuable comments and suggestions, leading to a better presentation of the paper.

References

1. Ciupa, A.: On the approximation by Favard–Szász type operators. Rev. Anal. Numer. Théor. Approx. **25**, 57–61 (1996)
2. Deo, N., Bhardwaj, N., Singh, S.P.: Simultaneous approximation on generalized Bernstein–Durrmeyer operators. Afrika Mat. **24**(1), 77–82 (2011)
3. Deo, N., Noor, M.A., Siddiqui, M.A.: On approximation by a class of new Bernstein type operators. Appl. Math. Comput. **201**, 604–612 (2008)
4. Gavrea, I., Rasa, I.: Remarks on some quantitative Korovkin-type results. Rev. Anal. Numer. Theor. Approx. **22**(2), 173–176 (1993)
5. Ismail, M.E.H.: Classical and Quantum Orthogonal Polynomials in One Variable. Cambridge University Press, Cambridge (2005)
6. Jakimovski, A., Leviatan, D.: Generalized Szász operators for the approximation in the infinite interval. Mathematica (Cluj) **34**, 97–103 (1969)
7. King, J.P.: Positive linear operators which preserve x^2. Acta Math. Hungar. **99**, 203–208 (2003)
8. Mazhar, S.M., Totik, V.: Approximation by modified Szász operators. Acta Sci. Math. (Szeged) **49**(1–4), 257–269 (1985)
9. Öksüzer, Ö., Karsli, H., Taşdelen, F.: Approximation by a Kantorovich variant of Szász operators based on Brenke-type polynomials. Mediterr. J. Math. **13**(5), 3327–3340 (2016)
10. Sucu, S., Büyükyazici, I.: Integral operators containing Sheffer polynomials. BMATHAA **4**(4), 56–66 (2012)
11. Szász, O.: Generalization of S. Bernstein's polynomials to the infinite interval. J. Res. Natl. Bur. Stand. **45**, 239–245 (1950)
12. Taşdelen, F., Aktaş, R., Altın, A.: A Kantorovich type of Szász operators including Brenke-type polynomials. Abstr. Appl. Anal. **2012**, Article ID 867203, 13 pages (2012)
13. Varma, S.: On a generalization of Szász operators by multiple Appell polynomials. Stud. Univ. Babes Bolyai Math. **58**, 361–369 (2013)
14. Varma, S., Taşdelen, F.: On a generalization of Szász–Durrmeyer operators with some orthogonal polynomials. Stud. Univ. Babes Bolyai Math. **58**(2), 225–232 (2013)
15. Varma, S., Taşdelen, F.: Szász type operators involving Charlier polynomials. MCM **56**, 118–122 (2012)
16. Varma, S., Sucu, S., İçöz, G.: Generalization of Szász operators involving Brenke type polynomials. CAMWA **64**, 121–127 (2012)
17. Zhuk, V.: Functions of Lip1 class and S. N. Bernstein's polynomials. Vestnik Leningrad. univ. Mat. Mekh. Astron. **1**, 25–30 (1989). (Russian)

ResearchGate

See discussions, stats, and author profiles for this publication at: https://www.researchgate.net/publication/311153464

Computational modeling of small molecule inhibitors of mitochondrial fusion

Article · November 2016

DOI: 10.2174/1574893611666161103152934

CITATIONS
0

READS
156

4 authors, including:

Vinod Scaria
Institute of Genomics and Integrative Biology
309 PUBLICATIONS **3,081** CITATIONS
SEE PROFILE

Salma Jamal
Jawaharlal Nehru University
38 PUBLICATIONS **119** CITATIONS
SEE PROFILE

Yasha Hasija
Delhi Technological University
49 PUBLICATIONS **369** CITATIONS
SEE PROFILE

Some of the authors of this publication are also working on these related projects:

Prediction of DNA-binding Proteins View project

rare rheumatic diseases View project

All content following this page was uploaded by Vinod Scaria on 06 January 2017.

The user has requested enhancement of the downloaded file.

Send Orders for Reprints to reprints@benthamscience.ae

Current Bioinformatics, **2017**, *12*, **000-000**

RESEARCH ARTICLE

Computational Modeling of Small Molecule Inhibitors of Mitochondrial Fusion

Sonam Arora[1,#], Salma Jamal[2,#], Sonam Gaba[3], Yasha Hasija[1] and Vinod Scaria[3,*]

[1]Department of Biotechnology, Delhi Technological University, Shahbad Daulatpur, Delhi, India; [2]Open Source Drug Discovery Unit, Anusandhan Bhawan, Delhi 110001, India and [3]GN Ramachandran Knowledge Center for Genome Informatics, CSIR Institute of Genomics and Integrative Biology (CSIR-IGIB), Mall Road, Delhi 110007, India

Abstract: ***Background:*** Mitochondria are membrane bound structures found in most eukaryotic cells.The most prominent function of this essential organelle is the generation of ATP and the regulation of cell metabolism. However, being a vital part of the cell, mitochondrial dysfunction has been associated to many diseases due to its influence on cellular metabolism. A range of disorders and diseases have been reported as a result of damage and dysfunction in mitochondria which include cancer, diabetes mellitus and neurodegenerative diseases that affect millions of people worldwide. This has made mitochondrial processes an attractive and novel target for potential therapeutic intervention. The application of cheminformatics tools has made possible prioritization and in-depth understanding of small molecules with mitochondrial phenotypes at a much faster rate and reduced cost compared to traditional high-throughput screening.

Results: We have used a publicly available dataset of inhibitors of mitochondrial fusion to build accurate predictive cheminformatics models. We have used the machine learning based classification algorithms and further enhanced this approach using a maximum common substructure (MCS) approach. Three classification algorithms, namely Naive Bayes, Random forest and J48 were used in the present study. Random forest based model was found to be the most accurate, with an accuracy of about 80%. As a proof of application, themodel was further used to prioritize a subset of drug like molecules from a large chemical library, ZINC as well as used to annotate potential new mechanisms of action of molecules with anti-cancer activities.

Conclusions: We show that machine learning approaches could be effectively used to build highly accurate classification models for high-throughput screen datasets. We show as proof of concept that such models could be used to screen and prioritize large datasets in silico, for further experimental validation and also assign potential mechanism of action for molecules.

ARTICLEHISTORY

Received: January 23, 2016
Revised: September 11, 2016
Accepted: October 11, 2016

DOI:
10.2174/1574893611666161103152934

Keywords: Apoptosis, Mitochondria, Mitochondrial fusion, Mitofusins, Machine learning.

INTRODUCTION

Mitochondria are essential organelles in eukaryotic cells primarily associated with cellular energetics. Apart from the well-studied roles in the cellular energetics [1-3], mitochondria play intricate roles in apoptosis [4, 5], cell signaling [6] and metabolism of iron [7, 8]. The organelle comprises of a double membrane enclosing a circular genome of 16 kilobases and codes for 37 proteins [9, 10]. In addition, a number of proteins and transcripts encoded by the nuclear genome are imported into the mitochondria to maintain its integrity and function. A number of genetic disorders have been mapped to mitochondrial loci [10]. Recent evidence also suggests the intricate role of mitochondria in modulating the nuclear epigenome of the cell [11]. A number of complex diseases including cancers and Diabetes Mellitus have recently been associated with mitochondrial dysfunction [12, 13].

Mitochondria in the cell form a rather complex and interconnecting network, modulated through mitochondrial fusion and fission. Mitochondrial fusion has been extensively studied in the recent past and in mammalian cells it has been primarily understood to be modulated by a set of proteins known as mitofusins- Mfn1 and Mfn2 [14]. Inner membrane fusions are modulated by *Opa1* and *Mgm* genes. A number of human diseases are presently known to be modulated by genetic mutations in the proteins modulating mitochondrial fusion. One of the most well characterized examples of disorders of mitochondrial fusion is the Charcot-Marie-Tooth disease which affects the

*Address correspondence to this author at the GN Ramachandran Knowledge Center for Genome Informatics, CSIR Institute of Genomics and Integrative Biology (CSIR-IGIB), Mall Road, Delhi 110007, India; E-mail: vinods@igib.in

#Both authors have contributed equally and would like to be known as joint first authors.

1574-8936/17 $58.00+.00 **© 2017 Bentham Science Publishers**

neuromuscular system [12, 14, 15]. A deranged mitochondrial dynamics and balance between mitochondrial fission and fusion has also been implicated in a number of cancers and neurodegenerative diseases including Alzheimer's disease.

Mitochondrial fusion has also been recently well studied in the context of cancers, and it has been suggested that mitochondria could rescue damage by fusion with other mitochondriae. Mitochondrial fusion thus provides for an attractive target for therapeutic intervention in cancers. It has been suggested that mitochondria evade apoptosis in cancers through activation of mitochondrial fusion [16]. Many distinct pathways associated with mitochondrial fusion have been shown to be activated in cancers. For example Drp1, the protein has been shown to be overexpressed in breast cancers and metastases [17], suggesting an intricate role of mitochondrial dynamics in maintaining the cancerous state. For example, CED-9, a *Caenorhabditis elegans* homolog of *BCL 2*, a gene overexpressed in lymphomas in humans have been shown to activate mitochondrial fusion through interactions with Mitofusins [18].

The recent availability of high-throughput chemical biology screen datasets in public domain provides a new opportunity to computationally model the biological activities of small molecules. A number of previous reports have attempted modeling biological activities from high-throughput screens using machine learning algorithms. These include activities as diverse as antimicrobial to RNA regulation [19, 20]. The numerical descriptors used to represent the molecules could be used as novel essential chemical features which can be employed to design novel compound with better pharmacological properties [21]. The machine learning approaches have been widely used for the generation of computational models which could be effectively used for the prioritization of active molecules. Li *et al*. 2014 [22] carried out in silico prediction of chemical acute oral toxicity using multiple machine learning modes. Maindola *et al*. 2015 [23] used machine learning algorithms for the identification of inhibitors against Plasmodium falciparum erythrocyte invasion. In the present report, we use computational approaches to model the activities of inhibitors of mitochondrial fusion using machine learning approaches based on physico-chemical properties or descriptors of molecules to create accurate classification models for the biological activity of small molecules. These models can be potentially employed to rapidly screen large molecular databases to prioritize and to discover potential new activities, thus significantly reducing the time and failures associated with high-throughput chemical biology screens.

MATERIALS AND METHODS

Dataset Source

The dataset comprising of high throughput assay for inhibitors of mitochondrial fusion containing 4,011 active and 1,90,149 inactive compounds was downloaded from PubChem [AID 1362], maintained by NCBI (National Centre for Biotechnology Information). The assay was a growth based assay in *S. cerevisiae* strains developed to identify small molecules that inhibit mitochondrial fusion activity. Mitochondrial fission and fusion are known to be involved in the regulation of apoptosis. Drp-1 (Dynamin related protein), which belongs to family of large GTPases, is a highly conserved protein regulates the process of mitochondrial division and fusion [24]. The loss in function of Drp increases mitochondrial fusion which further attenuates the process of apoptosis by controlling the release of cytochrome c from mitochondria. The assay was conducted using mitochondrial targeted GFP (Green Fluorescence Protein) and the effect of compounds on the morphology of mitochondria was observed. The small molecules were first screened using primary growth based assay, the molecules identified as active were further taken for secondary analysis. The activity of compounds was determined using PubChem activity score which is based on the IC50 values of compounds. The compounds having activity score between 0-40 were categorized as inactives while the compounds having activity score 0 were categorized as actives.

Preprocessing of Data and Computation of Molecular Descriptors

Molecular descriptors were computed for the Structure Data Files (SDF) obtained from PubChem We used popular and freely available software PowerMV [25] to compute molecular descriptors. A total of 179 descriptors were generated. The descriptors generated included pharmacophore fingerprints representing pharmacological properties of molecules, weighted burden number descriptors giving weightage to three important features i.e. atomic weight, charge and polarizability and properties like XlogP, BBB, toxicity etc. Pharmacophore based descriptors are binary fingerprints according to which the atoms or groups having similar bioactivity are given the same classification. These descriptors can be categorized into six categories which are hydrogen bond donors and acceptors, aromatic and hydrophobic centres containing ring systems and negatively and positively charged groups. Weighted burden numbers are continuous descriptors based on a burden connectivity matrix which considers three properties, partial charge electronegativity, and atomic lipophilicity. The property set of descriptors generated by PowerMV include eight properties, number of rotatable bonds, polar surface area, molecular weight, partition coefficient, H-bond donors and acceptors, blood-brain indicator and bad group indicator. The comma separated value (CSV) file obtained was then used to randomly split the dataset into train and test sets using a bespoke Perl script.

Model Building and Cross-Validation

We used Weka (Waikato Environment for Knowledge Analysis) 3.6.8 to generate the predictive classification models for the screening dataset. The CSV file was converted to Attribute Relation File Format (ARFF) as Weka takes input in ARFF format. The models were generated based on three different classification algorithms viz. Naive Bayes, Random Forest and J48. The base classifiers assume all misclassification errors as equal and thus are inefficient in handling imbalanced data. Since the dataset was biased, with far more inactives compared to actives, and this could bias

the efficiency of the mode, we employed a cost-sensitive classification approach. Cost sensitive classifiers use misclassification costs and the object is placed in class with lowest expected misclassification cost. Weka uses a confusion matrix to introduce misclassification costs. The confusion matrix consists of four sections: True positives (TP), True Negatives (TN), False Positives (FP) and False Negatives (FN). The cost was applied on false negatives and was incremented randomly so as to make the false positive rate around 20%. We used 5-fold cross-validation to test the accuracy of the models on independent dataset.

Evaluation of Predictive Models

Evaluation of the models was done using the test set and various parameters were taken into account for predicting the efficiency of model. We used different parameters generated by Weka to select the best model based on different misclassification costs applied. The parameters obtained from Weka include True positive rate (TPR), false positive rate (FPR), and accuracy. In addition, different accuracy estimates including sensitivity (the proportion of actual positives), specificity (proportion of actual negatives), Matthews Correlation Coefficient (depicts the correlation coefficient of observed and predicted classes), Balanced Classification Ratio (BCR) which is the average of specificity and sensitivity). In addition, Area under the curve for the Receiver Operator Characteristics (ROC) plot between the true positive rate and false positive rate was drawn to predict the ability of the model to correctly classify the compounds.

Substructure Search

A predictive model is just a mathematical equation explaining the descriptor space, which would provide no insights into the chemical structure or the structural motifs associated with the active dataset. In order to extract the substructures or structural motifs which were enriched or associated with the actives, we employed an additional substructure analysis approach. We used hierarchical clustering approach to cluster the active compounds in the dataset using LibMCS, available from ChemAxon [26, 27]. We initially generated the 3D SDF files using *molconvert* module of ChemAxon and clustered the compounds. We pruned the tree at an empirical level of 6 which retrieved 632 substructures. These substructures were further used to search through the active and inactive data sets using *jcsearch* algorithm from ChemAxon. The number of matches in active and inactive data sets was computed and statistical evaluation of the enrichment was performed using Chi-square test. Additionally, a measure, Enrichment Factor (EF) which denotes the number of times the substructures occur in actives versus inactives was computed for each of the substructure evaluated. All substructures with at least 1% matches among active dataset, p-value less than 0.01 and enrichment factor more than 10 were filtered.

Datasets of Anticancer Molecules

The datasets of anticancer molecules were downloaded from PubChem. This corresponds to a total of 9,410 molecules screened and found active against 66 cell lines.

Results and Discussion

The primary screen dataset obtained from PubChem contained a total of 194,156 molecules, out of which 4,011 were annotated as active and 190, 149 were annotated as inactive. A total of 179 molecular descriptors were generated for all the 4,011 molecules using PowerMV. We observed that 24 descriptors were not informative in demarcating between actives and inactives by virtue of either having the same values all across the datasets or having null values, and were removed from the further analysis. Further analysis was performed for the remaining potentially informative 155 descriptors (Supplementary Table **1**).

Table 1. Performance measures of models generated for small molecule inhibitors of mitochondrial fusion.

Classifier	True Positive Rate (TPR)	False Positive Rate (FPR)	ROC	Accuracy	BCR	MCC	Cost
Naïve Bayes	53.7	20.1	0.72	79.37	66.79	0.11	5
Random Forest	66.8	19.5	0.79	80.17	73.64	0.16	1460
J48	60.5	20.9	0.704	78.69	69.78	0.13	155

The descriptor files were transformed to native Weka formats using bespoke scripts and models were created using Naive Bayes, Random Forest and J48, a set of popular classification approaches extensively used by our lab and others for building models from high-throughput bioassay data sets. As described in the materials section, a cost-sensitive approach was used for the classification as the number of inactives far exceeded the number of actives. Different costs were applied on various classifiers. Naive Bayes used a minimum cost of 5 and Random Forest used maximum misclassification cost as 1,460. The classifiers used Metacost to convert the standard classifiers to cost sensitive classifiers. The Metacost is a procedure which renders the existing classifiers cost sensitive by relabeling the training examples with minimized costs and predict the class of test instances.

Model Validation

The models were evaluated on the test set as described in the materials and methods section and quantitative measures for the performance of the model was evaluated. Random Forest outperformed the other two methods in all the estimates of model accuracy (Table **1**, Fig. **1**). Additionally a receiver operator characteristic plot, which is the plot between the True positive and the false positive rate, was plotted and area under the curve for each of the model was evaluated. Random Forest model had an area under the curve of 0.79, while Naive Bayes and J48 had AUC values of 0.72 and 0.70 respectively (Fig. **2**).

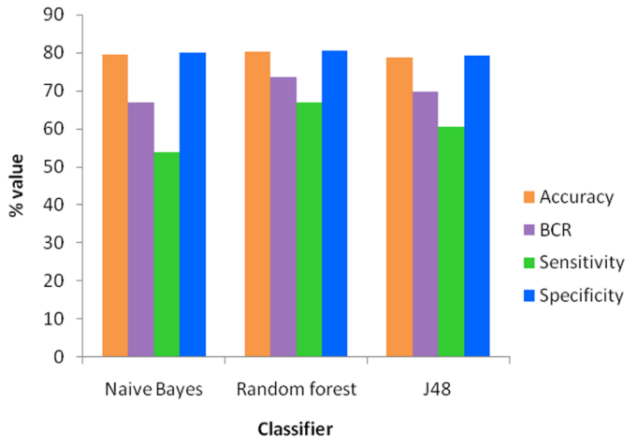

Fig. (1). Comparative plots depicting the various parameters for assessing the accuracy of predictive models.

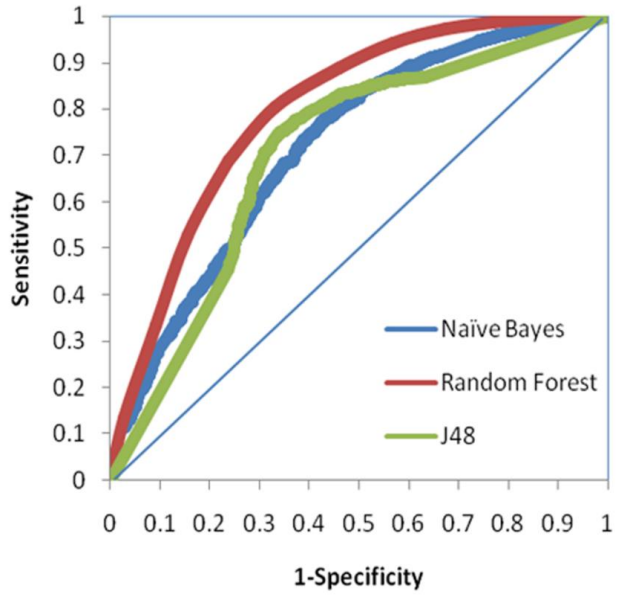

Fig. (2). Area under ROC curves for NB, RF and J48 depicting their predictive ability.

Evaluation of Significantly Enriched Sub-Structures

In order to find the potentially enriched substructures contributing to the activity of the molecules we used a maximum common substructure search approach. Similarity search of the compounds using LibMCS, and *jcsearch* software's from ChemAxon resulted in a total of 12 scaffolds that can act as potential drugs against the mitochondrial fusion enzymes. The MCS size was chosen to be 11 that gave up to 6 levels in the hierarchy. The cluster count at the top level was 632 and total cluster count was 4157. The singletons were removed after which we obtained 386 scaffolds. We used of more than 1% matches in actives, p-value less than 0.01 and enrichment factor more than 10 which gave us final 12 enriched scaffolds. Table **2** depicts the scaffold structures along with the p-value, chi-square and enrichment factor values of the significantly enriched 12 scaffolds (Table **2**). The structural motifs identified to be associated with the activity of the molecules could be used to prioritize large repertoire of chemical compounds and lead to the prediction of biologically active compounds.

Implementation of the Model Availability for In-Silico Screens

We have made available the model and scripts for prediction of potential biological activities at the 2C4C models repository. Briefly the package has the Weka Model and a set of preprocessing scripts which would pre-process the PowerMV descriptors to appropriate ARFF format files for Weka. Initially the user would require computing the descriptors using PowerMV and run a step-by-step set of instructions to preprocess the files. Further the models and the descriptor file would be required to be run on Weka to predict potential activities of molecules. A step-by-step set of instructions on how to use the prediction model has been made available at http://vinodscaria.rnabiology.org/2C4C/models.

Proof of Concept Application of Models to Understand Potential Mechanism of Action of Molecules with Anti-Cancer Effect

One of the major applications of a predictive model for specific molecular activities is to potentially understand the mechanisms of action of molecules. One of the major applications of inhibitors of mitochondrial fusion would be as anticancer agents [28, 29]. Such an approach would additionally enable prioritization of molecules for including or excluding a set of potential molecular activities. The recent availability of anticancer activities against a number of cell-lines using high-throughput screening provides an immense opportunity towards mapping potential additional molecular activities or mechanisms of action for these molecules. We briefly pre-processed the active molecules and molecular descriptors were computed as described in the materials section. The molecules were screened in-silico using the Random Forest model. Out of the total 9,410 molecules, a total of 2,732 molecules were predicted having potential inhibitory effect on mitochondrial fusion. The number of molecules active against each cell-line tested and the fraction of the molecules active against mitochondrial fusion are summarized in Table **3** and Supplementary Table **3**.

Proof of Concept Application of Model to Prioritize Molecules from Large Datasets

One of the major applications of such a predictive model for predicting molecular activities is to potentially prioritize molecules from large molecular databases. ZINC is one of the popularly used and well curated datasets for molecules, and has been extensively used for molecular studies [30]. We applied the computational model on the 'drug-like' subset of ZINC which included 15,798,630 molecules. The model with the best accuracy, and based on Random Forest was used for the analysis. In addition, we used a substructure based filtering approach and filtered for potential active molecules having one of the enriched substructures. Analysis revealed a total of 2,006,884 molecules predicted active by the Random Forest Model. Additional filtering using the

Table 2. Significantly enriched substructures obtained for Bioassay AID 1362 for small molecules inhibitors of mitochondrial fusion.

Scaffold No.	Scaffold Structure	No. of molecules active against mitochondrial fusion	No. of molecules inactive against mitochondrial fusion	Chi-square	P-value	Enrichment factor
1	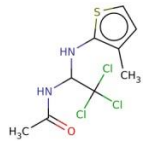	6	4	165.90	5.80E-38	71.11
2	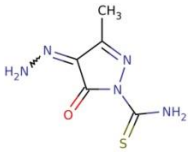	5	6	102.36	4.62E-24	39.50
3	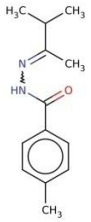	5	9	78.35	8.61E-19	26.33
4	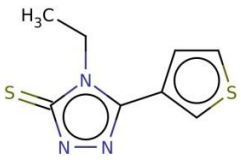	8	15	121.70	2.68E-28	25.28
5	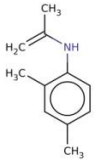	5	14	55.23	1.07E-13	16.93
6	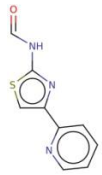	7	26	59.80	1.05E-14	12.76
7	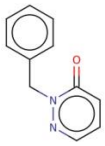	15	57	125.39	4.17E-29	12.47
8	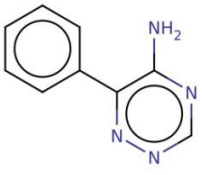	5	19	41.78	1.02E-10	12.47

9	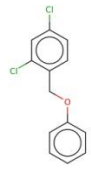	7	28	55.65	8.65E-14	11.85
10	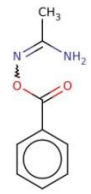	6	24	47.70	4.97E-12	11.85
11	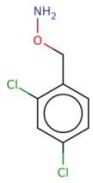	7	29	53.75	2.28E-13	11.44
12	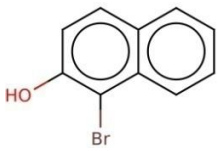	5	21	37.86	7.56E-10	11.28

substructure approach resulted in 224 molecules containing scaffold 12 (Supplementary Table **2**).

DISCUSSION AND CONCLUSIONS

Mitochondrial dynamics has been increasingly recognized as an important process to maintain the mitochondrial function and integrity. Processes which modulate mitochondrial dynamics, including mitochondrial shape, fission and fusion are also increasingly being molecularly deciphered to great detail and in context of their associations with human diseases [13]. In fact mitochondrial fusion has been recently one of the major areas of interest, due to its close association in the pathophysiology of a number of cancers and neurodegenerative processes [12]. Inhibition of mitochondrial fusion offers a novel alternative opportunity to target cancers. Nevertheless screening a large number of molecules for specific activities is both costly, tedious and time consuming.

The availability of high-throughput screens for inhibitors of specific assays provides a novel opportunity to model the activities based on machine learning approaches and molecular descriptors. Increasingly such models have been created for mining large datasets in silico and provide a new opportunity to create a systematic map of biological function or activities of molecules [31]. The recently available confirmatory dataset of small molecule inhibitors of mitochondrial fusion was used in this present study to create highly accurate computational models. Our analysis revealed Random Forest models to be highly accurate, with accuracies over 80 percent and Area under the curve of Receiver Operator Characteristics plot of 79.

Table 3. Number of molecules active against each cell-line tested and the fraction of the molecules active against mitochondrial fusion.

Cell lines	Total no. of molecules active against cell line (PubChem)	No. of molecules found active against mitochondrial fusion
Breast Cancer Cell line	352	101
CNS Cell line	476	126
Colon Cell line	479	142
Leukemia Cell line	4911	1482
Melanoma Cell line	477	117
Non-small Cell Lung Cell line	761	205
Ovarian Cell line	287	92
Prostate Cell line	43	13
Renal Cell line	492	129
Small Cell Lung Cell-line	1132	325
All	9,410	2,732

The potential application of such computational models is twofold. On one side, it offers a useful methodology to parse large molecular data sets presently available in public domain towards prioritizing molecules for experimental analyses. On the other end, it provides for a new way towards understanding mechanism of action of molecules. We have in this present manuscript provided a proof of concept application of the model in both the scenarios. On one end, we have used the model to prioritize potential actives from ZINC 'drug-like' molecule set [32], a well curated molecular dataset popularly used for molecular analyses. In addition, we have used the model to predict potential mechanisms of actions of a set of anticancer molecules screened against 66 cell lines.

The present analysis is not without caveats. The primary caveat being the un-availability of other well-curated datasets of inhibitors of mitochondrial inhibitors using comparable assays, which could potentially reflect experimental biases in the models. We hope, with the increasing interest in the field, a number of datasets of comparable assays in different assay systems would emerge, which could potentially be used to compare and create more robust computational methodologies. The second major caveat is the potential issues with extrapolating the models based on the yeast system to human systems. The mitochondrial systems, including the proteins modulating the mitochondrial integrity and function in eukaryotic systems are well conserved between eukaryotic systems [33] which makes a legitimate possibility of extending the model based on a yeast system to predict potential effects on human anticancer molecules. Nevertheless the additional molecular mechanisms of anticancer molecules suggested through this approach needs to be experimentally verified.

The utility of a computational model is intricately linked to the availability and ease of use. To this end, we have made available the computational model and associated scripts for preprocessing the molecular descriptors to enable researchers to be able to apply the methodology and model towards prioritizing large chemical libraries. The Weka Model, detailed instructions and scripts are available online [34].

CONFLICTS OF INTEREST

The authors declare that they have no competing interests.

ACKNOWLEDGEMENTS

Authors acknowledge Dr S Ramachandran and Dr Sridhar Sivasubbu for reviewing the manuscript. This manuscript is part of the Crowd Computing for Cheminformatics (2C4C) Programme involving undergraduate students. Authors acknowledge help and support from the CDAC-Garuda Grid Computing facility, National Knowledge Network, and the Open Source Drug Discovery Consortium for technical help and resources. The study was funded by the Council of Scientific and Industrial Research, India through Grant BSC0122 Centre for Cardiovascular and Metabolic Disease Research (CARDIOMED).

AUTHOR'S CONTRIBUTION

SJ and VS designed the study, SA, SG and SJ generated the classification models and performed the analysis under the guidance of VS and YH. SA, SJ and VS together wrote the manuscript and have approved the final manuscript. OSDDC was involved in regular discussions and supported the work.

SUPPLEMENTARY DATA

Supplementary Table 1: Zinc molecules containing scaffold no. 12 obtained using substructure based approach.

Supplementary Table 2: List of PowerMV descriptors used in predictive modeling.

Supplementary Table 3: Details of cancer cell lines datasets used for testing mitochondrial fusion inhibitors model.

REFERENCES

[1] Waterhouse NJ. The cellular energy crisis: mitochondria and cell death. Med Sci Sports Exerc 2003; 35(1): 105-10.

[2] David JM, Kenneth AS, Wayne AC, Donghoon L, Kevin EC. Reduced mitochondrial coupling in vivo alters cellular energetics in aged mouse skeletal muscle. J Physiol 2005; 569(2): 467-73.

[3] Glancy B, Balaban RS. Role of mitochondrial Ca in the regulation of cellular energetics. Biochemistry 2012; 51(14): 2959-73.

[4] Wang C, Youle RJ. The role of mitochondria in apoptosis. Annu Rev Genet 2009; 43: 95-118.

[5] Xiaodong W. The expanding role of mitochondria in apoptosis. Genes Dev 2001; 15: 2922-33.

[6] Tait SW, Green DR. Mitochondria and cell signalling. J Cell Sci 2012; 125(4): 807-15.

[7] Drysdale J, Arosio P, Invernizzi R, *et al.* Mitochondrial ferritin: a new player in iron metabolism. Blood Cells Mol Dis 2002; 29(3): 376-83.

[8] Richardson DR, Lane DJ, Becker EM. Mitochondrial iron trafficking and the integration of iron metabolism between the mitochondrion and cytosol. Proc Natl Acad Sci USA 2010; 107(24): 10775-82.

[9] Anderson S. Sequence and organization of the human mitochondrial genome. Nature 1981; 290: 457-65.

[10] Robert WT, Doug MT. Mitochondrial DNA Mutations in Human Disease. Nat Rev Genet 2005; 6(5): 389-402.

[11] Bellizzi D, D'Aquila P, Giordano M, Montesanto A, Passarino G. Global DNA methylation levels are modulated by mitochondrial DNA variants. Epigenomics 2012; 4(1): 17-27.

[12] Chen H, Chan DC. Mitochondrial dynamics–fusion, fission, movement, and mitophagy–in neurodegenerative diseases. Human Molecular Genetics 2009; 18(R2): R169-R76**.**

[13] Michael RD, Gyorgy S. Roles of mitochondria in human disease. Biochemical Society Essays Biochem 2010; 47: 115-37.

[14] Westermann B. Molecular Machinery of Mitochondrial Fusion and Fission. J Biol Chem 2008; 283(20): 13501-5.

[15] Der-Fen S, Kristi LN, Youle RJ. Mitochondrial dynamics and apoptosis. Genes Dev 2008; 22: 1577-90.

[16] Guido K, Lorenzo G, Catherine B. Mitochondrial Membrane Permeabilization in Cell Death. Physiol Rev 2007; 87(1): 99-163.

[17] Zhao J, Zhang J, Yu M, *et al.* Mitochondrial dynamics regulates migration and invasion of breast cancer cells. Oncogene 2013; 32(40): 4814-24.

[18] Delivani P, Adrain C, Taylor RC, Duriez PJ, Martin SJ. Role for CED-9 and Egl-1 as regulators of mitochondrial fission and fusion dynamics. Mol Cell 2006; 21(6): 761-73.

[19] Periwal V, Rajappan JK, Jaleel AU, Scaria V. Predictive models for anti-tubercular molecules using machine learning on high-throughput biological screening datasets. BMC Res Notes 2011; 4: 504.

[20] Jamal S, Periwal V, Scaria V. Computational analysis and predictive modeling of small molecule modulators of microRNA. J Chem 2012; 4: 16.
[21] Lee Y, Jana S, Acharya G, Lee CH. Computational analysis and predictive modeling of polymorph descriptors. Chem Cent J 2013; 7: 23.
[22] Xiao L, Lei C, Feixiong C, *et al.* In Silico Prediction of Chemical Acute Oral Toxicity Using Multi- Classification Methods. J Chem Inf Model 2014; 54: 1061-9.
[23] Maindola P, Jamal S, Grover A. Cheminformatics Based Machine Learning Models for AMA1-RON2 Abrogators for Inhibiting Plasmodium falciparum Erythrocyte Invasion. Mol Inf 2015; 34(10): 655-64.
[24] Smirnova E, Griparic L, Shurland DL, Bliek AM. Dynamin-related Protein Drp1 Is Required for Mitochondrial Division in Mammalian Cells. Mol Biol Cell 2001; 12: 2245-56.
[25] Liu K, Feng J, Young SS. PowerMV: a software environment for molecular viewing, descriptor generation, data analysis and hit evaluation. J Chem Inf Model 2005; 45: 515-22.
[26] Chemaxon: Budapest H. Library MCS, version 0.7; 2008.
[27] Chemaxon: Budapest H. Jcsearch version 5.8.2.
[28] Costantini P, Jacotot E, Decaudin D, Kroemer G. Mitochondrion as a Novel Target of Anticancer Chemotherapy. J Natl Cancer Inst 2000; 92(13): 1042-53.
[29] Irwin JJ, Shoichet BK. ZINC – A Free Database of Commercially Available Compounds for Virtual Screening. J Chem Inf Model 2005; 45(1): 177-82.
[30] Liesa M, Palacín M, Zorzano A. Mitochondrial Dynamics in Mammalian Health and Disease. Physiol Rev 2009; 89: 799-845.
[31] Vert JP, Jacob L. Machine Learning for *In Silico* Virtual Screening and Chemical Genomics: New Strategies. Comb Chem High Throughput Screen 2008; 11(8): 677-85.
[32] Ekins S, Mestres J, Testa B. Insilico pharmacology for drug discovery: applications to targets and beyond. Br J Pharmacol 2007; 152(1): 21-37.
[33] Hales KG. Mitochondrial Fusion and Division. Nature Education 2010; 3(9):12.
[34] http://vinodscaria.rnabiology.org/2C4C/models.

DISCLAIMER: The above article has been published in Epub (ahead of print) on the basis of the materials provided by the author. The Editorial Department reserves the right to make minor modifications for further improvement of the manuscript.

View publication stats

Dynamics of a delayed prey-predator model using modified Holling Tanner functional response with migration

Charu Arora, and Vivek Kumar

Citation: AIP Conference Proceedings **1897**, 020020 (2017); doi: 10.1063/1.5008699
View online: http://dx.doi.org/10.1063/1.5008699
View Table of Contents: http://aip.scitation.org/toc/apc/1897/1
Published by the American Institute of Physics

Articles you may be interested in

Preface: 2nd International Conference on Recent Advances in Mathematical Sciences and its Applications (RAMSA-2017)
AIP Conference Proceedings **1897**, 010001 (2017); 10.1063/1.5008679

Thermosolutal instability of Rivlin-Ericksen fluid under the effect of suspended particles and compressibility in porous medium
AIP Conference Proceedings **1897**, 020010 (2017); 10.1063/1.5008689

Influence of g–jitter on the Rayleigh-Bénard convection in nanofluids with internal heat source
AIP Conference Proceedings **1897**, 020013 (2017); 10.1063/1.5008692

Study of spectro-temporal variation in paleo-climatic marine proxy records using wavelet transformations
AIP Conference Proceedings **1897**, 020019 (2017); 10.1063/1.5008698

Inference on the parameters and reliability characteristics of the generalized inverse Weibull distribution based on records
AIP Conference Proceedings **1897**, 020001 (2017); 10.1063/1.5008680

Effect of non-homogeneity on orthotropic creep stresses in a pressurized circular cylinder
AIP Conference Proceedings **1897**, 020002 (2017); 10.1063/1.5008681

Dynamics of a Delayed Prey-Predator Model Using Modified Holling Tanner Functional Response With Migration.

Charu Arora[1,a),*] and Vivek Kumar[1,b),†]

[1]*Department of Applied Mathematics, Delhi Technological University, Delhi 110042, India.*

[a)]Corresponding author: charuarora099@gmail.com
[b)]vivekkumar.ag@gmail.com

Abstract. In the present paper, prey-predator relationship is discussed using Holling type IV functional response. Modified Holling-tanner prey-predator model has been considered and time delay has been incorporated in the system which is a parameter of bifurcation. The concept of migration in prey and predator population is induced in the system along with prey refuge and local stability analysis has been carried out. The direction of Hopf bifurcation along with the stability of periodic solutions is investigated using central manifold reduction and normal form theory. It is examined that delay plays a dominant role in stabilizing the system, as a consequence critical values of delay occurs below and above which, the dynamics of the system changes. Numerical simulation highlighting the role of migration and to validate theoretical results is presented at the end.

INTRODUCTION

Prey-predator relationship have been investigated by many ecologists and mathematicians due to its relevance by ecologists and biologists. The dynamics of the prey predator relationship has been examined from various prospects and the induction of delay concept is very affluential in prey-predator systems. Many mathematicians have induced delay in the study of prey predator relationship in literature.
The Leslie prey predator system with the use of Holling type II functional response has the following form;

$$\frac{dx}{dt} = rx(1 - \frac{x}{k}) - \frac{mx}{A + x}y, \frac{dy}{dt} = y[s(1 - h\frac{y}{x})], \tag{1}$$

where, x and y are the prey and predator density respectively with carrying capacity k. r is the intrinsic growth rate and m parameter is the per capita consumption rate of predators in its maximum. A is the density of prey required to attain one-half of the maximum rate m. The term $\frac{hy}{x}$ in model (1) is known to be Leslie Gower term[1]. Moreover, the model (1) has been reformed by Lu and Liu [2] and the mathematical form becomes;

$$\frac{dx}{dt} = rx(1 - \frac{x}{k}) - \frac{\alpha xy}{a + bx + cy}y, \frac{dy}{dt} = y[s(1 - h\frac{y(t-\tau)}{x(t-\tau)})], \tag{2}$$

where x and y denote the prey population and predator population respectively. The expression $\frac{\alpha xy}{a+bx+cy}$ is well known by Beddington-DeAngelis functional response. This model has been investigated in many ways in recent literature[3, 4]. The model (2) has further been modified by assuming $\widetilde{t} = rt$, $\widetilde{x} = \frac{x(t)}{k}$, $\widetilde{y} = \frac{\alpha y(t)}{rk}$ and ignoring the widetildes, a non dimensional form of the model becomes as;

$$\frac{dx}{dt} = x(1 - x) - \frac{xy}{a_1 + bx + c_1y}, \frac{dy}{dt} = y[(\delta - \beta\frac{y(t-\tau)}{x(t-\tau)})], \tag{3}$$

*First author charuarora099@gmail.com
†Second author-vivekkumar.ag@gmail.com

Advancement in Mathematical Sciences
AIP Conf. Proc. 1897, 020020-1–020020-7; https://doi.org/10.1063/1.5008699
Published by AIP Publishing. 978-0-7354-1585-0/$30.00

where $\delta = \frac{s}{r}, \beta = \frac{sh}{\alpha}, a_1 = \frac{a}{k}, c_1 = \frac{cr}{\alpha}, \widetilde{\tau} = r\tau$. Permanence, local stability with global stability of model (3) has been analysed in [2]. The Model as explained in (3) is modified by J.F Zhang [5] and the positive equilibrium stability is discussed along with the Hopf bifurcation study.
The model is again considered for study and the concept of prey refuge is induced which makes model (3) as;

$$\frac{dx}{dt} = x(1-x) - \frac{(1-m)xy}{a_1 + bx + c_1 y}, \frac{dy}{dt} = y[(\delta - \beta\frac{y(t-\tau)}{x(t-\tau)} + (1-m)x)], \tag{4}$$

where x and y denote the prey and predator densities respectively and m is the prey refuge and $(1-m)x$ is the measure of the quantity available for predator and its range is $0 < m < 1$. The concept of refuge has been studied in model (4) and stability conditions are determined in [6].

In this paper, we incorporate refuge and migration in both species using Holling type IV functional response and the model (2) and model (4) has been modified to become as;

$$\frac{dx}{dt} = rx(1-\frac{x}{k}) - \frac{(1-m)xy}{a' + bx + c'x^2} - m_1' x, \frac{dy}{dt} = y[s(1 - \frac{hy(t-\tau)}{x(t-\tau)})] - m_2' y, \tag{5}$$

For the sake of simplicity, the above system reduces in non dimensional form by assuming $\tilde{t} = rt, \tilde{x} = \frac{x}{k}, \tilde{y} = \frac{y}{rk}, \tilde{\tau} = r\tau$, $\frac{s}{r} = \delta, hr = \xi, \frac{m_2'}{r} = m_2, \frac{m_1'}{r} = m_1, \frac{a'}{k} = a, \frac{c'}{k} = c$ and dropping the tildes, we get;

$$\frac{dx}{dt} = x(1-x) - \frac{(1-m)xy}{a + bx + cx^2} - m_1 x, \frac{dy}{dt} = y[\delta(1 - \frac{\xi y(t-\tau)}{x(t-\tau)})] - m_2 y, \tag{6}$$

where, x and y are the prey population and predator population respectively. The parameters m_1, m_2 denote the migration in prey and predator population respectively. m denotes the refuge of prey.

In the present paper, the positive equilibrium stability and the Hopf bifurcation process has explained concisely. In the next section, the positive equilibrium stability along with the existence of Hopf bifurcation is discussed and further, the direction of Hopf bifurcation and the bifurcated solutions of periodic properties is discussed. The discussion part in the last section following the numerical simulations in second last section concludes the present article.

STABILITY OF POSITIVE EQUILIBRIUM WITH HOPF BIFURCATION

The model (6) possesses a unique positive nonzero equilibrium say $E^*(x^*, y^*)$ where the equation $cx^3 + Bx^2 + Dx + E = 0$, has a root $x = x^*$ with, $B = cm_1 + b - c$, $D = a + A + bm_1 - b$, $E = am_1 - a$ and $A = \frac{(1-m)(\delta - m_2)}{\delta\xi}$, and $y^* = \frac{(\delta - m_2)x^*}{\delta\xi}$

Initially, we examine the system (6) in the absence of delay. The Jacobian matrix at equilibrium point $E^*(x^*, y^*)$ takes the following form;

$$J = \begin{pmatrix} \alpha_{11} & \alpha_{12} \\ \alpha_{21} & \alpha_{22} \end{pmatrix},$$

where, $\alpha_{11} = 1 - 2x^* - \frac{(1-m)(ay^* - cy^*x^{*2})}{(a+bx^*+cx^{*2})^2}$, $\alpha_{12} = \frac{(m-1)x^*}{a+bx^*+cx^{*2}}$, $\alpha_{21} = \frac{\delta\xi y^{*2}}{x^{*2}}$, $\alpha_{22} = \delta - \frac{\delta\xi 2y^*}{x^*} - m_2$

and the corresponding characteristic equation is as follows;
$\lambda^2 - (Tr.J)\lambda + (Det.J) = 0$ or $\lambda^2 - (\alpha_{11} + \alpha_{22})\lambda + (\alpha_{11}\alpha_{22} - \alpha_{12}\alpha_{21}) = 0$,

Now, by Routh-Hurwitz principle to examine the stability of the model without delay. It is must to have,

$$(1 - 2x^* - \tfrac{(1-m)(ay^* - cy^*x^{*2})}{(a+bx^*+cx^{*2})^2})(\delta - \tfrac{\delta\xi 2y^*}{x^*} - m_2) - (\tfrac{(m-1)x^*}{a+bx^*+cx^{*2}})(\tfrac{\delta\xi y^{*2}}{x^{*2}}) > 0 \text{ and}$$

$$(1 - 2x^* - \tfrac{(1-m)(ay^* - cy^*x^{*2})}{(a+bx^*+cx^{*2})^2}) + (\delta - \tfrac{\delta\xi 2y^*}{x^*} - m_2) < 0$$

The above conditions are essential for the asymptotically stability of the model without delay. Hence, we have the theorem as,

Theorem 1 *Equilibrium point $E^*(x^*, y^*)$ of model (6) is locally asymptotically stable under the following conditions:*
H(1). $\alpha_{11}\alpha_{22} - \alpha_{12}\alpha_{21} > 0$
H(2). $\alpha_{11} + \alpha_{22} < 0$ *, where* $\alpha_{11}, \alpha_{12}, \alpha_{21}, \alpha_{22}$ *are same as defined above.*

The conditions for hopf bifurcation are examined now by the procedure as given in [5].

The characteristic equation of the system (6)is below as;

$$\lambda^2 - (\alpha_{11} + \alpha_{22})\lambda + (\beta_{12}\alpha_{11} - \beta_{12}\lambda - \alpha_{12}\beta_{11})e^{-\lambda\tau} + \alpha_{11}\alpha_{22} - \alpha_{21}\alpha_{12} = 0 \tag{7}$$

where, $\beta_{11} = \frac{\delta\xi y^{*2}}{x^{*2}}, \beta_{12} = \frac{-\delta\xi y^*}{x^*}$.

Substituting $\lambda = i\omega$ in (7), we get,

$$-\omega^2 - (\alpha_{11} + \alpha_{22})i\omega + (-\beta_{12}\omega i + \alpha_{11}\beta_{12} - \alpha_{12}\beta_{11})\cos\omega\tau - (-\beta_{12}\omega i + \alpha_{11}\beta_{12} - \alpha_{12}\beta_{11})i\sin\omega\tau + \alpha_{11}\alpha_{22} - \alpha_{12}\alpha_{21} = 0$$

Now simplifying with real and imaginary parts separated, we get,

$$-\omega^2 - (\alpha_{11}\beta_{12} - \alpha_{12}\beta_{11})\cos\omega\tau - \beta_{12}\omega\sin\omega\tau + \alpha_{11}\alpha_{22} - \alpha_{12}\alpha_{21} = 0 \tag{8}$$

$$-\beta_{12}\omega\cos\omega\tau - (\alpha_{11}\beta_{12} - \alpha_{12}\beta_{11})\sin\omega\tau - (\alpha_{11} + \alpha_{22})\omega = 0 \tag{9}$$

On squaring and adding (8) and (9), we get,

$$\omega^4 + (\alpha_{11}^2 + \alpha_{22}^2 + 2\alpha_{12}\alpha_{21})\omega^2 + (\alpha_{11}\alpha_{22} - \alpha_{12}\alpha_{21})^2 - (\alpha_{12}\beta_{11} - \alpha_{11}\beta_{12}) - \beta_{12}^2 = 0, \tag{10}$$

Let $z = \omega^2$, we get,

$$z^2 + (\alpha_{11}^2 + \alpha_{22}^2 + 2\alpha_{12}\alpha_{21})z + (\alpha_{11}\alpha_{22} - \alpha_{12}\alpha_{21})^2 - (\alpha_{12}\beta_{11} - \alpha_{11}\beta_{12}) - \beta_{12}^2 = 0, \tag{11}$$

being a quadratic equation, the roots are

$$z = \frac{-(\alpha_{11}^2+\alpha_{22}^2+2\alpha_{12}\alpha_{21}) \pm \sqrt{(\alpha_{11}^2+\alpha_{22}^2+2\alpha_{12}\alpha_{21})^2 - 4((\alpha_{11}\alpha_{22}-\alpha_{12}\alpha_{21})^2 - (\alpha_{12}\beta_{11}-\alpha_{11}\beta_{12}) - \beta_{12}^2)}}{2}$$

Considering the positive root, we get,

$$z = \frac{-(\alpha_{11}^2+\alpha_{22}^2+2\alpha_{12}\alpha_{21}) + \sqrt{(\alpha_{11}^2+\alpha_{22}^2+2\alpha_{12}\alpha_{21})^2 - 4((\alpha_{11}\alpha_{22}-\alpha_{12}\alpha_{21})^2 - (\alpha_{12}\beta_{11}-\alpha_{11}\beta_{12}) - \beta_{12}^2)}}{2}$$

Therefore,

$$\omega = \pm\sqrt{\frac{-(\alpha_{11}^2 + \alpha_{22}^2 + 2\alpha_{12}\alpha_{21}) + \sqrt{(\alpha_{11}^2 + \alpha_{22}^2 + 2\alpha_{12}\alpha_{21})^2 - 4((\alpha_{11}\alpha_{22} - \alpha_{12}\alpha_{21})^2 - (\alpha_{12}\beta_{11} - \alpha_{11}\beta_{12}) - \beta_{12}^2)}}{2}}. \tag{12}$$

Considering, again positive roots and denoting it by $\omega_{pos.}$, we get

$$\omega_{pos} = \sqrt{\frac{-(\alpha_{11}^2+\alpha_{22}^2+2\alpha_{12}\alpha_{21}) + \sqrt{(\alpha_{11}^2+\alpha_{22}^2+2\alpha_{12}\alpha_{21})^2 - 4((\alpha_{11}\alpha_{22}-\alpha_{12}\alpha_{21})^2 - (\alpha_{12}\beta_{11}-\alpha_{11}\beta_{12}) - \beta_{12}^2)}}{2}}.$$

Solving (8) and (9) to get the values of τ as below;

$\tau_j = \frac{1}{\omega_{pos}} \cos^{-1} \frac{\omega_{pos}^2(\alpha_{11}\beta_{12}-\alpha_{12}\beta_{11})-(\alpha_{11}\alpha_{22}-\alpha_{12}\alpha_{21})(\beta_{12}\alpha_{11}-\alpha_{12}\beta_{11})-(\alpha_{11}+\alpha_{22})\omega_{pos}^2\beta_{12}}{(\alpha_{11}\beta_{12}-\alpha_{12}\beta_{11})^2+\beta_{12}^2\omega_{pos}^2} + \frac{2\pi j}{\omega_{pos}}$, where j=0,1,2....

Considering the critical value of τ as τ_{cr}, we get as;
$\tau_{cr} = \frac{1}{\omega_{pos}} \cos^{-1} \frac{\omega_{pos}^2(\alpha_{11}\beta_{12}-\alpha_{12}\beta_{11})-(\alpha_{11}\alpha_{22}-\alpha_{12}\alpha_{21})(\beta_{12}\alpha_{11}-\alpha_{12}\beta_{11})-(\alpha_{11}+\alpha_{22})\omega_{pos}^2\beta_{12}}{(\alpha_{11}\beta_{12}-\alpha_{12}\beta_{11})^2+\beta_{12}^2\omega_{pos}^2}$

Now below is the lemma based on above discussion as in[3] by J.F Zhang.

Lemma 1 *If the positive equilibrium point of the model (6) in the absence of delay is locally asymptotically stable. At*
$\tau_j = \frac{1}{\omega_{pos}} \cos^{-1} \frac{\omega_{pos}^2(\alpha_{11}\beta_{12}-\alpha_{12}\beta_{11})-(\alpha_{11}\alpha_{22}-\alpha_{12}\alpha_{21})(\beta_{12}\alpha_{11}-\alpha_{12}\beta_{11})-(\alpha_{11}+\alpha_{22})\omega_{pos}^2\beta_{12}}{(\alpha_{11}\beta_{12}-\alpha_{12}\beta_{11})^2+\beta_{12}^2\omega_{pos}^2} + \frac{2\pi j}{\omega_{pos}}$, *(where j=0,1,2...), system has a pair of conjugate purely imaginary roots* $\pm i\omega_{pos}$, *with*
$\omega_{pos} = \sqrt{\frac{-(\alpha_{11}^2+\alpha_{22}^2+2\alpha_{12}\alpha_{21})+\sqrt{(\alpha_{11}^2+\alpha_{22}^2+2\alpha_{12}\alpha_{21})^2-4((\alpha_{11}\alpha_{22}-\alpha_{12}\alpha_{21})^2-(\alpha_{12}\beta_{11}-\alpha_{11}\beta_{12})-\beta_{12}^2)}}{2}}$ *and the following result is as below;*
(i) When $\tau \in [0, \tau_{cr})$, *then the roots of the system (6) have real negative parts.*
(ii) When $\tau = \tau_{cr}$, *then it has a pair of conjugate purely imaginary roots* $\pm\omega_{pos}$, *with negative real part of other roots.*

If $\lambda = v(\tau) + i\omega(\tau)$ is the root of the characteristic equation given by (7) along with the following condition as; $\tau = \tau_{cr}$,

$$v(\tau_{cr}) = 0, \omega(\tau_{cr}) = \omega_{pos}. \tag{13}$$

Now, differentiating (7) and on further simplification, we get the following result;

$[Re\left(\frac{d\lambda}{d\tau}^{-1}\right)]_{i\omega_{pos}} > 0,$
which proves the transversality condition. Hence, the bifurcation theorem can be stated for the model given in (6).

Theorem 2 *Let theorem 1 holds true. Then,*
(i) When $\tau \in [0, \tau_{cr})$, *the equilibrium point* $E^*(x^*, y^*)$ *of the system (6) is asymptotically stable.*
(ii) When $\tau > \tau_{cr}$, *the equilibrium point* $E^*(x^*, y^*)$ *of system (6) is unstable.*
(iii) Hopf bifurcation occurs for the system (6) at equilibrium point $E^*(x^*, y^*)$ *for* $\tau = \tau_j$ *which is given by;*
$\tau_j = \frac{1}{\omega_{pos}} \cos^{-1} \frac{\omega_{pos}^2(\alpha_{11}\beta_{12}-\alpha_{12}\beta_{11})-(\alpha_{11}\alpha_{22}-\alpha_{12}\alpha_{21})(\beta_{12}\alpha_{11}-\alpha_{12}\beta_{11})-(\alpha_{11}+\alpha_{22})\omega_{pos}^2\beta_{12}}{(\alpha_{11}\beta_{12}-\alpha_{12}\beta_{11})^2+\beta_{12}^2\omega_{pos}^2} + \frac{2\pi j}{\omega_{pos}}$, *(where j=0,1,2...)*

DIRECTION OF HOPF BIFURCATION

In the present section, Hopf bifurcation direction and stability of bifurcated periodic solutions has been discussed by the approach of normal form theory and central manifold theory in brief, which is initially proposed by Hassard et al [7]. This concept has been used much in recent literature. Using result of theorem 2, we can say that in system (6) Hopf bifurcation occurs at particular values of τ, which are represented by τ_j. and one of that value is $\overline{\tau}$. Therefore, at $\overline{\tau}$, the system (6) has one pair of imaginary roots $\pm i\omega_{pos}$ in its characteristic equation. As discussed in [7], system (6) is reduced by the approach of functional differential equation. Moreover, the term τ is denoted by $\tau = \overline{\tau} + \mu$ with $\mu \in \mathbb{R}$. Also, $\mu = 0$ is the value of Hopf bifurcation of system (6). On further taking time by $\rightarrow \frac{t}{\tau}$. System (6) becomes as;

$$u'(t) = L_\mu u(t) + F(u_t, \mu), \tag{14}$$

in Banach space $\mathbb{C}([-1, 0], \mathbb{R}^2)$, with u=$\begin{pmatrix} u_1 \\ u_2 \end{pmatrix} \in \mathbb{C}$ and $L_\mu : \mathbb{C} \rightarrow \mathbb{R}$, $F : \mathbb{R} \times \mathbb{C} \rightarrow \mathbb{R}$ as described in [5]. As discussed in [5] the following values can be obtained(with symbols similar as used in [5]):

$C_1(0) = \frac{i}{2\omega_{pos}\bar{\tau}}\left(g_{20}g_{11} - 2|\ g_{11}\ |^2 - \frac{|g_{02}|^2}{3}\right) + \frac{g_{21}}{2}$,
$\mu_2 = \frac{Re\{C_1(0)\}}{Re\{\lambda'(\bar{\tau})\}}$ and $\beta_2 = 2Re\{C_1(0)\}$.

Now, the following theorem can be stated;

Theorem 3 *(i) μ_2 decides about the Hopf bifurcation direction i.e. when $\mu_2 > 0 or < 0$, the Hopf bifurcation is supercritical or subcritical respectively;*
(ii) β_2 decides about the bifurcated periodic solutions stability i.e. when $\beta_2 > 0 (< 0)$, the bifurcated periodic solutions are stable or unstable.

NUMERICAL RESULTS

The section deals with the numerical simulations by considering assumed set of values for the parameters and the system (6) without migration becomes as;

$$\frac{dx}{dt} = x(1-x) - \frac{0.9xy}{2+2x+x^2}, \frac{dy}{dt} = y[3.5(1 - \frac{2y(t-\tau)}{x(t-\tau)})], \tag{15}$$

The above model is the case when there is no migration in prey as well as in predator population density($m_1 = m_2 = 0$). Dynamics of the system without migration is examined. System (15) with a unique equilibrium point as $(0.08670, 0.032206)$. System (15) is unstable for $\tau = 0.5$ (shown in figure 1). This is the case where only refuge is present and with no migration. Furthermore, the system with migration in both prey and predator population along with refuge is as follows;

$$\frac{dx}{dt} = x(1-x) - \frac{0.9xy}{2+2x+x^2} - 0.6x, \frac{dy}{dt} = y[3.5(1 - \frac{2y(t-\tau)}{x(t-\tau)})] - 0.6y, \tag{16}$$

Now the system is analysed with migration in both populations($m_1 = m_2 = 0.6$) along with the effect of delay. It is to be found that the system with a unique equilibrium point as $(0.377323, 0.412109)$ and using lemma 1, $\omega_{pos} = 2.909$ and $\tau_{cr} = 0.5$. It is to be noted that the equilibrium point $(0.3534, 0.146434)$ is asymptotically stable in the absence of delay τ in accordance with theorem 1. Using theorem 2, it is seen that the system (16) is asymptotically stable for $\tau \in [0, 0.52)$ and unstable for $\tau > 0.52$ with hopf bifurcation occurrence at $\tau = 0.52$(as shown in figure 2 and figure 3).
Further, the dynamics of the system is varied by increasing the value of migration as $m_1 = m_2 = 0.9$ and it is found that the prey population becomes stable for the otherwise unstable system at $\tau = 0.7$ with all other parameters same which depicts the significance of migration in changing the dynamics of the system.stabilising the system(as shown in figure 4). In this case, prey population is showing stable behaviour at the value of $\tau = 0.7$, where otherwise it is unstable.

$$\frac{dx}{dt} = x(1-x) - \frac{0.9xy}{2+2x+x^2} - 0.9x, \frac{dy}{dt} = y[3.5(1 - \frac{2y(t-\tau)}{x(t-\tau)})] - 0.9y, \tag{17}$$

DISCUSSION

In the proposed system, an attempt has been made to study prey predator relationship by incorporating refuge in prey and migration in both the populations using Holling type IV functional response. Much work has been done by inculcating refuge to examine the relationship between prey and predator using various functional responses[6, 8]. At the end, to verify the theoretical results, numerical simulation has been provided and suitable results are attained. System is analysed from the stability prospects and direction of hopf bifurcation is discussed in a concise manner.
In the future prospects, the same model can be enhanced or modified by incorporating the concept of allee effect and studying its role in amending the system dynamics.
In the paper, a delay version of prey-predator system using modified Holling-Tanner functional response is reviewed. In fact, system (15) can be elucidated as a particular case of the proposed system and in model (15), mainly the aspect

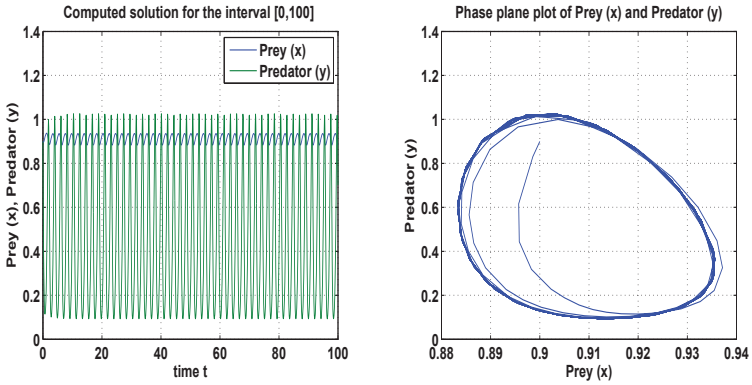

FIGURE 1. Numerical Simulation of the System without migration $m_1 = m_2 = 0$ and $\tau = 0.5$ in the interval [0,100]

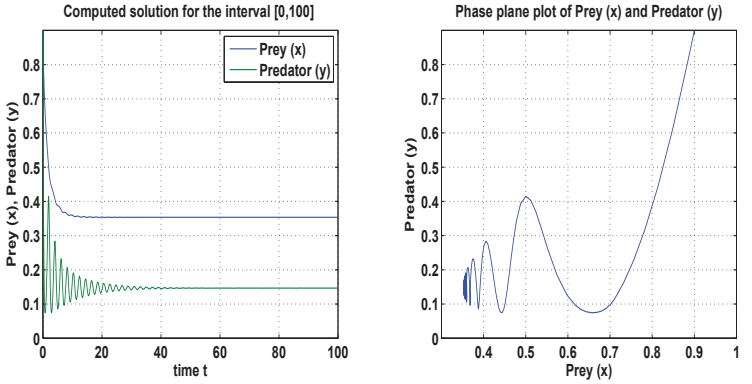

FIGURE 2. Numerical Simulation of the System with migration $m_1 = m_2 = 0.6$ and $\tau = 0.50 < \tau_{cr}$ in the interval [0,100]

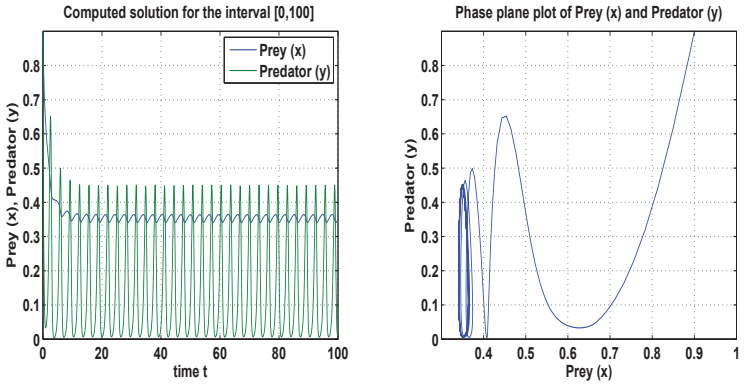

FIGURE 3. Numerical Simulation of System with migration $m_1 = m_2 = 0.6$ and $\tau > \tau_{cr} = 0.7$ in the interval [0,100]

of refuge is considered. Non feasibility of real parameters can be considered as a limitation of our study. Although numerical simulation carried out is consistent with the theoretical results. Also, for the different range of migration parameters(m_1, m_2),the system is analysed to signify its part.

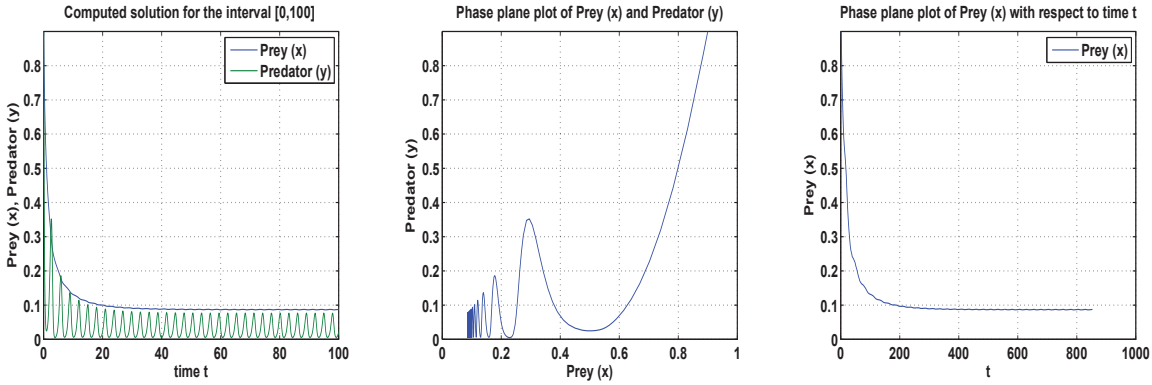

FIGURE 4. Numerical Simulation of the System with migration $m_1 = m_2 = 0.9$ and $\tau = 0.7 > \tau_{cr}$ in the interval [0,100]

REFERENCES

[1] Leslie, PH, Gower, J C: The properties of a stochastic model for the predator-prey type of interaction between two species. Biometrika 47, 219-234 (1960).

[2] Lu , Z, Liu ,X : Analysis of a predator prey model with modified Holling-Tanner functional response and time delay. Nonlinear Anal. Real World Appl. 9, 641-650 (2008). http://www.dx.doi.org/10.1016/j.nonrwa.2006.12.016.

[3] Negi, K., Gakkhar, S., 2007, Dynamics in a Beddington-DeAngelis preypredator system with impulsive harvesting. Ecological Modelling, 206, pp. 421-430.

[4] Naji, R.K., Balasim, A.T., 2007, Dynamical behavior of a three species food chain model with Beddington-DeAngelis functional response. Choas, Solitons and Fractals, 32, pp. 1853-1866.

[5] Zhang ,J-F: Bifurcation analysis of a modified Holling-Tanner predator-prey model with time delay. Applied Mathematical Modeling 36,1219-1231(2012).http://www.dx.doi.org/10.1016/j.apm.2011.07.071.

[6] Charu Arora, Vivek Kumar: Bifurcation Analysis of a Delayed Modified Holling-Tanner Predator-Prey Model with Refuge, Proceedings of International Conference on Mathematics and Computing (ICMC 2017), 246-254. http://www.dx.doi.org/10.1007/978.981.10.4642.1.21.

[7] Hassard B D, Kazarinoff , ND, Wan YH: Theory and Applications of Hopf Bifurcation, Camb. Uni. Press, Cambridge (1981).

[8] Shashi Kant, Vivek Kumar: Delayed prey-predator system with habitat complexity and refuge, Proceedings of International Conference on Mathematical Sciences (ICMS 2014), 584-591(2014). http://www.dx.doi.org/10.13140/2.1.3493.8884.

ResearchGate

See discussions, stats, and author profiles for this publication at: https://www.researchgate.net/publication/319975791

Effective sensitization of Eu 3+ and energy transfer in Sm 3+ /Eu 3+ co-doped ZPBT glasses for CuPc based solar cell and w-LEDs...

Article *in* Journal of Luminescence · September 2017

DOI: 10.1016/j.jlumin.2017.09.049

CITATIONS
0

READS
23

2 authors, including:

Kaushal Jha
Delhi Technological University
10 PUBLICATIONS **70** CITATIONS

SEE PROFILE

Some of the authors of this publication are also working on these related projects:

Synthesis and characterization of Glass and glass-ceramics for opto-electronic applications View project

All content following this page was uploaded by Kaushal Jha on 23 September 2017.

The user has requested enhancement of the downloaded file.

Author's Accepted Manuscript

Effective sensitization of Eu^{3+} and energy transfer in Sm^{3+}/Eu^{3+} co-doped ZPBT glasses for CuPc based solar cell and w-LEDs applications

Kaushal Jha, M. Jayasimhadri

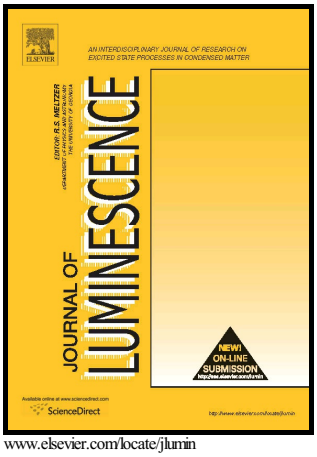

www.elsevier.com/locate/jlumin

PII: S0022-2313(17)31294-2
DOI: http://dx.doi.org/10.1016/j.jlumin.2017.09.049
Reference: LUMIN15057

To appear in: *Journal of Luminescence*

Received date: 25 July 2017
Revised date: 19 September 2017
Accepted date: 19 September 2017

Cite this article as: Kaushal Jha and M. Jayasimhadri, Effective sensitization of Eu^{3+} and energy transfer in Sm^{3+}/Eu^{3+} co-doped ZPBT glasses for CuPc based solar cell and w-LEDs applications, *Journal of Luminescence,* http://dx.doi.org/10.1016/j.jlumin.2017.09.049

This is a PDF file of an unedited manuscript that has been accepted for publication. As a service to our customers we are providing this early version of the manuscript. The manuscript will undergo copyediting, typesetting, and review of the resulting galley proof before it is published in its final citable form. Please note that during the production process errors may be discovered which could affect the content, and all legal disclaimers that apply to the journal pertain.

ACCEPTED MANUSCRIPT

Effective sensitization of Eu^{3+} and energy transfer in Sm^{3+}/Eu^{3+} co-doped ZPBT glasses for CuPc based solar cell and w-LEDs applications

Kaushal Jha, M. Jayasimhadri*

Luminescent Materials Research Lab (LMRL), Department of Applied Physics, Delhi Technological University, Delhi 110 042, India

Abstract:

Sm^{3+}/Eu^{3+} co-doped transparent Zinc Phosphate Barium Titanate (ZPBT) glasses have been successfully prepared via melt quenching technique. The photoluminescence properties and energy transfer mechanisms of these glasses were investigated in detail. The addition of Sm^{3+} as sensitizer expanded the excitation spectrum of Eu^{3+} in the Sm^{3+}/Eu^{3+}co-doped ZPBT glasses. The mechanism for energy transfer from Sm^{3+} to Eu^{3+} was dipole-dipole in nature, which was confirmed by Dexter energy transfer formula and Reisfeld's theory on emission spectra and Inokuti Hirayama (I-H) model on decay curves. The Sm^{3+}/Eu^{3+} co-doped ZPBT glasses reveal the capability to down-convert the n-UV and blue wavelength photons located in the weakest absorption of copper phthalocyanine (CuPc), to red-emitting photons in the optimal absorption of CuPc. The evaluated CIE chromaticity coordinates for the glasses move towards the red region with the increase in Eu^{3+} concentration under n-UV excitation wavelength. The above-mentioned results imply that the Sm^{3+}/Eu^{3+} co-doped ZPBT glasses are the potential candidate for applications in CuPc based solar cells and w-LEDs.

Keywords: Optical Glass, Photoluminescence; Energy transfer; Lifetime

Corresponding author e-mail: jayaphysics@yahoo.com

Accepted manuscript

ACCEPTED MANUSCRIPT

1. Introduction:

In recent years, white light emitting diodes (w-LEDs) have received enormous attention as solid state light sources as they offer characteristics like high brightness, low power consumption and are environment-friendly. At present, w-LEDs are fabricated using single/multitude phosphor with n-UV/blue excitation sources. The approach for w-LEDs fabrication with the combination of RGB (red, green, and blue) phosphors and n-UV LED chips are seeking attention as they offer better CRI, CCT and free from halo effect in comparison to yellow phosphor with the blue LED chip. However, the red phosphor prepared from nitride and sulfide suffers from low chemical stability, low luminous efficiency, and the red phosphor Y_2O_3:Eu^{3+} has intense excitation at 248 nm. Moreover, the quantum efficiency of InGaN LED chip has the maximum value at 400 nm, and "Droop" (where current density drops off) is also absent [1–4]. Therefore, there is an urgent need for red photoluminescent component excitable by n-UV LED chips. Among various activators, the trivalent europium (Eu^{3+}) has gained significant attention due to its emission in the red region upon excitation with the n-UV/blue wavelengths [5,6]. The addition of sensitizer to an activator could extend the excitation region and enhance the emission intensity of activator. Many researchers have successfully expanded the Eu^{3+} excitation by use of suitable sensitizers. Among various sensitizers, Sm^{3+} was found to be the most appropriate sensitizer. The incorporation of Sm^{3+} as the sensitizer enhanced the Eu^{3+} emission in different host matrices. Kang et al. increased the emission intensity by 35% under 410 nm in the $Na_2Y_2Ti_3O_{10}$ host, while Fang et al. revealed the increment in Eu^{3+} emission under 403 nm in $CaLa_2(MoO_4)_4$ host lattice [4,7]. Biju et al. showed the enhancement in Eu^{3+} emission under 402 nm in zinc phosphate glasses [8]. Lin et al. revealed the emission improvement under 482 nm in borate glasses owing to energy transfer from Sm^{3+} to Eu^{3+} [9]. Moreover, the process of energy

Accepted manuscript

ACCEPTED MANUSCRIPT

transfer can be used as a strategy to down convert unused photons of the solar spectrum to red emitting photons, which lie in the absorption region of the organic absorber material copper phthalocyanine (CuPC) [10,11]. The phosphor mentioned above is encapsulated in the organic resin made of polymer. The organic resin gets deteriorated at high temperatures, high power and/or high energy excitations light sources. Therefore, glasses doped with rare earth are preferred over phosphor as they have simpler manufacturing technique, lower production cost, highly durable, excellent thermal and mechanical stability [12–14]. Along with this, glasses serves the purpose of both the encapsulant and wavelength converter and is free from the organic resin.

Among various inorganic glasses, phosphate glasses have been extensively studied as they offer unique characteristics like transparency in the wide spectral region, low melting and softening temperature, and high mechanical and thermal stability. Phosphate glasses provide 1000 times greater rare earth ion solubility than in borate and silicate glasses which make them as an appropriate candidate as a host material for luminescence applications. However, the poor chemical durability and the hygroscopic nature of these glasses are a major limitation for practical applicability in devices. Zinc oxide (ZnO) offers unique properties like low toxicity, non-hygroscopic, direct band gap, low cost, intrinsic emitting property and large exciton binding and makes phosphate glasses moisture resistant due to the formation of P-O-Zn bonds. The addition of BaO to phosphate structure lowers the melting temperature as well as leads to disruption of the glass network. The heavy metal oxide like TiO_2 incorporation to the phosphate glasses significantly improves chemical durability and stabilization of the glass structure [12,14].

Therefore, in the present investigation Sm^{3+}/Eu^{3+} co-doped ZPBT glasses were synthesized for the first time via melt quenching technique and the energy transfer mechanisms were

Accepted manuscript

ACCEPTED MANUSCRIPT

discussed in detail. Furthermore, the efficiency and probability of energy transfer and CIE Chromaticity coordinates were calculated. The aim is to investigate these glasses for applications in the field of optoelectronics.

2. Experimental:

The Glasses were prepared with conventional melt-quenching technique with molar composition as mentioned below:

(1) $39ZnO\text{-}35P_2O_5\text{-}20BaO\text{-}5TiO_2\text{-}XSm_2O_3$ (X=0.1, 0.5, 1.0, 1.5, and 2.0) (Sample name with X= 1 was named as SM01)

(2) $39ZnO\text{-}35P_2O_5\text{-}20BaO\text{-}5TiO_2\text{-}1Eu_2O_3$ (Sample name = EU01)

Along with these two glass samples, a series of glasses doped with Sm_2O_3 and Eu_2O_3 were prepared in the molar composition as follows:

(3) $(39\text{-}X)ZnO\text{-}35P_2O_5\text{-}20BaO\text{-}5TiO_2\text{-}1Sm_2O_3\text{-}XEu_2O_3$

The values for X were 0.50, 1.0, 1.5 and 2.0 and the glasses were named as SE01, SE02, SE03, and SE04, respectively. The starting materials were Analytical Reagent (A.R) grade ZnO, TiO_2, $BaCO_3$, $NH_4H_2PO_4$, high purity Sm_2O_3, and Eu_2O_3. The chemicals were ground in an agate mortar for 1 hour using acetone as the wetting medium. The mixture was then placed in the muffle furnace at 1150 °C for 1 hour, and the melt was then poured on the preheated brass plate and annealed at 400 °C for 3 hours to remove mechanical and thermal stress. Finally, colorless and transparent glasses were obtained. The photoluminescence (PL) properties were measured using Shimadzu RF-5301PC spectrofluorophotometer fitted with xenon flash lamp. The decay analysis was performed using an Edinburgh FLS920, where xenon lamp was excitation source.

Accepted manuscript

ACCEPTED MANUSCRIPT

3. Results and discussion:

3.1 *Photoluminescence properties of Sm^{3+} doped ZPBT glasses*

Fig. 1 represents the excitation and emission spectrum Sm^{3+} doped ZPBT glasses. The excitation spectrum was recorded by monitoring emission at 599 nm. The excitation spectrum reveals several peaks originating from the $^6H_{5/2}$ ground level to different excited levels at 343, 359, 372, 399, 418, 437 and 467 nm corresponding to the $^4H_{9/2}$, $^4D_{3/2}$, $^6P_{7/2}$, $^4F_{7/2}$, $^6P_{5/2}$, $^4G_{9/2}$, and $^4I_{11/2}$ +$^4I_{13/2}$+$^4M_{15/2}$ transitions of Sm^{3+} ions, respectively. The emission spectra under different excitations (λ_{ex} = 399 and 467 nm) revealed three emission bands centered at 563, 599 and 645 nm corresponding to $^4G_{5/2}\rightarrow{}^6H_{5/2}$, $^4G_{5/2}\rightarrow{}^6H_{7/2}$, and $^4G_{5/2}\rightarrow{}^6H_{9/2}$ transitions, respectively. The $^4G_{5/2}\rightarrow{}^6H_{5/2}$ is magnetic dipole (MD) transition in nature following the selection rules ($\Delta J=0, \pm1$; J is angular momentum), whereas $^4G_{5/2}\rightarrow{}^6H_{9/2}$ is attributed to forced electric dipole (ED) transition following the selection rule ($\Delta J\leq6$; J or J´=0, when J=2, 4, and 6). The MD transition is insensitive to the crystal environment whereas forced ED transition is hypersensitive in nature, and the emission intensity of this transition gets strongly affected by the crystal field of the ligand atoms. The $^4G_{5/2}\rightarrow{}^6H_{7/2}$ transition arose due to both the MD and forced ED transition [15,16]. The intensity ratio of forced ED to MD transition indicate about the symmetry of environment around the rare earth. In the present case, the MD transition is more intense than ED transition which suggests that there is no deviation from the inversion symmetry. The emission intensity of the Sm^{3+} doped ZPBT glasses increased up to 1 mol % and decreased after that as shown in the inset of Fig. 1. The decrease in the emission intensity arises due to the concentration quenching phenomenon [17].

3.2 Photoluminescence properties of Sm^{3+}/Eu^{3+} co-doped ZPBT glasses:

Accepted manuscript

ACCEPTED MANUSCRIPT

Fig. 2 compares the excitation spectrum of EU01 and SE04 (1 mol% of Eu^{3+} and 2 mol% Sm^{3+}/Eu^{3+} co-doped ZPBT glasses) by monitoring emission at 613 nm. The emission at 613 nm is due to Eu^{3+}, but the excitation spectrum for the Sm^{3+}/Eu^{3+} co-doped ZPBT glass revealed peaks of Sm^{3+} also in addition to that of Eu^{3+}. The peaks at 343, 399, 437 and 473 nm are associated with Sm^{3+} as discussed previously, and the peaks at 360, 381, 392, 412, and 462 nm are attributed to $^7F_0 \rightarrow {}^5D_4$, $^7F_0 \rightarrow {}^5L_7$, $^7F_0 \rightarrow {}^5L_6$, $^7F_0 \rightarrow {}^5D_3$, and $^7F_0 \rightarrow {}^5D_2$ transitions, respectively of Eu^{3+} [18]. A few reports on the Sm^{3+} doped and Eu^{3+} doped glasses have been examined and revealed the excitation peaks of either Sm^{3+} or Eu^{3+} ions [19–24]. However, in the present case, the excitation spectrum of Eu^{3+} is extended and also enhanced the emission intensity by co-doping Sm^{3+}. Therefore, the introduction of Sm^{3+} has revealed the sensitization effect on Eu^{3+} in the Sm^{3+}/Eu^{3+} co-doped ZPBT glasses. The emission spectra of the co-doped ZPBT glasses i.e. Sm^{3+} (1 mol%) and Eu^{3+} (0.0, 0.5, 1.0, 1.5 and 2.0 mol%) under 399 nm are represented in Fig. 3. For 1 mol% Sm^{3+} doped ZPBT glasses under 399 nm, which matches well with excitation the n-UV LED chips, emission peaks due to only Sm^{3+} was observed at 563, 599 and 645 nm as discussed previously. When Eu^{3+} is co-doped with Sm^{3+}, in addition to Sm^{3+} peaks, Eu^{3+} emission peaks were also observed at 577, 591, 613, 655, and 701 nm corresponding to the transition arising from $^5D_0 \rightarrow {}^7F_0$, $^5D_0 \rightarrow {}^7F_1$, $^5D_0 \rightarrow {}^7F_2$, $^5D_0 \rightarrow {}^7F_3$, and $^5D_0 \rightarrow {}^7F_4$, respectively. The $^5D_0 \rightarrow {}^7F_2$ is forced ED transition which is hypersensitive in nature, and the emission intensity of this transition is strongly affected by the crystal field of ligand atoms. While the $^5D_0 \rightarrow {}^7F_1$ is MD transition which is insensitive to the crystal environment. The peak due to Sm^{3+} and Eu^{3+} at 645 and 655 nm are merged into one and hence not distinguishable. As the concentration of the Eu^{3+} is increased, the intensity of peaks due to Eu^{3+} is enhanced while that of Sm^{3+} are diminished. The decrease in the Sm^{3+} emission intensity with increase in Eu^{3+} concentration may be due to

Accepted manuscript

ACCEPTED MANUSCRIPT

the energy transfer from Sm^{3+} to Eu^{3+} [25,26]. The inset of Fig. 3 represents the comparison between the emission observed for SE04 (1 mol% Sm^{3+} and 2 mol % Eu^{3+} co-doped ZPBT glass) under both n-UV (399 nm) and blue (467 nm) excitation wavelengths. The emission spectra revealed all the peaks under both the excitations at the same position with variation in intensity. The intense excitation peaks (399 and 467 nm) for Sm^{3+}/Eu^{3+} co-doped ZPBT glasses lies in the weakest absorption of the region of CuPc solar cells. The above mentioned results indicate that Sm^{3+}/Eu^{3+} co-doped glasses has the capability to down-convert the photons in the n-UV and blue regions of the spectrum to red and orange region which is the strongest absorption region for CuPc based solar cells [11,27]. Hence, Sm^{3+}/Eu^{3+} co-doped ZPBT glasses can be placed on top of the CuPc based organic solar cells to down-convert the n-UV/blue and can lead to enhance the efficiency of the CuPc solar cells.

The energy transfer between rare-earth ions may take place by two interaction mechanisms: multipolar interaction and exchange interaction. Exchange interaction occurs only when the sensitizer/donor and the activator/acceptor are suited at the nearest neighbour positions. The interaction in Sm^{3+}/Eu^{3+} doped ZPBT glasses focuses on the mechanism of the multipolar interaction. To investigate the type of multipolar interaction, Dexter's energy transfer formula for multipolar interaction and Reisfeld's approximation was applied, as per the following equation [28]:

$$\frac{\eta_0}{\eta} \propto C^{n/3} \quad (1)$$

where η_0 and η are the luminescent quantum efficiency of the Sm^{3+} in the absence and presence of the Eu^{3+}, C is the sum of the mole percent of Sm^{3+} and Tb^{3+}, and the value of n is 6, 8 and 10 corresponding to dipole-dipole, dipole-quadrupole and quadrupole-quadrupole interaction,

Accepted manuscript

ACCEPTED MANUSCRIPT

respectively. The η_0/η value can be approximately estimated by the ratio of related luminescence intensities as:

$$\frac{I_{s0}}{I_s} \propto C^{n/3} \quad (2)$$

where I_{s0} is the intrinsic emission intensity of Sm^{3+} and I_s is the emission intensity of Sm^{3+} in the presence of Eu^{3+}. The graph was plotted between I_{s0}/I_s versus $C^{n/3}$ and the best fit was obtained for n=6 under 399 nm excitation as represented in Fig. 4. The value of n=6 suggests that the energy is transferred from the Sm^{3+} to Eu^{3+} due to the non-radiative dipole-dipole interaction.

The phenomenon of energy transfer process was studied on the basis of energy level diagram as presented in Fig. 5. In case of SM01 and EU01 glass samples, the excitation energy is absorbed by the rare earth ions (Sm^{3+} and Eu^{3+}), which in turns excites the electron from the ground state to the higher excited state. The excited electrons then rapidly falls to the lower energy states (Sm^{3+}:$^4G_{5/2}$ and Eu^{3+}:$^5D_0$) by non-radiative relaxation, and then relaxes to the lower states (Sm^{3+}:^6H_J (J=5/2, 7/2 and 9/2) and Eu^{3+}:^7F_J (J= 0 to 4)) liberating energy in the form of visible emission. The $^4G_{5/2}$ energy level of Sm^{3+} is 638 cm^{-1} higher than the $^5D_0$ energy level of Eu^{3+}. Therefore, it is possible that a part of the energy from Sm^{3+} is non-radiatively transferred to the Eu^{3+}, which results in decrement of Sm^{3+} emission as indicated in Fig. 3. The smaller energy difference between the $^4G_{5/2}$ and $^5D_0$ makes the energy transfer possible via phonon assisted non-radiative transition, which suggests that Sm^{3+} act as efficient sensitizer/donor for the Eu^{3+}.

3.3 Decay analysis and energy transfer efficiency/probability:

The decay profiles for different glasses (SM01, SE01, SE02, SE03 and SE04) were recorded by monitoring emission at 599 nm corresponding to $^4G_{5/2} \rightarrow {}^6H_{7/2}$ transition under the excitation of 399 nm as represented in Fig. 6. The decay curves were fitted with different

Accepted manuscript

ACCEPTED MANUSCRIPT

exponential equations and the best fit was obtained for bi-exponential equation as represented below [14]:

$$I = I_0 + A_1 exp\left(-\frac{t}{\tau_1}\right) + A_2\, exp\left(-\frac{t}{\tau_2}\right) \quad (4)$$

where I and I_0 are the luminescence intensities at time t and 0, τ_1 and τ_2 are the components of the lifetime, corresponding to the fast and slow lifetimes, respectively; A_1 and A_2 are the fitting constant, and t is the time. The average value of lifetime can be calculated for the bi-exponential as given by equation:

$$\tau_{avg} = \frac{A_1\tau_1^2 + A_2\tau_2^2}{A_1\tau_1 + A_2\tau_2} \quad (5)$$

The average lifetime values for SM01, SE01, SE02, SE03 and SE04 are represented in Table 1. A deeper insight on the process of energy transfer can be estimated from the lifetime values. It can be observed from Table 1, that the value of lifetime decreases with an increase in the Eu^{3+} concentration, which is a strong evidence of energy transfer from Sm^{3+} to Eu^{3+}. The energy transfer efficiency (η_T) value can be calculated from the equation as mentioned below [29]:

$$\eta_{T(Tb\rightarrow Sm)} = 1 - \left(\frac{\tau_d}{\tau_{d0}}\right) \quad (6)$$

The energy transfer probability rate in terms of lifetime can be expressed by the equation:

$$P_{T(Tb\rightarrow Sm)} = \frac{1}{\tau_d} - \frac{1}{\tau_{d0}} \quad (7)$$

where, τ_{d0} and τ_d are the decay time of the Sm^{3+} in the absence of the Eu^{3+} and in the presence of the Eu^{3+}, respectively. The values of the energy transfer efficiencies (η_T) and energy transfer probabilities (P_T) are represented in the Table 1. A graph showing variation in lifetime values and energy transfer efficiencies with increasing Eu^{3+} concentration is presented in Fig. 7. The

Accepted manuscript

ACCEPTED MANUSCRIPT

value of both η_T and P_T increase with an increase in the Eu^{3+} concentration, indicating that with the increase in Eu^{3+} concentration more energy is transferred from Sm^{3+} to Eu^{3+}.

The type of multipolar interaction can be obtained from decay curves by applying Inokuti-Hirayama (I-H) model. It gives a deeper insight on the type of interaction involved in the energy transfer process from the donor to acceptor. The decay of the luminescence given by equation [17,30]:

$$I_t = I_0 \exp\left\{\frac{-t}{\tau_0} - Q\left(\frac{t}{\tau_0}\right)^{\frac{3}{s}}\right\} \quad (8)$$

where, I_o the luminescence intensity at time t=0, I_t is the luminescence intensity at time t, t is time after excitation, Q is the energy transfer parameter, τ_0 is the intrinsic donor decay time in the absence of the acceptor. S is the multipole effect and takes the value 6, 8 and 10 for dipole-dipole, dipole-quadrupole and quadrupole-quadrupole interaction, respectively.

$$Q = \frac{4\pi}{3}\Gamma\left(1 - \frac{3}{s}\right).N_0.R_0^3 \quad (9)$$

where, Γ is gamma function, N_0 is the acceptor ion concentration and R_0 is the critical transfer distance, which is defined as the donor–acceptor separation when rate of energy transfer between a donor and acceptor ion is equal to the rate of intrinsic decay rate (τ_0^{-1}). The type of multipolar interaction was identified by fitting the decay curve for SE04 glass sample for different values of S=6, 8 and 10 and the best fit was obtained for S=6 as shown in Fig. 8 (a) and (b) represents the decay curve for SM01, SE01, SE02, SE03 and SE04 glass samples fitted with S=6. The results of the I-H model indicates that the interaction is dipole-dipole in nature and is in accordance with the Dexter energy transfer formula and Reisfeld's approximation. The donor–acceptor interaction parameter C_{DA} is calculated by the using the expression as mentioned below:

Accepted manuscript

ACCEPTED MANUSCRIPT

$$C_{DA} = R_0.\tau_0^{-1} \quad (10)$$

where, R_0 is critical energy transfer distance. The values of Q, R_0 and C_{DA} are given in Table 1. It can be observed that the Q value increases from 0.448 to 1.287, indicating that the dipole-dipole interaction becomes more dominant with increasing Eu^{3+} concentration. The values of C_{DA} and R_0 also increases with increasing concentration of Eu^{3+} concentration [31,32].

The CIE chromaticity coordinates calculated from emission spectra for SM01, SE01, SE02, SE03 and SE04 glass sample under 399 nm excitation are presented in Fig. 9, respectively and tabulated in Table 1. Under the excitation of 399 nm, it is observed that with increase in concentration of Eu^{3+}, the chromaticity coordinates shift towards the red region, which is due to the enhancement in the emission peak of Eu^{3+} due to efficient energy transfer from Sm^{3+} to Eu^{3+}. The CIE chromaticity coordinates for SE04 are (0.614, 0.384) under n-UV excitation and is close to the commercial available $Y_2O_2S:Eu^{3+}$ (0.647, 0.343) [12]. The CIE chromaticity coordinates values suggest the utility of Sm^{3+}/Eu^{3+} co-doped ZPBT glasses as the red fluorescent component for w-LEDs.

4. Conclusions:

A series of Sm^{3+}/Eu^{3+} co-doped transparent ZPBT glasses have been successfully prepared via melt quenching technique. The Sm^{3+} doped glasses show dominant emission at 599 nm corresponding to $^4G_{5/2} \rightarrow {}^6H_{7/2}$ transition, while Eu^{3+} doped glasses revealed strongest emission at 613 nm corresponding to $^5D_0 \rightarrow {}^7F_2$ transition. The energy transfer mechanism from Sm^{3+} to Eu^{3+} was dipole-dipole in nature, which was confirmed by applying Dexter energy transfer formula and Reisfeld's theory on emission spectra and I-H model on decay curves. The excitation spectrum for Sm^{3+}/Eu^{3+} co-doped ZPBT glasses of Eu^{3+} was expanded by addition of Sm^{3+} as a

Accepted manuscript

ACCEPTED MANUSCRIPT

sensitizer. The emission spectra of Sm^{3+}/Eu^{3+} co-doped ZPBT glasses revealed the down-conversion capability of the n-UV and blue wavelength photons located in the weakest absorption of copper phthalocyanine (CuPc) to red-emitting photons lying in the optimal absorption of CuPc. The calculated CIE chromaticity coordinates under n-UV excitation moves towards red region with increase in the Eu^{3+} concentration. These results strongly suggests the effective applicability of Sm^{3+}/Eu^{3+} co-doped ZPBT glasses as a potential candidate for CuPc based solar cells and n-UV/blue LED chips based w-LEDs.

Acknowledgements

Kaushal Jha is grateful to the University Grants Commission (UGC) for providing financial support in the form of senior Research Fellowship (SRF). The author (M. Jayasimhadri) is grateful to DST-SERB, Govt. of India for the sanction of a research project (No. SB/FTP/PS-082/2014, dt. 02/03/2015).

References:

[1] R. Xie, N. Hirosaki, M. Mitomo, K. Takahashi, K. Sakuma, R. Xie, N. Hirosaki, M. Mitomo, Highly efficient white-light-emitting diodes fabricated with short-wavelength yellow oxynitride phosphors, 101104 (2011) 2004–2007.

[2] J.S. Kim, P.E. Jeonny, J.C. Choi, H.L. Park, S.I. Mho, G.C. Kim, Warm-white-light emitting diode utilizing a single-phase full-color $Ba_3MgSi_2O_8:Eu^{2+}$, Mn^{2+} phosphor, Appl. Phys. Lett. 84 (2004) 2931–2933.

[3] H. Masai, Y. Yamada, Y. Suzuki, K. Teramura, Y. Kanemitsu, T. Yoko, Narrow energy gap between triplet and singlet excited states of Sn^{2+} in borate glass., Sci. Rep. 3 (2013) 3541.

Accepted manuscript

ACCEPTED MANUSCRIPT

[4] D. Kang, H.S. Yoo, S.H. Jung, H. Kim, D.Y. Jeon, Synthesis and Photoluminescence Properties of a Novel Red-Emitting $Na_2Y_2Ti_3O_{10}$:Eu^{3+},Sm^{3+} Phosphor for White-Light-Emitting Diodes, J. Phys. Chem. C. 115 (2011) 24334–24340.

[5] Y. Tian, B. Chen, B. Tian, R. Hua, J. Sun, L. Cheng, H. Zhong, X. Li, J. Zhang, Y. Zheng, T. Yu, L. Huang, Q. Meng, Concentration-dependent luminescence and energy transfer of flower-like $Y_2(MoO_4)_3$:Dy^{3+} phosphor, J. Alloys Compd. 509 (2011) 6096–6101.

[6] Y. Tian, B. Chen, R. Hua, J. Sun, L. Cheng, H. Zhong, X. Li, J. Zhang, Y. Zheng, T. Yu, L. Huang, H. Yu, Optical transition, electron-phonon coupling and fluorescent quenching of $La_2(MoO_4)_3$:Eu^{3+} phosphor, J. Appl. Phys. 109 (2011) 53511.

[7] Y.-C. Fang, S.-Y. Chu, P.-C. Kao, Y.-M. Chuang, Z.-L. Zeng, Energy Transfer and Thermal Quenching Behaviors of $CaLa_2(MoO_4)_4$:Sm^{3+},Eu^{3+} Red Phosphors, J. Electrochem. Soc. 158 (2011) J1.

[8] P.R. Biju, G. Jose, V. Thomas, V.P.N. Nampoori, N.V. Unnikrishnan, Energy transfer in Sm^{3+}:Eu^{3+} system in zinc sodium phosphate glasses, Opt. Mater. 24 (2004) 671–677.

[9] S. Sailaja, C. Nageswara Raju, C. Adinarayana Reddy, B. Deva Prasad Raju, Y.-D. Jho, B. Sudhakar Reddy, Optical properties of Sm^{3+}-doped cadmium bismuth borate glasses, J. Mol. Struct. 1038 (2013) 29–34.

[10] A.N. Meza-Rocha, A. Speghini, M. Bettinelli, U. Caldiño, Orange and reddish-orange light emitting phosphors: Sm^{3+} and Sm^{3+}/Eu^{3+} doped zinc phosphate glasses, J. Lumin. 167 (2015) 305–309.

[11] X. Min, Z. Huang, M. Fang, Y.-G. Liu, C. Tang, X. Wu, Energy Transfer from Sm^{3+} to

Accepted manuscript

ACCEPTED MANUSCRIPT

Eu $^{3+}$ in Red-Emitting Phosphor $LaMgAl_{11}O_{19}:Sm^{3+}$, Eu^{3+} for Solar Cells and Near-Ultraviolet White Light-Emitting Diodes, Inorg. Chem. 53 (2014) 6060–6065.

[12] K. Jha, M. Jayasimhadri, Structural and emission properties of Eu^{3+} -doped alkaline earth zinc-phosphate glasses for white LED applications, J. Am. Ceram. Soc. 100 (2017) 1402–1411.

[13] A.K. Vishwakarma, K. Jha, M. Jayasimhadri, A.S. Rao, K. Jang, B. Sivaiah, D. Haranath, Red light emitting $BaNb_2O_6:Eu^{3+}$ phosphor for solid state lighting applications, J. Alloys Compd. 622 (2015) 97–101.

[14] K. Jha, M. Jayasimhadri, Spectroscopic investigation on thermally stable Dy3+ doped zinc phosphate glasses for white light emitting diodes, J. Alloys Compd. 688 (2016) 833–840.

[15] A.K. Vishwakarma, M. Jayasimhadri, Pure orange color emitting Sm^{3+} doped BaNb2O6 phosphor for solid - state lighting applications, J. Lumin. 176 (2016) 112–117.

[16] A. Mohan Babu, B.C. Jamalaiah, T. Sasikala, S.A. Saleem, L. Rama Moorthy, Absorption and emission spectral studies of Sm^{3+}-doped lead tungstate tellurite glasses, J. Alloys Compd. 509 (2011) 4743–4747.

[17] S. N Rasool, L. R Moorthy, C.K. Jayasankar, Spectroscopic Investigation of Sm3+ doped phosphate based glasses for reddish-orange emission, Opt. Commun. 311 (2013) 156–162.

[18] W. Zhang, S. Ouyang, Z. Zhang, Y. Zhang, H. Xia, Luminescent properties of Eu^{3+}-doped glass ceramics containing $BaGdF_5$ nanocrystals under NUV-excitation for W-LEDs, Ceram. Int. 41 (2015) 14035–14040.

[19] F. Zaman, J. Kaewkhao, G. Rooh, N. Srisittipokakun, H.J. Kim, Optical and luminescence

Accepted manuscript

ACCEPTED MANUSCRIPT

properties of Li_2O-Gd_2O_3-MO-B_2O_3-Sm_2O_3 (MO=Bi_2O_3, BaO) glasses, J. Alloys Compd. 676 (2016) 275–285.

[20] N. Wantana, S. Kaewjaeng, S. Kothan, H.J. Kim, J. Kaewkhao, Energy transfer from Gd3+ to Sm3+ and luminescence characteristics of CaO–Gd_2O_3–SiO_2–B_2O_3 scintillating glasses, J. Lumin. 181 (2017) 382–386.

[21] P. Meejitpaisan, S. Insiripong, C. Kedkaew, H.J. Kim, J. Kaewkhao, Radioluminescence and optical studies of gadolinium calcium phosphate oxyfluoride glasses doped with Sm^{3+}, Radiat. Phys. Chem. 137 (2017) 62–67.

[22] J. Rajagukguk, J. Kaewkhao, M. Djamal, R. Hidayat, Suprijadi, Y. Ruangtaweep, Structural and optical characteristics of Eu^{3+} ions in sodium-lead-zinc-lithium-borate glass system, J. Mol. Struct. 1121 (2016) 180–187.

[23] J. Kaewkhao, K. Boonin, P. Yasaka, H.J. Kim, Optical and luminescence characteristics of Eu^{3+} doped zinc bismuth borate (ZBB) glasses for red emitting device, Mater. Res. Bull. 71 (2015) 37–41.

[24] E. Kaewnuam, H.J. Kim, C.K. Jayasankar, N. Chanthima, J. Kaewkhao, The photoluminescence, optical and physical properties of Sm^{3+}-doped lithium yttrium borate glasses, Phys. Chem. Glas. Eur. J. Glas. Sci. Technol. Part B. 57 (2016) 85–89.

[25] Y. Jin, Z. Hao, X. Zhang, Y. Luo, X. Wang, J. Zhang, Dynamical processes of energy transfer in red emitting phosphor $CaMoO_4$:Sm^{3+}, Eu^{3+}, Opt. Mater. 33 (2011) 1591–1594.

[26] Z. Wang, P. Li, Z. Yang, Q. Guo, Luminescence and energy transfer of Sm^{3+} and Eu^{3+} in Ca_2PO_4Cl, J. Lumin. 151 (2014) 170–175.

Accepted manuscript

ACCEPTED MANUSCRIPT

[27] H.-Y. Lin, Y.-C. Fang, S.-Y. Chu, Energy Transfer Sm^{3+}→Eu^{3+} in Potential Red Phosphor (Ca, Ba)$_3$(VO_4)$_2$:Sm^{3+}, Eu^{3+} for Use in Organic Solar Cells and White Light-Emitting Diodes, J. Am. Ceram. Soc. 93 (2010) 3850–3856.

[28] G. Li, D. Geng, M. Shang, C. Peng, Z. Cheng, J. Lin, Tunable luminescence of Ce^{3+}/Mn^{2+}-coactivated $Ca_2Gd_8(SiO_4)_6O_2$ through energy transfer and modulation of excitation: potential single-phase white/yellow-emitting phosphors, J. Mater. Chem. 21 (2011) 13334.

[29] W.J. Yang, L. Luo, T.M. Chen, N.S. Wang, Luminescence and energy transfer of Eu- and Mn-coactivated $CaAl_2Si_2O_8$ as a potential phosphor for white-light UVLED, Chem. Mater. 17 (2005) 3883–3888.

[30] M. Inokuti, F. Hirayama, Influence of Energy Transfer by the Exchange Mechanism on Donor Luminescence, J. Chem. Phys. 43 (1965) 1978.

[31] S. Mahamuda, K. Swapna, M. Venkateswarlu, A. Srinivasa Rao, S. Shakya, G. Vijaya Prakash, Spectral characterisation of Sm^{3+} ions doped Oxy-fluoroborate glasses for visible orange luminescent applications, J. Lumin. 154 (2014) 410–424.

[32] R. Shi, J. Xu, G. Liu, X. Zhang, W. Zhou, F. Pan, Y. Huang, Y. Tao, H. Liang, Spectroscopy and Luminescence Dynamics of Ce^{3+} and Sm^{3}+ in in $LiYSiO_4$, 120 (2016) 4529–4537.

Accepted manuscript

ACCEPTED MANUSCRIPT

Figure Captions:

Fig. 1. Excitation spectrum of SM01 glass by monitoring emission at 599 nm and emission spectrum under 399 excitation. (Inset: Represents variation in emission intensity of 599 nm peak with different Sm^{3+} concentration in ZPBT glasses)

Fig. 2. Excitation Spectra of EU01 and SE04 glasses by monitoring emission at 613 nm.

Fig. 3. Emission spectra of SM01, SE01, SE02, SE03, and SE04 glasses under 399 nm excitation. (Inset: Represents emission spectra of SE04 glass under 399 and 467 nm excitation)

Fig. 4. Dependence of I_{s0}/I_s of Sm^{3+} on $C_{Tb+Sm}^{6/3}$ x 10^4, $C_{Tb+Sm}^{8/3}$ x 10^5, $C_{Tb+Sm}^{10/3}$ x 10^6 of SM01, SE01, SE02, SE03, and SE04 glasses for 399 nm excitation.

Fig. 5. Energy level diagram showing energy transfer involved in Sm^{3+}/ Eu^{3+} co-doped ZPBT glasses.

Fig. 6. Decay profiles of SM01, SE01, SE02, SE03, and SE04 glasses under excitation of 399 nm fitted with bi-exponential equation.

Accepted manuscript

ACCEPTED MANUSCRIPT

Fig. 7. Variation of average decay time, energy transfer efficiency of Sm^{3+}/Eu^{3+} co-doped ZPBT glasses with Eu^{3+} concentration under 399 nm excitation.

Fig. 8. (a) Decay profiles fitted by I-H model (S=6, 8 and 10) for SE04 glasses and (b) Decay profiles fitted with I-H model (S=6) for SM01, SE01, SE02, SE03, and SE04 glasses under 399 nm excitation.

Fig. 9. CIE diagram representing chromaticity coordinates for SM01, SE01, SE02, SE03, and SE04 glasses under 399 nm excitation.

Accepted manuscript

ACCEPTED MANUSCRIPT

Table 1. Average lifetime (τ_{avg}), Energy transfer efficiency (η_T), Energy transfer probability rate (P_T), energy transfer parameter (Q), critical transfer distance (R_0), donor–acceptor interaction parameter (C_{DA}) and CIE chromaticity coordinates.

Sample name	τ_{avg} **(ms)**	η_T **(%)**	P_T	**Q**	**Ro (Å)**	C_{DA} **(10^{-44} cm^6s^{-1})**	**CIE Chromaticity coordinates**	
							Excitation wavelength	
							399 nm	**467 nm**
SM01	1.97	0.00	0.000	-	-	-	(0.570, 0.428)	(0.594, 0.398)
SE01	1.85	6.22	0.028	0.694	2.023	3.540	(0.578, 0.418)	(0.609, 0.382)
SE02	1.70	12.38	0.072	0.919	2.728	6.314	(0.584, 0.410)	(0.618, 0.372)
SE03	1.52	21.64	0.142	1.023	3.313	12.601	(0.595, 0.402)	(0.629, 0.365)
SE04	1.20	38.14	0.317	1.287	4.292	19.237	(0.614, 0.384)	(0.636, 0.357)

Accepted manuscript

ACCEPTED MANUSCRIPT

Fig. 1

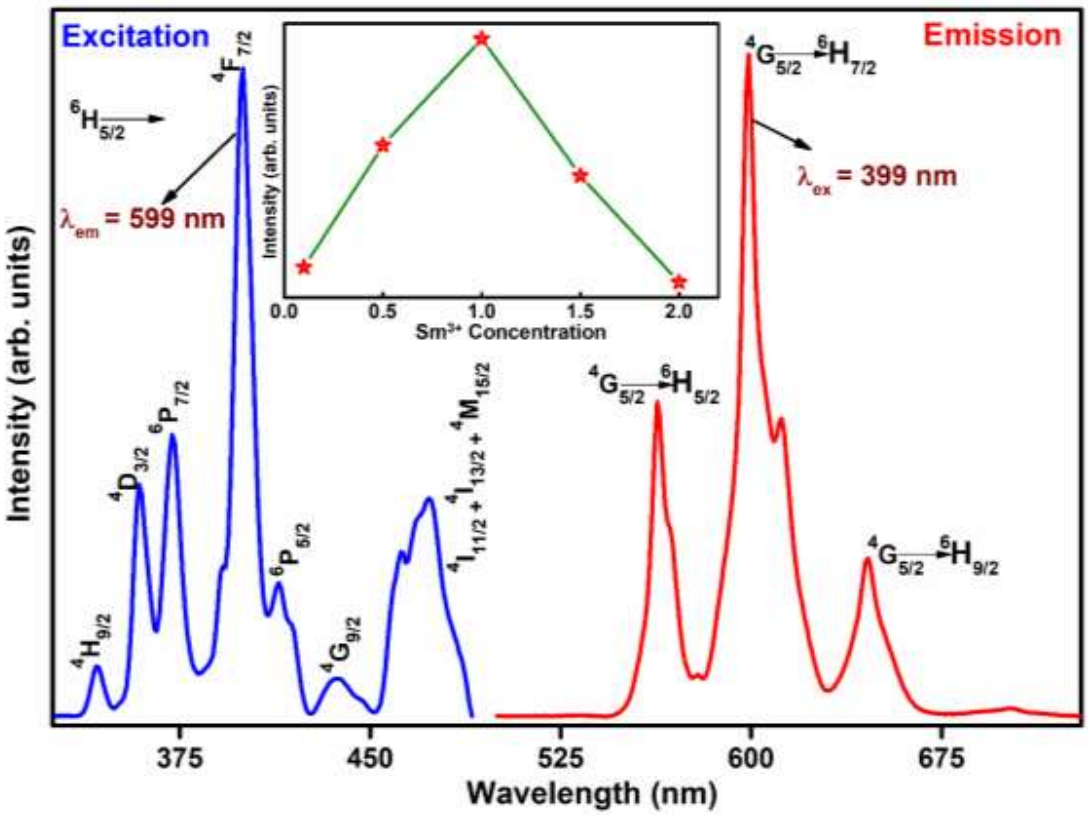

Accepted

ACCEPTED MANUSCRIPT

Fig. 2

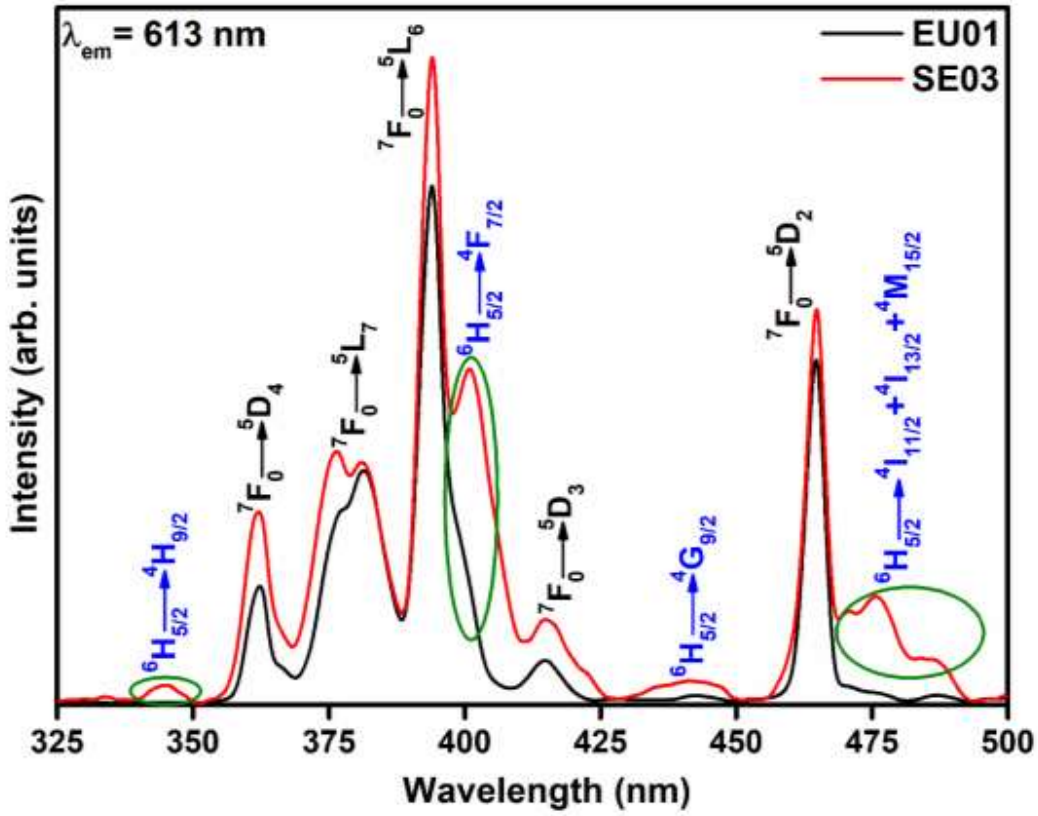

Accepted

ACCEPTED MANUSCRIPT

Fig. 3

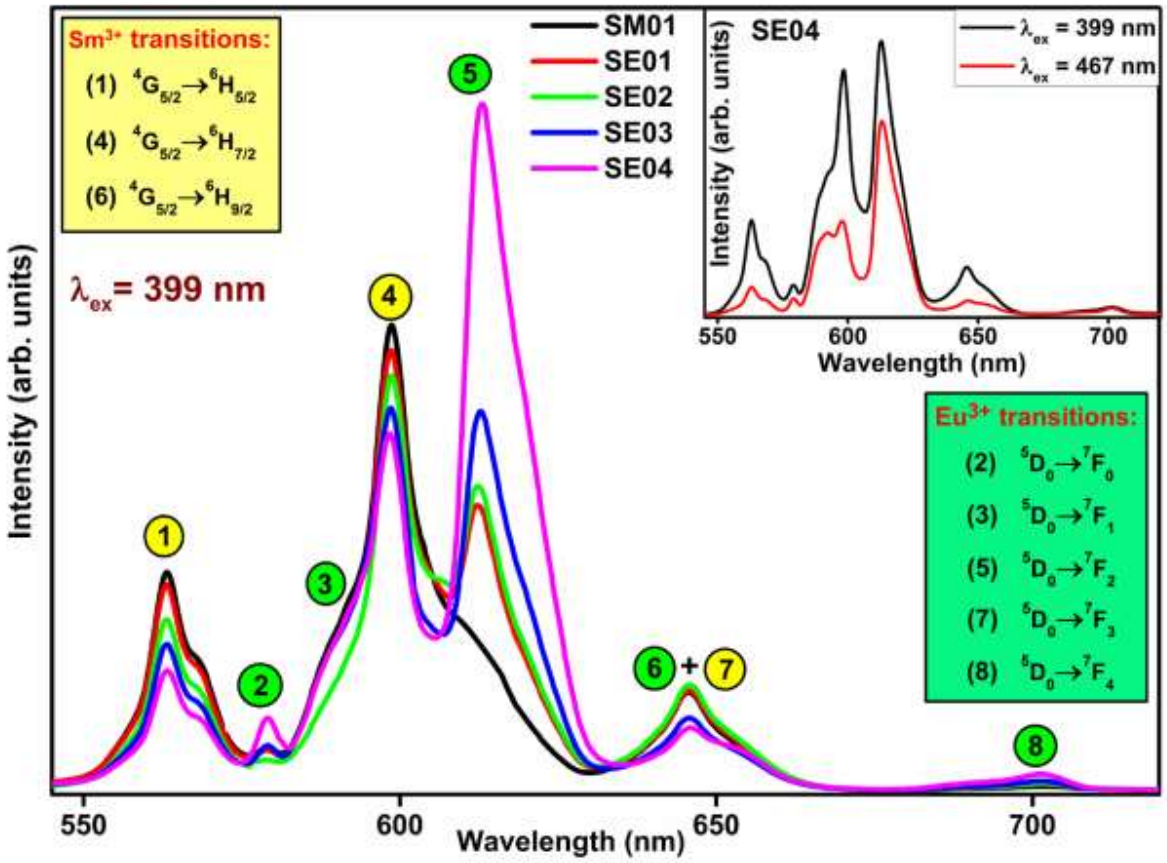

Accepted

ACCEPTED MANUSCRIPT

Fig. 4

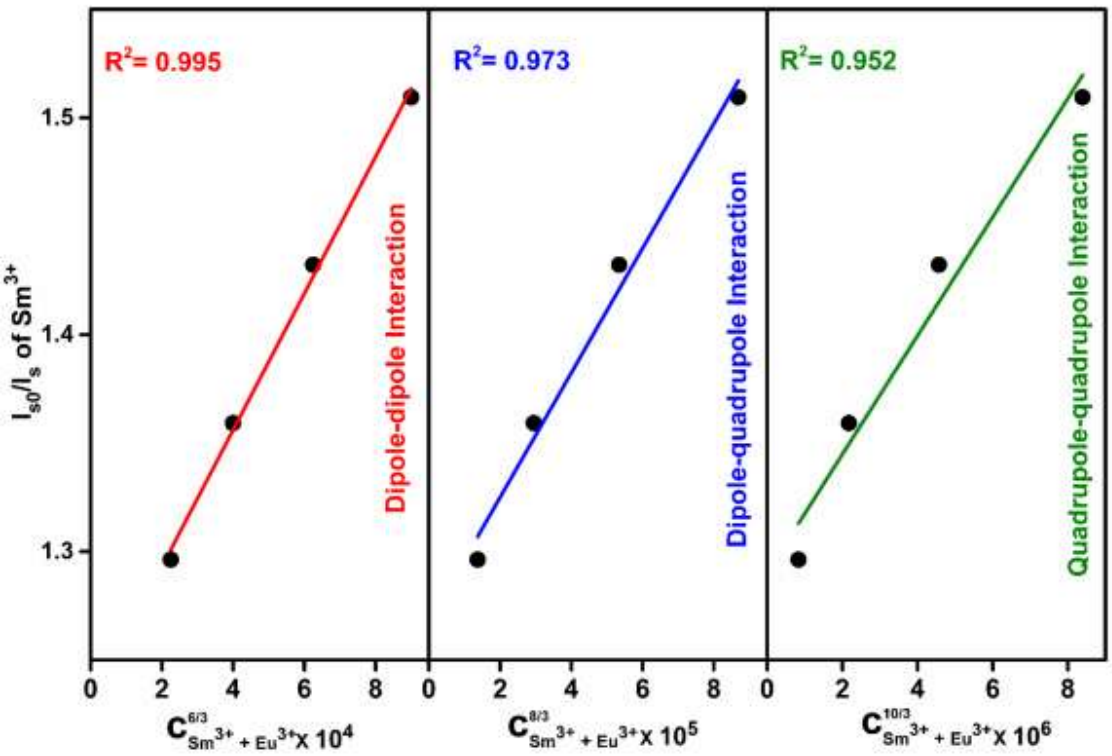

Accepted M

ACCEPTED MANUSCRIPT

Fig. 5

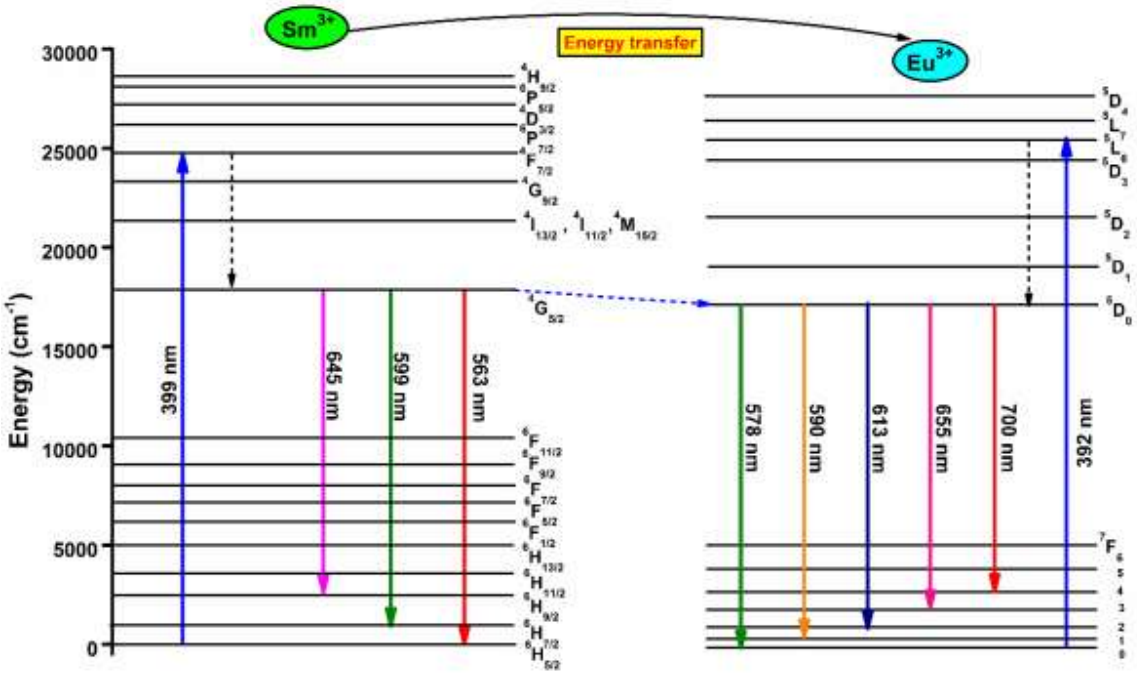

Accepted manuscript

ACCEPTED MANUSCRIPT

Fig. 6

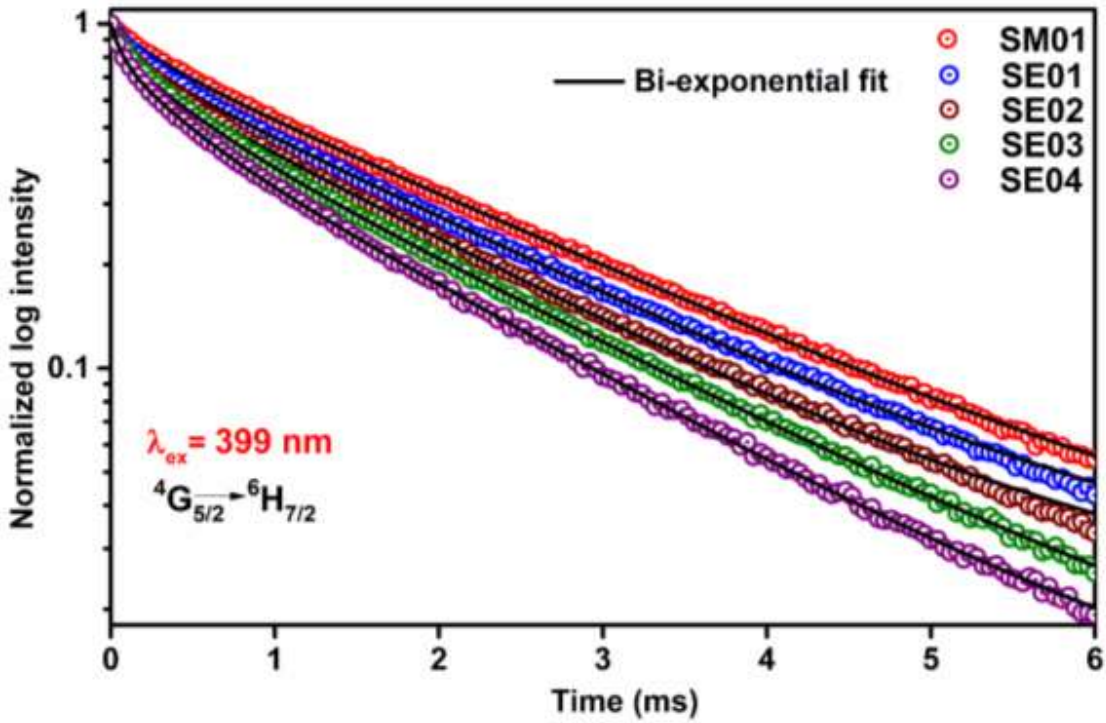

Accepted

ACCEPTED MANUSCRIPT

Fig. 7

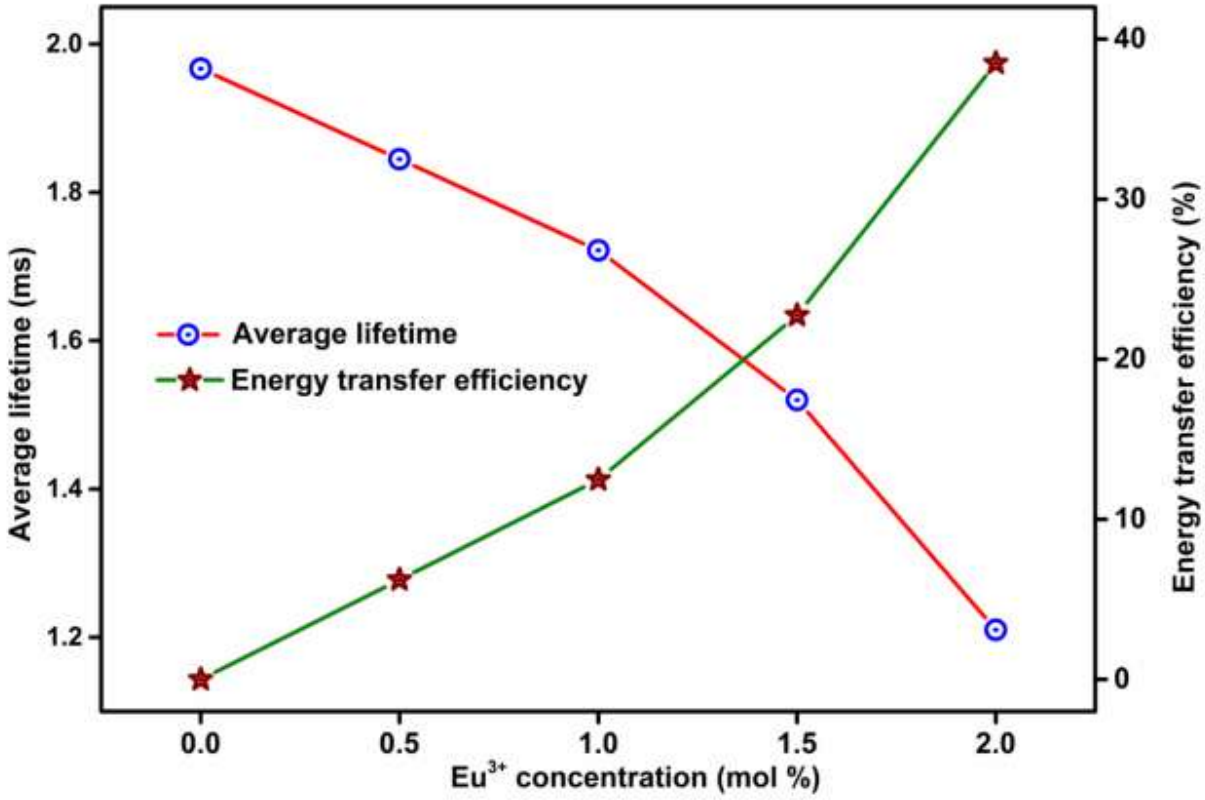

Accepted

ACCEPTED MANUSCRIPT

Fig. 8

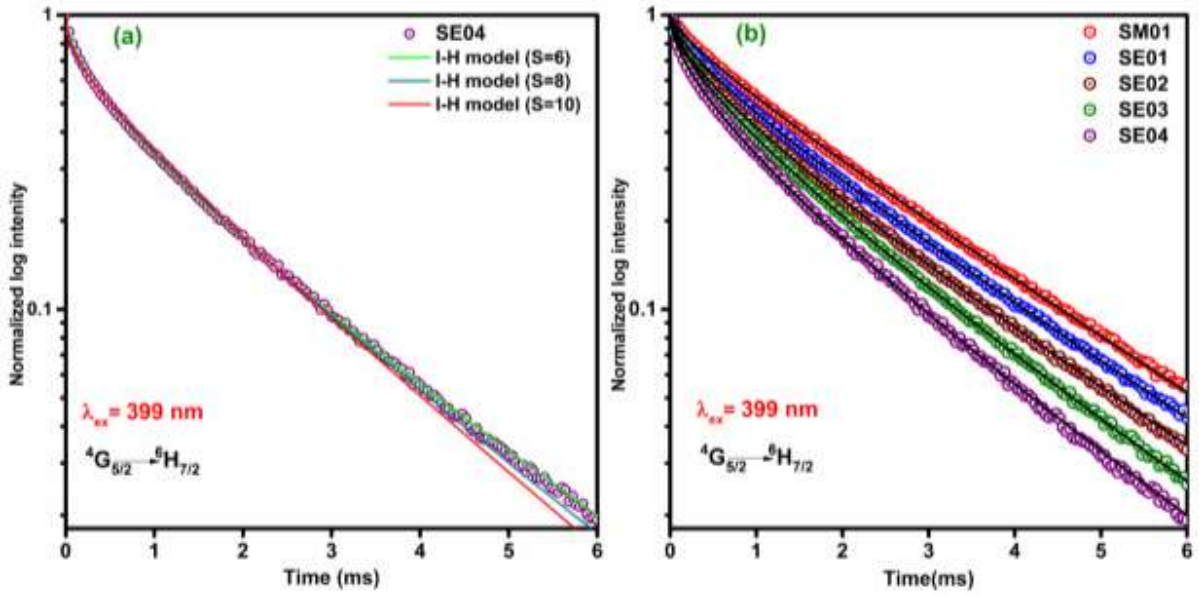

Accepted manuscript

ACCEPTED MANUSCRIPT

Fig. 9

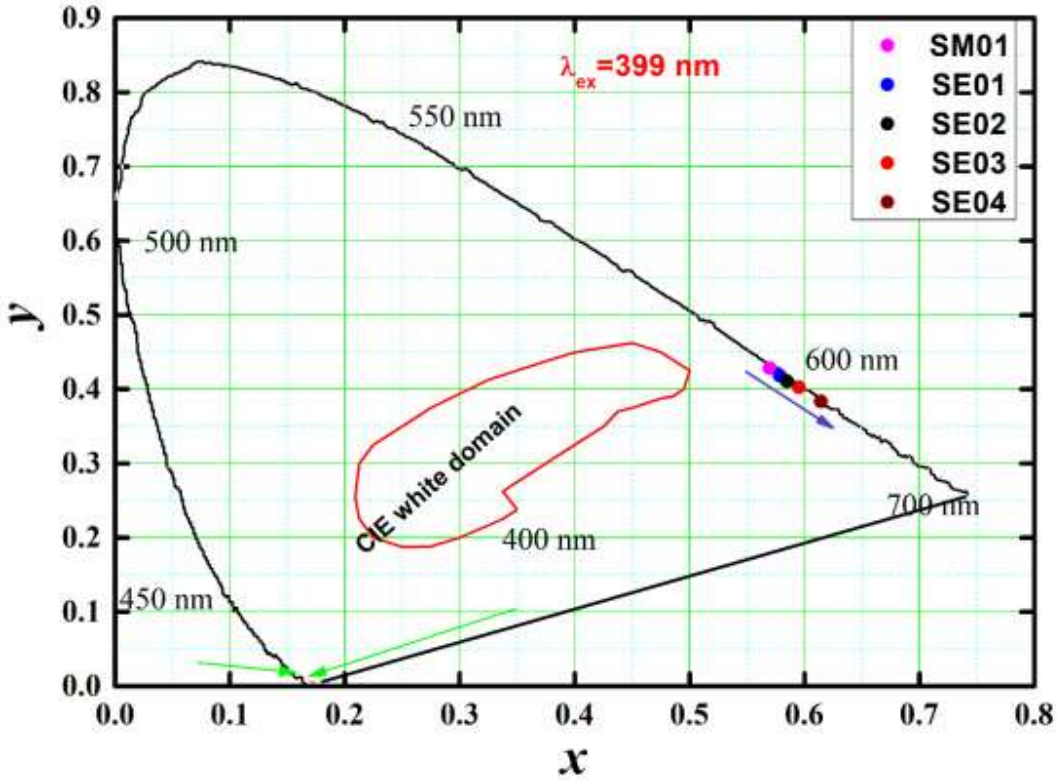

Accepted

View publication stats

Available online at www.sciencedirect.com

Science Direct

Materials Today: Proceedings 4 (2017) 7892–7902

materialstoday: PROCEEDINGS

www.materialstoday.com/proceedings

ICAAMM-2016

Effecton Surface Properties OF Mild SteelDuring Dry Turning& Wet Turning On Lathe

Ravi Butola[a], Jitendrakumar[b*], Vaibhavkhanna[c], ParveshAli[d] Vishesh Khanna [e]

[a,c,d,e]*Department of Mechanical, Production & Industrial and Automobile Engineering, Delhi Technological University, Delhi 11042, INDIA*

[b*] Department of Mechanical Engineering G.B Pant Govt. Engineering College, Delhi 110020, INDIA

Abstract.

In order to tackle a multi-objective optimization problemwhich seeks identification of the best process condition or parametric combination for the manufacturing processes, dry and wet turning, In the present experiment investigation on straight turning of mild- steel bar by using HSS tool. The experiment aimed at evaluating the best process environment which could simultaneously satisfy requirements of both quality and as well as productivity with special emphasis on reduction of cutting tool flank wear. Because reduction in flank wear ensures increase in tool life. The predicted optimal setting ensured minimization of surface roughness, height of flank wear of the cutting tool and maximization of MRR (Material Removal Rate).The experimental analysis showed that surface properties of mild steel improved when wet turning was carried out instead of dry turning.

© 2017 Elsevier Ltd. All rights reserved.

Selection and Peer-review under responsibility ofthe Committee Members of International Conference on Advancements in Aeromechanical Materials for Manufacturing (ICAAMM-2016).

*Keywords:*HSS Tool; Surface Roughness;Dryturning; Wet turning;

1. INTRODUCTION

This project was proposed to study and analyze the surface properties of steel during dry turning and wet turning on the lathe. The surface properties (surface roughness) of mild steel during dry turning and wet turning were dealt during the study. The project was intended towards the analysis, measurements, and output related parameters of Mild Steel after turning. There are many losses during turning operation due to which the roughness and other parameters of the material gets

* Corresponding author. Tel.: +919627834458

E-mail address:jkumarme80@gmail.com

2214-7853© 2017 Elsevier Ltd. All rights reserved.

Selection and Peer-review under responsibility ofthe Committee Members of International Conference on Advancements in Aeromechanical Materials for Manufacturing (ICAAMM-2016

affected. As the project dealt with the material whose specifications are not same every time therefore, the parameters, which were of prime concern, were very less. The project allowed us to check the roughness of steel we observe during different turning operations and apply the material accordingly in its different applications.

Lin et al. [1] selected an abdicative network to construct a prediction model for surface roughness and cutting force. The process parameters: cutting speed, feed rate and depth of cut were given which allowed the network to predict the surface roughness and cutting force. Regression analysis was also adopted as second prediction model for surface roughness and cutting force. Comparison was made on the results of both model indicating that adductive network was found more accurate than regression analysis.Feng and Wang [2] explored the prediction of surface roughness in finish turning operation by developing an empirical model by considering working parameters: work piece hardness (material), feed, cutting tool point angle, depth of cut, spindle speed, and cutting time. Data mining techniques, nonlinear regression analysis with logarithmic data transformation were used for developing the empirical model to predict the surface roughness. Suresh et al. [3] concentrated on machining mild steel by TiN-coated tungsten carbide (CNMG) cutting tools for developing a surface roughness prediction model by using Response Surface Methodology (RSM). Genetic Algorithms (GA) were used to optimize the objective function and compared with RSM results. It was observed that GA program provided minimum and maximum values of surface roughness and their respective optimal machining conditions. Lee and Chen [4]emphasized on artificial neural networks (OSRR-ANN) which used a sensing technique to monitor the effect of vibration produced by the motions of the cutting tool and work piece during the cutting process and developed an on-line surface recognition system. The authors utilized tri-axial accelerometer for determining the direction of vibration that significantly affected surface roughness and then analyzed by using a statistical method and compared prediction accuracy of the ANN and SMR. Choudhury and Bartarya [5] concentrated on design of experiments and the neural network for prediction of tool wear. The input parameters were cutting speed, feed and depth of cut and flank wear, surface finish and cutting zone temperature were selected as outputs. Empirical relation between different responses and input variables and also through neural network (NN) program helped in predicting all the three response variables and compared which method was best for prediction. Chien and Tsai [6] developed a model for the prediction of tool flank wear proceeded by an optimization model for the determination of optimal cutting conditions in machining 17-4PH stainless steel. The back-propagation neural network (BPN) was used to construct the predictive model. The genetic algorithm (GA) was used for the model optimization. Kirby et al. [7] developed the prediction model for surface roughness in turning method. The regression model was developed by a single cutting parameter. The vibrations along three axes were chosen for in-process surface roughness prediction system. By using multiple regression and Analysis of Variance (ANOVA) a strong linear relationship among the parameters (feed rate and vibration measured in three axes) and the response (surface roughness) was established. The authors validated that spindle speed and depth of cut might not necessarily have to be fixed for an effective surface roughness prediction model. Őzel and Karpat[8]analyzed the prediction of surface roughness and tool flank wear by utilizing the neural network model in comparison with regression model. The data set from measured surface roughness and tool flank wear were utilized to train the neural network models. Predictive neural network models were found to be capable of better predictions for surface roughness and tool flank wear within the range in between they were trained. Pal and Chakraborty [9] studied the development of a back propagation neural network model for prediction of surface roughness in turning operation and used mild steel work-pieces with high speed steel as the cutting tool for carrying out a large number of experiments. The authors used speed, feed, depth of cut and the cutting forces as inputs to the neural network model for prediction of the surface roughness. The

work obtained from the result predicted that surface roughness was very close to the experimental value. Zhong et al. [10]focused on the surface roughness of turned surfaces using networks with seven inputs namely tool insert grade, work piece material, tool nose radius, rake angle, depth of cut, spindle rate, and feed rate. Kumanan et al. [11] advocated the methodology for prediction of machining forces using multi-layered perceptron trained by genetic algorithm (GA). The data obtained from experimental analysis of a turning process were explored to train the proposed artificial neural networks (ANNs) with three inputs to get machining forces as output. The optimal ANN weights were obtained using GA search. This function-replacing hybrid made of GA and ANN was found computationally effective as well as accurate to predict the machining forces for the input machining conditions.

1.1. Turning operation

Turning is the removal of metal from the outer diameter of a rotating cylindrical work piece. Turning is used to reduce the diameter of the work piece, usually to a specified dimension, and to produce a smooth finish on the metal. Often the work piece will be turned so that adjacent sections have different diameters. Fig. 1. (a)shows a basic turning operation.Turning is the machining operation that produces cylindrical parts. In its basic form, it can be defined as the machining of an external surface:

- With the work piece rotating.
- With a single-point cutting tool, and
- With the cutting tool feeding parallel to the axis of the work piece and at a distance that will remove the outer surface of the work.

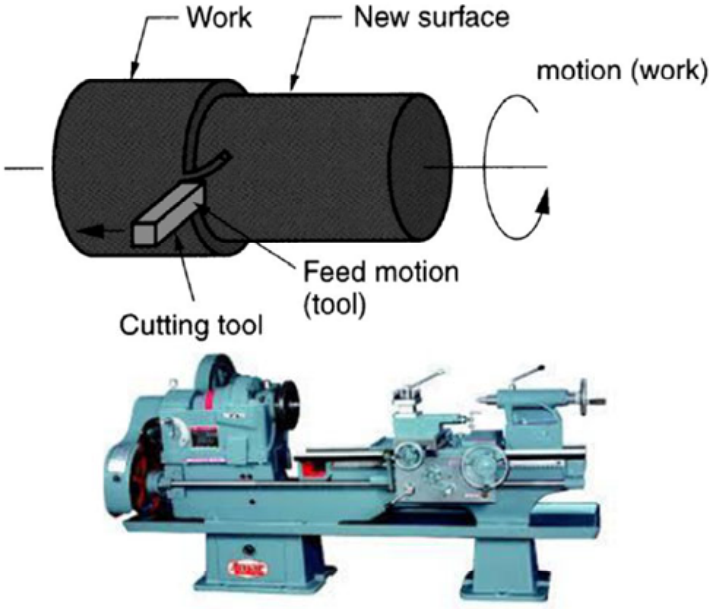

Fig. 1. (a) Turning Operation; (b) Lathe Machine

1.2. Turning machines

The turning machines are, of course, every kind of lathes. Lathes used in manufacturing can be classified as engine, turret, automatics, and numerical control etc. They are heavy duty machine tools and have power drive for all tool movements. They commonly range in size from 12 to 24 inches swing and from 24 to 48 inches centre distance, but swings up to 50 inches and centre

distances up to 12 feet are not uncommon. Many engine lathes are equipped with chip pans and built-in coolant circulating system.Fig. 1. (b) shows a lathe machine.

1.3. Material removal rate (m.r.r.)

The material removal rate (M.R.R.) in turning operations is the volume of material/metal that is removed per unit time in mm^3/min. For each revolution of the work piece, a ring shaped layer of material is removed as shown in Fig.2.

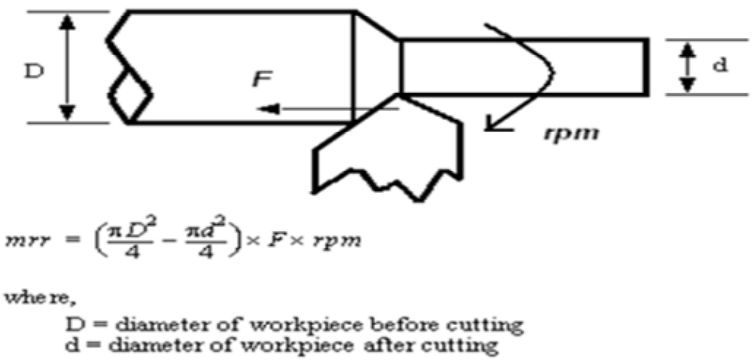

Fig. 2. Material Removal Rate in Turning

2. EXPERIMENTATION:

In this project we take six pieces of mild steel bars for compare the properties during turning. On first three pieces dry turning operation is performed, and on remaining three flood turning operation is performed. After the turning process the testing on the pieces performed to check and analyses the change in properties of mild steel in the terms of surface roughness.

DRY TURNING:

Dry turning promises the plant operations manager significant savings in fluid cost and treatment. With advanced Grade 4015 carbide cutting inserts and technical assistance from Sandvik Coromant, the auto parts maker also showed dry turning could double tool life (Fig.3). Dry turning axle shafts provided a triple payoff in chip control, process accuracy, and tool life. Like the wet turning operations on the gears and axle tubes, chip control for the finishing cuts on the axle shaft flange face posed a problem.

Fig. 3. Samples of Dry Turning

WET TURNING:

Cutting fluids are meant to lubricate cutting tools and reduce cutting zone temperatures to protect both tools and work pieces. They reduce cutting edge pressure. Fluids also flush away metal chips and suppress troublesome dust. Cutting fluids nevertheless pose workplace health hazards, and they impose a constant economic burden on machine shops. By one automotive industry estimate, cutting fluids account for up to 15% of the total cost of machining a part. At the high speeds encountered in computer numerically controlled lathes, just 15% of the coolant directed at the work piece evaporates on the cutting edge to dissipate heat. About 84% goes down the drain, and 1% remains on the part after machining, sometimes interfering with quality control measurements. While dry turning eliminates the expensive nuisance of cutting fluids, it takes special inserts to survive increased heat and tool pressure (Fig.4).

Fig. 4. Samples of Wet Turning

2.1. Type of steel used:

In this project we used mild steel as a work piece whose property is to be checked after the turning on lathe machine.

MILD STEEL: Mild steel , also known as plain-carbon steel, is the most common form of steel because its price is relatively low while it provides material properties that are acceptable for many applications, more so than iron. Low-carbon steel contains approximately 0.05–.15% carbon making it malleable and ductile. Mild steel has a relatively low tensile strength, but it is cheap and easy to form; surface hardness can be increased through carburizing(table.1).

2.1.1. Specification of specimen:

Percentage of Carbon = 0.05 – 0.15 %
Density = 7.85 g/cm3
Young's Modulus = 210 GPa

2.1.2. Parameters of specimen:

Table 1. PARAMETERS OF SPECIMEN.

Length of Specimen	100 mm
Diameter of Specimen	13 mm
Diameter After Machining	11 mm
Depth of Cut	1 mm
Time taken in Turning	39 sec
Material Removal Rate	18.84 mm^3/min

2.2. Machine used for surface testing of samples:

2.2.1. Profilometer:

Profilometer is a measuring instrument used to measure a surface's profile, in order to quantify its roughness (Fig.5). In this testing we used the contact based Profilometer (diamond stylus). A diamond stylus is moved vertically in contact with a sample and then moved laterally across the sample for a specified distance and specified contact force. It can measure small surface variations in vertical stylus displacement as a function of position. The height position of the diamond stylus generates an analog signal which is converted into a digital signal stored, analyzed and displayed.

Fig. 5. MitutoyoProfilometer

3. SURFACE ROUGHNESS TESTING RESULTS:

3.1. Dry Turning Sample 1 Results :

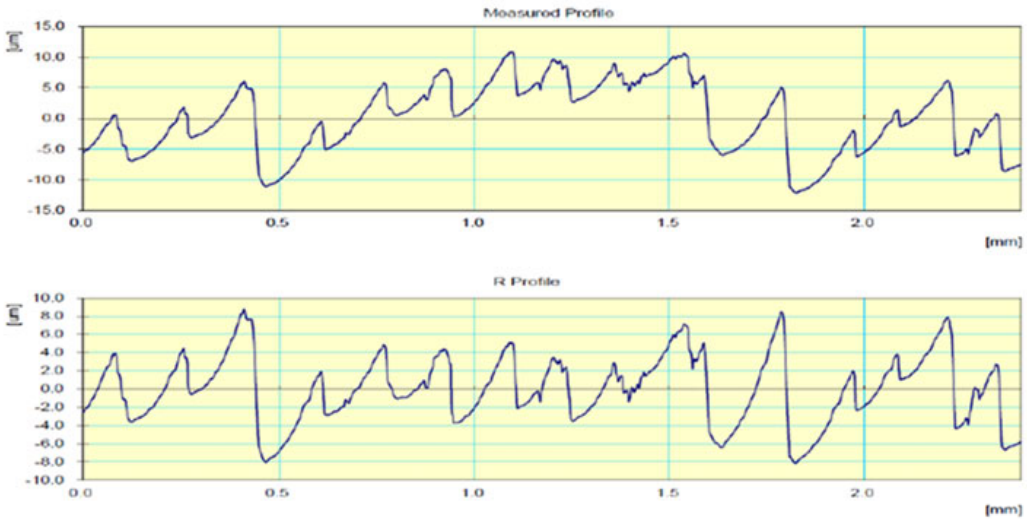

Fig. 6. Dry Turning Sample 1 Graph

Table 2. Result of Dry Turning Sample 1

Work Name	Sample	Operator	Mitutoyo
Measuring Tool	SurfTest SJ-400	Comment	Ver4.00
Standard	ISO 1997	N	3
Profile	R	Cutoff	0.8mm
Range	800 µm	FILTER	GAUSS
Ra	2.98µm		
Rz	14.9 µm		
Rq	3.66 µm		

3.2. Dry Turning Sample 2 Results :

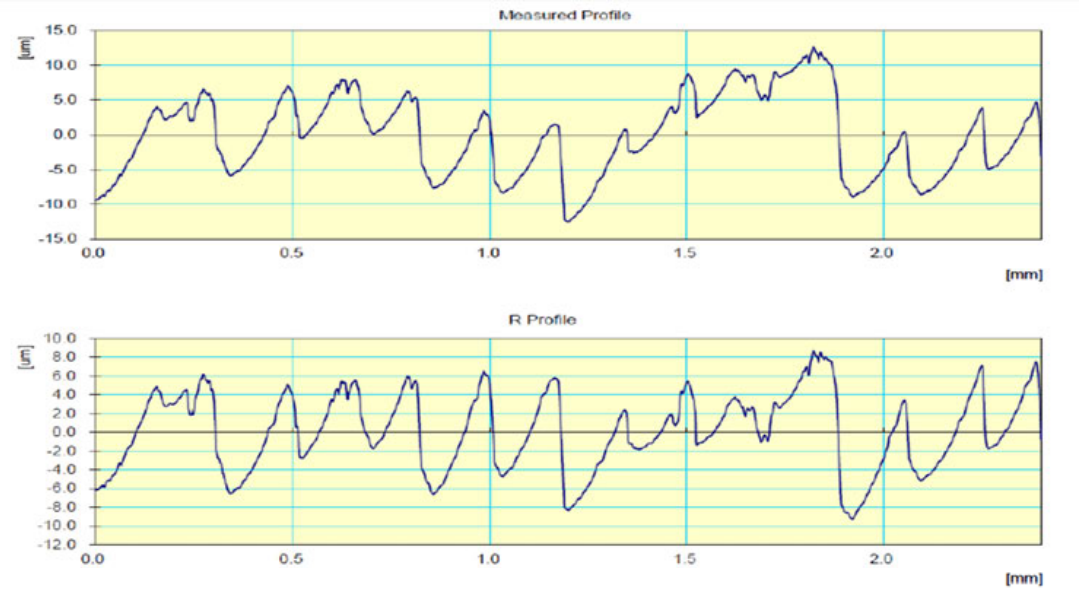

Fig. 7. Dry Turning Sample 2 Graph

Table 3. Result of Dry Turning Sample 2

Work Name	Sample	Operator	Mitutoyo
Measuring Tool	SurfTest SJ-400	Comment	Ver4.00
Standard	ISO 1997	N	3
Profile	R	Cutoff	0.8mm
Range	800 µm	FILTER	GAUSS
Ra	3.43µm		
Rz	15.2µm		
Rq	4.07µm		

3.3. Wet Turning Sample 1 Results

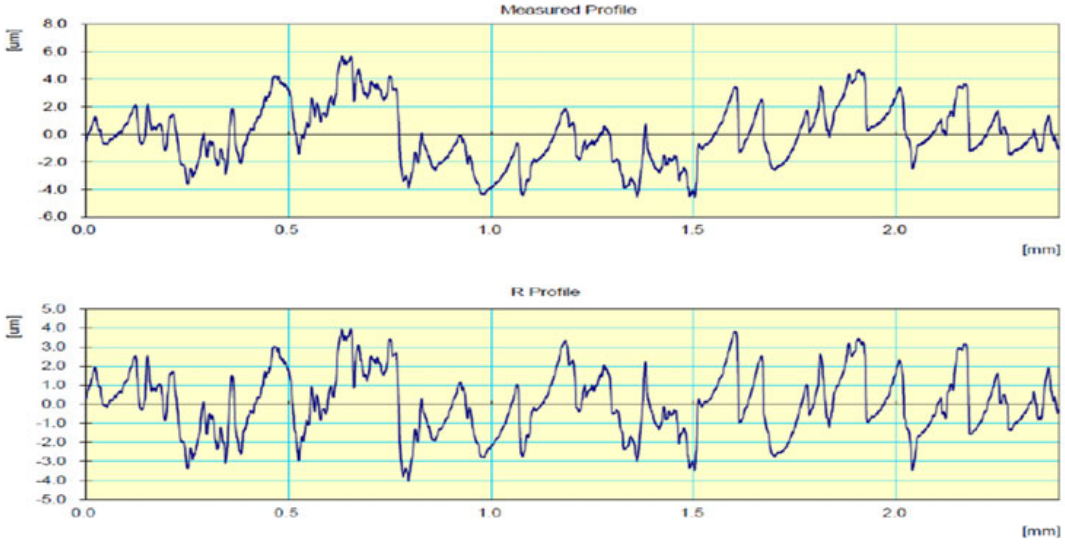

Fig. 8. Wet Turning Sample 1 Graph

Table 4. Result of Wet Turning Sample 1

Work Name	Sample	Operator	Mitutoyo
Measuring Tool	SurfTest SJ-400	Comment	Ver4.00
Standard	ISO 1997	N	3
Profile	R	Cutoff	0.8mm
Range	800 µm	FILTER	GAUSS
Ra	1.36 µm		
Rz	7.5 µm		
Rq	1.67 µm		

3.4. Wet Turning Sample 1 Results

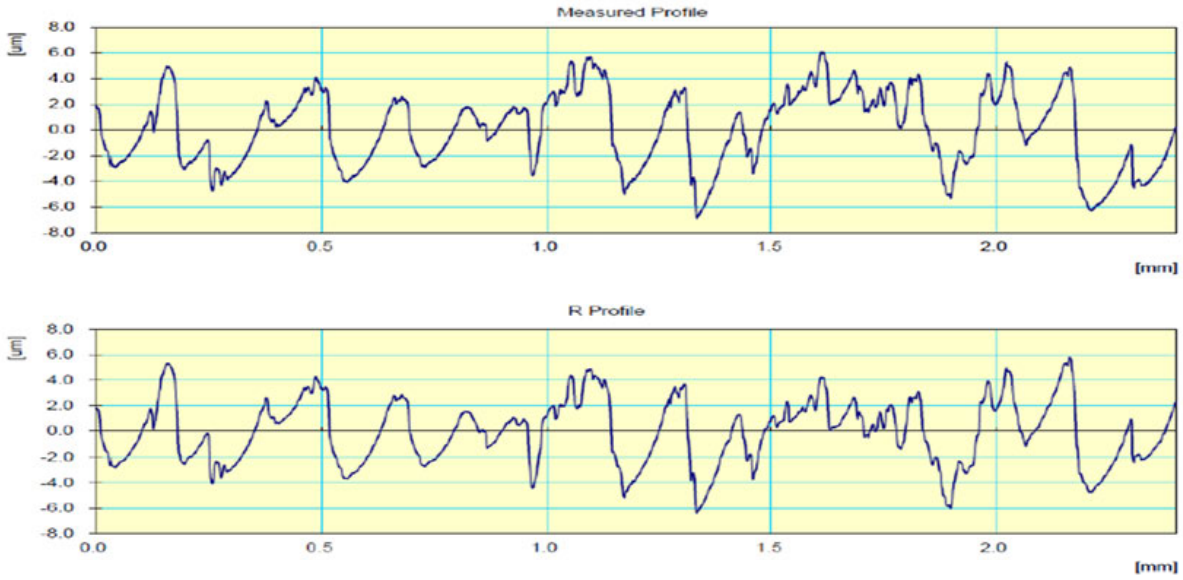

Fig. 9. Wet Turning Sample 2 Graph

Table 5. Result of Wet Turning Sample 2

Work Name	Sample	Operator	Mitutoyo
Measuring Tool	SurfTest SJ-400	Comment	Ver4.00
Standard	ISO 1997	N	3
Profile	R	Cutoff	0.8mm
Range	800 µm	FILTER	GAUSS
Ra	2.10 µm		
Rz	10.8 µm		
Rq	2.52 µm		

CONCLUSION:

This study deals with optimization of multiple surface roughness parameters along with material removal rate (M.R.R.) in search of an optimal parametric combination (favorable process environment) capable of producing desired surface quality of the turned product in a relatively lesser time. The following conclusions may be drawn from the results of the experiments and analysis of the experimental data. The Surface Roughness obtained after Dry Turning is 2.98 – 3.43 µm. The Surface Roughness obtained after Wet Turning is 1.36 – 2.10 µm.After comparing the all results we conclude that the surface properties improved when work- piece go through the wet turning rather than dry turning as shown in Fig.6 to 9 and Table 2 to 5.

References:

[1] Lin W. S., Lee B. Y., Wu C. L., "Modeling the surface roughness and cutting force for turning", Journal of Materials Processing Technology, Volume 108,(2001), pp. 286-293.

[2]Feng, C. X. and Wang X. 'Development of Empirical Models for Surface Roughness Prediction in Finish Turning', International Journal of Advanced Manufacturing Technology, Vol. 20,(2002),348-356.

[3] Suresh P. V. S., Rao P. V. and Deshmukh S. G., "A genetic algorithmic approach for optimization of surface roughness prediction model", International Journal of Machine Tools and Manufacture, Volume 42,(2002), pp. 675–680.

[4] Lee S. S. and Chen J. C., "Online surface roughness recognition system using artificial neural networks system in turning operations" International Journal of Advanced Manufacturing Technology, Volume 22,(2003), pp. 498–509.

[5].Choudhury S. K. and Bartarya G., "Role of temperature and surface finish in predicting tool wear using neural network and design of experiments", International Journal of Machine Tools and Manufacture, Volume 43,(2003), pp. 747–753.

[6].Chien W.-T. and Tsai C.-S., "The investigation on the prediction of tool wear and the determination of optimum cutting conditions in machining 17-4PH stainless steel", Journal of Materials Processing Technology, Volume 140,(2003), pp. 340–345.

[7]. Kirby E. D., Zhang Z. and Chen J. C., "Development of An Accelerometer based surface roughness Prediction System in Turning Operation Using Multiple Regression Techniques", Journal of Industrial Technology, Volume 20,(2004), pp. 1-8.

[8]. Özel T. and Karpat Y., "Predictive modeling of surface roughness and tool wear in hard turning using regression and neural networks", International Journal of Machine Tools and Manufacture, Volume 45,(2005), pp. 467–479.

[9]. Pal S. K. and Chakraborty D., "Surface roughness prediction in turning using artificial neural network", Neural Computing and Application, Volume14,(2005), pp. 319– 324

[10]. Zhong Z. W., Khoo L. P. and Han S. T., "Prediction of surface roughness of turned surfaces using neural networks", International Journal of Advance Manufacturing Technology, Volume 28,(2006), pp. 688–693.

[11]. Kumanan S., Saheb S. K. N. and Jesuthanam C. P., "Prediction of Machining Forces using Neural Networks Trained by a Genetic Algorithm", Institution of Engineers (India) Journal, Volume 87,(2006), pp. 11-15.

Journal of Plant Biochemistry & Physiology

ISSN: 2329-9029

Roy et al., J Plant Biochem Physiol 2017, 5:3
DOI: 10.4172/2329-9029.1000198

Research Article OMICS International

Estimation of Asiaticoside by Using RP-HPLC and FAME Analysis of Medicinally Important Plant *Centella asiatica*

Arpita Roy, Koyel Kundu, Gaurav Saxena and Navneeta Bharadvaja*

Department of Biotechnology, Plant Biotechnology Laboratory, Delhi Technological University, New Delhi, India

***Corresponding author:** Navneeta Bharadvaja, Plant Biotechnology Laboratory, Department of Biotechnology, Delhi Technological University, New Delhi, India, Tel: 01127294668; E-mail: navneetab@dce.ac.in

Received date: September 06, 2017; **Accepted date:** September 12, 2017; **Published date:** September 18, 2017

Copyright: © 2017 Roy A, et al. This is an open-access article distributed under the terms of the Creative Commons Attribution License, which permits unrestricted use, distribution, and reproduction in any medium, provided the original author and source are credited.

Abstract

Due to the presence of several bioactive compounds, *Centella asiatica* (L.) is used in traditional medicine for the treatment of various ailments. This usage of plant and its products created a huge demand which required an alternative method of its commercial production so that the loss of natural plant and its genetic pool can be prevented. A different investigation using biotechnological methods provided a wealth of information to enhance the biomass as well as different bioactive compounds. In the present study, we focused and reported the effect of different nitrogen sources on shoot proliferation of *Centella asiatica*. Effect of malt extract as plant elicitor on asiaticoside production as well as fatty acid methyl ester (FAME) profile was also worked out. Four different nitrogen sources i.e., NH_4NO_3 (1.65 g/l), KNO_3 (0.8 g/l), $NaNO_3$ (1.65 g/l), $Ca(NO_3)_2$ (0.825 g/l) on five different accessions of *Centella asiatica* were tested and accession number 347492 (14.66 ± 2.4) provided maximum shoot proliferation with ammonium nitrate. RP-HPLC analysis of accession number 347492 revealed that malt extract as plant extract enhanced 6 times asiaticoside in comparison to standard conditions. GC-MS analysis of five different accessions of *Centella asiatica* concluded that this plant is rich in the content of Pentadecanoic acid, 9, 12 Octadecadienoic acid (Linoleic acid) and 9, 12, 15 Octadecatrienoic acid (Linolenic acid). Most potential fatty acid methyl esters containing plant accession number is 281374.

Keywords *Centella asiatica*; Nitrogen source; Malt extract; Asiaticoside; Fatty acid methyl ester analysis

Introduction

Plants contains various active phytocompounds which includes vitamins, terpenoids, phenolic acids, lignins, stilbenes, tannins, flavonoids, quinones, coumarins, alkaloids, amines, betalains, and other metabolites which are well to do in antioxidant activity [1,2]. *Centella asiatica* (L.) is a polymorphous, perennial, medicinal creeping plant, rooting at nodes and belongs to the family Apiaceae (Umbeliferae). As the plant inhabits a various region in India, it is popular with its regional names such as Thankuni in Bengali, Gotukola in Sinhali, Manimunni in Assam, Valleri in Decan, Mandookaparni in Hindi, Indian pennywort in English [3], etc. This plant is found in abundance on moist, swampy, sandy or clay soils, often in large clumps, forming a dense green carpet. It is also used as a cover crop in plantations. The medicinal value of this plant was revealed in *Charaka Chikitsa* [4] and main active essential elements of *C. asiatica* (L.) are asiatic acid, madecasic acid, asiaticoside, madecassoside, brahmoside, brahmic acid, brahminoside, thankiniside, isothankunisode, centelloside, madasiatic acid, alkaloids, flavanoids, etc. [5-10] which are known to take care of skin problems, to heal wounds, for stimulating the nerves and brain cells, antileprotic, antifilarial, antibacterial, adaptogenic, antifeedant, anti-stress, anti-ulcer, anti-oxidative stress, anti-radiation properties, anti-heavy metal poisoning, antiviral properties, anticancer etc. [11-20].

It was also reported that asiaticoside, one of the important compound of *C. asiatica* shows anti-tumor activity by apoptosis of tumor cells and also used in the healing of leprosy or skin disorder by collagen I synthesis in human [21]. Due to its valuable medicinally important properties, this plant, as well as its extract, is in huge demand and such demand cannot be fulfilled by natural means. Thus, in the search for alternatives to production of desirable medicinal compounds from plants, biotechnological approaches, specifically, plant tissue cultures, are found to have more prospective as enhancement to traditional production of bioactive plant metabolites [22,23].

Several groups have worked out that carbon and nitrogen source are essential for the growth of the plant and they also have an important role in metabolic pathways [24] to enhance the formation of auxiliary buds and branching of adventitious roots [25]. Plant cells *in-vitro*, shows physiological and morphological responses to microbial, physical or chemical factors which are known as 'elicitors'. Elicitation is a process of induced or enhanced synthesis of secondary metabolites by the plants to ensure their survival. Treatment with elicitors was reported to enhance secondary metabolites in *C. asiatica* [26,27]. Therefore, in the present investigation, the focus has been done to record the effect of different nitrogen sources on shoot multiplication and effect of elicitor such as malt extract on the production of asiaticoside in different accessions of *Centella asiatica*. Another attempt has been made to investigate the fatty acid methyl ester (FAME) profile of this plant under normal environmental conditions. The purpose of this investigation was to find out potential culture conditions as well as potential accession which can provide high yield of plant material as well as active compounds. For this purpose, MS media supplemented with 6 Benzyl amino purine containing four different nitrogen sources {NH_4NO_3, KNO_3, $NaNO_3$ and $Ca(NO_3)_2$} were tested individually. Quantitative analysis of asiaticoside was carried out using the standard protocol of reverse phase high performance liquid chromatography with the plant's accession which

provided best results with malt extract. FAME analysis was done with GC-MS for five different accessions to access the potential fatty acid containing accession of *Centella asiatica*.

Materials and Methods

Plant material

Cultures of five different accessions i.e., 281374, 383913, 342109, 347492, 331514 of *Centella asiatica* were collected from National Bureau of Plant Genetic Resources (NBPGR), New Delhi, India.

In-vitro propagation in different culture conditions

In previous study effect of different carbon source and elicitors on the shoot multiplication of all the five accessions were done [28]. Roy et al. [29] also reported that MS media conatins highest number of shoots. In the present study the effect of nitrogen source on shoot multiplication, Murashige and Skoog (MS) [30] (Hi-media) media was prepared and pH was adjusted to 5.8 using 1 N HCl or 1 N NaOH solution. 0.8% plant agar was used to solidify the media. Sterilization of media was done by autoclaving for 20 min at 121°C and 15 lb pressure. MS media was supplemented with 1.5 mg/l 6-Benzylaminopurine (Hi-media) along with different nitrogen sources {NH_4NO_3 (1.65 g/l), KNO_3 (0.8 g/l), $NaNO_3$ (1.65 g/l), $Ca(NO_3)_2$ (0.825 g/l)}. After the solidification of media, sterile shoot nodes from each accession were inoculated in culture tubes (25 × 150 mm) separately. The cultures were incubated at 26 ± 2°C under 16 h photoperiod and light intensity of 3000 lux for four weeks. Each and every experiment was done in triplicates. Visual data was recorded after the 4th week of inoculation in terms of number of shoots and length of shoots for *in-vitro* growth measurement.

Estimation of asiaticoside by HPLC

For asiaticoside analysis, plant material of accession number 347492 was used which was found best in a previous study of effect of different plant elicitors on biomass of C. asiatica. Best results were found in case of malt extract as plant elicitor. 75 mg of air dried powdered leaf sample of plant was mixed with 20 ml of methanol and sonicated for 10 minutes with occasional shaking. After cooling sample was filtered with 0.45 µm filter paper and final volume made up to 30 ml by mixing additional methanol. Filtered a portion of this solution through a 0.2 µm polytetrafluoroethylene (PTFE) syringe filter and kept for HPLC analysis. 1 mg of standard of asiaticoside (Sigma) was dissolved in 10 ml methanol to prepare standard solution. For the analysis of asiaticoside, reverse phase high performance liquid chromatography (RP-HPLC) was used. HPLC system included a pump, an injection port, column compartment, and UV-VIS detector and fused core C18 HPLC column with chromatographic conditions i.e., mobile phase {Water: Methanol (3:7)}, flow rate (1 ml/min), injected volume (15 µl), column temperature (260°C), run time (10 minutes) and UV detection (220 nm). 15 µl standard solution was injected into HPLC machine and then injected the standard sample extract which was not treated with any plant elicitor. After that samples of accession number 347492 were injected in triplets.

Fatty Acid Methyl Ester (FAME) analysis using GC-MS

For FAME analysis, plants of all five accessions were cultured in MS media supplemented with 1.5 mg/L 6-Benzylaminopurine without using any extra source of carbon, nitrogen and plant elicitors etc. Sterile shoot nodes from each accession were inoculated in culture tubes (25 × 150 mm) separately at 26 ± 2°C under 16 h photoperiod and light intensity of 3000 lux for four weeks. Each and every experiment was done in triplicates. After four weeks, 100 mg chopped leaves of *Centella asiatica* were transferred to a screw-cap (teflon coated) glass tube and mixed with 1 ml of 2% methanolic HCl. The sample was then incubated at 90°C for an hour. After one hour, 1 ml of 0.9% NaCl was added followed by 2 ml of hexane and centrifuged at 2000 rpm for 2 minutes. The upper (hexane) layer of the sample was transferred into a fresh glass tube and dried under nitrogen flow. Dried sample was then diluted with 100 µl of hexane. 1 µl of samples was then injected into the GC-MS for analysis. Analysis was carried out by GC-MS electron impact ionization method. GC conditions included carrier gas (He), column temperature (50°C to 250°C) and run time (35 minutes). FAME of each accessions were analysed separately in triplets.

Data analysis

Observations were recorded and are presented as means ± standard deviation of 3 biological replicates to estimate the variability between the accessions.

Results

In-vitro propagation in different culture conditions

In previous study it was found that sucrose and malt extract showed highest amount of shoot multiplication [28]. Effect of nitrogen sources on shoot regeneration was observed in five accessions of *Centella asiatica*. Observation was recorded as mean value of triplicate samples after four weeks of inoculation (Table 1). A comparative study of four different nitrogen sources i.e., ammonium nitrate, potassium nitrate, sodium nitrate and calcium nitrate was carried out to test their potential on shoot regeneration. Each accession responded in its own way in MS media containing different nitrogen sources. Among five different accessions, 347492 showed the best result in presence of MS media supplemented with ammonium nitrate as nitrogen source. Maximum number of shoots was 14.66 ± 2.4 while maximum length of shoots 1.61 ± 0.59 cm has been reported in this accession. Although maximum length of shoot was reported in the same accession with sodium nitrate as nitrogen source but number of shoots were less than the number of shoots reported in case of ammonium nitrate. Thus, as combined results of both number and length of shoots, accession number 347492 was a potential accession among five accessions tested. Ammonium nitrate was found as best source of nitrogen among the four different sources tested.

Estimation of asiaticoside by HPLC

Among the five-different accession 347492 shows the best growth in MS media containing malt extract (1 mg/L) and supplemented with BAP (1.5 mg/L) in a previous study. So, the estimation of asiaticoside with and without malt extract was done by reverse phase high performance liquid chromatography (RPHPLC) analysis. Figure 1 show the chromatogram of standard asiaticoside and the retention time of asiaticoside was in 5.2 minutes. If we compare the two chromatograms (Figure 1) with chromatogram of standard asiaticoside, we can see that methanolic extract of malt extract treated sample (Figure 1) contains 8.03% of asiaticoside whereas without treated sample (Figure 1) contains 1.4% of asiaticoside. The

percentages of asiaticoside production in both the treated and untreated samples clearly indicate the 6 times increase in production of asiaticoside. Kim et al. [26] also reported the enhanced production of asiaticoside by the use of elicitors such as methyl jasmonate. They reported 116.8 mg/l production of asiaticoside with the use of 0.1 mM MJ in B5 liquid media. They further increased the yield of asiaticoside by combining 0.1 mM methyl jasmonate with 0.025 mg/l TDZ [thidiazuron, 1-phenyl-3-(1,2,3-thidiazol-5-yl) urea] and achieved a production of 342.72 mg/l. Kim et al. [31] also reported the use of methyl jasmonate in the increment of asiaticoside production in hairy root culture of *Centella asiatica*. Satheesan et al. [32] also reported two-fold increase in the asiaticoside production by root colonization of a fungus named *Piriformospora indica*. Fungal mediated elicitation of asiaticoside was also reported by Prasad et al. [27]. Nutrient mediated increment in the asiaticoside production along with high yield of biomass was reported by Prasad et al. [33] wherein they found this increment was due to reduction in the total nitrogen concentration and copper starvation.

Fatty Acid Methyl Ester (FAME) analysis by GC-MS

Table 2 lists the name of fatty acid as well as their relative percentage composition obtained from the gas chromatography mass spectrometry (GC-MS) analysis of the n-hexane extracts of five different accession of *Centella asiatica*. The analysis of fatty acid from five different accession of *Centella asiatica* by GC-MS showed that they contain both saturated and un-saturated fatty acids. In case of saturated fatty acids, three fatty acids i.e., Pentadecanoic, Hexadecanoic and Octadecanoic acid while in case of un-saturated fatty acids Octadecadienoic and Octadecatrienoic acid were reported. The percentage of Pentadecanoic and Octadecadienoic acids were very high while Octadecatrienoic acid was present in moderate amounts in all five accessions. Percentage of Hexadecanoic and Octadecanoic were very small in comparison to other fatty acids. These fatty acids have good therapeutic value such as Hexadecanoic (Palmitic acid) reduces the risk of cardiovascular disease, Octadecanoic (Stearic acid) used in baked food items, etc. Unsaturated fatty acids, Octadecadienoic (Linoleic acid) and Octadecatrienoic (Linolenic acid) are the most important essential fatty acids as because our body cannot synthesis these fatty acids. Linoleic acid is essential for maintenance of growth and found to be a potent cycloxygenase-2 (COX-2) catalyzed prostaglandin biosynthesis inhibitor.

Accession no. 281374 contain highest percent of Linoleic acid (approx. 24%) followed by 342109 (20.96%), 383913 (20.72%), 331514 (19.34%) and 347492 (18.62%). When we consider the presence of Linolenic acids, it is recorded that accession no. 347492 contains the highest percent (approx. 10%) followed by 281374 (9.6%), 383913 (7.11%), 383913 (6.41%) and 331514 (4.63%). These potential accessions can be utilized for the high yield of fatty acid production. Very less work has been reported related to the FAME profile of *Centella asiatica* which provided an opportunity to carry out this investigation. Jahan et al. [34] conducted a study related to elemental as well as fatty acid content of four medicinally important plant i.e., *Kaiempferia rotunda*, *Cuscuta reflexa*, *Centella asiatica* and *Asparagus racemosus*. Within *Centella asiatica*, they found good amount of Hexadecanoic acid (9.96%), Heptadecanoic acid (3.28%) and Octadecanoic acid (8.34%) but they also reported no presence of 9,12-Octadecadienoic acid. Although in our study, good amount of 9,12-Octadecadienoic acid has been investigated.

Nitrogen Source	Accession Numbers									
	383913		281374		331514		347492		342109	
	A	B	A	B	A	B	A	B	A	B
NH_4NO_3	4.67 ± 0.66	1.4 ± 0.33	6.33 ± 0.88	1.23 ± 0.26	10 ± 1.15	1.49 ± 0.27	14.66 ± 2.4	1.61 ± 0.59	5.33 ± 0.88	1.37 ± 0.62
KNO_3	7.66 ± 2.18	1.46 ± 0.41	3 ± 0.57	1.35 ± 0.23	7 ± 0.57	0.9 ± 0.22	5.66 ± 0.88	0.93 ± 0.29	7.66 ± 1.2	0.81 ± 0.3
$NaNO_3$	9.33 ± 2.4	1.17 ± 0.38	8 ± 0.1.5	0.76 ± 0.17	4 ± 0.57	0.75 ± 0.14	10 ± 1.15	1.94 ± 0.53	4.66 ± 0.66	0.64 ± 0.19
$Ca(NO_3)_2$	3 ± 0.57	0.25 ± 0.06	4.66 ± 0.66	1.01 ± 0.23	5.6 ± 1.2	0.97 ± 0.36	5.66 ± 1.2	1.04 ± 0.33	3.33 ± 0.88	0.84 ± 0.21

Table 1: Effect of different nitrogen sources on number and length of regenerated shoots in five different accession of *Centella asiatica* after four weeks of inoculation. Values are expressed as mean ± Standard Error (M ± SE). A represents number of shoots (M ± SE); B represents average length of shoot (M ± SE).

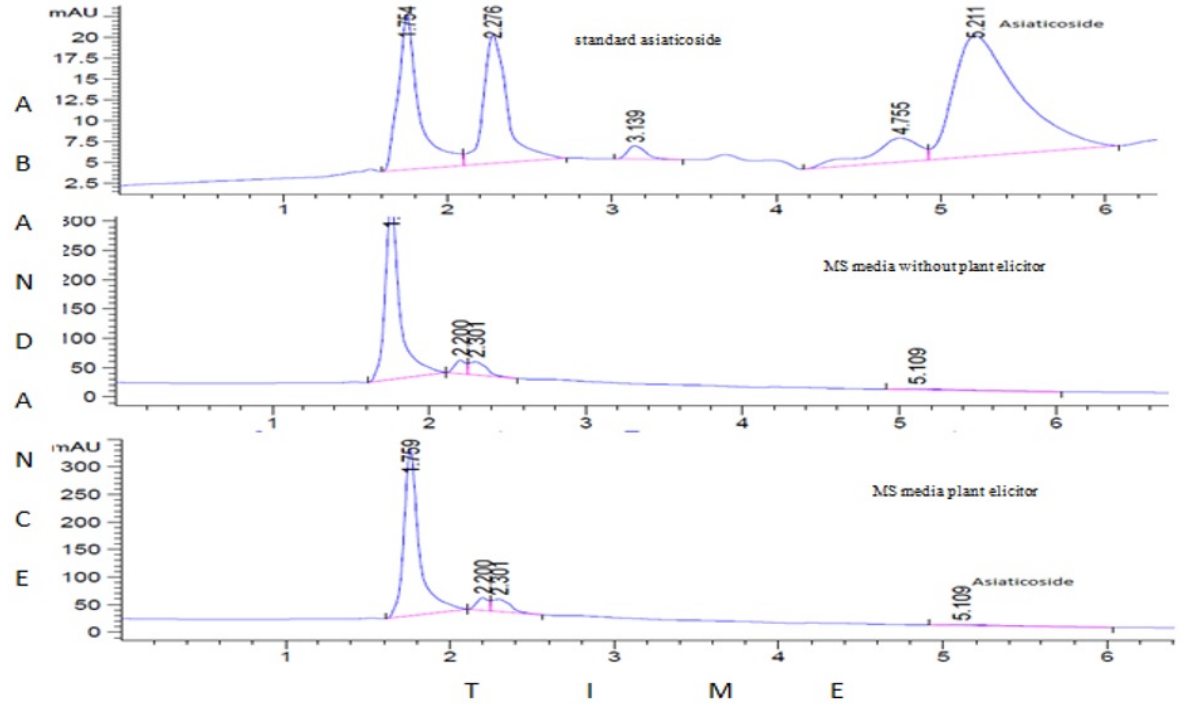

Figure 1: Chromatogram of standard asiaticoside, extract analysed from plant grown in MS media without plant elicitor and extract analysed from plant grown in MS media supplemented with malt extract as plant elicitor. Peaks of asiaticoside were found at 5.211, 5.109, 5.109 minutes in standard, without treated plant and treated plant respectively.

Fatty Acid	Relative %age of different Fatty acid in different accessions of *Centella asiatica*				
	281374	383913	342109	347492	331514
Saturated Fatty acids					
C15	17.31%	12.73%	15.08%	13.65%	12.54%
C16	1.91%	1.62%	1.90%	1.96%	1.58%
C18	1.70%	1.67%	1.65%	1.68%	1.15%
Un-saturated Fatty acids					
C18:2	23.95%	20.72%	20.96%	18.62%	19.34%
C18:3	9.59%	7.11%	6.41%	9.98%	4.63%

Table 2: Percentage of different saturated and un-saturated methylated fatty acids of five different accession of *Centella asiatica*. C15 - Pentadecanoic acid (Pentadecyclic acid) ($C_{15}H_{30}O_2$), C16 - Hexadecanoic acid (Palmitic acid) ($C_{16}H_{32}O_2$), C18 - Octadecanoic acid (Stearic acid) ($C_{18}H_{36}O_2$), C18:2-9,12 Octadecadienoic acid (Linoleic acid) ($C_{18}H_{32}O_2$) and C18:3-9,12,15 Octadecatrienoic acid (Linolenic acid) ($C_{18}H_{30}O_2$).

Conclusion

This study concluded that ammonium nitrate is a potential source of nitrogen for the proliferation of shoots in *Centella asiatica*. Accession number 347492 was found best among five different accessions for the maximum production of shoots. Accession number 347492 has also shown the capacity to produce 6 times more asiaticoside production in comparison to the standard environmental conditions when supplemented with malt extract as plant elicitors. GC-MS analysis of fatty acid methyl ester (FAME) of *Centella asiatica* revealed that accession number 281374 is the potential accession which can provide high yield commercially important fatty acids. These culture conditions and potential accessions can be used for high yield of biomass as well as asiaticoside and fatty acid production under lab conditions which may be beneficial for the fulfilment of their demand.

Acknowledgement

Sincere thanks to the Department of Biotechnology, Department of Applied Chemistry and Physics, Delhi Technological University for making necessary facilities during this study, National Bureau of Plant Genetic Resources, New Delhi for providing the plant materials and Dr Girish Mishra (Department of Botany, Delhi University) for providing the GC facility.

References

1. Zheng W, Wang SY (2001) Antioxidant activity and phenolic compounds in selected herbs. Journal of Agricultural and Food Chemistry 49: 5165-5170.
2. Cai YZ, Sun M, Corke H (2003) Antioxidant activity of betalains from plants of the Amaranthaceae. Journal of Agricultural and Food Chemistry 51: 2288-2294.
3. Jamil SS, Nizami Q, Salam M (2006) Centella asiatica (Linn.) Urban-A Review. Natural Product Radiance 6: 158-170.
4. Bhavna D, Jyoti K (2011) Centella asiatica: The elixer of life. International Journal of Research in Ayurveda & Pharmacy 2: 431-438.
5. Bonfill M, Mangas S, Cusidó RM, Osuna L, Piñol MT, et al. (2006) Identification of triterpenoid compounds of Centella asiatica by thin-layer chromatography and mass spectrometry. Biomedical Chromatography 20: 151-153.
6. Zhang FL, Wei YJ, Zhu J, Gong ZN (2008) Simultaneous quantitation of three major triterpenoid glycosides in Centella asiatica extracts by high performance liquid chromatography with evaporative light scattering detection. Biomedical Chromatography 22: 119–124.
7. Jiang ZY, Zhang XM, Zhou J, Chen JJ (2005) New triterpnoid glycosides from Centella asiatica. Helvetica Chimica Acta 88: 297-303.
8. Weng XX, Zhang J, Gao W, Cheng L, Shao Y, et al. (2012) Two New Pentacyclic Triterpenoids from Centella asiatica. Helvetica Chimica Acta 95: 255-260.
9. Krishnamurthy RG, Senut MC, Zemke D, Min J, Frenkel MB, et al. (2009) Asiatic Acid, a Pentacyclic Triterpene from Centella asiatica, Is Neuroprotective in a Mouse Model of Focal Cerebral Ischemia. Journal of Neuroscience Research 87: 2541–2550.
10. Subban R, Veerakumar A, Manimaran R, Hashim KM, Balachandran I (2008) Two new flavonoids from Centella asiatica (Linn.). Journal of Natural Medicines 62: 369–373.
11. Singh S, Gautam A, Sharma A, Batra A (2010) Centella asiatica (L.): A plant with immense medicinal potential but threatened. International Journal of Pharmaceutical Sciences Review and Research 4: 9-17.
12. Rao KGM, Rao SM, Rao SG (2006) Centella asiatica(L) leaf extract treatment during the growth spurt period enhances hippocample CA3 neuronal dendritic arborisation in rats. Evidence Based Complementary and Alternative Medicine 3: 349-57.
13. Gupta R, Flora SJS (2006) Effect of Centella asiatica on arsenic induced oxidative stress and metal distribution in rats. Journal of Applied Toxicology 26: 213–222.
14. Flora SJS, Gupta R (2007) Beneficial Effects of Centella asiatica Aqueous Extract against Arsenic-induced Oxidative Stress and Essential Metal Status in Rats. Phytotherapy Research 21: 980–988.
15. Shinomol GK, Ravikumar H, Muralidhara M (2010) Prophylaxis with Centella asiatica Confers Protection to Prepubertal Mice Against 3-nitropropionic-Acid-Induced Oxidative Stress in Brain. Phytotherapy Research 24: 885–892.
16. Heong S, Ariffin F, Kaur B, Karim AA, Huda N (2011) Antioxidant capacity and phenolic composition of fermented Centella asiatica herbal teas. Journal of the Science of Food and Agriculture 91: 2731–2739.
17. Joy J, Nair CKK (2009) Protection of DNA and membranes from gamma-radiation induced damages by Centella asiatica. Journal of Pharmacology and Pharmacotherapeutics 61: 941–947.
18. Saxena G, Flora SJS (2006) Changes in brain biogenic amines and haem biosynthesis and their response to combined administration of succimers and Centella asiatica in lead poisoned rats. Journal of Pharmacology and Pharmacotherapeutics 58: 547–559.
19. Roy A, Kundu K, Saxena G, Kumar L, Bharadvaja N (2016) Effect of different media and growth hormones on shoot multiplication of in-vitro grown Centella asiatica accessions. Advance Techniques in Biology Med 4: 172.
20. Roy A, Attre T, Bharadvaja N (2017) Anticancer agent from medicinal plants: A Review. New apects in medicinal plants and pharmacognosy. JB Books Publisher, Poland.
21. Bonte F, Dumas M, Chaudagne C, Maybeck A (1994) Influence of asiatic acid, madecassic acid and asiaticoside on human collagen I synthesis. Planta Medica 60: 133-135.
22. Vanisree M, Lee CY, Lo SF, Nalawade SM, Lin CY, et al. (2004) Studies on the production of some important secondary metabolites from medicinal plants by plant tissue cultures. Botanical Bulletin Academia Sinica 45: 1-22.
23. Sharma M, Sharma A, Kumar A, Basu SK (2011) Enhancement of secondary metabolites in cultured plant cells through stress stimulus. American Journal of Plant Physiology 6: 50-71.
24. Panathula CS, Mahadev MD, Naidu CV (2014) Effect of different carbohydrate on in vitro plant regeneration of Centella asiatica (L.), an important antijaundice medicinal plant. International Journal of Medicinal and Aromatic Plants 4: 41-47.
25. Saad AIM, Elshahed AM (2012) Plant tissue culture media. Recent advances in plant in vitro culture. Chapter 2. In Tech Publisher.
26. Kim OT, Kim MY, Hong MH, Ahn JC, Hwang B (2004) Stimulation of asiaticoside accumulation in the whole plant cultures of Centella asiatica (L.) Urban by elicitors. Plant Cell Reports 23: 339–344.
27. Prasad A, Mathur A, Kalra A, Gupta MM, Lal RK, et al. (2013) Fungal elicitor-mediated enhancement in growth and asiaticoside content of Centella asiatica L. shoot cultures. Plant Growth Regulation 69: 265–273.
28. Kundu K, Roy A, Saxena G, Kumar L, Bharadvaja N (2016) Effect of Different Carbon Sources and Elicitors on Shoot Multiplication in Accessions of Centella asiatica. Med Aromat Plants 5: 251.
29. Roy A, Bharadvaja N (2017) Effect of different culture medias on shoot multiplication and stigmasterol content in accessions of Centella asiatica. International Journal of Ayurvedic and Herbal Medicine 7: 2643–2650.
30. Murashige T, Skoog F (1962) A revised medium for rapid growth and bioassays with tobacco tissue cultures. Physiologia Plantarum 15: 473-497.
31. Kim OT, Bang KH, Shin YS, Lee MJ, Jung SJ, et al. (2007) Enhanced production of asiaticoside from hairy root cultures of Centella asiatica (L.) Urban elicited by methyl jasmonate. Plant Cell Reports 26: 1941–1949.
32. Satheesan J, Narayanan AK, Sakunthala M (2012) Induction of root colonization by Piriformospora indica leads to enhanced asiaticoside production in Centella asiatica. Mycorrhiza 22: 195–202.
33. Prasad A, Mathur A, Singh M, Gupta MM, Uniyal GC, et al. (2012) Growth and asiaticoside production in multiple shoot cultures of a medicinal herb, Centella asiatica (L.) Urban, under the influence of nutrient manipulations. Journal of Natural Medicines 66: 383–387.
34. Jahan IA, Akbar PN, Enayetullah M, Ahmmad N, Nuruddin M, et al. (2015) Elemental and Fatty Acid Content of Four Medicinal Plants: Kaiempferia rotunda, Cuscuta reflexa, Centella asiatica and Asparagus racemosus. European Journal of Medicinal Plants 10: 1-10.

International Journal of Research in Engineering and Innovation (IJREI)
journal home page: http://www.ijrei.com
ISSN (Online): 2456-6934

Experimental investigation on friction stir welding of copper alloys

R.S. Mishra, V Jeganathan

Department of Mechanical, Production & Industrial and Automobiles Engineering, Delhi Technological University, Delhi

Abstract

In this paper, the Friction stir welding successfully applied to join copper alloy and it was found that the defect free weld zone was formed with the condition of 800 rpm and 60 mm/min. The grain structure near weld zone was very different from that of the base metal. Heat affected zone (HAZ) were characterized by grain growth and stir zone had fine and equiaxed grain structure. The Slightly softening region was formed in the weld zone in spite of smaller grain size compare to that of base metal. Hardness of FSW copper weld zone mainly depended on the density of dislocation rather than grain size. Hardness variation also existed in the stir zone from the upper to the lower region with thermal and mechanical conditions and transverse tensile strength of FSW copper joint reached the 87% of tensile strength of base metal.
© 2017 ijrei.com. All rights reserved
Keywords: Friction Stir Welding, Copper Alloys, Microstructure Studies, improvement in Mechanical Properties

1. Introduction

The Friction Stir Welding (FSW) technique was invented by The Welding Institute (TWI) in 1991 [1]. Since then, the material flow mechanism during welding and the microstructures of the welds have been discussed vigorously. The FSW process is executed while the materials are in a solid state, thus preventing many of the metallurgical problems that occur with conventional fusion welding, such as distortion, shrinkage, porosity and splatter. Furthermore, improved mechanical properties can also be achieved using this technique. Due to increasing demand for lightweight parts and environmental protection, [2] applied this new welding technology to aluminum products in automotive and aerospace industries. In particular, [3] used the FSW technique to easily weld 2000 and 7000 grade aluminum alloy sheets, which are traditionally difficult to weld with fusion welding.

Few papers on the FSW process discussed the temperature history (such as the temperature range and other forming conditions for a successful FSW process) in a pure copper work piece, where the melting point and material properties of the copper are significantly different from those of aluminum alloys. In this paper, FSW experiments using pure C11000 copper will be discussed, along with the process control required for a successful FSW process. The Welding of copper is usually difficult by conventional fusion welding processes because the copper has the high. Thermal diffusivity, which is about 10 to 100 times higher than in many steels and nickel alloys. The hear input required is much higher than in almost any other material, and weld speeds are quiet low. To overcome these problems, the FSW which is one of the solid state welding techniques is applied to the joining of copper. In this present study we explored the friction stir welding of copper. This study especially characterized and compared the microstructures of the copper base metal with those of the residual FSW zones using optical metallographic (OM) and transmission electron microscopy (TEM). Micro hardness profiles through the weld zone and corresponding tensile strength test data were also correlated with these microstructures. The basic concept of FSW is very simple. A non-consumable rotating tool with a specially designed pin and shoulder is inserted into the abutting edges of sheets or plates to be joined and traversed along the line of joint. The two primary functions of tools are heating of work piece and stirring/intermixing of material to produce the joint.

Corresponding author: R.S. Mishra
Email Id: rsmishra@dce.ac.in

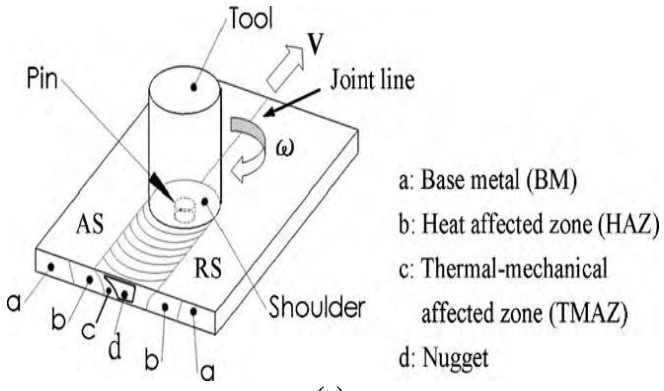

(a)

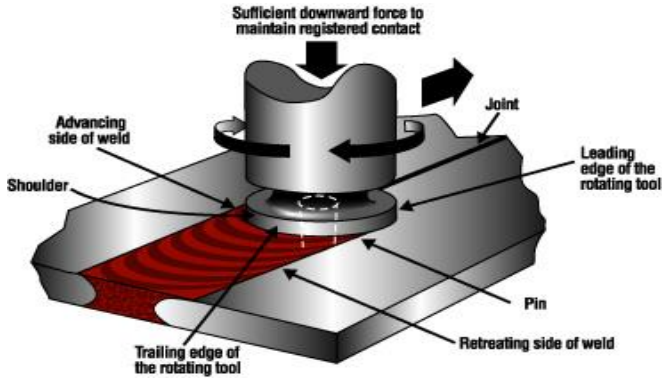

(b)

Figure 1(a)-(b) - Schematic diagram of FSW [1]

The heating is accomplished by friction between the tool and the work piece. During FSW process, the material undergoes intense plastic deformation at elevated temperature, resulting in the generation of fine and equiaxed recrystallized grains [4]. Heat generated by friction and deformation brings the material into a malleable state that promotes the forward displacement of the tool with the material flowing from the front to the back of the tool where it cools down, The weld is asymmetric since on one side of the weld, called the advancing side, the rotation of the tool is parallel to the advancing direction, while on the other side called the retreating side, the rotation is opposite to the direction of translation of the tool. The stirring of the tool minimizes the risk of having excessive local amounts of inclusions, resulting in a homogenous and void-free weld. Since the amount of heat supplied is smaller than during fusion welding, heat distortions are reduced and thereby the amount of residual stresses [5].

2. Literature Review

The weld quality is very dependent on the welding parameters such as tool rotation rate, the advancing speed and the tool geometry. A FSW joint consists of the various zones involving different microstructures and mechanical properties. The heat affected zone (HAZ) is the most distant from the joint center line. It is not deformed during the process but the microstructure evolves due to the welding thermal cycles, influencing the mechanical properties. The thermo-mechanically affected zone (TMAZ) and the nugget or stir zone (SZ) are highly deformed by the material rotational flow. The grains in the SZ are equiaxed with a much smaller size (several pm) than the base material. Under some welding conditions so-called onion rings are observed in the SZ [6].

2.1 Material flow and mechanism of joining

Recent literature and experimental works have provided significant insight about several features of materials flow during FSW and the joining process. Material flow occurs through the retreating side and the transport of the plasticized material behind the tool forms the welded joint. Three types of flow affect the overall transport of plasticized materials during FSW.

- First a slug of plasticized material rotates around the tool. This motion is driven by the rotation of the tool and the resulting friction between the tool and the work-piece.
- Another rotational motion of the threaded pin tends to push material downward close to the pin which drives an upward motion of an equivalent amount of material somewhat farther away.
- There is a relative motion between the tool and the work-piece. The overall motion of the plasticized material and the formation of the joint results from the simultaneous interaction of these three effects.

Several plastic flow models have been developed for understanding the material flow phenomena of FSW. These have been used to predict velocities around the tool pin. The velocities have also been estimated from strain rates which, in turn, were obtained from the correlation between grain-size and strain rate [7]. Comparison of the shape of the TMAZ predicted by flow models with microstructural observation has shown satisfactory match. Good agreement between the torque values obtained using dynamometers and the computed values from the flow models for 3ML stainless steel [8], 1 018 Mn steel [9] and Ti-6AI-4V alloy [10] indicates the usefulness of the models to understand the FSW process. Since torque is a measure of the shear stress on the tool and since the shear stress on the work-piece is responsible for both heat generation [11] and plastic flow, validation of the model predictions by experiments indicates that it is appropriate to use the models for the estimation of several important parameters. Though numerical modeling of plastic flow can aid tool design and the optimization of weld quality, there does not appear to have been an application of models towards the prediction of practical processing maps [12]. Arbegast et at. [13] Suggested that resultant microstructure and metal flow features of a friction stir weld closely resemble hot worked microstructure of typical aluminum extrusion and forging. Therefore, the FSW process can be modeled as a metalworking process in terms of five conventional metal working zones:

- Preheat Zone
- Initial deformation,

- Extrusion,
- Forging, and
- Post heat/cool down

The material flow during FSW is quite complicated and the understanding the phenomena of deformation process is difficult. It is important to point out that there are many factors that can influence the material flow during FSW. These factors include tool geometry (pin and shoulder design, relative dimensions of pin and shoulder), welding parameters (tool rotation rate and direction, traverse speed, plunge depth, spindle angle), material types, work piece temperature, etc. the material flow within the nugget during FSW consists of several independent deformation processes also [14].

2.2 Factors Affecting FSW

Friction Stir Welding depends upon various factors that affect the material flow pattern and temperature distribution which in turn affects the microstructural evolution of material.
Few major factors affecting FSW are—
1. Tool Geometry
2. Welding Parameters
3. Joint Design
4. Tool Tilt and Plunge Depth

2.3 Tool Geometry

The tool geometry has the highest impact on FSW. The tool geometry plays a critical role in material flow and hence the welding quality and maximum welding speed of the tool depends upon the design of the tool. As mentioned earlier, the tool has two primary functions [15] such as localized heating And material flow. The friction between the shoulder and workpiece results in the biggest component of heating. From the heating aspect. The relative size of pin and shoulder is important, and the other design features are not critical. The uniformity of microstructure and properties as well as process loads is governed by the tool design. Generally a concave shoulder and threaded cylindrical pins are used. The concave shoulder profile [16] acts as an escape volume for the material displaced by the pin and prevents material from extruding out of the sides of the shoulder. Maintains downwards pressure and hence good forging of the material behind the tool

2.4 Welding Parameters

For FSW, two parameters are very important—

(a) Tool rotation rate (how fast the tool rotates in clockwise or counter clockwise direction).

(b) Tool traverse speed (how quickly it traverses the interface) along the line of joint. The rotation of tool stirs and mixes the material around the rotating pin and the translation of tool moves the stirred material from the front to the back of the pin and finishes welding process. As temperature generated in FSW is due to friction between tool and material, so the higher tool rotation rates generate higher temperature because of higher friction heating and result in more intense stirring and mixing of material. A monotonic increase in heating with increasing tool rotation rate is not expected as the coefficient of friction at interface will change with increasing tool rotation rate. Similarly, the decrease in traverse speed results in generating higher temperatures. These parameters are optimized such that weld will have a sufficiently high heat input to ensure adequate material plasticity but not so high that the weld properties, are excessively deteriorated. In addition to the tool rotation rate and traverse speed, another important process parameter is the angle of spindle or tool tilt with respect to the workpiece surface. A suitable tilt of the spindle towards trailing direction ensures that the shoulder of the tool holds the stirred material by threaded pin and move material efficiently from the front to the back of the pin. Further, the insertion depth of pin into the work pieces (also called target depth) is important for producing sound welds with smooth tool shoulders. The insertion depth of pin is associated with the pin height. When the insertion depth is too shallow, the shoulder of tool does not contact the original workpiece surface. Thus, rotating shoulder cannot move the stirred material efficiently from the front to the back of the pin, resulting in generation of welds with inner channel or surface groove. [17-19].

2.5 Joint Design

The most common joint configurations for FSW are butt and lap joints. In butt Joint, two plates or sheets with same thickness are placed on a backing plate and clamped firmly to prevent the abutting joint faces from being forced apart. In lap joint two lapped plates or sheets are clamped on a backing plate. A rotating tool is vertically plunged through the upper plate and into the lower plate and traversed along desired direction, joining the two plates. In order to produce effective friction stir welded lap joints sufficient metallurgical and mechanical properties must be obtained by a nugget area as wide as possible together with satisfactory nugget integrity [17]. Cylindrical pins allow obtaining large nugget areas because of the large area they present at the sheet-sheet interface. Apart from butt and lap joint configurations, other types of joint designs, such as fillet joints, are also possible as needed for some engineering applications. Preheating or cooling can also be important for some specific FSW processes. For materials with high melting point such as steel and titanium or high conductivity such as copper, the heat produced by friction and stirring may be not sufficient to soften and plasticize the material around the rotating tool. Thus, it is difficult to produce continuous defect-free weld. In these cases, preheating or additional external heating source can help the material flow and increase the process window. On the other hand, materials with lower melting point such as aluminum and magnesium [18].

2.6 Tool Tilt and Plunge Depth

A suitable tilt of the spindle towards trailing direction ensures that the shoulder of the tool holds the stirred material by threaded pin and move material efficiently from the front to the back of the pin. Tilting the tool by 2-4 degrees, such that the rear of the tool is lower than the front, has been found to assist this forging process.
The plunge depth is defined as the depth of the lowest point of the shoulder below the surface of the welded plate and has been found to be a critical parameter for ensuring weld quality [19]. The insertion depth of pin is associated with the pin height. When the insertion depth is too shallow, the shoulder of tool does not contact the original workpiece surface. Thus, rotating shoulder cannot move the stirred material efficiently from the front to the back of the pin, resulting in generation of welds with inner channel or surface groove. When the insertion depth is too deep, the shoulder of tool plunges into the workpiece creating excessive flash. In this cases a concave weld is produced, leading to local thinning of the welded plates.

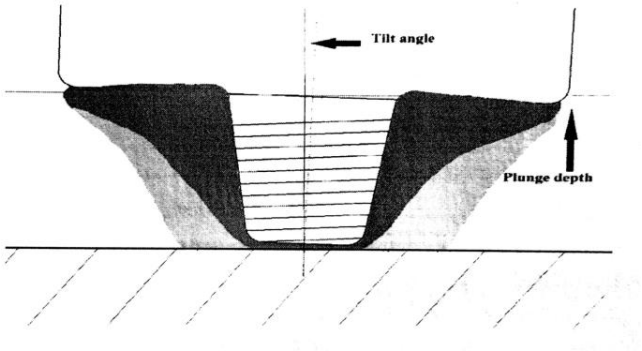

Figure 2: Plunge depth &Tilt angle

A survey of the researches which have been undertaken in this research area is outlined in this chapter. The materials which have been joined, similar or dissimilar, metallic or non-metallic will be discussed in relation to the welding conditions and parameters that gave different results. Here a brief discussion is provided and details will be given in the following sub topics. Traditional copper welding methods are associated with defects like porosity and voids, distortion, hot cracking and liquation cracking. Proper selection of FSW parameters results in a perfect joint which could be stronger than the base materials. Process parameters as well as tool geometry are the key factors that influence the soundness of the joint produced. Bahemmatet. et al recognized the importance of tool geometrical parameters which are height, shape, pin and shoulder that affect both the metal flow and the heat generation due to frictional forces developed.[20-23] Use of the proper tool gives the best results in an FSW weld. Traverse speed and rotational speed are factors that need to be taken into consideration when selecting welding parameters since these parameters determine the strength and overall performance of the joint.

2.7 Copper and its alloys

The similarity in external appearance of the various alloys, along with the different combinations of elements used when making each alloy, can lead to confusion when categorizing the different compositions. There are as many as 400 different copper and copper-alloy compositions loosely grouped into the categories: copper, high copper alloy, brasses, bronzes, copper, copper–nickel–zinc (nickel silver), copper, and special alloys. The table 2 shows the principal alloying element for four of the more common types used in modern industry, along with the name for each type. Historical types, such as those that characterize the, are vaguer as the mixtures were generally variable. Copper alloys are metal that have as their principal component. They have high resistance against. The best known traditional types are, where is a significant addition, and, using instead. Both these are imprecise terms, both having been commonly referred to as in the past. Copper is the oldest metal used by man. Its use dates back to prehistoric times. Copper has been mined for more than 10,000 years with a Copper pendant found in current day Iraq being dated to 8700BC. By 5000BC Copper was being smelted from simple Copper Oxides. Copper is found as native metal and in minerals cuprite, malachite, azurite, chalcopyrite and bornite. It is also often a by-product of silver production. Sulphides, oxides and carbonates are the most important ores. Copper and Copper alloys are some of the most versatile engineering materials available. The combination of physical properties such as strength, conductivity, corrosion resistance, machinability and ductility make Copper suitable for a wide range of applications. These properties can be further enhanced with variations in composition and manufacturing methods.
The largest end use for Copper is in the building industry. Within the building industry the use of copper based materials is broad. Construction industry related applications for Copper include:

- Roofing
- Cladding
- Rainwater systems
- Heating systems
- Water pipes and fittings
- Oil and gas lines
- Electrical wiring

2.8 Copper Application

The building industry is the largest single consumer of Copper alloys. The following list is a breakdown of Copper consumption by industry on an annual basis:

- Building industry – 47%
- Electronic products - 23%
- Transportation - 10%
- Consumer products - 11%
- Industrial machinery - 9%

There are around 370 commercial compositions for Copper alloys. The most common alloy tends to be C106/ CW024A -

the standard water tube grade of Copper. World consumption of Copper and Copper alloys now exceeds 18 million tonnes per annum.

2.9 Copper Designations

The table 1 shows the identifying chemical compositions. Property requirements are covered in EN, ASTM, government and military standards for each composition. The alloy designation system used in the UK and across Europe uses a 6 character alpha-numeric series. The 1st letter is C for Copper-based material the second letter indicates the product form
B = Ingot for re-melting to produce cast products
C = Cast products
F = Filler materials for brazing and welding
M = Master Alloys
R = Refined unwrought Copper
S = Scrap
W = Wrought products
X = Non-standard materials.
There is then a 3 digit number between 001 and 999 with the numbers being in groups as shown in the table below there is then a letter indicating the Copper or alloy grouping, also shown in the table-1.

Table- 1: Copper Designation

Number Series	**Letters**	**Materials**
001 – 099	A or B	Copper
100 – 199	C or D	Copper Alloys, Min. 95% Cu
200 – 299	E or F	Copper Alloys, <95% Cu
300 – 349	G	Copper-Aluminium Alloys
350 - 399	H	Copper-Nickel Alloys
400 - 449	J	Copper-Nickel-Zinc Alloys
450 - 499	L or M	Copper-Tin Alloys

Table 2 - Classification of copper and its alloys

Family	Principal alloying element	UNS numbers
Copper alloys, brass	Zinc (Zn)	C1xxxx–C4xxxx, C66400–C69800
Phosphor bronze	Tin (Sn)	C5xxxx
Al-bronzes	Aluminum (Al)	C60600–C64200
Silicon bronzes	Silicon (Si)	C64700–C66100
Copper nickel, nickel silvers	Nickel (Ni)	C7xxxx

3. Properties of copper alloys

Key Properties of Copper Alloys Copper is a tough, ductile and malleable material. These properties make copper extremely suitable for tube forming, wire drawing, spinning and deep drawing. The other key properties exhibited by Copper and its alloys include:

- Excellent heat conductivity
- Excellent electrical conductivity
- Good corrosion resistance
- Good bio fouling resistance
- Good machinability
- Retention of mechanical and electrical properties at cryogenic temperatures
- Non-magnetic Other Properties
- Copper and Copper alloys have a peculiar smell and disagreeable taste.
- These may be transferred by contact and therefore should be kept clear of foodstuffs, although some cooking pans.

3.1 Corrosion resistance

All Copper alloys resist corrosion by fresh water and steam. In most rural, marine and industrial atmospheres Copper alloys are also resistant to corrosion. Copper is resistant to saline solutions, soils, non-oxidising minerals, organic acids and caustic solutions. Moist ammonia, halogens, sulphides, solutions containing ammonia ions and oxidising acids, like nitric acid, will attack Copper. Copper alloys also have poor resistance to inorganic acids. The corrosion resistance of Copper alloys comes from the formation of adherent films on the material surface. These films are relatively impervious to corrosion therefore protecting the base metal from further attack. Copper Nickel alloys, Aluminium Brass, and Aluminium Bronzes demonstrate superior resistance to saltwater corrosion.

3.2 Electrical conductivity

The electrical conductivity of copper is second only to silver. The conductivity of Copper is 97% of the conductivity of Silver. Due to its much lower cost and greater abundance, Copper has traditionally been the standard material used for electricity transmission applications. However, weight considerations mean that a large proportion of overhead high voltage power lines now use Aluminium rather than Copper. By weight, the conductivity of Aluminium is around twice that of Copper. The Aluminium alloys used do have a low strength and need to be reinforced with a galvanised or Aluminium coated high tensile steel wire in each strand. Although additions of other elements will improve properties like strength, there will be some loss in electrical conductivity. As an example a 1% addition of Cadmium can increase strength by 50%. However, this will result in a corresponding decrease in electrical conductivity of 15%.

3.3 Surface oxidation

Most Copper alloys will develop a blue-green patina when exposed to the elements outdoors. Typical of this is the colour of the Copper Statue of Liberty in New York. Some Copper alloys will darken after prolonged exposure to the elements and take on a brown to black colour. Lacquer coatings can be used to protect the surface and retain the original alloy colour. An acrylic coating with benzotriazole as an additive will last several years under most outdoor, abrasion-free conditions.

3.4 Yield strength

The yield point for Copper alloys is not sharply defined. As a result it tends to be reported as either a 0.5% extension under load or as 0.2% offset. Most commonly the 0.5% extension yield strength of annealed material registers as approximately one-third the tensile strength. Hardening by cold working means the material becomes less ductile, and yield strength approaches the tensile strength.

3.5 Joining

Commonly employed processes such as brazing, welding and soldering can be used to join most Copper alloys. Soldering is often used for electrical connections. High Lead content alloys are unsuitable for welding. Copper and Copper alloys can also be joined using mechanical means such as rivets and screws.

4. Welding of Copper Alloys using Friction Stir Welding

Friction stir welding tool consists of a tool shoulder and a pin. Shoulder produces a majority of the deformational and frictional heat to the surface and subsurface regions and applies a forging pressure to welds, while the pin produces a majority of the heat in the thick work pieces and transports the material around it. Different tool designs will modify their effects on weld properties.

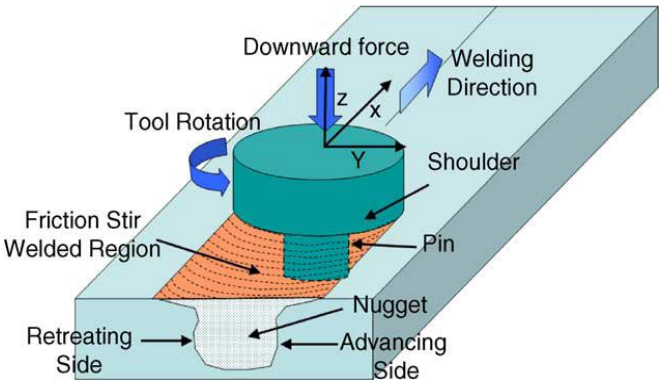

Figure 3 - Schematic diagram of FSW [5]

Tool geometry is the most influential aspect of process development. The tool geometry plays a critical role in material flow and in turn governs the traverse rate at which FSW can be conducted. An FSW tool consists of a shoulder and a pin as shown schematically in Fig. 2. As mentioned earlier, the tool has two primary functions: (a) localized heating, and (b) material flow. In the initial stage of tool plunge, the heating results primarily from the friction between pin and work piece. Some additional heating results from deformation of material. The tool is plunged till the shoulder touches the work piece. The friction between the shoulder and work piece results in the biggest component of heating. From the heating aspect, the relative size of pin and shoulder is important, and the other design features are not critical. The shoulder also provides confinement for the heated volume of material. The second function of the tool is to 'stir' and 'move' the material. The uniformity of microstructure and properties as well as process loads are governed by the tool design. Generally a concave shoulder and threaded cylindrical pins are used.

5. Mechanical Properties of Friction Stir Welding

The most commonly used testing methods to determine the properties of spot welds are lap-shear tension test, cross-tension test, fatigue test and micro hardness. Lap-shear test is a fast, convenient and practical method for evaluating weld property. This test was used in almost all current literature when considering the mechanical properties.
FSW/FSP results in significant micro structural evolution within and around the stirred zone, i.e., nugget zone, TMAZ, and HAZ. This leads to substantial change in post weld mechanical properties. In the following sections, typical mechanical properties, such as strength, ductility, fatigue, and fracture.

5.1 Strength and ductility

Mahoney investigated the effect of FSW on room-temperature tensile properties of C51000
.Tensile specimens were machined from the nugget zone in two directions, parallel (longitudinal) and normal (transverse) to the weld. Longitudinal tensile specimens contained only fully recrystallized grains from the nugget zone, whereas transverse tensile specimens contained microstructures from all four zones, i.e., parent material, HAZ, TMAZ, and nugget zone. Summarizes the longitudinal tensile properties of nugget zone. As-welded samples show a reduction in yield and ultimate strengths in the weld nugget, while elongation was unaffected. Mahoney attributed the reduced strength to the reduction in pre-existing dislocations and the elimination of the very fine hardening precipitates. In order to recover the lost tensile strength of the nugget zone, conducted a post weld aging treatment (121 8C/24 h) on the FSW sample, the aging treatment resulted in recovery of a large portion of the yield strength in the nugget, but at the expense of ultimate strength and in particularly ductility. The increase in the yield strength of post weld samples was attributed to the increase in the volume fraction of fine hardening precipitates, whereas the reduction in the ductility was accounted for by both the increase in the hardening precipitates and the development of precipitate-free zones (PFZs) at grain boundaries. The tensile properties in transverse orientation of FSW C51000 are summarized in. Compared to unwedded parent metal, samples tested in transverse direction show a significant reduction in both strength and ductility. Furthermore, the strength and ductility observed in transverse orientation are also substantially less than those in longitudinal orientation. The post weld aging treatment did not restore any of the strength to the as-welded condition and further reduced ductility. In

both as-welded and aged condition, failures occurred as shear fracture in the HAZ. As reported before, the tensile specimens in the transverse orientation cover four different microstructures, i.e., parent material, HAZ, TMAZ, and nugget zone. The observed ductility is an average strain over the gage length including various zones. The different zones have different resistances to deformation due to differences in grain size and precipitate size and distribution as discussed in Section 4. The HAZ has the lowest strength due to significantly coarsened precipitates and the development of the FPZs. Thus, during tension, strain occurs mainly in the HAZ, the low-strength HAZ locally elongated to high levels of strain (12–14%), eventually resulting in necking and fracture, whereas the nugget zone experiences only 2–5% strain. Therefore, fracture always occurred in the HAZ, resulting in a low strength and ductility along transverse orientation of the weld.

5.2 Fatigue

For many applications, like aerospace structures, transport vehicles, platforms, and bridge constructions, fatigue properties are critical. Therefore, it is important to understand the fatigue characteristics of FSW welds due to potentially wide range of engineering applications of FSW

5.3 Fracture toughness

It is usually accepted that all welded structures go into service with flaws ranging from volume defects like porosity, non-metallic inclusions to different planar defects like cracks induced by hydrogen or hot tearing. There are standards for acceptability of the welds pertaining to different inspection codes. The non-acceptable flaws must be repaired before the weld is put into service. Most existing codes cater toward weld elements made by conventional welding techniques. FSW is generally found to produce defect-free welds. However, no established code exists so far for FSW. Considering potential applications of FSW, there is a critical need for proper evaluation of the fracture behavior of the friction stir welds. 2.8 Work Piece Material
A commercial C51000 ASTM B103 plate which is solution heat treated, stress relieved by stretching then artificially aged is used as specimen for FSW. Chemical composition of work piece material is given in table

Table 3 – Chemical composition of C51000 (ASTM B103)

S.No	Element	Wt.%
1	Tin	4.2-5.8
2	Phosphorus	0.030-0.35
3	Iron, max	0.1
4	Lead, max	0.05
5	Zinc, max	0.3
6	Copper	89.75

5.4 FSW Tool Materials

Tool materials that can be applied during friction stir welding. These materials include tool steel for joining copper, aluminium and magnesium alloys; Polycrystalline cubic boron nitride (PCBN) tools for hard steel and titanium; tungsten based tools for steel and titanium alloys as well.
From the literature reviewed above, it has been shown that HSS, Die/Tool steels and Tungsten Carbide tools are commonly used in FSW of different material types. Straight tool profiles have always yielded best results as outlined by Palanivel and Koshy also carried out tests using HCH Cr steel tool. Five different tool pin profiles, (SS), (TS), (SH), (SO) and (TO) were identified. All the tools, the straight square pin profile yielded the best results at a speed of 60 mm/min in joining C69800.In another research friction stir welding tool pins like straight cylindrical, cylindrical taper, threaded cylindrical, square, and triangular with combinations of 15, 18, and 21mm shoulders were used by Elangovan and Balasubramanian to join copper alloy. In their investigation, square pins provided superior tensile properties with least number of defects.

Table 4 – Chemical composition of HSS M2 Steel

S.No	Element	Wt.%
1	C	0.78-0.88
2	Si	0.20-0.40
3	Mn	0.20-0.40
4	P	0.35
5	S	0.35
6	Cr	3.75-4.50
7	Mo	4.50-5.50
8	V	1.60-2.20
9	W	5.50-6.75

5.5 High speed steel grades

M2 is a high-speed steel in tungsten–molybdenum series. The carbides in it are small and evenly distributed. It has high wear resistance. After heat treatment, its hardness is the same as T1, but its bending strength can reach 4700 MPa, and its toughness and thermo plasticity are higher than T1 by 50%. It is usually used to manufacture a variety of tools, such as drill bits, taps and reamers. Its decarburization sensitivity is a little bit high.

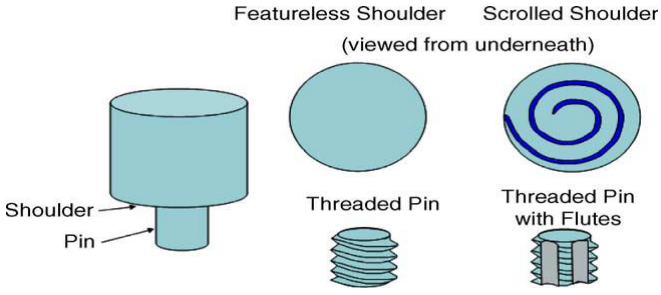

Figure 4 - FSW Tool tip Types

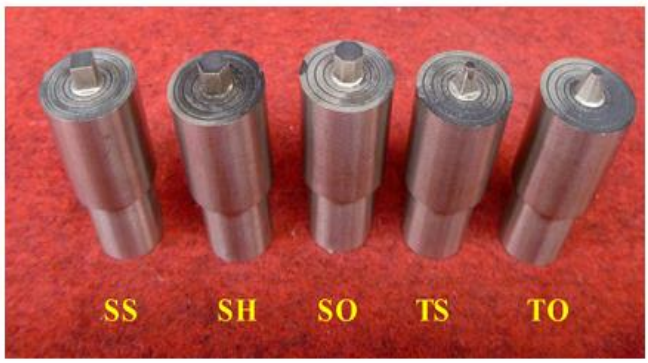

Figure 5 - Tool Pin Profiles

5.6 Microstructure Analysis

Microstructure of the welded joint achieved using the FSW procedure consists of: a) weld nugget, b) thermo mechanically affected zone (TMAZ), c) heat-affected zone (HAZ), and d) The parent metal. Depending on the microstructure of welded joint, there are three different mechanical properties of the weld. The present research is focused on welding copper and its alloys. Grains of the base material (copper) are elongated in shape and their size is about 30 microns.
Microstructure of the weld nugget is very fine, with a grain size of about 11 microns. This seam zone is characterized by dynamic recrystallization due to the influence of tribological processes (mechanical friction and plastic deformation), which results in higher hardness compared to the base material.

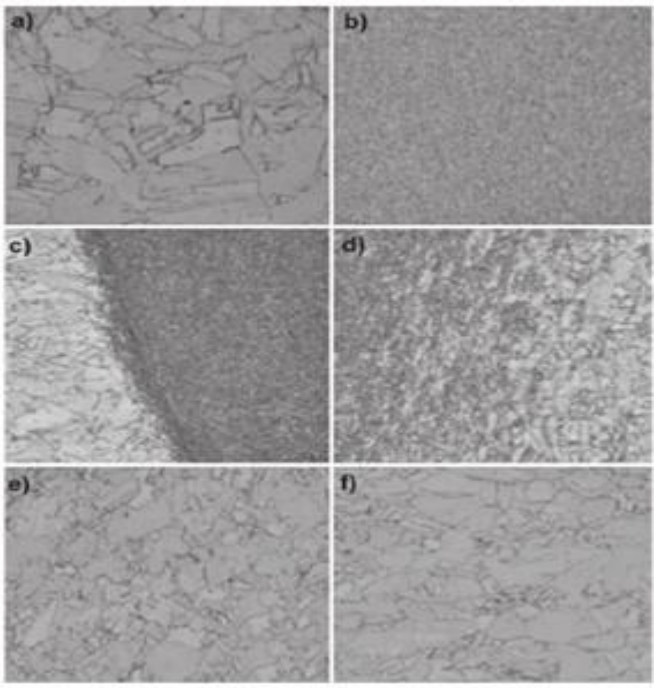

Figure 6: Microstructure of the welded copper joint
(a) base metal, (b) Nugget zone,(c) TMAZ of TMAZ,(d) TMAZ of RS, (e) HAZ of AS, (f) HAZ of RS

6. FSW Experimental Set-Up

A indigenous developed friction stir welding machine (R V machine tools, FSW-4T-HYD) (15 hp; 3000 rpm; 25 kN) as shown in figure 7 is used for welding process. This machine has a vertical spindle to hold the tool and a fixture with four hydraulic actuated clamps and a backing plate with groove (200mm x 80mm) to hold the work piece. Work holding fixture can move in X, Y and Z axis. Groove on backing plate is meant to strongly hold the work piece. Maximum operational speed of spindle is 3000 rpm. Rotational speed, welding speed and tool tilt angle can be altered easily but welding force cannot be changed on this machine.

Figure 7 –Friction stir welding machine (DTU)

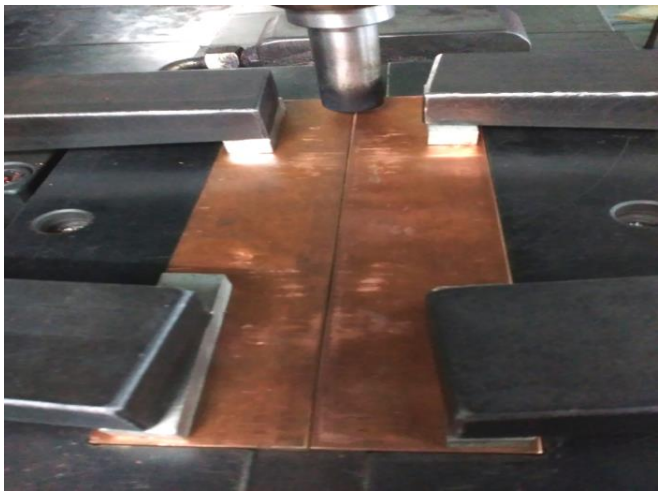

Figure 8 –Tool and work holding device

6.1 Experimental procedure

The 3mm thick plates were cut into the required sizes two plates (200 mm X 40mm) by power hacksaw cutting and milling. Square butt joints were prepared by FSW machine which is mention in section 3.1. The spindle of this self-

designed FSW apparatus can spin with rotational speeds from (800 rpm – 1200 rpm), and the fixture table, driven by a servomotor, can move with speeds 60 mm/min. Before welding, the work piece is polished and cleaned with acetone on the welding surface and is then placed on a backing plate and clamped rigidly by an anvil along the welding direction to prevent lateral movement (Figure 8). The dimension of the C11000 copper work piece is 200mm×40mm×3mm (L×W×H). The geometry and dimensions of the tool, made of M2 high-speed steel, are shown in Fig. 3. A concave part close to the shoulder is specially designed to prevent massive heat loss from the shoulder to the shank of the tool. Because the thickness of the work piece is only 3mm, the length of the pin is designed to be 2.7mm. The diameter of the shoulder, 19.95mm, is about four times of that of the pin, 4mm, at its root. An inclination angle of 1.5◦, with respect to the welding tool and the normal vector of the work piece, was set before welding to allow the tool to smoothly traverse the work piece.

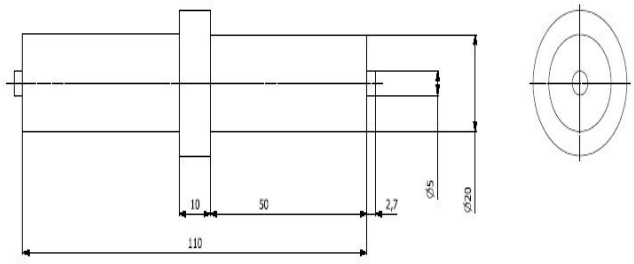

Figure 9 - Dimensions of the tool and pin

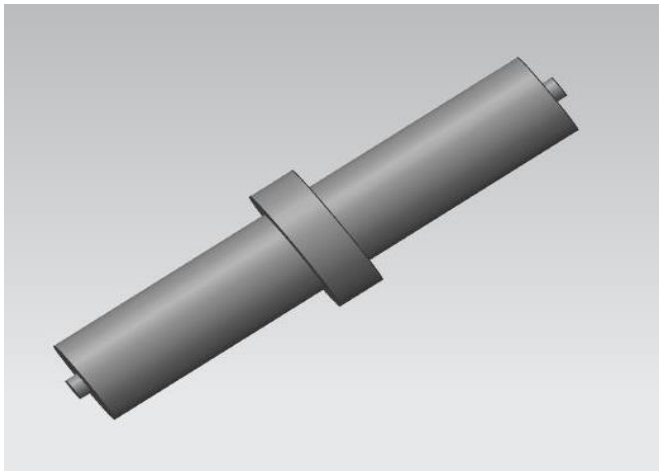

Figure 10- FSW Tool- circular tip

The rotation direction and the direction of motion of the tool are shown in Fig. 4. As further depicted in Fig. 4, two of the four thermocouples (TC1 and TC3) were placed on the advancing side, and the other two (TC2 and TC4) were placed on the retreating side. The distances between the tips of the thermocouples and the joint line are all 6mm. This kind of layout was used to measure the temperature histories on the advancing and retreating sides. Two kinds of welding conditions (a) ω= 800 rpm, *v* = 60mm/min and (b) ω= 1000 rpm, *v* = 60mm/min were selected for the welding experiments. During the FSW process, the pin is first plunged into the work piece with a depth of 2.85mm. At this moment, the downward force is about 5 kN. After the temperature increases to about 400 ◦C, the downward force increases to about 7.5 kN due to the expansion of the heated metal. Because of the capacity limitation of this FSW machine, the downward force has to be kept under 10 kN. The appearance of a welded product with condition (b) is shown in Fig. 5. Circular rings on the surface of the weld could be clearly observed, and a hole was left after the pin retracted from the work piece, just as happens in the standard FSW process.

Figure 11 - Friction Stir Welded for ω= 800rpm and v = 60 mm/min, downward force= 7.5kN

6.2 Tool geometry

Tool geometry is the most influential aspect of process development. The tool geometry plays a critical role in material flow and in turn governs the traverse rate at which FSW can be conducted. An FSW tool consists of a shoulder and a pin as shown schematically in Fig. 2. As mentioned earlier, the tool has two primary functions: (a) localized heating, and (b) material flow. In the initial stage of tool plunge, the heating results primarily from the friction between pin and work piece. Some additional heating results from deformation of material. The tool is plunged till the shoulder touches the work piece. The friction between the shoulder and work piece results in the biggest component of heating. From the heating aspect, the relative size of pin and shoulder is important, and the other design features are not critical. The shoulder also provides confinement for the heated volume of material. The second function of the tool is to ‘stir’ and ‘move’ the material. The uniformity of microstructure and properties as well as process loads are governed by the tool design. Generally a concave shoulder and threaded cylindrical pins are used. With increasing experience and some improvement in understanding of material flow, the tool geometry has evolved significantly. Complex features have been added to alter material flow, mixing and reduce process loads.

Figure 12 -FSW Tool –circular shape pin tool

6.3 Experimental procedure

In this study, commercial pure copper which had 200 mm in length, 40 mm in width and 3 mm in thickness was welded by butting two plates and stirring them together with a rotating tool assembly. The tool rotation speed was 800 rpm with lower welding speed providing optimum welding. A transverse speed of 60 mm/min was also employed. The butted plates were clamped on a steel backing plate. The welding tool titled by a 1.5 degree of angle with welded specimens was rotated in the clockwise direction and specimens, which were tightly fixed at the backing plate, were traveled. Micro structural changes from the weld zone to the unaffected base metal were examined with OM (Optical Microscopy), and TEM (Transmission Electron Microscope). For TEM observation, thin-foil disk specimens, 3 mm in diameter, were cut from the weld zone and the base metal using the electron discharge machine and were prepared by twin-jet electro polishing in nitric acid/methanol solution at 243 K. This thin foils were observed at 300 kv using a JEOL transmission electron microscope. The Vickers hardness profile of the weld zone was measured on a cross section and perpendicular to the welding direction using a Vickers indenter with a 200 gf load for 10 seconds. The tensile test was carried out using an Instron-type testing machine with crosshead speed of 1.67_10_2 mm/s.

Table-5: Tool Parameters

S.No.	Rotational Speed (rpm)	Transverse Speed (mm/min)	Tool Diameter(mm)
1	800	60	4
2	1000	60	5

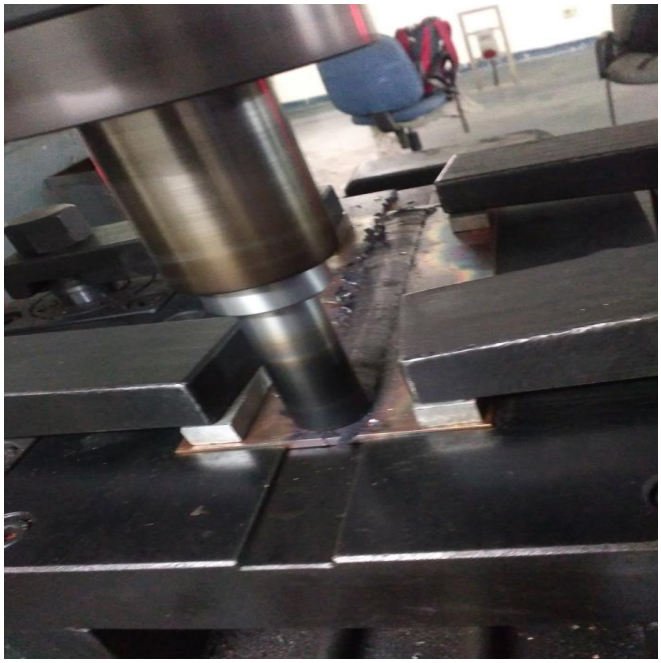

Figure 13 -Tool and work holding device of FSW

Figure 14 -Welded specimens before welding

Figure 15 - Welded specimens after FSW

7. Result and discussion

Uniaxial tensile test at room temperature were performed in order to evaluuate the mechanical properties of the joints.To determine the tensile strength of the stir zone ,small tensile test specimens were sectioned in transverse direction of the weld line with an electric discharge machine (EDM). Specimen is cut as per ASTM:B557-06 standard which is shown in figure. Tensile test is performed at a speed of 1mm/min.

Figure 16: Tensile Test Machine

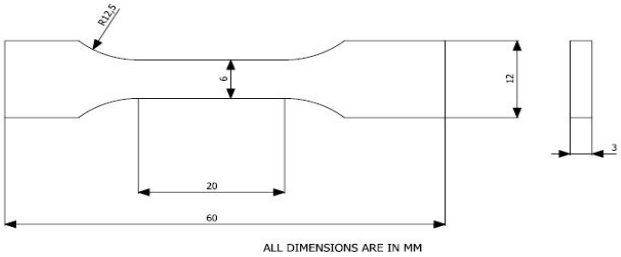

Figure 17 -Tensile Test Specimen

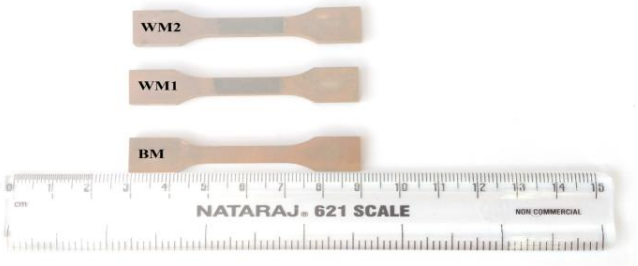

Figure 18 -Tensile Specimen Base Material 2&3. Welded Material

Figure 19 -Welded Plate after cutting Tensile Specimen

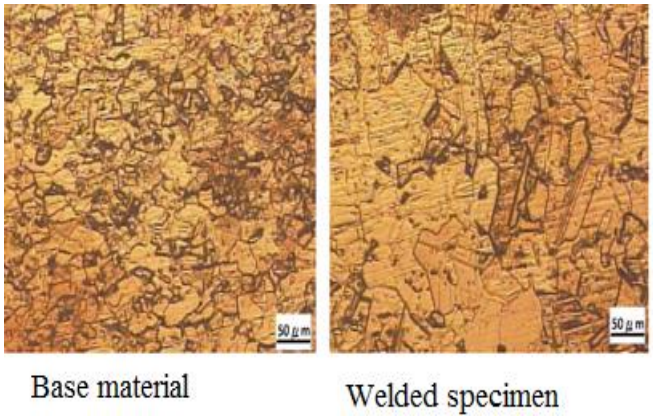

Figure 20-Microstrcture of copper specimen

The Similar joints C51000 ASTM B103 were successfully joined by the Friction Stir Welding process and showed no visible defects from the outside. The parameters for which joining was successful for all combinations

The tensile strength of all the joints were lower than those of the base material, regardless of the rotational speeds and welding speeds as previously noted. Tensile tests were carried out and Figure gives the results of the tests.

The Similar joints were successfully obtained at various speeds and feeds. The joint strongest had a maximum tensile strength of 241 MPa. This strength is 87% of C51000 ASTM B103 base material.

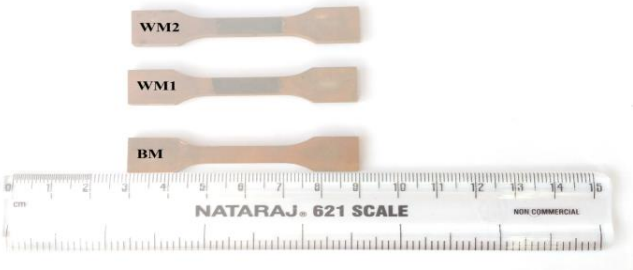

Figure 21: Tensile Test Specimen

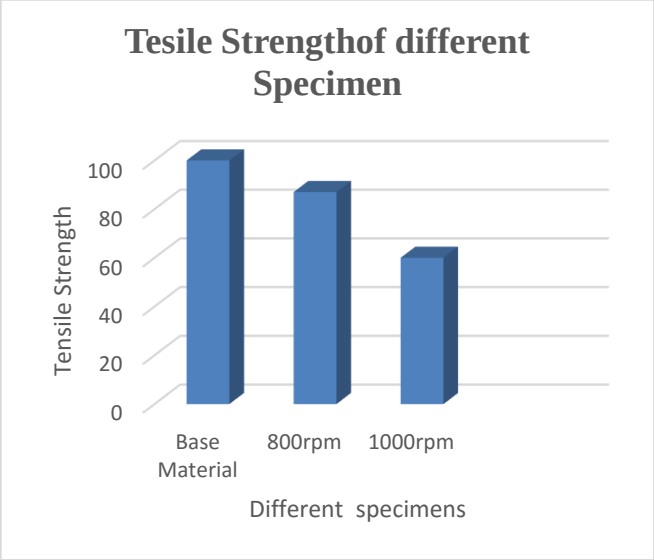

Figure 22 -Tensile strength of different specimen

Study on FSW of C51000 ASTM B103 with parameters ranging from 800 to 1200 rpm and 60mm/min is conducted. Tensile test results shows that, tensile strength of Friction Stir joint decreases with respect to the base material , When welding is done by FSW the best parameter of Friction Stir Welding for copper C51000 ASTM B103 of 3mm plate thickness is 800 rpm and 60mm/min in which 87% of tensile strength of base material.

8. Conclusions and Recommendations

Friction stir welding method can be successfully applied to join copper and acquired results are as follow

1. Defect free weld zone was formed with the condition of 800 rpm and 60 mm/min. The grain structure near weld zone was very different from that of the base metal. Heat affected zone (HAZ) were characterized by grain growth and stir zone had fine and equiaxed grain structure.
2. Slightly softening region was formed in the weld zone in spite of smaller grain size compare to that of base metal. Hardness of FSW copper weld zone mainly depended on the density of dislocation rather than grain size. Hardness variation also existed in the stir zone from the upper to the lower region with thermal and mechanical conditions.
3. Transverse tensile strength of FSW copper joint reached the 87% of tensile strength of base metal.

References

[1] Thomas, W.M., Nicholas, E.D., Needham, J.C., Murch, M.G., TempleSmith, P., Dawes,C.J., 1991. The Welding Institute, TWI, International Patent Application No.PCT/GB92/02203 and GB Patent Application No. 9125978.8.

[2] Colligan, K.J.,Konkol, P.J., Fisher, J.J., Pickens, J.R., 2003. Friction stir welding demonstrated for combat vehicle construction. Weld. J. 82, 34–40.

[3] Kakimoto, H., 2005. Study on application of FSW to aircraft. J. Jpn. Soc. Technol. Plast.46, 939–943.

[4] EI-Danaf E.A., El-Rayes M. M., Microstructure and mechanical properties of friction stir welded 6082 AA in as welded and post weld heat treated conditions, Materials and Design, 46 (2013) 561-572.

[5] Ericsson M., Sandstrom R., Influence of welding speed on the fatigue of friction stir welds, and comparison with MIG and TIG. International Journal of Fatigue, 25 (2003) 1379-87.

[6] Simar A., Brechet Y., Meester B., Denquin A., Gallais C., Pardoen T., Integrated modeling of friction stir welding of 6xxx series Al alloys: Process, microstructure and properties,Progress in Materials Science, 57 (2012) 95-183.

[7] Koumoulos E.P., Charitidis C.A., Daniolos N.M., Pantelis D.l., Nanomechanical properties of friction stir welded AA6082-T6 aluminum alloy, Materials Science and Engineering S, 176 (2011) 1585- 1589.

[8] Scialpi A., Filippis L.A.C., Cavaliere P., Influence of shoulder geometry on microstructure and mechanical properties of friction stir welded 6082 aluminium alloy, Materials and Design, 28 (2007) 1124-29.

[9] Cavaliere P., De Santis A., Panella F., Squillace A., Effect of welding parameters on mechanical and microstructural properties of dissimilar AA6082-AA2024 joints produced by friction stir welding, Materials and Design 30 (2009) 609-16.

[10] Liu H.J., Hou J.C., Guo H., Effect of welding speed on microstructure and mechanical properties of self-reacting friction stir welded 6061-T6 aluminum alloy, Materials and Design 50 (2013) 872-78.

[11] Jata K.V., Semiatin S.L., Continuous dynamic recrystallization during friction stirwelding, Scripta Materialia 43 (2000) 743-48.

[12] Nandan R., Roy G.G., Lienert T.J., Deb Roy T., Numerical modelling of 3D plasticflow and heat transfer during friction stir welding of stainless steel. Science and Technology of Welding and Joining, 11 (2006) 526-37.

[13] Nandan R., Roy G.G., Lienert T..I., Deb Roy T., Three-dimensional heat and material now during friction stir welding of mild steel, Acta Matcrialia, 55 (2007) 883-95.

[14] Nandan R., Lienert T.J., Deb Roy T., Toward reliable calculations of heat and plastic flow during friction stir welding of Ti- 6Al-4V alloy, International Journal of Materials Research, 99 (2008) 434-44.

[15] Khandkar M.Z.H., Khan J.A., Reynolds A.P., Prediction of temperature distribution and thermal history during friction stir welding: input torque based model. Science and Technology of Welding and Joining, 8 (2003) 165-74.

[16] Bhadeshia H.K.D.H., Mathematical models in materials science. Material Science Technology, 24 (2008) 128-35.

[17] Arbegast W.J., Jin Z., Beaudoin A., Bieler T.A., Radhakrishnan B., Hot Deformation of Aluminum Alloys III, TMS, Warrendale, PA, USA, 2003, page. 313.

[18] Arbegast W.J., Jin Z., Beaudoin A., Bieler T.A., Radhakrishnan B., Hot Deformation of Aluminum Alloys III, TMS, Warrendale, P A, USA, 2003, p. 313.

[19] Thomas W.M., Johnson K.l., Wiesner C.S., Friction stir welding-recent developments in tool and process technologies, Advanced Engineering Material, 5 (2003) 485-90.

[20] Thomas W.M., Friction stir welding-recent developments, Material Science Forum, 426,432 (2003) 229-36.

[21] Thomas W.M., Staines D.G., Johnsonand K.l., Evans P., Com-stir-compound motion for friction stir welding and machining, Advanced Engineering Material. 5 (2003) 273-4.
[22] Buffaa G., Campanileb G., Fratini L., Priscob A., Friction stir welding of lap joints: Influence of process parameters on the metallurgical and mechanical properties, Materials Science and Engineering A, 519 (2009) 19-26.
[23] Leonard A.J., Microstructure and aging behaviour of FSW in Al alloys 2014A-T651 and 7075-T65I. 2nd International Symposium on FSW (CD ROM). Gothenburg, Sweden, Composites Science and Technology, 65 (2005) 2526-40.
[24] Husain Mehdi, R.S. Mishra, Mechanical properties and microstructure studies in Friction Stir Welding (FSW) joints of dissimilar alloy- A Review, Journal of Achievements in Materials and Manufacturing Engineering 77/1 (2016) 31-40.
[25] Husain Mehdi, R.S. Mishra, Influences of Process Parameter and Microstructural Studies in Friction Stir Weldingof Different Alloys: A Review, International Journal of Advanced Production and Industrial Engineering, IJAPIE-SI-MM 509 (2017) 55–62.

Filters Modified ComplementarySplit-Ring Resonator Geometries with Face to Face Orientations in Substrate Integrated Waveguide for Applications as Band Pass

Jigyasa Sharma[1]*, Dhirendra Kumar[2], and Asok De[1]

[1]National Institute of Technology, Patna, Bihar, 800001, India;
[2] Raj Kumar Goel Institute of Technology, Ghaziabad, U.P. 201001, India.
*jigyasa.nsharma@gmail.com

Abstract. Novel face to face oriented square complementary split-ring resonators in substrate integrated waveguide (SIW) have been proposed and discussed. In the proposed structures the inner loop of the conventional CSRR is replaced by square and triangular slots. Like the conventional CSRRs, the proposed structures allow the implementation of a forward-wave passband which is propagating below the characteristic cutoff frequency of the waveguide. The proposed designs have the advantages of the better pass band and enhanced bandwidth compared to conventional CSRR for applications in miniaturized waveguide bandpass filters.

Keywords: Complementary split-ring resonators (CSRRs), electric dipoles, miniaturised planar waveguide filters, Substrate integrated waveguide (SIW).

1. Introduction

Split-ring resonators (SRR) and complementary split-ring resonators (CSRR) are the simplest metamaterial structures. The complementary split ring resonators (CSRRs) are the dual counterparts of split ring resonators (SRRs) and have been projected as effective constitutive elements for the synthesis of negative permittivity media based on resonant elements [1]. The dominant driving mechanism for CSRRs excitation is electric coupling, the condition being that the electric field must be applied in the axial direction. This is because in the complementary structure, the electric boundary conditions on the metal are replaced with magnetic ones and hence the structure becomes effectively dual. Due to this, the CSRRs electromagnetic behaviour is, in fact, an electric dipole excited by an axial electric field demonstrating propagation properties similar to an effective negative epsilon medium [2, 3]. Classical waveguide is not preferable in today's miniaturized electronic communications due to its bulk size and inability for post-tuning. When it comes to high-Q performance and low losses, even planar transmission lines are limited in performance. A solution to the aforementioned problems is a utilization of substrate integrated waveguides, which are very convenient for field transmission at high frequencies, especially, millimeter waves [4]. Furthermore, SIWs are highly applicable for mass production using well developed modern IC-technologies [5]. The field distribution in an SIW is similar to TE_{10} mode in a conventional rectangular waveguide. The electric field for TE_{10} mode within SIW is perpendicular to the surface and ground, and the direction of the magnetic field is parallel to the waveguide surface and perpendicular to the sidewalls. Hence the placement of CSRRs in an SIW is quite convenient.

As wireless communication relentlessly advances on frequency spectrum, there is a great need for designing small size active and passive circuits particularly filters at millimeter frequencies. Development of new compact, cheap components with low losses for Ka, V and W bands is strongly required from the point of satisfaction for fast increasing industrial needs. When the SIW is loaded with CSRRs, the CSRRs provide a stop band when they are resonant above the cutoff frequency [6-9] and this stop band switches to a pass band when the CSRRs are resonant below the cutoff frequency [10,11].There are derivations of CSRR orientations, such as face to face, back to back and side by side and each of these structures can be represented by equivalent circuit models [10]. In this paper, SIW loaded by novel unit cells of the modified CSRR pairs with face to face orientations are proposed and investigated. This alignment is able to provide strong coupling between the waveguide and the CSRRs since the electric field reaches maximum in the waveguide center.

In this paper, we present two novel structures which are obtained by appropriately modifying the conventional CSRR configuration in SIW with an inspection to their possible applications as pass band filters. As a validation of their working principles, the magnetic field distributions at the pass band centre frequency for the proposed structures have been presented. The transmission behavior both below and above the waveguide cutoff frequency has been considered on making this study distinctive from the previous research [6-8]. All simulations are performed using CST microwave studio [9].

2. SIW-CSRR structures and characterization

This part discusses the characteristics of CSRRs resonant below the waveguide cutoff frequency intending to their working principles and possible applications. According to the theory of evanescent-mode propagation, an additional pass band below the waveguide cutoff can be obtained for a waveguide by loading it with electric dipoles (CSRRs) [12], [13]. For the selected dielectric substrate RT/Duroid 5880

© 2017 IJAMT

with ε_r = 2.2 and thickness of 0.787mm, the width of the waveguide, w is set to 3.5 mm (SIW1) in the design to fix the nominal cutoff frequency of the waveguide to 30 GHz and to 4mm (SIW2) for a cutoff frequency of 25.65 GHz. The metalized vias have a diameter of 0.25 mm and a center to center spacing of 0.4mm. The structure of the conventional CSRR and the layout of the unit cells are depicted in Figure 1.

Figure 2 shows the transmission response for the SIW1 and SIW2 with conventional CSRR pairs in face to face orientations as illustrated in figure 1(b), simulated with CST MWS. The values of a_1=a_2=g=d are optimized at 0.08 mm, b=0.65 mm, t= 0.43 mm and l =1.365mm. A pass band with a center frequency of 29 GHz (3dB bandwidth = 1.884GHz) is observed in SIW1 and at a centre frequency of 28 GHz for SIW2. SIW2 has been employed to obtain the resonance of face to face coupled CSRRs in the frequency band of waveguide operation, and SIW1 is used to get the resonance below the cutoff frequency of 30GHz. Hence a pass band can be obtained in both ways by using coupled CSRRs in a SIW. A microstrip feed line is used to excite the SIW, with a tapered transition. The CSRRs have not been etched on the ground to preserve its integrity as in high- frequency system design noise and radiation losses may be introduced by the ring slots.

3. Proposed structures with improved performance

This section presents the configurations of the proposed SIW-CSRR unit cells, subsequently explaining the corresponding transmission behaviour followed by the filter applications of the proposed structures.

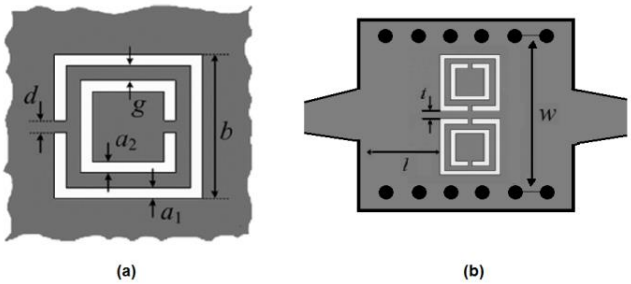

Fig.1. (a) The conventional square CSRR topology (grey zone represents metallization) (b) Face to face configuration of SIW-CSRR unit cells.

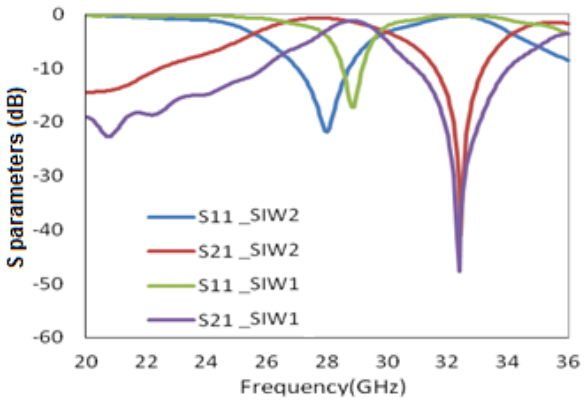

Fig.2. Transmission response for the SIW1 and SIW2 with conventional CSRR pairs.

3.1 Configurations and Transmission Responses

The layout of the SIW structure with a pair of modified CSRR pairs with face to face orientations is shown in Figure 3. In the structure in Figure 3(a), henceforth referred to as the structure-1, the inner loop of the conventional CSRR is replaced by a square slot of the same dimensions. In the second structure henceforth referred to as the structure-2, the square shape is replaced by an equilateral triangle with the same dimensions of the side as that of the original square. Figure 4(a) and 4(b) depicts the transmission responses of structure-1 and structure-2 respectively when incorporated in SIW1. Both the structures illustrate a better pass band with improved 3 dB bandwidths of 3.18 GHz and 7.0825 GHz for structures 1 and 2 respectively, in comparison to the conventional CSRRs in SIW1. The improved bandwidth of structure-1 is attributed to the increase in the resonant frequency of the effective capacitance between the central patch and ground for a conventional CSRR is nullified.

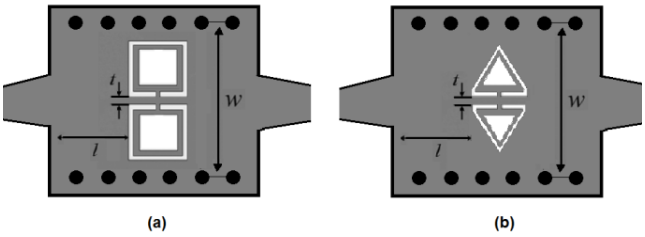

Fig.3. Configurations of the proposed SIW-CSRR unit cells: (a) Structure-1, (b) Structure-2.

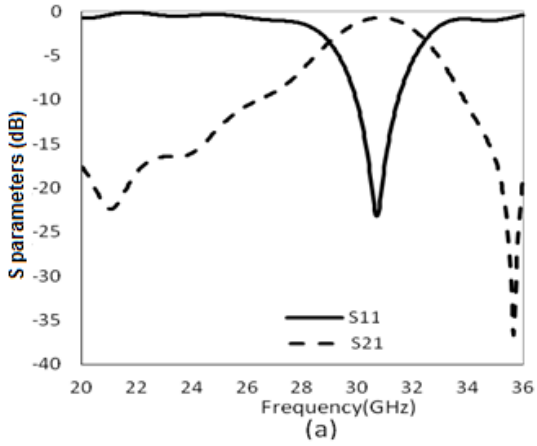

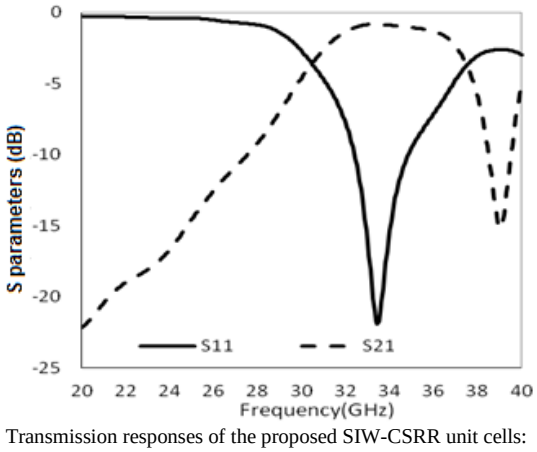

Fig.4. Transmission responses of the proposed SIW-CSRR unit cells: (a) Structure-1, (b) Structure-2.

© 2017 IJAMT

In structure-2 the perimeter of the inner slot of CSRR is reduced compared to structure-1, as a consequence, the centre frequency of the pass band increases further giving rise to a much wider pass band which is now above the waveguide cutoff.

Figure 5 depicts the simulation results of the magnetic field distributions in the middle plane of the substrate at the center frequency of the pass band for the conventional CSRR, structure-1 and structure-2 respectively. As evident from Figure 5 the propagation of the evanescent mode is highly reliant on the middle metal region between the two CSRRs and hence on altering the configurations of the inner ring of the CSRR no harm is done to this mode.

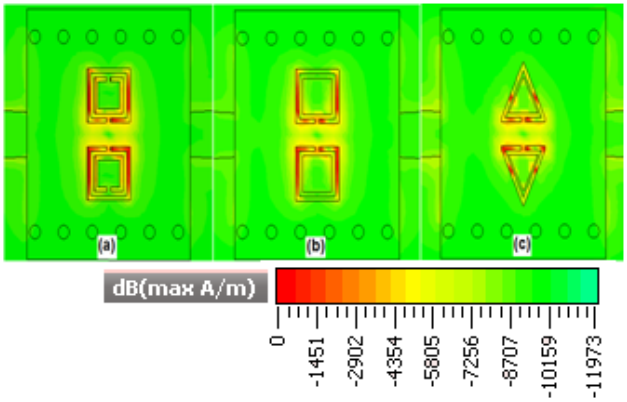

Fig.5. Magnetic field distributions of the (a) Conventional CSRR unit cell (b) Structure-1, (c) Structure-2.

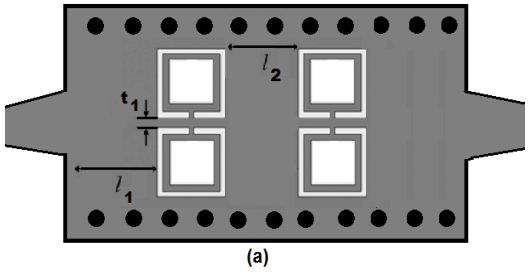

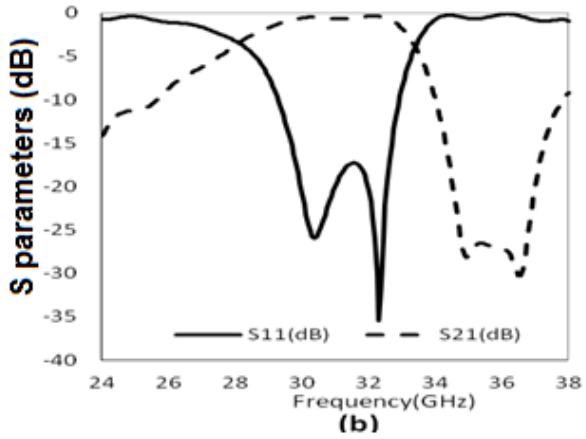

Fig. 6. (a) Two pole filter with Structure-1 unit cells (b) its transmission response.

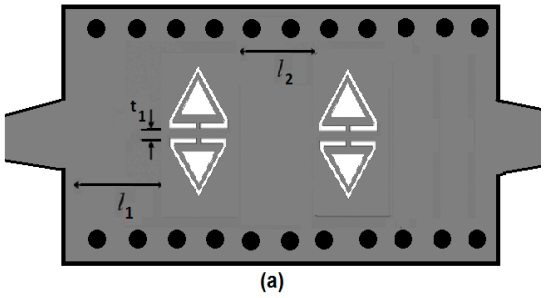

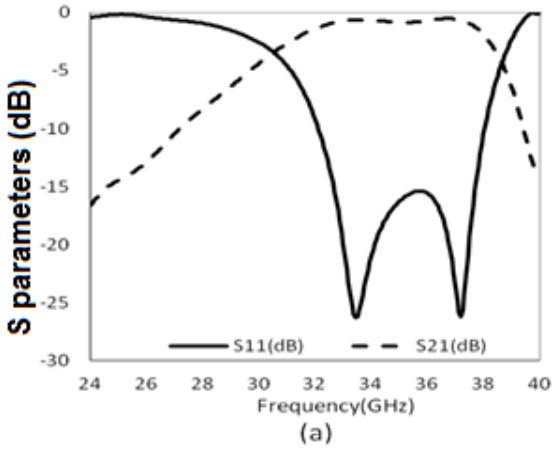

Fig. 7. (a) Two pole filter with Structure-1 unit cells (b) its transmission response.

3.2 Filter applications of the proposed structures

This section presents two types of filters based on the proposed new resonators (Structure-1 and Structure-2 unit cells respectively). The substrate, thickness, via diameter and center to center spacing of vias are same as for the above-mentioned cases. Figures 6(a) and 7(a) depict the two pole filters based on Structure-1 and Structure-2 unit cells respectively. For both the filters shown in Figure 6 and 7 l_1=l ,t_1=t and l_2=1.03mm.The transmission responses are shown in Figures 6(b) and 7(b).

4. Conclusion

Two novel structures are proposed as modifications of the conventional CSRRs in face to face configurations. Based on the theory of pass band created below the cutoff of SIW by CSRRs the proposed structures provide an enhanced bandwidth compared to the conventional CSRRs. By designing two pole filters based on the proposed structures it has been shown that the proposed structures are capable of providing suitable filtering characteristics.

References

[1] J. D. Baena, J. Bonache, F. Martin, R. Marques, F. Falcone, T. Lopetegi,M. A. G. Laso, J. Garcia, I. Gil, and M. Sorolla, Equivalent-circuit models for split-ring resonators and complementary split-ring resonators coupled to planar transmission lines, *IEEE Transactions on Microwave Theory and Techniques*, vol. 53, no. 4, pp. 1451-1461, Apr. 2005.

© 2017 IJAMT

[2] M. Gil, J. Bonache, J. Garcia, J. Martel, F. Martin, Composite right/left-handed metamaterial transmission lines based on complementary split-rings resonators and their applications to very wideband and compact Filter design', *IEEE Transactions on Microwave Theory and Techniques*, 2007, 55, (6), pp. 1296-1303.

[3] J. Bonache, M. Gil, I. Gil, J. Garcia, and F. Martin, On the electrical characteristics of complementary metamaterial resonators," *IEEE Microwave Wireless Components Letters*, vol. 16, no. 10, pp. 543-545, Oct. 2006.

[4] Deslandes D. and K. Wu, Design considerations and performance analysis of substrate integrated waveguide components, *European Microwave Conference*, pp, 881-884, 23 - 27 sept. 2002.

[5] Wu K., D. Deslandes, and Y. Cassivi, The substrate integrated circuits-a new concept for high-frequency electronics and optoelectronics, *TELSKIS 2003, NIS, Serbia and Montenegro*, October 2003.

[6] X. Zhang, Z. Yu, and J. Xu, Novel band-pass substrate integrated waveguide filter based on complementary split ring resonators, *Progress in Electromagnetic Research.*, vol. 72, pp. 39 - 46, 2007.

[7] W. Che, C. Li, K. Deng, and L. Yang, A novel bandpass filter based on complementary split rings resonators and substrate integrated waveguide, *Microwave and Optical Technology Letters*, vol. 50, no. 3, pp. 699 - 701, Nov.2008.

[8] Jin J. D and D. H Yu, Substrate Integrated Waveguide Band-pass Filter with Coupled Complementary Split Ring Resonators, in *General Assembly and Scientific Symposium (URSI GASS)*, 2014, pp. 1 - 4.

[9] CST Microwave Studio – www.cst.com

[10] Y. D. Dong, T. Yang, T. Itoh, Substrate integrated waveguide loaded by complementary split-ring resonators and its applications to miniaturized waveguide filters, *IEEE Transactions on Microwave Theory and Techniques*, 2009, 57, (9), pp. 2211‑2223

[11] Q. L. Zhang, W. Y. Yin., S. He, and L. S. Wu, Compact Substrate Integrated Waveguide (SIW) Bandpass Filter With Complementary Split-Ring Resonators (CSRRs), *IEEE Microwave Wireless Components Letters*, vol. 20, no. 8, pp. 428 - 428, August 2010.

[12] J. Esteban, C. C. Penalosa, J. E. Page, T. M. Martin-Guerrero, and E. Marquez-Segura, Simulation of negative permittivity and negative permeability by means of evanescent waveguide modes-theory and experiment, *IEEE Transactions on Microwave Theory and Techniques*, vol. 53, no. 4, pp. 1506 - 1514, Apr. 2005.

[13] P. Belov and C. Simovski, Subwavelength metallic waveguides loaded by uniaxial resonant scatterers, Physical Review E, vol. 72, pp. 0366181 - 03661811, Sep. 2005.

Biography of the authors

Jigyasa Sharma received her MSc degree in electronics from Banasthali Vidyapeeth, Rajasthan (1999) and Ph.D. in Applied Physics (Microwaves) from Delhi College of Engineering (University of Delhi) (2012). She worked as Assistant Professor with ABES Engineering college Ghaziabad. Currently, she is a post Doctoral fellow at NIT Patna with fellowship from University Grants Commission. Her current research activities include metamaterial design, microwave and millimeter wave filter design and substrate integrated waveguides.

Dhirendra Kumar received his ME (Electronics & Communication Engineering) and Ph.D. (ECE) from Delhi College of Engineering,(University of Delhi). He is presently Professor and Head of Electronics and Communication Engineering Department at Raj Kumar Goel Institute of Technology, Ghaziabad. His area of research is Microwave Technology and Antenna Engineering.

Asok De received the Bachelor of Engineering in Electronics & Telecommunication Engineering, Master of Engineering in Electronics & Telecommunication Engineering from Jadavpur University in 1978 and 1980 respectively. He received his Doctor of Philosophy (Ph.D.) from Indian Institute of Technology Kharagpur in 1986. He is, at present, professor in Electronics and Communication Engineering, Delhi Technological University and on lien, working as the Director of NIT Patna. His fields of interest are antennas, Numerical techniques in Electromagnetic, Transmission lines etc.

© 2017 IJAMT

Nucleic Acids Research, 2017 **1**
doi: 10.1093/nar/gkx957

FlavorDB: a database of flavor molecules

Neelansh Garg[1,2,†], Apuroop Sethupathy[1,3,†], Rudraksh Tuwani[1,4,†], Rakhi NK[5,†], Shubham Dokania[1,6,†], Arvind Iyer[1,†], Ayushi Gupta[1,†], Shubhra Agrawal[1,†], Navjot Singh[1,6,†], Shubham Shukla[1,7,†], Kriti Kathuria[1,8,†], Rahul Badhwar[5], Rakesh Kanji[5], Anupam Jain[5], Avneet Kaur[1], Rashmi Nagpal[1] and Ganesh Bagler[1,*]

[1]Center for Computational Biology, Indraprastha Institute of Information Technology (IIIT-Delhi), New Delhi, India, [2]University School of Information, Communication and Technology, Guru Gobind Singh Indraprastha University, New Delhi, India, [3]Ashoka University, Sonepat, Haryana, India, [4]Sri Venkateswara College, Delhi University, New Delhi, India, [5]Department of Bioscience and Bioengineering, Indian Institute of Technology Jodhpur, Jodhpur, India, [6]Delhi Technological University, New Delhi, India, [7]Northern India Engineering College, Guru Gobind Singh Indraprastha University, New Delhi and [8]Maharaja Agrasen College, Delhi University, New Delhi, India

Received August 15, 2017; Revised September 18, 2017; Editorial Decision October 05, 2017; Accepted October 06, 2017

ABSTRACT

Flavor is an expression of olfactory and gustatory sensations experienced through a multitude of chemical processes triggered by molecules. Beyond their key role in defining taste and smell, flavor molecules also regulate metabolic processes with consequences to health. Such molecules present in natural sources have been an integral part of human history with limited success in attempts to create synthetic alternatives. Given their utility in various spheres of life such as food and fragrances, it is valuable to have a repository of flavor molecules, their natural sources, physicochemical properties, and sensory responses. FlavorDB (http://cosylab.iiitd.edu.in/flavordb) comprises of 25,595 flavor molecules representing an array of tastes and odors. Among these 2254 molecules are associated with 936 natural ingredients belonging to 34 categories. The dynamic, user-friendly interface of the resource facilitates exploration of flavor molecules for divergent applications: finding molecules matching a desired flavor or structure; exploring molecules of an ingredient; discovering novel food pairings; finding the molecular essence of food ingredients; associating chemical features with a flavor and more. Data-driven studies based on FlavorDB can pave the way for an improved understanding of flavor mechanisms.

INTRODUCTION

Flavor is a complex, multi-sensory human experience with a rich evolutionary history (1). Molecules form the chemical basis of flavor expressed primarily via gustatory and olfactory mechanisms. The perception of flavor arises from interaction of flavor molecules with the biological machinery and could be perceived as an emergent property of a complex biochemical system. While some components of this puzzle have been unearthed, a holistic view of this phenomenon still eludes us (2–5). Taking a data-centric approach can provide a systems perspective of flavor sensation by offering ways to discern its key features.

Flavors derived from natural sources have shaped culinary habits throughout human history. Analogous to variations in regional languages, cultures have evolved variations in the way they cook. Traditional recipe compositions encode ingredient combinations that are not only palatable but appetizing. Heuristic associations between molecular properties and perception of flavors provide indications towards its chemical basis (1). For example, combinations of aliphatic esters play a major role in many fruit flavors. Ketones are known to impart metallic flavors in oxidized butter, and monoterpenoids provide the characteristic flavors of many herbs and spices. However, such knowledge remains largely unstructured and incomprehensive.

FlavorDB was created with the aim of integrating multidimensional aspects of flavor molecules and representing their molecular features, flavor profiles and details of natural source (Figure 1). FooDB, one of the efforts in similar direction, compiles molecules from food ingredients; although its focus is not on chemical basis of flavor or flavor pairing (http://foodb.ca). Flavornet is another resource, which provides a list of flavor molecules and their odor

*To whom correspondence should be addressed. Tel: +91 11 26907443; Email: bagler@iiitd.ac.in; ganesh.bagler@gmail.com
†These authors contributed equally to this work as first authors.
Present address: Ganesh Bagler, Center for Computational Biology, Indraprastha Institute of Information Technology (IIIT-Delhi), New Delhi 110020, India.

© The Author(s) 2017. Published by Oxford University Press on behalf of Nucleic Acids Research.
This is an Open Access article distributed under the terms of the Creative Commons Attribution License (http://creativecommons.org/licenses/by-nc/4.0/), which permits non-commercial re-use, distribution, and reproduction in any medium, provided the original work is properly cited. For commercial re-use, please contact journals.permissions@oup.com

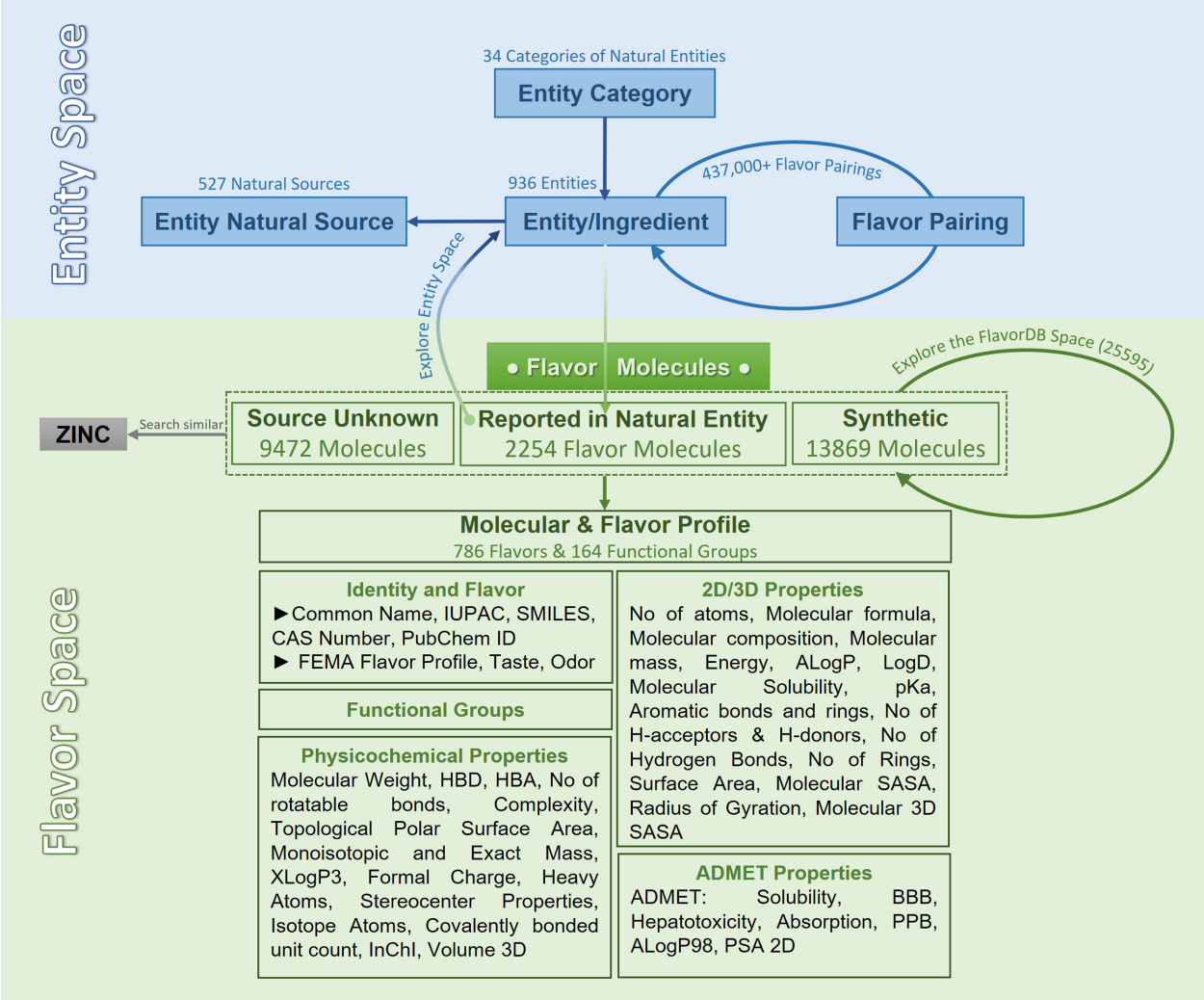

Figure 1. FlavorDB is a seamless amalgamation of 'entity space' and 'flavor space'. The resource provides a comprehensive dataset along with a user-friendly interface and interlinked search engines for exploring the flavor universe.

profiles, but does not furnish information of their natural sources (6). Other attempts in this direction have focused on compilation of data specific to aspects of flavors: tastes such as bitter (BitterDB) and sweet (SuperSweet), and volatile compounds of scents (SuperScent) (7–9). Certain others have targeted nutritional factors (NutriChem), polyphenols (Phenol-Explorer) and the medicinal value of food (10–13).

Among other sources, FlavorDB collates information from FooDB, Flavornet, SuperSweet and BitterDB to create a comprehensive repository of flavor molecules, flavor profiles, physicochemical properties and natural sources (Section S1, Supplementary Data). Compared to FooDB which has 2816 flavor compounds, FlavorDB covers 25,595 flavor molecules compiled from Fenaroli's Handbook of Flavor Ingredients and literature survey in addition to integrating data from all the above-mentioned sources. FlavorDB spans across 34 ingredient categories covering 936 ingredients of which 190 are unique. One of the features which sets FlavorDB apart from similar resources is that it presents information in a hierarchy of food category, ingredients, flavor molecules and their flavor profile, and chemical descriptors including functional groups and physicochemical properties. Through an extensive repertoire of ingredients and their constituent flavor molecules, FlavorDB also provides a tool for experimenting with flavor pairing. Thus, it offers an integrative platform for exploring the flavor space with the help of a feature-rich visual interface.

FlavorDB combines different dimensions of flavor constituting the 'entity space' and 'flavor space' (Figure 1). The former incorporates facets of ingredients which are entities from natural sources often used in food, whereas the latter represents molecules responsible for flavor sensation and their descriptors. By bringing relevant information under a single umbrella, FlavorDB provides a comprehensive dataset backed by a user-friendly interface, creative visualizations, and interlinked search engines for exploring features that contribute to the sensation of flavor. Thus, FlavorDB paves the way for an improved understanding of flavor perception arising out of complex interplay of flavor compounds with biological systems and allied applications.

DATABASE OVERVIEW

FlavorDB is a resource with extensive coverage of 25,595 flavor molecules (Figure 1). Among molecules listed in the database, 2254 have been reported to be found in 936 natural entities/ingredients. These natural ingredients have further been classified into 34 categories, and mapped to 527 distinct natural sources. An additional 13,869 compounds were identified as synthetic. For the remaining 9472 molecules, no specific source could be ascertained. The features provided as part of the detailed molecular and flavor profiles of these compounds have an impact on their taste and odor through gustatory and olfactory sensory mechanisms.

FlavorDB offers a user-friendly interface for querying and browsing flavor molecules, entities/ingredients, natural sources, as well as performing flavor pairing. Interactive data visualizations such as the flavor network and interlinked search options are provided to retrieve relevant information. Apart from searching via textual query or by drawing the chemical structure, FlavorDB also provides a 'Visual Search'. Using this a user can interactively browse through the ingredient categories to access corresponding natural entities and subsequently obtain details of their flavor molecules.

For any flavor molecule, the resource also facilitates lookup for structurally similar molecules within the database as well as those commercially available from external sources (ZINC (14)). Thus, through a blend of the entity and flavor space along with a dynamic interface and visualizations, FlavorDB provides a wide spectrum of information facilitating insights into the flavor universe.

DATA COMPILATION

One of the primary motivations behind the creation of this resource was to map the space of molecules critical for the sensations of taste and smell. To begin with, a list of ingredients was created using (15–17), FooDB (http://foodb.ca) and arXiv preprint arXiv:1502.03815, 2015. Each of the 936 ingredients were then manually classified into 34 categories: Additive, Animal Product, Bakery, Beverage, Beverage Alcoholic, Beverage Caffeinated, Cereal, Maize, Dairy, Dish, Essential Oil, Fish, Seafood, Flower, Fruit, Berry, Fruit Citrus, Fruit Essence, Fungus, Herb, Meat, Legume, Nut, Seed, Plant, Plant Derivative, Spice, Vegetable, Cabbage, Vegetable Fruit, Vegetable Gourd, Vegetable Root, Vegetable Stem, and Vegetable Tuber. Each entity was also mapped to its natural source, with a total of 527 unique sources being identified. The details of entities and their natural sources, related images, and scientific classification were obtained from Wikipedia using Python's BeautifulSoup4 library (https://www.crummy.com/software/BeautifulSoup) and MediaWiki's action API (MediaWiki The Free Wiki Engine).

The data of flavor molecules for each of these ingredients were compiled via flavor resources such as Fenaroli's handbook of flavor ingredients, previously reported data (16,17), FooDB (http://foodb.ca), arXiv preprint arXiv:1502.03815 and literature survey (Also see Section S2, Supplementary Data). Common names, scientific name and synonyms of ingredients were used to query PubMed to obtain articles that reported their flavor molecules. Flavor molecules associated with entities/ingredients were thus curated from existing sources (15–17) (FooDB; http://foodb.ca, arXiv preprint arXiv:1502.03815, 2015) and compiled manually. Molecules from Flavornet, BitterDB and SuperSweet were further included along with their flavor profiles (6,7,9). Additionally, information for 33 taste receptors (Sweet, Bitter, Sour, and Umami) and 1068 odor receptors is also available in FlavorDB. For each receptor, we provide its Uniprot ID, name, involvement in taste, and Uniprot link (18).

The chemical identifiers of molecules were obtained from various sources (FooDB; http://foodb.ca) (6,7,9,15,16) (Also see Section S2, Supplementary Data), and were standardized to procure their CAS (Chemical Abstract Service) numbers. CAS numbers were then mapped to their corresponding PubChem IDs, as the former are often degenerate with multiple CAS numbers pointing to the same molecule, and some pointing to multiple molecules. Thus, PubChem ID was used as the unique primary key for every flavor molecule. Using the PubChem ID, compound identifiers (such as common name, IUPAC, Canonical SMILES), physicochemical properties and 2D images were obtained from PubChem REST API (https://pubchem.ncbi.nlm.nih.gov/pug_rest/PUG_REST.html). The flavor profile of the molecule (Flavor Profile, FEMA Flavor Profile, FEMA Number, Taste, and Odor) was created by compiling information from FooDB (http://foodb.ca), Flavornet (6), SuperSweet (9), BitterDB (7) and PubChem.

Further 2D/3D, ADMET and physicochemical properties as well as Mol2 files for all 25,595 molecules were obtained using Discovery Studio 4.0 (DS4.0; Accelrys Inc.). The functional groups were obtained using Checkmol software (19). Functional group refers to an atom, or a group of atoms that have similar chemical properties whenever they occur in different compounds (20). Thus, it defines the characteristic physical and chemical properties of families of organic compounds.

Please refer to Supplementary Figures S1, S2, S3 and S4 in Supplementary Data for the statistics of entities, categories, flavor molecules, their flavors and functional groups.

DATABASE ARCHITECTURE AND WEB INTERFACE

FlavorDB facilitates easy comprehension of complex interrelations among flavor molecules, entities/ingredients and their natural sources (Figure 2; also see Figure S5 of Supplementary Data). Interactive data visualizations and a wide variety of user-friendly searches provide quick access to desired information. The following utilities and applications in FlavorDB enable visual explorations of 'flavor space' and 'entity space' to get insights into the flavor universe.

The flavor network

Flavor Network visualizes the graph of flavor-sharing across all entities/ingredients. To make it easier to observe flavor-sharing within and across categories, the entities are grouped category-wise and are spaced out along the circumference. To address dense pattern of interrelationships due to abundance of sharing, the backbone network showing

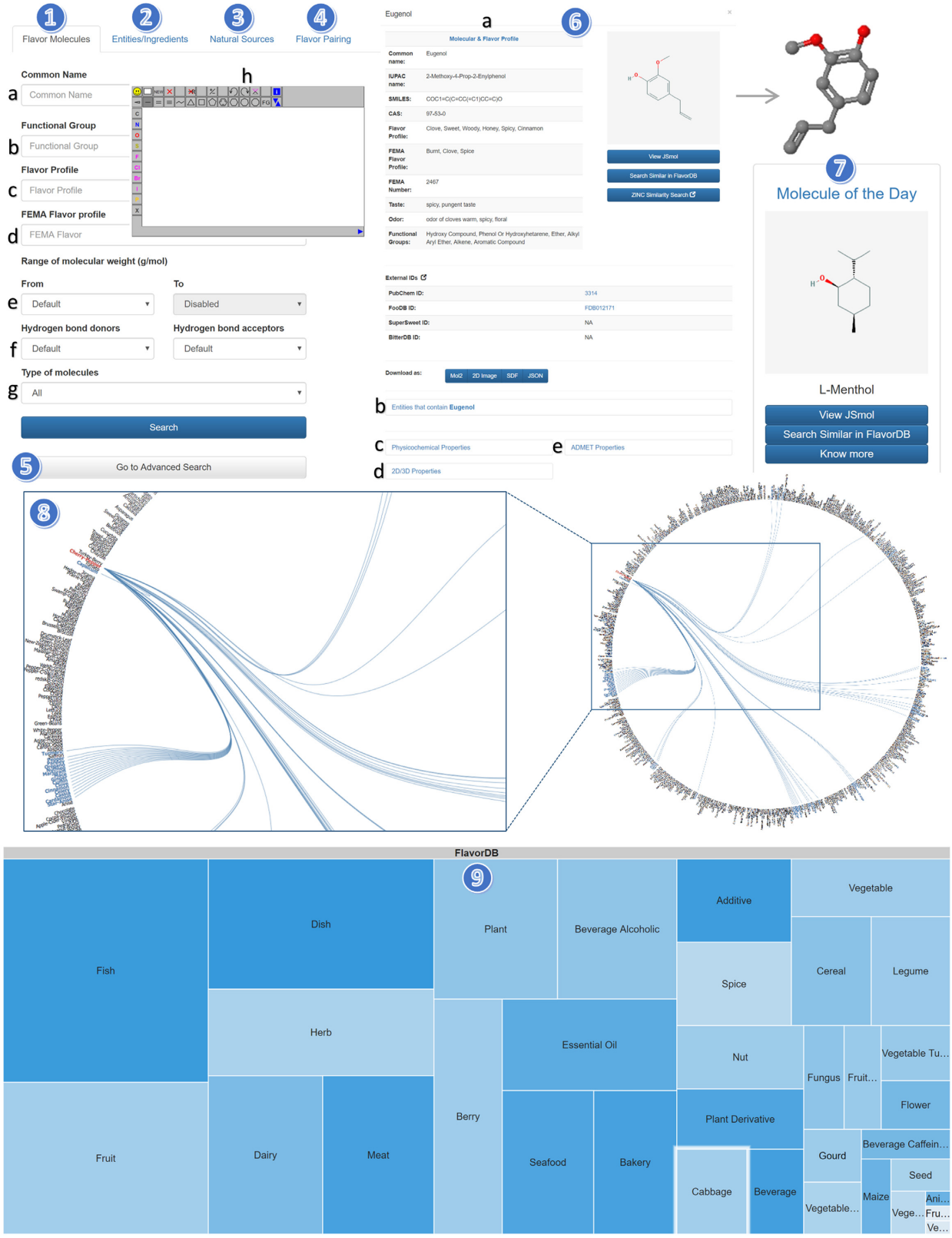

Figure 2. Schematic of FlavorDB user interface highlighting features for searching and graphical navigation of data. (**1**) Flavor Molecule Search, (**2**) Entity/Ingredient Search, (**3**) Natural Source Search, (**4**) Flavor Pairing, (**5**) Advanced Search, (**6**) Molecular & Flavor Profile (including features for finding related entities, searching for structurally similar molecules, external link-outs and data download), (**7**) Molecule of the Day, (**8**) The Flavor Network and (**9**) Visual Search.

statistically significant edges is depicted (21). Clicking on an entity shows its association with other entities by virtue of shared flavor molecules, thereby enabling search for similarities among seemingly disparate entities. The Flavor Network was implemented with the D3.js JavaScript library (https://d3js.org).

Visual search

Visual Search, implemented with the Google Charts library (http://developers.google.com/chart), provides an interactive way of exploring FlavorDB. At the top of the hierarchy, it displays all 34 ingredient categories as boxes. The size of each box is determined by the number of unique flavor molecules present in that category. Greater the number of molecules, larger the size of the box. Clicking through any of the categories, one can navigate to its constituent ingredients and their respective flavor profiles. Thus, visual search enables multi-level, open-ended exploration of FlavorDB.

Molecular search

By virtue of extensive molecular and flavor features provided in FlavorDB, 'Molecular Search' forms a key query mechanism. It facilitates querying on the basis of a host of features including Common Name, Functional Group, FEMA Flavor, Molecular Weight, Number of Hydrogen Bond Donors/Acceptors, and Type of Molecules (Natural, Synthetic, Unknown). Additionally, the JSME Molecule Editor enables search based on structural similarity (22). The editor facilitates creation of molecules using SMILES, MOL or SDF files. Structurally similar compounds can also be found using the 'Search Similar in FlavorDB' button provided on the molecules' profile page.

Molecular search yields matching flavor compounds with detailed 'molecular and flavor profile'. A 3D visualization of the molecule is provided with the JSmol library along with an external link to PubChem. Further an option for downloading the molecule in different formats (MOL2, SMILES, 2D images) is also available. The flavor molecules can be filtered using search and sort functionality provided by 'data tables' plugin.

The algorithm for performing structural similarity computes molecular fingerprints (FP2) of all flavor molecules using OpenBabel (11). For any molecular structure that is queried, its fingerprint is computed using an OpenBabel protocol and is compared with the database using the Tanimoto coefficient of structural similarity. Molecules with at least 30% similarity are returned. FlavorDB also facilitates browsing all 25,595 flavor molecules by doing a null search (no constraints; all query fields empty). 'Molecule of the Day' feature offers a peek into the flavor universe, from where the user can start exploring the resource.

Advanced search

Advanced search provides an option for refined search by querying FlavorDB data on the basis of a variety of molecular properties (number of rings, rotatable bonds, energy, surface area etc.) apart from those provided in basic search. For numeric fields either a range or discrete values can be provided as a query.

Entity and natural source search

These searches facilitate querying on the basis of 'Entity/Ingredient Name' as well as 'Category Name' to retrieve detailed information of entity, category, natural source, scientific classification, Wiki page link, synonyms, images, and flavor molecules associated with the entity. Additionally, we facilitate search based on synonyms, knowing that many ingredients are often known by a variety of alternative names. For example, to search for 'Eggplant', one may as well search by either 'Aubergine' or 'Brinjal'. All text search fields are assisted by jQuery UI autocomplete.

Flavor pairing

'Flavor Pairing' (also known as 'Food Pairing') is a heuristic with empirical evidence (15,16), (arXiv preprint arXiv:1505.00155, 2015), used for finding ingredient pairs that are expected to go well together in a recipe/food product. On the foundation of extensive repertoire of 936 entities and their constituent flavor molecules (2254), 'Flavor Pairing' tool provides a powerful engine for spanning through >437,000 pairings to reveal flavor profile overlaps across categories and disparate entities. The app provides pairing results through interactive visualization for easy comprehension. Detailed analysis yields the number of shared flavor molecules between the queried entity and all the other entities having at least one shared flavor molecule. The results can be further filtered using data tables to probe the list of shared flavor molecules.

Webserver tech stack

FlavorDB has been designed as a Relational Database using MySQL (https://www.mysql.com). The webserver has been built using the Python web development framework, Django (https://www.djangoproject.com). Django has a built in ORM (Object Relational Mapper) for querying the database, thus optimizing queries and making it easier to perform complex queries, apart from reducing the development period. The front-end has been built using HTML, CSS and JavaScript. The jQuery, Bootstrap, D3.js and Google Charts libraries were used to add to the functionality of FlavorDB. An Apache HTTP Server has been used to route requests to the Django app and to enable data compression for faster page load times. The site is best viewed in latest versions of Google Chrome, Firefox, Opera, Internet Explorer, and Microsoft Edge.

EXAMPLES

Below we provide a few case studies illustrating the utility of FlavorDB for various applications.

Applications for Flavor/Food pairing

The food pairing principle suggests that ingredients which taste similar tend to be used together in recipes (23). Historically practiced on a trial-and-error basis, food pairing has relied heavily on human judgment and the intuition of food connoisseurs. Evidence-based understanding of rules that

dictate food choices can facilitate informed experiments to pair ingredients in a recipe. While many Western cuisines are reported to be characterized with 'uniform food pairing', Indian cuisine tends to follow 'contrasting food pairing' pattern (15,16) (arXiv preprint arXiv:1505.00155, 2015, arXiv preprint arXiv:1502.03815, 2015). Based on data of ingredients and flavor molecules, FlavorDB offers an app by which users can experiment with food pairing of desired ingredients.

Let's consider the case where a user wants to find a substitute for oregano. Using the Flavor Network, one can quickly get an overview of ingredients that share flavor molecules with oregano. Via the Flavor Pairing app, it can be observed that oregano and thyme have the most number of common molecules. Hence, by virtue of uniform food pairing, thyme can be a possible substitute for oregano. This example demonstrates the utility of different features of FlavorDB for making informed decisions on flavor pairing and choice of ingredients.

Searching for drug-like compounds

Find molecules structurally similar to a compound satisfying Lipinski's rule of five. This example demonstrates use of FlavorDB's 'Advanced Search' and 'Structural Similarity Search' features to find molecules matching desired chemical properties. Lipinski's rule is a heuristic to evaluate drug-likeness; the suitability of a chemical compound to have pharmacological or biological activity making it a likely candidate for orally active drug. It states that, an orally active drug has no more than one violation of the following criteria: no more than five hydrogen bond donors; no more than 10 hydrogen bond acceptors; Molecular mass less than 500 Da; an octanol–water partition coefficient (log *P*) not >5.

Using the above mentioned criteria in the 'Advanced Search', one can search for molecules that satisfy Lipinski's rule. This query can be refined further by using the structural search provided through the JSME tool, to find drug-like compounds that are structurally related to a certain compound. As an example, one may specify the conditions for Lipinski's rule in the 'Advanced Search' and draw the chemical structure for Pyridine. The resulting search returns all molecules that are potentially suitable for being tested as a drug, ranked in descending order of structural similarity with Pyridine.

Finding flavor molecules similar to any desired compound

Allicin (SMILES: O=S(SC\C=C)C\C=C) is one of the primary molecules present in garlic. Using the structural search, one can get a list of similar molecules in FlavorDB. The top result for this example is Diallyl Disulfide with 66.7% similarity. Interestingly, as reflected in its 'Molecular and Flavor Profile', Diallyl Disulfide has a 'sharp, garlic taste'. Thus it can be a possible substitute for Allicin and used as a scaffold to create a synthetic garlic flavor. One may also search for flavor molecules matching a particular FEMA flavor term and/or functional group among naturally occurring as well as synthetic compounds.

Exploring flavor properties of ingredients

Wasabi is empirically known to have a pungent odor. Using the 'Entity Search' option, it can be discovered that there are five known flavor molecules for Wasabi in FlavorDB. Of these, one molecule, Allyl Isothiocyanate is reported to exhibit characteristics of a 'very pungent' odor. It can be speculated that the pungent smell of wasabi is primarily due to the presence of Allyl Isothiocyanate.

The above examples illustrate how FlavorDB and its features can be interactively used to make data-driven decisions that cater to various aspects of flavor.

SUMMARY AND OUTLOOK

Study of molecules and mechanisms involved in flavor sensation has been of interest for its applications for food and fragrances (1–13) (http://www.pherobase.com). Contributing to the efforts on compilation of molecules from food and their flavors, FlavorDB provides a detailed perspective into the 'entity space', 'flavor space' and the latent connections between the two. In doing so, it lays down the foundation for conducting data driven analysis which can aid in building applications meant for molecular gastronomy, culinary food pairing, novel recipe generation, aroma blending and predicting odor from chemical features (24–26).

Despite our best efforts, FlavorDB is not an exhaustive repository of all flavor molecules and ingredients. Our data on flavor molecules of an ingredient is limited by the availability of information about them from literature survey. Similarly, the ingredients represented in the database are not exhaustive in themselves as their choice is limited by the reports of flavor compounds. Also, at present the database focuses on flavor profiles of natural ingredients and thus, the crux of our flavor space is made up of flavor molecules from natural sources.

In future, we intend to increase the coverage of flavor molecules and look for their latent effects on human health. Our endeavor is to integrate aspects of flavor profiles with those of entities and molecules that has hitherto been unexplored.

AVAILABILITY

FlavorDB is available at http://cosylab.iiitd.edu.in/flavordb

SUPPLEMENTARY DATA

Supplementary Data are available at NAR Online.

ACKNOWLEDGEMENTS

G.B. thanks the Indraprastha Institute of Information Technology (IIIT-Delhi) for providing computational facilities and support. N.G., A.S., R.T., S.D., N.S., S.S. and K.K. were Summer Research Interns in Dr. Bagler's lab at the Center for Computational Biology, and are thankful to IIIT-Delhi for the support and fellowship. A.I., A.G. and S.A., M.Tech. (Computational Biology) students, thank IIIT-Delhi for the fellowship. R.N.K., R.B. and R.K. thank the Ministry of Human Resource Development, Government of India and Indian Institute of Technology Jodhpur for the senior research fellowship.

FUNDING

The open access publication charge for this paper has been waived by Oxford University Press - *NAR*.
Conflict of interest statement. None declared.

REFERENCES

1. Fisher,C. and Scott,T. (1997) *Food Flavours: Biology and Chemistry Royal Society of Chemistry*.
2. Shepherd,G. (2013) *Neurogastronomy – How the Brain Creates Flavor and Why it Matters* Columbia University Press.
3. Malnic,B., Hirono,J., Sato,T. and Buck,L.B. (1999) Combinatorial receptor codes for odors. *Cell*, **96**, 713–723.
4. Mouritsen,O.G. (2015) The science of taste. *Flavour*, **4**, 1–2.
5. Newcomb,R.D. and Ohla,K. (2013) The genetics and neuroscience of flavour. *Flavour*, **2**, 17.
6. Arn,H. and Acree,T.E. (1998) Flavornet: a database of aroma compounds based on odor potency in natural products. *Dev. Food Sci.*, **40**, 27.
7. Wiener,A., Shudler,M., Levit,A. and Niv,M.Y. (2012) BitterDB: a database of bitter compounds. *Nucleic Acids Res.*, **40**, 413–419.
8. Dunkel,M., Schmidt,U., Struck,S., Berger,L., Gruening,B., Hossbach,J., Jaeger,I.S., Effmert,U., Piechulla,B., Eriksson,R. *et al.* (2009) SuperScent – a database of flavors and scents. *Nucleic Acids Res.*, **37**, 291–294.
9. Ahmed,J., Preissner,S., Dunkel,M., Worth,C.L., Eckert,A. and Preissner,R. (2011) SuperSweet-A resource on natural and artificial sweetening agents. *Nucleic Acids Res.*, **39**, D377–D382.
10. Scalbert,A., Andres-Lacueva,C., Arita,M., Kroon,P., Manach,C., Urpi-Sarda,M. and Wishart,D. (2011) Databases on food phytochemicals and their health-promoting effects. *J. Agric. Food Chem.*, **59**, 4331–4348.
11. Rothwell,J.A., Perez-Jimenez,J., Neveu,V., Medina-Remón,A., M'Hiri,N., García-Lobato,P., Manach,C., Knox,C., Eisner,R., Wishart,D.S. *et al.* (2013) Phenol-Explorer 3.0: a major update of the Phenol-Explorer database to incorporate data on the effects of food processing on polyphenol content. *Database*, **2013**, bat070.
12. Jensen,K., Panagiotou,G. and Kouskoumvekaki,I. (2015) NutriChem: a systems chemical biology resource to explore the medicinal value of plant-based foods. *Nucleic Acids Res*., **43**, D940–D945.
13. Neveu,V., Perez-Jimenez,J., Vos,F., Crespy,V., du Chaffaut,L., Mennen,L., Knox,C., Eisner,R., Cruz,J., Wishart,D. *et al.* (2010) Phenol-Explorer: an online comprehensive database on polyphenol contents in foods. *Database*, **2010**, bap024.
14. Sterling,T. and Irwin,J.J. (2015) ZINC15—ligand discovery for everyone. *J. Chem. Inf. Model.*, **55**, 2324–2337.
15. Jain,A., Rakhi,N.K. and Bagler,G. (2015) Analysis of food pairing in regional cuisines of India. *PLoS One*, **10**, e0139539.
16. Ahn,Y.-Y., Ahnert,S.E., Bagrow,J.P. and Barabási,A.-L. (2011) Flavor network and the principles of food pairing. *Sci. Rep.*, **1**, 196.
17. Burdock,G.A. (2010) Fenaroli's handbook of flavor ingredients.
18. Wasmuth,E.V. and Lima,C.D. (2016) UniProt: the universal protein knowledgebase. *Nucleic Acids Res.*, **45**, 1–12.
19. Haider,N. (2010) Functionality pattern matching as an efficient complementary structure/reaction search tool: an open-source approach. *Molecules*, **15**, 5079–5092.
20. IUPAC (2014) Compendium of chemical terminology.
21. Serrano,M.A., Boguna,M. and Vespignani,A. (2009) Extracting the multiscale backbone of complex weighted networks. *Proc. Natl. Acad. Sci. U.S.A.*, **106**, 6483–6488.
22. Bienfait,B. and Ertl,P. (2013) JSME: a free molecule editor in JavaScript. *J. Cheminform.*, **5**, 1–6.
23. Blumenthal,H. (2008) The Big Fat Duck Cookbook Bloomsbury Publishing.
24. Keller,A., Gerkin,R.C., Guan,Y., Dhurandhar,A., Turu,G., Szalai,B., Mainland,J.D., Ihara,Y., Yu,C.W., Wolfinger,R. *et al.* (2017) Predicting human olfactory perception from chemical features of odor molecules. *Science*, **355**, 820–826.
25. Spence,C., Hobkinson,C., Gallace,A. and Fiszman,B.P. (2013) A touch of gastronomy. *Flavour*, **2**, 14.
26. This,H. (2002) Molecular gastronomy. *Angew. Chem. Int. Ed.*, **41**, 83–88.

International Journal of Research in Engineering and Innovation (IJREI)
journal home page: http://www.ijrei.com
ISSN (Online): 2456-6934

Friction stir processing of magnesium alloys used in automobile and aerospace applications

R.S. Mishra, Sumit Jain

Department of Mechanical, Production & Industrial and Automobiles Engineering, Delhi Technological University, Delhi

Abstract

A new microstructural modifications technique was developed by the Welding Institute (TWI) of United Kingdom in 1991 is known as friction stir processing (FSP). The FSP is a newer technique used for refining and homogenizing the grain structure of metal sheet. Friction stir processing is a great potential in the field of super-plasticity and metal matrix composites. Many investigators observed that the FSP greatly enhances super plasticity in many Al alloys. It is a solid-state processing technique based on friction stir welding technique in which a specially designed rotating cylindrical tool that comprises of a probe and shoulder. The probe of the tool is inserted into the sheet material while rotating and the shoulder moves over the surface of the sheet, and then traverses in the desired direction. The contact between the rotating probe and the sheet material generate heat due to friction which softens the material and the mechanical stirring caused by the probe, the material within the processed zone undergoes intense plastic deformation yielding a dynamically-recrystallized fine grain microstructure.

This paper mainly deals with friction stir processing of magnesium alloys with different reinforcement and different input parameters. The study consist of the effect of different reinforcement addition methods that i.e. groove method and drill hole method on tribological and mechanical properties. The result shows that the addition of reinforcements improves the ultimate tensile strength, strain rate and wear resistance.

© 2017 ijrei.com. All rights reserved

Keywords: Friction Stir Processing (FSP), Tool Rotation Speed (TRS), Transverse Speed (TS).

1. Introduction

Friction stir processing is a novel technique used for improving material properties with the help of a rotation tool by plastic deformation. Friction stir processing is used to make the grain structure homogenous that enhance the properties of material. Friction stir processing is totally based on the friction stir welding technique in which there is a rotating tool consists of a shoulder and a probe. The probe of the tool plunged into the material and produces heat due to friction with the work material. The shoulder produces the additional heat and also capped the material extruded out during the process. Friction stir processing is mostly used for making surface composite, bulk composite and super-plasticity

2. Literature Review

The literature consists of the work conducted on various magnesium alloys by friction stir processing. The study consist of various parameters, tool materials, tool dimensions, response parameters and results obtained by various researchers on magnesium alloys by friction stir processing. The literature in the tabular form is given below:

Corresponding author: R.S. Mishra
Email Id: rsmishra@dce.ac.in

S.N	Author	Title of paper	Work-Piece/ Tool and groove size	Input parameters	Output parameters	Finding
1	C.I. Chang et al. (2004)	Relationship between grain size and Zener–Holloman parameter during friction stir processing in AZ31 Mg alloys	AZ31B billets ➢ Tool Pin length- 6 mm. ➢ Pin dia- 6 mm ➢ Shoulder dia- 18 mm ➢ Tilt angle- 3 degree	➢ RS range- 1000-1800 rpm. ➢ TS range- 6-24 mm/min	➢ Strain rate. ➢ grain size ➢ temperature range	(1) The temperature rise during FSP is traced, and the maximum temperature can reach 250–450^0 C, depending on the FSP pin rotation speed. (2) X-ray diffraction results show that, in the FSP dynamically recrystallized zone, the (0002) basal plane tends to lie on the transverse plane at lower pin rotation speeds, and approaches to nearly random orientation at higher rotation speeds.
2	Morisada. Y.,et al (2006)	Effect of friction stir processing with SiC particles on microstructure and hardness of AZ31	SiC powder was filled into a groove (1mm×2 mm) on the AZ31 plate SKD61 has a columnar shape	➢ Probe Diameter 4 mm. ➢ Probe length 1.8 mm. ➢ Tool rotating speed 1500 rpm ➢ Tool travel speed - 25 to 200 mm/min. ➢ Tool tilt angle 3◦	➢ Microstructure and micro hardness. ➢ Effect of SiC particles on grain size. ➢ Grain growth at elevated temperatures	(1) The SiC particles lead the grain to be refined by the FSP. (2) The micro hardness of the stir zone with the SiC particles increases to about 80 Hv. (3) The fine grain structure of the AZ31 fabricated by the FSP is unstable above 300 ◦C. (4) The fine grain fabricated by the FSP with the SiC particles is maintained at the elevated temperatures (∼400 ◦C).
3	A.H. Feng and Z.Y. Ma (2006)	Enhanced mechanical properties of Mg–Al–Zn cast alloy via friction stir processing	Mg–Al–Zn cast alloy		➢ UTS ➢ % EL	(1) The FSP Mg–Al–Zn sample exhibited an ultimate tensile strength of 337 MPa and an elongation of 10%. (2) FSP combined with aging is a simple and effective approach to enhance the mechanical properties of Mg–Al–Zn casting.
4	Chang. C.I ., et al (2007)	Microstructure and Mechanical Properties of Nano-ZrO2 and Nano-SiO_2 Particulate Reinforced AZ31-Mg Based Composites Fabricated by Friction Stir Processing	10~20 vol% nano-sized ZrO2 and 5~10 vol% nano-sized SiO2 particles into an Mg-AZ31 alloy Thickness - 10 mm	➢ Tool Shoulder diameter 18 mm. ➢ Tool pin diameter 6 mm. ➢ Tool pin length - 6 mm. ➢ Tool rotation speed - 800 rpm. ➢ Tool traverse speed - 45 mm/min	➢ Microstructures. ➢ XRD Results. ➢ Hardness ➢ Measurement ➢ Mechanical Properties	(1) The distribution of Nano particles measuring ~20 nm after four FSP passes resulted in satisfactorily uniform distribution. (2) The hardness and tensile properties at room temperature of the AZ31 composites with nano-fillers were appreciably improved, as compared with the AZ31 cast billet (3) The crystalline ZrO2 phase is very stable, no reaction between ZrO2 and Mg occurred during the FSP mixing ZrO2 into Mg-AZ31 matrix.

5	Darras. B.M., et al (2007)	Friction stir processing of commercial AZ31 magnesium alloy	AZ31B-H24 magnesium alloy Thickness - 0.125 in Tool Material -H-13 tool steel	➢ Tool Shoulder diameter - 0.5 in. ➢ Tool pin dia 0.25 in. ➢ Tool pin length - 0.12 in. ➢ Tool rotation speed - 1200–2000 rpm ➢ Tool traverse speed - 20–30 in./min	➢ Temperature ➢ Microstructure ➢ Hardness	(1) The preliminary results on FSP of AZ31 magnesium alloy are promising; grain refinement and homogenization of the microstructure are achieved in a single FSP pass. (2) The thermal histories presented in these studies give useful results on the peak temperature, cooling and heating rates which are critical to control and optimize the process
6	C. J. Lee et al. (2007)	Using Multiple FSP Passes to Cure Onion Splitting of Mg Alloys Deformed at Elevated Temperatures	AZ61A Mg (130*60*10) tool: Shoulder dia.18mm Pin dia.-6mm pin lenth-6mm	➢ Multi-pass (4) ➢ TRS-800 rpm ➢ TS- 45-90mm/min	➢ Microstructure ➢ Strain rate ➢ True stress- true strain	The multi-passes FSP could effectively cure the onion premature splitting by accumulating a higher degree of strain to fully recrystallize the initial grains and to improve the inhomogeneous microstructure.
7	Chen Ti-jun et al. (2009)	Friction stir processing of thixoformed AZ91D magnesium alloy and fabrication of Al-rich surface	thixoformedAZ91D magnesium alloy 100 mm×40 mm×15 (Al powder) GROOVE- 4.2 mm in depth and 1.25 mm in width	➢ TRS-450 RPM. ➢ TS-60 mm/min	➢ Corrosion resistance ➢ Microstructure ➢ grain size and distribution	(1) Compared with the PMC alloy, the microstructural evolution of the TF alloy is slower because the operation efficiency of the grain refinement mechanisms is relatively low. (2) An Al-rich surface layer can be produced on the thixoformed alloy by FSP and the corrosion resistance in NaCl aqueous solution is obviously improved.
8	Faraji.G., et al (2010)	Effect of Process Parameters on Microstructure and Micro-hardness of AZ91/Al2O3 Surface Composite Produced by FSP Effect of Process Parameters on Microstructure and Micro-hardness of AZ91/Al2O3 Surface Composite Produced by FSP	Al2O3 powder with three different sizes (ranging from nanometer to micrometer scale) 3000, 300, and 30 nm, and 99.9% pure & as-cast AZ91 plate Groove - 0.8 mm (width) & 2 mm (depth) Tool Material - H13 tool	➢ Tool type - Square & Triangular ➢ Particle size - 0.03 , 3 ➢ Pass number - 1, 3 ➢ Tool Shoulder diameter - 15 mm ➢ Tool pin diameter - 5 mm ➢ Tool pin height - 1.8 mm ➢ Tool tilt angle - 3° ➢ Tool rotation speed - 900 rpm	➢ Microstructure ➢ Micro-hardness ➢ X-ray diffraction	(1) Grain structures in the SZ had fine and equiaxed grains due to the recrystallization, while nano-sized alumina particles distributions were different because they received a different stirring action. (2) Grain size and cluster size in the specimen produced by the triangular tool is smaller than that of square tool. (3) Decreasing the particle size leads to increase in the hardness. (4) Hardness of the specimen produced by triangular tool is higher than that of square tool and increasing the number of passes leads to monotonous hardness curve.

9	Azizieh. M., et al (2010)	Effect of rotational speed and probe profile on microstructure and hardness of AZ31/Al2O3 nanocomposites fabricated by friction stir processing	AZ31 billets Three kinds of Al_2O_3 particles with mean diameters of 35 nm , 350 nm and 1000 nm Thickness - 10 mm Tool Material = H13 Steel Groove- 1.2 mm * 5 mm	➢ Shoulder dia. (mm) – 18 ➢ pin dia. – 6 ➢ pin length (mm) - 5.7 ➢ TRS (rpm) - 800, 1000 and 1200 rpm ➢ Welding Feeds (mm/min) - 45 ➢ Tilt angle-2 ^{0}	➢ Material flow in the stir zone ➢ Microstructure of the stir zone ➢ Hardness measurement	(1) The effects of probe profile, rotational speed and the number of FSP passes on nanoparticle distribution and matrix microstructure were studied. (2) The grain refinement of matrix and improved distribution of nanoparticles were obtained after each pass. (3) By increasing the rotational speed, as a result of greater heat input, grain size of the base alloy increased and simultaneously more shattering effect of rotation, cause a better nanoparticle distribution.
10	Asadi.P., et al (2012)	On the role of cooling and tool rotational direction on microstructure and mechanical properties of friction stir processed AZ91	AZ91 Magnesium alloy Thickness - 5 mm Tool material - 2344 hot working steel	➢ Tool shoulder diameter (mm) 15. ➢ Tool square pin diameter – 5 ➢ Tool square pin length (mm) - 2.5 ➢ Tool rotating speed (rpm) – 900 ➢ Welding Feeds (mm/min)- 63 ➢ Tilt angle -3 ^{0}	➢ Microstructure ➢ Hardness ➢ Tensile properties ➢ Wear properties	(1) Water cooling enhances the hardness and reduces the final grain size, while the amount of oxide particles in the processed area increases. (2) The oxide particles reduce the final grain size because of limiting grain growth due to pinning of the grain boundaries. (3) Changing the RD in each pass reduces the grain size noticeably, because of creating more suitable sites for nucleation during DRX, and increases the hardness and tensile strength considerably.
11	Zheng.F. Y.,et al (2013)	Microstructures and mechanical properties of friction stir processed Mge2.0Nde0.3Zne1.0Zr magnesium alloy	NZ20K (nominal Mge2.0Nde0.3Zne1.0Zr, wt.%) alloy Thickness - 7 mm Tool Material - Steel	➢ Tool Shoulder diameter - 16 mm ➢ Tool pin length - 6mm ➢ Tool rotation speed - 800 rpm ➢ Tool traverse speed - 200 mm/ min	➢ XRD patterns analysis ➢ SEM images & EDS analyses	(1) The alloy was friction stir processed with different passes: single-pass, three-pass and five-pass, under a tool rotation rate of 800 rpm and a traverse speed of 200 mm/ min. with the increase of pass, the average grain size in the stir zone (SZ) is decreased firstly and then increases. (2) The Vikers hardness of SZs in all FSPed samples is higher than that of the parent material (3) Tensile strengths of the stir zones along the FSP advancing direction are slightly lower than those of PM.
12	Lee.W., et al (2013)	Joint properties of friction stir welded AZ31B– H24 magnesium alloy	AZ31B –H24 alloy Thickness – 4 Tool material- D2 (SKD11)	➢ Tool shoulder diameter (mm) - 20 ➢ Tool rotating speed (rpm) - 1250 - 2500 rev/ min ➢ Welding Feeds (mm/min) - 87 - 507 ➢ Tilt angle - 3 ^{0}	➢ Change of top surface roughness ➢ Macrostructure ➢ Microstructure ➢ Grain size distribution ➢ Hardness distribution	(1) The microstructure of the weld zone was composed of +ve regions: base metal, HAZ, thermomechanical affected zone, stir zone I & stir zone (2) Stir zones I and II were characterized by partial dynamic recrystallization and full dynamic recrystallization, respectively. (3) The hardness of the weld zone was lower than that of the base metal owing to grain growth. (4) The maximum tensile strength was 240 MPa, which was ~85% of the base metal value.

13	Gupta.A ., et al (2015)	Effect of Tool rotation speed and feed rate on the formation of tunnel defect in Friction Stir Processing of AZ31 Magnesium alloy	AZ31 magnesium thickness - 6 mm Tool Material - H-13	➢ Tool Rotational speed (RPM) – 2000 ➢ Feed rate (mm/min.) 40,50 ➢ Tool Shoulder dia. -18 mm ➢ Tool pin dia. 6 mm ➢ Tool pin length 5.36 mm. ➢ Tool tilt angle 1.8°	Defects	(1) Truncated conical tool produced much less tunnel defect as compare to the cylindrical tool. (2) Tunnel defect increases along the weld length as the welding proceeds and it was inclined towards the retreating side of the weld in all the specimens. (3) Negligible tunnel defect was found during FSP with the truncated conical tool at the rotational speed of 2000 rpm and welding speed of 40 mm (4) Excessive flash was observed during FSP with the cylindrical tool at the feed rate of 50 mm/min.
14	Azizieh M.et al.(2016)	Effect of friction stir processing on the microstructure of pure magnesium castings	pure magnesium (110*70*10) Tool: Shoulder dia.-18mm Pin dia.-6mm pin lenth-6mm	➢ Cylindrical non-threaded pin, a cylindrical threaded pin and a conical pin. ➢ TRS- 400, 500, 630, 800, 1000, 1250 and 1600 rpm ➢ TS- 50 mm/min.	➢ Material flow ➢ Hardness	(1) Threaded pin produced the best material flow and the least cavities. (2) The hardness measurements demonstrated increase in the FSP specimens compared with the initial pure Mg castings.
15	Li.J., Chai.F., et al (2014)	Influence of processing speed on microstructures and mechanical properties of friction stir processed Mg–Y–Nd–Zr casting alloy	Cast WE43 magnesium alloy plates (6 mm)	➢ Tool angle - 2.5° ➢ Tool rotational speed -800 rev/ min ➢ Tool travel speed -30, 60, 90 and 120 mm/ min. ➢ Tool concave shoulder dia - 15 mm	➢ Microstructure of BM and FSP samples ➢ X-ray diffraction patterns of WE43 samples ➢ Mechanical properties of BM and FSP samples	(1) Friction stir processing results in the generation of fine grained microstructures and fundamental break-up and dissolution of the coarse second phases. (2) Owing to much finer microstructure, the mechanical properties of the WE43 alloy after FSP are significantly improved. (3) High temperature tensile tests show that the FSP WE43 alloys exhibit excellent HSRS, with a large elongation of 631% at 748 K with a strain rate.
16	Morishige .T., et al (2013)	Microstructural modification of cast Mg alloys by friction stir processing	Mg–Y–Zn cast alloys Thickness - 10 mm AZ91D die cast	➢ Tool angle - 2° ➢ Tool rotational speed -450,600 rpm ➢ Tool travel speed -50,100 mm/min ➢ Tool shoulder diameter -20 mm.	➢ Microstructures of as cast and homogenised Mg–Y–Zn alloys and die cast AZ91D alloy ➢ Microstructures 3) Hardness	(1) For Mg–Y–Zn cast alloy, FSP was a very efficient method for grain refinement, higher hardness (.120 HV) and finer structure (grain size of y1 mm) than that of AZ91D was achieved. (2) In AZ91D alloy, the grain refinement level and hardness in the stir zone were less than Mg–Y–Zn because of the partly dissolved second phase particles.

17	Ahmadkhaniha.D., et al (2013)	Optimisation of friction stir processing parameters to produce sound and fine grain layers in pure magnesium	10*5* 7 mm were prepared from a pure Mg ingot. H-13 tool steel	➢ Tool angle 2 .5° ➢ Tool rotational speed 1000, 1250, 1600 w/rev /min ➢ Tool travel speed -3,31.5,12 v/mm /min ➢ Tool shoulder diameter -15 mm.	➢ Qualification of friction stir processed workpieces. ➢ Micro hardness ➢ Microstructure	(1) FSP's window process for pure Mg is quite narrower than that of AZ alloys. Achieving a defect free layer of friction stir processed pure Mg is very sensitive to the processing temperature and friction mode. (2) Rotational and traverse speeds play key roles in achieving a sound friction stir processed pure Mg layer. (3) At constant rotational and traverse speeds, when the PD increases, the title angle must also increase in order to have a defect free workpiece.
18	Husain Mehdi et al (2017)	Mechanical properties and microstructure studies in Friction Stir Welding (FSW) joints of dissimilar alloy – a review	CY16, W-La, WC-411 tool	➢ 350 rpm and 15 mm/min ➢ 2236 rpm to 1500 rpm	➢ Mechanical Properties ➢ Wear Property ➢ Microstructure ➢ Macrostructure	Welding parameter such as tool rotation, transverse speed and axial force have a significant effect on the amount of heat generated and strength of FSW joints. Microstructure evaluation of FSW joints clearly shows the formation of new fine grains and refinement of reinforcement particles in the weld zone with different amount of heat input by controlling the welding parameter
19	Husain Mehdi et al (2017)	Influences of Process Parameter and Microstructural Studies in Friction Stir Welding of Different Alloys: A Review	CY16, W-La, WC-411 tool	➢ 2236 rpm and travel speed of 2.33 mm/s ➢ 700 rpm and a traverse speed of 203 mm/min ➢ Tool rotation rate of 300,700, 900 and 1100 rpm and a traverse speed 2 and 8 ipm	➢ Mechanical Properties ➢ Microstructure ➢ Macrostructure ➢ Wear Properties	The mechanical properties of welded joint by friction stir welding are largely dependent on the combined effect of both the composition of alloying element and processing parameter.

20	Jamshidijam.M., et al (2013)	Wear Behavior of Multiwalled Carbon Nanotube/AZ31 Composite Obtained by Friction Stir Processing	AZ31 billet AISI-H13 steel tool	➢ Tool angle - 3° ➢ Tool rotational speed -1500 rpm ➢ Tool travel speed -80 mm /min ➢ Tool shoulder diameter -20 mm. ➢ Tool cylindrical pin diameter - 4 mm ➢ Tool cylindrical pin length - 3 mm	➢ Micro hardness profile. ➢ Optical micrographs ➢ Friction coefficient of the FSP AZ31 with the MWCNTs as a function of sliding distance.	(1) Multiwalled carbon nanotubes were used as reinforcement in the FSP AZ31. The grain size of the AZ31 alloy containing MWCNTs reduced to less than 0.5 μm after FSP. (2) The micro hardness was increased due to grain refinement and high interfacial strength at the MWCNT-AZ31 interface. (3) The difference in wear resistance of the specimens was more pronounced under high applied loads. The wear resistance of the AZ31 alloy containing MWCNTs also doubled under an applied load of 20 N due to the low coefficient friction and higher hardness.
21	Karthikeyan.L., et al (2010)	Biaxial Stressing of Sheets of friction Stir Processed Aluminum Alloy A319	A319 aluminum alloy 100mm×100mm×10 mm. High carbon steel	➢ Tool angle -2° ➢ TRS -1200 rpm ➢ TS -40 mm/min ➢ Cylindrical threaded tool shoulder dia-18 mm. ➢ cylindrical pin diameter - 6 mm ➢ cylindrical length -5.7 mm	➢ Thickness Distribution ➢ Microstructures	(1) FSP is a viable technique for inducing at least extended plasticity in materials. (2) The sheets subjected to gas forming exhibited behavior similar to what has been reported earlier in similar alloys processed by other techniques. (3) The sheets were found to thin by ∼53.3% from the outer flange to the bottom portion (pole).
22	Azizieh.M., et al (2016)	Effect of friction stir processing on the microstructure of pure magnesium castings	Mg ingot 100 mm3 × 70 mm3 × 10 mm3	➢ FSP tool shapes: a non-threaded cylindrical, b threaded cylindrical and c conical pins ➢ Tool rotational speed -400, 500, 630, 800, 1000, 1250 and 1600 rpm ➢ Tool travel speed -50 mm/min	➢ Microstructure ➢ XRD results ➢ Hardness measurements	(1) The threaded pin produced the best material flow and the least cavities. (2) The temperature rise during the FSP was traced, and the maximum temperature reached 360–550 °C, depending on the FSP pin rotational speed. (3) The grain size of the specimens was refined to 13.5–35.5 μm, compared with 200 μm in the initial Mg ingot. (4) The grain growth in high rotational speed resulted from the higher temperatures in this processing condition.

23	Naser.A.Z et al (2016)	Experimental investigation of Mg/SiC composite fabrication via friction stir processing	Magnesium AZ31B sheets with a thickness of 5 mm groove with a width of 2 mm and a depth of 0.5 mm	➢ Tool angle - 2° ➢ Tool rotational speed - 800–2000 rpm ➢ Tool travel speed -25–200 mm/min ➢ Tool shoulder diameter -15 mm ➢ Tool cylindrical pin diameter -5 mm. ➢ Tool cylindrical pin length - 4 mm	➢ Temperature ➢ Microstructure ➢ Micro hardness	(1) FSP was successfully used to fabricate the Mg/Sic surface composite, and the process was found to be very sensitive to the process parameters (the rotational and translational speeds and the groove geometry). (2) Significant grain refinement was attained by FSP, and an average grain size as low as 1.46 μm was achieved for a specific combination of the process parameters. (3) The addition of the SiC particles tends to slightly increase the peak temperature during processing.

3. Conclusions & Recommendation

- The surface composite layer of Nano reinforcement particles by friction stir processing on magnesium alloys improves tensile behavior, hardness, corrosion resistance, percentage and wear resistance behavior of the workpiece material.
- The friction stir processing with multiple passes could effectively cure the onion premature splitting by accumulating a higher degree of strain and the initial grains gets fully recrystallize and to improve the microstructure.
- Increasing the tool rotational speed results greater heat input and increases grain size of the metal alloy and simultaneously more shattering effect of rotation, results a better distribution of Nano particles.
- Water cooling during friction stir welding on magnesium MZ91 enhances the hardness and reduces the final grain size, while the amount of oxide particles in the processed area increases.
- The hardness increases in the FSPed specimens compared with the initial pure Magnesium castings.

References

[1] Chang, C. I., Lee, C. J., & Huang, J. C. (2004). Relationship between grain size and Zener – Holloman parameter during friction stir processing in AZ31 Mg alloys, 51, 509–514.

[2] Morisada, Y., Fujii, H., Nagaoka, T., & Fukusumi, M. (2006). Effect of friction stir processing with SiC particles on microstructure and hardness of AZ31, 433, 50–54.

[3] Materialia, S., Natural, N., Foundation, S., No, G., Sciences, F., & View, C. A. S. (2007). Enhanced Mechanical Properties of Mg-Al-Zn Cast Alloy via Friction Stir Processing Enhanced mechanical properties of Mg – Al – Zn cast alloy via friction stir processing, (51471171).

[4] Chang, C. I., Wang, Y. N., Pei, H. R., Lee, C. J., Du X. H., Huang, J. C., (2007). Microstructure and Mechanical Properties of Nano-ZrO2 and Nano-SiO2 Particulate Reinforced AZ31Mg Based Composites Fabricated by Friction Stir Processing 2015.

[5] Darras, B.M., Khraisheh, M.K., Abu-Farha, F.K., Omar, M.A. (2007). Friction stir processing of commercial AZ31 magnesium alloy Friction stir processing of commercial AZ31 magnesium alloy, (October 2014).

[6] Lee, C. J., Huang, J. C., & Du, X. H. (2007). Using Multiple FSP Passes to Cure Onion Splitting of Mg Alloys Deformed at Elevated Temperatures, 48(4), 780–786.

[7] Ti-jun, C., Zhan-ming, Z., Yuan-dong L., Ying, M., Yuan, H. (2010). Friction stir processing of thixoformed AZ91D magnesium alloy and fabrication of Al-rich surface, (January).

[8] Faraji, G., Dastani, O., Mousavi , S.A.A.A. (2011). Microstructures and mechanical properties of produced by friction stir processing Effect of Process Parameters on Microstructure and Micro-hardness of AZ91 / Al 2 O 3 Surface Composite Produced by FSP).

[9] Azizieh, M., Kokabi, A. H., & Abachi, P. (2011). Effect of rotational speed and probe profile on microstructure and hardness of AZ31 / Al 2O 3 nanocomposites . Journal Of Materials&Design, (April).

[10] Asadi , P., Besharati Givi, M. K., Parvin, N., Araei, A.,Taherishargh, M., Tutunchilar, S., (2012). On the role of cooling and tool rotational direction on microstructure and mechanical properties of friction stir processed AZ91 on microstructure and mechanical properties, (December).

[11] Lee, W. B., Yeon, Y. M., Jung, S. B., Lee, W. B., Yeon, Y. M., & Jung, S. B. (2017). Joint properties of friction stir welded AZ31B – H24 magnesium alloy Joint properties of friction stir welded AZ31B – H24 magnesium alloy, 836(May).

[12] Gupta, A., Singh, P., Gulati, P., & Shukla, D. K. (2015). Effect of Tool rotation speed and feed rate on the formation of tunnel defect in Friction Stir Processing of AZ31 Magnesium alloy Effect of Tool rotation speed and feed rate on the formation of tunnel defect in Friction Stir Processing of AZ31 Magnesium alloy. Materials Today: Proceedings, 2(4–5), 3463–3470.

[13] Zheng, F. Y., Wu, Y. J., Peng, L. M., Li, X. W., Fu, P. H., & Ding, W. J. (2013). Microstructures and mechanical properties of friction stir processed Mg e 2 . 0Nd e 0. 3Zn e 1. 0Zr magnesium alloy, 1, 122–127.

[14] Journal, I., Azizieh, M , Bahadori, R., Abbasi, M., Yoon, E. Y., Kim, H. S. (2016). Effect of friction stir processing on the microstructure of pure magnesium castings Effect of friction stir processing on the, (December 2015).

[15] Li, J., Zhang, D., Chai, F., Li, J., Zhang, D., & Chai, F. (2017). Influence of processing speed on microstructures and mechanical properties of friction stir processed Mg – Y – Nd – Zr casting alloy Influence of processing speed on microstructures and mechanical properties of friction stir processed Mg – Y – Nd – Zr casting alloy, 8917(July).

[16] Morishige, T., Tsujikawa, M., Hino, M., Hirata, T., Oki, S., Higashi, K., Higashi, K. (2017). Microstructural modification of cast Mg alloys by friction stir processing Microstructural modification of cast Mg alloys by friction stir processing, 461(July).

[17] Ahmadkhaniha, D., Sohi, M. H., Ahmadkhaniha, D., & Sohi, M. H. (2014). Optimisation of friction stir processing parameters to produce sound and fine grain layers in pure magnesium Optimisation of friction stir processing parameters to produce sound and fine grain layers in pure magnesium, 1718(July 2017).

[18] Husain Mehdi, R.S. Mishra, Mechanical properties and microstructure studies in Friction Stir Welding (FSW) joints of dissimilar alloy- A Review, Journal of Achievements in Materials and Manufacturing Engineering 77/1 (2016) 31-40.

[19] Husain Mehdi, R.S. Mishra, Influences of Process Parameter and Microstructural Studies in Friction Stir Weldingof Different Alloys: A Review, International Journal of Advanced Production and Industrial Engineering, IJAPIE-SI-MM 509 (2017) 55–62.

[20] Jamshidijam, M., Akbari-fakhrabadi, A., Morteza, S., Hasani, G. H., Mangalaraja, R. V, Jamshidijam, M., … Masoudpanah, S. M. (2013). Wear Behavior of Multiwalled Carbon Nanotube / AZ31 Composite Obtained by Friction Stir Processing Wear Behavior of Multiwalled Carbon Nanotube / AZ31, 2004(July 2017).

[21] Karthikeyan, L., Senthilkumar, V. S., & Padmanabhan, K. A. (2017). Biaxial Stressing of Sheets of Friction Stir Processed Aluminum Alloy A319 Biaxial Stressing of Sheets of Friction Stir Processed, 6914(July).

[22] Azizieh, M., Bahadori, R., Abbasi, M., Yoon, E. Y., Kim, H. S., Bahadori, R., Kim, H. S. (2017). Effect of friction stir processing on the microstructure of pure magnesium castings Effect of friction stir processing on the microstructure of pure magnesium castings. International Journal of Cast Metals Research, 28(6), 345–351.

[23] Naser, A. Z., & Darras, B. M. (2017). Experimental investigation of Mg / SiC composite fabrication via friction stir processing, 781–790.

This article has been accepted for publication in a future issue of this journal, but has not been fully edited. Content may change prior to final publication. Citation information: DOI 10.1109/TIE.2017.2758739, IEEE Transactions on Industrial Electronics

Generalized input impedance modelling of TL-network-based HFDPS for validating frequency-dependent criteria for power-signal integrity

Ankit Gupta, Nikhil Kumar, *Student Members*, IEEE, Sudip K Mazumder, *Fellow*, IEEE

***Abstract*— Adjusting the transmission-line (TL) length or using active compensation is pursued in high-frequency distributed power systems (HFDPSs) as a possible remedy for addressing the TL effects. While adjusting the TL length is primarily limited to printed-circuit-board (PCB) level implementations, active compensation yields higher expense and complexity. To mitigate TL effects under periodic condition, generalized input impedance modelling of a TL network- based HFDPS feeding linear load(s) is provided. Using this generalized model, a frequency-dependent criterion for maintaining power-signal integrity is outlined for scenario centric single-/ multiple-input single-/ multiple-output (SISO/ SIMO/ MIMO) HFDPS topologies. Selection of such a transmission frequency is important for designing a HFDPS to avoid deterioration of voltage and current, rupturing the TL insulation, and increased losses owing to the TL effect. Validations of the frequency dependent criteria have been carried out using simulation and experiments in time and frequency domains.**

***Index Terms*— Transmission line, characteristic impedance, high frequency, power transfer.**

I. Introduction

Conventionally, DPSs are based on dc or low-frequency ac power delivery. Fig. 1 displays a HFDPS, which offers a promising alternative with several flexible applications [1][2]. A HFDPS is outlined in [3][4] to minimize system complexity, reduce power-electronics stages, and enhance the efficiency, power density, and system dynamics. Improvements in the device technology have facilitated HFDPS by enabling HF operation at reduced losses. This has accelerated the applications of the HFDPS in areas such as hybrid-electric vehicle, all-electric ships, telecommunication, computers, and digitization of electricity [1], [5]-[12].

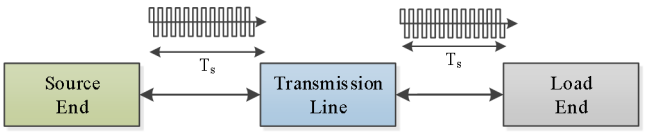

Fig. 1. Illustration of a HFDPS overview.

On the basis of the span of a HFDPS and the frequency of wave transmission through a TL, HFDPS is subdivided into two categories: one which encounters TL effect [13]-[22] and the other, which does not [23]-[26]. When the physical length of a TL is comparable to the length of the wave being transmitted through it, TL effect comes into play. The latter leads to loss of integrity of the power signal being transmitted through the TL [27]-[29].The simulation result in Fig. 2 captures the variations in the length of a TL (with the parameters tabulated in Table I) at which the onset of TL effect occurs as a function of the frequency of wave transmission [27]. Fig. 2 shows that, as the frequency of the wave transmission increases, the length at which the TL effect onsets decreases. Such effects, often accompanying over-voltages in circuits which may lead to damage to the insulation of a motor or a TL [14]-[22].

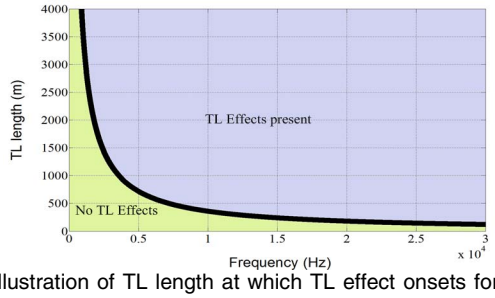

Fig. 2. Illustration of TL length at which TL effect onsets for a given frequency. The parameters of the TL are captured in Table I.

One way to mitigating the TL effect is via active compensation along the TL [30]-[32], which ensures signal integrity for a wide range of frequency of wave transmission. However, such an active-compensation scheme is often limited by an increase in the associated cost and complexity of the compensated system. Therefore, it is preferred to design an alternative strategy to eliminate the TL effects. A unique approach was presented in [33]-[37] for exploiting the periodicity property exhibited by the input impedance of the TL with varying length of wave transmission. It was demonstrated that, by choosing a particular TL length and keeping the frequency of wave transmission constant, voltage and current profile of a system can be modified in any desired manner. However, such a methodology is not applicable when the length of the TL cannot be varied. Further, past research mainly dealt with SISO HFDPS topologies that lack scalability for SIMO and MIMO HFDPS topologies [33]-[37].

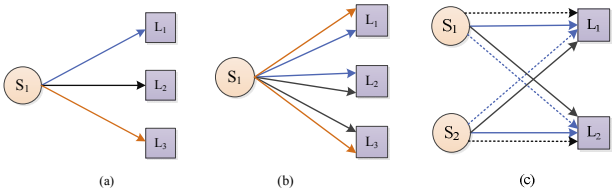

Fig. 3. HFDPS (a) SISO, (b) SIMO, and (c) MIMO network topologies. The links marked with same colors can transfer power simultaneously while dotted lines in (c) show the interference (leakage) path for power.

In this paper, to extend the analysis and validate the scalability of SIMO and MIMO HFDPS topologies as illustrated in Fig. 3, we have outlined a methodology for generalized input impedance modelling of spatiotemporal coupled TL network. Using this methodology, scenario-centric input-impedance model is extracted which leads to a frequency selection criterion. The frequency selection criterion exploits the periodic property of a TL exhibited by

Manuscript received April 09, 2017; revised August 29, 2017; accepted September 18, 2017. This work was supported by U.S. National Science Foundation under Award No.1239118.

The authors are with the Laboratory of Energy and Switching-Electronics Systems, Department of Electrical and Computer Engineering, University of Illinois at Chicago, IL 60607 USA (e-mail: agupta70@uic.edu; nkumar22@uic.edu; mazumder@uic.edu)

0278-0046 (c) 2017 IEEE. Personal use is permitted, but republication/redistribution requires IEEE permission. See http://www.ieee.org/publications_standards/publications/rights/index.html for more information.

This article has been accepted for publication in a future issue of this journal, but has not been fully edited. Content may change prior to final publication. Citation information: DOI 10.1109/TIE.2017.2758739, IEEE Transactions on Industrial Electronics

its input impedance as a function of the frequency of wave transmission to ensure the integrity of a power signal being transmitted to an unmatched load in a HFDPS.

This paper is divided into five sections. In Section II, input impedance modeling of a HFDPS with TL network has been outlined. In Section III, various HFDPS topologies are discussed in detail and frequency-selection criterion is derived for each topology. Next, in Section IV, an experimental setup for validation is outlined along with detailing of the experimental results and their analyses. Also, simulated parametric plots are provided for demonstrating the periodic property exhibited by the input impedance for scenario-centric SISO, SIMO and MIMO topologies. A brief conclusion of our work is outlined in Section V.

II. Generalized Input Impedance Modeling of a HFDPS with TL Network

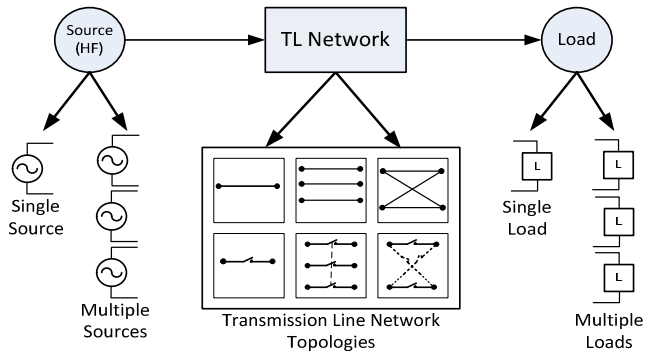

Fig. 4. Illustration of a simplified representation of a HFDPS, which provides a power-transfer pathway between the energy source(s) and load(s) (which may/may not be monolithic) over a TL network that may have a singular/plural path-invariant/path-varying TL(s).

Fig. 4 illustrates a simplified representation of a generalized HFDPS. Essentially, the HFDPS provides a pathway for power transfer between energy source(s) and application load(s) over a TL network that may have a singular/plural path-invariant/path-varying TL(s). Such a HFDPS may have multiple topological manifestations including SISO, SIMO, and MIMO topologies. Further, the load in Fig. 4 may not be a monolithic load. Thus, a generalized analysis of n number of sources feeding n number of loads simultaneously through a TL network as shown in Fig. 4 is provided. The TL network is composed of n spatiotemporal coupled TL(s).

Starting from n mutually coupled TLs of different characteristics, TL equations in a matrix form is written as

$$\partial_z V = -L\partial_t I,\ \partial_z I = -C\partial_t V \qquad (1), (2)$$

where ∂_z and ∂_t are the partial differential operators w.r.t space and time respectively. Also V, I are $n \times 1$ voltage and current column vectors and are represented as $V = [v_1 \quad \dots \quad v_n]^T$ and $I = [i_1 \quad \dots \quad i_n]^T$. Symbols L and C are matrices of order n×n. The principal diagonal elements of L and C matrices are L_{jk} and C_{jk}, where $(j = k)$ represents self-inductance and capacitance per unit length of individual TL while off diagonal elements L_{jk} and C_{jk}, where $(j \neq k)$ represent mutual inductance and mutual capacitance per unit length between TLs in the TL network. To study the input impedance as seen by the sources $S_1\ S_2 \dots S_n$, an equivalent form of (1) and (2) in frequency domain is written as follows:

$$\partial_z V = -jX_L I\ ,\ \partial_z I = -jX_c V \qquad (3), (4)$$

where X_L and X_c are $n \times n$ matrices and are represented as

$$X_L = \begin{bmatrix} \omega_1 L_{11} & \dots & \omega_n L_{1n} \\ \vdots & \ddots & \vdots \\ \omega_1 L_{n1} & \dots & \omega_n L_{nn} \end{bmatrix},\ X_c \begin{bmatrix} \omega_1 C_{11} & \dots & -\omega_n C_{1n} \\ \vdots & \ddots & \vdots \\ -\omega_1 C_{n1} & \dots & \omega_n C_{nn} \end{bmatrix}.$$

On differentiating (3) with respect to ∂z and subsequent substitution of (4) in (3), one obtains the following expression:

$$\partial_z{}^2 V + X_L X_c V = 0,\ \partial_z{}^2 I + X_L X_c I = 0. \qquad (5), (6)$$

The matrix $X_L X_c$ is of order $n \times n$ and has distinct eigenvalues $\beta_1\ \beta_2 \dots \beta_n$. For such a matrix, eigenvectors $p_1, p_2 \dots, p_n$ corresponding to $\beta_1, \beta_2 \dots, \beta_n$ will be linearly independent and can be used to yield a diagonal matrix D:

$$D = P(X_L X_c)P^{-1} = \mathrm{diag}[\,\beta_1 \quad \dots \quad \beta_n]. \qquad (7)$$

In (5) and (6), since matrix $X_L X_c$ couples each element of $(\partial_z{}^2 V, \partial_z{}^2 I)$ to each element of (V, I) respectively, a decoupled system of equations is generated using transformation $U = pV$ and $J = pI$ yielding the following:

$$\partial_z{}^2 U + D'U = 0,\ \partial_z{}^2 J + D'J = 0. \qquad (8), (9)$$

Solving (8) and (9), one obtains

$$U = [U_1 \quad \dots \quad U_n]^T, J = \quad [J_1 \quad \dots \quad J_n]^T \quad (10), (11)$$

where the n^{th} element of U and J are given, respectively, by ${U_n}^+ e^{-j\sqrt{\beta_n} z} + {U_n}^- e^{+j\sqrt{\beta_n} z}$ and ${J_n}^+ e^{-j\sqrt{\beta_n} z} + {J_n}^- e^{+j\sqrt{\beta_n} z}$. Now, (10) and (11) can be transformed back to coupled system of equations by using following transformations:

$$V = P^{-1}U,\ I = P^{-1}J. \qquad (12), (13)$$

If matrix P^{-1} is a $n \times n$ matrix represented by $[p_{jk}]$, where p_{jk}, (12) and (13) is expressed as follows:

$$V = [v_1 \quad \dots \quad v_n]^T, I = [i_1 \quad \dots \quad i_n]^T \quad (14), (15)$$

and the n^{th} element of V and I are, respectively, given by $p_{n1}U_1 + p_{n2}U_2 + \dots + p_{nn}U_n$ and $p_{n1}J_1 + p_{n2}J_2 + \dots + p_{nn}J_n$. Matrix I can also be expressed in terms of U using (3):

$$I = jX_L{}^{-1}\left[\sum_{i=1}^{i=n} p_{1i}(\partial_z U_i) \cdots \sum_{i=1}^{i=n} p_{ni}(\partial_z U_i)\right]^T. \qquad (16)$$

Equations (14) and (16) represent voltage and current at any z on a TL in a n spatiotemporal coupled TL network.

For simplification, n spatiotemporal coupled TL(s) are assumed to have same characteristics such that the principal diagonal elements of matrix L and C are equal, i.e. $L_{jk} = L$ and $C_{jk} = C$, where $(j = k)$. Further, it is assumed that the off diagonal elements of matrix L and C are equal, i.e. $L_{jk} = L_m$ and $C_{jk} = C_m$, where $(j \neq k)$. Thus, using (14) and (16) the voltage and current at any point z on n^{th} TL in a n spatiotemporal coupled TL network can be represented as follows:

$$v_n = \left[\sum_{m=1}^{n} p_{nm}({U_m}^+ e^{-j\sqrt{\beta_m} z} + {U_m}^- e^{+j\sqrt{\beta_m} z})\right] \qquad (17)$$

$$i_n = j\begin{bmatrix} c_{11} & \dots & c_{12} \\ \vdots & \ddots & \vdots \\ c_{12} & \dots & c_{11} \end{bmatrix}\left[\sum_{m=1}^{n} p_{nm}({U_m}^+ e^{-j\sqrt{\beta_m} z} + {U_m}^- e^{+j\sqrt{\beta_m} z})\right] \qquad (18)$$

where $c_{11} = \frac{L+(n-2)L_m}{N_c}$, $c_{12} = \frac{-L_m}{N_c}$, and $N_c = \omega_1\left(\left(L^2 - (n-1){L_m}^2\right) + (n-2)LL_m\right)$. On applying boundary conditions at load and source end, input impedance as seen by the source S_n is represented as

$$Z_{inn} = F_n(Z_{L1} \dots Z_{Ln}, L, C,\ \omega_n,\ \beta_1 \dots \beta_n,\ l_1 \dots l_n, L_m, C_m). \qquad (19)$$

A detailed analysis for a 2×2 scenario-centric HFDPS in which two sources S_1 and S_2 feeds two loads L_1 and L_2 via two spatiotemporal coupled TL(s) is presented in Appendix A. Following the methodology presented in Section II, Appendix A further details the expression of the input impedance as seen by S_1 and S_2.

III. Input-Impedance based Frequency-Dependent Criteria for TL-Network based HFDPS Topologies

Analyses of three distinct scenario-centric HFDPS topologies is conducted next using input-impedance modeling methodology provided in Section II. They lead to

0278-0046 (c) 2017 IEEE. Personal use is permitted, but republication/redistribution requires IEEE permission. See http://www.ieee.org/publications_standards/publications/rights/index.html for more information.

This article has been accepted for publication in a future issue of this journal, but has not been fully edited. Content may change prior to final publication. Citation information: DOI 10.1109/TIE.2017.2758739, IEEE Transactions on Industrial Electronics

corresponding frequency–selection criteria that ensure the integrity of the transmitted signal under periodic condition.

A) Case A: HFDPS with SISO Topology

Fig. 5 shows a HFDPS with a pathway marked in red illustrating a SISO power transfer originating at a single source (S_1) and terminating at a single load (L_1) with an impedance of Z_{L1} by closing the source and load-side switches u_{S1} and u_{L1}, respectively. It is noted that a SISO realization for the HFDPS can be obtained in several other ways by linking any one source to any one load with/without a preceding TL. For these scenarios, the scenario-centric analysis carried out next is applicable with small variations that will be outlined at the end of the analysis.

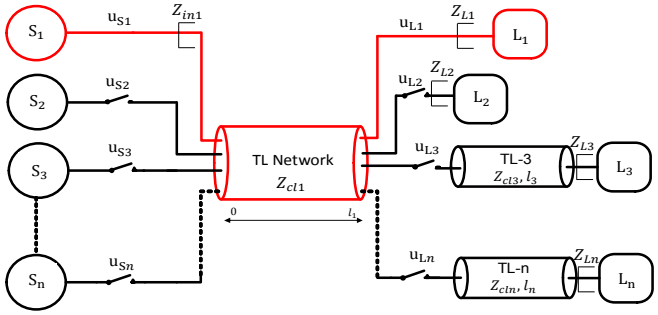

Fig. 5. SISO power transfer for a HFDPS. The TL network can be configured to realize multiple other SISO realizations by connecting any one source to any one load with/without a preceding TL.

As mentioned earlier, we assume that S_1 is connected to L_1 (with an impedance of Z_{L1}) via the TL network of length l_1. Further, let Z_{in1} represent the impedance reflected at the input (or source-end) of the SISO topology as illustrated in Fig. 5. If there is no mutual coupling between the TL(s) in TL network such that $L_m = 0$ and $C_m = 0$, then using (A3), as provided in Appendix A, input impedance as seen by the source S_1 for SISO topology is given by the following:

$$Z_{in1} = \frac{\left[(Z_{L1}) + j\sqrt{L/C}\tan(2\pi f_1\sqrt{LC}l_1)\right]\sqrt{L/C}}{\left(\sqrt{L/C} + jZ_{L1}\tan(2\pi f_1\sqrt{LC}l_1)\right)}. \quad (20)$$

It is important to note that substitution of $f_1 = n/2\sqrt{LC}l_1$ (where n is an integer) in (20) always yields

$$Z_{in1} = Z_{L1}. \quad (21)$$

For any other frequency of wave transmission that does not satisfy $f_1 = n/2\sqrt{LC}l_1$, (20) is not satisfied as well. Instead, Z_{in1} could exhibit resistive or reactive impedance for the same load [38], [39]. Above outlined hypothesis can be extended to other cases with minor adjustments. For instance, if one considers, that S_1 has to transfer power to L_3 which is preceded by an additional TL (TL-3), the same procedure can be followed in two steps. First, a set of frequencies ($f_3 = n/2\sqrt{LC}l_3$) have to be determined using parameters of TL-3 and then a subset of the obtained frequency set ($f_1 \subseteq f_3$) is to be establish using the parameters of the TL network such that the input impedance (Z_{in1}) becomes equal to the load impedance (Z_{L3}). Similar analysis can also be applied if air is chosen as the transmission medium instead of a waveguide. The difference will appear in the obtained set or subset of frequencies as L and C assume different values for air.

B) Case B: HFDPS with SIMO Topology

In Fig. 6, the section of the HFDPS marked in red illustrates a SIMO topology. It comprises S_1 that feeds power to L_1 and L_3 over the TL network. While L_1 is directly connected to the TL network of length l_1, L_3 is connected to the TL network via a TL marked TL-3 of length l_3. Similar to Case A, a SIMO topology can be obtained in plurality of ways by connecting any single source to multiple loads among L_1 through L_n with or without a preceding TL. It is assumed that the TL network and TL-3 have same characteristics. For the illustrated SIMO topology, if coupling between the TLs in TL network is assumed to be zero, then using (A3), the input impedance (Z_{in1}) as seen by S_1 is given by

$$Z_{in1} = \sqrt{\frac{L}{C}}\left[\frac{\left\{\frac{(Z_{L1}Z_{L3}(\sqrt{L/C})+jZ_{L1}(L/C)\tan(2\pi f_1\sqrt{LC}l_3))}{((\sqrt{L/C})(Z_{L1}+Z_{L3})+j\tan(2\pi f_1\sqrt{LC}l_3)(Z_{L2}+(L/C)))}\right\}+j\sqrt{L/C}\tan(2\pi f_1\sqrt{LC}l_1)}{j\left\{\frac{(Z_{L1}Z_{L3}(\sqrt{L/C})+jZ_{L1}Z_{cl}{}^2\tan(2\pi f_1\sqrt{LC}l_2))\tan(2\pi f_1\sqrt{LC}l_1))}{\sqrt{L/C}(Z_{L1}+Z_{L3})+j\tan(2\pi f_1\sqrt{LC}l_3)((L/C)+Z_{L1}Z_{L3})}\right\}+\sqrt{L/C}}\right]. \quad (22)$$

It is important to note that, in (22) substitution of $f_1 = \frac{n}{2\sqrt{LC}l_1} = \frac{m}{2\sqrt{LC}l_3}$ (where m is an integer) always yields

$$Z_{in1} = Z_{L1} * Z_{L3}/Z_{L1} + Z_{L3} \quad (23)$$

Following Case A, for a given l_1 and l_3, if the frequency of wave transmission is so selected such that $f_1 = \frac{nv}{2l_1} = \frac{mv}{2l_3}$, then (23), which represents the impedance matching condition, is satisfied. The latter ensures signal integrity by mitigating the TL effects between S_1 and L_1 and L_3. For any other frequency of wave transmission, (23) is not satisfied. It is noted that, the outlined approach is applicable for any other SIMO topology shown in Fig. 6 and even if air instead of a conductive waveguide is the medium of transmission.

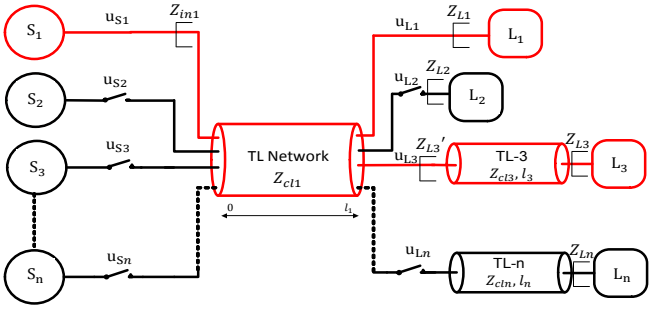

Fig. 6. An illustration of a SIMO topology marked in red. It comprises S_1 that feeds L_1 and L_3 over the TL network; L_1 is directly connected to the TL network and L_3 is connected to the TL network via a TL-3.

C) Case C: HFDPS with MIMO Topology

While several HFDPSs may emulate SISO and SIMO topologies, MIMO topologies, which involve simultaneous power transfer from a plurality of sources to a plurality of loads is often a reality. Consider a scenario in Fig. 7, where S_1 and S_2 transfers power to load L_1 and L_2 simultaneously, as a result of cross-coupling between the TLs in the TL network, a part of S_1's (S_2's) power is fed to L_2 (L_1) which is undesirable. Crosstalk in a MIMO topology due to a finite mutual coupling between the TL(s) can be understood in the form of either spatiotemporal (distributive coupling) coupling as presented in Appendix A or a temporal coupling for a 2 × 2 HFDPS as shown in Fig. 7. The generalized and case specific analysis for the spatiotemporal coupled TL is provided in section II and appendix B respectively. This sub-section is attributed to the scenario-centric analysis for a finite mutual temporal coupling represented by coupled inductor as shown in Fig. 7. TL-1 and TL-2 are assumed to have the same characteristics.

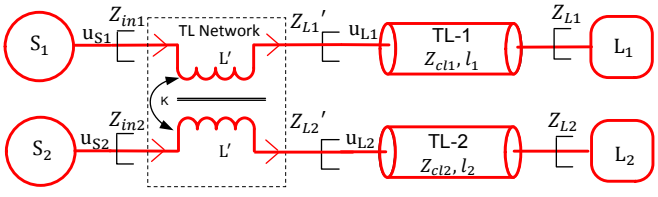

Fig. 7. A simple embodiment of crosstalk in a MIMO topology with TL network replaced with a coupled inductor.

0278-0046 (c) 2017 IEEE. Personal use is permitted, but republication/redistribution requires IEEE permission. See http://www.ieee.org/publications_standards/publications/rights/index.html for more information.

This article has been accepted for publication in a future issue of this journal, but has not been fully edited. Content may change prior to final publication. Citation information: DOI 10.1109/TIE.2017.2758739, IEEE Transactions on Industrial Electronics

Using the input impedance expression as obtained in case A for the SISO topology, $Z_{L_1}{}'$ and $Z_{L_2}{}'$ are given by

$$Z_{L_1}{}' = \frac{\left[(Z_{L1}) + j\sqrt{L/C}\tan(2\pi f_1\sqrt{LC}l_1)\right]\sqrt{L/C}}{\left(\sqrt{L/C} + jZ_{L1}\tan(2\pi f_1\sqrt{LC}l_1)\right)} \quad (24)$$

$$Z_{L_2}{}' = \frac{\left[(Z_{L2}) + j\sqrt{L/C}\tan(2\pi f_2\sqrt{LC}l_2)\right]\sqrt{L/C}}{\left(\sqrt{L/C} + jZ_{L2}\tan(2\pi f_2\sqrt{LC}l_2)\right)} \quad (25)$$

To calculate the input impedance seen by S_1, S_2 is short-circuited such that $v_{in2} = 0$. This yields Z_{in1} to be

$$Z_{in1} = \left(\frac{\left[(Z_{L1}) + j\sqrt{L/C}\tan(2\pi f_1\sqrt{LC}l_1)\right]\sqrt{L/C}}{\left(\sqrt{L/C} + jZ_{L1}\tan(2\pi f_1\sqrt{LC}l_1)\right)} + j\omega_1 L'\right) + \left(jM\omega_1 \frac{\left[\frac{\left[(Z_{L2}) + j\sqrt{L/C}\tan(2\pi f_1\sqrt{LC}l_2)\right]\sqrt{L/C}}{\left(\sqrt{L/C} + jZ_{L2}\tan(2\pi f_1\sqrt{LC}l_2)\right)} + j\omega_1(L'-M)\right]}{\left(\frac{\left[(Z_{L2}) + j\sqrt{L/C}\tan(2\pi f_1\sqrt{LC}l_2)\right]\sqrt{L/C}}{\left(\sqrt{L/C} + jZ_{L2}\tan(2\pi f_1\sqrt{LC}l_2)\right)} + jL'\omega_1\right)} - j\omega_1 M\right). \quad (26)$$

Similarly, Z_{in2} as seen by S_2 can be calculated by short-circuiting S_1 such that $v_{in1} = 0$ and is given by

$$Z_{in2} = \left(\frac{\left[(Z_{L2}) + j\sqrt{L/C}\tan(2\pi f_2\sqrt{LC}l_2)\right]\sqrt{L/C}}{\left(\sqrt{L/C} + jZ_{L2}\tan(2\pi f_2\sqrt{LC}l_2)\right)} + j\omega_2 L'\right) + \left(jM\omega_2 \frac{\left[\frac{\left[(Z_{L1}) + j\sqrt{L/C}\tan(2\pi f_2\sqrt{LC}l_1)\right]\sqrt{L/C}}{\left(\sqrt{L/C} + jZ_{L1}\tan(2\pi f_2\sqrt{LC}l_1)\right)} + j\omega_2(L'-M)\right]}{\left(\frac{\left[(Z_{L1}) + j\sqrt{L/C}\tan(2\pi f_2\sqrt{LC}l_1)\right]\sqrt{L/C}}{\left(\sqrt{L/C} + jZ_{L1}\tan(2\pi f_2\sqrt{LC}l_1)\right)} + jL'\omega_2\right)} - j\omega_2 M\right) \quad (27)$$

where M represents the mutual inductance between the two temporally-coupled TL(s) in the TL network and its expression is given by $M = KL'$, K being the mutual coupling coefficient. To ensure signal integrity, the following conditions need to be satisfied:

(i) $Z_{in1} = Z_{L1} + j\omega_1 L'$, $Z_{in2} = Z_{L2} + j\omega_2 L'$ (28)

(ii) Signal to interference noise ratio (SINR) should be high.

One way to practically satisfy both conditions is to ensure negligible K for the system and chose frequency of wave transmission $f_1 = \frac{n}{2\sqrt{LC}l_1}$ and $f_2 = \frac{m}{2\sqrt{LC}l_2}$. However, for large value of K, using the frequency set $f_1 = \frac{n}{2\sqrt{LC}l_1}$ and $f_2 = \frac{m}{2\sqrt{LC}l_2}$ alone will not ensure signal integrity. An alternative approach to ensure signal integrity in a MIMO topology, as shown in Fig. 8, is to use a band-stop filter in the power transmission path between S_1 (S_2) and L_1 (L_2). We use a TL-based band-stop filter [26], outlined in Appendix B, to exploit the periodic property of such a filter. The basic idea, following Case A, is to initially select a set of frequencies of wave transmission between S_1 (S_2) and L_1 (L_2) such that the condition for signal integrity following (28) is achieved assuming no crosstalk. Next, the band-stop filter for each of these paths is placed and so tuned so that they only let go the power signal at the selected frequency of wave transmission. Thus, for the MIMO topology, any cross talk between S_1 (S_2) and L_2 (L_1) is essentially eliminated and power flows from S_1 (S_2) and L_1 (L_2) without signal-integrity issues.

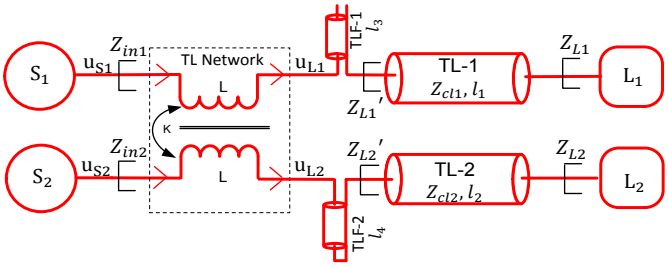

Fig. 8. Mitigation of crosstalk using tuned TL based band-stop filters TLF-1 and TLF-2.

IV. Results

An experimental setup shown in Fig. 9, is developed to conduct experimental validations of the frequency-selection criterion outlined in Section III and extended for SISO, SIMO, and MIMO topologies. Frequency-domain experimentations and validations are carried out using an HP3577A vector network analyzer (VNA). The HP 35677A S-parameter test set is used to study the scattering (S) parameters [28] of the TL network (Figs. 5-7) for the various network topologies. A Belden 7977A co-axial cable has been chosen as the TL (with following parameters: characteristic impedance - 50 Ω, inductance - 0.1968 μH/m, capacitance - 80.688 pF/m, velocity of propagation – 84%, delay – 3.96 ns/m, and dc resistance – 11.7384 mΩ/m) and Bourns radio-frequency (RF) resistive loads have been used. Time-domain analyses is carried out at a frequency of 10 MHz to limit the size of the experimental setup. An RF power amplifier (ENI 503L from Bell Electronics) is used to generate the HF power signals.

Fig. 10(a) shows the variation of the input impedance with frequency of wave transmission using a Smith chart for the SISO topology marked in red in Fig. 5. It can be seen from the Smith chart that, the input impedance varies between 0.5-2 p.u. of the characteristic impedance, which corresponds to a range of 25 Ω through 100 Ω. Further, even though the input impedance is purely resistive at integer multiples of 5 MHz, it matches the load impedance of 100 Ω only at integer multiples of 10 MHz. At odd integral multiples of 5 MHz, which according to (20) yields an input impedance of $Z_{in1} = L/CZ_L = 25$ Ω and is shown by the intersection of the circle with the Smith's chart at 0.5 on the horizontal axis.

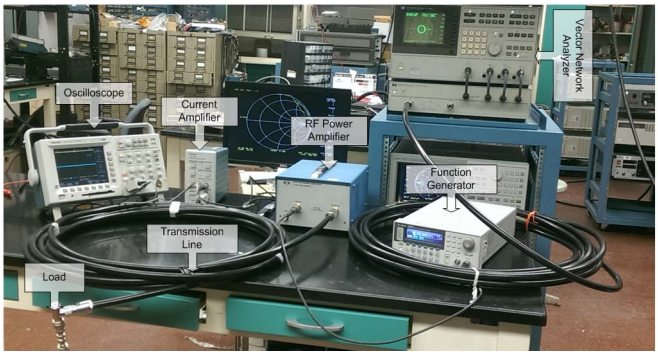

Fig. 9. Experimental setup for validating frequency-selection criterion.

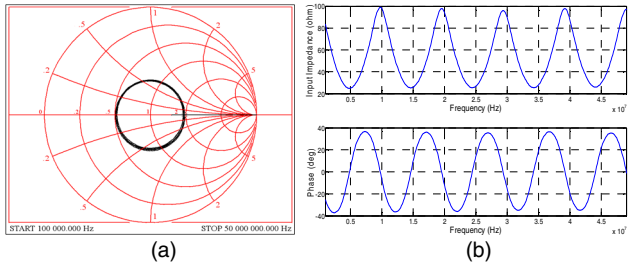

(a) (b)

Fig. 10. Experimental results showing (a) variation in the input impedance with frequency of wave transmission for SISO topology (marked in red in Fig. 5); and (b) magnitude and phase variations of the input impedance with frequency for the same SISO topology.

The magnitude and phase variations of the input impedance as a function of the frequency of wave transmission for the SISO topology (Fig. 5) are shown in Fig. 10(b). Following [28], the data points for Fig. 10(b) are extracted from the S_{11} parameter obtained using the VNA. Fig. 10(b) shows that, at integral multiples of 5 and 10 MHz, the input impedance is resistive in nature indicated by zero phase angles; however, its

0278-0046 (c) 2017 IEEE. Personal use is permitted, but republication/redistribution requires IEEE permission. See http://www.ieee.org/publications_standards/publications/rights/index.html for more information.

This article has been accepted for publication in a future issue of this journal, but has not been fully edited. Content may change prior to final publication. Citation information: DOI 10.1109/TIE.2017.2758739, IEEE Transactions on Industrial Electronics

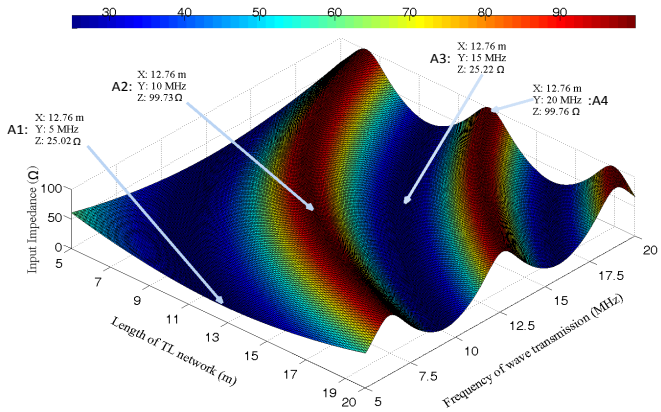

Fig. 11. Variation in input impedance with frequency of transmission and TL network length for a SISO topology. TL length, the frequency of transmission, and input impedance are marked by X, Y, and Z.

magnitude matches the load impedance only at integral multiples of 10 MHz. It can also be observed that, the input impedance shows a periodic nature and follows our simulation result in Fig. 11 for a TL-network length of 12.75 m.

Fig. 12 displays the time-domain results for the same SISO topology. The designed setup was tested at 10, 12, 15 and 20 MHz. At 10, 15 and 20 MHz, the voltage and current at the input of the TL network are in phase but the input impedance closely matches the load impedance ($Z_{L1} = 100\ \Omega$) only at 10 MHz and 20 MHz. This is because for propagation velocity of 84% (Table I) and TL network length of 12.75 m, (21) is satisfied only at input wave frequencies which are integer multiples of 10 MHz. However, at 15 MHz the present length of TL network (12.75 m) is equivalent to $3\lambda/4$, and the input impedance is found to be $Z_{in1} = L/CZ_{L1} = 23.7\ \Omega$. At a frequency of 12 MHz, the input impedance is found to be inductive in nature and does not match the load impedance. The time-domain results obtained in Fig. 12 closely match the simulation result shown in Fig. 11 for a TL network length of 12.75 m and frequency-domain results in Figs. 10(a) and 10(b). This serves as a clear proof for the SISO frequency-selection criterion provided in Section III.

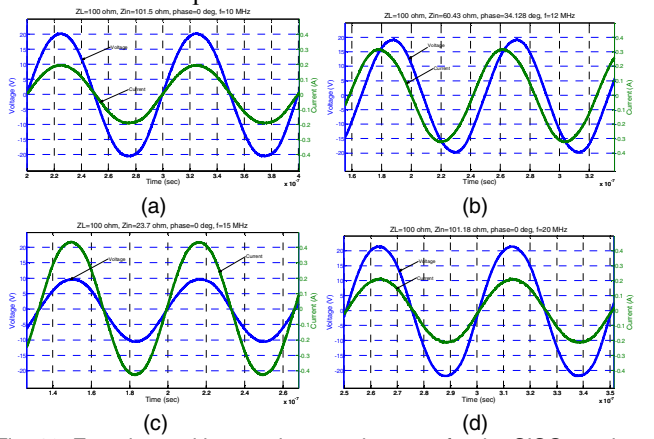

Fig. 12. Experimental input voltage and current for the SISO topology (Fig. 5) at (a) 10 MHz, (b) 12 MHz, (c) 15 MHz, and (d) 20 MHz.

Frequency-domain results for the SIMO topology marked in red in Fig. 5 are presented in Fig. 13(a) in the form of Smith's chart and in Fig 13(b) as magnitude and phase plots. Both the TL network and TL-3 were chosen to have a length of 12.75 m and L_1 and L_3 were chosen to be 100 Ω each. It can be observed from the Smith chart as shown in Fig. 13(a) that the input impedance curve intersects the horizontal axis at 0.66, 1 and 2.46 p.u. of the characteristic impedance. This signifies a resistive input impedance of 33 Ω, 50 Ω and 123 Ω respectively. Similar results can also be inferred from the frequency-domain results shown in Figs. 13(b). It is noted that in Figs. 13(a) and 13(b) the magnitude of input impedance decreases in successive cycles as a result of lossy TL characteristics. At odd integer multiple of 5 MHz, the input impedance is resistive in nature and approaches 125 Ω. However, at integer multiples of 10 MHz, using (22) the value of the input impedance is given by the parallel combination of Z_{L1} and Z_{L3} and approaches 50 Ω. As can be inferred from Fig. 13(b), in a single period there are four points on the graph at which phase angle is zero. The input impedance at these points can be calculated using (22) by equating the imaginary part of Z_{in1} to zero.

Frequency-domain and simulation results for the SIMO topology are provided in Fig. 13 and Fig. 14, respectively. These are also validated by the time-domain results as shown in Fig. 15 for TL-3 of length 12.75 m. Fig. 13 displays that at 10 and 20 MHz the input impedance is resistive in nature and has a magnitude close to 50 Ω which satisfies (23). Also, at 15 MHz the input impedance is still resistive in nature; however, at this frequency, the magnitude of the input impedance is 122.65 Ω which matches the frequency- domain results provided in Fig 13. Likewise, it can be observed that at 13 MHz, the input impedance is inductive in nature which follows from (22). These results provide a proof for the SIMO frequency selection criterion provided in Section II.

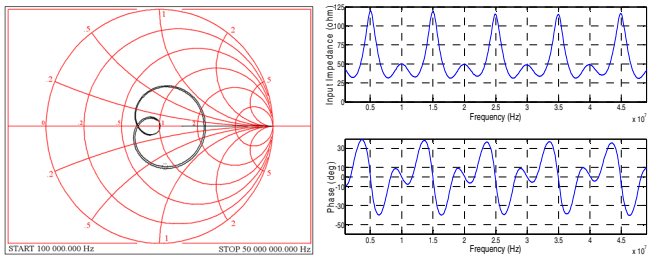

Fig. 13. Experimental variation in the (a) input impedance and (b) magnitude and phase variations of the input impedance with frequency of wave transmission for the SIMO topology marked in red in Fig. 6.

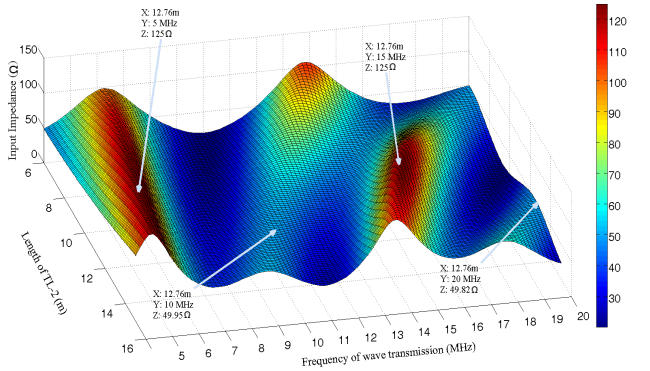

Fig. 14. Variation in input impedance with variation in frequency of wave transmission and TL-3 length for the SIMO topology marked in red in Fig. 6. TL-network length is marked by X, the frequency of wave transmission is marked by Y and input impedance is marked with Z.

Next, an experimental setup was developed for ascertaining the validity of (28) for power flow in the MIMO topology as shown in Fig. 7. Condition (28) is satisfied by setting frequencies of wave transmissions or signal frequencies corresponding to S_1 and S_2 to be 10 MHz and 20 MHz, respectively. This ensures, following Case A and in the absence of crosstalk, mitigation of noise in the transmitted power signals being fed to two 100 Ω loads through two temporal coupled TL(s) each with a physical length of 12.75 m. Fig. 16 demonstrates the variation in the signal-to-interference-noise ratio (SINR) of voltage and current as a

0278-0046 (c) 2017 IEEE. Personal use is permitted, but republication/redistribution requires IEEE permission. See http://www.ieee.org/publications_standards/publications/rights/index.html for more information.

This article has been accepted for publication in a future issue of this journal, but has not been fully edited. Content may change prior to final publication. Citation information: DOI 10.1109/TIE.2017.2758739, IEEE Transactions on Industrial Electronics

function of K. Due to coupling in the TL network, the crosstalk noise frequency for the path between S_1 and L_1 and S_2 and L_2 are found to be 20 MHz and 10 MHz, respectively. It is evident from Fig. 16 that, the SINR increases as K is decreased because with progressively lower values of K, Z_{in1} and Z_{in2} in (26) and (27) approaches (28), thereby further reducing the impact of crosstalk noise.

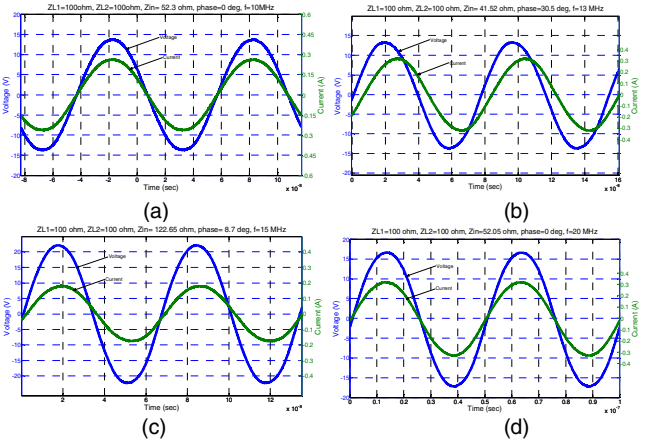

Fig. 15. Experimental input voltage and input current for the SIMO topology at (a) 10 MHz, (b) 12 MHz, (c) 15 MHz, and (d) 20 MHz.

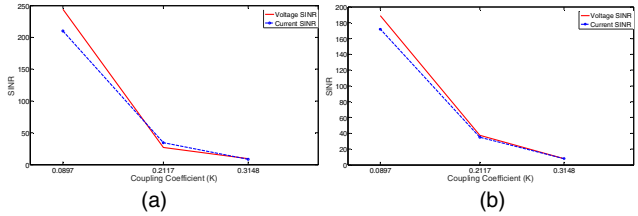

Fig. 16. Variations in experimental SINRs of the voltage and current as a function of K. At the input of (a) TL-1 and (b) TL-2 having fundamental component of 10 MHz with a 20 MHz noise frequency.

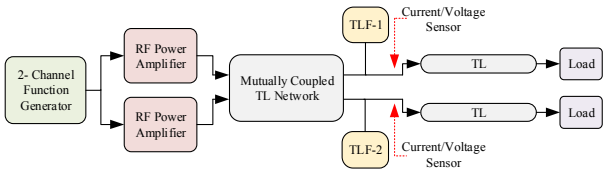

Fig. 17. Mitigation of crosstalk in Fig. 7 using tuned TL based band-stop filters TLF-1 and TLF-2.

To satisfy (28), we pursue an alternate approach by placing band-stop filters, tuned at band-stop frequencies of 20 MHz and 10 MHz, in the paths between S_1 and L_1 an S_2 and L_2, respectively. Fig. 17 captures the flow of the experimental setup that is used to investigate the impacts of adding TL filters (TLF-1 and TLF-2) on SINR of current and voltage signals. For simplicity, the band-stop filter was designed using TL, as outlined in Appendix B. Fig. 18 compares the variation in SINR for K= 0.3148 with and without the use of band-stop filters. The results show a significant improvement in SINR for both the current and voltage waveforms at the input of TL-1 and TL-2.

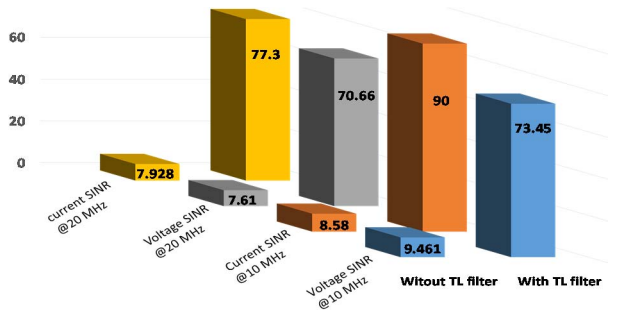

Fig. 18. Comparison of experimentally-obtained SINRs with and without the band-stop filter for the MIMO topologies in Figs. 7 and 8.

Finally, we explore the impact of transmitting a periodic signal synthesized using a plurality of frequencies in the presence of TL effect. It is demonstrated that, if the selection of these frequency components of the time-domain signal are carefully selected then, the impact of TL effect is mitigated. Even though we demonstrate the outcome of the analysis for the SISO topology shown in Fig. 5, the concept extends to SIMO and MIMO cases as well. To ensure the integrity of the transmitted power signal in a SISO topology, the frequency of wave transmission must satisfy condition (21), which, as outlined in Section II, yields a set of discrete frequencies that exhibit a periodic property. So, instead of transmitting a signal comprising only one of these discrete frequency components, if a signal comprising a plurality of these discrete-frequency components is transmitted, then one can expect no signal-integrity issue in the power signal as well. Fig. 19 shows the outcome of such a prediction using a bipolar square-wave signal (of 0.5 duty ratio) that has a fundamental frequency of 10 MHz and superharmonics that are multiples of 10 MHz yielding $V(t) = \sum \frac{4V_p}{(2N-1)\pi} \sin(2N-1)\omega t$, where V_p represents the peak voltage of the square wave and N represents consecutive positive integer with an initial value of 1. It is noted that, the 10 MHz frequency component and the superharmonics are chosen from a set that satisfy are chosen from a set that satisfy (21). In Fig. 19, RMS voltage of each harmonic component at the source is plotted for two cases: one when the signal is sent through a TL network of length 12.75 m and the other when no TL network is used. It is apparent from Fig. 19 that, and as expected, for the case under consideration, the magnitudes of the harmonic components for these two cases do not show any significant difference. However, when the two scenario-centric analyses were repeated for 8 MHz and 15 MHz base frequency of the bipolar square wave, a tangible difference was observed in the amplitudes of the base and superharmonic-frequency components. This is because both 8 MHz and 15 MHz base frequency and their superharmonic components do not satisfy the impedance criterion (21).

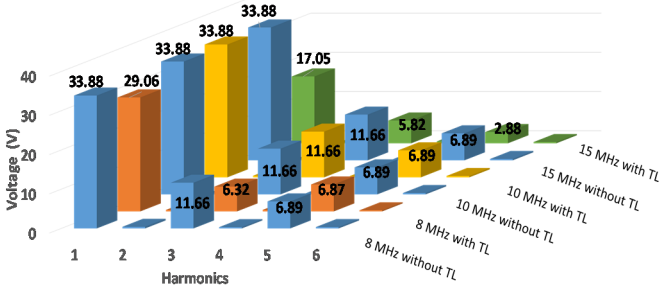

Fig. 19. Experimental result showing comparison of harmonic-voltage components when a square wave is transmitted in the absence or presence of TL effect.

V. Conclusions

The maturity of standalone high-frequency power electronics has opened the possibility for HFDPSs, which have the potential for yielding multi-pronged advantages including high power density, rapid power flow, reduced localized storage requirements, and high network control bandwidth. However, distribution of high-frequency power signals over a HFDPS (that may assume SISO, SIMO, and MIMO topologies) brings forth the increasing possibility of encountering TL effects that can yield poor signal quality. At the PCB level, such TL effects have been addressed by using active-compensation techniques or by adjusting the physical length of the TL.

0278-0046 (c) 2017 IEEE. Personal use is permitted, but republication/redistribution requires IEEE permission. See http://www.ieee.org/publications_standards/publications/rights/index.html for more information.

This article has been accepted for publication in a future issue of this journal, but has not been fully edited. Content may change prior to final publication. Citation information: DOI 10.1109/TIE.2017.2758739, IEEE Transactions on Industrial Electronics

In contrast, in this paper, using generalized input-impedance modelling of SISO/SIMO/MIMO HFDPS, we have explored frequency as the modulation parameter for addressing the TL effects. The applicability of the outlined analysis is not limited to fixed type and magnitude of the impedances. To determine frequency sets that ensure signal integrity in presence of TL effects, a generalized input impedance modeling for n mutually coupled TLs is presented. Next, the generalized input impedance expression is simplified for a 2×2 HFDPS as shown in Appendix A. Using this input impedance expression, frequency sets that ensure signal integrity are calculated. With regard to the overall analysis, we observed that the procedure for determining the frequency set that ensures impedance criterion for SISO and SIMO topologies remain essentially the same, while for the MIMO topology, an additional criterion that requires mitigating the crosstalk or high SINR needs to be addressed. Two mechanisms for mitigation of the crosstalk noise are explored: one, that is based on reducing the coupling strength among the transmission channels while the other is based on using band-stop filters to mitigate the crosstalk noise. Finally, we illustrate a bipolar time-domain square-wave signal synthesized using a discrete set of frequencies that individually satisfy the impedance-matching condition for a SISO topology also mitigates the TL effect.

APPENDIX A

For a 2×2 HFDPS, where two sources S_1 and S_2 feeds two loads L_1 and L_2 via two spatiotemporal coupled TLs of length l_1 and l_2 represented by TL network as shown in Fig. A1, using (17) and (18), voltages and currents at any point z on the TL network are given by the following steps:

$$V = [v_1\ v_2]^T = [p_{11}\sigma_1 + p_{12}\sigma_2 \quad p_{21}\sigma_1 + p_{22}\sigma_2]^T \quad \text{(A1)}$$

$$I = [i_1\ i_2]^T = \begin{bmatrix} \frac{\sqrt{\beta_1}(Lp_{11}-p_{21}L_m)\sigma_3+\sqrt{\beta_2}(Lp_{12}-p_{22}L_m)\sigma_4}{(L^2-L_m^2)\omega_1} \\ \frac{\sqrt{\beta_1}(Lp_{21}-p_{11}L_m)\sigma_3+\sqrt{\beta_2}(Lp_{22}-p_{12}L_m)\sigma_4}{(L^2-L_m^2)\omega_1} \end{bmatrix} \quad \text{(A2)}$$

where

$\sigma_1, \sigma_3 = U_1^{+}e^{-j\sqrt{\beta_1}z} \pm U_1^{-}e^{+j\sqrt{\beta_1}z}$

$\sigma_2, \sigma_4 = U_2^{+}e^{-j\sqrt{\beta_2}z} \pm U_2^{-}e^{+j\sqrt{\beta_2}z}.$

Symbols $\sqrt{\beta_1}$ and $\sqrt{\beta_2}$ represent propagation constant of individual TL(s) in a coupled TL network. The description of notations $\beta_1, \beta_2, p_{11}, p_{12}, p_{21}, p_{22}$ are given below:

$$\beta_{1,}\beta_2 = \frac{1}{2}(LC\omega_1^2 - 2C_mL_m\omega_1\omega_2 + CL\omega_2^2 \pm \sqrt{(LC\omega_1^2 - CL\omega_2^2)^2 + 4\omega_1\omega_2(CL_m\omega_1 - LC_m\omega_2)(-LC_m\omega_1 + CL_m\omega_2)}$$

$$p_{11} = -p_{21} - \omega_1(CL_m\omega_1 - LC_m\omega_2)/N$$

$$p_{12}, p_{22} = -\frac{-CL\omega_1^2+CL\omega_2^2 \pm N}{2N}$$

where

$$N = \sqrt{C^2L^2\omega_1^4 - 4CLC_mL_m\omega_1^3\omega_2 - 2C^2L^2\omega_1^2\omega_2^2 + 4L^2C_m^2\omega_1^2\omega_2^2 + 4C^2L_m^2\omega_1^2\omega_2^2 - 4CLC_mL_m\omega_1\omega_2^3 + C^2L^2\omega_2^4}.$$

To calculate the input impedance as seen by the sources S_1 and S_2, following steps were carried out:

(i) Using initial conditions on (17) and (18) at $z = 0$ (input of TL-2 and Tl-3 respectively), constants $U_1^{+}, U_1^{-}, U_2^{+}, U_2^{-}$ can be calculated in terms of $i_{L1}, i_{L2}, Z_{L1}, Z_{L2}$;

(ii) Using boundary conditions at the input, Z_{in1} (Z_{in2}) - input impedances seen by $S_1(S_2)$ when S_2 (S_1) is off are calculated:

$$Z_{in1} = \big(2\omega_1(2j\cos[l\sqrt{\beta_1}]\cos[l\sqrt{\beta_2}](L^2 - L_m^2)Z_{L1}Z_{L2}\sqrt{\beta_1}\sqrt{\beta_2} + (L - L_m)(L + L_m)(Z_{L1} + Z_{L2})(-\cos[l\sqrt{\beta_1}]\sin[l\sqrt{\beta_2}](L + L_m)\sqrt{\beta_1} + \cos[l\sqrt{\beta_2}]\sin[l\sqrt{\beta_1}](-L + L_m)\sqrt{\beta_2})\omega_1 - 2j\sin[l\sqrt{\beta_1}]\sin[l\sqrt{\beta_2}](L^2 - L_m^2)^2\omega_1^2)\big)/ \big((\omega_1(-jZ_{L2}(\sin[l\sqrt{\beta_1}]\sin[l\sqrt{\beta_2}](L + L_m)^2\beta_1 - 2(1 + \cos[l\sqrt{\beta_1}]\cos[l\sqrt{\beta_2}])(L^2 - L_m^2)\sqrt{\beta_1}\sqrt{\beta_2} + \mathrm{si}[l\sqrt{\beta_1}]\sin[l\sqrt{\beta_2}](L - L_m)^2\beta_2) + 2(L^2 - L_m^2)(-\cos[l\sqrt{\beta_1}]\sin[l\sqrt{\beta_2}](L + L_m)\sqrt{\beta_1} + \cos[l\sqrt{\beta_2}]\sin[l\sqrt{\beta_1}](-L + L_m)\sqrt{\beta_2})\omega_1) + jZ_{L1}(-2jZ_{L2}(-\cos[l\sqrt{\beta_2}]\sin[l\sqrt{\beta_1}](L + L_m)\beta_1\sqrt{\beta_2} - \cos[l\sqrt{\beta_1}]\sin[l\sqrt{\beta_2}](L - L_m)\sqrt{\beta_1}\beta_2) - (\sin[l\sqrt{\beta_1}]\sin[l\sqrt{\beta_2}](L + L_m)^2\beta_1 - 2(-1 + \cos[l\sqrt{\beta_1}]\cos[l\sqrt{\beta_2}])(L^2 - L_m^2)\sqrt{\beta_1}\sqrt{\beta_2} + \sin[l\sqrt{\beta_1}]\sin[l\sqrt{\beta_2}](L - L_m)^2\beta_2)\omega_1)\big) \quad \text{(A3)}$$

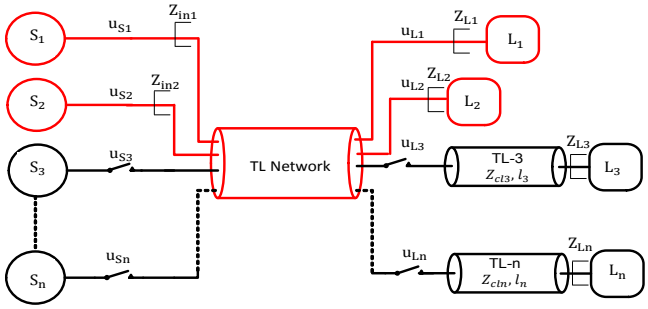

Fig. A1. A MIMO topology showing activation of sources and loads.

$$Z_{in2} = (2(L^2 - L_m^2)\omega_2(-2j\cos[l\sqrt{\beta_1}]\cos[l\sqrt{\beta_2}]Z_{L1}Z_{L2}\sqrt{\beta_1}\sqrt{\beta_2} + (Z_{L1} + Z_{L2})(\cos[l\sqrt{\beta_1}]\sin[l\sqrt{\beta_2}](L + L_m)\sqrt{\beta_1} + \cos[l\sqrt{\beta_2}]\sin[l\sqrt{\beta_1}](L - L_m)\sqrt{\beta_2})\omega_2 + 2j\sin[l\sqrt{\beta_1}]\sin[l\sqrt{\beta_2}](L^2 - L_m^2)\omega_2^2))/ (\omega_2(2j(L^2 - L_m^2)Z_{L2}\sqrt{\beta_1}\sqrt{\beta_2} + 2\cos[l\sqrt{\beta_2}](L^2 - L_m^2)\sqrt{\beta_2}(-j\cos[l\sqrt{\beta_1}]Z_{L2}\sqrt{\beta_1} + \sin[l\sqrt{\beta_1}](L - L_m)\omega_2) + \sin[l\sqrt{\beta_2}](j\sin[l\sqrt{\beta_1}]Z_{L2}((L + L_m)^2\beta_1 + (L - L_m)^2\beta_2) + 2\cos[l\sqrt{\beta_1}](L - L_m)(L + L_m)^2\sqrt{\beta_1}\omega_2)) + Z_{L1}(-2j(L^2 - L_m^2)\sqrt{\beta_1}\sqrt{\beta_2}\omega_2 + 2\cos[l\sqrt{\beta_2}](L + L_m)\sqrt{\beta_1}\sqrt{\beta_2}(\sin[l\sqrt{\beta_1}]Z_{L2}\sqrt{\beta_1} - j\cos[l\sqrt{\beta_1}](L - L_m)\omega_2) + \sin[l\sqrt{\beta_2}](2\cos[l\sqrt{\beta_1}](L - L_m)Z_{L2}\sqrt{\beta_1}\beta_2 + j\sin[l\sqrt{\beta_1}]((L + L_m)^2\beta_1 + (L - L_m)^2\beta_2)\omega_2))) \quad \text{(A4)}$$

APPENDIX B

Low-, high-, and band-pass and band-stop filters can be designed using a co-axial TL. A TL having length $\lambda/4$ for a frequency behaves as a quarter-wave transformer yielding

$$Z_{in} = Z_{cl}\frac{Z_L + jZ_{cl}\tan(\beta l)}{Z_{cl} + jZ_L\tan(\beta l)}. \quad \text{(B1)}$$

Using (B1), when TL of electric length $\lambda/4$ is terminated by an open ($Z_L = \infty$) or short circuit ($Z_L = 0$), the TL input impedance Z_{in} transforms to a short or an open circuit, respectively, for that frequency. In Fig. 8, two TL(s) TLF-1 and TLF-2 are connected to a mutually-coupled SISO networks in series with the source as a quarter-wave transformer for 10-MHz signal. The lengths of the TL(s) are

0278-0046 (c) 2017 IEEE. Personal use is permitted, but republication/redistribution requires IEEE permission. See http://www.ieee.org/publications_standards/publications/rights/index.html for more information.

This article has been accepted for publication in a future issue of this journal, but has not been fully edited. Content may change prior to final publication. Citation information: DOI 10.1109/TIE.2017.2758739, IEEE Transactions on Industrial Electronics

chosen such that TLF-1 and TLF-2 have an electric length of $\lambda/4$ for 10 MHz and $\lambda/2$ for 20 MHz. TLF-1 is terminated by an open circuit; hence, it acts as a band-pass filter for 10 MHz and band-stop filter for 20 MHz. TLF-2 is terminated by a short circuit; it acts as band-stop and band-pass filters for 10-MHz and 20-MHz power signals. Using TL configuration evident in Fig. 8, it is ensured that L_1 and L_2 are feed power at 10 and 20 MHz, respectively. A TL filter also exhibits periodic property like a normal TL; hence, TLF-1 and TLF-2 act as band-pass and band-stop filters for frequencies in multiple of $2n$-1 and $2n$, (where n is an integer), respectively. The bandwidth and attenuation of these TL filters depend on the length of TL being used to design these filters. Fig. B1 displays an experimental comparison between two notch filters of different TL lengths. Dotted and solid curves in Fig. B1 show band-stop filter characteristics for the TL having an electrical length of $\lambda/4$ and $3\lambda/4$, respectively, for a wave-transmission frequency of 10 MHz. It is observed from Fig. B1 that, TL filter of longer length ($3\lambda/4$) has shorter bandwidth (3.65 MHz) and a sharper roll off; whereas, TL filter of shorter length ($\lambda/4$) has a wider bandwidth (6.85 MHz) with a comparatively gentle roll-off.

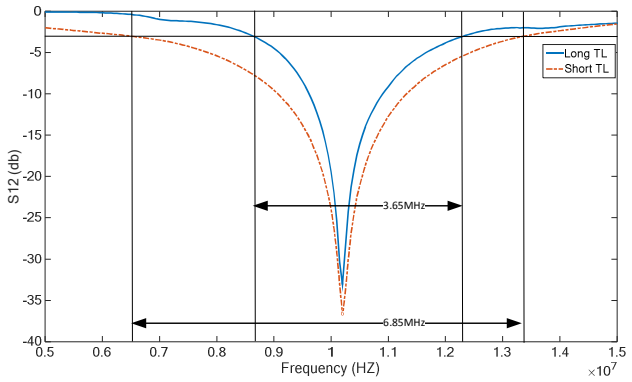

Fig. B1. Experimental result of variation in S_{12} parameter with frequency for TL band-stop filters with different TL lengths.

REFERENCES

[1] P. Jain, M. Pahlevaninezhad, S. Pan, and J. Drobnik, "A review of high-frequency power distribution systems: for space, telecommunication, and computer applications," IEEE Transactions on Power Electronics., vol. 29, no. 8, pp. 3852–3863, Aug. 2014.

[2] J. Liu, J. Zeng, R. Hu and K. W. E. Cheng, "A valley-fill driver with current balancing for parallel LED strings used for high-frequency ac power distribution of vehicle," in IEEE Transactions on Transportation Electrification, vol. 3, no. 1, pp. 180-190, March 2017.

[3] N. Aeronautics, "NASA Contractor Report 178208," 1987.

[4] I.G Hansen, "Status of 20 kHz space station power distribution technology." NASA, Washington, DC, USA, TM 100781, Jan 1988.

[5] Y. J. Kim, D. Ha, W. J. Chappell and P. P. Irazoqui, "Selective wireless power transfer for smart power distribution in a miniature-sized multiple-receiver system," in IEEE Transactions on Industrial Electronics, vol. 63, no. 3, pp. 1853-1862, March 2016.

[6] A. Musolino, M. Raugi, R. Rizzo and M. Tucci, "Optimal design of EMALS based on a double-sided tubular linear induction motor," in IEEE Trans. on Plasma Science, vol. 43, no. 5, pp. 1326-1331, 2015.

[7] Z. Ye, P. K. Jain and P. C. Sen, "Circulating current minimization in high-frequency ac power distribution architecture with multiple inverter modules operated in parallel," IEEE Transactions on Industrial Electronics, vol. 54, no. 5, pp. 2673-2687, Oct. 2007.

[8] Lourdes, S., S. Y. Ng, and P. C. K. Luk. "An alternative power grid-High frequency ac power distribution platforms," IEEE Power Electronics and Motion Control Conference, 2009.

[9] W. A. Fernando and D. D. C. Lu, "Feasibility study of existing 50/60Hz electrical appliances for HFAC power distribution systems," 2016 IEEE INTELEC, Austin, TX, pp. 1-8, 2016.

[10] J. Liu, K. W. E. Cheng and J. Zeng, "A unified phase-shift modulation for optimized synchronization of parallel resonant inverters in high frequency power system," IEEE Transactions on Industrial Electronics, vol. 61, no. 7, pp. 3232-3247, July 2014.

[11] PT. Sivasubramanian, S.K. Mazumder, H. Soni, A. Gupta and N. Kumar, " A dc/dc modular current-source differential-mode inverter," IEEE Journal of Emerging and Selected Topics in Power Electronics, vol. 4, Issue: 2, pp. 489 - 503, 2016.

[12] Wennan Guo and P. K. Jain, "A power-factor-corrected ac-ac inverter topology using a unified controller for high-frequency power distribution architecture," IEEE Transactions on Industrial Electronics, vol. 51, no. 4, pp. 874-883, Aug. 2004.

[13] A. Deutsch, G. V. Kopcsay, P. Restle, G. Katopis, W. D. Becker, H. Smith, P. W. Coteus, C. W. Surovic, B. J. Rubin, R. P. Dunne, T. Gallo, K. A. Jenkins, L. M. Terman, R. H. Dennard, G. A. Sai-Halasz, and D. R. Knebel, "When are transmission-line effects important for on-chip interconnections," Electronic Components and Technology Conference, pp. 704–712, 1997.

[14] V. Dzhankhotov, J. Pyrhonen, P. Silventoinen, M. Kuisma and T. A. Minav, "A new passive hybrid air-core foil filter for modern power drives," IEEE Transactions on Industrial Electronics, vol. 58, no. 5, pp. 1757-1762, 2011.

[15] K. K. F. Yuen and H. S. H. Chung, "A low-loss "RL-plus-C" filter for overvoltage suppression in inverter-fed drive system with long motor cable," IEEE Trans. on Power Elec., vol. 30, no. 4, pp. 2167-2181, 2015.

[16] Y. Jiang, W. Wu, Y. He, H. S. H. Chung and F. Blaabjerg, "New passive filter design method for overvoltage suppression and bearing currents mitigation in a long cable based PWM inverter-fed motor drive system," in IEEE Trans. on Power Elec., vol. 32, no. 10, pp. 7882-7893, 2017.

[17] X. Chen, D. Xu, F. Liu and J. Zhang, "A novel inverter-output passive filter for reducing both differential- and common-mode dv/dt at the motor terminals in PWM drive systems," IEEE Transactions on Industrial Electronics, vol. 54, no. 1, pp. 419-426, Feb. 2007.

[18] M. J. Melfi, "Low-voltage PWM inverter-fed motor insulation issues," in IEEE Trans. on Industry App., vol. 42, no. 1, pp. 128-133, 2006.

[19] G. Kan, S. Huang and X. Zou, "Active damping of output LCL filter in PWM inverter-fed drive system with long motor cable," International Conference on Electrical Machines and Systems, 2016, pp. 1-4.

[20] A. F. Moreira, P. M. Santos, T. A. Lipo and G. Venkataramanan, "Filter networks for long cable drives and their influence on motor voltage distribution and common-mode currents," IEEE Transactions on Industrial Electronics, vol. 52, no. 2, pp. 515-522, April 2005.

[21] K. Hatua, A. K. Jain, D. Banerjee and V. T. Ranganathan, "Active damping of output LC filter resonance for vector-controlled VSI-fed ac motor drives," in IEEE Transactions on Industrial Electronics, vol. 59, no. 1, pp. 334-342, Jan. 2012.

[22] M. A. Mannah, N. Ginot and C. Batard, "Effect of the power cable on data transmission over a pulse-width-modulated network," IEEE Trans. on Industrial Electronics, vol. 61, no. 8, pp. 4238-4245, 2014.

[23] P. K. Sood and T. A. Lipo, "Power conversion distribution system using a high-frequency ac link," IEEE Transactions on Industrial Applications, vol. 24, no. 2, pp. 288–300, 1988.

[24] T. Mishima, S. Sakamoto and C. Ide, "ZVS phase-shift PWM-controlled single-stage boost full-bridge ac-ac converter for high-frequency induction heating applications," IEEE Transactions on Industrial Electronics, vol. 64, no. 3, pp. 2054-2061, March 2017.

[25] S. Jain and V. Sonti, "A highly efficient and reliable inverter configuration based cascaded multilevel inverter for PV systems," IEEE Transactions on Industrial Electronics, vol. 64, no. 4, pp. 2865-2875, April 2017.

[26] S. S. Lee and Y. E. Heng, "Improved single-phase split-source inverter with hybrid quasi-sinusoidal and constant PWM," IEEE Transactions on Industrial Electronics, vol. 64, no. 3, pp. 2024-2031, March 2017.

[27] A. Gupta, N. Kumar and S.K. Mazumder, "Frequency-dependent criterion for mitigation of transmission line effects in high frequency distributed power systems," IEEE Energy Conversion Congress and Exposition, pp. 4624 - 4631, 2015.

[28] C. Li and K. Xiaole," Effects of ground vias on high-speed signal transmission in high-speed PCB design," IEEE Electronic Packaging Technology & High Density Packaging (ICEPT-HDP), pp 88-91, 2010.

[29] A. Deutsch, G.V. Kopcsay , V.A. Ranieri, J.K. Cataldo, E.A. Galligan, W.S. Graham, R.P. McGouey, S.L. Nunes, J.R. Paraszczak, J.J. Ritsko, R.J. Serino, D.Y. Shih, and J. S. Wilczynski," High-speed signal propagation on lossy transmission lines", IBM Journal of Research & Development, vol. 34, Issue: 4, pp 601 - 615, 1990.

[30] I. Takahashi and G. J. Su, "A 500 Hz power system-power converter and transmission lines," in Conference Record of the IEEE Industry Applications Society Annual Meeting, 1989, pp. 988–995.

[31] T. Nakamura , G. J. Su and I. Takahashi, "A 500 Hz power system - microprocessor control of the power converter," Record of the 1988 KANSAI-section Joint Conv. of I.E.E., Japan, 1988

[32] J. M. Correa, S. Chakraborty, M. G. Simoes, and F. A. Farret, "A single phase high frequency ac microgrid with an unified power quality

0278-0046 (c) 2017 IEEE. Personal use is permitted, but republication/redistribution requires IEEE permission. See http://www.ieee.org/publications_standards/publications/rights/index.html for more information.

This article has been accepted for publication in a future issue of this journal, but has not been fully edited. Content may change prior to final publication. Citation information: DOI 10.1109/TIE.2017.2758739, IEEE Transactions on Industrial Electronics

conditioner," in 38th IAS Annual Meeting on Conference Record of the Industry Applications Conference, 2003., 2003, vol. 2, pp. 956–962.
[33] H. Ohguchi, M. H. Ohsato, T. Shimizu, G. Kimura, and H. Takagi, "A high-frequency electronic ballast for HID lamps based on a λ/4-long distributed constant line," IEEE Transactions on Power Electronics, vol. 13, no. 6, pp. 1023–1029, 1998.
[34] S. Sander, "Buck and boost converters with transmission lines," in IEEE Trans. on Power Electronics, vol. 27, no. 9, pp. 4013-4020, Sept. 2012.
[35] T. Kawahara, T. Shimizu, M. Shioya, and G. Kimura, "High frequency power transmission by lumped constant circuit replaced distributed constant line," in 15th Annual Conference of IEEE Industrial Electronics Society, 1989, pp. 77–81.
[36] S. Suzuki and T. Shimizu, "A high-frequency current-output-type inverter aimed for wireless power transmission system," IEEE Energy Conversion Congress and Exposition, 2015, pp. 5732-5740.
[37] S. Sander and A. Karvonen, "Semiconductor component reduction in AC/DC converters with transmission lines," European Conference on Power Electronics and Applications, pp. 1-10, 2013.
[38] D. M. Pozar, Microwave engineering, 4th Edition, in John Wiley and Sons Inc., Nov 2011, p. 728.
[39] M. Zahn, Electromagnetic field theory: a problem solving approach, Malabar, FL: Krieger Publishing Company, 2003.

Ankit Gupta (S'11) received his B.E. degree in Electrical Engineering from Delhi College of Engineering (DCE), Delhi, India in 2011. From 2011-2013, he worked as an engineer at the super critical Turbo-Generator manufacturing facility of Bharat Heavy Electrical Ltd (BHEL), HEEP, Haridwar unit. In 2013, Ankit joined the Laboratory of Energy and Switching Electronics System (LESES) at the University of Illinois, Chicago, USA, and is currently working on his Ph.D. degree. He is an active member of IEEE MGA comity and in 2015 served as the IEEE Region 4 student representative. His research interests include but not limited to GaN based high density power converters, high frequency power transmission, microgrids and grid integration of renewable energy. He also serves as a reviewer for the IEEE Transaction on Power Electronics and IEEE transaction on Industrial Electronics.

Nikhil Kumar (S'15) received the B.E. degree in Electrical Engineering from Delhi College of Engineering, Delhi, India in 2011. He also worked as executive engineer at Larsen & Toubro, Mumbai, India from 2011-13. He received his M.S. degree in Electrical and Computer Engineering from University of Illinois at Chicago, USA in 2015. His MS Thesis project at UIC was on developing frequency-dependent criterion to mitigate effects of transmission line terminated with linear loads. In 2015, Nikhil joined Laboratory of Energy and Switching Electronics Systems (LESES) at UIC and is currently working on his Ph.D. degree. His research area includes but are not limited to high frequency link converters, formulation of network control, dc/dc converters and GaN based switching power converters.

Sudip K. Mazumder (S'97–M'01–SM'03-F'16) received his Ph.D. degree from Virginia Tech in 2001 and M.S. degree from Rensselaer Polytechnic Institute in 1993. He is a Professor at the University of Illinois, Chicago (UIC) and is the President of NextWatt LLC. He has over 25 years of professional experience and has held R&D and design positions in leading industrial organizations and has served as a Technical Consultant for several industries.

He has published over 200 refereed papers, delivered over 80 invited presentations, and received and carried out about 50 sponsored research since joining UIC. He is the recipient of UIC's Inventor of the Year Award (2014), University of Illinois' University Scholar Award (2013), ONR Young Investigator Award (2005), NSF CAREER Award (2003), and IEEE PELS Transaction Paper Award (2002). He has served on several prestigious NSF panels.

In 2016, he was elevated to the rank of an IEEE Fellow and he was elected to serve as a Distinguished Lecturer for IEEE PELS beginning in 2016. He has served/ is serving as the Guest Editor-in-Chief/Editor for IEEE PELS/IES Transactions between 2013-2017, as the first Editor-in-Chief for Advances in Power Electronics (2006-2009), and as an Editorial Board Member for IEEE IES/PELS/TII/JESTPE/TAES Transactions. Currently, he serves as the Chair for IEEE PELS TC on Sustainable Energy Systems.

0278-0046 (c) 2017 IEEE. Personal use is permitted, but republication/redistribution requires IEEE permission. See http://www.ieee.org/publications_standards/publications/rights/index.html for more information.

Available online at www.sciencedirect.com

ScienceDirect

Materials Today: Proceedings 4 (2017) 7208–7218

materialstoday: PROCEEDINGS

www.materialstoday.com/proceedings

ICAAMM-2016

Hybrid Abrasive Flow Machining for Nano Finishing - A Review

Parvesh Ali[a], Sachin Dhull[b], R.S.Walia[c], Q.Murtaza[d], Mohit Tyagi[e*]

[a,b]*Research scholar,Delhi Technological University, Delhi-110042, India*
[c,d,e]*Faculty, Delhi Technological University, Delhi-110042, India*

Abstract

Abrasive flow machining (AFM) is a fine finishing process for difficult to reach internal surfaces through the action of extrusion pressure, combined with the abrading action of the polymer media laden with abrasive particles. To improve the material removal and surface finishing, various variants of AFM process have been developed. The present paper describes various hybrid AFM processes and compares their working principle and process parameters. In addition, the different polymers used for finishing have been described in an elaborate manner. After literature review, an effort is made to develop the optimum hybrid combination of various variants of AFM process incorporating a suitable polymer media so as to achieve high material removal and fine surface finish.

© 2017 Elsevier Ltd. All rights reserved.
Selection and Peer-review under responsibility of the Committee Members of International Conference on Advancements in Aeromechanical Materials for Manufacturing (ICAAMM-2016).

Keywords: AFM; polymer; process parameters

1. Introduction

Abrasive Flow Machining is a non-traditional process used for micro finishing of difficult to reach surfaces like intricate shapes [1]. With advent of super alloys, ceramics, polymers etc., the requirement to machine complex geometries with high accuracy needed for development of advanced finishing processes such as abrasive flow machining (AFM), magnetic abrasive finishing (MAF), magnetic float polishing (MFP), magneto-rheological finishing (MRF) etc. The above mentioned variants improve the efficiency of conventional AFM process. Finishing process is obtained by abrasion, by the contact of abrasives and workpiece. It is a better process for finishing in comparison to the traditional process. Traditional process removes the material in form of chips of larger size but

*Corresponding author
E-mail: mohitmied@gmail.com

2214-7853 © 2017 Elsevier Ltd. All rights reserved.
Selection and Peer-review under responsibility of the Committee Members of International Conference on Advancements in Aeromechanical Materials for Manufacturing (ICAAMM-2016).

Abrasive Flow Machining removes material in form of micro chips. The media is a combination of polymer, gel and abrasives, which passes through the restricted path and removes the material.

Nomenclature

PE	polyethylene
PS	polystyrene
PMMA	polymethylmethacrylate
SBR	styrene butadiene rubber
AFM	abrasive flow machining
CFG	centrifugal force generated
UAAFM	ultrasonic assisted abrasive flow machining
EC^2A^2FM	electrochemical and centrifugal assisted abrasive flow machining
FMAB	flexible magnetic brush
MAF	magnetic abrasive finishing
MAP	magnetic abrasive polishing
MFP	magnetic float polishing
MRF	magnetic rheological finishing

2. Role of polymer media

The media plays a crucial role in abrasive flow finishing process. The polymer media should be selected so as to achieve better machining, it should have the desired flow ability, it should properly hold the abrasive particles and its viscosity must be retained during the finishing operation i.e. is should not fail at higher temperatures. The various mechanical properties and different type of polymers used in AFF process are explained below.

2.1. Mechanical properties of polymer used in AFF

The different mechanical properties like elasticity, viscosity and viscoelasticity which are the basic requirement of any polymer used in AFF process are explained as under.

- *Continuous extension*
  The ratio of stress to strain is called modulus. In the low strain region, the stress and strain are directly proportional to each other, as shown in fig.1.

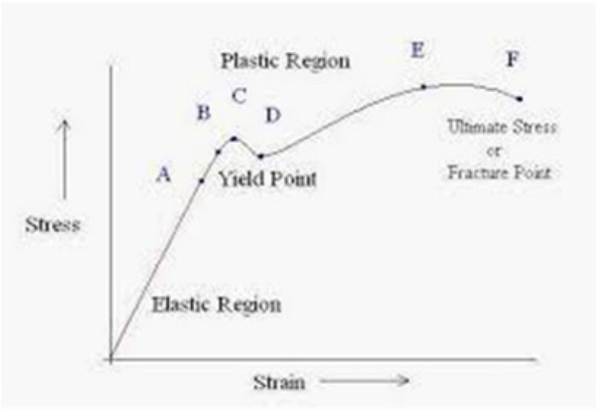

Fig.1. Stress vs strain diagram [2].

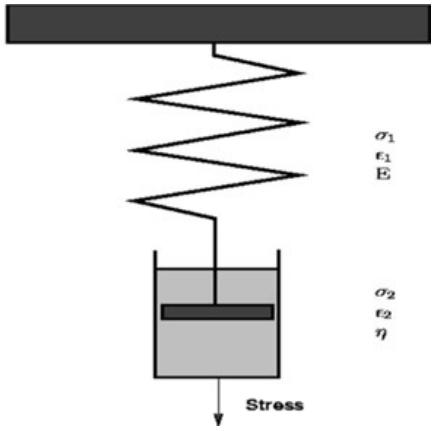

Fig.2. Maxwell model for viscoelasticity [2].

When the strain reaches a yield value, the curve becomes non-linear. (a) Soft and weak material such as unfilled silicon rubber -"soft" refers to the fact that initial slope is small, which means low value of modulus. "Weak" refers to low ultimate strength. (b) Hard and brittle (Polystyrene) -"Hard" refers to initial slope or modulus is large. "Brittle" refers to the fact that maximum extensibility is small.

- *Hookean elasticity*

$$\text{Young's modulus } G = \frac{s}{\gamma} \tag{1}$$

- *Rubber-like elasticity*

A good operational definition of rubber-like elasticity is high deformability with essentially complete recoverability. The equation of state is

$$f^* = \frac{f}{A^*} = \vartheta kT(\alpha - \alpha^{-2}) \tag{2}$$

where f^* is nominal stress, f is equilibrium force, A^* is undeformed cross section, ϑ is number density of network chains, k is Boltzmann constant, T is absolute temperature, $\alpha = L/L_i$ is relative length of sample [2]. The eq. (2) is similar to ideal gas law P = NkT/V, N is no. of gas molecules, V is volume, p is pressure.

- *Viscosity*

The viscosity n of a fluid may be defined by the eq. (3)

$$S = n\frac{d\gamma}{dt} = n\dot{\gamma} \tag{3}$$

where S is force per unit area, $\dot{\gamma}$ is rate of shear.

- *Viscoelasticity*

It is the combination of viscous characteristics with elastic characteristics to describe the viscoelasticity of polymeric materials. The combination of spring and dashpot in series is called the Maxwell model as shown in fig.2. It is used to describe the viscoelastic behavior of uncrossed-linked polymer.

The general differential equation (4) which describes the Maxwell model is

$$\dot{\gamma} = \frac{s}{n} + \left(\frac{1}{G}\right)\left(\frac{ds}{dt}\right) \tag{4}$$

2.2. Properties of various polymeric materials

The various properties of different polymeric materials used for making media for AFF process are listed below.

- *Polyethylene (PE)*

The crystallinity, melting point, tensile strength, stiffness, hardness, abrasion resistance, dissolution temperature in benzene and chemical resistance increases with increase in density of PE.

- *Polystyrene (PS)*

It is an amorphous polymer with high degree of branching. It has good chemical stability towards acids, alkalies, water. The most important weaknesses are its brittleness, low thermo stability, low resilience and flammability. The last property can be improved by introduction of halogen atoms in benzene ring [3].

- *Polymethylmethacrylate (PMMA)*

It is amorphous, has better thermal stability. The solubility and viscosity of this group of polymers depend on the alcoholic group. Polymethacrylates are superior to polyacrylates in chemical stability, thermal stability and stability to water. When heated, polyacrylates soften before the corresponding polymethacrylates.

- *Styrene butadiene rubber (SBR)*

It is a general purpose rubber. Its permeability, heat resistance, resistance to wear, and aging is superior to natural rubber. SBR requires more severe milling than natural rubber; however over milling causes a considerable decrease in tensile strength. Larger amounts of plasticizer and softener are required. At an increased vulcanization temperature, a decrease of young's modulus, relative elongation and even abrasion resistance has been observed [4].

3. Types of AFM

There are three types of Abrasive Flow Machining Process, One way AFM, Two way AFM, Orbital AFM.

3.1. One way AFM

One way AFM has a hydraulically actuated piston and a media chamber which has the capability to receive the media and pressurizes to pass the media through the internal passage of the workpiece in a single direction. The process of one way AFM is shown in fig.3. Fixture holds the workpiece and directs the media coming from the media cylinder to pass through the internal surface of workpiece. There is a media collector which collects the extruded media coming out from the workpiece. It has a advantage of finishing of larger workpiece, faster process cycle, no need of controlling the media temperature, simple tooling and part change over but it has also a disadvantage of poor process control and radius generation. One way AFM and Two way AFM both was developed by Extrudes Hone Corporation in 1960.

3.2. Two way AFM

Two way AFM consist two hydraulic cylinders and two media chamber. The media flows from upper cylinder to lower cylinder and lower cylinder to upper cylinder due to pressure difference. The motion of media from upper to lower and lower to upper comprises a cycle. The figure of two way AFM is as shown in fig.4. The piston of hydraulic cylinder pressurizes the media to flow between the two cylinders depending upon the pressure difference created between the cylinders. Work piece material is removed by abrasion caused by abrasion laden media flowing co-axially to the work surface. It has the advantage of better process control, can finish both internal and outer diameter and good control of radius generation.

3.3. Orbital AFM

In orbital AFM, low amplitude vibration is given to the workpiece. The vibration causes more number of abrasive particles to contact with the work surface and increases the surface finish. The tool has a layer of abrasive-laden elastic plastic medium having high viscosity and elastic in nature. The figure of Orbital AFM is as shown in fig.5.

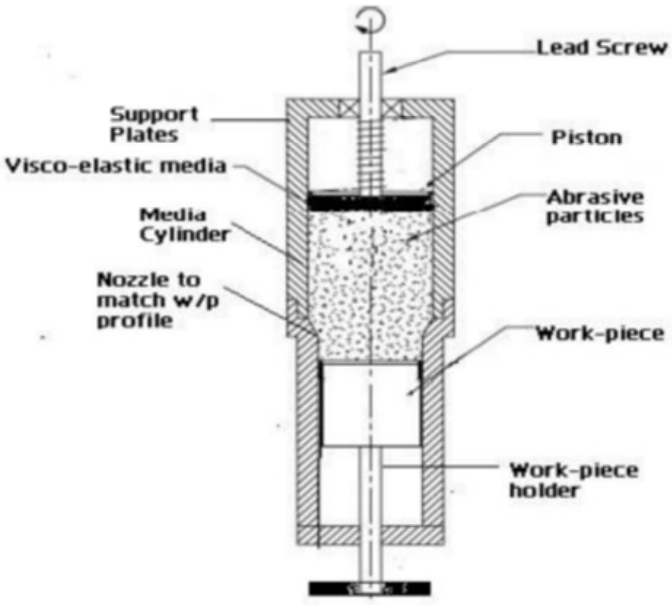

Fig.3. Shown operation of one way AFM [5]

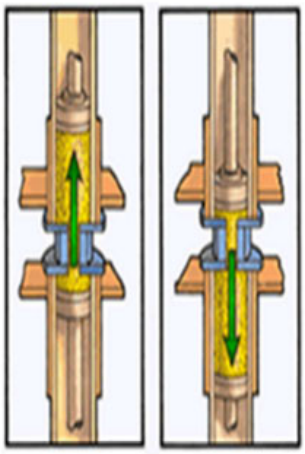

Fig.4. Shown operation of two way AFM [6]

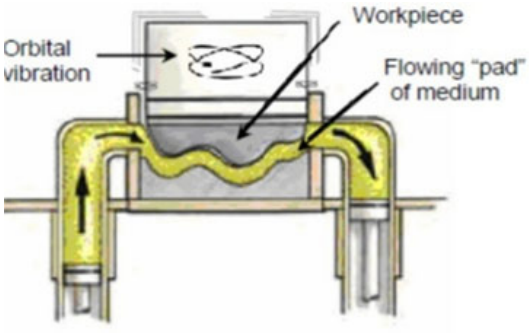

Fig.5. Shown operations of orbital AFM [7]

4. Various Hybrid Abrasive Flow Machining Processes

Now a day's, efforts are being made to make AFM process better by hybridizing it with other processes. Hybridization is important to get a better performance between many modern nontraditional processes. AFM has a limitation of low material removal, so Hybridization of AFM is required to get better material removal and surface finishing.

4.1. Magnetic force assisted AFM process

The magnetic Assisted AFM process was developed by Singh and Shan in 2002. The researchers used magnetic force to enhance the material removal and surface finishing. Singh and Shan [8] applied magnetic field around the full length of cylindrical workpiece in AFM and found that material removal and surface roughness is significantly affected by magnetic field. When the magnetic field is applied around the workpiece, less number of cycles is required for the higher material removal. In magnetic abrasive flow machining higher material removal and higher improvement in surface roughness are observed, when brass is used as workpiece material with high magnetic flux density and low flow rate of medium. In Magnetic abrasive flow machining the abrasive particle are used in magnetic nature so ferromagnetic particle are sintered with fine abrasive particles (CBN, Al_2O_3 or diamond, Sic), and these particles are called ferromagnetic abrasive particles. The magnetic field retains ferromagnetic abrasive particles in the machining gap and also acts as a binder. When magnetic field is applied around the work piece then normal component of magnetic force is responsible for abrasive penetration inside the work piece while rotation of the ferromagnetic abrasive brush intact to north-pole results in tangential force. At magnetic flux density of 0.4 tesla material removal is maximum and there is some variations up to 0.6 tesla after that the material removal decreases [9]. It has excellent capability to finish machining of inaccessible regions of a component. The process of Magnetic Assisted AFM is shown in fig.6 as given below. The magnitude of magnetic force on a small ferromagnetic particle of mass m in magnetic field at a distance x is given by eq. (5)

$$F_m(x)=\frac{m\aleph_m}{\mu_0}B(x) \tag{5}$$

where μ_0 is magnetic permeability of free space, $\aleph_m$ is magnetic susceptibility of MRP medium, B(x) is magnetic induction [10].

4.2. Centrifugal force assisted AFM

Walia et.al. [11] developed a setup for centrifugal force assisted abrasive flow machining to improve the surface finish and material removal with low viscosity media in 2006. In centrifugal force assisted AFM, different size of tiny rod were rotated at the centre of medium flow path and used a low viscosity medium to finish the surface.

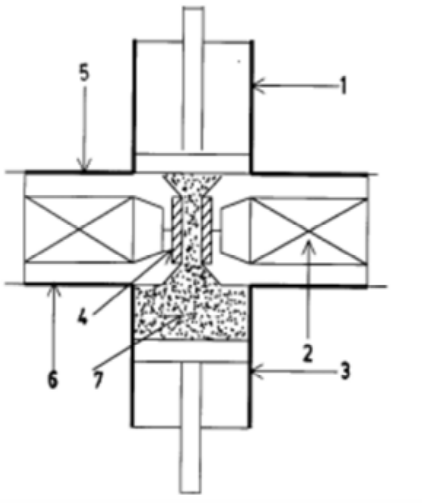

1. Upper media cylinder and flange; 2. DC electromagnet; 3. Lower media cylinder and flange; 4. Workpiece; 5. Upper fixture plate; 6. Lower fixture plate; 7. Magnetic Abrasive particles ;

Fig.6. Magnetic assisted AFM set up [8]

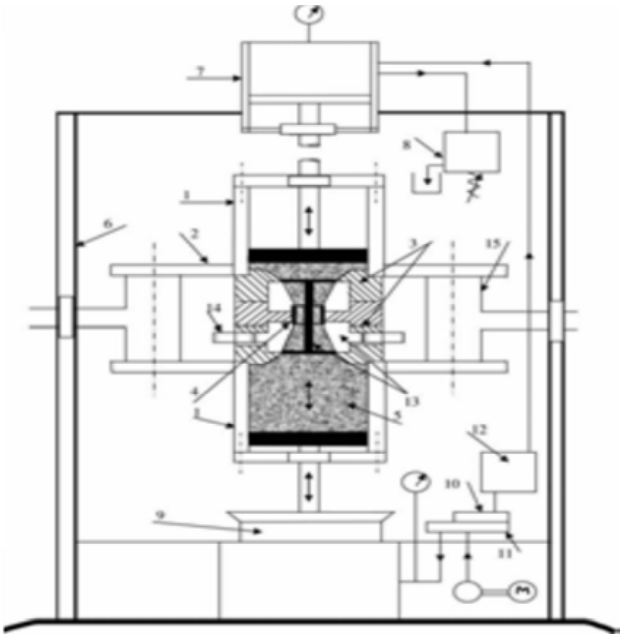

1. Cylinder containing media; 2. Flange; 3. Fixture; 4. Workpiece 5. Abrasive laden media; 6. Hydraulic Press; 7.Auxillary cylinder; 8. Modular relief valve; 9. Piston of hydraulic press; 10. Direction Control Valve; 11 and 12. Manifold blocks; 13. Rotating CFG rod Assembly; 14. Idle gear; 15. Eye bolt

Fig.7. Schematic illustration of the CFAAFM process setup [18]

The abrasive laden media is rotated by using centrifugal force generated rod (CFG) due to the action of centrifugal force and hence more number of abrasive particles will come into the contact of surface as shown in fig.7. In this process, centrifugal force acts on the abrasive particles normal to the axis of the work piece [11]. Material is removed by erosion process from the work piece due the interaction of the abrasives particle. The increase in the rate of material removal is due to an increasing number of active particles in the medium [12]. Surface area of abrasives in contact with inner work surface = $\pi[D^2 - (D - 2d)^2]/4 = \pi(Dd\text{-}d^2)$
Number of abrasive particles in contact with work surface can be computed as:

$$N_A = \frac{\text{Surface area of abrasives in contact with inner work surface}}{\text{Surface area of work passage}} = 4N\frac{Dd-d^2}{D^2} \quad (6)$$

Where‘d’ is abrasive diameter, ‘N’ is number of abrasive particles in full volume media.

4.3. Ultrasonic AFM

Ultrasonic Abrasive flow machining was developed by Sharma et al. [13]. Ultrasonic assisted abrasive flow machining (UAAFM) is a new hybrid process in which ultrasonic vibration is given to the workpiece in perpendicular to the media flow direction [13]. In this process, high frequency and low amplitude vibration is applied. The range of frequency ranges between 5 to 20 kHz and amplitude in the range of 10-50 μm. The vibration was given to the work piece with the help of a piezo actuator and special fixture. Ultrasonic vibration increases the relative velocity of abrasives with which they hit the work piece asperities [14]. Since the velocity of the work piece taken is much more than the velocity of the abrasive particles flowing with the media, there is a significant increase in active abrasive grain density. This arrangement helps in providing better cutting conditions and causes more depth of penetration. Hence, surface finish and material removal could be improved easily. In the UAAFM process, the work piece is in dynamic condition, which vibrates radially at a high frequency and is subjected to additional radial forces along with the conventional AFM process.

4.4. Drill-bit guided AFM

Drill bit guided AFM was developed in 2009 by Ravi Sankar et.al. [15]. A drill bit is placed in the medium flow path, so called drill bit guided abrasive flow finishing and improves the finish rate, material removal and surface texture as shown in figure 8.When the inner part of medium slug flows along the helical flute that creates random motion among the abrasives in the medium. Due to this reshuffling of abrasive particles occurs at outer region and more number of active grains interacts with the workpiece surface. The result shows that the abrasive traverse path is longer than the AFM abrasive traverse path in each cycle which causes higher finishing rate in DBG-AFF than the simple AFM. It is also found that material removal decreases with decrease in drill diameter. In conventional abrasive flow finishing machine circular fixture plate is used which restricts the flow of medium in a cylindrical region. In this abrasive particle follows the shortest contact length, due to which material removal is not good but in drill guided AFM process the fixture plate used is of twins slots that assist the aligning drill bit along the finishing zone. Due to intermixing of different flows the abrasive and work piece contact length is no longer a straight line, it becomes a curved line. It causes shearing of more number of peaks and improves material removal. The figure of drill bit guided AFM is as shown in fig.8.

4.5. Rotational AFM

Shankar et al. developed rotational AFM in 2010 [16]. Rotational abrasive flow finishing process is similar to CFAAFM, the only difference being that instead of the use of a rod to generate the centrifugal force; the work piece itself is rotated using a suitable setup as shown in fig.9. The rotation of the work piece along with the extrusion pressure on the medium increases the contact length between work surface and abrasives, which improves the material removal. It has four main components, named as machine structure, rotational set-up, tooling, hydraulic power pack and medium [16]. Rotational AFM can produce 44% better smoothness and 81.8% more material removal in comparison of AFF process. It can be used to produce micro cross hatch pattern on the finished surface that will improve lubricant holding capabilities [17].

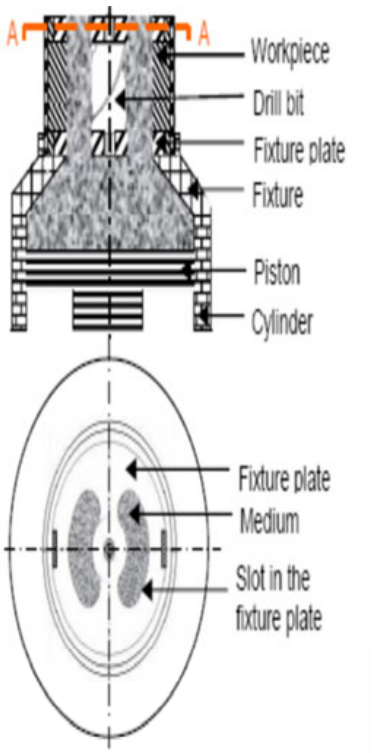

Fig.8. Sectional front view of tooling in finishing region in DBG-AFF process and top view of medium splitting through twin slotted [15]

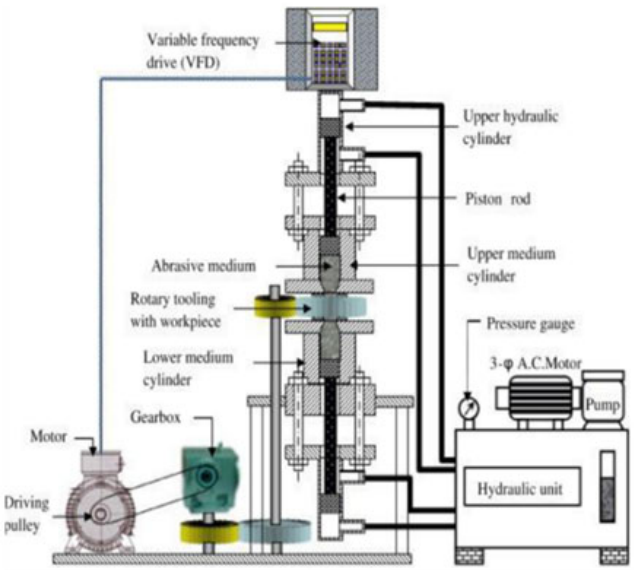

Fig.9. Rotational AFM set up

4.6. Electrochemical assisted AFM

Electro-chemical aid along with the AFM, as has been experienced by Dabrowski et al. [20 & 21] in 2011, for the fine finishing of flat surfaces and for cylindrical surface [19]. AFM with Electro- chemical machining process has been termed as Electrochemical Assisted Abrasive Flow Machining (ECAAFM) as shown in fig.11. The principle of electrochemical machining (ECM) involves dissolving an anodic workpiece in the form of atoms. ECM can be utilized as a micro scale or nano scale machining method. With an increasing need for micro scale parts, such as medical implants, micro scale batteries, and fuel cells, more and more attempts are being made to use ECM for micromachining. At higher operating voltage the surface becomes rough due to more material electrolytic dissolution resulting in the deeper scratches on surface at 10V, 87.43% improvement in surface roughness was observed for brass material [22]. The workpiece used with the initial surface roughness of 4.02 microns leading to final surface roughness 0.49 microns.
The volume of material removal follows Faraday's law and removal height of workpiece is given by the equation (7) [23]

$$h = \frac{a}{A\rho ZF}.I.t \tag{7}$$

where 'I' is current, 't' is time taken, ρ is density of electrolyte, 'Z' is atomic mass and 'F' is faraday's constant.

4.7. Helical AFM

Walia et.al. [24] developed Helical abrasive flow machining in 2012. It uses no extra power drive and is simple and rugged in construction. It was named as Helical Abrasive flow machining because drill bit used co-axially with workpiece has a helical profile. The medium is forced to flow through annular space between the stationary drill bit and work piece [24], so that more number of abrasive grains interact with work surface by which surface finish and material removal is improved. Material removal is dependent upon the parameters helical drill bit status, extrusion pressure, number of cycle, flow rate. The contribution of helix 78.89% and number of cycle is 6.70% in the material removal. The combine effect of axial, radial and centrifugal force produced due to use of helical drill bit increases the material removal. The centrifugal force causes better mixing of media and abrasive that results more number of active grains. Walia et.al [25, 26] observed that same phenomena used with rotation of different profile and drill bit in the medium results in 10 and 2.35 times improvements in material removal whereas using helical AFM process improves 2.66 times material removal than in AFM process. Helical AFM process improves the surface roughness up to 2 microns [24].

4.8. Centrifugal- magnetic force assisted AFM

Centrifugal-Magnetic force Assisted Abrasive Flow Machining was developed by Singh & Walia in 2015 [27]. In this research, fixture was made in three parts. The central part consist the workpiece, CFG rod of different shapes, for applying centrifugal force and the arrangement for applying the magnetic field. The arrangement is adjusted in such a way that the magnetic field can be applied to the full length of workpiece. When the dc supply is given, it produces a magnetic field which causes the abrasive particles to pull towards the inner surface of the workpiece and causes more material removal. Magnetic force developed was in the range of 0-0.6 Tesla and the rotation of CFG rod was taken up to 60 rpm. The researcher made an optimization model based on Taguchi and Utility Concept to optimize the process parameters and found that the maximum utility function was obtained at 0.3 Tesla Magnetic Force, 60 rpm of CFG rod, Triangular shape of rod, 4 No. of cycles, 200 mesh size of abrasive grains, 1.1 % by weight of abrasive to iron ratio [27].

4.9. Hybrid electrochemical and centrifugal force assisted abrasive flow machining

EC^2A^2FM was developed by Vaishya et al. in 2015 [28]. The researcher has clubbed the advantages of the two processes ECM and Centrifugal AFM. Taguchi L_{27} standard was used to determine the significant parameters.

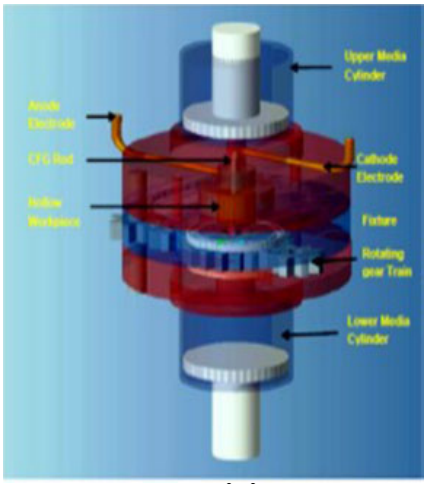

Fig.10. Shown a EC^2A^2FM setup [25]

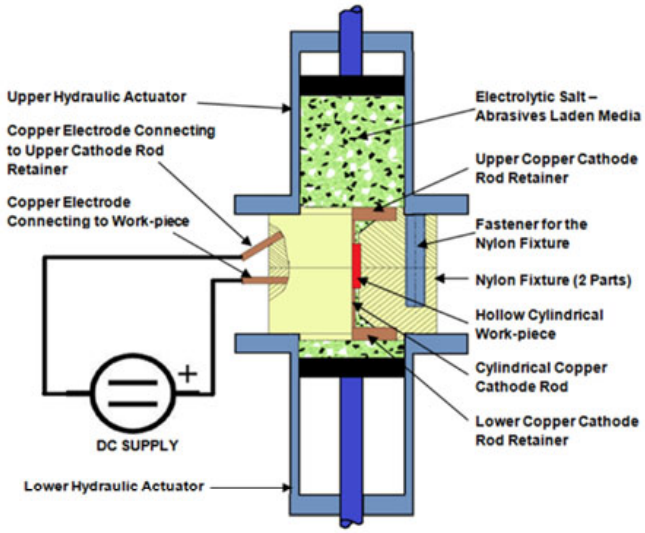

Fig.11. Schematic of ECA^2FM process [19]

In this research the nylon fixture is made of three parts which consists a CFG rod within it held by retainer and fasteners. In this process the extrusion pressure is kept low up to 6 N/mm^2 because of using very thin components. Two copper electrodes were used to connect one electrode to the CFG rod and other to the workpiece. The power supply used was of 0- 30V. The polymeric media was made by adding KI to produce the ECM effect. The figure of EC^2A^2FM is as shown in fig.10. The result shows that clubbing the rotating CFG rod and the ECM process reduces 70-80 percent of the machining time and also it is operated at low extrusion pressure. The result also showed that the surface finish obtained was in the range of 0.5-0.6 Ra [28].

5. Comparison of different AFM processes

The comparison of different variants of abrasive flow machining process is explained in the table 1. The table describes the different process parameters, working and different media used in various AFM processes.

Table 1. Comparison of various AFM processes

Process	CFAAFM	ECAAFM	MAFM
Media	Polymer media Hydrocarbon gel Abrasive grains	Polymer media Hydrocarbon gel Abrasive grains Electrolytic salt like NaI	Polymer media Hydrocarbon gel Abrasive grains
Special feature	Use of centrifugal force generating rod	Electrochemical action increases the rate of machining Work piece used as anode, and a copper electrode as cathode.	MAP (ferromagnetic + abrasive particles) used to finish the surface. Flexible magnetic abrasive brush (FMAB) is formed by these MAP particles, behaving like a multi-point cutting tool to remove material.
Process specific parameters	RPM of the centrifugal rod	Applied voltage to the electrodes	Magnetic flux density Working gap

	Shape of the rod		Work-piece material properties, Size, Type and Volume fraction of abrasives.
Media	Polymer media Hydrocarbon gel Abrasive grains Ferromagnetic particles	Polymer media Hydrocarbon gel Abrasive grains	Polymer media Hydrocarbon gel Abrasive grains
Special feature	FMAB is formed, which acts as a multipoint cutting tool. Longitudinal movement (due to the transducer) of the work piece for better finishing.	A gear system used to rotate the work piece	A drill bit inserted into the medium flow path. A twin slotted fixture plate used.
Process specific parameters	Voltage Rotation of magnet (rpm) Abrasive weight percentage, Pulse on time (Ton)of ultrasonic vibrations	Rotational speed of the work piece Composition of the medium	Drill bit diameter Flute angle

6. Conclusion

AFM process is one of the emerging non conventional micro finishing operation, which is used in various modern industries to replace conventional hand finishing operation. AFM has one of the serious limitations of low material removal so that hybridization improves the efficiency of process by adding the advantage of different machining process and avoiding limitations. AFM is used for finishing intricate, complex edges and deburring, radiusing in a single operation. Many researchers have done a lot of work in AFM but still there is gap for the development of more hybrid AFM processes to enhance the material removal and surface finish with lesser time and cost. Since, the most crucial part of any abrasive flow machine is the abrasive-laden media, therefore a lot of scope for further work lies in developing new cost effective media that result in achieving high removal of material and better surface finish.

References

[1]. R.K. Jain, V.K. Jain, , P.M. Dixit, Modelling of material removal and surface roughness in abrasive flow machining process. International Journal of Machine Tool & Manufacture, 39 (12) (1999), pp. 1903–1923.

[2]. J.E. Mark, H.R. Allcock , R. West, Inorganic Polymers book, Oxford University Press,2nd edition.

[3]. J.L. Wang. and N.A. Favstritsky. Polym. Preprints, 35(2) (1994), pp.701-709.

[4]. F. Gharavi and A.A. Katbab, Prog. Rubber Plast.Technology, 6(2) (1990), pp.120-129.

[5]. L.J. Rhoades, T.A. Kohut, N.P. Nokovich, D.W. Yanda, Unidirectional abrasive flow machining, US patent number 5, 367, 833, Nov 29th(1994).

[6]. E. Uhlmann, Modelling the AFM process on advanced ceramic materials, Journal of materials processing technology, 209 (20)(2009), pp. 6062-6066.

[7]. M.R. Sankar, V.K. Jain and J. Ramkumar, Abrasive flow machining (AFM): An Overview, Indo-US Workshop on Smart Machine Tools, Intelligent Machining Systems and Multi-scale Manufacturing. December (2008).

[8]. S. Singh and H.S. Shan, Development of magneto abrasive flow machining process, International Journal of Machine Tool & Manufacture 42 (2002), pp. 953-959.

[9]. R. Singh and R.S. Walia, Hybrid Magnetic Force Assistant Abrasive Flow Machining Process Study for Optimal Material Removal , International Journal of Applied Engineering Research, ISSN 0973-4562 7 (11) (2012).

[10]. A.W. Sradling, The physics of open gradient dry magnetic separation, International Journal of Mineral Processing, 39 (1993), pp.19-29.

[11]. R. Singh, R.S. Walia, Study The Effects of Centrifugal Force on Abrasive Flow Machining Process, ISSN : 2249-5762 (Online) | ISSN : 2249-5770 (Print) 2 (1) (2012).

[12]. R.S. Walia, H.S. Shan, P. Kumar, Morphology and Integrity of Surfaces Finished by Centrifugal Force Assisted Abrasive Flow Machining, International Journal of Advanced Manufacturing Technology 39 (11-12) (2008), pp. 1171–1179.

[13]. A.K. Sharma, P. Kumar and S. Rajesha, An improved ultrasonic abrasive flow machining, Patent number 3578/DEL/201, India (2011).

[14]. S. Rajesha , Some Studies to Enhance the Capabilities of Abrasive Flow Machining Process. Ph. D dissertation, IIT Roorkee (2011).

[15]. M.R. Sankar, S. Mondal, J. Ramkumar, V.K. Jain, Experimental Investigations and Modelling of Drill Bit Guided Abrasive Flow Finishing (DBG-AFF) Process, International Journal of Advanced Manufacturing Technology, DOI: 10.1007/s00170-008-1642 42 (2009), pp.678-688.

[16]. M.R. Sankar, V.K. Jain, J. Ramkumar, Rotational abrasive flow finishing process and its effects on finished surface, International journal of machine tools and manufacture 50 (7) (2010), pp.637-650.

[17]. M.R. Sankar, V.K. Jain, J. Rajkumar, Experimental investigations into rotating workpiece abrasive flow finishing, Wear, 267 (1-4) (2009), pp. 43-51.

[18]. M.R. Shankar, S. Mondal, J. Ramkumar, V.K. Jain, Experimental investigations and modeling of drill bit guided abrasive flow finishing (DBG-AFF) process, International Journal of Advanced manufacturing Technology, 42 (7-8) (2009), pp.678-688.

[19]. B.S. Brar, R.S. Walia, V.P. Singh, Electrochemical aided abrasive flow machining (ECA^2AFM) process: a hybrid machining process , International Journal of Advanced manufacturing Technology,79 (1-4) (2015), pp. 329-342.

[20]. L. Dabrowski, M. Marciniak, W. Wieczarek, and A. Zygmunt, Advancement of Abrasive Flow Machining Using an Anodic Solution, Journal of New Materials for Electrochemical Systems 9 (2006), pp.439-445.

[21]. L. Dabrowski, M. Marciniak, T. Szewczyk, Analysis of abrasive flow machining with an electrochemical process aid, Proc. Institution of Mechanical Engineers (220) (2006).

[22]. B.S. Brar, R.S. Walia, V.P. Singh, Electro Chemical aid to abrasive flow machining process: harnessed for improved surface finishing, International Conference on Advancements and Futuristic Trends in Mechanical and Materials Engineering (2012).

[23]. E. Brinksmeier, O. Riemer, A. Gessenharter, Finishing of structured surfaces by abrasive polishing, Precision Engineering 30 (3) (2006), pp. 325–336.

[24]. B.S. Brar, R.S. Walia, V.P. Singh, M. Sharma, Helical abrasive flow machining (hlx-afm) process, International Journal of Surface engineering and Materials Technology 2 (2) (2012), pp. 48-52.

[25]. R.S. Walia., H.S. Shan., P. Kumar, Enhancing AFM process productivity through improved fixturing, International Journal of Advanced Manufacturing Technology, 44 (7) (2009), pp. 700–709.

[26]. R.S. Walia, Ph.D. Thesis: Development and Investigations in Centrifugal Force Assisted Abrasive Flow Machining Process, IIT, Roorkee (2006).

[27]. R. Singh, R.S. Walia, N.M Suri, Parametric optimization of Centrifugal- magnetic force Assisted Abrasive Flow Machining Process Using utility Concept, International Journal of Research in Engineering and Technology, 4(8),pp. 2321-730, 2015.

[28]. R. Vaishya, R.S. Walia, P. Kalra, Design and Development of Hybrid Electrochemical and Centrifugal force Assisted Abrasive Flow Machining, Materials Today: Proceedings, 2 (4-5) (2015), pp. 3327-3341.

This article has been accepted for publication in a future issue of this journal, but has not been fully edited. Content may change prior to final publication. Citation information: DOI 10.1109/TII.2017.2756703, IEEE Transactions on Industrial Informatics

Hybrid Control of High Efficient Resonant Converter for Renewable Energy System

H. M. Suryawanshi, *Senior Member, IEEE*, Snehal P. Pachpor, T.Ajmal , Girish G. Talapur, Shelas Sathyan, M. S. Ballal, *Senior Member, IEEE* , V. B. Borghate , *Member, IEEE* and M. R. Ramteke, Member, IEEE

***Abstract*-- This paper presents the hybrid control of DC-DC resonant converter for DC micro-grid. The hybrid control is the simultaneous variation of frequency and duty ratio which can provide excellent voltage regulation and maintain zero voltage switching (ZVS) over wide load range. Hence excellent conversion efficiency is also maintained over wide load range using hybrid control. However, the conventional control methods for DC-DC resonant converter using either variable switching frequency or duty ratio have their own limitations. The frequency control requires wide variation in switching frequency for output voltage regulation which leads to higher switching losses at turn-off of switches and lower efficiency particularly at light load. The duty ratio control has a limitation of loosing of ZVS at light loads. The simulation and experimental results of hybrid control of resonant converter operating above 100 kHz with maximum duty ratio of 0.48 for 3kW are presented from full load to no load. The maximum efficiency of the resonant converter is found to be 98% which was achieved at 75% of full load.**

***Index Terms*-- Hybrid control, zero voltage switching (ZVS), duty ratio control, conventional switching frequency control, DC-DC converters.**

I. INTRODUCTION

RENEWABLE energy sources like wind, solar (PV) have been gaining more and more attention from the last few decades due to increased demand of electrical power and clean power generations. Multi-pronged strategies are being adopted to tackle the impending energy crisis. With increasing worldwide popularity of renewable energy, intelligent power electronic interfaces between these sources and electrical DC grid are being extensively focused for better energy yield and power quality [1]. These renewable energy sources are highly intermittent in nature and operate at medium power levels. The control implementation for these interfaces is an emerging challenge. In order to meet high current requirements, parallel connection of converters can be used which leads to significant improvement in reliability. But unequal current sharing can adversely impact energy yield. So, the concept of modular power systems has been prominently suggested to circumvent the problem of series/parallel stacks. The modular converter systems are more efficient than the conventional centralized structures and can be integrated to DC grid through dedicated DC-DC converters [2]. In the systems requiring high voltage, step-up converters have been used for each module. The increased voltage gain in isolated converters can be achieved by using large turns ratio of transformer. Current fed converters have also been used for high power applications. But presence of isolation transformer and additional inductor increases the weight and reduces power density [3]-[5]. Non-isolated converters have good efficiency, higher power density compared to isolated converters. A non-isolated converter with multiplier cells with reduced duty cycle operation can also be used to achieve high voltage gain [6]. Smart grid power systems also require bidirectional topology for interface between dc bus and generation along with energy storage. The number of soft switching bidirectional converters have been suggested for eliminating switching losses, EMI and increased power density [7]-[9].

In the last 2-3 decades, there has been growing interest in the area of designing control strategies for soft switched DC-DC resonant converters. Soft switched *LCLC* resonant converters have been extensively reported to improve overall conversion efficiency, reduced switching losses, reduced voltage stress on switches and high power density [10]-[14]. Resonant converters conventionally implemented using switching frequency as a control variable in order to achieve desired voltage regulation. But depending upon required gain and load handled by resonant tank, frequency excursions are seen to be very high [15], [16]. This sharply increases the switching losses, complicates design of EMI filter, and other associated problems. Series resonant converters have limitation that, it is extremely difficult to regulate voltage at light loads. To overcome problems associated with switching frequency control of resonant converters, numerous approaches have been discussed in literature. Some of them have employed phase shifted control of inverter to obtain quasi-square voltage output of desirable magnitude [17]. It can also be achieved by using series connected inverters along with transformer connected at the output. However, it increases the component count, control circuit complexity making it a costly. Another possibility of two stage configurations has been reported in [18]-[20] wherein first stage acts as regulator for the voltage input to the next stage. The major limitation of the configuration is increased cost and reduced efficiency due to two stages being used. Another two stage converter consisting of one non-isolated and an isolated stage is presented in [21], [22]. Non-isolated stage was used for voltage regulation and power flow control whereas, isolated stage was designed for optimized components' ratings. Even though power was passing through two stages, enhanced conversion efficiency could be achieved over a wide voltage range. The other approach was to employ constant-frequency DC-DC converter with single stage and through magnetic control. The concept of variable inductance as an additional control parameter is employed and inductance of resonant tank has been varied by current flowing through an

Manuscript received January 17, 2017; revised May 15, 2017, August 14 2017 and accepted September 11, 2017. This work was supported by Department of Science and Technology (DST), Government of India, under the project grant No. DST/TM/SERI/FR/104/(G) dated:15/06/2015.

H. M. Suryawanshi, , G. G. Talapur, S. Sathyan, M. S. Ballal, V. B. Borghate , M.R.Ramteke are with the Department of Electrical Engineering, VNIT, Nagpur 440010, India , S.P Pachpor is working as an Associate Professor in KITS, Ramtek, Dist. Nagpur, India and T. Ajmal is working as an Engineer in TATA Elxsi Ltd. Trivandrum, India.

1551-3203 (c) 2017 IEEE. Personal use is permitted, but republication/redistribution requires IEEE permission. See http://www.ieee.org/publications_standards/publications/rights/index.html for more information.

This article has been accepted for publication in a future issue of this journal, but has not been fully edited. Content may change prior to final publication. Citation information: DOI 10.1109/TII.2017.2756703, IEEE Transactions on Industrial Informatics

additional winding [23]. Using this methodology, it was possible to regulate output voltage from full load to no load maintaining reasonable variations in controlled inductance in parallel converters. But in series resonant inverter, variation in inductance was found to be very high to regulate voltage during light loads. Therefore, it was not suitable for applications with wide load range. Another drawback of this technique was medium efficiency as operation was away from resonant frequency. Dual active bridge (DAB) converters have modular and symmetrical configuration and it can attain ZVS at turn on with no auxiliary components. But, it has a narrow ZVS range and also circulating currents are high when a wide voltage variation is required. The current has high ripple factor and they are problematic for low voltage applications [24].

The various control techniques for resonant converters such as phase shifted modulation (PSM), self-sustained oscillation control (SSOC), and self-sustained phase shift modulation (SSPSM) have been compared quantitatively in terms of transient response, converter ratings, allowable range of ZVS and frequency variation in [25]. This comparison has showed that SSOC is a good alternative and SSPSM offers the best optimized component ratings with high operating efficiency of the resonant converter. In yet another study an asymmetrical voltage cancellation control (AVC) technique was employed as a generalized phase shift and asymmetrical duty cycle ratio control technique [26]. A multi-resonant switch concept could be used to overcome limitation of HF quasi-resonant converters (QRCs). It provides favorable ZVS conditions for active switch as well as rectifier diodes thereby reducing voltage stress compared to ZVS QRCs. But this concept was applied for comparatively low power and high operating frequency ranges which are in MHz [27].

To overcome aforementioned limitations of existing control techniques, a hybrid controller which utilizes simultaneous variation of both switching frequency and duty cycle control to regulate the output voltage is presented in this paper. Particularly this approach is based on the use of combined effect of switching frequency as well as duty ratio as the control variables in order to achieve advantages of both the control schemes together. The other objectives of the proposed technique are to design a programmable/intelligent control which can be extended for other resonant converter topologies and for modular converters with minimum modification in control hardware. Modified series parallel resonant converter (MSPRC) which has features of both series and parallel resonant converter has been used for demonstrating the effectiveness of the proposed hybrid control. The mathematical modeling of hybrid control and comparative analysis of control using switching frequency and proposed control are presented in section II. In section III, design of laboratory prototype converter and simulation results with hybrid control are presented. Experimental results and its analysis are discussed in section IV and paper is concluded in section V.

II. DESIGN AND ANALYSIS OF HYBRID CONTROL

The proposed control technique is implemented on full bridge MSPRC which is a higher order resonant tank circuit as shown in Fig.1. Equivalent circuit of the resonant converter is

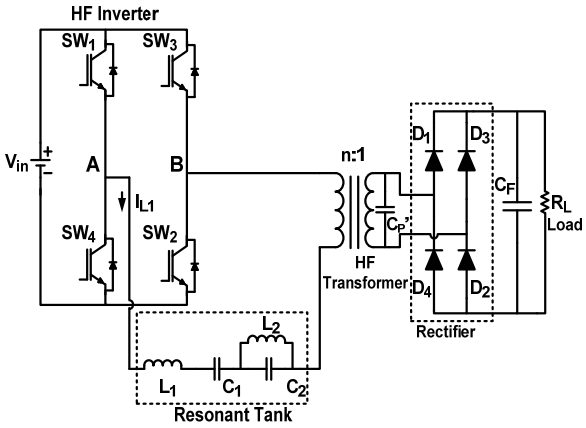

Fig. 1. Full bridge modified series parallel resonant tank converter.

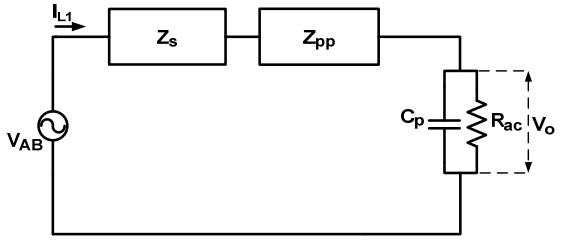

Fig. 2. Equivalent circuit of modified series parallel resonant converter.

shown in Fig.2. The resonant converters operating above resonant frequency give nearly sinusoidal current and voltage waveforms [28]. L_1, C_1, L_2 and C_2 form the series branch of resonant tank circuit. C_P' is the capacitor connected across secondary side of high frequency transformer, so leakage inductance of HF transformer used as a part of L_1.

A. Conventional Switching frequency control

In conventional frequency control, the variation in switching frequency alters the impedance of reactive elements of resonant tank circuit and hence output voltage is regulated. Therefore, in order to reduce gain large frequency excursion is required. In duty ratio control, variation in duty ratio alters the input voltage to the resonant tank circuit, and hence output voltage is regulated with respect to load. But there is limitation on variation of duty cycle due to loosing of ZVS at light load.

In switching frequency control, converter voltage gain, M is given by (1), where V_{AB} is the voltage input applied to resonant tank network and V_O is the output voltage of converter.

$$M = \frac{V_o}{V_{AB}} = \frac{Z_P}{Z_{in}} \tag{1}$$

where, Z_P is parallel combination of R_{ac} and C_P. Capacitance C_P is equivalent capacitance of C_P' referred to primary side of HF transformer. The R_{ac} is equivalent ac resistance representing load, rectifier and filter. Z_S and Z_{PP} together represent impedances of series branch of resonant tank of MSPRC. The n is turns ratio of high frequency transformer, R_L'=n^2R_L, and k = 8 / π^2. Q is a quality factor of the converter as expressed in (2) and the resonant frequency of the MSPRC tank circuit, f_0 can be expressed as follows [28];

1551-3203 (c) 2017 IEEE. Personal use is permitted, but republication/redistribution requires IEEE permission. See http://www.ieee.org/publications_standards/publications/rights/index.html for more information.

This article has been accepted for publication in a future issue of this journal, but has not been fully edited. Content may change prior to final publication. Citation information: DOI 10.1109/TII.2017.2756703, IEEE Transactions on Industrial Informatics

$$Q = \frac{\omega_0 L_1}{R_L^{'}} = \frac{\sqrt{L_1/C_1}}{R_{ac}} \tag{2}$$

$$\text{Where, } \omega_0 = \sqrt{[(\frac{1}{2L_1C_1})a(b+\sqrt{b^2-4})]}$$

$$f_0 = \frac{1}{\pi\sqrt{8L_1C_1}}\sqrt{(a(b+\sqrt{b^2-4})}$$

$$a = \sqrt{\frac{L_1}{L_2}\frac{C_1}{C_2}}$$

$$b = \sqrt{\frac{L_1}{L_2}\frac{C_1}{C_2}} + \sqrt{\frac{L_2}{L_1}\frac{C_1}{C_2}} + \sqrt{\frac{L_2}{L_1}\frac{C_2}{C_1}}$$

$$R_{ac} = \frac{8R_L^{'}}{\pi^2} = k\,R_L^{'}$$

$$Z_S = j(\omega_s L_1 - \frac{1}{\omega_s C_1}) \tag{3}$$

$$Z_{PP} = \frac{-j\,\omega_s L_2}{(\omega_s^2 L_2 C_2 - 1)} \tag{4}$$

$$Z_P = \frac{-j\,R_{ac}}{(\omega_s C_P R_{ac} - j)} \tag{5}$$

The impedance that is viewed from the input port of the resonant tank is Z_{in} which depends on switching frequency ω_s, parameters of resonant tank, load resistance R_L and is expressed as follows:

$$Z_{in} = Z_S + Z_{PP} + Z_P \tag{6}$$

The angle of impedance Z_{in} of resonant tank, ϕ can be expressed as a function of switching frequency, ω_s using (7).

$$\phi = f(\omega_s) = \tan^{-1}[\frac{\omega_s L_1 - \frac{1}{\omega_s C_1} - \frac{\omega_s L_2}{\omega_s^2 L_2 C_2 - 1} - \frac{\omega_s C_p R_{ac}^2}{1+\omega_s^2 C_p^2 R_{ac}^2}}{\frac{R_{ac}}{1+\omega_s^2 C_p^2 R_{ac}^2}}] \tag{7}$$

The converter voltage gain is a function of normalized switching frequency $Y_S = f_S/f_0$. Due to variation in frequency, impedance of reactive elements of resonant tank varies and output voltage is modified. The quality factor, Q is function of load. The variation of voltage gain, M with normalized switching frequency, Y_S, for different loads i.e. for different Q values is shown in Fig. 3. This shows that wide range of switching frequency is required for voltage regulation from full load to light load condition with conventional frequency control and hence performance is degraded due to sharply increased switching losses.

B. Proposed Hybrid control

The Hybrid control method is the simultaneous variation of both frequency and duty ratio. Therefore range of the switching frequency and duty ratio is limited. If the switching frequency and duty cycle both together are suitably adjusted with respect to load, the output voltage can be regulated with narrow

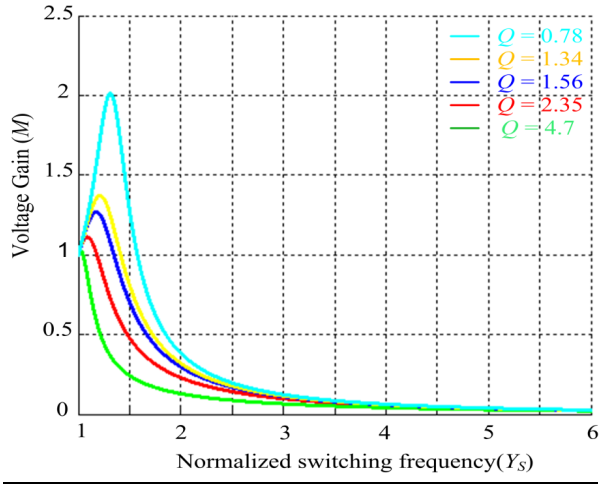

Fig. 3. Variation of gain with normalized switching frequency for different Q factors.

variation in switching frequency as well as duty ratio, since both impedance of reactive elements and input voltage to resonant tank are varied during hybrid control. Reduction in switching frequency reduces switching losses, reduction in duty ratio reduces conduction losses and consequently enhances the conversion efficiency. The judicious/appropriate variation in frequency and duty cycle can maintain ZVS even at very light load. Thus, for designing the hybrid control, it is required to model and study an expression for converter gain in terms of both duty ratio, and frequency.

In order to simplify the analysis, all components are assumed to be ideal and converter is assumed to be operating under steady state condition. Assuming that duty ratio is D for the switches in both the legs, the input voltage applied to the tank circuit v_{AB}(t) which is symmetrical and can be expressed as shown below. Due to symmetrical nature, dc component is zero in an expression for v_{AB}(t) [31].

$$v_{AB}(t) = \sum_{h=1}^{\infty} 2\sqrt{2}[\frac{V_{in}}{h\pi}\sqrt{1-\cos(2\pi hD)}\,\sin(h\omega t + \psi_h)$$

Where, ψ_h is phase angle of h^{th} harmonic voltage v_{AB}(t) and ψ is phase angle of fundamental component of voltage v_{AB}(t) which can be estimated using (8),

$$\psi = g(D) = \tan^{-1}[\frac{\sin(2\pi D)}{1-\cos(2\pi D)}] \tag{8}$$

The filtering action of the resonant capacitor blocks dc component and allows the ac component of v_{AB}(t) to pass through HF transformer. The fundamental ac component of the v_{AB}(t) that forces current i_L(t) in resonant tank circuit (h=1) is given by,

$$v_{ABac}(t) = 2\sqrt{2}[\frac{V_{in}}{\pi}\sqrt{1-\cos(2\pi D)}\,\sin(\omega t + \psi)] \tag{9}$$

The ψ is a function of duty ratio D and during conventional frequency control where D = 0.5, phase angle of $v_{AB}(t)$ i.e. ψ is zero. In hybrid control, duty cycle, D is less than 0.5 and ZVS condition of two bridge arms is same because of symmetrical switching of switches in both the arms. It can be determined by a lagging of resonant current behind voltage applied to the tank circuit v_{AB}(t). The effective value of the fundamental

1551-3203 (c) 2017 IEEE. Personal use is permitted, but republication/redistribution requires IEEE permission. See http://www.ieee.org/publications_standards/publications/rights/index.html for more information.

This article has been accepted for publication in a future issue of this journal, but has not been fully edited. Content may change prior to final publication. Citation information: DOI 10.1109/TII.2017.2756703, IEEE Transactions on Industrial Informatics

component of voltage contributing towards active power transfer to load can be calculated by,

$$V_{AB} = \frac{2V_{in}}{\pi}\sqrt{1-\cos(2\pi D)} \tag{10}$$

$$M = \frac{V_0}{V_{in}} = \frac{2Z_P}{n\pi Z_{in}}\sqrt{1-\cos 2\pi D} = K_1\frac{Z_P}{Z_{in}}\sin(\pi D) \tag{11}$$

$$K_1 = \frac{2\sqrt{2}}{n\pi} \tag{12}$$

Equation (11) shows that overall converter gain can be controlled by varying both switching frequency and duty ratio. Z_P and Z_{in} are the functions of switching frequency. The variation of converter voltage gain, M with normalized switching frequency, Y_S at different duty cycles for full load and for 30% rated load are shown in Fig. 4(a)-(d). It can be seen that the effect of duty cycle variation is more prominently observed at lighter load conditions compared to full load.

The proposed algorithm to regulate the output voltage according to load variations requires decision algorithm to calculate control voltage, v_C which is proportional to the difference between actual load voltage, V_O and desired reference load voltage V_{Oref}. The k' is the scaling factor. An algorithm is developed to estimate new values of switching frequency f_S' and duty cycle D' corresponding to the control voltage. Actual load voltage can be easily detected by using voltage sensor in order to calculate v_C. By measuring output voltage V_O, control voltage v_C can be estimated as,

$$v_C = k'\left(V_o - V_{Oref}\right) \tag{13}$$

$$M' = M - \frac{V_o - V_{oref}}{V_{in}} \tag{14}$$

When load is reduced, output voltage tends to be increased and to regulate output voltage reduction in gain, M is required. This reduction in gain should depend on change in output voltage. Here change in output voltage is measured in terms of v_C and M' is the new converter gain for reduced load.

In order to achieve desired gain, M' to maintain constant voltage with load changing from full load to no load, increase in switching frequency and decrease in duty ratio are required. The new values of switching frequency f_S' and duty ratio D' can be calculated using (15) and (16) respectively.

$$f'_S = f_S + v_C k_f \tag{15}$$

$$D' = D - v_C k_d \tag{16}$$

The frequency constant k_f can be suitably calculated for desired frequency variation and required upper and lower limits of the switching frequency range. The duty ratio constant k_d can be fixed for desired duty ratio variation and required range of upper and lower limits on duty ratio. The new frequency and duty ratio are independent of resonant converter parameters. The novelty in the proposed algorithm is that it is symmetrical i.e. ON times of all the switches are same and DC component in an expression for v_{AB}(t) is zero which reduces the possibility of saturation of HF transformer.

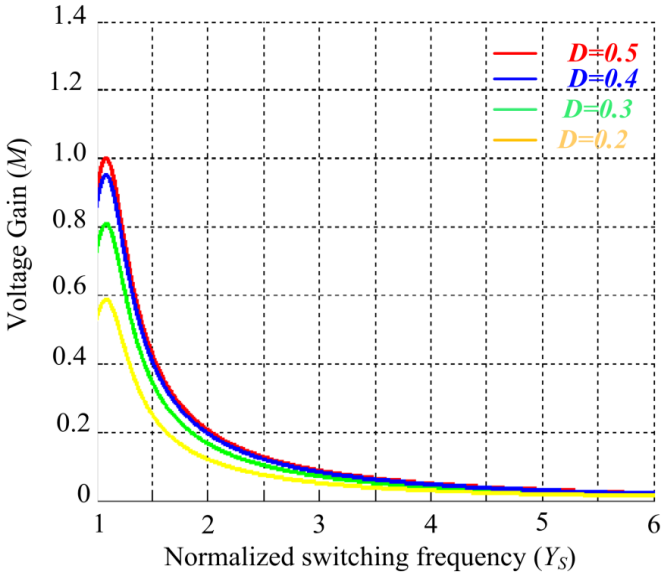

(a)

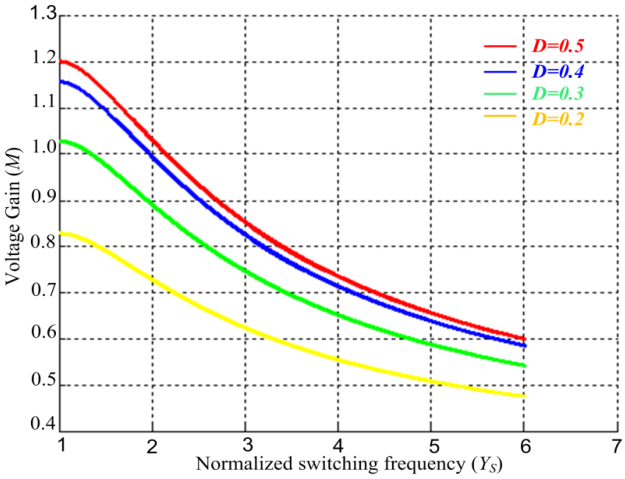

(b)

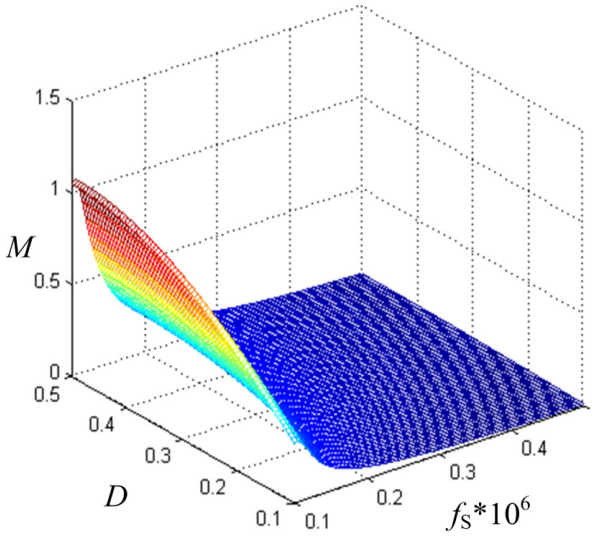

(c)

1551-3203 (c) 2017 IEEE. Personal use is permitted, but republication/redistribution requires IEEE permission. See http://www.ieee.org/publications_standards/publications/rights/index.html for more information.

This article has been accepted for publication in a future issue of this journal, but has not been fully edited. Content may change prior to final publication. Citation information: DOI 10.1109/TII.2017.2756703, IEEE Transactions on Industrial Informatics

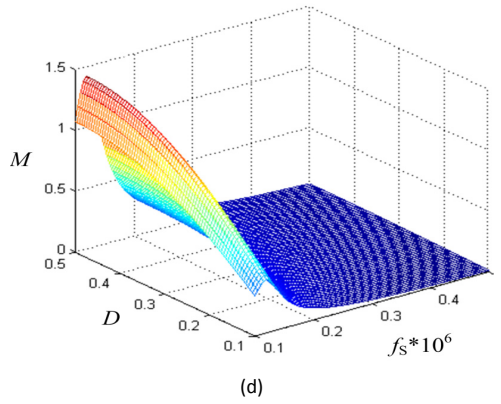

Fig. 4. Variation of gain with switching frequency as a function of duty ratio at: (a) rated, (b) 30% rated load, (c) variation of gain with both frequency and duty ratio at full load 3D and (d) variation of gain with both frequency and duty ratio at light load 3D.

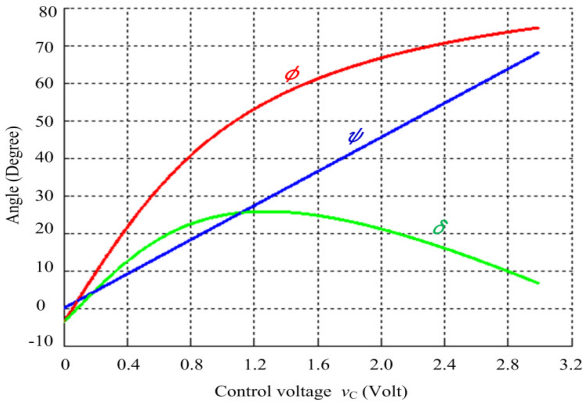

Fig. 5. Variation in angles with respect to control voltage using proposed hybrid control.

The other important parameter for soft switching operation is fundamental component of resonant current, $i_{L1}(t)$ flowing through the resonant network. The instantaneous value of this current is $i_{L1}(t)$.

$$i_{L1}(t) = \frac{2\sqrt{2}V_{in}}{\pi Z_{in}}\sqrt{1-\cos(2\pi D)}\sin(\omega t + \psi - \phi) \qquad (17)$$

Where, ϕ is the phase angle with which $i_{L1}(t)$ lags the inverter output voltage $v_{AB}(t)$. The condition for ZVS operation is the resonant current $i_{L1}(t)$ lagging the voltage $v_{AB}(t)$ applied to the tank circuit i.e. angle δ should be greater than zero.

$$\delta = \phi - \psi > 0 \qquad (18)$$

$$\phi > \psi \qquad (19)$$

In other words, phase angle of total impedance, ϕ should be greater than ψ, the phase angle of $v_{AB}(t)$. In case of conventional frequency control in which duty cycle is fixed i.e. D=0.5, ψ is zero as per (8) and the angle ϕ increases with frequency, hence current i_{L1} through inductor L_1 always lags and maintain ZVS. However, in hybrid control both the phase angles ϕ and ψ change. The angle ψ is inversely proportional to duty cycle and ϕ is directly proportional to switching frequency. Hence in order to ensure ZVS operation, variables ψ and ϕ are determined. Fig.5. shows variation of angles ϕ, ψ and δ with respect to control voltage v_C during hybrid control.

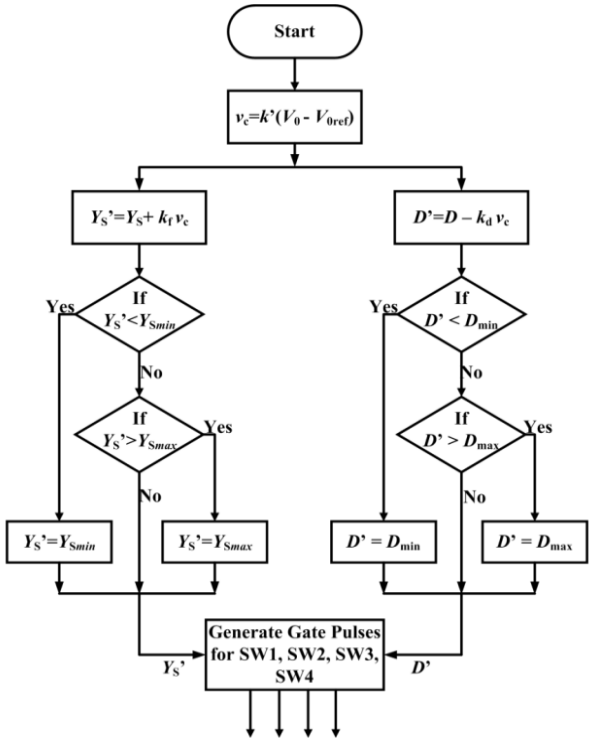

Fig. 6. Flow chart for proposed hybrid control.

It is seen that for the switching frequency and duty ratio estimated using proposed control, angle δ is positive over wide range and it can be ensured that current i_{L1} lags behind $v_{AB}(t)$ and qualifies the condition for ZVS operation. Hence the proposed hybrid control is reliable. The proposed hybrid control algorithm to decide appropriate normalized switching frequency and duty ratio in terms of v_C for voltage regulation with respect to load is shown in flow chart of Fig. 6. The normalization is used for common conclusion. It is implemented in digital controllers DSP TMS320F28335. For every value of control voltage v_C, there is unique value of f_s' and D'. During control, v_C is control voltage applied to ADC port of DSP and its phase angle is zero as it is a DC voltage. For inductive mode of operation, it is required that the frequency should always be greater than resonant frequency. Therefore lower limit is put on frequency Y_{Smin}. i.e. Y_{Smin} is set greater than the resonant frequency so as to avoid operating frequency below resonant frequency. The algorithm ensures that the new normalized switching frequency is always greater than Y_{Smin} and less than Y_{Smax}. The range of frequency is set to be f_{min}=106 kHz to f_{max}= 190kHz whereas the range of duty ratio is set to be D_{min}= 0.16 to D_{max}= 0.48 for ZVS and stable operation of the converter. The range of control voltage, v_C where ZVS can be realized is 0.1V < v_C < 3V.

To justify the applicability and validity of the proposed technique, it is tested on various resonant topologies such as *LLC*, *LCLC* higher order and *LC* series resonant converters. The simulation results using conventional frequency control, conventional duty ratio control and hybrid control are presented in Table.I-Table.III. It is seen that proposed hybrid control can be easily implemented and gives satisfactory results for other topologies as well.

1551-3203 (c) 2017 IEEE. Personal use is permitted, but republication/redistribution requires IEEE permission. See http://www.ieee.org/publications_standards/publications/rights/index.html for more information.

This article has been accepted for publication in a future issue of this journal, but has not been fully edited. Content may change prior to final publication. Citation information: DOI 10.1109/TII.2017.2756703, IEEE Transactions on Industrial Informatics

TABLE I
2kW LLC Series Resonant converter. [33]

Parameter	Full Load		No Load (1% FL)		
	Conventional frequency control	Hybrid control	Conventional frequency control	Duty ratio control	Hybrid control
Switching freq, *fs* (kHz)	107	107	315	107	275
Duty Ratio, *D*	0.5	0.5	0.5	0.12	0.2
ZVS	Yes	Yes	Yes	No	Yes

TABLE II
3kW LCLC Higher Order Resonant Converter. [32]

Parameters	Full Load		No Load (1% FL))		
	Conventional frequency control	Hybrid control	Conventional frequency control	Duty ratio control	Hybrid control
Switching freq, *fs* (kHz)	100	100	131	100	107
Duty Ratio, *D*	0.5	0.5	0.5	0.175	0.26
ZVS	Yes	Yes	Yes	No	Yes

TABLE III
3.3kW LC Series Resonant Converter.

Parameters	Full Load		No Load (1% FL))		
	Conventional frequency control	Hybrid control	Conventional frequency control	Duty ratio control	Hybrid control
Switching freq, *fs* (kHz)	87	87	305	87	133
Duty Ratio, *D*	0.5	0.5	0.5	0.115	0.3
ZVS	Yes	Yes	Yes	No	Yes

TABLE IV
Specifications and parameters of proposed converter.

Input voltage	220V
Output Voltage	400V
Power	3kW
Minimum switching frequency	100kHz
Series resonant tank	L_1=51.35µH (MPP core), C_1 = 54.32nF
Parallel resonant tank	L_2 = 513.5µH (Ferrite core), C_2 = 543.2nF
Parallel capacitor	C_P=5.432nF, $C_P'=n^2C_P$ =1.643nF
Filter capacitor	200 µF
Ultra-fast switches, IGBTs	30N60A4D
HF Transformer	PM 62 ferrite core, n = 0.55
Rectifier Diodes	RHRG75120 hyper fast

III. SIMULATION RESULTS

For the given specifications and designed components values, the proposed converter is simulated in PSIM simulation package. Parameters for simulation are V_0 = 400V, V_{in} = 220V, output power Po = 3kW, inductor ratio L_1/L_2 = 0.1, capacitor ratio C_1/C_2 = 0.1 and Turns ratio n = 0.55. During converter design, M = 1 at full load and switching frequency is equal to resonant frequency. The specifications of designed converter are given in Table IV. For these specifications, a=0.1, b=11.11 and resonant frequency is f_0 =100 kHz. Using hybrid control, the values of switching frequency and duty ratio are computed for different load conditions and for desired output voltage.

TABLE V
Simulation results using hybrid control at different loads.

Parameters	Full load	75% FL	50% FL	10% FL	5% FL
R_L (Ω)	53.33	71.1	106.66	533.33	1066.6
Switch freq. (*kHz*) (Frequency control)	106	112	125	333.5	397.8
Switch freq. (*kHz*) and duty ratio (Hybrid control)	f_S'=106 D'=0.48	f_S'=110 D'=0.46	f_S'=117 D'=0.44	f_S'=147 D'=0.3	f_S'=169 D'=0.28

TABLE VI
Simulation results using duty ratio control at different loads.

Parameters	Full load	75% FL	50% FL	10% FL	5% FL
Switching frequency (*kHz*)	106	106	106	106	106
Duty ratio	0.48	0.46	0.43	0.26	0.16
R_L (Ω)	53.33	71.1	106.6	533.3	1066.6
Load current (*A*)	7.46	5.72	3.73	0.746	0.373
Efficiency (%)	97.6	96.5	95.78	92.2	80

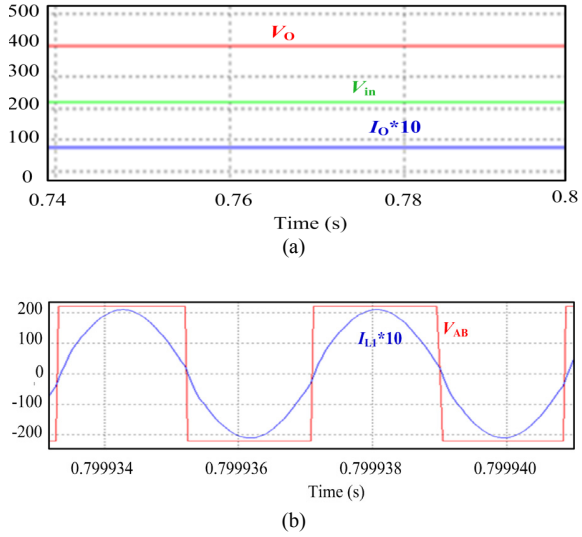

Fig. 7. Simulation results: (a) Input-output dc voltage and load current of converter, (b) variation of input voltage to resonant tank and inductor current i_{L1}.

The simulation waveforms are shown in Fig.7 (a)-(b). Fig.7 (a) shows input DC voltage V_{in}, output DC voltage V_0 and load current I_0 at full load. Fig.7 (b) shows variation of voltage input to resonant tank v_{AB}(t) and resonant current, I_{L1} through inductor L_1 at rated load. Table.V shows the values of switching frequency and duty ratio during hybrid control as well as the frequency variation required if conventional frequency control is employed from full load to no load conditions. From TABLE.V-VI, it is observed that when load is reduced to 5% of full load, switching frequency is 397.8 kHz to regulate output voltage if conventional frequency control is used and duty ratio is 0.16 if conventional duty ratio

1551-3203 (c) 2017 IEEE. Personal use is permitted, but republication/redistribution requires IEEE permission. See http://www.ieee.org/publications_standards/publications/rights/index.html for more information.

This article has been accepted for publication in a future issue of this journal, but has not been fully edited. Content may change prior to final publication. Citation information: DOI 10.1109/TII.2017.2756703, IEEE Transactions on Industrial Informatics

control is used. Whereas with the proposed hybrid control, switching frequency reduces to 169 kHz with duty ratio D=0.28.

IV. EXPERIMENTAL RESULTS

The proposed hybrid control of resonant converter for DC micro-grid has been experimentally tested for 3 kW, 220/400V with minimum switching frequency of 106 kHz with specifications shown in TABLE IV. This design is based on the optimum operating point of MSPRC. The optimum operating point is selected based on design curves given in [30], [32]. The resonant tank circuit is optimized for minimum inverter output current, maximum efficiency, excellent voltage regulation and minimum kilo volt-ampere rating of tank per kilowatt of output power. The high frequency transformer is designed using PM 62 ferrite core and litz wires are used for transformer as well as inductor windings. Slightly higher values of inductors (52µH) are used to get smoother waveforms, inductor winding is tightly wound, and multilayer ceramic capacitors (MLCC) are used which have negligible internal resistance to improve the performance specifically at lighter loads. The full bridge rectifier is made using four hyper fast diodes (RHRG75120). Photograph of prototype converter is shown in Fig. 8. Control circuit for the converter is developed by using DSP TMS320F28335. Isolated gate driver circuits are designed using MIC 4425 for all the switches. The critical point for resonant converters is the regulation of output voltage at very light load, since minimum gain is desired at this condition within the operating frequency range. The experimental results are taken from full load to 5% FL for inverter output voltage, resonant current. Fig.9-14 show the key experimental waveforms when converter was operated from rated load to 5% of rated load using hybrid control. Fig.9 illustrates the inverter output voltage, v_{AB} and inverter output current, i_{L1} operating under hybrid control at rated load of 3 kW. This operation is at 106 kHz and D=0.48. The Current is nearly sinusoidal and lagging behind v_{AB}. Fig.10 shows voltage across SW_1 and current through SW_1 and it can be seen that switch (SW_1) of converter is being turned ON with ZVS. In fact, all the switches are turned ON with ZVS using proposed approach. Fig.11 shows waveform of converter operating at 50% of full load. The output voltage is regulated with switching frequency of 117 kHz, D=0.438 at 50% rated load. Fig.12-13 show experimental waveforms of converter operating at 25% and 10% of full load respectively. The output voltage is regulated with switching frequency of 131 kHz, D=0.381 at 25% rated load and 144.5 kHz, D=0.29 at 10% rated load. It is seen from Fig.14 that resonant current is kept lagging even at 5% rated load with proposed hybrid control at a switching frequency of 161 kHz and D=0.27. TABLE.VII shows that the output voltage is regulated with a frequency of only 161 kHz at 5% rated load which was 397.8 kHz during conventional frequency control. Due to this drastic reduction in switching frequency, switching losses, EMI are reduced and conversion efficiency is improved with proposed hybrid control. Further, due to decrease in duty ratio conduction losses are reduced and converter efficiency is enhanced. All the experimental results at different load conditions are summarized in Table.VII.

TABLE VII
Experimental results using hybrid control at different loads.

Parameters	Full load	75% FL	50% FL	10% FL	5% FL
Switching frequency (kHz)	106	110	117	144.5	161
Duty ratio	0.48	0.46	0.438	0.29	0.27
R_L (Ω)	53.33	71.1	106.6	533.33	1066.6
I_{L1} (A,peak)	21	15.87	10.77	3.75	2.4
I_{L2} (A,peak)	0.185	0.149	0.0809	0.03027	0.016
V_{C1} (V,peak)	613.6	453.49	298	64.17	44.41
V_{C2} (V,peak)	61.89	46.43	30.17	7.12	4.68
Load current (A)	7.46	5.72	3.73	0.746	0.373
Efficiency (%)	97.6	98	97.68	91.519	86.63

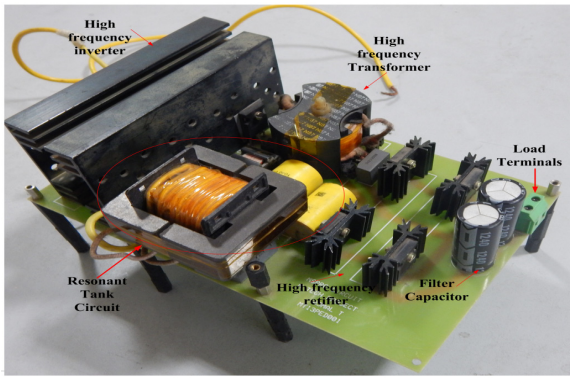

Fig. 8. Experimental setup.

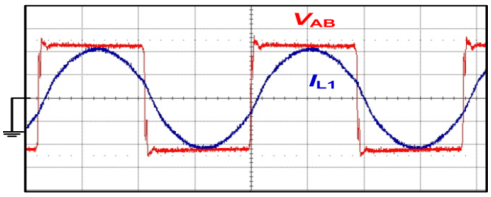

Fig. 9. Input voltage to resonant tank and resonant current at full load (100V/Div, 10A/Div, 2.5µs/Div).

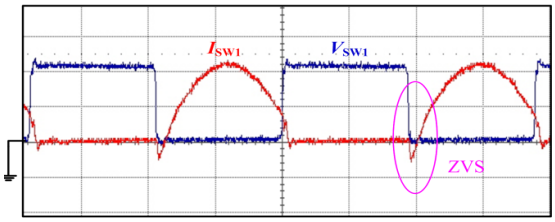

Fig. 10. Voltage across switch,V_{SW1} and switch current, I_{SW1} at full load (100V/Div,10A/Div,2.5µs/Div).

The various angles are estimated for the new values of switching frequency, f_s' and duty ratio, D' as shown in TABLE.VIII. It is seen that δ is positive and ZVS of all primary switches is well realized at minimum load as well as at rated load conditions.

The comparison of the efficiency with the classical frequency control technique, duty ratio control and the proposed hybrid control at different load conditions is presented in TABLE. IX. It is clear that the efficiency with proposed hybrid control is improved more specifically at lighter loads and explains the effectiveness of this control.

1551-3203 (c) 2017 IEEE. Personal use is permitted, but republication/redistribution requires IEEE permission. See http://www.ieee.org/publications_standards/publications/rights/index.html for more information.

This article has been accepted for publication in a future issue of this journal, but has not been fully edited. Content may change prior to final publication. Citation information: DOI 10.1109/TII.2017.2756703, IEEE Transactions on Industrial Informatics

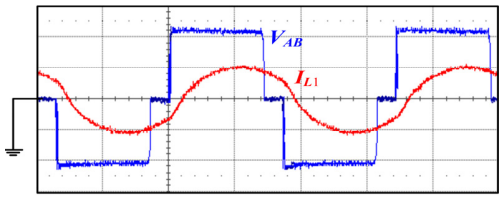

Fig. 11. Input voltage to resonant tank and resonant current at 50% full load (100V/Div,10A/Div,2.5µs/Div).

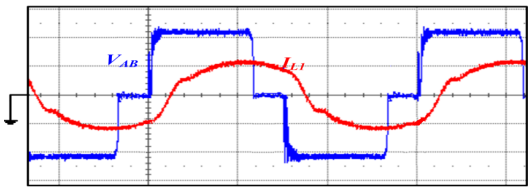

Fig. 12. Input voltage to resonant tank and resonant current at 25% full load (100V/Div, 5A/Div, 2.5µs/Div).

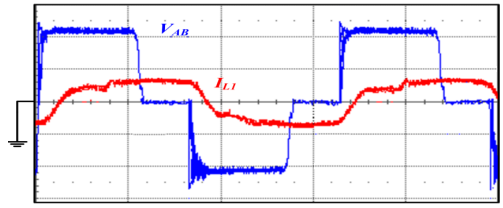

Fig. 13. Input voltage to resonant tank and resonant current at 10% full load (100V/Div, 5A/Div, 2.5µs/Div).

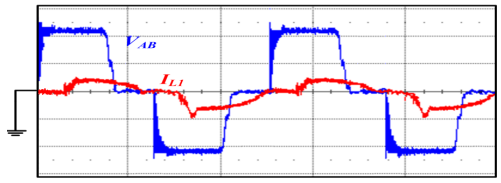

Fig. 14. Input voltage to resonant tank and resonant current at 5% full load (100V/Div, 5A/Div, 2.5µs/Div).

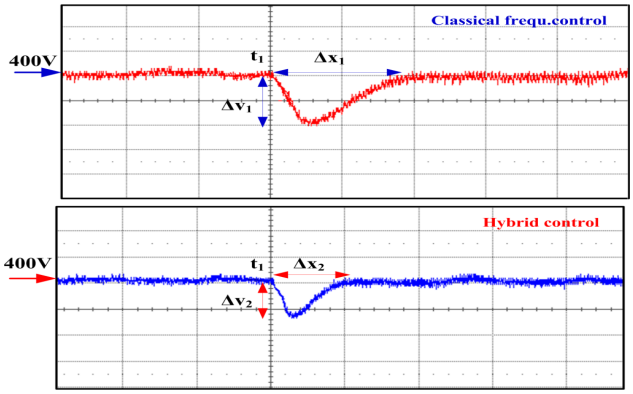

Fig. 15. Comparison between classical frequency and hybrid control of output voltage dynamic response due to step change of load from 10% full load to full load; voltage scale:5V/div, time scale:0.05ms/div.

For evaluating the performance during dynamical operation, the output voltage to the step change of loads from light load to full load is observed. The load is increased from 10% of full load to full load at instant t_1. Fig.15 shows the comparison of the dynamic responses when classical and proposed hybrid controls are used. It is evident that in classical approach i.e. during conventional frequency control, the time required for the system to reach the reference output voltage value i.e.

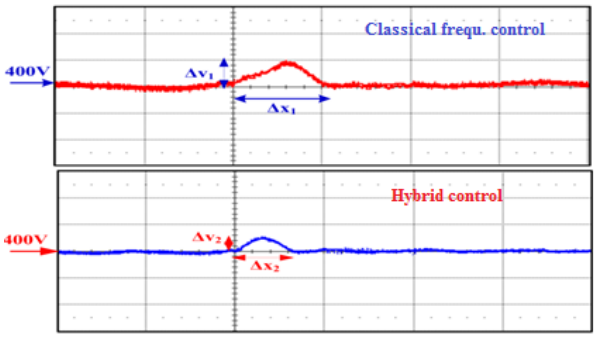

Fig. 16. Comparison between classical frequency and hybrid control of output voltage dynamic response due to step change of load from full load to 50% full load; voltage scale; voltage scale: 5V/div, time scale:0.05ms/div.

TABLE.VIII

Various angles at new values of switching frequency and duty ratio

Load	f_S', D'	Φ	ψ	δ
10%Full load	f_S'=144.5kHz, D'=0.29	57.63	37.80	19.83
5%full load	f_S'=161kHz, D'=0.27	84.788	41.4014	43.3

TABLE.IX.

Comparison of the efficiency with classical control technique

% Full Load	Conventional frequency control	Proposed Hybrid Control	Conventional duty ratio control
Full load	97.6 %	97.6 %	97.6 %
75% Full load	97 %	98 %	96.5%
50% Full load	96.1%	97.68 %	95.78%
10% Full load	82.94 %	91.51 %	92.2%
5% Full load	73.47 %	86.63 %	80%

settling time is Δx_1=0.1ms and the peak undershoot is Δv_1=10V (2.5%), whereas with proposed hybrid control the settling time is reduced to Δx_2=0.05ms and the peak undershoot is reduced to Δv_2=6V (1.5%). Further, Fig. 16 shows the dynamic response when load is reduced from full load to 50% of full load, output voltage is increased to 405V with classical method. The peak overshoot is Δv_1= 5V (1.25%) and settling time is Δx_1=0.05ms. However with hybrid control the settling time is reduced to Δx_2=0.03ms and the peak overshoot is reduced to Δv_2=2.5V (0.625%).

V. CONCLUSION

The hybrid control of DC-DC resonant converter for DC micro-grid has been presented in this paper. The proposed hybrid control is simple as well as effective technique to achieve enhanced conversion efficiency, reduced frequency excursions and ZVS operation of converter switches especially at very light loads. The hybrid control based on both switching frequency and duty ratio together as control variables can overcome the limitations of conventional frequency and conventional duty ratio controls and provide fast dynamic response. The results are verified on converter operating at 3 kW. The experimental results reveal that the proposed hybrid control regulates output voltage with a

1551-3203 (c) 2017 IEEE. Personal use is permitted, but republication/redistribution requires IEEE permission. See http://www.ieee.org/publications_standards/publications/rights/index.html for more information.

This article has been accepted for publication in a future issue of this journal, but has not been fully edited. Content may change prior to final publication. Citation information: DOI 10.1109/TII.2017.2756703, IEEE Transactions on Industrial Informatics

switching frequency of 161 kHz and duty ratio D=0.27 at 5% rated load which was 397.8 kHz during conventional frequency control. This reduction in frequency results in reduced switching losses, improved efficiency, reduced size of EMI filter, and high power density. ZVS is also achieved for all the switches during very light load condition. The maximum efficiency of the resonant converter is 98% and is achieved at 75% of full load. The proposed control technique can be implemented to control the performance of other similar resonant converter topologies with minimum modification in algorithm using same control hardware. It is important to note that the converter operation under proposed hybrid control is symmetrical i.e. duty cycle or ON time of all the switches is equal at a given operating condition. This helps to regulate output voltage within a narrow range of switching frequency and also reduces the possibility of saturation of core of HF transformer and inductor.

REFERENCES

[1] J. M. Guerrero, F. Blaabjerg, T. Zelev, K. Hemmes, E. Monmasson, and J. I. Frau, "Distributed generation: Toward a new energy paradigm." IEEE Industrial Electronics Magazine 1.4, pp. 52-64, 2010.

[2] R. Giri, V. Choudhary, R. Ayyanar, and N. Mohan, "Common-duty ratio control of input-series connected modular dc-dc converters with active input voltage and load-current sharing," IEEE Transactions Industry Applications, vol. 42, no. 4, pp. 1101–1111, 2006.

[3] U. Prasanna and A. K. Rathore, "Extended range zvs active-clamped current-fed full-bridge isolated dc/dc converter for fuel cell applications: Analysis, design, and experimental results," IEEE Transactions Industrial Electronics, vol. 60, no. 7, pp. 2661–2672, 2013.

[4] S. Lee, J. Park, and S. Choi, "A three-phase current-fed push–pull dc–dc converter with active clamp for fuel cell applications," IEEE Transactions Power Electronics, vol. 26, no. 8, pp. 2266–2277, 2011.

[5] E. Adib and H. Farzanehfard, "Zero-voltage transition current-fed full bridge pwm converter," IEEE Transactions Power Electronics, vol. 24, no. 4, pp. 1041–1047, 2009.

[6] M. Prudente, L. L. Pfitscher, G. Emmendoerfer, E. F. Romaneli, and R. Gules, "Voltage multiplier cells applied to non-isolated dc–dc converters," IEEE Transactions Power Electronics, vol. 23, no. 2, pp. 871–887, 2008.

[7] Xu, C. Zhao, and H. Fan, "APWM plus phase-shift control bidirectional dc-dc converter," IEEE Trans. Power Electron., vol. 19, no. 3, pp. 666–675, May 2004.

[8] F. Z. Peng, H. Li, G.-J. Su, and J. S. Lawler, "A new ZVS bidirectional dc-dc converter for fuel cell and battery application," IEEE Trans. Power Electron., vol. 19, no. 1, pp. 54–65, Jan. 2004.

[9] S. Inoue and H. Akagi, "A bidirectional dc-dc converter for an energy storage system with galvanic isolation," IEEE Trans. Power Electron., vol. 22, no. 6, pp. 2299–2306, Nov. 2007.

[10] J. H. Jung and J.-G. Kwon, "Theoretical analysis and optimal design of LLC resonant converter," Proceedings, Eur.Conf. Power Electronics Appl., pp. 1–10, Sep. 2007.

[11] J. H. Jung, J.-M. Choi, and J.-G. Kwon, "Design methodology for transformers including integrated and center-tapped structure for LLC resonant converters," J. Power Electron., vol. 9, no. 2, pp. 215–223, Mar. 2009.

[12] S.Y.Chen, Z. R. Li, and C.-L. Chen, "Analysis and design of single-stage ac/dc LLC resonant converter,"IEEETrans.Ind.Electron., vol.59,no.3, pp. 1538–1544, Mar. 2012.

[13] X.Fang, H.Hu, Z.J.Shen, and I.Batarseh, "Operation mode analysis and peak gain approximation of the LLC resonant converter," IEEE Trans. Power Electron., vol. 27, no. 4, pp. 1985–1995, Apr. 2012.

[14] J.Zhang, J. Liao, J. Wang, and Z. Qian, "A current-driving synchronous rectifier for an LLC resonant converter with voltage-doubler rectifier structure," IEEE Trans. Power Electron., vol. 27, no. 4, pp. 1894–1904, Apr. 2012.

[15] Jung, Jee-Hoon, Ho-Sung Kim, Myung-Hyo Ryu, and Ju-Won Baek, "Design methodology of bidirectional CLLC resonant converter for high-frequency isolation of DC distribution systems," IEEE Transactions Power Electronics, 28.4, pp. 1741-1755, 2013.

[16] R. Lenk, "Practical Design of Power Supplies," Hoboken,NJ:JohnWiley & Sons, 2005.

[17] S. Kislovski, "Linear variable inductor (LVI) in single-phase off-line telecom rectifiers," Proceeding IEEE Int. Telecom. Energy Conf. (INTELEC), pp. 93–98, 1995.

[18] B.-C. Kim, K.-B. Park, C.-E. Kim, B.-H. Lee, and G.-W. Moon, "LLC resonant converter with adaptive link-voltage variation for a high-power density adapter," IEEE Trans. Power Electron., vol. 25, no. 9, pp. 2248–2252, Sep. 2010.

[19] Klumpner and M. Corbridge, "A two-stage power converter for welding applications with increased efficiency and reduced filtering," in Proc. IEEE Int. Symp. Ind. Electron. (ISIE), Jun. 30, 2008–Jul. 2, 2008, pp. 251–256.

[20] J. Marcos Alonso, M. S. Perdigao, D. G. Vaquero, A. J. Calleja, and E. S. Saraiva, "Analysis, design, and experimentation on constant-frequency DC-DC resonant converters with magnetic control." Power Electronics, IEEE Transactions Power Electronics, 27.3, 1369-1382, 2012.

[21] H. Huang, "Designing an LLC resonant half-bridge power converter," Texas Instruments 2010–2011 Power Supply Design Seminar, SEM1900, 2011.

[22] H. Xiao and S. Xie, "A ZVS bidirectional DC–DC converter with phase shift plus PWM control scheme," IEEE Trans. Power Electron., vol. 23, no. 2, pp. 813–823, Mar. 2008.

[23] Gautam, F. Musavi, M. Edington, W. Eberle, and W. G. Dunford, "An automotive on-board 3.3 kW battery charger for PHEV application," in Proc. IEEE Vehicle Power Propuls. Conf, pp. 1–6, Sep. 6–9, 2011.

[24] D. Fu, F. C. Lee, Y. Liu, and M. Xu, "Novel multi-element resonant converters for front-end dc/dc converters," in Proc. 39th IEEE Annu. Power Electron. Spec. Conf., pp. 250–256, Jun. 15–19, 2008.

[25] Z. Mohamed Youssef, and Praveen K. Jain, "A review and performance evaluation of control techniques in resonant converters," Industrial Electronics Society, 2004. IECON 2004. 30th Annual Conference of IEEE. Vol. 1. IEEE, 2004.

[26] M. Jose Burdio, L. A. Barragan, D. Npvarro, and J. Acero, "Asymmetrical voltage-cancellation control for full-bridge series resonant inverters," IEEE Transactions Power Electronics, 19.2, pp. 461-469, 2004.

[27] W. Tabisz, and C. Y. Lee Fred, "Zero-voltage-switching multi resonant technique-a novel approach to improve performance of high-frequency quasi-resonant converters." IEEE Transactions Power Electronics, 4.4, pp. 450-458, 1989.

[28] H. M. Suryawanshi, K. L. Thakre, S. G. Tarnekar, D. P. Kothary, and A. G. Kothari, "Power factor improvement and closed loop control of an AC-to-DC resonant converter." IEE Proc.-Electric Power Applications, Vol. 149. No. 2. IET, 2002.

[29] H. M. Suryawanshi, S. G. Tarnekar, "Modified LCLC-type series resonant converter with improved performance" IEE Proc.-Electr. Power Appl, Vol. 143, No 5, September 1996.

[30] H. M. Suryawanshi, S. G. Tarnekar, "Improvement of power factor using modified series-parallel resonant converter" IEEE conference on power quality, 1998.

[31] Ye. Zhongming, Praveen K. Jain, Paresh. C. Senan, "A Two stage resonant inverter with control of the phase angle and magnitude of output voltage," IEEE transactions industrial electronics, vol.54, no. 5, October 2007.

[32] S. P. Pachpor, and H. M. Suryawanshi, "Design of DC-DC Converter for Integration of Sources," IEEE International Conference on Power Electronics Drives and Energy Systems (PEDES), Dec. 2014.

[33] Reza Beiranvand, Bizhan Rashidian, Mohammad Reza Zolghandri, Seyed Mohammad Hossein Alavi, "A Design Procedure for Optimizing the LLC Resonant Converter as a Wide Output Range Voltage Source," IEEE transactions power electronics, vol.27, no. 8, pp. 3739–3763, August 2012.

Hiralal M. Suryawanshi (M'06-SM'12) received the B.E. degree in Electrical Engineering from Walchand College of Engineering, Sangli, India, in 1988 and M.E. degree in Electrical Engineering from Indian Institute of Science, Bangalore, in 1994. He has been

1551-3203 (c) 2017 IEEE. Personal use is permitted, but republication/redistribution requires IEEE permission. See http://www.ieee.org/publications_standards/publications/rights/index.html for more information.

This article has been accepted for publication in a future issue of this journal, but has not been fully edited. Content may change prior to final publication. Citation information: DOI 10.1109/TII.2017.2756703, IEEE Transactions on Industrial Informatics

awarded Ph.D. degree by Nagpur University, Nagpur (India) in 1999. He is currently working as Professor in the Department of Electrical Engineering, Visvesvaraya National Institute of Technology, Nagpur, (India). He is Chair Professor of INAE. He is an Associate Editor of IEEE Transaction on Industrial Electronics, USA. He has received Fellow of Indian National Academy of Engineering (FNAE) in 2012 for his outstanding research. He has received IETE-Bimal Bose Award in 2009 and IETE-Biman Behari Sen Memorial Award in 2017 for his leadership in Power Electronics in India. His research interests include the field of Power Electronics, emphasising developmental work in the area of resonant converters, power factor correction, active power filters, FACTs devices, multilevel converters and electric drives.

Snehal P. Pachpor received B.E. degree in Electrical Engineering from Government College of Engineering, Amravati, India, in 1991 and M.Tech. degree in Integrated Power Systems from Visvesvaraya National Institute of Technology, Nagpur, India, in 2007. She is currently pursuing Ph.D. in Electrical Engineering at Visvesvaraya National Institute of Technology, Nagpur, India. She is an Associate Professor in the department of electrical engineering, at KITS, Ramtek, India. Her research interests include power electronics, resonant converters and power quality.

Ajmal T received his B.Tech degree in electrical engineering from government engineering college Thrissur, Kerala in 2012. He obtained his masters degree from Visvesvaraya National Institute of Technology Nagpur in power electronics anddrives in 2015. He is currently working as an Engineer in TATA Elxsi Ltd. Trivandrum. His area of interests include power electronics, soft switching DC-DC converters, Embedded hardware development etc.

Girish G. Talapur received the B.Tech. degree in Electrical and Electronics Engineering from RGM College of Engineering and Technology, Nandyal, India in 2009, M.Tech. degree in Power Systems from Delhi Technological University, New Delhi, India in 2012. He is currently working towards Ph.D. degree in Electrical Engineering at VNIT, Nagpur, India. His research interests include high density power converters, distributed generation, AC Micro-grid, power quality and DC Micro-grid.

Shelas Sathyan received the B.Tech. degree in electrical and electronics engineering from the Government College of Engineering Kannur, Kerala, India, in 2009, and M.Tech. and Ph.D. degree in electrical engineering from the Visvesvaraya National Institute of Technology, Nagpur, India, in 2012 and 2017 respectively. He is currently an assistant Professor with the Department of Electrical Engineering, Shiv Nadar University, Greater Noida, India. His research interests include dc–dc converters for renewable energy sources, soft switching converters, and power factor correction.

Makarand S. Ballal (M'15-SM'16) received B.E. degree in electrical engineering from Government College of Engineering, Aurangabad, India in 1993, M.Tech. degree in integrated power system from VNIT, Nagpur, India in 1997 and Ph.D. in electrical engineering from R.T.M. Nagpur University, India in 2007. He is currently an Associate Professor in the department of electrical engineering, VNIT, Nagpur, India.His current research interests include condition monitoring of electrical machines, power quality, power electronics and drives.

Vijay B. Borghate (M'12) received B.E. (electrical engineering), M.Tech. (integrated power system) and Ph.D. (electrical engineering) from VNIT, Nagpur, India, in 1982, 1984 and 2007 respectively.He is currently working as a Professor in the department of electrical engineering, in the same institute. His area of research includes resonant converters, multilevel inverters.

Manoj R. Ramteke (M'15) received M.Tech. and Ph.D. degrees in electrical engineering from Nagpur University, India, in 1994 and 2008 respectively. He is currently working as an Associate Professor in the department of electrical engineering, VNIT, Nagpur. His research interest includes resonant converters and power quality.

1551-3203 (c) 2017 IEEE. Personal use is permitted, but republication/redistribution requires IEEE permission. See http://www.ieee.org/publications_standards/publications/rights/index.html for more information.

ResearchGate

See discussions, stats, and author profiles for this publication at: https://www.researchgate.net/publication/318987540

KDR Mutation: A High-Frequency Rare Mutation and its Correlation with other Somatic Mutations in Indian Colorectal Cancer...

Article · July 2017

DOI: 10.4172/2469-9853.1000148

CITATIONS
0

READS
18

6 authors, including:

Vani Gupta
Delhi Technological University
1 PUBLICATION **0** CITATIONS

SEE PROFILE

All content following this page was uploaded by Vani Gupta on 08 August 2017.

The user has requested enhancement of the downloaded file.

Journal of Next Generation Sequencing & Applications

Jauhri et al., Next Generat Sequenc & Applic 2017, 4:2
DOI: 10.4172/2469-9853.1000148

Research Article OMICS International

KDR Mutation: A High-Frequency Rare Mutation and its Correlation with other Somatic Mutations in Indian Colorectal Cancer Patients

Mayank Jauhri[1*], Vani Gupta[2], Yogender Shokeen[1], Sachin Minhas[1], Sunita Bhalla[3] and Shyam Aggarwal[1]

[1]*Department of Medical Oncology, Sir Ganga Ram Hospital, New Delhi - 110060, India*

[2]*Department of Biotechnology, Delhi Technological University, New Delhi – 110042, India*

[3]*Department of Pathology, Sir Ganga Ram Hospital, New Delhi – 110060, India*

[*]**Corresponding author:** Mayank Jauhri, Department of Medical Oncology, Sir Ganga Ram Hospital, New Delhi - 110060, India, Tel: +91-9999991433; E-mail: mayank.jauhri@yahoo.com

Rec date: July 06, 2017; **Acc date: July 25**, 2017; **Pub date:** July 27, 2017

Copyright: © 2017 Jauhri M, et al. This is an open-access article distributed under the terms of the creative commons attribution license, which permits unrestricted use, distribution, and reproduction in any medium, provided the original author and source are credited.

Abstract

Aim: This study aims to find out the frequency of KDR mutation in colorectal cancer patients and if any correlation exists between KDR mutation and demographical features or with other common and uncommon gene mutations occurring in colon cancer.

Methods: FFPE samples of 112 patients were analyzed using next generation sequencing.

Results: KDR gene was found to be mutated most frequently (19.6%) as compared to other uncommon gene mutations occurring among patients. 21/22 patients had the p.Q472H type of KDR mutation. It was significantly associated with mutations in PTEN (p=0.003), KRAS (p=0.026), APC (p=0.033), EGFR (p=0.036), NOTCH1 (p=0.029) and ERBB4 (p=0.008) mutations. More number of males (22.06%) harbored KDR mutations than the number of females (15.9%). A higher number of KDR mutations in Stage III (31%) as compared to other stages – I-II (19.23%) and IV (7.31%) was reported. KDR mutations were found to be in greater number in patients with lymph node metastasis (27.3%) as compared to liver metastasis (8%). However, a statistically significant association of any clinical parameter was not found.

Conclusion: Our results suggest that although KDR is a rare somatic mutation in CRC, it plays a pivotal role in the development of colon cancer via angiogenesis pathway.

Keywords: Colorectal cancer; KDR; Mutation; Next generation sequencing; Rare mutation

Introduction

According to World Cancer Reports 2014, cancer accounted for 8.2 million deaths in year 2012 where colorectal cancer (CRC) was the third most common cancer in men and the second most common in women worldwide [1]. Also, as per the statistics given by Indian Council of Medical Research, CRC incidence in India is reported to be 4 patients per every hundred thousand people. CRC is a fatal disease caused and affected by various genetic mutations in biological pathways. This has been shown in KEGG (Kyoto Encyclopedia of Genes and Genomes) pathway database, that colorectal cancer is associated with and occurs via various biological pathways like Wnt, MAPK, PI3K, mTOR, VEGF, cAMP, p53 and other signaling pathways. These pathways may affect the processes of angiogenesis, gene repair, apoptosis, proliferation and differentiation.

Although all other pathways are equally crucial in development of CRC, VEGF pathway is mainly associated with angiogenesis and is responsible for its regulation in tumors. VEGF Pathway is followed through different signaling cascades depending on the type of signaling stimulus received by VEGF receptors, and thus leading to proliferation, migration, permeability or survival [2]. Any mutation in the proto-oncogenes involved in these pathways may lead to cancer by transformation into oncogenes. The VEGF signaling pathway has a key element namely KDR, also known as VEGFR-2 (Vascular Endothelial Growth Factor Receptor-2), stands for Kinase Insert Domain Receptor for VEGF-A. It is known to be a proto-oncogene, thus, affecting tumor angiogenesis. KDR gene is located on chromosome 4 at location 4q12. As per Cancerindex.org and Cancer Genetics Web, KDR gene mutation has been previously reported to be associated with lung and breast cancers. Importantly, KDR gene has been previously shown to play an important role in Cancer development via induction of vascularity, metastasis, apoptosis and proliferation in human colon cancer and breast cancer [3,4].

Thus, it highlights the fact that CRC is well known to be associated with and caused by mutations and epigenetic alterations in certain common as well as rare genes regulating cellular signaling pathways like *KRAS, BRAF, PIK3CA, KDR, PTEN, VHL, SMAD4* and others leading to cell proliferation and metastasis. The association of the disease with commonly occurring genetic mutations like those in *KRAS, BRAF* and *PIK3CA* has been shown in various studies [5-7] but less attention has been given to the role and correlation of genetic mutations which occur rarely such as those in *KDR, PTEN, SMAD4* and others. For such a heterogeneous disease, insights into the role of a rare mutation, in this case – KDR, can open new opportunities for treatment based research with KDR as a novel target. Therefore, in this study, we aim to find out frequency of KDR mutation in patients and if

any correlation exists between KDR and demographical features or between KDR and other genes.

Material and Methods

Patients and samples

This study was initially conducted with 146 patients admitted at Sir Ganga Ram Hospital, New Delhi but after tumor content estimation only samples from 112 CRC patients remained. Clinical features of the patients including gender, age, anatomical site, depth of invasion, tumor size, distant metastasis etc. were recorded. December 2015 was the Follow-up end point of the patients under study.

Formalin fixed paraffin embedded (FFPE) blocks, obtained from Department of Histopathology, with tumor content >30% were used for the study and those rejected were because they were old tissue blocks. Microtome was used for extraction of DNA from five to eight sections of 10 µm each. The DNA was isolated using Qiagen ALL Prep DNA FFPE kit following manufacturer's instructions.

NGS analysis

All isolated dsDNA (double stranded DNA) samples and protein contamination were quantified using Nanodrop and QuBit respectively. The DNA samples with 260/280 ratio between 1.7-2.0 were selected for the study. For further qualification, IlluminaInfinium Assay was performed and only those samples having delCT value less than or equal to 2 were chosen. Sequencing library was created using 200-300 ng of dsDNA added to True Seq Amplicon Cancer Panel (Cat. No. FC-130-1008, Illumina) containing a 48 gene panel. Cancer Panel involved 212 amplicons of length 170-190bp which targeted hot spot mutations in 48 cancer related genes. DNA library was denatured, diluted and processed according to Illumina Protocol. MiSeq Reagent Kit V2 (Cat. No. MS-102-2002, Illumina) and MiSeq Reporter (V2.6.2, Illumina) were used to run samples, generate trimmed FASTQ files and align reads against whole genome build hg19.

Strand NGS V2.1.6 was used for further analysis and filtering of reads. The sequencing depth was 200x and target coverage was 5000x. Filtering out of read was done on the basis of failed vendor QC, average quality less than 20, alignment score below 90 and those with ambiguous characters. For detection of variants at locations in target regions covered by a minimum of 10 reads with at least 2 variant reads and variants with a decibel score of at least 50, Strand NGS variant caller was used. Substitution variants with StrandBias greater than 100% and InDel variants in homopolymer stretches greater than 4 with supporting reads of less than 10% were filtered out. 'SNP Effect Analysis" functionality in Strand NGS was used for analyzing the effect on protein and final variants were annotated using COSMIC (Catalogue of Somatic Mutations in Cancer) database.

Statistical analysis

SPSS 17.0 software was used for the analysis of data. Analysis was performed on two main categories of data; comparison of different clinical characteristics with mutations and co-existence of two or more genes together. Pearson's Chi Square test, Chi-square test or Fischer test of association were used to determine the relation between the above mentioned groups. P value of less than 0.05 was considered to be statistically significant.

Results

In the current study, 112 CRC patient samples were analyzed for mutations occurring commonly and uncommonly in 48 genes. The total number of patients characterized according to their demographical characters is given in Table 1. We calculated the per capita statistics of each clinical parameter for all patients having KDR mutation. It is noteworthy that more number of males (22.06%) harbored KDR mutations than the number of females (15.9%). KDR mutation might be associated with people with age >60 as these people were found to have higher number of KDR mutations (23.07%) as compared to those with age ≤ 60 (19.2%). KDR mutation was found to occur more frequently in Rectum (25%) than in Colon (18.5%).

Clinical Parameters	Total no. of patients (n=112)	No. of patients with KDR mutation	(%)
Sex			
M	68	15	22.06%
F	44	7	15.91%
Age			
≤60	73	14	19.18%
>60	39	9	23.07%
Anatomical site			
Colon	92	17	18.48%
Rectum	20	5	25.00%
Location			
Right	46	13	28.30%
Left	46	8	17.40%
Stage			
I-II	26	5	19.23%
III	45	14	31.11%
IV	41	3	7.31%
Depth of invasion			
T2	8	3	37.50%
T3	75	14	18.67%
T4	79	5	6.33%
Metastasis	--	22	--
Liver	25	2	8.00%
Lymph node	22	6	27.30%
No. of Nodes			
N0 (0)	34	5	14.70%
N1 (1-3)	41	6	14.60%
N2 (>3)	37	11	29.30%

Size of Tumor			
<5 cm	35	13	37.10%
≥ 5 cm	77	9	11.70%

Table 1: Clinical characteristics of 112 colorectal cancer patients.

The right side of colon might be linked to KDR mutations due to occurrence of higher frequency of KDR mutations in Right side (28.3%) while the left side only contained 17.4% mutations. Our study reports higher number of KDR mutations in Stage III (31%) as compared to other stages I and II (19.23%) and IV (7.31%). The T2 stage of depth of invasion with KDR mutation accounts for 37.5% of total patients with T2 stage. KDR mutations were found to be in greater number in patients with lymph node metastasis (27.3%) as compared to liver metastasis (8%).

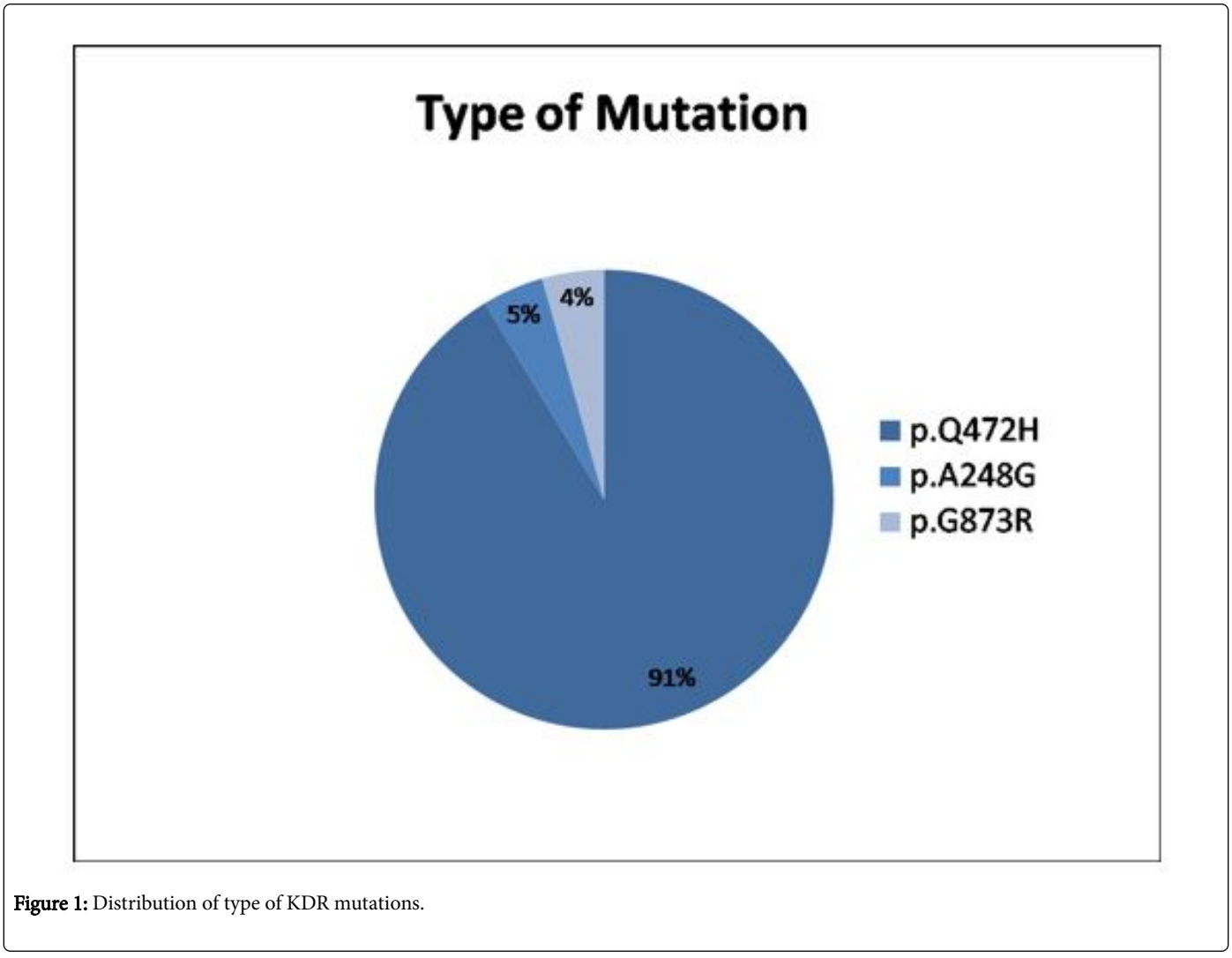

Figure 1: Distribution of type of KDR mutations.

However, our study does not report any statistically significant association of KDR mutation with clinical parameters. In our knowledge, this is the first study targeting at KDR gene mutation in colon cancer using NGS. Out of the mutations in these 48 genes, mutation in KDR was found to be present in 19.6% patients. This is a comparatively high frequency with respect to rarely occurring mutations in other genes. KDR gene was found to contain three types of substitution mutations p.Q472H, p.A248G and p.G873R. The distribution of these mutations among patients is given in Figure 1. 21 patients out of 22 had p.Q472H out of which one had two mutations including p.Q472H and p.A248G. 1 out of 22 patients was reported to have p.G873R type of mutation.

Upon correlation analysis of the 48 genes, we found significant correlation of KDR with six other genes: KRAS (p=0.026), APC (p=0.033), PTEN (p=0.003), ERBB4 (p=0.008), EGFR (p=0.036), and NOTCH1 (p=0.029) where KRAS, APC, PTEN, ERBB4, EGFR and NOTCH1 occurred in common with 12, 11, 10, 4, 3 and 2 out of 22 patients having KDR mutations respectively. Figure 2 shows the distribution of mutations among patients.

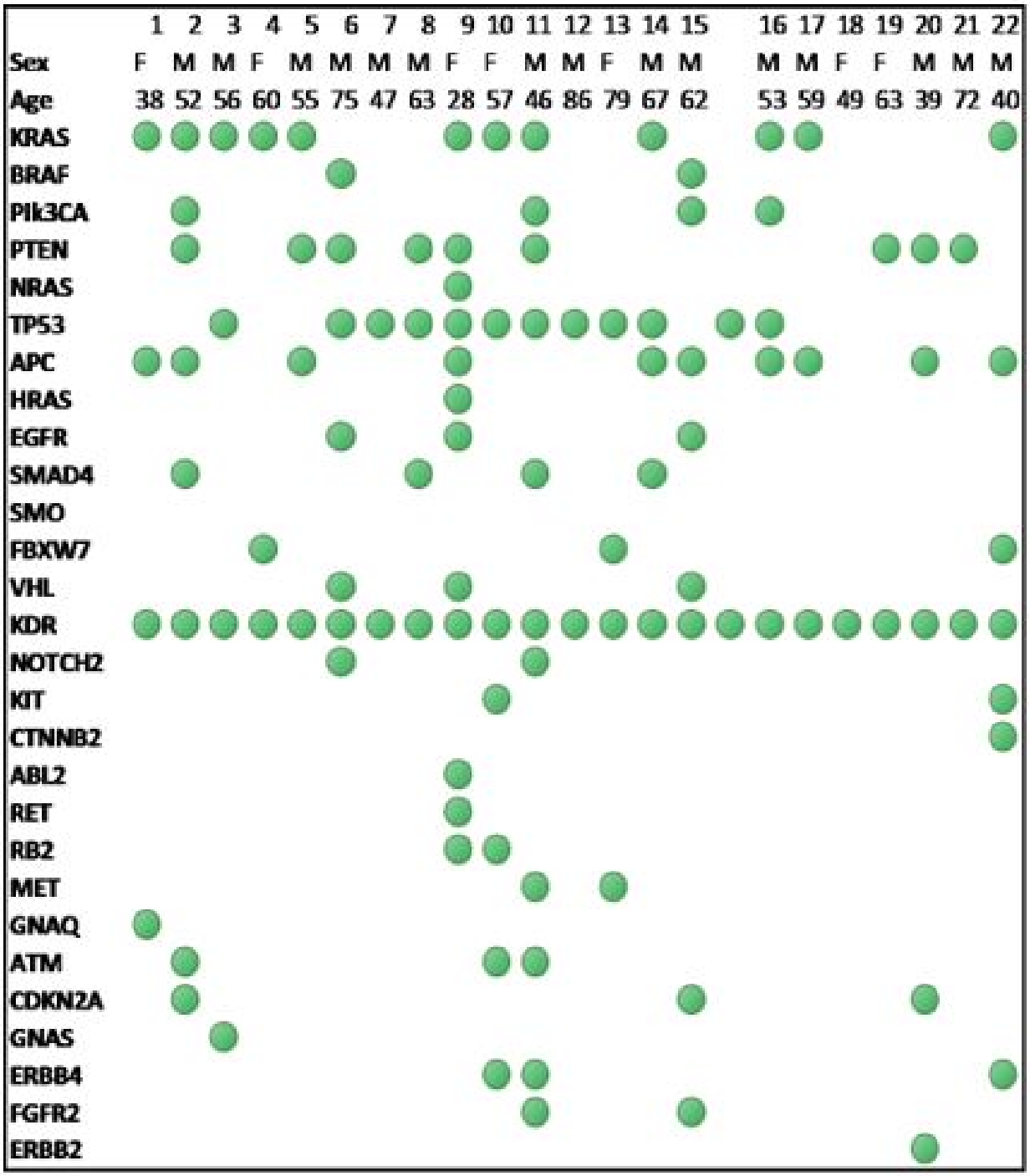

Figure 2: Co-existence of other gene mutations in patients with KDR mutation.

Also, 12 cases of TP53 mutations occurred in coexistence with KDR mutations but the correlation was not of clinical significance. Other genes of the panel did not occur in coexistence with KDR in even a single patient. Figure 3 shows significantly associated double mutations with KDR.

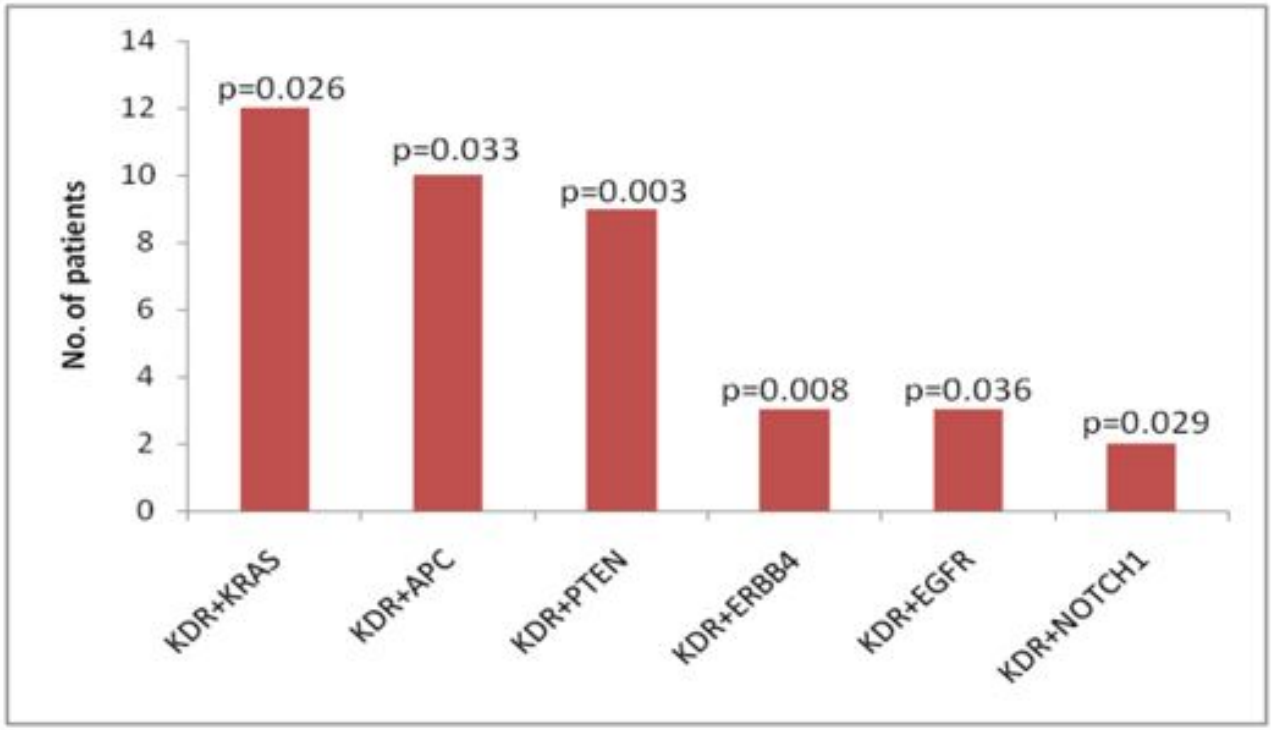

Figure 3: Significantly associated double mutations with KDR. X-axis represents number of patients with double mutations; Y-axis represents double mutations.

Discussion

Colorectal cancer is widely known to be associated with genetic mutations. These genetic mutations usually contribute to one or the other biological pathway involved in carcinogenesis. Pathways involved in development of CRC majorly include Wnt, MAPK, PI3K, mTOR, VEGF, cAMP, p53 and others (KEGG Pathway Database). But out of all these pathways, VEGF pathway plays a major role in development and progression of CRC by the process of angiogenesis. Vascular Endothelial Growth Factor Receptor (VEGFR), also known as KDR (Kinase Domain Receptor) is a protein involved in functioning of VEGF pathway. Mitogens like VEGF-A bind to KDR and signal cell proliferation and angiogenesis.

Thus, mutations in KDR have been previously found to play a role in increasing cell proliferation and angiogenesis. This brings forth the significance of studies conducted to find association between mutations in KDR and clinicopathological parameters as clinically significant results would help open avenues for new drug formulations. In the light of this, activating mutations in KDR gene have been found to be associated with increased KDR protein expression in human angiosarcoma but it has not been found to be correlated with histological type or grade. Despite no significant correlation with the histology, the same study has been successful in bringing forward the frequency of KDR mutation among the patients under study. A 10% mutation frequency of KDR gene has been reported [8]. Another study reported a frequency of 38/123 patients (30.9%) with mutation in KDR gene in Malignant Pleural Mesothelioma [9]. It is noteworthy to mention here that, a study on non-small cell lung cancer reported high Q472H type of KDR mutation number in 33.3% patients [10] and in another study, it has been suggested to play a role of proto-oncogene in Lung Adeno-carcinoma [11]. Therefore, a high frequency (19.6%) of KDR mutation among the patients in our study may also indicate its role in developing cancer. Interestingly, our study also reports high occurrence of p.Q472H (21 out of 22 patients) type of mutation which highlights the role of p.Q472H mutation in the KDR gene. This is also substantiated by the study in which p.Q472H has been found to be mutated in large intestine carcinomas [12].

Mutation in KDR gene was found to be higher in Lymph node metastasis as compared to liver metastasis in our study. This supports the study in which expression of VEGF-C, (which upon proteolytic processing binds to VEGFR-2 (KDR)), was significantly associated with lymph node metastasis in gastric carcinoma [13]. But on the other hand, this result is also in contrast to a previous study in which 27% cases with KDR mutations were associated with Colorectal Liver metastasis [12]. This difference might be present due to the small patient population size in our study. KDR gene has been associated with VEGF signaling pathway which is also linked with PIK3CA and PTEN proteins. Our study reports a significant correlation between KDR and PTEN gene mutations which suggests their associated role in development of colon cancer. However, this is in contrast to one study conducted in Small cell lung cancer patients in which PI3K/AKT/mTOR pathway status did not correlate with KDR gene [14]. This difference might be present due to different cancer groups and the small number of patients studied. Furthermore, in a recently reported case study [15], KDR mutation, KRAS mutation and APC mutation were found together in a patient of colon cancer although no clinical significance was reported for their correlation. This case study collectively with our results indicates that KRAS and KDR mutation

can together play a role in proliferation of tumor cells when VEGF signaling pathway proceeds via MAPK signaling route. Not only this, APC and KDR mutations have been independently reported to play a role in tumorigenesis of gastrointestinal cancer and colon cancer but no previous reports of correlation between APC and KDR were found [16-18]. Also, our study suggests a significant correlation between NOTCH1 and KDR (VEGFR2) but we found no literature supporting the same. However, NOTCH1 has been associated with VEGFR1 in previous studies [19]. Moreover, a discussion on NOTCH and VEGF signaling proposes a model where NOTCH1 and VEGFR2 may play symbiotic roles in angiogenesis [20]. This indicates that there might also be an association of NOTCH1 and VEGFR2 in combined development towards angiogenesis which strengthens our results. Interestingly, KDR (VEGFR2) and EGFR have been identified as potential targets for many anti-cancer therapies [21-23] but no studies could be found showing direct correlation between KDR and EGFR. The combined therapeutic targeting to treat cancer is also suggestive of their significant association in regulating cancer pathways which can be seen in our results which shows a significant correlation between mutations in EGFR and KDR genes. Not only this, drugs targeting EGFR, ERBB4 and KDR together have also been studied previously [24]. Moreover, EGFR and ERBB4 belong to the same Receptor Tyrosine Kinase family and work in close association. Thus, a correlation between EGFR and KDR mutations may also indicate the possibility of ERBB4 and KDR mutation. But the results need to be validated by performing assays in larger number of patients.

However, high KDR protein expression has been previously reported in many cancer studies projecting its role in tumorigenesis and angiogenesis [8,25,26]. Overall, this can mean that the KDR mutation leads to high expression of KDR protein. In addition, KDR gene mutation has been previously reported to play a therapeutic role using Regorafenib in metastatic colon cancer [14] as well as in Non-small cell lung cancer [27]. On the contrary, it has also been reported to occur as an adverse effect of Ramucirumab therapy [28] and may lead to side effects when used with FGFR inhibitors for treatment. Additionally, COSMIC database suggests its association with Sorafenib. So, mutation in KDR gene is therapeutically important and any association with clinical parameters or pathways can further help in embarking research focused on drugs targeting KDR. Intriguingly, KDR gene as a potential therapeutic target for angiogenesis inhibitor drugs has been reported previously [29-31].

Conclusion

Our results in combination with previous studies suggest a role for KDR in colon cancer also making it a potential therapeutic target for various drugs like Regorafenib and Sorafenib. Thus, the results from our study can be used for employing targeted therapy in patients with KDR mutations. Besides, it might also be associated with one or more clinical parameters which can help prognostic studies. Significant correlations of KDR mutation with other gene mutations – KRAS, APC and PTEN has shown a new possibility for association of signaling pathways in development of tumors and angiogenesis in Colorectal Cancer. Further studies on KDR and other genes' expression and polymorphisms in colorectal cancer using a larger patient cohort are required for the validation of these results.

Acknowledgement

The study was funded by Merck Serono India. The authors express their gratitude to Strand Life Sciences for their support during data preparation and to Mrs. Parul Takkar for her help in statistical analysis.

Permissions

Ethics approval

Institutional and/or National Committee ethical standards were followed throughout the study. All procedures involving human participants in the study were in accordance with the 1964 Helsinki declaration and its later amendments or comparable ethical standards. This article does not contain any studies with animals performed by any of the authors.

Informed consent

Informed consent was obtained from all individual participants included in this study.

References

1. International Agency for Research of Cancer, WHO (2012) Fact sheets of cancer.
2. KEGG Pathway Database (2005) Kanehisa Laboratories, Japan.
3. Takahashi Y, Kitadai Y, Bucana CD, Cleary KR, Ellis ML (1995) Expression of vascular endothelial growth factor and its receptor, KDR, correlates with vascularity, metastasis, and proliferation of human colon cancer. Cancer Res 55: 3964-3968.
4. Zhang X, Ge YL, Zhang SP, Yan P, Tian RH (2014) Down regulation of KDR expression induces apoptosis in breast cancer cells. Cell Mol Biol Lett 19: 527-541.
5. Arrington A, Heinrich E, Lee W, Duldulao M, Patel S, et al. (2012) Prognostic and predictive roles of KRAS mutation in colorectal cancer. Int J Mol Sci 13: 12153-12168.
6. Barras D (2015) BRAF mutation in colorectal cancer: An update. Biomark Cancer 7: 9-12.
7. Cathomas G (2014) PIK3CA in colorectal cancer. Front Oncol 4: 1-4.
8. Antonescu CR, Yoshida A, Guo T, Chang NE, Zhang L, et al. (2009) KDR activating mutations in human are sensitive to specific kinase inhibitors. Cancer Res 69: 7175–7179.
9. Lo Iacono M, Monica V, Righi L, Grosso F, Libener R, et al. (2015) Targeted next-generation sequencing of cancer genes in advanced stage malignant pleural mesothelioma: A retrospective study. J Thorac Oncol 10: 492–499.
10. Masago K, Fujita S, Muraki M, Hata A, Okuda C, et al. (2015) Next-generation sequencing of tyrosine kinase inhibitor-resistant non-small-cell lung cancers in patients harboring epidermal growth factor-activating mutations. BMC Cancer 15: 908.
11. Tanoue LT (2010) Somatic mutations affect key pathways in lung adenocarcinoma. Yearbook of Pulmonary Disease 115–117.
12. Lee SY, Haq F, Kim D, Jun C, Jo HJ, et al. (2014) Comparative genomic analysis of primary and synchronous metastatic colorectal cancers. PLoS one 9: e90459.
13. Onogawa S, Kitadai Y, Amioka T, Kodama M, Cho S, et al. (2005) Expression of vascular endothelial growth factor (VEGF)-C and VEGF-D in early gastric carcinoma: correlation with clinicopathological parameters. Cancer Lett 226: 85–90.
14. Cheng H, Shcherba M, Pendurti G, Liang Y, Piperdi B, et al. (2014). Targeting the PI3K/AKT/mTOR pathway: Potential for lung cancer treatment. Lung Cancer Manag 3: 67–75.

View publication stats

15. Loaiza-Bonilla A, Jensen CE, Shroff S, Furth E, Bonilla-Reyes PA, et al. (2016) KDR mutation as a novel predictive biomarker of exceptional response to regorafenib in metastatic colorectal cancer. Cureus 8: e478.
16. Morin PJ, Vogelstein B, Kinzler KW (1996) Apoptosis and APC in colorectal tumorigenesis. Proc Natl Acad Sci USA 93: 7950–7954.
17. Taketo MM (2006) Wnt signaling and gastrointestinal tumorigenesis in mouse models. Oncogene 25: 7522–7530.
18. Warren RS, Yuan H, Matli MR, Gillett NA, Ferrara N (1995) Regulation by vascular endothelial growth factor of human colon cancer tumorigenesis in a mouse model of experimental liver metastasis. J Clin Invest 95: 1789–1797.
19. Paiva T, De Jesus V, Marques R, Anastácio Da-Costa AA, Petaccia De-Macedo M, et al. (2015) Angiogenesis-related protein expression in bevacizumab-treated metastatic colorectal cancer: NOTCH1 detrimental to overall survival. BMC Cancer 15: 643.
20. Hellstrom M, Phng L, Gerhardt H (2007) VEGF and Notch Signaling. Cell Adh Migr 1: 133-136.
21. Ciardiello F, Troiani T, Bianco R, Orditura M, Morgillo F, et al. (2006) Interaction between the epidermal growth factor receptor (EGFR) and the vascular endothelial growth factor (VEGF) pathways: A rational approach for multi-target anticancer therapy. Ann Oncol 7: vii109-114.
22. Traxler P, Allegrini PR, Brandt R, Brueggen J, Cozens R, et al. (2004) AEE788: A dual family epidermal growth factor receptor/ErbB2 and vascular endothelial growth factor receptor tyrosine kinase inhibitor with antitumor and antiangiogenic activity. Cancer Res 64: 4931-4941.
23. Yokoi K, Thaker PH, Yazici S, Rebhun RR, Nam DH, et al. (2005) Dual inhibition of epidermal growth factor receptor and vascular endothelial growth factor receptor phosphorylation by AEE788 reduces growth and metastasis of human colon carcinoma in an orthotopic nude mouse model. Cancer Res 65: 3716–3725.
24. Pan Y, Xu Y, Feng S, Luo S, Zheng R, et al. (2012) SKLB1206, a novel orally available multikinase inhibitor targeting EGFR activating and T790M mutants, ErbB2, ErbB4, and VEGFR2, displays potent antitumor activity both in vitro and in vivo. Mol Cancer Ther 11: 952-962.
25. Teicher BA (2012) Searching for molecular targets in sarcoma. Biochem Pharmacol 84: 1–10.
26. Phillips HS, Kharbanda S, Chen R, Forrest WF, Soriano RH, et al. (2006) Molecular subclasses of high-grade glioma predict prognosis, delineate a pattern of disease progression and resemble stages in neurogenesis. Cancer Cell 9: 157–173.
27. Veldore VH, Patil S, Satheesh CT, Shashidhara HP, Tejaswi R, et al. (2015) Genomic profiling in a homogeneous molecular subtype of non-small cell lung cancer: An effort to explore new drug targets. Indian J Cancer 52: 243-248.
28. Lim YH, Odell ID, Ko CJ, Choate KA (2015) Somatic p.T771R KDR (VEGFR2) Mutation arising in a sporadic angioma during ramucirumab therapy. JAMA Dermatol 151: 1240-1243.
29. Gavilondo JV, Hernández-Bernal F, Ayala-Ávila M, De La Torre AV, De La Torre J, et al. (2014) Specific active immunotherapy with a VEGF vaccine in patients with advanced solid tumors. Results of the CENTAURO antigen dose escalation phase I clinical trial. Vaccine 32: 2241–2250.
30. Li Q, Wang Y, Zhang L, Chen L, Du Y, et al. (2016) Naringenin exerts anti-angiogenic effects in human endothelial cells: Involvement of ERRα/VEGF/KDR signaling pathway. Fitoterapia 111: 78–86.
31. Yu DH, Lu Q, Xie J, Fang C, Chen HZ (2010) Peptide-conjugated biodegradable nanoparticles as a carrier to target paclitaxel to tumor neovasculature. Biomaterials 31: 2278–2292.

Accepted Manuscript

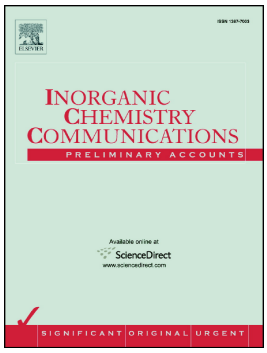

Manganese(III) mediated synthesis of A2B Mn(III) corroles: A new general and green synthetic approach and characterization

Omprakash Yadav, Atul Varshney, Anil Kumar

PII: S1387-7003(17)30542-7
DOI: doi:10.1016/j.inoche.2017.10.018
Reference: INOCHE 6806

To appear in: *Inorganic Chemistry Communications*

Received date: 2 July 2017
Revised date: 16 October 2017
Accepted date: 17 October 2017

Please cite this article as: Omprakash Yadav, Atul Varshney, Anil Kumar , Manganese(III) mediated synthesis of A2B Mn(III) corroles: A new general and green synthetic approach and characterization. The address for the corresponding author was captured as affiliation for all authors. Please check if appropriate. Inoche(2017), doi:10.1016/j.inoche.2017.10.018

This is a PDF file of an unedited manuscript that has been accepted for publication. As a service to our customers we are providing this early version of the manuscript. The manuscript will undergo copyediting, typesetting, and review of the resulting proof before it is published in its final form. Please note that during the production process errors may be discovered which could affect the content, and all legal disclaimers that apply to the journal pertain.

ACCEPTED MANUSCRIPT

Manganese(III) mediated synthesis of A_2B Mn(III)corroles: A new general and green synthetic approach and characterization

Omprakash Yadav, Atul Varshney and Anil Kumar*

Department of Applied Chemistry, Delhi Technological University, Bawana Road, Delhi-42, India.

E-mail: *anil_kumar@dce.ac.in*

Abstract: A new general and green synthetic protocol for the synthesis of manganese(III) metallocorroles has been developed from substituted aryl aldehydes and 5-(4-nitrophenyl)dipyrromethane using manganese salt as template. This is the first report in the synthesis of corroles: the formation of direct C-C bond through metal initiation. This method allows higher working concentrations than those previously reported. The new A_2B manganese(III) metallocorroles were synthesized in good yield for different applications. The single crystal X-ray structure of 10-(3,4,5-fluorophenyl)-5,15-bis(4-nitrophenyl)manganese(III) corrole is also reported and shows that manganese atom is situating atop on macrocyclic plane.

Keywords: Corroles, Metallocorroles, Green Chemistry, dipyrromethane, one-pot method

ACCEPTED MANUSCRIPT

ACCEPTED MANUSCRIPT

Graphical abstract

A new general and green protocol for metallocorroles using metal as template and report for direct C-C bond formation in corroles synthesis.

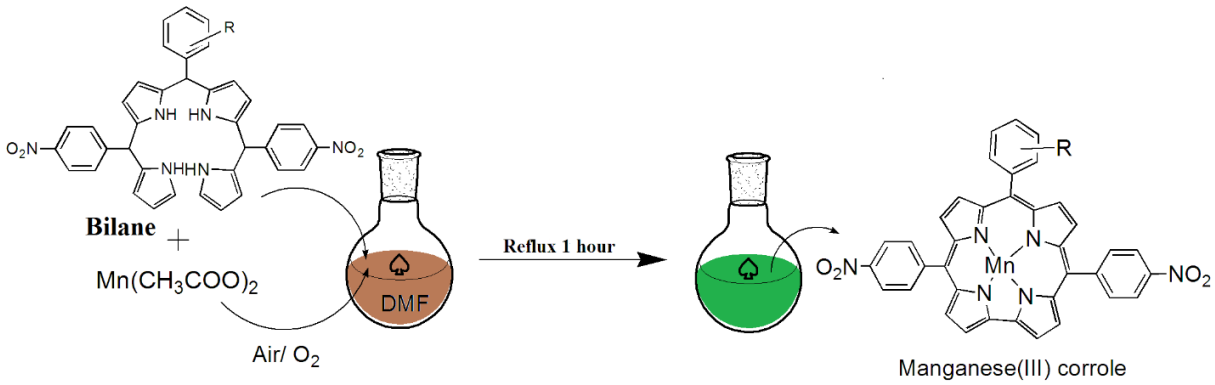

Corrole chemistry increased exponentially after the discovery of facile, convenient and high yield synthetic methods developed by Paloesse, Gross, Gryko and their coworkers.[1-6] In recent years, metallocorroles are of great interest due to their exceptional properties that free base corroles, an trianionic ligand, induces on metal chelated to it.[7] The important property imparted by free base ligand is the stability of metal in high oxidation states.[7] Because of this utility of, metallocorroles are responsible for important aspects related to energy, photochemistry, luminescence spectroscopy and other biological applications.[8-9] The important are activation of small molecules such as O_2, CO_2, H^+, H_2O_2, HOONO and more.[10-14] Manganese and iron complexes have already been introduced as robust catalyst for such type of applications: oxygen atom transfer reactions, oxygen, carbon dioxide and protons reduction reactions and antioxidants in biological systems.[11,12,15-30] It has been clearly seen that manganese corroles have performed excellently in advanced applications.[9,31] Therefore, corroles and metallocorroles synthesis have attracted great attention in recent years.[31] Looking back into the synthesis of corroles, the first corrole was synthesized by Johnson and Kay by cyclisation of 5,5'-bi-(5'-bromodipyrromethenes)

ACCEPTED MANUSCRIPT

and introduced a *meso* carbon atom, cyclisation of bilene and biladienes with the introduction of link between two α-carbon atoms but resulted into the formation of a palladium(II)-10-oxacorrole instead.[32]Later on biladenedihydrobromide derivative was used for the synthesis of corrole using different metal salts as template and rhodium metal complex was confirmed by X-ray crystallographic method.[33] The metallocorroles were obtained only in the case of manganese and iron metal salts used.[33-34] Manganese as a template has been used to synthesize corrole with the condensation of dipyrrins in DMF.[34] Paolesse and co-workers reported first direct synthesis of cobalt corrole using 3,4-Dimethyl-2-(a-hydroxybenzyl)- pyrrole-5-carboxylic acid as monopyrrolic sourse.[35] Superoxide induced cyclizations of metallo-2,2'-bidipyrrins was found to be selective for the synthesis of corrole.[36] Alternatively, the reaction of free base octaethylcorrole with carbonyl complex of manganese in toluene also gave metallocorroles.[37]Till now, the methods developed by Murakami,[38] Gross[3-4]and Gryko,[6] the oxidative cyclization of α, ω-didesoxybiladienes-*a,c* are being used for the preparation of corroles. The most convenient method to obtain manganese(III) corroles after the facile syntheses of free base corroles is the reaction of free base corroles with manganese(II) acetate dihydrate in polar solvents.[2-7]To date, there is no report available in the literature for the synthesis of A_2B manganese(III) corroles directly by a reaction between bilane and metal salt to yield metallocorroles via difficult C-C bond formations.

In this paper, we report first the direct C-C bond formation in the synthesis of manganese(III) corroles with various substituents, which can be used with a large variety of substituted benzaldehydes including sterically hindered, electron withdrawing, electron releasing group substituted (Scheme 1). The idea of selecting 5-(4-nitrophenyl)dipyrromethane is that the large number of applications were reported on such corroles and metallocorroles which contain C_6F_5

ACCEPTED MANUSCRIPT

groups on their *meso*-carbon positions.[3-6] Usually, these corroles have high stability and ease of an excellent characterization tool: the ^{19}F NMR spectroscopy. It is very important to develop protocols for such types of corroles which do not contain the strong electron withdrawing and very expensive C_6F_5 groups on *meso* positions. The choice of 5-(4-nitrophenyl)dipyrromethane seems to be practically interesting candidate to fulfill the desired requirement.[3] Further, reduction of nitro group will certainly enhance the corroles electron – richness and reduced product 4-aminophenyl moieties may be used as synthetic models for further modifications.

All the manganese(III) corroles were characterized by UV–visible spectroscopy, elemental analysis and mass spectrometry. Due to paramagnetic nature of manganese(III) corroles, NMR spectroscopy was not performed to characterize the compounds. The electronic spectra of manganese(III) corroles reported, herein, are similar to those of previously reported manganese(III) porphyrins and corroles.[16-17] The UV-visible spectrum as shown in Fig. 1 confirms the formation of desired manganese corroles and calculated yield were found to be comparable to available literature.[16-17] They display split Soret bands (λ_{max} = 400-425 nm), a ligand-sensitive absorbance at λ_{max} = 480-490 nm and broad Q bands at 600 nm (Fig. 1).

The present reaction conditions were optimized with respect to solvent, temperature, time of the reaction and use of reactants used. Initially, we planned to follow the procedure as reported for metalloporphyrins.[39] The 5-(4-nitrophenyl)dipyrromethane and pentafluorobenzaldehyde was dissolved in DMF and HCl was added dropwise over a period of 10 min. and the resulting reaction mixture was refluxed. The progress of the reaction was checked with TLC and UV-visible spectroscopy. But we could not succeed to get desired metallocorroles. So we changed our strategy and follow the path of first synthesizing bilane using 5-(4-nitrophenyl)dipyrromethane and aryl aldeydes in methanol-water containing HCl mixture. The

ACCEPTED MANUSCRIPT

bilane was extracted and dissolved in DMF. This reaction was carried out with two different routes. In Route-**I** as shown in Scheme 1 produced manganese(III) corroles after the continuous stirring of reactants overnight and yielded desired product in low yield. Whereas in Route-**II** the reaction mixture was refluxed and yielded desired product in 1 hr. The progress of the reaction was checked with TLC and UV-visible spectroscopy which shows the formation of product after the refluxing of 15 min. only but completion of the reaction was confirmed after 1 hr in the form of high yield of product. The yield of the manganese(III) corroles also depend upon the nature of substituents present on the aldehyde used in the reaction. In the case of synthesis of A_2B corroles, pentafluorobenzaldehyde and 5-(4-nitrophenyl)dipyrromethane were used to optimize the reaction conditions. The different arylaldeydes used are tabulated in Table 1. Using this method, we have synthesized a variety of manganese (III) corroles including complexes with sterically encumbered, electron withdrawing and electron releasing group substituted corroles in good yields.

ACCEPTED MANUSCRIPT

ACCEPTED MANUSCRIPT

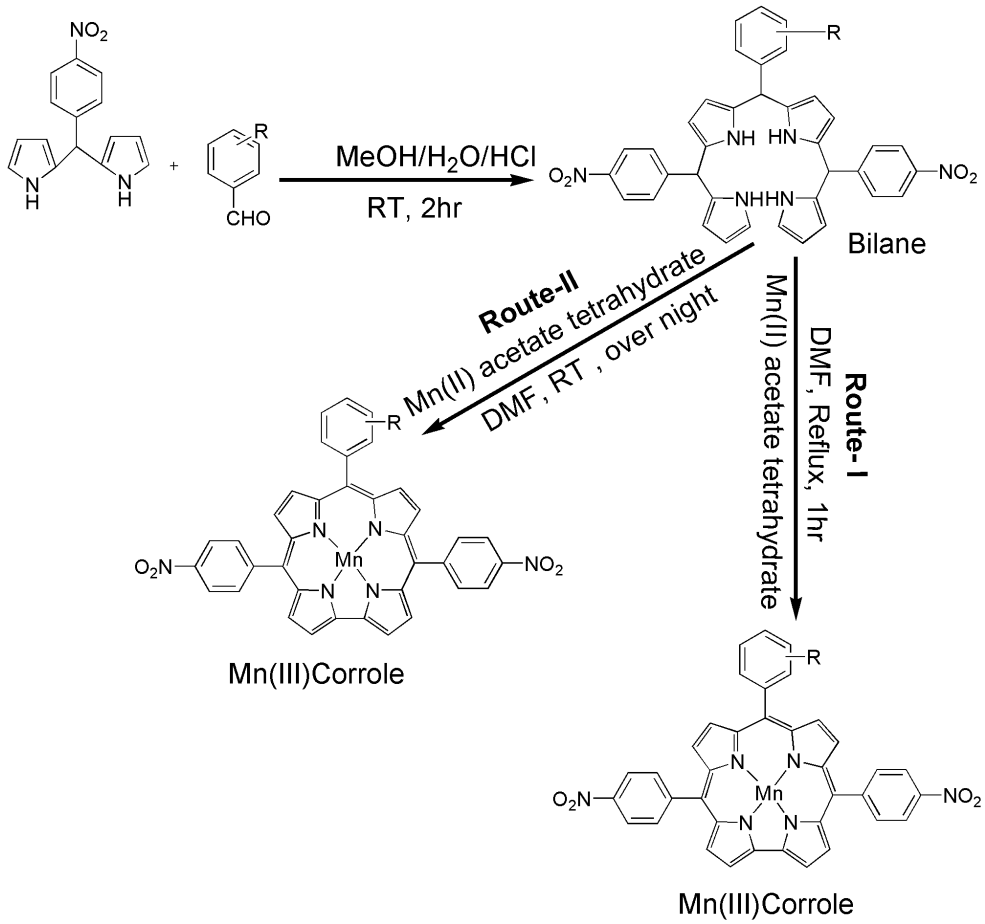

Scheme 1

ACCEPTED

ACCEPTED MANUSCRIPT

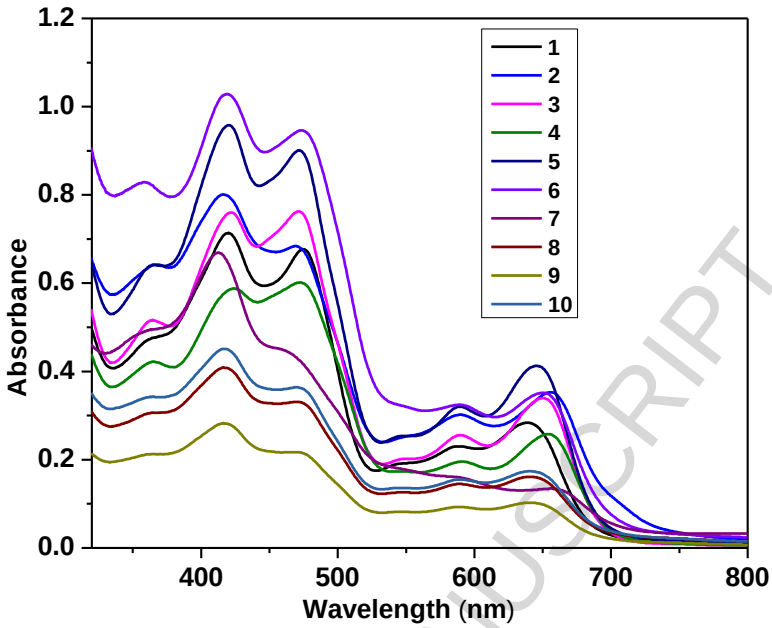

Fig. 1: UV-visible spectra of synthesized manganese(III) corroles.

In a typical reaction freshly distilled pentafluorobenzaldehyde (130 µL, 0.5 mmol) and 5-(4-nitrophenyl)dipyrromethane[40] (566 mg, 1.0 mmol) was dissolved in methanol (200 mL) and mixture and water (100 mL) containing HCl (36%, 10 mL) was added slowly. The reaction mixture was kept on stirring for two hours at room temperature under air. After two hours of stirring, the crude product was washed and extracted several times with chloroform and dried over anhydrous sodium sulfate. The solvent was removed using a vacuum pump. The extracted product was dissolved in 50 ml of argon-purged dimethylformamide. The mixture was stirred and 2.5 equiv. of manganese (III)acetatetetrahydrate was added. The final reaction mixture was refluxed for 1 h in air. The rate of the reaction was monitored with TLC. After 1 hr refluxing, DMF was removed in *vacuo*. The dark colored product was dissolved in dichloromethane and purified by flash chromatography over silica gel using ethyl acetate as eluent. The final product

ACCEPTED MANUSCRIPT

was purified over alumina using ethyl acetate-hexane (7:3) mixture as eluent. The purified product was recrystallized using ethyl acetate and hexane and afforded dark green crystals, **185 mg, 24 % yield**.

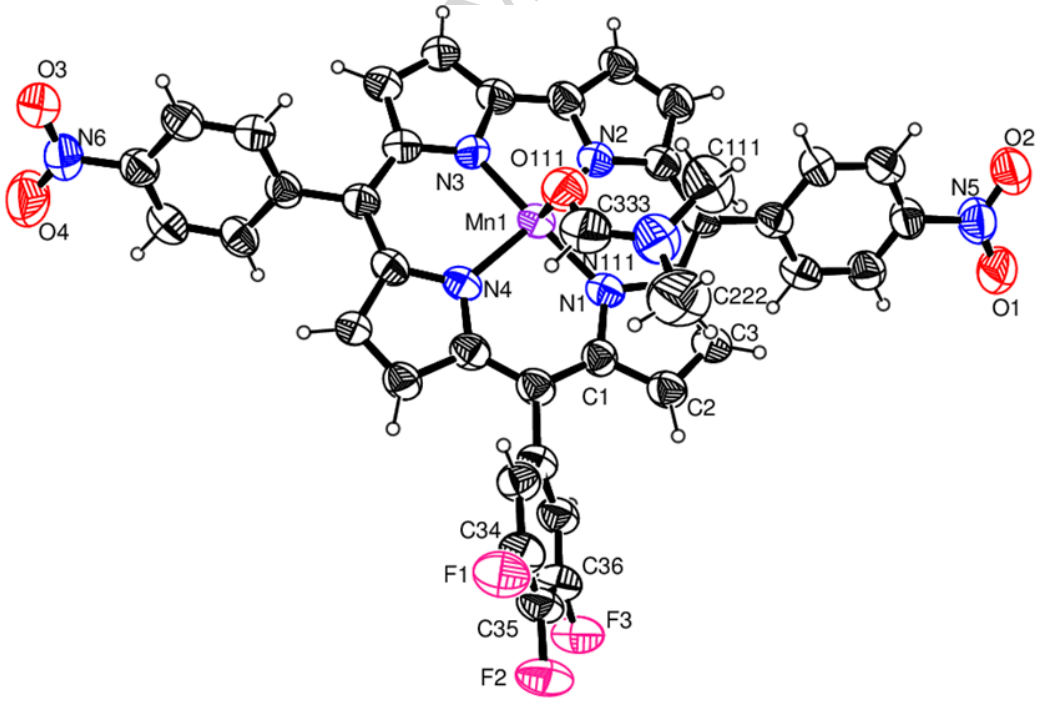

Fig. 2. Single crystal X-ray structure of **3.**

ACCEPTED MANUSCRIPT

The single crystal X-ray structure of one of the manganese(III) corrole, **3**, obtained is shown in Fig. 2. Manganese atom is axially coordinated to oxygen atom of dimethylformamide. Manganese atom is situated 0.257 Å above the mean plane of 4 pyrrolic nitrogens and 0.32 Å above the mean plane of macrocyclic core atoms. These values are comparable to axial coordination to the manganese atoms in corroles and values are comparable to the literature value reported earlier.[17, 41]

In conclusion, we first report that metal ion initiates the cyclisation of bilane through carbon-carbon bond formation to yield manganese(III) corroles under aerobic conditions. The advantage of our method is the general nature of the reaction which is valid for any type of substituted aldehyde and aryldipyrromethane. This method also avoids the difficult steps to form firstly C-C bond formation and then cyclization of dipyrrin using metal as reported in the literature. So, methodology reported in this paper follow the principles of *Green Chemistry* so protocol is *Green* in nature. The yield of the manganese(III) corroles was reasonably good and the reaction time was shorter than in other methods reported. Also, higher concentration of reagents can be employed.

ACCEPTED MANUSCRIPT

ACCEPTED MANUSCRIPT

Table 1: Analytical data of manganese(III) corroles. (Elemental analysis given in ref. no. 42)

Compound		Bilane 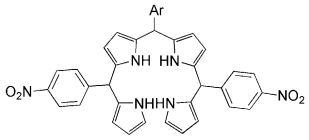	Yield (%)	UV-visible data (in nm)	HRMS Calculated (Found)
1	Ar =	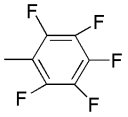	24%	419,474,591, 639	758.0534 (758.0521)
2	Ar =	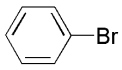	14%	416,471,591, 656	746.0110 (746.0138)
3	Ar =	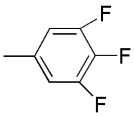	20%	423,470,590, 639	722.0722 (722.0706)
4	Ar =	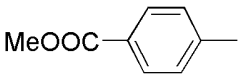	22%	420,473,588, 644	726.1060 (727.1126)
5	Ar =	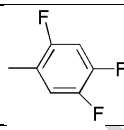	19%	419,474,590, 651	722.0722 (722.0718)
6	Ar =	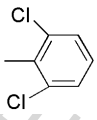	11%	412,464,590, 660	736.0225 (737.2099)
7	Ar =	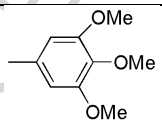	17%	418,474,590, 639	758.1322 (758.1302)
8	Ar =	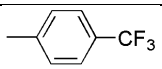	07%	418,472,590, 660	736.0879 (736.0863)
9	Ar =	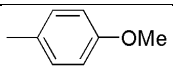	10%	419,472,589, 641	698.1110 (698.1122)
10	Ar =	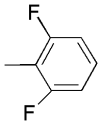	20%	418,471,591, 641	704.0816 (705.0866)

ACCEPTED MANUSCRIPT

Acknowledgment

OPY thanks to CSIR and AV thanks to UGC for fellowship and AK thanks to DTU for infrastructural facilities.

Supporting Information

HRMS of the reported metallocorroles can be found in supporting information file.

References

1. Paolesse, R. in *The Porphyrin Handbook*, ed. Kadish, K. M.; Smith, K. M.; Guilard, R. Academic, San Diego, CA, **2000**, vol. 2, ch. 11,p. 201–232.(b) Erben, C.; Will, C. S.; Kadish, K. M. in *The Porphyrin Handbook*, ed. Kadish, K. M.; Smith, K. M.; Guilard, R. Academic, San Diego, CA, **2000**, vol. 2, ch. 12, p. 233–300.
2. (a) Paolesse, R.; Licoccia, S.; Fanciullo, M.; Morgante, E.; Boschi, T. *Inorg. Chim. Acta*, **1993**, *203*, 107-114. (b) Paolesse, R.; Licoccia, S.; Bandoli, G.; Dolmella, A.; Boschi, T. *Inorg. Chem.*, **1994,** *33*, 1171-1176. (c) Adamian,V. A.; Souza, F. D.; Licoccia, S.; Di Vona, M. L.; Tassoni, E.; Paolesse, R.; Boschi, T.;Smith, K. M. *Inorg. Chem.*, **1995**, *34*, 532-540.
3. (a) Gross, Z.; Galili, N.; Saltsman, I. *Angew. Chem., Int. Ed.*, **1999**, *38*, 1427-1429. (b) Gross, Z.; Galili, N.; Simkhovich, L.; Saltsman, I.; Botoshansky, M.; Blaser, D.; Boese, R.; Goldberg, I.*Org. Lett*, **1999,** *1*, 599-602. (c) Gryko, D. T. *Chem. Commun.*, **2000**, 2243-2244. (d) Paolesse, R.; Nardis, S.; Sagone, F.; Khoury, R. G. *J. Org. Chem.*, **2001**, *66*, 550-556. (e) Gryko, D. T and K. Jadach, *J. Org. Chem.*, **2001**, *66*, 4267-75. (f) Asokan, C. V.; Smeets, S.; Dehaen, W.*Tetrahedron Lett.*, **2001**, *42*, 4483-4485.
4. (a) Gross, Z.; Simkhovich, L.; Galili, N. *Chem. Commun.*, **1999**, 599-600. (b) Gross, Z.; Golubkov, G.; Simkhovich, L. *Angew. Chem., Int. Ed.*, **2000**, *39*, 4045-4047. (c) Golubkov, G.;

ACCEPTED MANUSCRIPT

Bendix, J.; Gray, H. B.; Mahammed, A.; Goldberg, I.; DiBilio, A. J.; Gross, Z. *Angew. Chem., Int. Ed.*, **2001,** *40*, 2132-2134.

5. (a) Paolesse, R.; Pandey, R. K.; Forsyth, T. P.; Jaquinod, L.;Gerzevske, K. R.; Nurco, J.; Senge, M. O.; Licoccia, S.; T. Boschi, T.; Smith, K. M. *J. Am. Chem. Soc.*, **1996**, *118*, 3869-3882. (b) Jérome, F.; Gros, C. P.; Tardieux, C.; Barbe, J.-M.; Guilard, R. *Chem. Commun.*, **1998**, 2007-2008. (c) Paolesse, R.; Macagnano, A.; Monti, D.; Tagliatesa, P.; Boschi , T. *J. Porph. Phthal.* **1998**, *2*, 501.-510 (d) Jérome, F.; Gros, C. P.; Tardieux, C.; Barbe, J.-M.; Guilard, R. *New J. Chem.* **1998**, 1327-1329. (e) Paolesse, R.; Sagone, F.; Macagnano, A.; Boschi,T.;Prodi,L.;Mantalti,L.;Zaccheroni,N.;Bolettaand,F.;Smith,K. M.*J. Porph. Phthal.***1999**, *3*, 364-370. (f) Paolesse, R.; Froiio, A.; Nardis, S.; Mastroianni, M.; Russo, M.; Nurco, D. J.; Smith,K. M.*J. Porph. Phthal.***2003**, 7, 585-595.
6. (a) Gryko, D. T. *Eur. J. Org. Chem.* **2002**, 1735–1743. (b) Ghosh, A. *Angew. Chem., Int. Ed.* **2004**, *43*, 1918-1931. (b) Gryko, D. T.; Koszarna, B. *Synthesis* **2004**, *13*, 2205–2209. (c)Koszarna, B.; Gryko, D. T. *J. Org. Chem.* **2006**, *71*, 3707–3717. (d) Broring, M.; Funk, M.; Milsmann, C. *J. Porph. Phthal.* **2009**, *13*, 107–113.
7. (a)Sessler, J. L.; Weghorn, S. J. Expanded, Contracted, & Isomeric Porphyrins; Pergamon Press: Oxford, U.K., **1997**; Vol. 15, Chapter 2. (b) Gross, Z.; Gray, H. B. *Comments Inorg. Chem*. **2006**, *27*, 61-72.
8. (a)Palmer,J. H.; Durrell,A. C.;Gross,Z.;Winkler,J. R.;Gray,H. B.*J.Am. Chem. Soc.* **2010**, *132*, 9230–9231. (b) Reith,L. M.; Himmelsbach,M.; Schoefberger,W.; Knör,G.*J. Photochem. Photobiol.A: Chem.* **2011**, *218*, 247–253. (c) Kadish,K. M.;Frémond,L.; Shen,J.;Chen,P.; Ohkubo,K.;Fukuzumi,S.; El Ojaimi, M.; Gros,C. P.;Barbe,J.-M.;Guilard,R.*Inorg. Chem.* **2009**, *48*, 2571– 2582. (d) Liu,S.;Mase,K.;Bougher,C.; Hicks,S. D.; Abu-Omar,M. M.; Fukuzumi,S.*Inorg. Chem.***2014**, *53*, 7780–7788.(e) Agadjanian,H.; Ma,J.;A. Rentsendorj,A.;Valluripalli,V.;Hwang,J. Y.;Mahammed,A.;Farkas,D. L.;Gray,H. B.;Gross,Z.; Medina-Kauwe,L. K.*Proc. Natl. Acad. Sci. USA* **2009**, *106*, 6105–6110.

ACCEPTED MANUSCRIPT

9. (a) Aviv-Harel I.;Gross, Z. *Chem. Eur. J.* **2009**, *15*, 8382–8394.(b)Abu-Omar, M. M. *Dalton Trans.* **2011**, *40*, 3435–3444.(c) Dogutan, D. K.; Stoian, S. A.; McGuire Jr, R.; Schwalbe, M.; Teets, T. S.; Nocera, D. G. *J. Am. Chem. Soc.* **2011**, *133*, 131–140.

10. (a) Mahammed, A.; Gray, H. B.; Meier-Callahan, A. E.; Gross, Z. *J. Am. Chem. Soc*. **2003**, *125*, 1162-1163. (b) Collman, J. P.; Kaplum, M.; Decréau, R. A. *Dalton Trans*. **2006**, 554-559. (c) Prokop, K. A.; Neu, H. M.; Visser, S. D.; Goldberg, D. P. *J. Am. Chem. Soc*. **2011**, *133*, 15874-15877.

11. Grodkowski, J.; Neta, P.; Fujita, E.; Mahammed, A.; Simkhovich, L.; Gross, Z. *J. Phys. Chem. A.* **2002**, *106*, 4772-4778.

12. Schechter, A.; Stanevsky, M.; Mahammed, A.; Gross, Z. *Inorg. Chem*. **2012**, *51*, 22-24.

13. Mahammed, A.; Gross, Z. *J. Am. Chem. Soc*. **2005**, *127*, 2883-2887.

14. Mahammed, A.; Gross, Z. *Angew. Chem., Int. Ed*. **2006**, *45*, 6544-6547.

15. (a) Flamigni, L.; Gryko, D. T.; *Chem. Soc. Rev*. **2009**, *38*, 1635–1646. (b) Nastasi, F.; Campagna, S.; Ngo, T. H; Dehaen,W.;Maes,W.;Kruk,M. *J. Photochem. Photobiol. A: Chem.* **2011**, *10*, 143–150. (c) Rohand, T.; Dolusic, E.; Ngo, T. H.; Maes, W.; Dehaen. *ARKIVOC* **2007**, 307-314.

16. (a) Golubkov, G.; Gross, Z. *Angew. Chem., Int. Ed*. **2003**, *42*, 4507-4510. (b) Golubkov, G.; Gross, Z. *J. Am. Chem. Soc*. **2005**, *127*, 3258-3259. (c) de Visser, S. P.; Ogliaro, F.; Gross, Z.; Shaik, S. *Chem.Eur. J*. **2001**, *7*, 4954-4960. (d) Meier-Callahan, A. E.; Gray, H. B.;Gross, Z. *Inorg. Chem*. **2000**, *39*, 3605-3607. (e) Zhao, H.; Pierloot, K.; Langner, E. H. G.; Swarts, J. C.; Conradie, J.; Ghosh, A. *Inorg. Chem*. **2012**, *51*, 4002-4006. (f) Wabotton, I.; Ghosh, A. *Inorg. Chem*. **2006**, *45*, 4910-4913. (g) Harischandra, D. N.; Zhang, R.; Newcomb, M. *J. Am. Chem.Soc*. **2005**, *127*, 13776-13777.

17. Kumar, A.; Goldberg, I.;Botoshansky, M.; Buchman, Y.; Gross, Z.*J. Am. Chem. Soc*. **2010**, *132*, 15233–15245.(b) Balazas, Y. S.; Saltsman, I.; Mahammed, A.; Tkachenko, E.; Golubkov, G.; Levine, J.; Gross, Z. *Magn. Reson. Chem.* **2004**, *42*, 624–635.

ACCEPTED MANUSCRIPT

18. Paolesse, R.; Mini, S.; Sagone, F.; Boschi, T.; Jaquinod, L.; Nurco, D. J.; Smith, K. M. *Chem. Commun.* **1999**, 1307–1308.

19. (a) Davies, H. M. L. *Angew. Chem., Int. Ed*. **2006**, *45*, 6422-6425. (b) Callot, H. J.; Mets, F. *Tetrahedron Lett*. **1982**, *23*, 4321-4324. (c) Li, Y.; Huang, J. S.; Zhou, Z. Y.; Che, C. M.; You, X. Z. *J. Am. Chem. Soc*. **2002**, *124*, 13185-13193. (d) Li, Y.; Huang, J. S.; Zhou, Z. Y.; Che, C. M. *Chem. Commun*. **2003**, 1362-1363. (e) Li, Y.; Huang, J. S.; Zhou, Z. Y.; Che, C. M. *J. Am. Chem. Soc*. **2001**, *123*, 4843-4844. (f) Aviv, I.; Gross, Z. *Synlett.***2006**, *6*, 951-953. (g) Aviv, I.; Gross, Z. *Chem. Commun*. **2006**, 4477-4779.

20. (a) Kadish, K. M.; Fremond, L.; Ou, Z.; Shao, J.; Shi, C.; Anson, F. C.; Burdet, F.; Gros, C. P.; Barbe, J. M.; Guilard, R. *J. Am. Chem. Soc*. **2005**, *127*, 5625-5631. (b) Mahammed, A.; Giladi, I.; Goldberg, I.; Gross, Z. *Chem.Eur. J*. **2001**, *7*, 4259-4265. (c) Dogutan, D. K.; Stoian, S. A.;McGuire, R., Jr.; Schwalbe, M.; Teets, T. S.; Nocera, D. G. *J. Am. Chem. Soc*. **2010**, *133*, 131-140.

21. Mahammed, A.; Gray, H. B.; Weaver, J. J.; Sorasaenee, K.; Gross, Z. *Bioconjugate Chem*. **2004**, *15*, 738-746.

22. Gross, Z.; Galili, N. *Angew. Chem., Int. Ed*. **1999**, *38*, 2366-2369.

23. Saltsman, I.; Mahammed, A.; Goldberg, I.; Tkachenko, E.;Botoshansky, M.; Gross, Z. *J. Am. Chem. Soc*. **2002**, *124*, 7411-7420.

24. Paolesse, R.; Nardis, S.; Sagone, F.; Khoury, R. G. *J. Org. Chem*. **2001,** 66, 550-556.

25. (a) Han, Y.; Lee, Y.; Mariappan, M.; Fukuzumi, S.; Nam, W.*Chem. Commun*. **2010**, 8160-8162. (b) Fryxelius, J.; Eilers, G.; Feyziyev, Y.; Magnuson, A.; Sun, L.; Lomoth, R. J. *J. Porphyrins Phthalocyanine*s **2005**, *9*, 379-386. (c) Gao, Y.; Åkermark, T.; Liu, J.; Sun, L.; Åkermark, B. *J. Am. Chem. Soc.***2009**, *131*, 8726-8727.

26. (a) Joseph, C. A.; Ford, P. C. *J. Am. Chem. Soc*. **2005**, *127*, 6737-6743. (b) Joseph, C. A.; Lee, M. S.; Iretskii, A. V.; Wu, G.; Ford, P. C. *Inorg. Chem*. **2006**, *45*, 2075-2082. (c) Singh, P.; Saltsman, I.; Mahammed, A.; Goldberg, I.; Tumanskii, B.; Gross, Z. *J. Porph. Phthal*. **2012**, *16*,

ACCEPTED MANUSCRIPT

663-673. (d) Singh, P.; Dutta, G.; Goldberg, I.; Mahammed, A.; Gross, Z. *Inorg. Chem*. **2013**, *52*, 9349-9355.

27. Ou, Z.; Erben, C.; Autret, M.; Will, S.; Rosen, D.; Lex, J.; Vogel, E.; Kadish, K. M. J. *Porph. Phthal.* **2005**, *9*, 398-412.
28. (a) Mandoj, F.; Nardis, S.; Pomarico, G.; Stefanelli, M.; Schiafinno, L.; Ercolani, G.; Prodi, L.; Genovese, D.; Zaccheroni,N.; Franczek, F. R.; Smith, K. M.; Xiao, X.; Shen, J.; Kadish, K. M.; Paolesse, R. *Inorg. Chem.***2009**, *48*, 10346-10357. (b) Mandoj, F.; Stefanelli, M.; Nardis, S.; Mastroianni, M.; Franczek, F. R.; Smith, K. M.; Paolesse, R. *Chem. Commun*. **2009**, 1580-1582.
29. (a) Eikey, R. A.; Khan, S. I.; Abu-Omar, M. M. *Angew. Chem., Int. Ed*. **2002**, *41*, 3591-3595. (b) Zdilla, M.; Abu-Omar, M. M. *J. Am. Chem. Soc*. **2006**, *128*, 16971-16979. (c)Lansky, D. E.; Kosack, J. R.; Sarjeant, A. N.; Goldberg, D. P. *Inorg. Chem.***2006**, *45*, 8477-8479.
30. Palmer, J. H.; Nannestad, T. B.; Mahammed, A.; Durrell, A. C.; Vandervelde, D.; Virgil, S.; Gross, Z.; Gray, H. B. *Angew. Chem., Int. Ed*. **2011**, *50*, 9433-9436.
31. Liu, H.-Y.; Mahmood, M. R.; Wue, S.-X(Samuel).; Chang, C. K. *Coord. Chem. Rev*. **2013**, *257*, 1306-1333.
32. Johnson, W.; Kay, I. T.*J. Chem. Soc. C*, **1961,** 2418-2423.
33. (a) Boschi, T.; Licoccia, S.; Paolesse, R.; Tagliatesa, P.; Azarnia, M. *J. Chem. Soc. Dalton Trans.***1990**, *1*463-1476. (b) Boschi, T.; Licoccia, S.; Paolesse, R.; Tagliatesa, P. *Inorg. Chim. Acta***1988**, *141*,169-171.
34. Broring, M.; Hell, C. *Chem. Comm.***2001**, 2336-2337.
35. Paolesse, R.; Licoccia, S.; Bandoli, G.; Dolmella, A.; Tagliatesa, P. *Inorg. Chem.* **1994**, 33, 1171-1176.
36. (a) Bröring, M. *Synthesis*, **2000**, 1291-1294. (b) Bröring, M.; D. Griebel, D.; Hell, C.; Pfister, A. *J. Porph. Phthal.* **2001**, *5*, 708-714.
37. Kadish, K. M.;Adamian, V.A.; Van Caemelbecke,E.; Gueletii, E.; Will,S.; Erben,C.; Vogel,E. *J. Am. Chem. Soc*. **1998**, *120*, 11986-11993.

ACCEPTED MANUSCRIPT

38. (a) Murakami, Y.; Matsuda, Y.; Sakata, K.; Yamada, S.; Tanaka, Y.; Aoyama, Y. *Bull. Chem. Soc. Jpn.*, **1981**, *54*, 163-169.

39. Kumar, A.; Maji, S.; Dubey, P.; Abhilash, G. J.; Pandey, S.; Sarkar, S. *Tetrahedron Lett.* **2007**, *48*, 7287-7290.

40. The pyrrole (3 equiv.) was added to the 100 mL of 0.18 M aqueous HCl (1.5:98.5), followed by the addition of the 4-nitrobenzaldehyde (1 equiv., 2.0 g, 0.010–0.019 mol). The resulting reaction mixture was stirred at room temperature and the progress of the reaction was monitored by TLC. After 2 hr stirring, the precipitated yellow solid product was filtered off and washed with water and dried yellow product was again washed with petroleum ether to afford 5-(4-nitrophenyl)dipyrromethane in high yields (97%).

41. The chemical formula and ring labeling system is shown in Figure 2. Crystal data for compound **3**: $C_{40}H_{25}F_3MnN_7O_5$, Mw, 795.61; system, monoclinic; space group, P 21/c; unit cell dimensions, a= 8.0405(6) Å; b = 23.987(3) Å; c = 18.1125(13) Å; $\alpha = 90^0$; $\beta = 92.293(6)^0$; $\gamma = 90^0$; V =3490.5(5)Å^3; Z = 4; T = 150 K; R_{int}, 0.1239; R(all), 0.1979; *Gof* = 1.019; $\Delta_{\rho max}$ = 1.035 e Å^3; $\Delta_{\rho min}$= -1.119 e Å^3. The resolution obtained for the structure of the compounds was limited by the poor quality of the available crystals. Intensity data were collected at 150(2) K on Bruker diffractometer (a single wavelength Enhance X-ray source with MoK_α radiation, λ = 0.71073 Å). The selected suitable single crystals were mounted using paratone oil on the top of a glass fiber fixed on a goniometer head and immediately transferred to the diffractometer. Pre-experiment, data collection, data reduction and analytical absorption corrections were performed with the Bruker SAINT program. The crystal structures were solved with SHELXS-97 using direct methods. The structure refinements were performed by full-matrix least-squares on F^2 with SHELXL-97. All programs used during the crystal structure determination process are included in the WINGX software. CCDC no. 1556509.

42. CHN data. Calculated (Found); **1**: C 58.59 (59.60), H 2.13 (2.23), N 10.08 (11.11); **2**: C 59.46 (57.47), H 2.70 (3.57), N 11.24 (11.05); **3**: C 61.51 (61.80), H 2.51 (2.65), N 11.63 (12.01); **4**: C 64.47 (64.46), H 3.19 (3.39), N 11.57 (11.47); **5**: C 61.51 (61.46), H 2.51 (2.36), N 11.63 (11.47);

ACCEPTED MANUSCRIPT

6: C 60.26 (55.16), H 2.70 (3.57), N 11.40 (7.48); **7**: C 63.33 (61.62), H 3.59 (3.30), N 11.08 (11.04); **8**: C 61.97 (61.46), H 2.74 (2.63), N 11.41 (11.24); **9**: C 65.33 (65.75), H 3.32 (3.50), N 12.03 (11.74); **10**: C 63.08 (63.24), H 2.72 (2.90), N 11.93 (12.66).

ACCEPTED MANUSCRIPT

ACCEPTED MANUSCRIPT

Highlights

- We report direct C-C bond through metal initiation in corrole.
- It is a green synthetic protocol.
- It is a synthesis of metallocorroles directly from bilane.
- Manganese(III) as template has been used for the synthesis of metallocorroles.

ACCEPTED MANUSCRIPT

Asia Pacific Journal of Research

ISSN (Print): 2320-5504
ISSN (Online): 2347-4793

Asia Pacific Journal of Research
A peer reviewed international Journal
IMPACT FACTOR : 6.58
Print -ISSN -2320 - 5504
Online-E-ISSN - 2347 - 4793

MEASURING THE IMPACT OF GREEN HUMAN RESOURCE FACTORS ON ENVIRONMENTAL PERFORMANCE USING STRUCTURE EQUATION MODELING

[1] Anu Singh Lather ,[1,2] Shikha Goyal

[1]Pro Vice Chancellor, Delhi Technological university Delhi, India

[2]PDM College of Engineering, Bahadurgarh, Haryana, India

ABSTRACT

The purpose of this paper is to investigate the effect of green human resource factors (Non-technical factors) on environmental performance as perceived by employees of the organization. A survey was conducted on 360 employees of manufacturing companies implementing environmental management system (EMS) in Delhi-NCR region. A conceptual model is drawn up based on the existing literature. In order to validate the scale and test the model confirmatory factor analysis and structure equation modeling was used, using AMOS software. The green human resource practices are measured with the help of seven first order factors such as Top management commitment, Environmental Communication, Environmental Trainings, Environmental Teams, Employee Involvement, Rewards, and Green Programs. A questionnaire with 42 items on these factors and 7 items on environmental Performance was constructed. These seven factors represent the green human resource practices for the effective implementation of EMS. The results revealed that all the green human resource factors have a significant impact on environmental performance.

Keywords: Environmental Management System, EMS, Green Human Resource factors, Environmental Performance, Structure Equation Modeling, Confirmatory Factor analysis

1. Introduction

In present era of globalization, organizations are becoming proactive for protection of their environment by implementing Environmental Management System(EMS) in their organizations. It helps the companies to identify , measure and control the harmful effects of business processes on the environment. It is a continuous improvement programme for dealing with environmental problems by acquiring and developing instruments and methodologies (Borri & Boccaletti, 1995).But organizations cannot embark on the journey to organization environmental objective without focus on the most vital asset of the organization i.e. Human Resource. So organizations have to develop green human resource management practices for promoting environmental management initiatives. Green Human Resource Management practices and policies promote HRM to ecological usage of business resources. It comprises of all activities aimed at helping an organization carry out its agenda for environmental management, to reduce carbon footprints and earn carbon credits. Several Researches have identified the human resource factors for EMS implementation.(Bonnie F. Daily & Huang, 2001; Govindarajulu & Daily, 2004; Jabbour, 2013; Jabbour, Santos, Fonseca, & Nagano, 2013; Jabbour, Santos, & Nagano, 2008; Wee & Quazi, 2005) but few researches have talked about their effects on environmental performance (Bonnie F Daily, Bishop, & Steiner, 2011; Ramus, 2001; Renwick, Redman, & Maguire, 2008; Wee & Quazi, 2005).

Hence this study was carried out to study the relationship between green human resource factors and environmental performance in manufacturing companies implementing EMS in Delhi-NCR region, India. Firstly, through literature review it developed a scale measuring the green human resource factors. Secondly it proposed and tested a conceptual model which links green human resource factors and environmental performance as perceived by the employees of the organization.

ISSN (Print): 2320-5504
ISSN (Online): 2347-4793

2. Review of Literature

Green HRM as referred by (Renwick et al., 2008) is the process of support from Human resource to Environmental Management objectives. A greater integration between human resource management constructs and environmental issues helps firms to implement Environmental Management System effectively. For this study, a number of human resource management constructs for environmental management were operational zed and measured in the organizations of Delhi-NCR region, India. These constructs include: Top Management Commitment, Environmental communication, environmental trainings, environmental teams, rewards and green programs. The green human resource factors will be defined and discussed briefly below.

2.1. ***Top Management commitment***. It is considered to be the most important aspect in the implementation and maintenance of environmental management system (Daily & Huang,2001) Management clearly establishes its commitment to environmental improvement by forming environmental policy. It establishes an environmental vision and guide the company's efforts to achieve it (Wee& Quazi,2005,Govindarajula &Daily,2004).With the top management support environmental strategies could be adopted that leads to low emissions, reduce wastes and environmentally responsible products that can lead to continual improvement in environmental performance. Hence we propose the following hypothesis:

Hypothesis 1: "*There exists a significant impact of top management support on environmental performance of the organization"*

2.2. ***Environmental Communication***. Environmental goals should be clearly communicated to workers ,subject to continuous improvement overtime to reach to the goal of zero emission and zero waste.(Gupta & Sharma, 1996). Employees should have a clear understanding to company's environmental policy. The messages delivered should be clear, practical and easy to implement, tailored according to different employee groups based upon its relevancy to their jobs (Uusi-Rauva and Nurkka,2010). But studies show that employees do not feel properly informed regarding environmental issues(Madsen & Ulhøi, 2001). It is also felt that if the line managers inform employees and adopt a democratic and open style of communication in regard to environmental ideas environmental performance will automatically increase(Ramus, 2001). Hence we propose another hypothesis:

Hypothesis 2: "*There exists a significant impact of environmental communication on environmental performance of the organization"*

2.3. ***Environmental trainings*** provide opportunity to organizational members to be more aware of environmental issues and develop the need for environmental control (Bonnie F Daily et al., 2011; Rothenberg, 2003; Wee & Quazi, 2005; Zutshi & Sohal, 2004). These trainings are provided to make them learn and adapt environmental friendly practices(recycling, waste management, teleconferencing etc).They are also conducted to inform employees about changes in corporate environmental policy and address concern towards environmental liabilities(Wee & Quazi, 2005). Apart from these companies also celebrates annual 'environmental day 'and organize many competitive programs for employees and families of employees to inculcate eco-values among them.(Jabbour, Teixeira, Oliveira, & Soubihia, 2010) has also addressed the issue of environmental training in organizations and has presented a literature review that highlights the importance of environmental training for organizations. It emphasized the need to devote more attention to different trainings at different levels i.e. strategic, tactical and operational. It can create value for the stakeholders and can differentiate organizations that are pioneers from their direct competitors by creating a competitive advantage. These trainings should be provided frequently for employees engagement in environmental issues. The content of trainings should be regularly reviewed and revised. Daily et al.(2011) concluded that employees do not perceive environmental training to be directly impacting environmental performance but an indirect effect was found through environmental team acting as a mediating variable. Hence it leads to the following hypothesis:

Hypothesis 3: "*There exists a significant impact of environmental trainings on environmental teams of the organization"*

2.4. ***Employee Involvement***. Employees should be actively involved in setting specific environmental goals to achieve corporate environmental vision (Wee & Quazi, 2005) Employees should be involved at each and every stage of introduction and change of any policy or programme (Zutshi & Sohal, 2003). (Kirk-Davidoff, Hintsa, Anderson, & Keith, 1999) found employee involvement as an essential factor for improving pollution control in Dow Chemical as it believes that "if pollution control is a cost to you (my competitor) and a cost to me, I win if my costs are lower". Controlling these costs require people to think about it a lot. Everybody should accept ownership for pollution. (Rothenberg, 2003) used data from an automobile plant i.e. New United Motor Manufacturing (NUMMI) which was well known for its participative work structures to look more closely at the dynamics of worker participation in environmental management. It was found that workers possess contextual knowledge but with knowledge of intra-organizational processes, external knowledge makes the role of workers important for environmental improvement. The various practices the company can adopt for employee involvement could be participatory decision making by employees in environmental management(Berry & Rondinelli, 1998), establishing individual environmental goals(Epstein & Research, 1996), suggestion schemes, employee empowerment, setting of environmental teams, setting of environmental targets. The two gains seen from introducing environmental employee involvement are improvement in environmental and worker health and safety, and development of more knowledgeable employees and supervisors (Govindarajulu & Daily, 2004). Also it can have a strong effect on changing working routines, affecting behavior and increasing environmental consciousness (Kaur, 2011). Once the employees are involved they will be

ISSN (Print): 2320-5504
ISSN (Online): 2347-4793

motivated to work in teams in order to achieve the team objectives(Bonnie F Daily et al., 2011). As environmental projects require not only individual efforts but more of team efforts so we propose the hypothesis:

Hypothesis 4: "*There exists a significant impact of employee involvement on environmental teams of the organization"*

2.5. *Environmental Teams*. (Beard & Rees, 2000) describes "green teams" as the teams used to: "generate ideas, enhance learning experiences, explore issues, identify conflict and focus action to enhance understanding about why, what, how, where and when to pursue the best practicable environmental options".(p.27).Environmental teams gives an opportunity for individuals to work together to solve complex problems.(Bonnie F Daily et al., 2011). They will motivate the engagement of workers and will affect their performance.(Neto & Jabbour, 2010). The companies have both cross functional teams(members from different departments) or functional teams(individual department teams). Organization with more advanced environmental management systems used EMS teams more intensively than organization with less advanced environmental management systems. (Jabbour et al., 2013). So seeing the importance of green teams for the successful implementation of EMS we can propose that:

Hypothesis 5: "*There exists a significant impact of environmental teams on environmental performance of the organization"*

2.6. *Environmental rewards*. It can be implemented in the form of monetary rewards (bonuses, cash premiums), non-monetary rewards (sabbaticals, leave, gifts) and recognition awards(awards, dinners, daily praise) (Bonnie F. Daily & Huang, 2001; Govindarajulu & Daily, 2004; Renwick et al., 2008). It can motivate and increase employee's commitment to be more environmentally responsible which can help both the company and its workers and environmental performance will be enhanced (Bonnie F Daily et al., 2011). It can reinforce empowerment and good decision making, improving corrective and preventive measures employees initiate (Bonnie F. Daily & Huang, 2001). In order to produce desirable behaviors in environmental management companies require effective employment of both incentives and disincentives (Rees, 1996). Incentives as discussed above could be awards, rewards or recognition for employee suggestion, feedback, participation and disincentives could be criticism, warnings, disciplinary actions such as suspension for lapses (Renwick et al., 2008). Based on the discussion we believe that rewards could be used to motivate employees to perform well in teams to achieve environmental performance. So we propose that:

Hypothesis 6: "*There exists a significant impact of environmental rewards on environmental teams of the organization"*

2.7. *Green Programs*. Green Programs are certain environmentally responsible practices from the perspective of HR professionals and employees. These practices could lead to more environment-friendly and ecologically responsible decisions. Society for Human Resource Management (SHRM) conducted a survey (2007) in U.S. and explored environmentally responsible practices from the perspective of HR professionals and employees. The practices were: Encouraging employees to work more environmentally friendly(e.g., double sided photocopies, using energy efficient bulbs for desk lamps, powering down computers after few minutes of inactivity), offering recycling program for office products (e.g. paper, plastic, glass and cans), donating or discounting used office furniture, using energy efficient lighting systems and equipments(energy star equipment, changing from desktops to laptops, occupancy sensors), Installing automatic shut off for equipments, promoting walking, biking, public transit, participating in or sponsoring projects/events in the community to improve the environment (a trash pick –up day, plant a tree day etc).The top three practices reported were encouraging employees to work more environmentally friendly, offering recycling programs for office products and donating/discounting office furniture. The greening of HR survey (2009) conducted by Buck Surveys examined the green initiatives taken by companies involving their workforce. It found the following green programs in place such as using internet or teleconferencing, putting summary plan description or other information online for reducing printing, reduction of paper usage, offering work from home opportunities, ride/share programs. We have included these programs in our survey to find out the environmental initiatives taken by Indian companies. Hence we propose that:

Hypothesis 7: "*There exists a significant impact of green programs on environmental performance of the organization"*

3. Research Methodology

3.1 Research Design

A descriptive research was conducted in 40 manufacturing companies adopting environmental management system in Delhi-NCR region. Manufacturing companies from different industrial sectors were included in the study as they are the major source of pollution.

3.2 Sample and Data collection

One coordinator from every company served as a liaison to get the data filled from employees of various departments. The coordinator selected the employees, distributed the questionnaire and finally collected the questionnaire. The questionnaire was administered to a total of 360 employees from 40 manufacturing companies, selecting 9 employees from each company. The questionnaire studied the perceptions of the employees working up to executive level from the selected manufacturing companies.

ISSN (Print): 2320-5504
ISSN (Online): 2347-4793

3.3 Tool

The various items of the questionnaire pertaining to different HR constructs were developed based upon different studies in literature such as Daily et al (2001,2007), Kaur(2011), Wee and Quazi (2005), Jabbour(2008), Greening of HR survey(2009), SHRM survey(2008) depending upon the requirements of the study. The items were measured using 5-point likert scale (1=strongly disagree to 5=strongly agree).

4. Data analysis and Interpretation

This study proposes to study the green human resource factors for EMS implementation and its effect on environmental performance in Indian manufacturing firms of Delhi-NCR. Seven first order Green HR factors were identified through literature review. The statements related to these selected factors are included in the questionnaire. The measurement model is designed in the AMOS software and confirmatory factor analysis is applied in order to test the reliability and construct validity (convergent as well as discriminant validity) of the green human resource factor.

The results of the measurement model are shown below in table1.

Table 1 : Regression Weights

Statements	Variables		Construct Name	Unstandardized Estimate	Standardised Estimates	Standard Errors	Critical Ratio	P Value
Being set up to handle environmental problems	Envt1	<---	Environmental teams	1.000	.835			
Provide large amount of information regarding environmental issues.	Envt2	<---		1.006	.861	.051	19.603	***
Free to express opinions regarding environmental issues in team meetings.	Envt3	<---		1.027	.799	.058	17.581	***
Can be contacted at any time to discuss about environmental issues	Envt4	<---		.972	.761	.059	16.426	***
Encouraged for making suggestions regarding environmental improvements	EI1	<---	Employee Involvement	1.000	.801			
Completely aware about my environmental responsibilities related to my job.	EI2	<---		.999	.830	.057	17.588	***
Participate in environmental decisions related to my job	EI3	<---		.884	.851	.049	18.175	***
Employees can express their opinions openly and freely.	EI4	<---		.968	.834	.055	17.704	***
Proper feedback is provided to employees regarding their environmental saving efforts	EI5	<---		.964	.737	.064	15.074	***
Cash rewards to employees for achieving environmental initiatives	Rew1	<---	Rewards	1.000	.867			
Environmental award/special recognition to individuals	Rew2	<---		.904	.868	.041	21.818	***
Provides environmental award/special recognition to teams	Rew3	<---		.948	.892	.041	22.909	***
Disciplinary actions for violating environmental policies and procedures	Rew4	<---		.766	.754	.044	17.223	***
Put summary plan description or other company information online to reduce printing	Green1	<---	Green Program	1.075	.712	.082	13.118	***
Videoconferencing/teleconferencing over flying for meetings	Green2	<---		1.004	.728	.075	13.423	***
Offer opportunities for employees to telework or work from home	Green3	<---		1.082	.727	.081	13.403	***
Promotes Public Transport	Green4	<---		1.000	.721			
Car Pooling	Green5	<---		1.052	.720	.079	13.270	***

ISSN (Print): 2320-5504
ISSN (Online): 2347-4793

Statements	Variables		Construct Name	Unstandardized Estimate	Standardised Estimates	Standard Errors	Critical Ratio	P Value
Use energy efficient sensor based light turn on/off	Green6	<---		1.009	.692	.079	12.749	***
Building design for cooling and lighting load Efficiency	Green7	<---		.951	.745	.069	13.733	***
Procure energy efficient energy star certified devices	Green8	<---		.973	.710	.074	13.071	***
Replace desktops with laptops	Green9	<---		1.059	.744	.077	13.724	***
Encourages employees to participate in trash pickup day	Green10	<---		1.066	.745	.078	13.737	***
Top Management emphasizes environmental policy.	Topm1	<---	Top Management	1.000	.681			
Environmental policy of my company is assessed periodically and revised.	Topm2	<---		.985	.745	.076	12.938	***
Top Management takes environmental issues at priority	Topm3	<---		1.163	.839	.081	14.370	***
Top management allocates sufficient funds for environmental activities	Topm4	<---		1.113	.817	.079	14.036	***
Top management allows employees to spend time for environmental activities.	Topm5	<---		1.030	.786	.076	13.573	***
Takes follow up of suggestions to bring changes in the company's system to save environment.	Topm6	<---		1.032	.782	.076	13.504	***
Continuously review the environmental management system and make the required improvements.	Topm7	<---		1.160	.769	.087	13.313	***
Formally communicates its environmental policy and strategy to all its employees.	Ecom1	<---	Environmental Communication	1.000	.779			
Quite often meetings are organized for raising employee's awareness about environmental issues	Ecom2	<---		1.138	.830	.067	16.950	***
Develops awareness among employees for promotion of their health, hygiene and healthy environment.	Ecom3	<---		.832	.730	.057	14.509	***
Provides clear directions to me about what i can do to save my environment.	Ecom4	<---		1.003	.823	.060	16.787	***
Provides information regarding cost benefit initiatives relating to the environment	Ecom5	<---		.988	.775	.063	15.580	***
Information regarding environmental audits is communicated to employees for further improvements	Ecom6	<---		.786	.658	.061	12.831	***
Trainings regarding environmental improvements are provided at regular intervals	ET1	<---	Environmental Trainings	1.000				
Trainings are provided to new hires to avoid environmental mistakes	ET2	<---		.930	.793	.066	14.025	***
Environmental training has contributed to my understanding of the environmental impacts of the company.	ET3	<---		1.215	.690	.067	18.131	***
I am satisfied with environmental trainings provided in my organization.	ET4	<---		1.268	.842	.063	20.099	***
I am able to use my environmental trainings effectively	ET5	<---		1.166	.908	.060	19.445	***
I feel better equipped to make environmentally responsible decisions due to environmental training.	ET6	<---		.866	.886	.060	14.446	***

ISSN (Print): 2320-5504
ISSN (Online): 2347-4793

The result of the measurement model comprising the seven green human resource factors indicates that the p value of all the critical ratio is found to be less than 5 percent level of significance. Therefore with ninty five percent confidence level it can be concluded that all the statements of green practices included in the study significantly represents the related factors/constructs. The results of CFA also indicates that the standardized regression coefficients (construct loading) of different statements related to green human resource practices are found to be more than 0.5. Hence, it can be concluded that each statements of green human resource practices have significant correlation with their respective construct. Therefore, convergent validity of all the included construct of green human resource practices is ensured.

In the study the Pearson coefficient of correlations between different pairs of the green human resource constructs is also estimated. The correlation as measured by coefficients of Pearson Correlation between different green human resource construct is shown below in table2:

Table 2: Pearson correlation for the green human resource constructs.(N=360)

	Variable	1	2	3	4	5	6	7
1	Top Management Support	1						
2	Environmental Communication	.707	1					
3	Environmental Trainings	.251	.346	1				
4	Environmental Teams	.647	.694	.419	1			
5	Employee involvement	.555	.547	.206	.582	1		
6	Rewards	.624	.689	.286	.758	.500	1	
7	Green Programs	.552	.579	.312	.622	.459	.639	1

The result of the correlation analysis between the different green human resource constructs indicates that the coefficients of Pearson correlation between the green HR constructs is found to be positive and greater than zero. This indicates that the selected green human resource constructs have positive correlation between them. The results also indicate the presence of moderately high coefficients of correlation in most of the cases. This represents the absence of very high positive correlation between the green human resource constructs. The moderately positive correlation between the included green human resource constructs of EMS implementation ensures the presence of discriminant validity in the used scale of EMS management. In the study, the CR statistic, AVE, MSV indicators of all the included constructs of green human resource practices is estimated. The results are shown below in the table:

Table 3: Validity indicates of the measurement model

	CR	AVE	MSV	ASV
Environmental Communication	0.896	0.590	0.500	0.368
Environmental Team	0.887	0.664	0.575	0.396
Employee involvement	0.906	0.658	0.339	0.242
Rewards	0.910	0.717	0.575	0.363
Green Programs	0.917	0.526	0.408	0.291
Top Management Support	0.913	0.602	0.500	0.368
Environmental Training	0.921	0.662	0.176	0.097

The results of the CFA analysis of the measurement model as represented by CFA diagram indicate that the CR indicator of the included green HR constructs are found to be greater than 0.7 and AVE indicator is greater than 0.5. Hence, the convergent validity of the included green human resource constructs of EMS implementation is ensured. In addition to this AVE is found to be greater than MSV ensuring the existence of discriminant validity among the green human resource factors included in the study. The statistical fitness of the green human resource measurement model is also estimated in the study. The different statistical indices representing the statistical fitness of the measurement model is shown below in table.

ISSN (Print): 2320-5504
ISSN (Online): 2347-4793

Table 4: Showing the Model Fit statistics of each construct

	Chi-Square	CFI (Comparative Fit Index)	GFI (Goodness of Fit index)	SRMR (Standardized Root Mean Residual)	RMSEA (Root Mean Square Error of Approximation)
Acceptable levels	Non-Significant	≥.92	≥.90	≤.08	Upto 0.1
Top Management Support	31.427	.988	.974	.026	.059
Environmental Communication	35.859	.977	.969	.034	.091
Environmental Training	20.628	.992	.982	.020	.060
Environmental Team	2.858	.998	.995	.015	.043
Employee Involvement	20.703	.986	.977	.021	.094
Employee Rewards	4.150	.998	.994	.013	.055
Green Programs	84.225	.973	.955	.044	.063

The results indicates that the measurement model is statistically fit and furthur statistical analysis can be done in the study.

Figure 1Hypothesized Structural Model

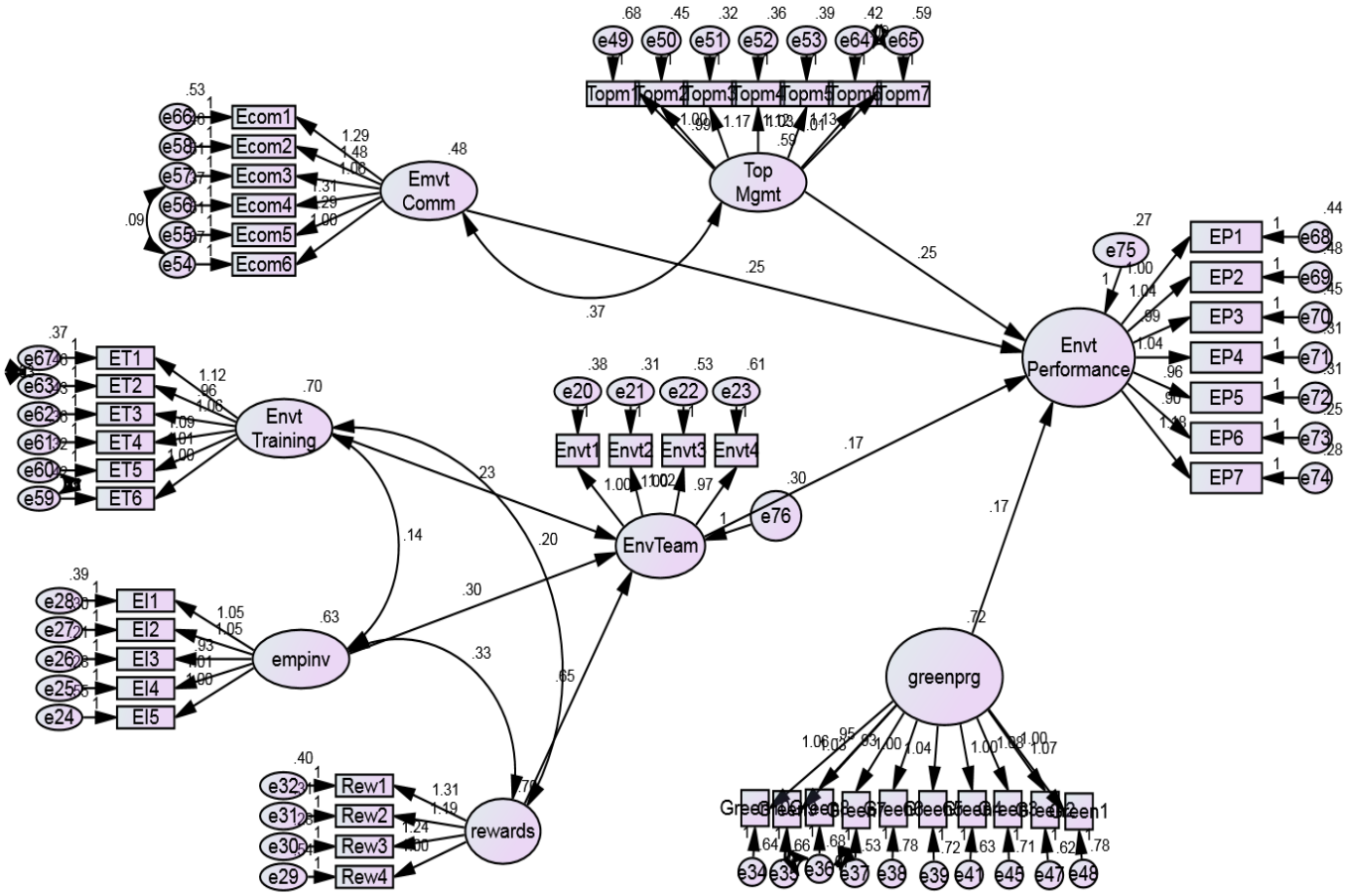

ISSN (Print): 2320-5504
ISSN (Online): 2347-4793

The results of SEM approach is shown below in table 5

Table 5: SEM results

Endogenous Construct		Exogenous Construct	Unstandardized Regression coefficient	Standardised Regression coefficient	Standard Error (S.E.)	Critical Ratio (C.R.)	P Value	R Square
Environmental Team	<---	Environmental Training	.226	.201	.048	4.764	***	.665
Environmental Team	<---	Employee Involvement	.296	.249	.058	5.131	***	.665
Environmental Team	<---	Rewards	.651	.577	.065	10.072	***	.665
Environmental Performance	<---	Top Management Support	.252	.294	.066	3.814	***	.378
`Environmental Performance	<---	Environmental communication	.254	.266	.074	3.444	***	.378
Environmental Performance	<---	Green Programs	.171	.219	.039	4.341	***	.378
Environmental Performance	<---	Environmental Team	.175	.250	.035	4.944	***	.378

The results of the SEM analysis indicate that the p values of the critical ratio in case of all the assumed inter-relationships are found to be less than 5 percent level of significance. Thus all of the framed hypothesis as mentioned above can be accepted.

5. Discussion and conclusion

This study contributes to the environmental management literature in several ways. Firstly it developed a scale measuring the green human resource factors through confirmatory factor analysis. Secondly a step further to CFA , structural equation modeling was applied to test the proposed relationships between green human resource factors and environmental performance.

Our hypothesized model proposed 7 relationships including 4 between HR factors(Top Management support, Environmental communication, Environmental team and green programs) and environmental performance and 3 to environmental teams from the other HR factors(environmental training, employee involvement and rewards.)All the relationships were found to be significant thus supporting our hypothesis H1, H2, H3, H4, H5, H6, H7.

So our result suggests that managers should emphasize on green human resource factors while implementing EMS in the organization. Results of our study are in continuity with a number of studies having a positive influence of Top management support on environmental performance (Zutshi and Sohal 2004; Daily et al 2001, 2007), Environmental communication on environmental performance (Uusi-Rauva & Nurkka, 2010), environmental training, environmental involvement and rewards on environmental performance with environmental team acting as mediating variable(Daily et al, 2007) and Green environmental friendly practices(SHRM survey,2008 ; Greening of HR survey,2009).

6. Managerial Implications

Beyond the technical aspects of EMS, we have taken care of non-technical or softer issues that could be very critical for the success of EMS implementation. Our study provides a model to managers in understanding how Green HR factors could be related to

Environmental Management System of a company. So HR practices could be significant predictors of EMS success or failure. It could help the managers in knowing the importance of integrating human resource practices with companies' environmental management system. The managers will be able to determine the role of different HR factors in implementing a successful environmental management system in the organization. The Green HR practices will motivate employees to become more involved in environmental activities and develop proactive strategies to prevent environmental problems and attain environmental sustainability. It will enhance business efficiencies and help the company's to gain competitive advantage.

REFERENCES

1. Beard, C., & Rees, S. (2000). Green teams and the management of environmental change in a UK county council. *Environmental Management and Health, 11*(1), 27-38. doi: doi:10.1108/09566160010314161
2. Berry, M. A., & Rondinelli, D. A. (1998). Proactive corporate environmental management: A new industrial revolution. *The Academy of Management Executive, 12*(2), 38-50.
3. Borri, F., & Boccaletti, G. (1995). From total quality management to total quality environmental management. *The TQM Magazine, 7*(5), 38-42. doi: doi:10.1108/09544789510098614
4. Buck Surveys (2009),*Greening of HR Survey*. Retrieved from http://buckimplementsgreen.com/pdfs/Go_Green_Survey.pdf
5. Daily, B. F., Bishop, J. W., & Steiner, R. (2011). The mediating role of EMS teamwork as it pertains to HR factors and perceived environmental performance. *Journal of Applied Business Research (JABR), 23*(1).
6. Daily, B. F., & Huang, S. c. (2001). Achieving sustainability through attention to human resource factors in environmental management. *International Journal of Operations & Production Management, 21*(12), 1539-1552. doi: doi:10.1108/01443570110410892
7. Epstein, M. J., & Research, I. F. f. A. (1996). *Measuring corporate environmental performance: best practices for costing and managing an effective environmental strategy*: McGraw-Hill.
8. Govindarajulu, N., & Daily, B. F. (2004). Motivating employees for environmental improvement. *Industrial Management & Data Systems, 104*(4), 364-372. doi: doi:10.1108/02635570410530775
9. Gupta, M., & Sharma, K. (1996). Environmental operations management: an opportunity for improvement. *Production and Inventory Management Journal, 37*(3), 40.
10. Jabbour, C. J. C. (2013). Environmental training in organisations: From a literature review to a framework for future research. *Resources, Conservation and Recycling, 74*, 144-155.
11. Jabbour, C. J. C., Santos, F. C. A., Fonseca, S. A., & Nagano, M. S. (2013). Green teams: understanding their roles in the environmental management of companies located in Brazil. *Journal of Cleaner Production, 46*, 58-66.
12. Jabbour, C. J. C., Santos, F. C. A., & Nagano, M. S. (2008). Environmental management system and human resource practices: is there a link between them in four Brazilian companies? *Journal of Cleaner Production, 16*(17), 1922-1925.
13. Jabbour, C. J. C., Teixeira, A. A., Oliveira, J. H. C. d., & Soubihia, D. F. (2010). Managing environmental training in organizations: Theoretical review and proposal of a model. *Management of Environmental Quality: An International Journal, 21*(6), 830-844. doi: doi:10.1108/14777831011077673
14. Kaur, H. (2011). Impact of human resource factors on perceived environmental performance: An empirical analysis of a sample of ISO 14001 EMS companies in Malaysia. *Journal of Sustainable Development, 4*(1), 211.
15. Kirk-Davidoff, D. B., Hintsa, E. J., Anderson, J. G., & Keith, D. W. (1999). The effect of climate change on ozone depletion through changes in stratospheric water vapour. *Nature, 402*(6760), 399.
16. Madsen, H., & Ulhøi, J. P. (2001). Greening of human resources: environmental awareness and training interests within the workforce. *Industrial Management & Data Systems, 101*(2), 57-65. doi: doi:10.1108/02635570110384320
17. Neto, A. S., & Jabbour, C. J. C. (2010). Guidelines for improving the adoption of cleaner production in companies through attention to non-technical factors: A literature review. *African Journal of Business Management, 4*(19), 4217-4229.
18. Ramus, C. A. (2001). Organizational support for employees: Encouraging creative ideas for environmental sustainability. *California management review, 43*(3), 85-105.
19. Rees, W. E. (1996). Revisiting carrying capacity: area-based indicators of sustainability. *Population & Environment, 17*(3), 195-215.
20. Renwick, D., Redman, T., & Maguire, S. (2008). Green HRM: A review, process model, and research agenda. *University of Sheffield Management School Discussion Paper, 2008*(1), 1-46.
21. Rothenberg, S. (2003). Knowledge content and worker participation in environmental management at NUMMI. *Journal of Management Studies, 40*(7), 1783-1802.
22. SHRM survey(2008),*Green Worlplace*, Retrieved from
23. aceclifehealthtrust.com/wpcontent/.../SHRM-Green-Workplace-Survey-Brief1.pdf
24. Uusi-Rauva, C., & Nurkka, J. (2010). Effective internal environment-related communication: An employee perspective. *Corporate Communications: An International Journal, 15*(3), 299-314. doi: doi:10.1108/13563281011068140
25. Wee, Y. S., & Quazi, H. A. (2005). Development and validation of critical factors of environmental management. *Industrial Management & Data Systems, 105*(1), 96-114. doi: doi:10.1108/02635570510575216
26. Zutshi, A., & Sohal, A. S. (2003). Stakeholder involvement in the EMS adoption process. *Business Process Management Journal, 9*(2), 133-148. doi: doi:10.1108/14637150310468362
27. Zutshi, A., & Sohal, A. S. (2004). Adoption and maintenance of environmental management systems: Critical success factors. *Management of Environmental Quality: An International Journal, 15*(4), 399-419. doi: doi:10.1108/14777830410540144

The Egyptian Journal of Remote Sensing and Space Sciences xxx (2017) xxx–xxx

HOSTED BY

ELSEVIER

Contents lists available at ScienceDirect

The Egyptian Journal of Remote Sensing and Space Sciences

journal homepage: www.sciencedirect.com

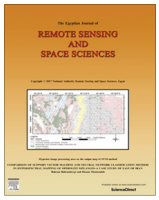

Research Paper

Parameters affecting target detection in VNIR and SWIR range

Deepti Yadav [a,*], M.K. Arora [a], K.C. Tiwari [b], J.K. Ghosh [a]

[a] Department of Civil Eng. (Geomatics), IIT Roorkee, Roorkee, Uttarakhand 247667, India
[b] Civil Engineering Dept., Delhi Technological University, Delhi 110042, India

ARTICLE INFO

Article history:
Received 6 April 2017
Revised 29 July 2017
Accepted 21 August 2017
Available online xxxx

Keywords:
Target detection
Shadow
Background
Material composition
Color

ABSTRACT

Hyperspectral data due to its fine spectral resolution facilitates detection of targets with high accuracies and thus has been used in many applications. A target detection application differs from most other remote sensing applications in the fact that targets are often too small and contained in only a few pixels. However, HSI detection gets limited by several parameters which can be broadly categorized in three groups: sensor parameters (noise, calibration *etc.*), spatial parameters (size, shape *etc.*), scene parameters (illumination variation, background *etc.*). These parameters may have varying effect on detectability of targets and thus need further investigations. Two specific spectral ranges VNIR and SWIR have been selected based on literature review to study effect of four scene parameters namely illumination, background, material composition and color of target on detection of known targets. The detection has been implemented using three popular detection algorithms namely, ACE, MF, SAM. Results indicate that scene parameters play a major role and affect detectability of targets differently in different spectral ranges.
© 2017 National Authority for Remote Sensing and Space Sciences. Production and hosting by Elsevier B. V. This is an open access article under the CC BY-NC-ND license (http://creativecommons.org/licenses/by-nc-nd/4.0/).

1. Introduction

Target detection using hyperspectral imaging (HSI) is an important application in many civilian and defence activities. HSI due to its high spectral resolution, is widely used by several researchers for accurate detection of targets. Many target detection algorithms have been reported in literature. Typically, these algorithms are categorised in two groups-spectral matching and anomaly detection algorithms such as Spectral Angle Mapper, Constrained Energy Minimization and Reed–Xiaoli *etc.* respectively (Nasarbadi, 2014). These algorithms have been evolved and tested with different data sets under various assumptions to provide improved detection results. However in real-world applications, algorithms have to address several issues which may severely affect accuracy of detection. Primarily because spectral reflectance for a specific material may show great variability in actual operating conditions *i.e.* reflectance of same material may vary in two images captured in different geographic locations or within same image. This variability can get introduced due to numerous parameters such as atmospheric propagation, sensor noise, target size, mixed pixel, illumination *etc.* Herweg et al. (2011) demonstrated that signature of fabrics worn by pedestrian might have variations due to cluttered environment, background and illumination variation. Kerekes and Hsu (2004) performed target detection using HYDICE hyperspectral data captured over forest and desert backgrounds. Results demonstrated that several parameters such as spectral resolution, ground sample distance, SNR, and scene complexity may affect spectral quality of image and thus detection probability. Additionally, issues like viewing angle, mixed pixels *etc.* may also influence detectability. Additionally, spectral resolution *i.e.* number of bands and the choice of bands may also have a bearing on performance of detection algorithms (Bris et al., 2016). Target detection using hyperspectral data may get benefitted by a suitable selection of bands. The process of selection, however, depends on type of data, target and background and scene complexities *etc.* In addition, operational parameters may influence detection differently in different spectral ranges.

Therefore, large number of parameters can affect the performance of detection algorithms in HSI. According to its place in the end to end remote sensing system, these parameters can be categorised into three groups, namely, sensor, spatial and scene parameters (Kerekes and Goldberg, 2013). The sensor parameters include aperture size, focal length, spectral and spatial resolutions *etc.* Spatial parameters include target location (*Surface/Subsurface/Air*), shape (*Point/Linear/Area*), size (*Group of pixels/pixel/subpixel*) and scene parameters refer to atmospheric/illumination conditions, target condition (*Open/Hidden/buried*), background, color

Peer review under responsibility of National Authority for Remote Sensing and Space Sciences.
* Corresponding author.
E-mail address: deepti.soni11@gmail.com (D. Yadav).

http://dx.doi.org/10.1016/j.ejrs.2017.08.004
1110-9823/© 2017 National Authority for Remote Sensing and Space Sciences. Production and hosting by Elsevier B.V.
This is an open access article under the CC BY-NC-ND license (http://creativecommons.org/licenses/by-nc-nd/4.0/).

and material composition of target. The uncertainties in reflectance spectra under influence of all such parameters may decrease accuracy of detection. However, target detection applications demand high accuracies and therefore it is important to investigate the effect of these parameters on performance of detection algorithms. The effect of most of the sensor related parameters may be corrected during pre-processing of data. However, the effect of spatial and scene parameters can't be solved theoretically and needs an empirical investigation. Also, since targets are generally contained in only a few pixels, so assessment of impact of parameters will help in increasing the effectiveness of a detection system and may also help in reducing false alarms.

This paper investigates the effect of four scene parameters namely background, illumination, material composition and color of target on detection of targets from hyperspectral data. Further, in one of the earlier works by the authors, it was found that the detection rate was high in VNIR and SWIR ranges of hyperspectral data used. Therefore, in this study, the impact of parameters has been studied in these two spectral ranges of hyperspectral image, referred as image_VNIR and image_SWIR.

2. Dataset

Data used here is an airborne hyperspectral data collected using ProSpecTIR-VS2 sensor over Rochester Institute of Technology, New York during July 26–29, 2010 (Herweg et al., 2012). An orthorectified true color image of the area is shown in Fig. 1(a). The data has been captured in 360 bands ranging from 390 to 2450 nm with spectral resolution of 10 nm. Spatial resolution of the data is 1 m. Extensive reference data consisting of position and reflectance spectrum of several objects in the area, measured using ASD FieldSpec Pro, have also been provided.

The image has been subset, size 161 × 61pixels, to generate two spectrally different images in two spectral ranges, namely, VNIR range (400–1000 nm) consisting of 108 bands (image_VNIR), and SWIR range (2100–2450 nm) consisting of 56 bands (image_SWIR). The image contains eight instances of each of two polyester fabric targets namely Red felt and Blue felt targets. These instances has been assigned a unique ID *i.e.* RF1 to RF8 and BF1 to BF8 respectively, as shown in Fig. 1(b). Few of these targets are full pixel such as RF1, RF5, RF7 (9 pixels each) and RF2, RF3, RF6, RF8 (4 pixels each), and one is sub pixel target *i.e.* RF4. Similar is the case with Blue felt targets. The description of these targets along with experimental plan is given in Table 1.

3. Methodology and implementation

The aim here is to assess the impact of four scene parameters namely, background, illumination, color and material composition of target on detectability of the two fabric targets in VNIR and SWIR ranges. All implementations have been done in MATLAB and ENVI software using following steps, also summarized in Fig. 2:

a. The details of experiments are given in Table 1. Each row gives details of the parameter being assessed. Each column describes the name of parameter, desired target and source of reference spectrum for each spectrum and remarks. While impact of one parameter has been assessed, other parameters have been kept constant.

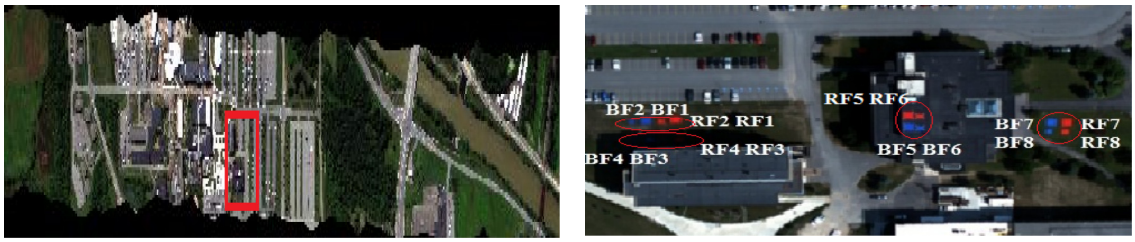

(a) (b)

Fig. 1. (a) True color image, (b) Subset image.

Table 1
Details of experiments performed for investigating effect of each parameter.

Parameter considered		Desired targets and source of reference spectrum		Remarks
		Red felt	Blue felt	
Background	Grass	Target: RF1, RF2, RF7, RF8 Reference: RF1, RF5	Target: BF1, BF2, BF7, BF8 Reference: BF1, BF5	Targets with same illumination, color and material composition
	Roof	Target: RF5, RF6 Reference: RF1, RF5	Target: BF5, BF6 Reference: BF1, BF5	
Illumination	Illumination	Target: RF1, RF2, RF7, RF8 Reference: RF1, RF3	Target: BF1, BF2, BF7, BF8 Reference: BF1, BF3	Targets with same background, color and material composition
	Shadow	Target: RF3, RF4 Reference: RF1, RF3	Target: BF3, BF4 Reference: BF1, BF3	
Color of target	Red	Target: RF1, RF2 Reference: RF1, BF1		Targets with same illumination, background and material composition
	Blue	Target: BF1, BF2 Reference: RF1, BF1		
Material composition of target	Polyester	Target: RF1, RF2 Reference: RF1, BF1	Target: BF1, BF2 Reference: RF1, BF1	Targets with same material, illumination and background

Please cite this article in press as: Yadav, D., et al.. Egypt. J. Remote Sensing Space Sci. (2017), http://dx.doi.org/10.1016/j.ejrs.2017.08.004

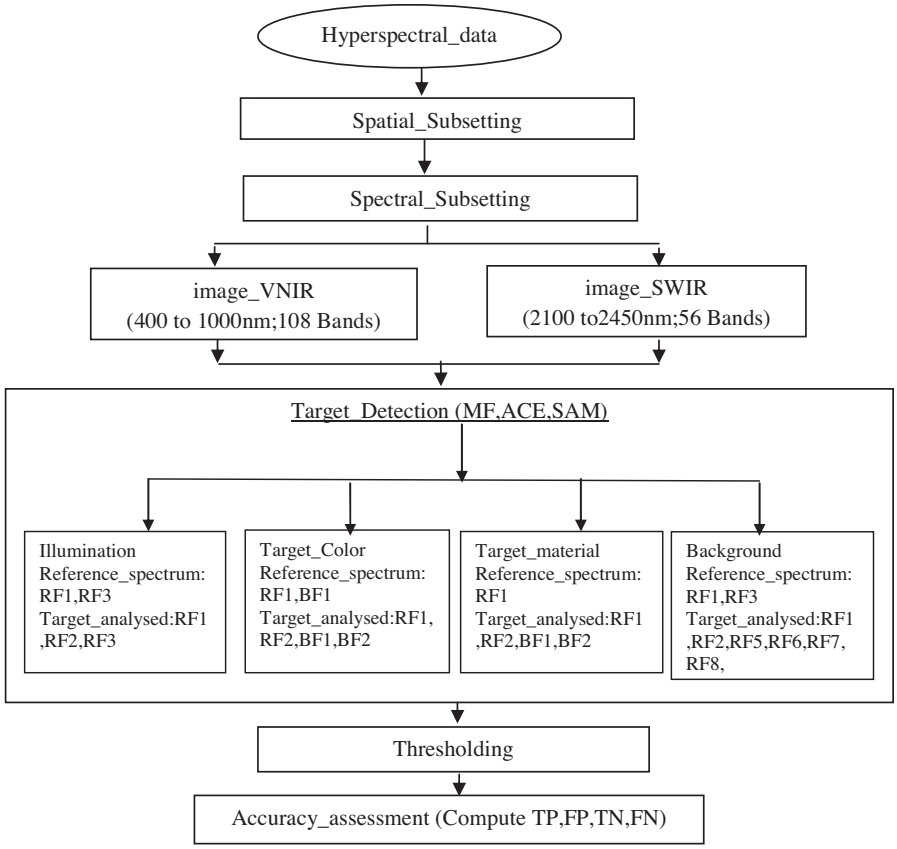

Fig. 2. Flow chart of overall methodology.

b. Three spectral matching algorithms namely Adaptive Cosine Estimator (ACE), Matched Filter (MF), Spectral Angle Mapper (SAM) have been implemented using *in scene* reference spectra. The sources used for drawing reference spectra have been summarized in Table 1. For example in order to investigate effect of illumination on detection, four experiments have been performed for Red felt target under illumination and shadow using reference spectrum drawn from RF1 as well as RF3 in both VNIR and SWIR range.
c. For each algorithm, appropriate thresholds have been applied by trial and error on the values of each metric computed in the respective spectral matching algorithm. The thresholded data have been converted into binary images to indicate the presence or absence of a target.
d. For evaluating performance of target detection, the statistics namely true positives (TP), true negatives (TN), false positives (FP) and false negatives (FN) have been computed by selecting a small window covering the desired targets and few neighbouring pixels. In the present case, windows with two different sizes (decided on the basis of size of targets) have been used. Firstly, three windows, each of size 13×9 pixels, have been used for assessment of three sets of targets such as one window each for set of RF1 & RF2, RF5 & RF6 and RF7 & RF8. The window has been designed to cover set of two targets instead of individual target because location of both of these targets is near and two single windows might overlap leading to miscalculation. Secondly, a window of size 6×6 pixels, covering a single target *i.e.* RF3 has been used for computing statistics for target under shadow.

Fig. 2 summarises the implementation of experiments discussed in this section.

4. Results and discussion

Following sub-sections discuss the results obtained for investigating effect of four selected parameters on detectability of fabric targets. Theories to explain the effects are introduced.

4.1. Effect of illumination

4.1.1. Effect of illumination in VNIR range

The detections obtained for detection of Red felt targets placed under illumination and shadow are shown in Fig. 3 and corresponding detection statistics are summarized in Table 2.

From the binary images shown in Fig. 3, it may be observed that all the algorithms have been able to accurately detect targets under illumination.

Following observations have also been drawn,

a. When a reference spectra drawn from a target under illumination (RF1) is used to detect targets under illumination (RF1, RF2, RF7, RF8), it is observed that all three algorithms are able to detect most of the pixels (TP $\geq$ 12 *out of* 13) (refer Table 2(a)). However, when the same reference spectra (RF1) is used to detect targets under shadow (RF3, RF4), it is observed that none of the algorithms are able to detect correctly and completely (refer Table 2(c)).
b. When a reference spectra drawn from a target under shadow (RF3) is used to detect targets under illumination (RF1, RF2, RF7, RF8), then it is observed that ACE is not able to detect any target pixels, MF detects few of the target pixels (TP = 8 *out of* 13) and SAM detects all target pixels with very high FP (refer Table 2(b)). However, when the same reference spectra (RF3) is used to detect targets under shadow

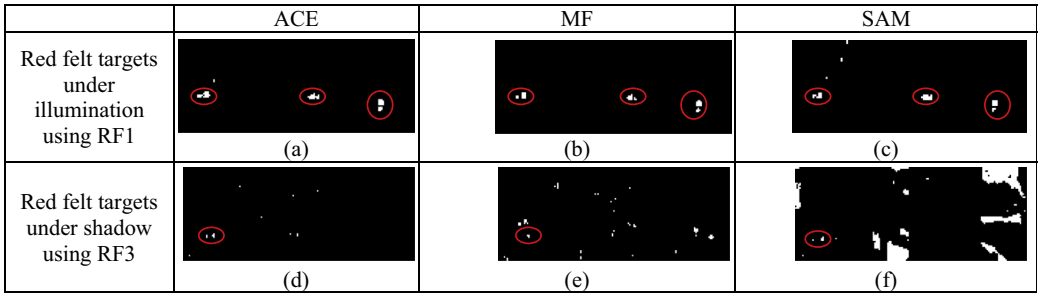

Fig. 3. Detection of Red felt target under illumination and shadow in VNIR range.

Table 2
Statistics for detections of Red felt target under illumination and shadow (VNIR range).

	Using reference spectrum: Red felt under illumination (RF1)					Using reference spectrum: Red felt in shadow (RF3)				
	(a)					(b)				
Red felt targets under illumination (RF1, RF2)	Algorithm	Red felt targets under Illumination (No. of pixels:- window:117, target:13)				Algorithm	Red felt targets under Illumination (No. of pixels:- window:117, target:13)			
		TP	FN	FP	TN		TP	FN	FP	TN
	ACE	13	0	5	99	ACE	0	13	0	104
	MF	13	0	5	99	MF	8	5	2	102
	SAM	12	1	3	101	SAM	13	0	90	14
	(c)					(d)				
Red felt targets under shadow (RF3)	Algorithm	Red felt targets in Shadow (No. of pixels:-window:36, target:4)				Algorithm	Red felt targets in Shadow (No. of pixels:-window: 36, target:4)			
		TP	FN	FP	TN		TP	FN	FP	TN
	ACE	1	3	0	32	ACE	2	2	0	32
	MF	1	3	0	32	MF	2	2	0	32
	SAM	2	2	0	32	SAM	4	0	30	2

(RF3, RF4), it is observed that ACE and MF algorithms are able to detect few target pixels (TP = 2) and though SAM detects all target pixels (TP = 4) but with very high FP (refer Table 2(d)). The probable reason for this appears to be the fact that SAM is a illumination invariant algorithm.

It may, therefore, be inferred that shadow degrades the detectability of target in VNIR range for some of the algorithms except illumination invariant algorithms. This may be due to the fact that shadow not only affects the magnitude of spectra but also its spectral properties (Ientilucci, 2012).

4.1.2. Effect of illumination in SWIR range

Similar experiments have been performed for each fabric target (Red felt and Blue felt) in image_SWIR. Results obtained have been shown in Fig. 4 and Table 3.

From the binary images (Fig. 4), it may be observed that all the algorithms fail to detect targets in shadow. In addition, detections obtained by using reference spectra of target under shadow is very low for targets under illumination and shadow.

Following observations have been made from Fig. 4 and Table 3,

a. When a reference spectra drawn from a target under illumination (RF1) is used to detect targets under illumination (RF1, RF2, RF7, RF8), it is observed that all three algorithms are able to detect most of the pixels (TP $\geq$ 9 *out of* 13) (refer Table 3(a)). However, when the same reference spectra (drawn from target under illumination (RF1)) is used to detect targets under shadow (RF3, RF4), it is observed that none of the algorithms are able to detect any pixel of shadowed target (Table 3(c)).
b. When a reference spectra drawn from a target under shadow (RF3) is used to detect targets under illumination (RF1, RF2, RF7, RF8), it is observed that none of the algorithms are able to detect any pixel of target under illumination. Similarly, when the same reference spectra (RF3) is used to detect targets under shadow (RF3, RF4), then very low detections are obtained (Table 3(b) and (d)).

Therefore, on the basis of results, it appears that shadow degrades the detectability of targets in VNIR range and almost limits or stops detectabilty of targets in SWIR range. This is due to the fact that spectra of target is likely to be at variance from spectra of targets under illumination. This is also seen corroborated from the reflectance spectra of Red felt target as shown in Fig. 5.

As seen from Fig. 5, the shape and amplitude of reflectance spectrum of shadowed target reduces in VNIR. However in SWIR range, the reflectance spectrum almost flattens and thus it appears that shape and amplitude of spectrum are severely affected due to shadow. Thus, illumination has a significant bearing on spectra and hence in the detection. Similar conclusions have been drawn by Ientilucci (2012).

4.2. Effect of target color

4.2.1. Effect of target color in VNIR range

Fig. 6 and Table 4 shows results of experiments performed for assessing target color in VNIR range.

It may be observed that Red felt reference spectra detects Red felt target only (Fig. 6(a)–(c)). Similarly, Blue felt reference spectra detects Blue felt targets only (Fig. 6(d)–(f)).

Following observations have been made from Fig. 6 and Table 4,

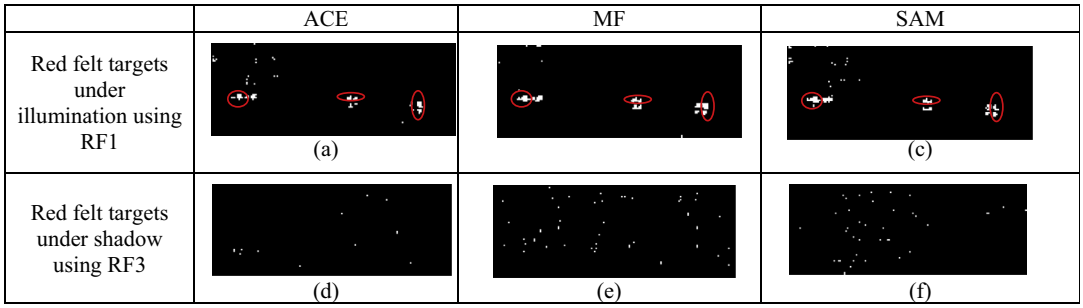

Fig. 4. Detection of Red felt target under illumination and shadow in SWIR range.

Table 3
Statistics for detections of Red felt target under illumination and shadow (SWIR range).

	Using reference spectrum: Red felt under illumination (RF1)				Using reference spectrum: Red felt under shadow (RF3)				
	(a)				(b)				
Red felt targets under illumination (RF1, RF2)	Algorithm	Detection of Red felt targets in Illumination (No. of pixels window:117, target:13)			Algorithm	Detection of Red felt targets Illumination (No. of pixels:- window:117, target:13)			
		TP	FN	FP	TN		TP	FN	FP	TN
	ACE	9	4	6	98	ACE	0	13	0	104
	MF	11	2	10	94	MF	0	13	2	102
	SAM	11	2	13	91	SAM	0	13	0	104
	(c)					(d)				
Red felt targets under shadow (RF3)	Algorithm	Detection of Red felt targets in Shadow (No. of pixels:- window:36, target:4)			Algorithm	Detection of Red felt targets in Shadow (No. of pixels:- window:36, target:4)			
		TP	FN	FP	TN		TP	FN	FP	TN
	ACE	0	4	0	32	ACE	1	3	1	31
	MF	0	4	3	32	MF	1	3	0	32
	SAM	0	4	0	32	SAM	0	4	0	32

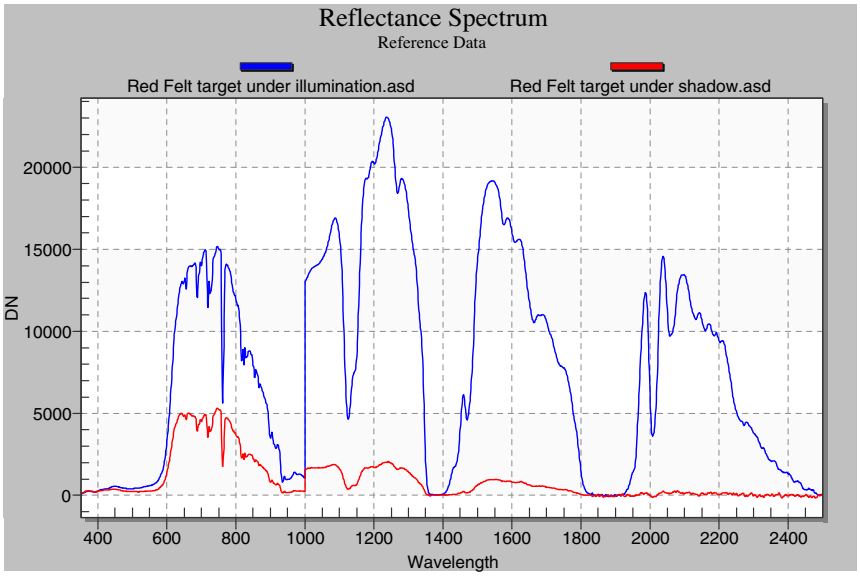

Fig. 5. Reflectance spectrum of Red felt target under illumination and shadow.

a. For detection performed using Red felt RF1, both Red felt targets (RF1, RF2) have been detected by all algorithms with TP $\geq$ 12 *out of* 13 pixels (Table 4(a)). However, none of the pixels of Blue felt targets have been detected (TP = 0) (Table 4(c)).
b. For detection performed using Blue felt BF1, both of the Blue felt targets (BF1, BF2) have been detected by all algorithms (Table 4(d)). However, none of the pixels of Red felt have been detected (TP = 0) (Table 4(b)).

It is observed that despite the fact that both fabric targets (Red felt and Blue felt) are made of same material composition, the Red felt spectra detects only Red felt targets and Blue felt spectra

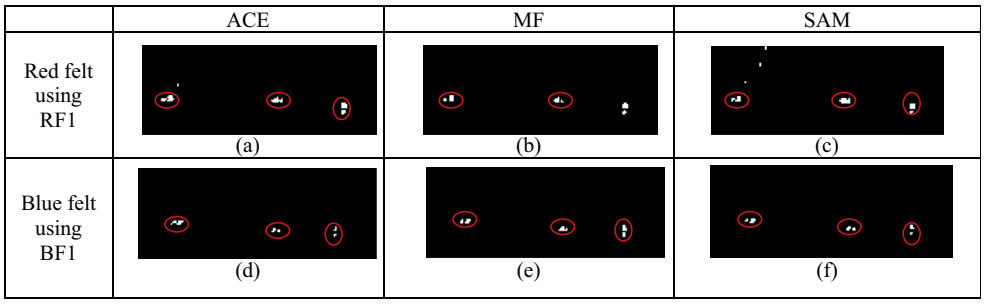

Fig. 6. Detection of Red felt and Blue felt targets in VNIR range.

Table 4
Statistics for detections of Red felt and Blue felt target (VNIR range).

	Using Red felt reference spectrum RF1					Using Blue felt reference spectrum BF1				
	(a)					(b)				
Red felt targets (RF1, RF2)	Algorithm	Detection of Red felt targets (No. of pixels window:117, target:13)				Algorithm	Detection of Red felt targets (No. of pixels window:117, target:13)			
		TP	FN	FP	TN		TP	FN	FP	TN
	ACE	13	0	5	99	ACE	0	13	5	99
	MF	13	0	5	99	MF	0	13	5	99
	SAM	12	1	3	101	SAM	0	13	3	101
	(c)					(d)				
Blue felt targets (BF1, BF2)	Algorithm	Detection of Blue felt targets (No. of pixels window:117, target:13)				Algorithm	Detection of Blue felt targets (No. of pixels window:117, target:13)			
		TP	FN	FP	TN		TP	FN	FP	TN
	ACE	0	13	2	102	ACE	10	3	6	98
	MF	0	13	3	101	MF	12	1	12	92
	SAM	0	13	1	102	SAM	10	3	2	102

detects only Blue felt targets. Thus, color has an impact of target detection in VNIR range. This may be due to characteristics of VNIR range which has absorption features associated with paint pigments. Similar observation has been reported by Adler-Golden and Sundberg (2016). They performed detection of vehicles in VNIR-SWIR hyperspectral images captured using Headwall Photonics, Inc. Hyperspec VNIR and SWIR sensors in RIT campus on October 8, 2015. The results demonstrated that when data is preprocessed with whitening, VNIR range alone can provide discrimination of vehicle spectra from background.

4.2.2. Effect of target color in SWIR range

Results of detection in SWIR have been shown in Fig. 7 and Table 5.

The binary images shown in Fig. 7 indicate that all the algorithms have detected both Red felt and Blue felt targets.

Following observations have been made from Fig. 7 and Table 5,

a. For detection performed using Red felt (RF1), both of the Red felt targets (RF1, RF2) have been detected by all algorithms with TP $\geq$ 12 *out of* 13 pixels (Table 5(a)). In addition, as seen from Table 5(c), both of the Blue felt targets (BF1, BF2) have also been detected with Red felt reference spectrum (TP > 8 *out of* 13 pixels).
b. Similarly for detection performed using Blue felt (BF1), both of the Blue felt targets (BF1, BF2) have been detected by all algorithms with TP > 8 as shown in Table 5(d). Also, both of the Red felt targets have been detected with Blue felt reference spectrum (TP > 4 *out of* 13) as shown in Table 5(b).

Thus for detection of targets with same material in SWIR, it is observed that despite difference in color, both targets have been detected using reference spectrum drawn from either of them, unlike the results obtained in VNIR range. Therefore, it appears that color of the target influences its detectability in VNIR range but

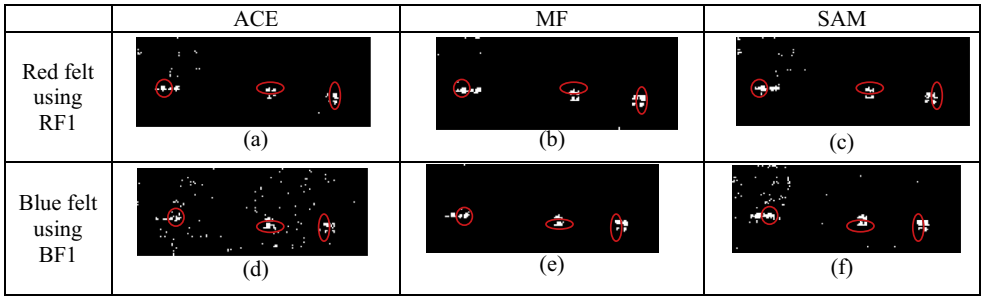

Fig. 7. Detection of Red felt and Blue felt target in SWIR range.

Please cite this article in press as: Yadav, D., et al.. Egypt. J. Remote Sensing Space Sci. (2017), http://dx.doi.org/10.1016/j.ejrs.2017.08.004

Table 5
Statistics for detections of Red felt and Blue felt target (SWIR range).

	Using reference spectrum RF1					Using reference spectrum BF1				
Red felt Target (RF1, RF2)	(a)					(b)				
	Algorithm	Detection of Red felt targets (No. of pixels window:117, target:13)				Algorithm	Detection of Red felt targets (No. of pixels: window:117, target:13)			
		TP	FN	FP	TN		TP	FN	FP	TN
	ACE	9	4	6	98	ACE	4	9	3	101
	MF	11	2	10	94	MF	8	5	6	98
	SAM	11	2	13	91	SAM	12	1	19	85
Blue felt Target (BF1, BF2)	(c)					(d)				
	Algorithm	Detection of Blue felt targets (No. of pixels window:117, target:13)				Algorithm	Detection of Blue felt targets (No. of pixels window:117, target:13)			
		TP	FN	FP	TN		TP	FN	FP	TN
	ACE	9	4	11	93	ACE	8	5	12	92
	MF	10	3	15	89	MF	11	2	11	93
	SAM	8	5	18	86	SAM	9	4	24	80

doesn't effect its detectability in SWIR range. This may be because VNIR includes Visible alongwith NIR range. wherein color is used for distinguishing objects in Visible range and material properties are used for distinguishing the objects in NIR range. Overall, VNIR range has absorption features associated with paint pigments for painted surfaces (Mohamed et al., 2017). Therefore, color of target surface may influence its detection in VNIR range. However, SWIR imaging do not capture color and thus color has no contribution in detection.

4.3. Effect of material composition of target

Due to brevity, similar results displayed in previous sections has been referred here.

4.3.1. Effect of material composition of target in VNIR range

Results displayed in first row of Fig. 6 and corresponding detection statistics as summarized in Table 6 are used for assessing effect of material composition in VNIR range.

It may be observed from Fig. 6 and Table 6 that when detections of polyester fabric targets (Red felt and Blue felt) are performed using a reference spectra drawn from a polyester target *i.e.* RF1, all algorithms detect only Red felt targets but fail to detect Blue felt targets (despite of same material composition). The probable reason may be that VNIR is influenced by color characteristics of the surface accurately in addition to various other surface characteristics associated with NIR range (as seen in Section 4.2.1) (Wilczynski et al., 2016).

4.3.2. Effect of material composition of target in SWIR range

Results displayed in first row of Fig. 7 and corresponding detection statistics as summarized in Table 7 have been used for assessing effect of material composition in SWIR range.

It may be observed from Fig. 7 and Table 7 that when detections are performed in image_SWIR for polyester fabric targets (Red felt and Blue felt both) using a reference spectra drawn from a polyester fabric *i.e.* Red felt (RF1), then all three algorithms are able to detect both polyester targets *i.e.* Red felt and Blue felt polyester targets.

Therefore, it is seen that although the material composition is same for both Red felt and Blue felt targets *i.e.* polyester but detections obtained are different in VNIR and SWIR ranges. With Red felt reference spectra, only Red felt targets are detected in VNIR range. However, both Red felt and Blue felt targets are detected in SWIR range. Thus, it appears that material composition affects detectability of targets in SWIR whereas it doesn't seem to affect detectability of same targets in VNIR. This can be attributed to the fact that SWIR can distinguish targets which have similar or even identical coating but differ in terms of composition (Wilczynski et al., 2016). Therefore it may be established that SWIR can provide improved detection performance particularly in case of visibly similar targets (such as Red felt and Red cotton) (Gross et al., 2015). Literature also suggests that SWIR supports higher detection rate for many targets (Neumann et al., 2012). Bris et al. (2016) has confirmed the importance of SWIR region for supporting good discrimination between common urban materials such as cement, gravel, metal stone, tile slate, asphalt *etc.*

4.4. Effect of background

Due to brevity, only detections statistics have been included.

4.4.1. Effect of background in VNIR range

The detection statistics of detection of Red felt target placed on grass and roof in VNIR range are summarized in Table 8.

The observations based upon Table 8 are summarized as under,

Table 6
Statistics for detection of Red felt target (VNIR range).

	Detection of Red felt (RF1, RF2) using reference spectrum RF1					Detection of Blue felt (BF1, BF2) using reference spectrum RF1				
Detection in image_VNIR	(a)					(b)				
	Algorithm	Detection of Red felt targets (No. of pixels:- window:117, target:13)				Algorithm	Detection of Blue felt targets (No. of pixels:- window:117, target:13)			
		TP	FN	FP	TN		TP	FN	FP	TN
	ACE	13	0	5	99	ACE	0	13	2	102
	MF	13	0	5	99	MF	0	13	3	101
	SAM	12	1	3	101	SAM	0	13	1	102

Please cite this article in press as: Yadav, D., et al.. Egypt. J. Remote Sensing Space Sci. (2017), http://dx.doi.org/10.1016/j.ejrs.2017.08.004

Table 7
Statistics for detection of Red felt target (SWIR range).

	Detection of Red felt (RF1, RF2) using reference spectrum RF1				Detection of Blue felt (BF1, BF2) using reference spectrum RF1				
	(a)					(b)			
Detection in image_SWIR	Algorithm	Detection of Red felt targets (No. of pixels:- window:117, target:13)				Algorithm	Detection of Blue felt targets (No. of pixels:- window:117, target:13)		
		TP	FN	FP	TN		TP	FN	FP	TN
	ACE	9	4	6	98	ACE	9	4	11	93
	MF	11	2	10	94	MF	10	3	15	89
	SAM	11	2	13	91	SAM	8	5	18	86

Table 8
Statistics for detection of Red felt targets placed on grass and roof (VNIR range).

	Using reference spectrum from Red felt on grass (RF1)					Using reference spectrum from Red felt on roof (RF3)				
	(a)					(b)				
Detection of Red felt on grass (RF1, RF2, RF7, RF8)	Algorithm	Targets on Grass (No. of pixels:- window:234, target:26)				Algorithm	Targets on Grass (No. of pixels:- window:234, target:26)			
		TP	FN	FP	TN		TP	FN	FP	TN
	ACE	26	0	52	156	ACE	26	0	40	168
	MF	26	0	51	157	MF	26	0	17	191
	SAM	26	0	16	192	SAM	26	0	16	192
	(c)					(d)				
Detection of Red felt on roof (RF5, RF6)	Algorithm	Targets on Roof (No. of pixels: window:117,target:13)				Algorithm	Targets on Roof (No. of pixels:- window:117, target:13)			
		TP	FN	FP	TN		TP	FN	FP	TN
	ACE	13	0	16	88	ACE	13	0	12	92
	MF	13	0	17	87	MF	13	0	4	100
	SAM	13	0	11	93	SAM	13	0	11	93

a. Red felt targets on both backgrounds have been detected by all three algorithms.
b. Using RF1, targets on grass background produces detections with TP = 26 and on roof background produces detections with TP = 13. Since RF1 is drawn from target on grass background, it was expected that it would have detected more pixels of targets on grass and less pixels of targets on roof. However, all the pixels of targets on both the backgrounds have been detected.
c. Using RF5, targets on grass background produces detections with TP = 26 and on roof background produces detections with TP = 13. Since RF5 is drawn from target on roof background, it was expected that it would have detected more pixels of targets on roof and less pixels of targets on grass. However, all the pixels of targets on both the backgrounds have been detected.

Therefore, it may be seen that all target pixels have been detected in VNIR range despite variation in the background. Thus, it appears that background does not interfere with detection of desired fabric targets in VNIR range. It may be because of very fine spectral resolution of hyperspectral data, the effect of background gets almost nullified or the pixel vector captured with narrow spectral resolution may be able to capture unique characteristics

Table 9
Statistics for detection of Red felt targets placed on grass and roof (SWIR range).

	Using reference spectrum from Red felt on grass (RF1)					Using reference spectrum from Red felt on roof (RF3)				
	(a)					(b)				
Detection of Red felt on grass (RF1, RF2, RF7, RF8)	Algorithm	Targets on Grass (No. of pixels: window:234, target:26)				Algorithm	Targets on Grass (No. of pixels: window:234, target:26)			
		TP	FN	FP	TN		TP	FN	FP	TN
	ACE	12	14	5	203	ACE	14	12	19	189
	MF	21	5	25	183	MF	18	8	21	187
	SAM	23	3	40	169	SAM	11	15	32	176
	(c)					(d)				
Detection of Red felt on roof (RF5, RF6)	Algorithm	Targets on Roof (No. of pixels: window:117,target:13)				Algorithm	Targets on Roof (No. of pixels: window:117, target:13)			
		TP	FN	FP	TN		TP	FN	FP	TN
	ACE	3	10	3	101	ACE	9	4	23	81
	MF	9	4	9	95	MF	10	3	11	93
	SAM	10	3	15	89	SAM	8	5	19	85

Please cite this article in press as: Yadav, D., et al.. Egypt. J. Remote Sensing Space Sci. (2017), http://dx.doi.org/10.1016/j.ejrs.2017.08.004

of the target and thus supports discrimination of the target from background. Moreover, VNIR captures reflectance of the surface only and thus underlying background might not be contributing much in the reflectance captured.

4.4.2. Effect of background in SWIR range

The detection statistics of detection of Red felt target placed on grass and roof in SWIR range are summarized in Table 9.

It may be observed from Table 9 that all Red felt targets placed on grass and roof have been detected. However, it may be observed that probability of detection in SWIR is lower than that of VNIR (Tables 8 and 9). Thus, it appears that background affects detectability of fabric targets in SWIR range. This may be due to the fact that reflectance obtained in SWIR range captures characteristics of surface and under the surface (up to few microns depending on material structure and properties) in contrast to surface characteristics captured in VNIR (Wilczynski et al., 2016). The targets considered here are fabrics which are thin and thus may allow penetration. Therefore, the reflectance of underlying background appears to influence the overall reflectance spectrum and thus reduce the detection in SWIR range.

5. Conclusions

Accuracy demand from a detection algorithm is very high but there exist large number of parameters which can adversely affect the accuracy of detection algorithms. Therefore for improving effectiveness of detection algorithm, it is fruitful to perform detailed assessment of impact of the parameters. In this paper, an empirical analysis of impact of four scene parameters namely illumination, background, color and material composition of target on accuracy of target detection have been performed. For this, in-depth performance evaluation of the three detection algorithms namely ACE, MF and SAM for detection of two fabric targets namely Red felt and Blue felt as applied to VNIR and SWIR regions of hyperspectral imagery is presented. From the analysis of results, following conclusions have been drawn,

(i) The impact of parameters on performance of detection algorithm varies for different spectral regions of HSI.
(ii) The variation in illumination has high impact on the detectability of the target. In particular, shadow reduces detectability of targets in VNIR range and restricts detection in SWIR range considerably.
(iii) The impact of background on detection of target in VNIR is not prominent but it has an impact in SWIR range.
(iv) In case of targets made of same material but with different colors, it has been shown that color influence detection of target in VNIR range but has no role in detection in SWIR range.
(v) The material composition has an impact on detection of targets in SWIR but not in VNIR range (for same category of targets *i.e.* both cotton fabric and polyester fabric are fabrics).

The experimental study presented here demonstrated that scene parameters can influence the accuracy of detection and severity of the influence may vary from one spectral range to the other. This experiment setup can be applied to any kind of targets, different spectral ranges, parameters and detection algorithms. This can provide good reference for deciding the suitable range and parameters requiring specialized processing for achieving more effective detection in real remote sensing applications.

References

Adler-Golden, S., Sundberg R., 2016. Identifying vehicles with VNIR-SWIR hyperspectral imagery: sources of distinguishability and confusion. Proc. SPIE-9976. Imaging Spectrometry-XXI.99760K.

Bris, L., Chehata, N., Briottet, X., Paparoditis, N., 2016. Spectral band selection for urban material classification using Hyperspectral libraries. ISPRS Annals of Photogrammetry, Remote Sensing & Spatial Information Sciences. Volume III-7, 2016, XXIII ISPRS Congress, 12–19, July 2016, Prague.

Gross, W., Boehler, J., Schilling, H., Middelmann, W., Weyermann, J., Wellig, P., Oechslin, R., Kneubuehler, M., 2015. Assessment of target detection limits hyperspectral data. Target & background signatures. Proc. SPIE 9653, 96530J–10.

Herweg, J.A., Kerekes, J.P., Ientilucci, E.J., Eisman, M.T., 2011. Spectral variations in HSI signatures of thin fabrics for detecting & tracking pedestrians. Active & Passive Signatures-II, Proc. of SPIE, vol. 8040.

Herweg, J.A., Kerekes, J.P., Weatherbee, O., Messinger, D., Aardt, J.V., Ientilucci, E.J., Ninkov, Z., Faulring, J., Raqueño, N., Meola, J., 2012. SpecTIR Hyperspectral Airborne Rochester Experiment Data Collection Campaign. SPIE. Proc. SPIE, vol. 8390.

Ientilucci, E.J., 2012. Leveraging LiDAR data to aid hyperspectral image target detection radiance domain. Proc.of SPIE, vol. 8390, Algorithms & Technologies for Multispectral, Hyperspectral, Ultraspectral Imagery-XVIII, 839007.

Kerekes, J., Goldberg, D., 2013. Hyperspectral image quality for unmixing and subpixel detection applications. Proc. Image Qual. Syst. Perform.-X, SPIE 8653, 865304.

Kerekes, J., Hsu, S., 2004. Spectral quality metrics for VNIR and SWIR hyperspectral imagery. Proceedings of Algorithms & Technologies for Multispectral, Hyperspectral & Ultraspectral Imagery-X. Proc. of SPIE, vol. 5425, Defense & Security Symposium, Orlando, Florida.

Mohamed, E.S., Saleh, A.M., Belal, A.B., Abd_Allah, 2017. Application of near-infrared reflectance for quantitative assessment of soil properties. Egypt. J. Remote Sens. Space Sci., Elsevier.

Nasarbadi, N.M., 2014. Hyperspectral target detection: an overview of current and future challenges. IEEE Signal Proc. Mag. 31 (1), 34–44.

Neumann, J., Kruer, M., Allman, E., Downes, T., Howard, G., Leathers, R., Yetzbacher, M., Kutteruf, M., Colbert, M., Frawley, S., Butikofer, Z., Meadows, C., Lee, J., 2012. Long Range Automated Hyperspectral Target Detection. US Naval Research Laboratory.

Wilczynski, S., Koprowski, R., Marmion, M., Duda, P., Fajfrowska, B.B., 2016. The use of hyperspectral imaging in VNIR 400–1000 nm and SWIR range1000–2500 nm for detecting counterfeit drugs with identical API composition, vol. 160. Elsevier, Talanta, pp. 1–8.

This is an open access article published under an ACS AuthorChoice License, which permits copying and redistribution of the article or any adaptations for non-commercial purposes.

ACS OMEGA

Article

Cite This: ACS Omega 2017, 2, 6782-6785

http://pubs.acs.org/journal/acsodf

Probing Charge-Transfer and Short-Lived Triplet States of a Biosensitive Molecule, 2,6-ANS: Transient Absorption and Time-Resolved Spectroscopy

Mohan Singh Mehata,*[,†] Yang Yang,[‡] and Keli Han*[,‡]

[†]Laser-Spectroscopy Laboratory, Department of Applied Physics, Delhi Technological University, Bawana Road, Delhi 110042, India

[‡]State Key Laboratory of Molecular Reaction Dynamics, Dalian Institute of Chemical Physics (DICP), Chinese Academy of Sciences, Dalian 116023, China

Supporting Information

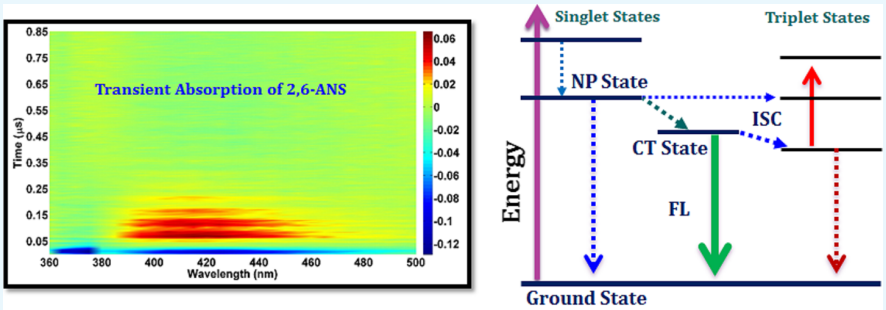

Transient absorption and Energy level diagram of 2,6-ANS

ABSTRACT: We report the existence of a short-lived triplet electronic state of 2,6-ANS (2-anilinonaphthalene-6-sulfonic acid), which, together with nonplanar (NP) and planar [charge-transfer (CT)] states, is produced following photoexcitation; these results are based on nanosecond transient absorption and time-resolved decays. The short-lived triplet state has a lifetime of ∼126 ns and is observed via triplet−triplet (T−T) transitions after exciting 2,6-ANS with a pump laser pulse of 355 nm (probe wavelength range of 360−500 nm). Moreover, the CT state, which is very close to the NP state produced from the locally excited state/NP state, emits active fluorescence with a lifetime of ∼11 ns. The solvent plays a major role in the rotation of the phenylamino group during the conversion of the NP state to the CT state, and vice versa. Intersystem crossing occurs from the CT state. Thus, investigating the triplet state together with the CT/NP states of 2,6-ANS, a commonly used probe for sensing proteins and other biomolecules, is highly relevant and helps reveal its photoexcitation dynamics.

INTRODUCTION

Probes containing the anilinonaphthalene sulfonate (ANS) fluorophore, which is characterized by the dependence of its absorption, fluorescence (FL), FL quantum yield (QY), and lifetime on its environment, have been used for studying the structures of biological macromolecules for the past several years.[1−4] ANS and the related molecules 1-anilinonaphthalene-8-sulfonate and 2,6-ANS (2-anilinonaphthalene-6-sulfonic acid) are the most widely used molecules featuring this fluorophore. A dramatic change in the FL QY with different solvents, a change in FL intensity with the local environment, and a drastic blue shift of the FL wavelength maximum in low-polarity solvents relative to that in higher polarity solvents such as water have been observed.[1−3] An increase in FL intensity in a hydrophobic environment was also reported in 1954.[4] In biological fields, ANS has been used as a hydrophobicity probe for protein folding and for cell surface studies.[5] The characteristic features of the ANS fluorophore have been used successfully to evaluate the micropolarity of the local environment in proteins and lipid nanotubes.[6,7] These photoinduced electron-transfer-based probes are also sensitive to the pH and the presence of transition-metal ions in the environment.[8] The mechanism of ANS involves the intramolecular rotation of the phenylamino group and the subsequent conversion of its nonplanar (NP) state to the stable charge-transfer (CT) state immediately after photoexcitation. However, different explanations for the massive solvent effects on the excited-state lifetime have been given.[1−11]

Here, we applied nanosecond transient absorption (TA) and time-resolved FL techniques to 2,6-ANS dissolved in degassed methanol and measured the nanosecond TA and FL decays. On the basis of the TA and FL decay curves, along with the steady-state spectra, the S−S (singlet−singlet) and T−T (triplet−triplet) transitions that occur following the photoexcitation

Received: July 4, 2017
Accepted: October 2, 2017
Published: October 17, 2017

 © 2017 American Chemical Society

DOI: 10.1021/acsomega.7b00921
ACS Omega 2017, 2, 6782−6785

have been confirmed, and the nonradiative transition through intersystem crossing (ISC) was found to be responsible for the decrease in FL QY.

RESULTS AND DISCUSSION

Figure 1a shows the absorption, FL, and FL excitation spectra of 2,6-ANS in methanol. The absorption spectrum shows the

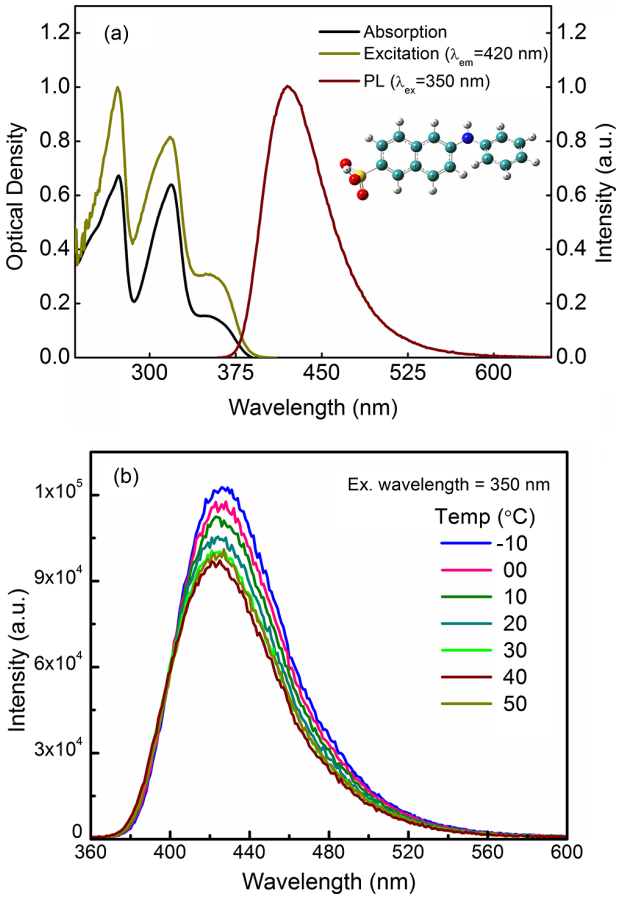

Figure 1. (a) Absorption, normalized FL, and corrected FL excitation spectra of 2,6-ANS dissolved in methanol. The inset shows the chemical structure of 2,6-ANS. (b) FL spectra of 2,6-ANS in methanol as a function of temperature. The excitation and emission wavelengths were 350 nm (a,b) and 420 nm (a), respectively.

lowest energy band at approximately 350 nm as well as strong bands at approximately 319 and 273 nm, whereas the FL spectrum shows a band maximum at 420 nm. The FL excitation spectrum is nearly the same as the absorption spectrum, as shown in Figure 1a, which indicates that the QY does not change with excitation. Thus, the steady-state absorption represents the locally excited singlet state transitions. The FL may arise from the NP state and/or from a CT state produced following the rotation of the phenylamino group in polar solvents. FL from the NP state is observed in less polar solvents.[3] Furthermore, the FL spectra were also measured at temperatures varying from −10 to 50 °C and are shown in Figure 1b. Cooling from room temperature to −10 °C was expected to double the solvent viscosity relative to that at room temperature, but the intensity of the FL band increases without any significant shift in wavelength. The increase in FL intensity is due to the slowdown of the nonradiative deactivation. When the temperature increases above room temperature, the FL intensity decreases without a considerable shift in band position, indicating that the FL originates from the CT state only, that is, from the planar molecule. However, the NP and CT states are very close to each other in alcoholic solvents and water, and both of them may exist.[9,11] When the temperature increases further above 40 °C, the FL intensity again starts increasing without any significant shift, which may affect the rate of the ISC process.

In addition, FL decay analysis was performed with a 336 nm excitation wavelength and was monitored using a 420 nm emission wavelength under degassed conditions and atmospheric conditions, both of which are shown in Figure 2. Both

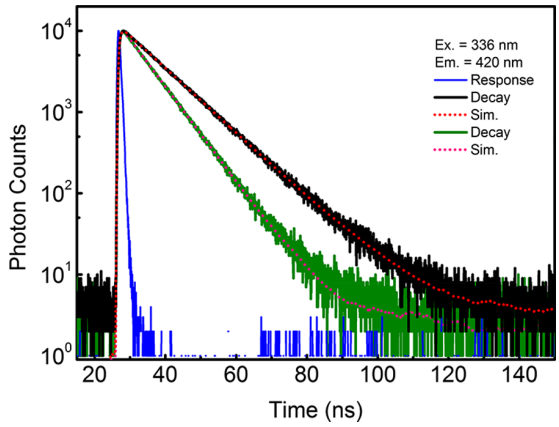

Figure 2. FL decay curves of 2,6-ANS in methanol (solid black line) obtained at 298 K under degassed conditions and simulated curve (dotted red line). The excitation and emission wavelengths were 336 and 420 nm, respectively. The FL decay curve (solid green line) and simulated curve (dotted red line) obtained without degassing. The instrumental response function is shown with the solid blue line.

decay profiles could be well-simulated by assuming a single-exponential decay function, that is, $A_1 \exp(-t/\tau_1)$, and the lifetime τ_1 is determined. The fitted lifetime is 10.89 ± 0.02 ns with χ^2 = 1.29. Under atmospheric conditions, the lifetime becomes 7.43 ± 0.02 ns (χ^2 = 1.17). Thus, the observed lifetime is a single exponential and is quenched reasonably in the presence of oxygen. The observed FL lifetime originates from the relaxed state which is designated the CT state. Furthermore, the single lifetime of 2,6-ANS in methanol is ascribed to the fast interconversion between the CT and NP states. The reported lifetime of 2,6-ANS varies with different solvents and mixtures of solvents and is typically 0.3 ns of the CT state FL and approximately 1−5 ns of the NP state in water, which is debatable.[3] In addition to the solvent, oxygen is an important factor that can alter the lifetime of such biomolecules, as observed in this study. Thus, the lifetime of ANS strongly depends on the solvent system.

Figures 3 and 4 show the TA spectrum and dynamical curves, respectively, of 2,6-ANS in methanol under degassed conditions. The measurements were carried out at 5 mJ@355 nm excitation and every 10 nm interval in the 360−500 nm region. The corresponding instrumental response function of the dynamical curve is provided in Figure S1 in the Supporting Information. The pulse energy was maintained as small as possible to still obtain the transient signal while avoiding

DOI: 10.1021/acsomega.7b00921
ACS Omega 2017, 2, 6782−6785

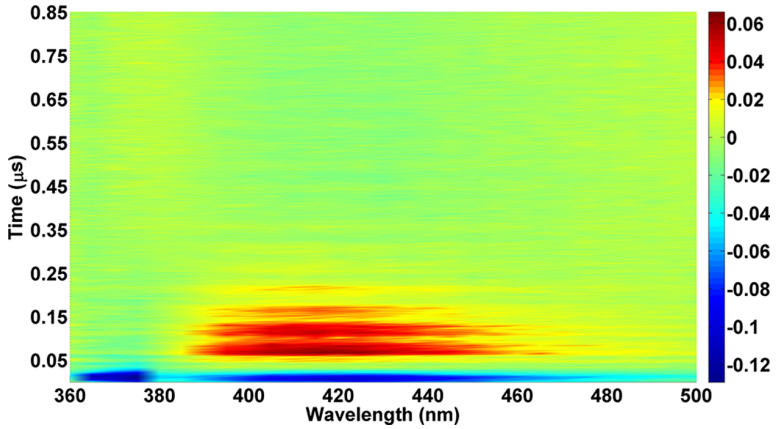

Figure 3. TA spectrum of 2,6-ANS in methanol as a function of probe wavelength under degassed conditions. The pumped wavelength was 355 nm with a pulse energy of 5 mJ.

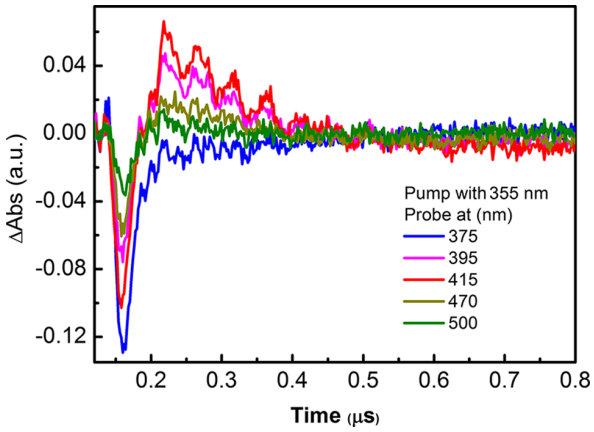

Figure 4. TA dynamical curves of 2,6-ANS in methanol at different probe wavelengths under degassed conditions. The pumped wavelength was 355 nm with a pulse energy of 5 mJ.

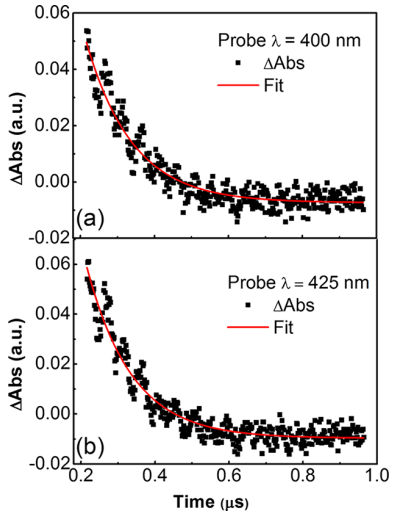

Figure 5. TA dynamical curves/absorbance (ΔAbs) of 2,6-ANS in methanol at probe wavelengths of 400 nm (a) and 425 nm (b) pumped by nanosecond laser pulses of 355 nm at 5 mJ under degassed conditions. The black and red curves represent the original data and the single-exponential fit, respectively.

additional reactions.[12] It can be seen from Figure 3 that a series of absorption/emission peaks last for several sub-microseconds. The positive (red color) and negative (blue) signals are attributed to the T−T and S−S transitions, respectively. Strong S−S transitions appear at approximately 360−380 nm, which may be due to the ground-state bleaching effect. Above this point, both positive and negative lobes were obtained at each probe wavelength, indicating that both T−T absorption and S−S emission occur (Figures 4 and 5). Different dynamical curves were selected because of their high signal-to-noise ratios for fitting. However, only the dynamical curves obtained at 400 and 425 nm are shown in Figure 5. The positive part of the TA signal is well-fitted with the single-exponential fit component: $\Delta\mathrm{Abs}(t) = A_2 \exp(-t/\tau_2)$, where τ_2 and A_2 are the lifetime and the pre-exponential factor, respectively. The fitted lifetime is 0.126 ± 0.004 μs with an adjustment R^2 of >0.9. Similarly, the negative part of the dynamical curves is fitted with the single-exponential fit. However, the fitted lifetime could not be considered accurate, as the lifetime of the FL is approximately 10.89 ns, which is beyond the resolution of the TA system. The long lifetime corresponds to the positive amplitude of the TA signal designated to the T−T transitions (absorption), that is, assigned to the short-lived triplet state. Thus, the TA signal of 2,6-ANS demonstrates the existence of a short-lived triplet state. However, the emission measurement, which was conducted between −10 and 50 °C, did not show any emission from the triplet state, even at −10 °C.

Following photoexcitation, an NP state is initially produced and subsequently forms a CT state that emits FL. However, the NP and CT states of 2,6-ANS lay very close to each other in alcoholic solvents[9] and are not distinguishable in water.[11] We did not observe any significant shift in the FL spectrum with decreasing temperature, that is, upon increasing the viscosity of the solvent, and vice versa, which indicates that the FL may originate from the CT state and that the solvent methanol allows the rotation of the phenylamino group. Importantly, both the NP and CT states can yield triplets.[9,10] The CT state that emits active FL undergoes a nonradiative transition through ISC. The TA, together with FL decay analysis and steady-state spectra, indicates the existence of NP/CT (due to fast interconversion) and triplet states of 2,6-ANS; among these species, the CT state emits strong FL with a lifetime of ∼11 ns, as demonstrated in Figure 6.

DOI: 10.1021/acsomega.7b00921
ACS Omega 2017, 2, 6782−6785

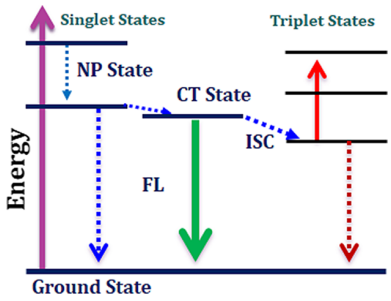

Figure 6. State diagram of the photoexcitation dynamics of 2,6-ANS.

The molecule 2,6-ANS has been studied based on the TA spectra/dynamical curves and time-resolved FL decay curves. The fitted TA and FL decay curves show the existence of NP/CT and triplet states with lifetimes of approximately 11 and 126 ns, respectively. Thus, the present investigation of 2,6-ANS, a molecule commonly used to probe biomolecules, is highly important and unusual, as it opens up new avenues to understand the existence of the CT and triplet states of ANS and the variable QY.

METHODS AND MATERIALS

2,6-ANS was obtained from Molecular Probes, USA, and was used without further purification. Steady-state absorption and FL spectra were recorded with a LAMBDA-750 UV/vis/NIR spectrometer (PerkinElmer) and a Fluorolog-3 spectrofluorometer (HORIBA Jobin Yvon), respectively. The details about the equipment were described in our previous report.[13] A sample heater/cooler Peltier thermocouple device (FI-3004) equipped with a Fluorolog-3 was used for recording the temperature from −10 to 50 °C. Time-resolved FL decay curves were collected on a time-correlated single-photon counting system (DeltaFlex, HORIBA Jobin Yvon) with a PPD-850 detector using a delta diode as an excitation source.

Nanosecond TA measurements were performed with pump−probe techniques, as described in our previous reports.[12,14,15] All samples were thoroughly degassed (N_2) before obtaining the spectra, FL decays, TA spectra, and dynamical curves. The concentration of the samples was 20 μM, and the path length of the sample quartz cuvette was 10 mm.

ASSOCIATED CONTENT

Supporting Information

The Supporting Information is available free of charge on the ACS Publications website at DOI: 10.1021/acsomega.7b00921.

Instrumental response function of the TA system recorded with a pulse energy of 5 mJ at 355 nm with a neat solvent (PDF)

AUTHOR INFORMATION

Corresponding Authors

*E-mail: msmehata@gmail.com (M.S.M.).
*E-mail: klhan@dicp.ac.cn (K.H.).

ORCID

Mohan Singh Mehata: 0000-0003-4564-5243
Keli Han: 0000-0001-9239-1827

Notes

The authors declare no competing financial interest.

ACKNOWLEDGMENTS

M.S.M. thanks the Chinese Academy of Science (CAS), China, for supporting his stay at DICP, CAS, Dalian, China, under the CAS visiting scholar program and Dr. H.C. Joshi, IPR, India, for valuable comments. This work was financially supported by the National Basic Research Program of China (2013CB834604), the Natural Science Foundation of China (NSFC, grant no. 21403226), the Science and Engineering Research Board (SERB), DST (grant no. EMR/2016/001110), and the DST-FIST project (SR/FST/PSI-164/2011(C)).

REFERENCES

(1) Robinson, G. W.; Robbins, R. J.; Fleming, G. R.; Morris, J. M.; Knight, A. E. W.; Morrison, R. J. S. Picosecond studies of the fluorescence probe molecule 8-anilino-1-naphthalenesulfonic acid. *J. Am. Chem. Soc.* **1978**, *100*, 7145−7150.
(2) Brand, L.; Gohlke, J. R. Fluorescence probes for structure. *Annu. Rev. Biochem.* **1972**, *41*, 843−868.
(3) Someya, Y.; Yui, H. Fluorescence lifetime probe for solvent microviscosity utilizing anilinonaphthalene sulfonate. *Anal. Chem.* **2010**, *82*, 5470−5476.
(4) Weber, G.; Laurence, D. J. Fluorescent indicators of adsorption in aqueous solution and on the solid phase. *Biochem. J.* **1954**, *31*, 56.
(5) Royer, C. A. Probing protein folding and conformational transitions with fluorescence. *Chem. Rev.* **2006**, *106*, 1769−1784.
(6) Pal, S. K.; Peon, J.; Zewail, A. H. Ultrafast surface hydration dynamics and expression of protein functionality: α-chymotrypsin. *Proc. Natl. Acad. Sci. U.S.A.* **2002**, *99*, 15297−15302.
(7) Yui, H.; Guo, Y.; Koyama, K.; Sawada, T.; John, G.; Yang, B.; Masuda, M.; Shimizu, T. Local environment and property of water inside the hollow cylinder of a lipid nanotube. *Langmuir* **2005**, *21*, 721−727.
(8) Dimov, S. M.; Georgiev, N. I.; Asiri, A. M.; Bojinov, V. B. Synthesis and sensor activity of a PET-based 1,8-naphthalimide probe for Zn^{2+} and pH determination. *J. Fluoresc.* **2014**, *24*, 1621−1628.
(9) Kosower, E. M.; Tanizawa, K. Analysis of fluorescence emission and quenching for molecules bearing latent donors. *Chem. Phys. Lett.* **1972**, *16*, 419−425.
(10) Kosower, E. M. Intramolecular donor-acceptor systems. 9. Photophysics of (phenylamino)naphthalenesulfonates: a paradigm for excited-state intramolecular charge transfer. *Acc. Chem. Res.* **1982**, *15*, 259−266.
(11) Hamai, S. Fluorescence polarization of inclusion complexes of β-cyclodextrin with 6-anilino-2-naphthalenesulfonate and 8-anilino-1-naphthalenesulfonate in aqueous D-glucose solutions. *Bull. Chem. Soc. Jpn.* **1999**, *72*, 2177−2182.
(12) Mehata, M. S.; Yang, Y.; Qu, Z.-J.; Chen, J.-S.; Zhao, F.-J.; Han, K.-L. Spin mixed charge transfer states of iridium complex $Ir(ppy)_3$: Transient absorption and time-resolved photoluminescence. *RSC Adv.* **2015**, *5*, 34094−34099.
(13) Ratnesh, R. K.; Mehata, M. S. Synthesis and optical properties of core-multi-shell CdSe/CdS/ZnS quantum dots: Surface modifications. *Opt. Mater.* **2017**, *64*, 250−256.
(14) Yang, Y.; Liu, L.; Yin, H.; Xu, D.; Liu, G.; Song, X.; Liu, J. White light assisted photosensitized synthesis of Ag nanoparticles: Excited-state hydrogen bonding roles. *J. Phys. Chem. C* **2013**, *117*, 11858−11865.
(15) Chen, J.-S.; Zhao, G.-J.; Cook, T. R.; Han, K.-L.; Stang, P. J. Photophysical properties of self-assembled multinuclear platinum metallacycles with different conformational geometries. *J. Am. Chem. Soc.* **2013**, *135*, 6694−6702.

DOI: 10.1021/acsomega.7b00921
ACS Omega 2017, 2, 6782−6785

Appl. Phys. A (2017) 123:677
DOI 10.1007/s00339-017-1295-5

Applied Physics A
Materials Science & Processing

Quantifying phase separation in terms of magnetoresistive hysteresis loops in strongly phase-separated manganite thin films

Sandeep Singh[1,2] · Pawan Kumar Tyagi[2] · H. K. Singh[1]

Received: 26 April 2017 / Accepted: 1 October 2017
© Springer-Verlag GmbH Germany 2017

Abstract The present work reports the scaling behaviour of thermomagnetic hysteresis in temperature and magnetic field-dependent resistivity [(ρ–T) and (ρ–H)] measured during cooling/warming and H increasing/decreasing cycles in single crystalline $La_{0.21}Pr_{0.42}Ca_{0.37}MnO_3$ thin films. The zero-magnetic field ($H=0$) insulator–metal transition temperature (IMT) measured in warming cycle ($T_{IM}^{W}\sim 163$ K) is higher than that in the cooling cycle ($T_{IM}^{C}\sim 116$ K) and the difference between the two IMTs shrinks as H is increased. The magnetic field dependence of the two IMTs is well fitted by the equation $T_{IM}=T_{IM}^{0}+\beta H^{\alpha}$. Here, T_{IM}^{0} is the H-independent contribution and the constants, pre-factor β and exponent α determine the H-dependent part of the IMT. The ρ–T loop area diminishes with the increasing H and its scaling with H in the regime which is akin to a magnetic liquid and unstable towards external H ($H<30$ kOe) is nicely described by $A_T=A_{T0}e^{-\Gamma H}$. Here, A_{T0} is the zero-field normalized area and Γ is a constant related to the degree of phase separation. The analysis of the isothermal ρ–H loop area, which increases with H shows a scaling behaviour of the type $A(H)=a(H-H_{IM})^{\eta}$. Here, the constant H_{IM} corresponds to the induced AFMI–FMM phase transition and decreases with temperature, while the exponent 'η' measures the degree of phase separation.

✉ H. K. Singh
hks65@nplindia.org

[1] National Physical Laboratory (Council of Scientific and Industrial Research), Dr. K. S. Krishnan Marg, New Delhi 110012, India

[2] Department of Applied Physics, Delhi Technological University, Delhi 110042, India

1 Introduction

Manganese incorporating perovskite oxides represented generically by $RE_{1-x}AE_xMnO_3$, where RE and AE are rare earth and alkaline earth cations have engaged the interest of the physics community for nearly a quarter century now because of their highly enriched nature regarding the electronic phases [1–3]. The electronic phase affluence is amply demonstrated by the existence paramagnetic insulator (PMI), ferromagnetic metal (FMM), a ferromagnetic insulator (FMI), an antiferromagnetic insulator (AFMI) and charge ordered/orbital ordered (CO/OO) phases [1–3]. The nature and relative fraction of the phases are controlled by the RE/AE ratio, their average cationic size and thermomagnetic variables like temperature (T) and magnetic field (H). At sufficiently small average RE/AE cation radii, which manifests it in the form of reduced one electron bandwidth (BW), the interphase boundaries become permeable making the cross boundary electronic phase diffusion noticeable. This cross-boundary phase diffusion is called phase separation, which is the axial attribute of the physics of manganites [1–3]. As BW is lowered, the nature of the PM and FM phases and the associated phase transition deviates from the canonical one due to the phase separation. In low BW manganites like $Sm_{1-x}Sr_xMnO_3$ and $La_{1-x-y}Pr_yCa_xMnO_3$, the dominant phase separation tendencies are considered as intrinsic having mesoscopic dimensionality [4–12]. $La_{1-x-y}Pr_yCa_xMnO_3$ has emerged as the generic representative of the manganites showing mesoscale phase separation with coexisting AFMI/CO and FMM clusters [6].

As demonstrated by the work of Ghivelder and Parisi [7], in bulk $La_{5/8-y}Pr_yCa_{3/8}MnO_3$ ($y\approx 0.4$), the CO transition at T_{CO} ~ 230 K is followed by AFM spin order T_N ~ 180 K and at T_C ~ 80 K the FM transition is observed. Large relaxation effects are also observed due to the temporal and

Published online: 11 October 2017

dimensional fluctuations in the relative fraction of the FMM and AFM/COI phases [7]. Sharma et al. [8] in a similar material showed that the magnetic phase in the phase-separated regime has liquid-like character; it has non-ergodic nature and is ultra-sensitive to magneto-thermal perturbations. Wu et al. [9] and Singh et al. [10] have demonstrated that $La_{5/8-y}Pr_yCa_{3/8}MnO_3$ ($y \approx 0.4$) thin films exhibit a supercooled glass transition with huge difference between the cooling and warming cycle FM transition temperature (T_C) insulator metal transition temperatures (IMTs). More recently Agarwal et al. [11, 12] demonstrated that depending on the growth conditions and the degree of microstructural inhomogeneity, the difference between cooling and warming cycle T_C and IMTs can be as large as ~ 73–75 K in $La_{1-x-y}Pr_yCa_xMnO_3$ ($x \sim 0.42$, $y \sim 0.40$) thin films. Such huge differences in the magneto-metallic transitions and the devitrification of the glassy phase during warming yields extraordinary hysteresis in FCC–FCW and cooling and warming cycle IMTs. The typical signatures of strongly phases-separated manganites are (1) pronounced divergence of the zero-filed cooled (ZFC) and field cooled warming (FCW) magnetization, (2) noticeable hysteresis between the field cooled cooling (FCC) and FCW magnetization, and (3) strong thermomagnetic hysteresis in resistivity measured during cooling/warming and H increasing/decreasing cycles [6–20].

The hysteresis loops are common manifestations of non-equilibrium states and are generally associated with the first-order phase transition in which there is a finite barrier to the nucleation of the new phase. It is also related to a glass phase frozen into a nonequilibrium. In case of low BW manganites like $La_{1-x-y}Pr_yCa_xMnO_3$, the finite barrier to the growth of the low temperature ordered FM phase is provided by the high temperature ordered AFM phase and the non-equilibrium states are manifested in the form of the thermomagnetic hysteresis in ρ–T and ρ–H measured during cooling/warming and H increasing/decreasing cycles. The prominent members of the family are the low BW manganites with intrinsic phase separation like $Pr_{1-x}Ca_xMnO_3$ ($x \approx 0.3$–0.5) [3, 21–25], $Sm_{1-x}Sr_xMnO_3$ ($x \approx 0.35$–0.5) [3–5, 26, 27] and $La_{1-x-y}Pr_yCa_xMnO_3$ ($x \approx 0.3$–0.5, $y \approx 0.3$–0.5) [3, 6–20, 28]. Among these, the last member has emerged as the prototypical system to study the magnetic field-induced first-order phase transition, the supercooling glass transition, and the associated thermomagnetic hysteresis. The hysteretic behaviour of $La_{1-x-y}Pr_yCa_xMnO_3$ ($x \approx 0.3$–0.5, $y \approx 0.3$–0.5) (LPCMO) as observed in the ρ–T and ρ–H measurements has been studied in fair detail during the last decade [6–20, 28]. Depending on the values of the compositional variables x and y, the zero field ($H = 0$) difference between the cooling and warming cycle IMTs (T_{IM}^{C} and T_{IM}^{W}) can be as large as 50–75 K [10–12] and as H is increased, both T_{IM}^{C} and T_{IM}^{W} rise up, with simultaneous shrinking of the difference between them and the enclosed loop area. Similar differences are seen in the T_C obtained from the FCC and FCW M-T. The isothermal ρ–H curves of LPCMO also show pronounced hysteresis in the magnetic liquid regime. Despite several detailed studies focussed on the phase separation in LPCMO, not much attention has been paid to the scaling behaviour of the ρ–T and ρ–H hysteresis loops as a function of thermomagnetic variable T and H. We believe that in view of the mesoscopic cluster coexistence, the scaling behaviour of the ρ–T and ρ–H hysteresis loops can prove to be an alternative tool to analyse and understand the intrinsic phase separation. In the present work, we have grown high-quality ~ 70 nm thin single crystalline films of $La_{0.21}Pr_{0.42}Ca_{0.37}MnO_3$ (LPCMO) and investigated the scaling behaviour of T_{IM}^{C} and T_{IM}^{W}, ρ–T and ρ–H hysteresis loops.

2 Experimental details

Target (~ 2″ diameter) of $La_{5/8-y}Pr_yCa_{3/8}MnO_3$ ($x \sim 0.42$ and $y = 0.36$) was prepared by solid state reaction route with desired amount of high purity (> 3N) La_2O_3, Pr_2O_3, $CaCO_3$, and MnO_2. The thoroughly mixed powder was heat treated at 900 °C for 24 h and with an intermediate grinding; the second heat treatment was given at 1000 °C for 24 h. Then, fine powder was pressed in the form of a disc of 2″ diameter and ~ 3 mm thickness and sintered at 1200 °C for 24 h. The films were deposited by RF magnetron sputtering under ~ 200 mtorr of $Ar + O_2$ (~ 80 + ~ 20%) mixture. The crystal STO (110) substrates ($5 \times 3 \times 0.5$ mm^3) were maintained at temperature ~ 820 °C. Ex situ annealing in oxygen ambient at ~ 900 °C for 10 h was done to achieve optimum oxygen content. The X-ray reflectivity (XRR) measurement was used to estimate the film thickness. The structural and topological characteristics were probed by high-resolution X-ray diffraction (HRXRD, PANalytical PRO X'PERT MRD, Cu-Kα1 radiation $\lambda = 1.5406$ Å) and atomic force microscopy (AFM, VEECO Nanoscope V), respectively. The temperature and magnetic field magnetotransport properties were measured by commercial PPMS (Quantum Design) with linear four contact configurations. The current was supplied through the two outer probes and the voltage was measured across the two inner electrodes. The contacts were made by 50 µm diameter Pt coated Cu wires and EPO-TEK (Epoxy Technology) conductive epoxy.

3 Results and discussions

3.1 Structural characterization

The film thickness was measured by X-ray reflectivity and found to be ≈ 70 nm. The doped bulk $La_{5/8-y}Pr_yCa_{3/8}MnO_3$ ($x \sim 0.42$ and $y = 0.36$) used for target has Pbnm symmetry and the lattice constants obtained after the Rietvelt

refinement are found to be $a = 0.548$ nm, $b = 0.546$ nm, and $c = 0.772$ nm. Thus, the average in-plane lattice parameter is $a_{av} = 0.387$ nm. The pseudo-cubic lattice of manganites is defined as lattice with a lattice parameter of $a_{sc} = c/2 = 0.386$ nm. For the cubic STO substrate, the lattice constants are $a_c = 0.3905$ nm. As a result, epitaxial deposition of LPCMO film on STO substrate can give rise to an in-plane tensile strain of − 1.06% if we take into account the average in plane lattice constant of the bulk LPCMO or − 1.26% if $c/2$ of the bulk is taken as the pseudo-cubic lattice constant. Whichever may be the case, the film grown on STO (110) is expected to grow with its (110) plane parallel to that of the substrate and will experience almost uniform strain because the difference between the orthorhombic 'a' and 'b' lattice constants is very small. A representative HRXRD symmetric $2\theta/\omega$ scan of the film deposited on STO (110) substrates is shown in Fig. 1. The occurrence of the diffraction maxima of the LPCMO film and the substrate in close proximity and the absence of any other peaks in the HRXRD pattern clearly demonstrate that the former (LPCMO film) has adopted the structural symmetry of the latter (substrate). The $2\theta-\omega$ scan presented in Fig. 1 shows two diffraction peaks corresponding to the LPCMO thin film. The broad low intensity peak corresponds to the cubic lattice parameter of 0.3824 nm, which is appreciably smaller than the lattice constant of the bulk and hence is signature of the large tensile strain. The higher intensity peak which appears closer to the substrate peak yields a cubic lattice constant of 0.3871 nm, which is the same as that of the bulk cubic unit cell and thus corresponds to the strain relaxed part of the film. The rocking curve of the (220) diffraction peak is plotted in the inset of Fig. 1. The half width at full maximum of the rocking curve is ≈ 0.27°. This shows that the film has fairly good crystallinity.

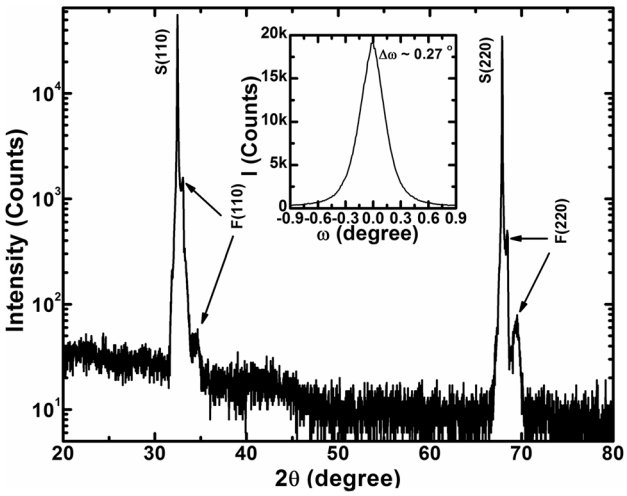

Fig. 1 $2\theta/\omega$ scan of the LPCMO film on STO (110). The arrow indicates the strained and strain relaxed diffraction peaks of the film. The inset shows rocking curve of (220) diffraction peak

Finally, we would like to point out that the the distribution of the cations is expected to be of disordered type. Ordering of the cationic species (La^{3+}, Pr^{3+} and Ca^{2+}) is indeed important but not a critical factor governing the magnetic and transport behaviour of the strongly phase-separated systems like LPCMO. As shown by Zhu et al. [29], the ordering of the cations leads to (1) lower resistivity, (2) higher magnetic moment, (3) less sharp IMT at higher temperature, and (4) narrower hysteresis in the cooling and warming cycle ρ–T. Zhu et al. achieved the cationic ordering only in the 2LCMO-PCMO superlattices on (001)-$SrTiO_3$ by laser MBE. But such ordering is extremely difficult to achieve in films prepared from a compound target of LPCMO and the resulting films are generally cation disordered. Here, we would like to point out that in contrast to the manganites like different doped variants of $LaMnO_3$, the cationic ordering plays far greater role in determining the properties of double perovskites manganites like $LnBaMn_2O_6$ system (Ln = Y and rare earth ions) [30, 31].

Apart from the cationic ordering, the oxygen vacancies/stoichiometry also play a crucial role in governing the magnetic and magnetotransport properties of manganites. Oxygen vacancies break the symmetry in the arrangement of d-orbitals of manganese ions and hamper the orbital ordering. Through his systematic study of the effect of oxygen stoichiometry in $La_{0.70}Sr_{0.30}MnO_{3-d}$ ($0 \le d \le 0.25$), $La_{1-x}Ba_xMnO_{3-x/2}$ and $Pr_{0.70}Ba_{0.30}MnO_{3+\delta}$ Trukhanov has established that decrease in oxygen vacancy (1) lowers the Curie temperature T_C and spontaneous magnetization, (2) gradually increases the resistivity towards the semiconducting regime, (3) induces structural changes, and (4) results in the formation of cluster spin glass with freezing of magnetic moments at low temperature due to competition between ferromagnetic and antiferromagnetic interactions [32–34]. In a study on the large BW manganite $La_{0.5}Ba_{0.5}MnO_3$, Tukhanov et al. have observed a monotonic increase in the T_C and the spontaneous magnetic moment with an increase in the average crystallite size. It has been established that anomalous magnetic properties in large BW manganites could be explained in terms of the two competing size effects, (1) frustration of indirect exchange interaction Mn^{3+}–O–Mn^{4+} on the nanocrystallite surface and (2) crystal lattice compression due to crystallite surface tension [35].

3.2 Thermomagnetic hysteresis and T_{IM}–H scaling

The temperature-dependent resistivity (ρ–T) measured during cooling and warming cycles at several magnetic fields upto $H = 70$ kOe are shown in Fig. 2. The resistivity (ρ_{RT} ($H = 0$ kOe) = 0.048 Ω cm) increases on lowering the temperature and ρ–T first shows insulator like behaviour and

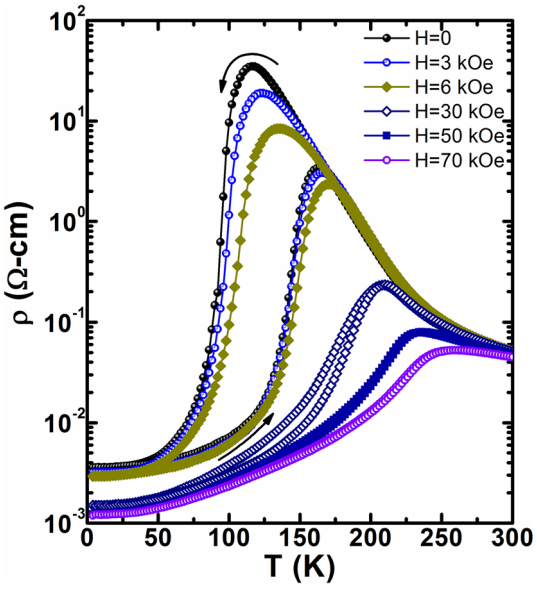

Fig. 2 ρ–T measured during cooling and warming (2 K/min) cycles at different H

then insulator to metal transition (IMT) appears at $T_{IM}{}^{C}$ = 116 K [$\rho_{IM}{}^{C}$ (H = 0 kOe) = 34.921 Ω-cm; an increase of nearly three orders of magnitude]. At $T < T_{IM}{}^{C}$ the zero-field resistivity decreases sharply [ρ_{4K} (H = 0 kOe) = 0.0035 Ω cm; a decrease by nearly four orders of magnitude]. Such sharp IMT is the hall mark of the strongly phase-separated manganite families, like $La_{1-x-y}Pr_yCa_xMnO_3$ [3, 6–20] and $Sm_{1-x}Sr_xMnO_3$ [3–5, 25, 26] and is caused by the competing mesoscopic FMM and AFMI/CO clusters. During the warming cycle, the metal–insulator transition is observed at $T_{IM}{}^{W}$ = 163 K ($\rho_{IM}{}^{W}$ (H = 0 kOe) = 3.422 Ω cm) and in the higher temperature regime the resistivity approaches the cooling cycle value. The application of magnetic field (H) pushes the IMT up with concomitant reduction in its sharpness and narrowing of the thermal hysteresis in ρ–T. The drastic difference between the zero field IMT measured during cooling and warming thermal cycles (≈47 K) has been understood in terms of the accommodation strain and the energy barrier provided by the AFMI phase to the nucleation of the lower temperature ordered FMM phase. This results in the formation of a magnetic phase which is akin to a magnetic liquid [8]. The electrical transport characteristics of the magnetic liquid phase should depend on the relative fractions of FM and AFM/COI phases at the instant from where the low temperature state is approached and consequently IMT temperature corresponding to liquid-like magnetic phase should be non-unique [10]. The lower value of the $T_{IM}{}^{C}$ is caused by the non-equilibrium magnetic liquid and the magnetic frustration is a direct evidence of supercooling of the magnetic liquid formed by the competing AFM and FM phases [9–12]. During the warming cycle, the system is much closer to the equilibrium due to the dominantly higher fraction of the FMM phase and hence the IMT occurs at almost the actual transition [7–16].

The ρ–T hysteresis, which is very pronounced in the absence of H nearly vanishes at H = 70 kOe and cooling and warming cycle IMTs coincide with $T_{IM}{}^{C} = T_{IM}{}^{W}$ =262 K. The evolution of $T_{IM}{}^{C}$ and $T_{IM}{}^{W}$ with H plotted in Fig. 3 shows that during the cooling cycle the IMT shows a sharp nonlinear rise at $H \leq 45$ kOe and above it rises linearly. In contrast, during warming the IMT scales up almost linearly with H. The nonlinear behaviour of $T_{IM}{}^{C}$–H is a signature of the non-equilibrium magnetic liquid, which is created by the low energy barrier to the nucleation of the FM phase by the AFM phase. In the warming cycle, the system is closer to the equilibrium and hence the $T_{IM}{}^{W}$–H is nearly linear. To parametrize the IMT-H scaling in terms of some physically relevant empirical law, we analysed the data in terms of several power laws. It is found that the scaling of the IMT during the two thermal cycles is well fitted by the power law:

$$T_{IM}(H) = T^0_{IM} + \beta H^{\alpha} \quad (1)$$

Here T^0_{IM} is the characteristic H-independent contribution to the T_{IM}, which can be taken as a measure of the zero field FMM fraction. The second term in Eq. (1) in which the constant β and the exponent α determine the magnetic field-dependent part of the IMT and can be considered as a measure of the relative fraction of the AFMI/CO and FMM phases. The $T_{IM}{}^{C} - H$ experimental data except the zero-field value are well fitted by the above equation with, $T^0_{IM} = 64.44 \pm 19.50$ K, $\beta = 35.81 \pm 4.02$ K/(kOe)$^{\alpha}$, and $\alpha = 0.40 \pm 0.07$ ($R^2 = 0.99803$). During the warming cycle, small deviation is observed for the zero-field data but all

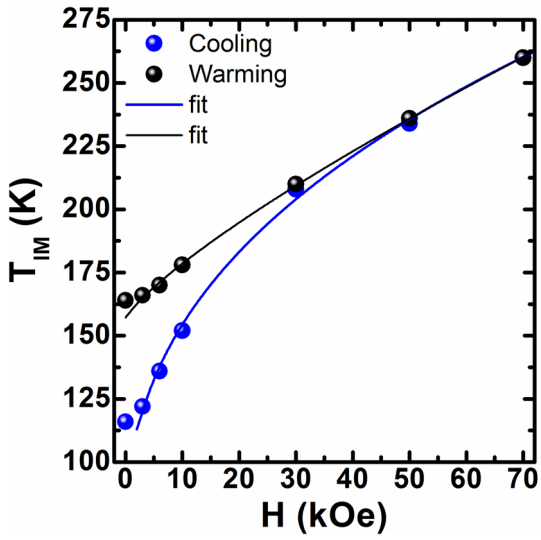

Fig. 3 Variation of $T_{IM}{}^{C}$ and $T_{IM}{}^{W}$ with H. The solid lines are fit to power law Eq. 1 (see text)

other data points are well fitted by the above equation with, $T^0_{IM} = 156.41 \pm 1.78$ K, $\beta = 3.53 \pm 0.61$ K/(kOe)$^{\alpha}$, and $\alpha = 0.80 \pm 0.04$ ($R^2 = 0.99803$). In Fig. 3 the fit to the experimental data using Eq. (1) is shown by the solid lines. The large difference in the value of the constants exponent β and α is attribute of the contrasting difference in the nature of the overall magnetic phase realized during the two thermal cycles. The large difference in the cooling and warming cycle values of β in conjunction with fact that it is measure of the H-dependent contribution to IMT suggests that H-induced AFMI–FMM phase transition is quite robust during the cooling cycle. As discussed above, in the cooling cycle the magnetic phase is akin to a magnetic liquid phase and is extremely unstable against the fluctuations arising due to external perturbations like H. This causes the robust H-induced AFMI–FMM first-order phase transition. At $H > 45$ kOe, because of the dominance of the FMM over AFMI, the H-induced phase transition may not be of the first order and hence the linear behaviour. During the warming cycle, the magnetic phase is dominated by FMM fraction and more akin to a solid and hence less sensitive to fluctuations caused by external stimuli such as H. Consequently, the H-dependent contribution to T_{IM} is very small and hence a small value of β. The small value of the exponent α for the cooling cycle is consistent with the non-linear behaviour of the non-equilibrium and fluctuation-dominated magnetic liquid phase. The nearly equilibrium magnetic phase is manifested by the appreciably larger value of the pre-factor β and exponent α during the warming cycle. Hence, the proposed model with a H-independent contribution and H-dependent part appears to be reasonably successful in explaining the behaviour of T_{IM}–H scaling.

Another interesting feature in the ρ–T data shown in Fig. 2 is the hysteresis between the cooling and warming cycle curves. The zero-field ρ–T curves enclose the largest area, which gradually diminishes as H is increased. Such hysteresis apart from being signature of the first-order AFM/COI–FMM phase transition also manifests the strong magnetic frustration created by the delicate balance between these coexisting phases. At $H = 70$ kOe the area enclosed by the cooling and warming cycle ρ–T curves negligible. The scaling of ρ–T loop area with H can be taken as a signature of the strength of phase separation. The larger loop area signatures stronger phase separation. The decrease in the loop area with increase in H clearly shows the weakening of the phase separation tendencies due to H-induced AFMI–FMM phase transition. Hence, a more detailed analysis of the loop area scaling appears pertinent. For further analysis, the area (A_T) enclosed by the hysteretic ρ–T curves was calculated after normalizing the measured ρ–T data with the room temperature resistivity [ρ (RT)]. The variation of the loop area with H is plotted in Fig. 4.

While developing models for the scaling of the thermomagnetic hysteresis in temperature- and magnetic field-dependent [(ρ–T) and (ρ–H)] loops, (1) the intrinsic mesoscale nature of the phase separation, (2) nonergodic and liquid-like behavior of magnetic state during the cooling cycle, and (3) nearly equilibrium magnetic solid-like behavior of the magnetic state while warming have been taken into account. Our analysis shows that for the $A_T - H$ scaling upto a certain value of H the follows the exponential decay given by

$$A_T(H) = A_{T0} e^{-\Gamma H} \tag{2}$$

Here, A_{T0} is the zero-field normalized area and Γ is a constant which could be related to the degree of phase separation. The experimental data is well fitted with the above equation up to $H \approx 30$ kOe (the solid line in Fig. 4). At $H > 30$ kOe, the loop area is very small and therefore can be regraded as well outside the strongly phase-separated regime with mesoscale magnetic clusters. The value of the constant $\ln(A_{T0}) = 10.18 \pm 0.06$ and $\Gamma = 0.241 \pm 0.004$/kOe with $R^2 = 0.99887$. Thus, it is clear that the exponential decay given (2) describes the ρ–T loop area scaling with H quite nicely in the regime which is akin to a magnetic liquid. The linear behavior of the $\ln <A>$–H curve upto $H \sim 30$ kOe is the map of the exponential decrease in the ρ–T loop area with increasing H. This is clearly due to extreme sensitivity of the magnetic liquid phase to the applied magnetic field. The magnetic liquid undergoes a first-order AFMI–FMM transition at relatively small H. The deviation from the exponential behavior at $H > 30$ kOe is due to the substantial decrease (increase) in the AFMI (FMM) phase fraction

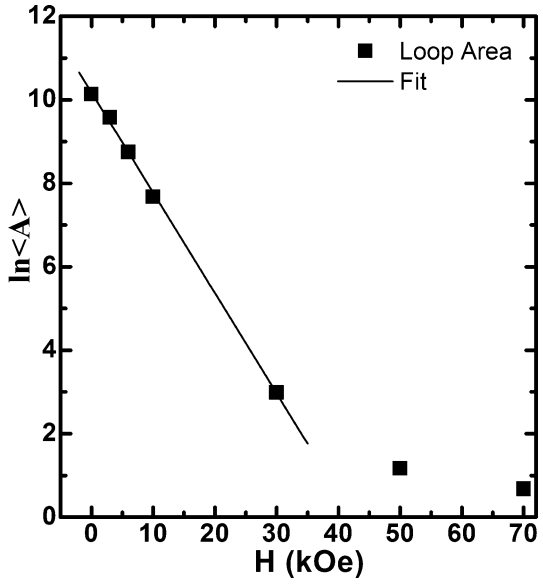

Fig. 4 Scaling of normalized loop area enclosed by hysteretic (ρ–T) curves at different H. Solid line represents the fit to Eq. (2) (see text)

which is detrimental to the magnetic liquid-like behaviour and favours the appearance of an equilibrium magnetic phase. We believe that the nature of the constant Γ can be ascertained if similar analysis is carried out on thin films having different degree of phase separation that may be induced by either changing the substrate or the composition.

3.3 Isothermal magnetoresistive hysteresis and *ρ–H* scaling

Another hallmark of the manganites exhibiting strong mesoscopic phase separation is the hysteresis in isothermal resistivity versus magnetic field (*ρ–H*) measurements [3, 4, 9, 12, 13, 25–27]. However, the scaling of the *ρ–H* loop area with the applied DC magnetic field has not been studied so far and hence no scaling laws are existent in the literature. In the present study, we have measured the isothermal *ρ–H* loops using a protocol, which is used to study the B–H and P–E hysteresis dynamics as function of the field amplitude and frequency in ferromagnetic and ferroelectric materials, respectively [36–44]. Theoretical and experimental studies spread over the last two decades have shown that the dynamic M–H loop area scaling follows the following scaling relation:

$$A \propto H^{\eta}\Omega^{\beta}T^{-\gamma} \tag{3}$$

Here, H is the amplitude of the AC magnetic field, Ω is its frequency and T is the temperature. The exponents, α, β and γ depend on the dimensionality and the symmetry of the system and their universality is still under debate. The continuous spin system model predicts $\alpha = \beta = 1/2$ [37, 38]. In the present case, we assume that the isothermal ρ - H curves would follow the above scaling law with frequency Ω taken as a constant (as there is no AC magnetic field). Since the *ρ–H* measurements are isothermal, T = constant. Thus, in the present case the scaling law should appear like:

$$A \propto H^{\eta} \tag{4}$$

In case of manganites or other magnetoresistive materials, the common practice in *ρ–H* measurements has been that during the virgin cycle H is varied from zero to the desired value (+ H) in the positive field direction, then reversed and brought via $H = 0$ kOe to the same value (− H) in the negative field direction. Afterwards, H is again reversed and allowed to pass via $H = 0$ kOe to the desired value on the positive side (+ H). To investigate the evolution of the isothermal *ρ–H* loops measured at different reversal magnetic fields, we have employed a measurement protocol in which the loops were traced during the positive cycle only and the reversal magnetic field was increased in the steps of 10 kOe from $H = 0$ to 70 kOe. Thus, for the first *ρ–H* measurement, the field was varied from 0 to 10 kOe and then reversed back to the initial value. In the next cycle H was increased to 20 kOe and reversed back to $H = 0$ kOe. This procedure was followed for field up to $H = 70$ kOe. All the measurements were done in the cooling cycle. The *ρ–H* loops measured at different temperatures with the above-mentioned protocol are shown in Fig. 5. Figure 5a shows the *ρ–H* loop measurements at $T = 185$ K. For the first H cycle up to $H = 10$ kOe there is no significant change in resistivity and no hysteresis is observed. However, at all higher H cycles (1) the magnetic field-induced drop in resistivity increases successively, (2) the *ρ–H* curves show hysteretic behaviour with progressively include larger area and (3) loops traced at smaller H lie inside those traced at higher H. At $H = 70$ kOe the decrease in resistivity is more than two orders of magnitude. Since the measurement temperature is well above the cooling and warming cycle IMTs and FCC/FCW T_C values therefore this temperature regime consists mainly of AFMI/CO phases. Hence the decrease in resistivity is principally due to AFMI–FMM phase transition. The hysteretic behaviour, although weak suggests the first-order nature of this field-induced phase transition. Despite the irreversibility, the zero-field value is recovered in all the cycles, confirming a FMM–AFMI/CO transition during the reverse cycle.

The temperature for the second set of measurement ($T = 150$ K) was chosen to be the beginning of the magnetic liquid phase, which is just below $T_{IM}^{W} = 163$ K and well above $T_{IM}^{C} = 116$ K. This temperature regime is still dominated by the AFMI phase. The *ρ–H* loops measured at $T = 150$ K are plotted in Fig. 5b. The resistivity decreases sharply during the first H increasing cycle and when H is reversed the initial state is not recovered. In the $H = 20$ kOe cycle the resistivity drop is even sharper and the initial state is still not recovered after the field is reversed to zero. However, in subsequent cycles the initial resistivity state is recovered and the *ρ–H* loops lie well within those traced at higher H values. The behaviour of the *ρ–H* curves in this case clearly has two contributions; (1) at $H \leq 30$ kOe the initial resistivity state is not recovered after reversing H to zero and (2) at $H > 30$ kOe, the initial resistivity state is almost fully recovered after reversing H to zero. This clearly shows that during the first two H cycles a fraction of the AFMI phase after the H-induced transition to the FMM phase remains permanently in that phase even after the reversing the field to zero. Thus, it can be said that the softer magnetic liquid with a higher AFMI fraction is transformed into a stiffer magnetic liquid with a lower fraction of the AFMI phase. At higher H values the induced phase transition is irreversible but with fully recoverable zero field values. The hysteretic behaviour outlines the first-order nature of the phase transition.

The next set of measurements was carried out at a temperature $T = 110$ K, which is lower than $T_{IM}^{C} = 116$ K. The *ρ–H* loops measured at $T = 110$ K are plotted in Fig. 5c. The resistivity decreases nearly by an order of magnitude at $H = 10$ kOe during the first H increasing cycle and when H is reversed it

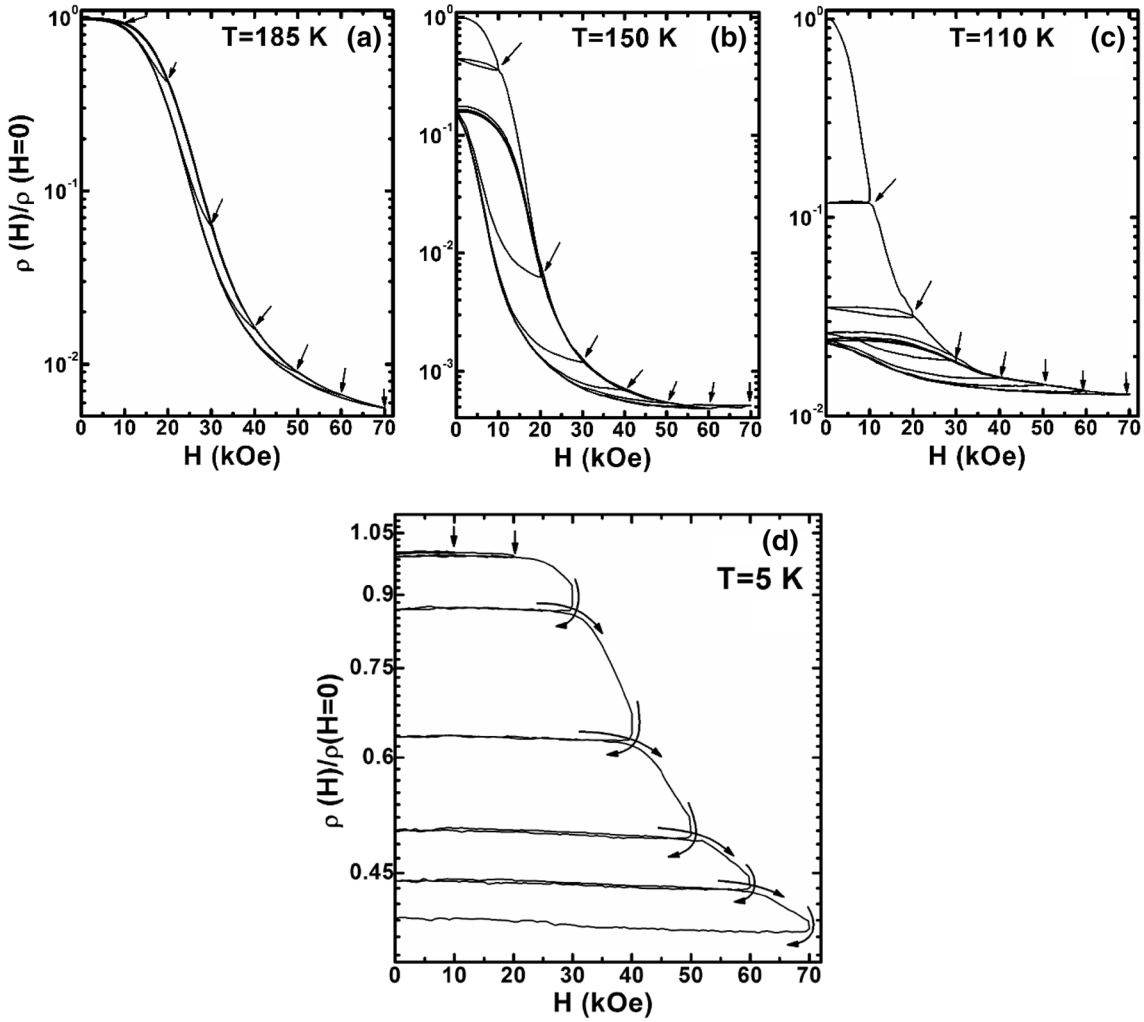

Fig. 5 Isothermal ρ–H loop measurements at temperatures $T = 185$ K (**a**), 150 K (**b**), 110 K (**c**) and in the glassy region at 5 K (**d**)

remain almost constant till $H = 0$ kOe. This clearly shows that appreciable fraction of the AFMI that has been permanently transformed to FMM. During the second H cycle, the resistivity first increases and then decreases sharply by nearly 70% when H is increased to 20 kOe. After H reversal, the resistivity increases slightly and the $H = 0$ kOe value lies well below the initial value of the second H cycle. Thus in this case too, some of the AFMI remains permanently in AFM phase. The next H cycle also shows a similar behaviour. In the subsequently cycles, the initial resistivity state is recovered and the ρ–H loops lie well within those traced at higher H values. However, in this case the influence of the magnetic field is much subtle than in case at $T = 150$ K. Nearly similar behaviour is observed around 80 K also. However, at $T < 20$ K, that is in the glassy region, the behaviour of the ρ–H curves changes dramatically. The ρ–H loops measured at 5 K, which lies well within the glassy region formed by the freezing of the magnetic liquid are shown in Fig. 6. In this case for all H cycles, the resistivity remains constant and then decreases after a certain H value during each field increasing cycle. During each field decreasing cycle the resistivity remains nearly constant and follows the same path even during the next H increasing cycle. As seen in Fig. 5d, the hysteretic behaviour is conspicuously absent and replaced by a reversible behavior. Such behaviour appears consistent with the low temperature glassy phase.

To look into the further details of the nature and scale of phase separation, we measured the ρ–H loop area in all the case and studied their scaling as a function of the external perturbation H. As in the previous case of the ρ–T loop, the area was calculated from after normalizing with the zero-filed data, viz. ρ ($H = 0$). The loop area–magnetic field (A–H) scaling is plotted in Fig. 6. To have an idea of the scaling behaviour, we have employed, instead of the Eq. (4), the following Eq. to fit the A–H data:

$$A(H) = A_{\mathrm{H}}(H - H_{\mathrm{IM}})^{\eta} \tag{5}$$

In this equation, the constant H_{IM} is the magnetic field at which the induced AFMI–FMM phase transition appears

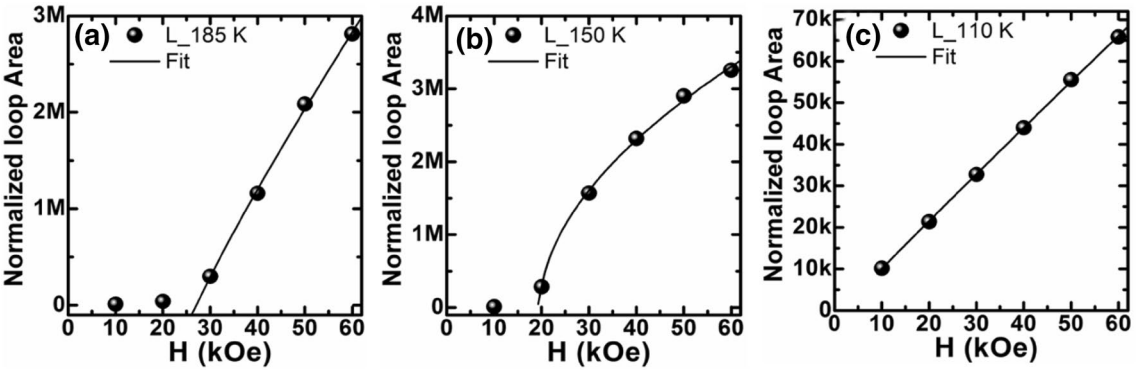

Fig. 6 Scaling of normalized loop area enclosed by hysteretic (ρ–H) curves at different H. Solid line represents the fit to Eq. (5) (see text)

and is expected to decrease with lowering of the temperature, the exponent 'η' may be taken as a measure phase separation. The deviation from the scaling Eq. (4) could be due to the intrinsic phase-separated nature and the ensuing H-induced AFMI/CO–FMM first-order phase transition [45]. As seen in Fig. 6a, the loop area of the ρ–H curves measured at $T = 185$ K remains constant at lower magnetic fields and rises linearly at H higher than ~ 20 kOe. Equation (4) fits the observed data quite nicely at $H \geq 30$ kOe. In this case, the value of the constants yielding the best fit ($R^2 = 0.9906$) is found to be $A_H = 120560 \pm 4639$, $H_{IM} = 27.4 \pm 1.3$ kOe and $\eta = 0.91 \pm 0.03$. In case of the ρ–H curves measured at $T = 150$ K, the loop area scales non-linearly at $H \geq 20$ kOe and the best fitting ($R^2 = 0.9973$) parameters are found to be $A_H = 465052 \pm 51206$, $H_{IM} = 19.6 \pm 1$ kOe and $\eta = 0.53 \pm 0.03$. It is interesting to note that the area of the ρ - H loops measured at 110 K below the $T_{IM}^{C} = 116$ K all the observed data points are extremely well fitted by the curve in Eq. (4). The best fitting ($R^2 = 0.9993$) parameters are found to be $A_H = 2199 \pm 262$, $H_{IM} = 7.6 \pm 0.6$ kOe and $\eta = 0.90 \pm 0.03$. From the fitting parameters, it is clear that the AFMI/CO melting field decreases with lowering of the temperature, that is, the dominance of the FMM over AFMI/CO phase increases. The exponent 'η' is found to be close to unity in the higher temperature region ($T > T_{IM}^{W} = 163$ K) which is dominantly AFMI/CO with H-induced FMM phase only and in the lower temperature region ($T > T_{IM}^{C} = 116$ K) where FMM dominants over AFMI/CO phase (hence less prominent magnetic liquid phase). In the intermediate temperature regime enclosed by the IMTs, which is dominated by the magnetic liquid-like phase, the value of the exponent is ~ 0.5.

The fact that $H_{IM} \approx 27.4$ kOe clearly shows that the slow increase in the ρ–H loop area at lower H values is due to weak AFMI–FMM phase fraction. The much sharper and nearly linear rise the loop area at $H > H_{IM}$ is due to the H-induced AFMI–FMM phase transition. In this temperature region, the magnetic phase dominantly remains a solid-like AFMI and hence the nearly linear ρ–H area scaling at $H > H_{IM}$. As the temperature is lowered below the warming cycle $T_{IM}{}^{W}$, the magnetic liquid state acquires dominant contribution due to the appearance of FMM clusters and ensuing delicate balance between AFMI and FMM. This enhances the H sensitivity of the resistivity and H-induced IMT occurs at much lower field (19.6 kOe) than at $T > 185$ K. The non-linear ρ–H scaling is consistent with the magnetic liquid behavior at $T = 150$ K. At $T < T_{IM}{}^{C}$ the magnetic state behaves more like solid FMM with much smaller AFMI phase fraction. Hence the IMT occurs at very small field $H_{IM} \approx 7.6$ kOe and the ρ–H loop area scaling is linear.

4 Conclusions

The thermal and magnetic field scaling of the thermomagnetic hysteresis observed in the temperature- and magnetic field-dependent electric transport properties of ~ 70 nm thick single crystalline thin films of $La_{0.21}Pr_{0.42}Ca_{0.37}MnO_3$ (LPCMO) grown on STO (110) substrates by RF magnetron sputtering have been investigated. The supercooling of the magnetic liquid during the cooling cycle and the near equilibrium behaviour during warming result in a pronounced ρ–T hysteresis. The scaling of the IMT with the applied magnetic field during the two thermal cycles is well fitted by the power law of the type $T_{IM}(H) = T_{IM}^{0} + \beta H^{\alpha}$. The fitting parameters β and α are related to the strength of the phase separation and the H-induced AFMI–FMM transition. The scaling of the area of the ρ–T hysteresis loop with the magnetic field follows a power law of the type $A_T(H) = A_{T0}e^{-\Gamma H}$ in the region of strong phase separation. The isothermal ρ–H loop area is found to follow a scaling law of the type $A(H) = A_H(H - H_{IM})^{\eta}$. The constant H_{IM} is the magnetic field at which the induced IMT occurs due to AFMI–FMM phase transition and the exponent η measures the strength of phase separation; being close to unity in the

weakly phase-separated regimes and ~0.5 in the strongly phase separated or the magnetic liquid regime. We emphasise that the critical ingredients of the phenomenological models used to explain the observed hysteresis in temperature- and magnetic field-dependent [(ρ–T) and (ρ–H)] loops are the mesoscale phase separation, appearance of magnetic liquid during the cooling cycle, and nearly equilibrium magnetic solid-like behavior while warming.

Acknowledgements The authors are grateful to Director, CSIR-NPL for persistent encouragement. Financial support from CSIR (AQUARIUS, Grant No. PSC0110) thankfully acknowledged.

References

1. E. Dagotto, T. Hotta, A. Moreo, Phys. Rep **344**, 1 (2001)
2. E. Dagotto, New J. Phys **7**, 67 (2005)
3. Y. Tokura, Rep. Prog. Phys **69**, 797 (2006)
4. Y. Tomioka, H. Hiraka, Y. Endoh, Y. Tokura, Phys. Rev. B **74**, 104420 (2006)
5. M.K. Srivastava, A. Kaur, K.K. Maurya, V.P.S. Awana, H.K. Singh, Appl. Phys. Lett. **102**, 032402 (2013)
6. M. Uehara, S. Mori, C.H. Chen, S.-W. Cheong, Nature **399**, 560 (1999)
7. L. Ghivelder, F. Parisi, Phys. Rev. B **71**, 184425 (2005)
8. P.A. Sharma, S.B. Kim, T.Y. Koo, S. Guha, S.-W. Cheong, Phys. Rev. B **71**, 224416 (2005)
9. W. Wu, C. Israel, N. Hur, S. Park, S.-W. Cheong, A. de Lozanne. Nat. Mater. **5**, 882 (2006)
10. S. Singh, P. Kumar, P.K. Siwach, P.K. Tyagi, H.K. Singh, Appl. Phys. Lett. **104**, 212403 (2014)
11. V. Agarwal, G. Sharma, P.K. Siwach, K.K. Maurya, H.K. Singh, Appl. Phys. A **119**, 899 (2015)
12. V. Agarwal, G. Sharma, P.K. Siwach, K.K. Maurya, V.P.S. Awana, H.K. Singh, Solid State Commun. **202**, 43 (2015)
13. V. Podzorov, B.G. Kim, V. Kiryukhin, M.E. Gershenson, S.-W. Cheong, Phys. Rev. B **64**, 140406R (2001)
14. T. Dhakal, J. Tosado, A. Biswas, Phys. Rev **B75**, 092404 (2007)
15. H. Jeen, A. Biswas, Phys. Rev. B **88**, 024415 (2013)
16. T.Z. Ward, S. Liang, K. Fuchigami, L.F. Yin, E. Dagotto, E.W. Plummer, J. Shen, Phys. Rev. Lett. **100**, 247204 (2008)
17. V.G. Sathe, A. Ahlawat, R. Rawat, P. Chaddah, J. Phys. Cond. Matter **22**, 176002 (2010)
18. D.K. Mishra, V.G. Sathe, R. Rawat, V. Ganesan, J. Phys.: Condens. Matter. **25**, 175003 (2013)
19. D. Gillaspie, J.X. Ma, H.-Y. Zhai, T.Z. Ward, H.M. Christen, E.W. Plummer, J. Shen, J. Appl. Phys **99**, 08S901 (2006)
20. S. Singh, M.R. Fitzsimmons, T. Lookman, J.D. Thompson, H. Jeen, A. Biswas, M.A. Roldan, M. Varela, Phys. Rev. Lett. **108**, 077207 (2012)
21. Y. Tomioka, A. Asamitsu, Y. Moritomo, Y. Tokura, J. Phys. Soc. Japan **64**, 3626 (1995)
22. Y. Tomioka, A. Asamitsu, H. Kuwahara, Y. Moritomo, Y. Tokura, Phys. Rev. B **53**, R1689 (1996)
23. A. Asamitsu, Y. Tomioka, H. Kuwahara, Y. Tokura, Nature **388**, 50 (1997)
24. V. Agarwal, R. Prasad, M.P. Singh, P.K. Siwach, A. Srivastava, P. Fournier, H.K. Singh, Appl. Phys. Lett. **96**, 052512 (2010)
25. V. Agarwal, P.K. Siwach, G.D. Varma, VPS Awana, A.K. Srivastava, H.K. Singh, Mater. Res. Express **1**, 046117 (2014)
26. Y. Tomioka, A. Asamitsu, H. Kuwahara, Y. Tokura, J. Phys. Soc. Jpn **66**, 302 (1997)
27. M.K. Srivastava, S. Singh, P.K. Siwach, K.K. Maurya, V.P.S. Awana, A. Kaur, H.K. Singh, Mater. Res. Express **1**, 016110 (2014)
28. V. Agarwal, L.M. Kandpal, P.K. Siwach, V.P.S. Awana, H.K. Singh, J. Magn. and Magnet. Mater **394**, 299 (2015)
29. Zhu et al., (Nature Communication **7**, 11260 (2016)
30. S.V. Trukhanov, JETP **101**, 513 (2005)
31. S.V. Trukhanov, A.V. Trukhanov, H. Szymczak, R. Szymczak, M. Baran, J. Phys. Chem. Solids **67**, 675 (2006)
32. S.V. Trukhanov, JETP **100**, 95 (2005)
33. S.V. Trukhanov, J. Mater. Chem **13**, 347352 (2003)
34. S.V. Trukhanov, A.V. Trukhanov, C.E. Botez, A.H. Adair, H. Szymczak, R. Szymczak, J. Phys.: Condens. Matter. **19**, 26621418 (2007)
35. S.V. Trukhanov, A.V. .Trukhanov, S.G. Stepin, H. Szymczak, C.E. Botez, Phys. Sol. State **50**, 886893 (2008)
36. S. Sengupta, Y. Marathe, S. Puri, Phys. Rev. B **45**, 7828 (1992)
37. D. Dhar, P.B. Thomas, J. Phys. A **25**, 4967 (1992)
38. D. Dhar, P.B. Thomas, J. Phys. A **26**, 3973 (1993)
39. M. Rao, H.R. Krishnamurthy, R. Pandit, Phys. Rev. B **42**, 856 (1990)
40. J.-M. Liu, H.L.W. Chan, C.L. Choy, C.K. Ong, Phys. Rev. B **65**, 014416 (2001)
41. J.-M. Liu, H.L.W. Chan, C.L. Choy, Y.Y. Zhu, S.N. Zhu, Z.G. Liu, N.B. Ming, Appl. Phys. Lett. **79**, 236 (2001)
42. S.S. Bhattacharyya, M. Rahman, A. Mukherjee, B.K. Chaudhuri, A. Yoshizawa, 92, 122909 (2008)
43. J.-M. Liu, B. Pan, H. Yu, S.T. Zhang, J. Phys.: Condens. Matter. **16**, 1189 (2004)
44. W.Y. Lee, B.-Ch.. Choi, J. Lee, C.C. Yao, Y.B. Xu, D.G. Hasko, J. A. C. Bland, Appl. Phys. Lett **74**, 1609 (1999)
45. A. Yadav, S. Singh, A. Vashist, G. Sharma, P.K. Siwach, H.K. Singh, Mater. Res. Express **4**, 066102 (2017)

Aryabhatta Journal of Mathematics & Informatics Vol. 9, No. 2, July-Dec., 2017
Scientific Journal Impact Factor SJIF (2016) : 5.856

ISSN (Print) : 0975-7139
ISSN (Online) : 2394-9309

SECOND HANKEL DETERMINANT FOR CERTAIN CLASS CLOSE TO CONVEX FUNCTIONS

Kanika Khatter* and S. Sivaprasad Kumar**
** & **Department of Applied Mathematics, Delhi Technological University, Delhi-110042, India*
E-mail : kanika.khatter@yahoo.com, spkumar@dce.ac.in

ABSTRACT :

In the present investigation, we determine the second Hankel determinant $H_2(2)$ ***for a class of close-to-convex functions for which*** $-z^2 f'(z)/g(z)g(-z) \prec \varphi(z)$ ***where*** $\varphi(z)$ ***is an analytic function with the positive real part satisfying*** $\varphi(0)=1$ ***and*** $\varphi'(z)>0, f$ ***is analytic and g is starlike of order 1/2.***

2010 Mathematics Subject Classi_cation. 30C80, 30C45.

Key words and phrases : ***Second Hankel determinant; close-to-convex functions; subordination; functions with positive real part***

www.IndianJournals.com
Members Copy, Not for Commercial Sale
Downloaded From IP - 14.139.251.107 on dated 25-Oct-2017

1. INTRODUCTION

Let *A* be the class of all analytic functions of the form $f(z)=z+\sum_{n=2}^{\infty}a_n z^n$ normalized by the conditions $f(0)=0$ and $f'(0)=1$ in the open unit disk $\mathsf{D}:=\{z\in\mathbb{C}:|z|<1\}$ and *S* be the subclass of *A* consisting of univalent functions in Δ. The *q*th Hankel determinant (denoted by $H_q(n)$ for q = 1, 2, ... and n = 1, 2, 3, ... of the function *f* is given by

$$H_q(n):=\begin{vmatrix} a_n & a_{n+1} & a_{n+q-1} \\ a_{n+1} & a_{n+2} & a_{n+q} \\ \vdots & \vdots & \vdots \\ a_{n+q-1} & a_{n+q} & a_{n+2q-2} \end{vmatrix}$$

Hankel determinant has been extensively studied in the literature. Among the first few papers was a paper by Pommerenke [20] in the year 1966. He investigated the Hankel determinant of a really *p*-valent functions, univalent functions and starlike functions. A little later, Noonan [14-16] investigated the Hankel determinants of a really mean *p*-valent functions. The bounds on Hankel determinant of close-to-convex functions has been studied by Noor in [17-19]. Pommerenke [21] established the fact that Hankel determinant of univalent functions satisfies the following relation: $|H_q(n)|<Kn^{-\left(\frac{1}{2}+\beta\right)q+\frac{3}{2}}\ (n=1,2,...;q=1,2...)$, where $\beta>1/40000$ and *K* depends on *q*. Afterwards, Hayman [8] proved that $|H_2(n)|<An^{1/2}\ (n=1,2,...)$; A is an absolute constant for a really mean univalent functions. In 1986, Elhosh [3,4] investigated the Hankel determinant for univalent functions with a

positive Hayman index α and *k*-fold symmetric and close-to-convex functions. The second Hankel determinant $H_2(2) := a_2a_4 - a_3^2$ for the class of functions whose derivative has positive real part, the classes of starlike and convex functions, close-to-starlike and close-to-convex functions with respect to symmetric points have been studied in [7,9] respectively. Lee *et.al.*[11] obtained bounds on second Hankel determinant for the classes of Ma-Minda starlike and convex functions with respect to φ and two other similar subclasses. One may refer to the survey given by Liu, Xu and Yang [12] for the other work done in the research of Hankel determinant for univalent functions. They also obtained the second Hankel determinant for some other subclasses of analytic functions.

An analytic function *f* is said to be subordinate to *F,* written $f \prec F$ or $f(z) \prec F(z), (z \in \mathsf{D})$ if there exists an analytic function $w : \mathsf{D} \to \mathsf{D}$ satisfying $w(0) = 0$ and $f(z) = F(w(z))$ in Δ. If *F* is univalent in D, then $f(z) \prec F(z)$ if and only if $f(0) = F(0)$ and $f(\mathsf{D}) \subseteq F(\mathsf{D})$. A function $f \in A$ is starlike with respect to symmetric point in Δif for every *r*less than and sufficiently close to one and every ξ on $|z| = r$, the angular velocity of $f(z)$ about the point $f(-\xi)$ is positive at $z = \xi$ as z traverses the circle $|z| = r$ in the positive direction. Analytically, a function $f \in A$ is starlike with respect to symmetric points if

$$\mathrm{Re}\left(\frac{zf'(z)}{f(z) - f(-z)}\right) > 0 \qquad (z \in \mathsf{D})$$

The class S_s^* of all functions starlike with respect to symmetric points was introduced and studied by Sakaguchi [22]. The functions belonging to this class are close-to-convex and hence univalent. Motivated by this class, Gao and Zhou [5] introduced a new subclass K_s of close-to-convex univalent functions given by

$$K_s = \left\{ f : \mathrm{Re}\left(\frac{z^2 f'(z)}{g(z)\, g(-z)}\right) < 0 \right\}, \tag{1.1}$$

where the function *g* is starlike of order 1/2. This is assumed in order to make the functions in this class univalent. Recently, Wang *et.al.* [23] generalised this class by expressing it in terms of subordination. For a function φ with the positive real part and satisfying $\varphi(0) = 1$ and $\varphi'(z) > 0$, they studied the class $K_s(\varphi)$ defined as follows

$$K_s(\varphi) = \left\{ f : -\frac{z^2 f'(z)}{g(z)\, g(-z)} \prec \varphi(z) \right\}, \mathrm{X} \tag{1.2}$$

where the function *g* is starlike of order 1/2. Cho *et.al.*[1] studied coefficient estimates and some distortion and growth theorems for the class $K_s(\varphi)$. Motivated by this we determine the bounds on the second Hankel determinant $H_2(2)$ for the functions in the class $K_s(\varphi)$.We have also investigated the second Hankel determinant bounds for some special subclasses of $K_s(\varphi)$.

2. MAIN RESULTS

Let $\varphi : \Delta \to \mathrm{X}$ be a function with positive real part with

$$\varphi(z) = 1 + B_1 z + B_2 z^2 + B_3 z^3 + \ldots \quad (B_1 > 0; B_1, B_2, B_3 \in R). \tag{2.1}$$

The class $K_s(\varphi)$ consists of functions $f \in A$ satisfying the following subordination

www.IndianJournals.com Members Copy, Not for Commercial Sale Downloaded From IP - 14.139.251.107 on dated 25-Oct-2017

$$-\frac{z^2 f'(z)}{g(z)\,g(-z)} \prec \varphi(z),$$

where the function g is starlike of order 1/2. For functions in the class $K_s(\varphi)$, we have the following result.

Theorem 2.1. Let the function $f \in K_s(\varphi)$ be given by $f(z) = z + a_2 z^2 + a_3 z^3 + \ldots$.

(1) If B_1, B_2 and B_3 satisfy the conditions

$$4\left|16B_2 - 9B_1^2\right| - 28B_1^2 + 8B_1B_2 - 64B_1 \le 0$$

and

$$\left|9B_1^2 - 16B_2\right| + \left|8B_2^2 - 9B_1B_3\right| \le 8B_1(2 + B_1)$$

then the second Hankel determinant satisfies

$$\left|a_2a_4 - a_3^2\right| \le \frac{1}{9}\left(1 + 2B_1 + B_1^2\right).$$

(2) *If B_1, B_2 and B_3satisfy the conditions*

$$4\left|16B_2 - 9B_1^2\right| - 28B_1^2 + 8B_1B_2 - 64B_1 \ge 0$$

and

$$\left|9B_1^2 - 16B_2\right| + 2\left|8B_2^2 - 9B_1B_3\right| \ge B_1(16 + 9B_1 + 2B_2);$$

or the conditions

$$4\left|16B_2 - 9B_1^2\right| - 28B_1^2 + 8B_1B_2 - 64B_1 \le 0,$$

and

$$\left|9B_1^2 - 16B_2\right| + \left|8B_2^2 - 9B_1B_3\right| \ge 8B_1(2 + B_1),$$

then the second Hankel determinant satisfies

$$\left|a_2a_4 - a_3^2\right| \le \frac{1}{72}\left(8 + \left|9B_1^2 - 16B_2\right| + \left|8B_2^2 - 9B_1B_3\right|\right).$$

(3) *If B_1, B_2 and B_3 satisfy the conditions*

$$4\left|16B_2 - 9B_1^2\right| - 28B_1^2 + 8B_1B_2 - 64B_1 > 0,$$

and

$$\left|9B_1^2 - 16B_2\right| + 2\left|8B_2^2 - 9B_1B_3\right| \le B_1(16 + 9B_1 + 2B_2),$$

then the second Hankel determinant satisfies

$$\left|a_2a_4 - a_3^2\right| \le \frac{M}{144\left(B_1^2 + 2B_1B_2 - \left|9B_1B_3 - 8B_2^2\right|\right)},$$

where,

$$M = 144B_1^2 + 144B_1^3 + 81B_1^4 + 32B_1B_2 - 112B_1^2B_2 + 18B_1^3B_2$$
$$+128B_2^2 + 2B_1^2B_2^2 + B_1\left(-7B_1 + 2\left(-8 + B_2\right)\right)\left|9B_1^2 - 16B_2\right|$$
$$-16\left(1 + B_1\right)^2\left|8B_2^2 - 9B_1B_3\right|.$$

www.IndianJournals.com
Members Copy, Not for Commercial Sale
Downloaded From IP - 14.139.251.107 on dated 25-Oct-2017

The bounds obtained here are sharp.

We prove Theorem 2.1 by expressing the coefficient of the function f in terms of the coefficient of a functionwith positive real part. Recall that the class $P$of functions with positive real part consists of all analytic function $p(z)=1+\sum_{n=0}^{\infty}c_n z^n$ with $\operatorname{Re} p(z)>0$ for $z\in \mathsf{D}$. It is known that for $p(z)=1+c_1z+c_2z^2+c_3z^3+...\in P$, $|c_n|\le 2\ (n=1,2,3,...)$ [2]. Let Ω be the class of all analytic functions $w:\mathsf{D}\to\mathsf{D}$ of the form $w(z)=w_1z+w_2z^2+....$ To prove our result, we need the following lemma:

Lemma 2.2.*[6] If the function given by $p(z)=1+c_1z+c_2z^2+c_3z^3+...$ is in P, then,*

(2.2) $$2c_2=c_1^2+x\left(4-c_1^2\right),$$

(2.3) $$4c_3=c_1^3+2\left(4-c_1^2\right)c_1x-c_1\left(4-c_1^2\right)x^2+2\left(4-c_1^2\right)\left(1-|x|^2\right)y,$$

for some x, y with $|x|\le 1$ and $|y|\le 1$.

Proof of Theorem 2.1. Since $f\in K_s(\varphi)$, there is an analytic function $w(z)=w_1z+w_2z^2+...\in\Omega$, such that

(2.4) $$-\frac{z^2f'(z)}{g(z)g(-z)}=\varphi(w(z))$$

Define $p_1(z)$ by

$$p_1(z)=\frac{1+w(z)}{1-w(z)}=1+c_1z+c_2z^2+...$$

Then

(2.5) $$w(z)=\frac{p_1(z)-1}{p_1(z)+1}=\frac{1}{2}\left(c_1z+\left(c_2-\frac{c_1^2}{2}\right)z^2+...\right).$$

Clearly p_1 is analytic in Δ with $p_1(0)=1$ and $p_1\in P$. Since $\varphi(z)=1+B_1z+B_2z^2+B_3z^3+...,$ we get

(2.6) $$\varphi\left(\frac{p_1(z)-1}{p_1(z)+1}\right)=1+\frac{1}{2}B_1c_1z+\left(\frac{1}{2}B_1\left(c_2-\frac{c_1^2}{2}\right)+\frac{1}{4}B_2c_1^2\right)z^2+....$$

Next, we try to compute the series expansion for $-z^2f'(z)/g(z)g(-z)$. In order to do this, we proceed by taking $g(z)=z+g_2z^2+g_3z^3+...,$ and therefore it is seen that

(2.7) $$-\frac{z}{g(z)g(-z)}=\frac{1}{z}+\left(g_2^2-2g_3\right)z+\left(g_2^4-4g_2^2g_3+3g_3^2+2g_2g_4-2g_5\right)z^3+...,$$

and the Taylor series expansion of f gives

(2.8) $$zf'(z)=z+2a_2z^2+3a_3z^3+4a_4z^4+....$$

Hence using the equations (2.7) and (2.8), we get

(2.9) $$-\frac{z^2f'(z)}{g(z)g(-z)}=1+2a_2z+\left(3a_3+g_2^2-2g_3\right)z^2+\left(4a_4+2a_2g_2^2-4a_2g_3\right)z^3+....$$

Then from (2.4), (2.6) and (2.9), we get

www.IndianJournals.com Members Copy, Not for Commercial Sale Downloaded From IP - 14.139.251.107 on dated 25-Oct-2017

(2.10) $a_2 = \frac{B_1 c_1}{4}.$

(2.11) $a_3 = \frac{1}{12}\left(\left(B_2 - B_1\right)c_1^2 + 2B_1 c_2 - 4g_2^2 + 8g_3\right).$

(2.12) $a_4 = \frac{1}{32}\left(\left(B_1 - 2B_2 + B_3\right)c_1^3 + 4\left(B_2 - B_1\right)c_1 c_2 + 4B_1 c_3 - 4B_1 c_1 g_2^2 + 8B_1 c_1 g_3\right).$

Therefore,

$$a_2 a_4 - a_3^2 = \frac{1}{1152}\Big[\left(B_1^2 - 2B_1B_2 - 8B_2^2 + 9B_1B_3\right)c_1^4 + \left(4B_1B_2 - 4B_1^2\right)c_1^2 c_2$$
$$-32B_1^2 c_2^2 + 36B_1^2 c_1 c_3 - 128g_2^4 + 512g_2^2 g_3 - 512g_3^2 + 128c_2\left(B_1 g_2^2 - 2B_1 g_3\right)$$
$$+c_1^2\left(64\left(B_2 - B_1\right)g_2^2 - 36B_1^2 g_2^2 + 128B_1 g_3 + 72B_1^2 g_3 - 128B_2 g_3\right)\Big].$$

Since the function $p(e^{i\theta} z)(\theta \in \mathrm{P})$is in the class P for any $p \in P$ without loss of generality, we can assume that $c_1 = c > 0.$ Substituting the values of $c_2$and $c_3$from (2.2) and (2.3) in the above expression, we get

$$\left|a_2 a_4 - a_3^2\right| = \frac{1}{1152}\Big|\left(9B_1B_3 - 8B_2^2\right)c^4 - 128\left(g_2^2 - 2g_3\right)^2 + 64B_1\left(4 - c^2\right)\left(g_2^2 - 2g_3\right)x$$
$$-8B_1^2\left(4 - c^2\right)^2 x^2 - 4\left(9B_1^2 - 16B_2\right)\left(g_2^2 - 2g_3\right)c^2 + 2B_1B_2c^2\left(4 - c^2\right)x$$
$$-9B_1^2 c^2\left(4 - c^2\right)x^2 + 18B_1^2 c\left(4 - c^2\right)\left(1 - x^2\right)y\Big|.$$

Using triangle inequality in the above expression for $\left|a_2 a_4 - a_3^2\right|$ and after a little simplification, we get

$$\left|a_2 a_4 - a_3^2\right| \le \frac{1}{1152}\Big(\left|9B_1B_3 - 8B_2^2\right|c^4 + 512\left|g_3 - g_2^2/2\right|^2 + 128B_1\left(4 - c^2\right)\left|g_3 - g_2^2/2\right||x|$$
$$+8B_1^2\left(4 - c^2\right)^2|x|^2 + 8\left|9B_1^2 - 16B_2\right|\left|g_3 - g_2^2/2\right|c^2 + 2B_1B_2c^2\left(4 - c^2\right)|x|$$
$$+9B_1^2c^2\left(4 - c^2\right)|x|^2 + 18B_1^2c\left(4 - c^2\right)\left(1 - |x|^2\right)|y|\Big)$$

Since the function $g(z) = z + g_2 z^2 + g_3 z^2 + \ldots$ is starlike of order 1/2, we have $\left|g_3 - g_2^2/2\right| \le 1/2.$ Using this estimate in the above inequality, replacing $|x|$ by $\mu$and making use of the fact that $|y| \le 1,$ we get

$$\left|a_2 a_4 - a_3^2\right| \le \frac{1}{1152}\Big(\left|9B_1B_3 - 8B_2^2\right|c^4 + 32 + 32B_1\left(4 - c^2\right)\mu + 8B_1^2\left(4 - c^2\right)^2\mu^2$$
$$+2\left|9B_1^2 - 16B_2\right|c^2 + 2B_1B_2c^2\left(4 - c^2\right)\mu + 9B_1^2c^2\left(4 - c^2\right)\mu^2$$
$$+18B_1^2c\left(4 - c^2\right)\left(1 - \mu^2\right)\Big)$$

(2.13) $= F(c, \mu).$

We shall now maximize $F(c, \mu)$ for $(c, \mu) \in [0, 2] \times [0, 1]$. Differentiating $F(c, \mu)$ in (2.13) partially with respect to μ, we get

(2.14) $$\frac{\partial F}{\partial \mu} = \frac{1}{1152}\left(2B_1\left(4 - c^2\right)\left(16 + B_2c^2 + B_1\left(32 - 18c + c^2\right)\mu\right)\right)$$

For $0 < \mu < 1$, and for any fixed $c \in [0, 2]$, we observe that $\partial F / \partial \mu > 0$. Thus $F(c, \mu)$ is an increasing function of μ, and for $c \in [0, 2]$, $F(c, \mu)$ has a maximum value at $\mu = 1$. Thus, we have

(2.15) $$\max F(c, \mu) = F(c, 1) = G(c).$$

www.IndianJournals.com
Members Copy, Not for Commercial Sale
Downloaded From IP - 14.139.251.107 on dated 25-Oct-2017

The equations (2.13) and (2.15), upon a little simplification, yield

$$G(c)=\frac{1}{1152}\Big[\Big(\big|9B_1B_3-8B_2^2\big|-B_1^2-2B_1B_2\Big)c^4+\Big(2\big|9B_1^2-16B_2\big|-32B_1-28B_1^2$$
$$+8B_1B_2\Big)c^2+\Big(32+128B_1+128B_1{}^2\Big)\Big]$$

$$=\frac{1}{1152}\Big(Pc^4+Qc^2+R\Big), \tag{2.16}$$

where

$$P=\big|9B_1B_3-8B_2^2\big|-B_1^2-2B_1B_2, \tag{2.17}$$

$$Q=2\big|9B_1^2-16B_2\big|-32B_1-28B_1^2+8B_1B_2, \tag{2.18}$$

and

$$R=32+128B_1+128B_1{}^2. \tag{2.19}$$

We know that

$$\max_{0\le t\le 4}\Big(Pt^2+Qt+R\Big)=\begin{cases} R, & Q\le 0,\ P\le -\dfrac{Q}{4};\\ 16P+4Q+R, & Q\ge 0,\ P\ge -\dfrac{Q}{8}\ \text{ or }\ Q\le 0,\ P\ge -\dfrac{Q}{4};\\ \dfrac{4PR-Q^2}{4P} & Q>0,\ P\le -\dfrac{Q}{8}. \end{cases}$$

Thus, we have, from (2.16),

$$\big|a_2a_4-a_3^2\big|\le\frac{1}{1152}\begin{cases} R, & Q\le 0,\ P\le -\dfrac{Q}{4};\\ 16P+4Q+R, & Q\ge 0,\ P\ge -\dfrac{Q}{8}\ \text{ or }\ Q\le 0,\ P\ge -\dfrac{Q}{4};\\ \dfrac{4PR-Q^2}{4P} & Q>0,\ P\le -\dfrac{Q}{8}. \end{cases}$$

where *P, Q, R* are given by (2.17), (2.18) and (2.19), respectively. To prove the sharpness of our result, consider the function defined as

$$f_0(z)=\int_0^z\frac{\varphi(w)}{1-w^2}$$

Let $g(z)=z/(1-z)$. Then the function $f_0(z)$ clearly belongs to the class $K_s(\varphi)$. Now, since $\varphi(z)=1+B_1z+B_2z^2+B_3z^3+\ldots$ and $w(z)$ is as defined in (2.5), therefore we have

$$\frac{\varphi(w)}{1-w^2}=1+\frac{1}{2}B_1c_1w+\frac{1}{4}\Big(4-B_1c_1^2+B_2c_1^2+2B_1c_2\Big)w^2+\ldots.$$

and hence the function $f_0(z)$ is given by

$$f_0(z)=z+\frac{1}{4}B_1c_1z^2+\frac{1}{12}\Big(4-B_1c_1^2+B_2c_1^2+2B_1c_2\Big)z^3+\ldots \tag{2.20}$$

which shows that the result is sharp.

www.IndianJournals.com
Members Copy, Not for Commercial Sale
Downloaded From IP - 14.139.251.107 on dated 25-Oct-2017

Remark 2.3. (1) When $\varphi(z)=(1+z)/(1-z)=1+2z+2z^2+2z^3+...$, our class $K_s(\varphi)$ reduces to the class K_s of close-to-convex univalent functions and thus we have for $f \in K_s$, $|H_2(2)| \le 1$.

(2) When $\varphi(z)=e^z=1+z+z^2/2!+z^3/3!+...$, $|H_2(2)| \le 4/9$

(3) When $\varphi(z)=\sqrt{1+z}=1+z/2-z^2/8+z^3/16$, $|H_2(2)| \le 1/4$

(4) When

$$\varphi(z)=\sqrt{2}-(\sqrt{2}-1)\sqrt{\frac{1-z}{1+\sqrt{2}(\sqrt{2}-1)z}}$$

$$=1+\frac{5-3\sqrt{2}}{2}z+\frac{71-51\sqrt{2}}{8}z^2+\frac{589-415\sqrt{2}}{16}z^3+...,$$

we have that $|H_2(2)| \le (67-42\sqrt{2})/4$.

REFERENCES

1. *N. E. Cho, O. S. Kwon and V. Ravichandran, Coefficient, distortion and growth inequalities for certain close-to-convexfunctions, J. Inequal. Appl. 2011, 2011:100, 7 pp.*
2. *P. L. Duren, Univalent Functions, GTM 259, Springer, New York, 1983.*
3. *M. M. Elhosh, On the second Hankel determinant of univalent functions, Bull. Malays. Math. Soc. (2) 9 (1986), no. 1, 23-25.*
4. *M. M. Elhosh, On the second Hankel determinant of close-to-convex functions, Bull. Malaysian Math. Soc. (2) 9 (1986), no. 2,67-68.*
5. *C. Gao and S. Zhou, On a class of analytic functions related to the starlike functions, Kyungpook Math. J. 45 (2005), no. 1,123-130.*
6. *U. Grenander and G. Szegö, Toeplitz Forms and Their Applications, California Monographs in Mathematical Sciences, Univ.California Press, Berkeley, 1958.*
7. *S. A. Halim, A. Janteng and M. Darus, Classes with negative coefficients and starlike with respect to other points. II, TamkangJ. Math. 37 (2006), no. 4, 345-354.*
8. *W. K. Hayman, On the second Hankel determinant of mean univalent functions, Proc. London Math. Soc. (3) 18 (1968),77-94.*
9. *A. Janteng, S. A. Halim and M. Darus, Coefficient inequality for a function whose derivative has a positive real part, J. Inequal.Pure Appl. Math. 7 (2006), no. 2, Art. 50, 5 pp.*
10. *Y. C. Kim, J. H. Choi and T. Sugawa, Coefficient bounds and convolution properties for certain classes of close-to-convex functions, Proc. Japan Acad. Ser. A Math. Sci. 76 (2000), no. 6, 95-98.*
11. *S. K. Lee, V. Ravichandran and S. Supramaniam, Bounds for the second Hankel determinant of certain univalent functions,J. Inequal. Appl. 2013, 2013:281, 17 pp.*
12. *M.-S. Liu, J.-F. Xu and M. Yang, Upper bound of second Hankel determinant for certain subclasses of analytic functions,Abstr. Appl. Anal. 2014, Art. ID 603180, 10 pp.*

www.IndianJournals.com
Members Copy, Not for Commercial Sale
Downloaded From IP - 14.139.251.107 on dated 25-Oct-2017

13. *W. C. Ma and D. Minda, A united treatment of some special classes of univalent functions, in Proceedings of the Conferenceon Complex Analysis (Tianjin, 1992), 157-169, Conf. Proc. Lecture Notes Anal., I, Int. Press, Cambridge.*

14. *J. W. Noonan and D. K. Thomas, On the Hankel determinants of areally mean p-valent functions, Proc. London Math. Soc.(3) 25 (1972), 503-524.*

15. *J. W. Noonan, Coefficient differences and Hankel determinants of a really mean p-valent functions, Proc. Amer. Math. Soc. 46(1974), 29-37.*

16. *J. W. Noonan and D. K. Thomas, On the second Hankel determinant of a really mean p-valent functions, Trans. Amer. Math.Soc. 223 (1976), 337-346.*

17. *K. I. Noor, Higher order close-to-convex functions, Math. Japon. 37 (1992), no. 1, 1-8.*

18. *K. I. Noor, On the Hankel determinant problem for strongly close-to-convex functions, J. Natur. Geom. 11 (1997), no. 1,29-34.*

19. *K.I. Noor, On certain analytic functions related with strongly close-to-convex functions, Appl. Math. Comput. 197 (2008),no. 1, 149-157.*

20. *Ch. Pommerenke, On the coefficients and Hankel determinants of univalent functions, J. London Math. Soc. 41 (1966), 111-122.*

21. *Ch. Pommerenke, On the Hankel determinants of univalent functions, Mathematika 14 (1967), 108-112.*

22. *K. Sakaguchi, On a certain univalent mapping, J. Math. Soc. Japan 11 (1959), 72-75.*

23. *Z. Wang, C. Gao and S. Yuan, On certain subclass of close-to-convex functions, Acta Math. Acad. Paedagog. Nyházi. (N.S.)22 (2006), no. 2, 171-177.*

www.IndianJournals.com
Members Copy, Not for Commercial Sale
Downloaded From IP - 14.139.251.107 on dated 25-Oct-2017

Silver Nanoparticles Synthesis from a Pharmaceutically Important Medicinal Plant *Plumbago Zeylanica*

Abstract

Purpose: In the Ayurvedic system of medicine, *Plumbago zeylanica* is one of the important medicinal plants which possess several pharmaceutical activities such as antiplasmodial, anti-microbial, antitumour, hepatoprotective, antifungal, anti-inflammatory and anticancer activity. It contains several active constituents and the most important bioactive compound is plumbagin which is a naphthoquinone. Recently nanoparticles have gained its significance in the medical fields due to its higher surface area to volume ratio. In this study silver nanoparticles were synthesised from the *in-vitro* grown accession of Plumbago zeylanica.

Materials and Methods: Aqueous extract of aerial part of *Plumbago zeylanica* accession number 524441 was analyzed for the presence of steroid, reducing sugar, flavonoids, alkaloids, tannin, terpenoids and saponins. Silver nanoparticles were synthesized by mixing the aqueous and silver nitrate solution for 24hrs. Ultraviolet-visible spectroscopy (UV-Vis) was used to detect the formation of silver nanoparticles and scanning electron microscopy (SEM) was used to check the shape of the synthesized nanoparticles.

Results: Present investigation deals with the qualitative analysis of phytocompounds present in the *Plumbago zeylanica* accession number 524441 was done using aqueous extract of the aerial part. It showed positive results for reducing sugar, terpenoid, steroid, flavonoid, glycoside and alkaloid. Further silver nanoparticles synthesis was done and synthesized nanoparticles were characterized by UV-VIS spectroscopy and SEM.

Conclusion: This is the first report on rapid and efficient synthesis of silver nanoparticles from the *in-vitro* grown accession of Plumbago zeylanica. It can be concluded that aerial part of *Plumbago zeylanica* can be a good source for the silver nanoparticles synthesis.

Keywords: Plumbago zeylanica; Silver nanoparticles; Bioactive compounds; Phytocompounds

Research Article

Volume 3 Issue 5 - 2017

Arpita Roy and Navneeta Bharadvaja*

Department of Biotechnology, Delhi Technological University, India

***Corresponding author:** Navneeta Bharadvaja, Plant Biotechnology Laboratory, Delhi Technological University, New Delhi-110042, India, Email: navneetab@dtu.co.in

Received: July 20, 2017 | **Published:** August 14, 2017

Introduction

Plumbago zeylanica is a medicinal plant commonly called "White leadwort" in English and "Chitrak" in Sanskrit, it belonging to the Plumbaginaceae family. It's a perennial herb which is found in West Bengal, Uttar Pradesh and Maharashtra and also to some parts of South India. Most commonly used name persisted with the plant is chitraka [1]. It having multi-purpose medicinal property and is most commonly used in the traditional medicinal system of India. The plants consist of various bioactive compounds like alkaloids, flavonoids, naphthoquinones, glycoside, saponins, steroids, triterpenoids, coumarins, phenolic compounds, tannins, carbohydrate, fixed oils, fats and proteins are present in different parts of the plant which have been reported to show anti-bacterial, anti-plasmodial, anti-tumour, hepatoprotective, central nervous system stimulatory activity, anti-fungal, anti-inflammatory, anti-hyperglycemic, anti-cancer and anti-atherosclerotic activity [2]. Roots of *P. zeylanica* are long and slightly branched with very less secondary roots, having a smooth and unbroken texture. These roots are usually very strong having a bitter taste and a distinct odour with acrid [2]. Medicinal properties of the plants are due to the presence of various phytocompounds. Qualitative analysis reveals the presence of different phytocompounds present in the plant.

In recent times nanotechnology is one of the fast growing fields. It mainly concerns to the synthesis and designing of nanomaterials within the range of 1-100nm. Nanoparticles exhibit new properties due to its specific characteristics such as size, morphology and distribution if compared to with the large particles of bulk material. Nanoparticles present a high surface to volume ratio with decreasing size. Generally, nanomaterials synthesized by using physical and chemical methods but the by-products from these methods are toxic in nature and the process is also costly. Chemically synthesized silver nanoparticles also showed poor antibacterial activity compared to biologically synthesized nanoparticles. This could be due to the protein coating of NPs obtained from the biological extract [3]. To

overcome this problem there is a need for environment-friendly methods of synthesis. Synthesis of nanoparticles using plant extract is an important branch [4]. Several nanoparticles have been synthesized by this plant like silver, gold and copper oxide. Utilization of plant for nanoparticles synthesis can be advantageous over other biological processes as it eliminates the elaborate process of cell culture maintenance. Among several metal nanoparticles, silver nanoparticles gained special focus due to its stability, good conductivity and antimicrobial activity.

Materials and Methods

Accessions number 524441 of *Plumbago zeylanica* was collected from NBPGR, New Delhi and maintained at the plant tissue culture laboratory of Department of Biotechnology, Delhi Technological University.

Inoculation and incubation of explants

The laminar air flow chamber was properly surface sterilized with alcohol and UV lights for 30 minutes. The explants were trimmed to a suitable size of about 2cm by keeping it in sterile Petri-dishes. Then a cut was given on both basal and top portion to remove the undesirable or dead portion. The forceps were rinsed in 70% ethanol and were flamed and then kept for some time to get cool. Each explant was then aseptically inoculated on the MS medium containing 1mg/l BAP in an erect position with long forceps without touching the rim of the culture tube. Inoculated culture tubes were incubated in the culture room at 25±2°C, with a light intensity of 2500lux and a photoperiod of 16 hour light, 8 hour dark and 65% humidity.

Preparation of aqueous plant extract

In-vitro grown plant materials were dried for seven days. Dried plant material was used for the preparation of extract. 100mg of dried plant material mixed with 10ml of mili-Q water and boiled for 15 minutes. Then the plant extract was filtered through Whatman No.-1 filter paper and transferred into autoclaved vials and stored at 4°C for further analysis.

Analysis of phytochemicals

Terpenoid test (salkowski test): 100µl of plant extract was mixed with 2ml of chloroform and 3ml of concentrated sulphuric acid to form a layer. A reddish brown color at interface shows the presence of terpenoid and triterpenoids.

Steroid test (salkowski test): 100µl of plant extract was dissolved in 2ml of chloroform. Sulphuric acid was carefully added to form a lower layer. A reddish brown color at interface shows the presence of steroidal ring.

Saponin test (foam test): Add 100mg of powdered plant material to 10ml of distilled water. Mixture was heated and observed for persistent froth. Formation of froth shows the presence of saponins.

Flavonoid test (NaOH test): 100µl of plant extract was treated with few drops of sodium hydroxide solution. Formation of intense yellow colour, which becomes colourless on the addition of dilute HCL, indicates the presence of flavanoids.

Tannin test ($FeCl_3$ test): 100µl of plant extract was treated with few drops of freshly prepared 6% $FeCl_3$. Green colour formation indicates the tannin presence.

Glycosides test (fehling's test): Equal volume of Fehling A and Fehling B reagents were mixed together and 2ml of it was added to the 100µl of plant extract and gently boiled. Formation of brick red precipitate at the bottom of the test tube indicates the reducing sugars presence.

Alkaloids (mayer's reagent): One milli-liter aqueous extract was taken in test tube and 2ml of 2N HCL was added to it then solution was shaken vigorously to mix and kept for 10 minutes. Few drops of Mayer's reagent were added to it. Formation of creamy colour precipitation indicates the presence of alkaloids.

Synthesis of silver nanoparticles

Preparation of silver nitrate solution: Silver nitrate ($AgNO_3$) was collected from Fisher Scientific. For the preparation of 1mM $AgNO_3$ solution, 16.987mg of $AgNO_3$ was added to 100ml of mili-Q water and mixed. Solution was stored in flask covered with aluminium foil.

Synthesis of silver nanoparticles: Potential of biosynthesis of silver nanoparticles of *Plumbago zeylanica* was tested by using leaf extract. Leaves of *P. zeylanica* were taken and dried under room temperature for 5 days. Then the dried leaves were crushed using pestle and mortar. The crushed material was then boiled in 10ml of distilled water. Then the extract was left to cool at room temperature. The cooled extract was filtered into fresh vials. 8.5mg of silver nitrate was dissolved in 50ml of distilled water. The extract was then added in the ratio of 1:10. Solution was mixed well and kept in incubator shaker at 37°C, 150 rpm for 24 hours. Then the sample was analysed by using UV-Vis spectrometry for the confirmation of silver nanoparticles synthesis. Further SEM was used for the detection of shape of the synthesized nanoparticles.

Characterization of silver nanoparticles

UV-Vis spectroscopy: Silver nanoparticles exhibits yellowish brown colour in aqueous solution due to the phenomenon of Surface Plasmon Resonance. Thus silver nanoparticles formed were separated from the residual and characterized by UV-VIS absorption spectroscopy. Bio-reduction of pure silver ion was monitored. Deionised water was used as a blank. The wavelength range for the silver nanoparticles detection was 300 to 700nm and the presence of reduced silver ions was highlighted by a peak of absorption in the range of 350 to 500nm.

Scanning electron microscope (SEM) analysis: SEM analysis was done by using Hitachi 3700N SEM machine. A thin films of sample was prepared on a carbon coated copper grid by dropping very small amount of sample on the grid, extra solution was removed by using blotting paper and then film on the SEM grid was allowed to dry by putting it under a mercury lamp for 5 minutes.

Results and Discussion

Analysis of phytochemicals

Qualitative analysis of phytochemicals in *Plumbago zeylanica* revealed the presence of terpenoid, saponin, steroid, flavonoid, saponin and alkaloid. These photochemical compounds are major compounds which impart medicinal value of this plant. Dhale & Markandeva [5] a reported the presence of glycoside, alkaloids, reducing sugar, tannins, flavonoids and saponins in the leaves of *Plumbago zeylanica*. Borhade et al. [6] also reported similar kinds of results. Tyagi & Menghani [7] also reported that the presence of reducing sugars, flavanoids, alkaloids and terpenoids and absence of tannins in aqueous extract of *P. zeylanica* (Table 1).

Table 1: Details of presence and absence of phyto-chemicals in *P. zeylanica*.

Phytochemicals	Result	Observation
Steroid	+	Formation of Reddish Brown Ring
Reducing Sugars	+	Reddish Brown Color
Flavanoids	+	Color Changes from Light Yellow Color to Colorless
Alkaloids	+	Formation of Turbid Solution
Tannins	-	No Colour Change
Terpenoids	+	Formation of Reddish Brown Ring
Saponin	+	Formation of Froth

Silver nanoparticles synthesis

Aqueous extract of *Plumbago zeylanica* were tested for their potential to form silver nano-particle by using aqueous extract of whole plant. Change in the colour of solution from slightly yellow to dark brown after overnight incubation the solution of silver nitrate confirms the potential of extract of the plant to form silver nano-particles. Characterisation of silver nanoparticle was done by using UV-Vis spectrophotometer and Scanning electron microscopy (SEM) (Figure 1).

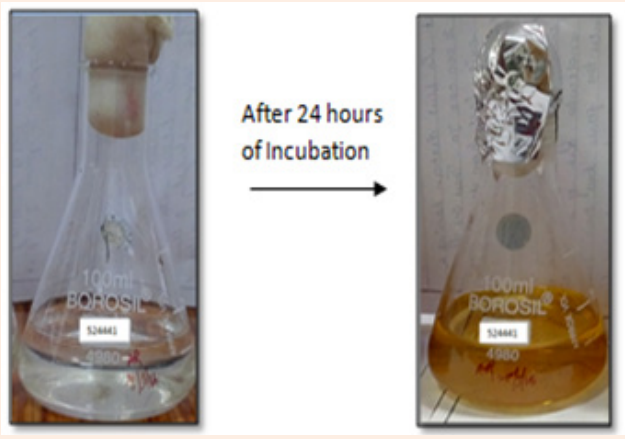

Figure 1: Synthesis of silver nanoparticles using plant extract.

UV-Vis spectroscopy

UV-Vis analysis was done to check the formation of silver nanoparticles based on the absorbance at 350 to 450nm which indicates the presence of silver nanoparticles. Peak of silver nanoparticles was found approximately at 446nm at absorbance of 1.97 which corresponds to Plasmon excitation of silver nanoparticles (Figure 2). Broadening of peak indicates that the particles are poly dispersed. Renisheya Joy Jeba Malar & Johnson [8] also characterised the silver nanoparticles prepared from leaf extract of *P. zeylanica* by using UV-Vis. They have also reported the absorbance lying at the range of 430 to 470nm. Salunke et al. [3] also reported that absorbance of silver nanoparticles was maximum at 440nm. Ponarulselvam et al. [9] reported the absorbance of synthesized silver nanoparticles from *C. roreus* was maximum at 400nm. It was observed that nanoparticles solution was stable for more than six months with little signs of aggregation [10].

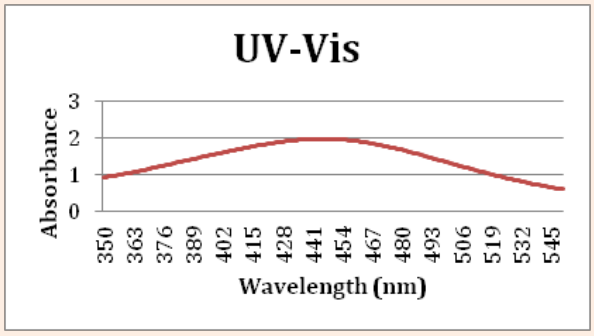

Figure 2: UV-Vis spectra of synthesized silver nanoparticles.

Scanning electron microscope (SEM)

Scanning Electron Microscope (SEM) Analysis SEM provides the details about the morphology of the silver nanoparticles. SEM image was taken at 500nm. Size of synthesized nanoparticles was more than the size of nanoparticles which should be between 1-100nm. Size was more than the desired size due to the protein which were bound in the surface of nanoparticles. Result shows that the particles were of relatively spherical in shape (Figure 3).

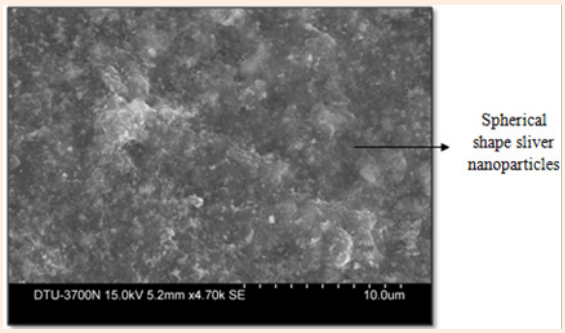

Figure 3: SEM image of silver nanoparticles.

Conclusion

Qualitative analysis of phytochemicals revealed the presence of steroids, terpenoids, saponin flavonoids, alkaloid and reducing sugar in *Plumbago zeylanica*. Presence of these compounds suggests the medicinal properties of this plant. There is a need of further studies to know their biological effects which could be beneficial in the treatment of various diseases.

Biosynthesis of silver nanoparticles using *Plumbago zeylanica* aqueous extract provides a simple, efficient and environment friendly method for the synthesis of nanoparticles. UV-VIS showed that maximum peak was obtained at 446nm. SEM image showed that the synthesized silver nanoparticles were relatively spherical in shape. These silver nanoparticles have potential application in biomedical field; they have several advantages such as cost effective, compatible for medical and pharmaceutical applications.

Acknowledgement

Sincere thanks to the Department of Biotechnology, Delhi Technological University for making necessary facilities during this study, National Bureau of Plant Genetic Resources, New Delhi for providing the plant materials and Department of Applied Physics, Delhi Technological University for providing SEM facility.

References

1. Yuvaraj D Mandavkar, Sunil S Jalalpure (2011) A comprehensive review on *Plumbago zeylanica* Linn. African journal of Pharmacy and Pharmacology 5(25): 2738-2747.
2. Kumar R, Kumar S, Patra A, Jayalakshmi S (2009) Hepatoprotective activity of aerial parts of *Plumbago zeylanica* linn against carbon tetrachloride-induced hepatotoxicity in rats. International Journal of Pharmacy and Pharmaceutical Sciences 1(Suppl 1): 171-175.
3. Salunke GR, Ghosh S, Santosh Kumar RJ, Khade S, Vashisth P, et al. (2014) Rapid efficient synthesis and characterization of silver, gold, and bimetallic nanoparticles from the medicinal plant *Plumbago zeylanica* and their application in biofilm control. Int J Nanomedicine 9: 2635-2653.
4. Logeswari P, Silaqmbarasan S, Abraham J (2013) Eco-friendly synthesis of silver nanoparticles from commercially available plant powders and their antibacterial properties. Scientia Iranica 20(3): 1049-1054.
5. Dhale DA, Markandeya SK (2011) Antimicrobial and phytochemical screening of *Plumbago zeylanica* Linn (*plumbaginaceae*) leaf. Journal of Experimental Science 2(3).
6. Borhade PS, Deshmukh TA, Patil VR, Khandelwal KR (2014) Pharmacognostic and Phytochemical Investigations of *Plumbago zeylanica* Linn, root. Journal of Pharmacognosy and Phytochemistry 2(6): 83-88.
7. Tyagi R, Menghani E (2014) Phytochemical screening of *Plumbago zeylanica*: A potent Herb. International Journal of Pharma Sciences and Research 5(3): 71-72.
8. Renisheya Joy Jeba Malar T, Johnson M (2015) Biosynthesis of Silver nanoparticles using *Plumbago zeylanica* leaves extracts and their bio-efficacy. Research in Pharmacy 5: 49-53.
9. Ponarulselvam S, Panneerselvam C, Murugan K, Aarthi N, Kalimuthu K, et al. (2012) Synthesis of silver nanoparticles using leaves of *Catharanthus roseus* Linn. G. Don and their antiplasmodial activities. Asian Pac J Trop Biomed 2(7): 574-580.
10. Saifuddin N, Wong CW, Nur Yasumira AA (2009) Rapid biosynthesis of silver nanoparticles using culture supernatant of bacteria with microwave irradiation. E Journal of Chemistry 6(1): 61-70.

Author's Accepted Manuscript

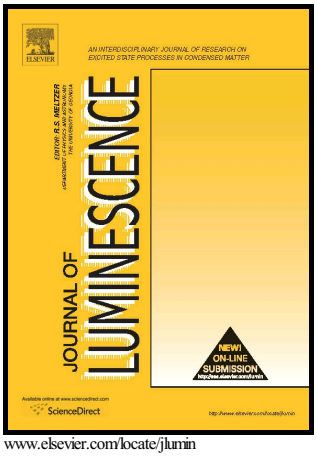

www.elsevier.com/locate/jlumin

Spectroscopic Studies of single Near Ultraviolet pumped Tb^{3+} doped Lithium Lead Alumino Borate Glasses for Green Lasers and Tricolour w-LEDs

Nisha Deopa, A.S. Rao

PII: S0022-2313(17)31446-1
DOI: https://doi.org/10.1016/j.jlumin.2017.09.057
Reference: LUMIN15065

To appear in: *Journal of Luminescence*

Received date: 18 August 2017
Revised date: 25 September 2017
Accepted date: 29 September 2017

Cite this article as: Nisha Deopa and A.S. Rao, Spectroscopic Studies of single Near Ultraviolet pumped Tb^{3+} doped Lithium Lead Alumino Borate Glasses for Green Lasers and Tricolour w-LEDs, *Journal of Luminescence,* https://doi.org/10.1016/j.jlumin.2017.09.057

This is a PDF file of an unedited manuscript that has been accepted for publication. As a service to our customers we are providing this early version of the manuscript. The manuscript will undergo copyediting, typesetting, and review of the resulting galley proof before it is published in its final citable form. Please note that during the production process errors may be discovered which could affect the content, and all legal disclaimers that apply to the journal pertain.

ACCEPTED MANUSCRIPT

Spectroscopic Studies of single Near Ultraviolet pumped Tb^{3+} doped Lithium Lead Alumino Borate Glasses for Green Lasers and Tricolour w-LEDs

Nisha Deopa and A. S. Rao*

Department of Applied Physics, Delhi Technological University, Bawana Road, New Delhi-110 042, India.

Abstract

Terbium ions (Tb^{3+}) doped Lithium Lead Alumino Borate (LiPbAlB) glasses with the chemical composition $10Li_2O - 10PbO - (10\text{-}x)\ Al_2O_3 - 70B_2O_3 - xTb_2O_3$ (where x = 0.5, 1.0, 1.5, 2.0 and 2.5 in mol%) were synthesized via melt quench method and characterized by absorption, photoluminescence (PL) and PL decay spectral measurements. The Judd-Ofelt (J-O) intensity parameters evaluated from the oscillator strength values are further used to evaluate the radiative parameters for the prominent fluorescent levels ($^5D_4 \rightarrow {}^7F_j$) of Tb^{3+} ions. The intensity of all the emission bands increases up to 2 mol% of Tb^{3+} and beyond concentration quenching took place. The decay profiles of $^5D_4$ show single exponential for lower concentration and non-exponential for higher concentration resulting decrease in experimental lifetime (τ_{exp}) with increase in rare earth ion concentration. Such decrease in τ_{exp} and decay conversion from single to non-exponential has been attributed to the cross-relaxation processes and subsequent concentration quenching observed. The Inokuti-Hiryama (I-H) model applied to the decay spectral profiles confirms the energy transfer process between Tb^{3+}-Tb^{3+} ions as dipole-dipole in nature. Higher values of stimulated emission cross-section, quantum efficiency, gain bandwidth and optical gain obtained for $^5D_4 \rightarrow {}^7F_5$ transition of LiPbAlB glass with 2 mol% of Tb^{3+} ions suggests its suitability for green lasers. The CIE-chromaticity co-ordinates, color purity (CP) and correlated color temperature (CCT) confirms the suitability of these glasses in tricolor w-LEDs.

Keywords: Terbium, glasses, photoluminescence, Inokuti-Hiryama model, w-LEDs.

*Corresponding author, ***E-mail: drsrallam@gmail.com, Tel: +91 85860 39007, Fax: +91 01127871023.***

Accepted manuscript

ACCEPTED MANUSCRIPT

1. Introduction

Recently the scientific interest in fabrication and characterization of glasses doped with rare earth (RE) ions have attracted many scientist because of their applications in diversified fields such as lasers, optical waveguides, hole burning memories and white Light Emitting Diodes (w-LEDs) [1–6]. RE doped glasses are also useful in fabricating visible and infrared optical devices due to the transitions observed within their 4f shells. Quite recently, the lighting industries have witnessed tremendous growth because of the replacement of conventional lighting sources with w-LEDs. It is because of the fabulous characteristics features of w-LEDs such as longer lifetime, environment friendly nature, higher reliability and lower fabrication cost [7,8]. The commercial approach for fabricating w-LED is to combine blue emitting LED InGaN chip with yellow emitting YAG:Ce^{3+}phosphor. However this method suffers from halo effect and poor Color Rendering Index (CRI) [9,10]. To overcome these drawbacks, scientists have adopted another method in which RGB phosphors are excited with Near Ultra Voilet (NUV) LEDs. This method helps in improving CRI and minimizing the halo effect [8-10]. Nevertheless in both the methods, phosphors are encapsulated in an epoxy region, which gets deteriorated at higher temperatures, energy and excitation sources resulting in reducing the output gradually. Quite recently RE ions doped glasses are considered to be the potential candidates for fabricating w-LEDs as there is no epoxy region present in the glasses. The design as well as development of RE doped glassy systems for the aforementioned application needs the thorough study of optical properties by using absorption, PL and PL decay spectral analysis. The optical property of doped glasses highly depends upon the environment surrounded by RE ions in the amorphous matrix and on the phonon energy of the host matrix.

Accepted manuscript

ACCEPTED MANUSCRIPT

Among the glass former available, borates are said to be the excellent hosts matrices for RE ions due to their unique properties such as high transparency, thermal stability, good RE ion solubility and lower melting point [11]. Despite having the aforementioned fantastic advantages, borate glasses are encountering a major setback due to their high phonon energies (1300 cm^{-1}). Presence of such redundant phonon energies in borate glasses can reduce the radiative emissions in them. Consequently emission cross-sections and quantum efficiency of borate glasses are getting effected very badly [12]. To overcome this drawback, some heavy metal oxides (HMO) such as lead oxide (PbO) or bismuth oxides (Bi_2O_3) can be added to B_2O_3 [13]. Depending upon the concentration of PbO in B_2O_3, it acts as a network modifier or as a network former. As the Pb^{2+} content in the boron network increases, conversion from BO_3 to BO_4 units takes place which may be a strong reason for suppressing the non-radiative decay process [14]. Addition of aluminium trioxides (Al_2O_3) to B_2O_3-PbO network can improve mechanical strength and thermal stability [15]. Al^{3+} ions involve in the glassy network along with AlO_4 and AlO_6 structural units and combine to evaluate the radiation sensitivity of glass system [16]. Introducing lithium oxide (Li_2O) in a ternary system (PbO-Al_2O_3- B_2O_3) can enhance stability, produce moisture resistance and remove air bubbles from the glassy matrix. Further, it can increase the glass transition temperature (T_g) and reduces thermal expansion coefficient [6,17]. Considering the aforementioned valuable scientific patronages offered by the chemical constituents such as B_2O_3, PbO, Al_2O_3 and Li_2O, in the present work we prepared a glassy system namely Lithium Lead Alumino Borate (LiPbAlB) glass.

Among the RE ions, Tb^{3+} is the most efficient ion for strong green emission, originating from $^5D_4 \rightarrow {}^7F_5$ transition located at 544nm. The luminescence intensity of Tb^{3+} ions doped matrices depend upon the excitation wavelength, host matrix composition and Tb^{3+} ions concentration.

Accepted manuscript

ACCEPTED MANUSCRIPT

Recently, Tb^{3+} doped glassy systems in large industrial scale were synthesized and studied by using their PL spectroscopy [18]. When Tb^{3+} ions doped glassy systems are pumped by NUV light, two types of energy transfer takes place from $^5D_3 \rightarrow {}^7F_j$ (blue emission) and $^5D_4 \rightarrow {}^7F_j$ (green emission) where j=0 to 6, therefore the PL property is very useful for evaluating energy level structure as well as for identifying different transitions present in the system [19]. Tb^{3+} doped glasses can also be pumped by co-operative energy transfer process in which the excited Yb^{3+} ions simultaneously transfer its energy to an unexcited Tb^{3+} ion. Many researchers have reported the co-operative energy transfer between Yb^{3+} to Tb^{3+} [20-23]. Nowadays, Tb^{3+} doped materials are attracting researchers as well as industry due to their diversified applications in w-LEDs, solid state lasers, evolution of electromagnetic transmission window of sea water and green color emitting phosphors [24, 25]. In this report, the role of Tb^{3+} ions in LiPbAlB glass has been studied thoroughly using spectroscopic techniques such as absorption, PL and PL decay spectra to understand the utility of these glasses in green lasers as well as in tricolor w-LEDs.

2. Experimental

Tb^{3+} doped LiPbAlB glasses with the nominal molar composition $10Li_2O$-10PbO-(10-x) Al_2O_3 - $70B_2O_3$-xTb_2O_3, where x is 0.5, 1.0, 1.5, 2.0 and 2.5 in mol% were synthesized by using conventional melt quenching technique. For convenience these glasses are designated as glass A, B, C, D and E. All the raw materials used in the present work such as Li_2O, PbO, Al_2O_3, B_2O_3 and Tb_2O_3 are of analar grade in quality. The above constituents in the given proportions were melted in a silica crucible by heating at 1100^0 C in an electrical furnace for about 5 hours and the desired melts were prepared. The melts were then quenched between two preheated brass plates to form the glass samples of uniform thickness. The glasses were annealed for 4 hours in another electrical furnace at 350^0C to eliminate thermal strains and to improve structural stability. The

Accepted manuscript

ACCEPTED MANUSCRIPT

resultant glasses are amorphous and transparent with 3mm thickness and used directly for their optical characterization.

Densities of the as-prepared glasses were measured by using Archimedes principle taking water as an immersion fluid with an accuracy of ±0.01 gm/cm^3. Brewster's angle method was employed to determine the refractive index of titled glasses using He-Ne laser (650 nm line) with ± 0.01 accuracy. The optical absorption spectra for glasses were recorded by using a Perkin Elmer Tensor-27 UV-vis-NIR spectrophotometer in the wavelength range of 350-550nm having a spectral resolution of 0.1nm. The PL spectra for the titled glasses were recorded using Shimadzu RF-5310 PC-Spectrofluorophotometer with a spectral resolution of 0.5nm in a steady state mode. The PL decay spectral recordings were done using an Edinburgh FLSP900 Fluorescence Spectrometer with a spectral resolution of 0.1nm taking xenon lamp as an excitation source.

3. Results and discussion

3.1 Absorption spectral analysis and J-O parameters

The absorption spectrum of 2 mol% Tb^{3+} ions in LiPbAlB glass (Glass D) is shown in Fig. 1 as a representative. While the rest of the absorption spectra for various Tb^{3+} concentrations show similar band positions but their respective absorption intensities and absorption band edges shows systematic variation with concentration, which will be discussed in the following sections. From Fig. 1 it can be seen that all the transition starts from the ground state ($^7F_6$) of Tb^{3+} ions and consists of 3 transitions corresponding to $^7F_6 \rightarrow {}^5G_6$, $^5D_3$ and $^5D_4$. The band assignments have been done as per the Carnall report [26]. All the absorption bands are originated from induced electric dipole-dipole transition following the selection rules $\Delta S=0$, $|\Delta L| \leq 6$, $|\Delta J| \leq 6$ [27]. From

Accepted manuscript

ACCEPTED MANUSCRIPT

Fig. 1 it can be noticed that Tb^{3+} ions in LiPbAlB glass shows weak absorption in UV/blue region, which is due to the forbidden character of 4f-4f transition. The absorption spectra are used to evaluate oscillator strengths by taking area under the absorption curves using the procedure explained elsewhere [5, 28-31]. The energy levels within the $4f^5$ configuration of the Tb^{3+} ion have been examined applying J-O theory [27, 32] to the experimental oscillator strengths. The values of J-O intensity parameters thus estimated are presented in Table 1 along with some reported values [25, 33-35].

The J-O intensity parameters (Ω_2, Ω_4 and Ω_6) will play a vital role in understanding the glass structure as well as transitions among the RE energy levels in a host matrix. Generally, the Ω_2 J-O parameter is very sensitive towards local environment and assigned to degree of covalence between Tb^{3+} ion and oxygen ligands. Higher the Ω_2 parameter, higher will be the covalency between Tb^{3+} ion and oxygen ligands along with lower symmetry around Tb^{3+} ion. From Table 1, it is observed that the bonding between terbium ions with the surrounding ligands is covalent in nature and the RE ion sites are having lower asymmetry in these glasses. Among all the glasses studied in the present work, glass D possesses more covalent nature than the other glasses. The Ω_4 and Ω_6 parameters are related to long range effects and bulk properties such as viscosity and rigidity. From Table 1, it can be seen that the J-O parameters are following the same trend ($\Omega_2 > \Omega_4 > \Omega_6$) for all the as-prepared glasses under investigation.

3.2 Optical band gap and Urbach energy analysis

The optical band gap energy is an essential parameter for studying the properties of solid state materials. The fundamental absorption edge in the UV-region is a useful tool for evaluating electronic band structure and optical transitions in crystalline as well as amorphous materials. In the absorption edge, two types of optical transition can occur which are direct and indirect. The

Accepted manuscript

ACCEPTED MANUSCRIPT

optical band gap for the as-prepared glasses were evaluated from the absorption spectra, by using Davis and Mott's expression [36]

$$\alpha h\vartheta = B(h\vartheta - E_{opt})^n \quad (1)$$

where, B is bonding trailing parameter, α is absorption coefficient, ϑ is frequency, and E_{opt} is optical band gap energy. The values of n can be 1/2, 2, 1/3 and 3 for direct allowed, indirect allowed, direct forbidden and indirect forbidden transitions respectively. The absorption coefficient parameter can be evaluated by using the following expression [37]

$$\alpha(\vartheta) = \frac{1}{d}\ln\left(\frac{I_0}{I_t}\right) \quad (2)$$

where, d is thickness of the glass sample, I_0 and I_t are intensity of incident and transmitted radiations. From Tauc's plot, the optical band gap energies (E_{opt}) are estimated by extrapolating the liner region of the plot drawn for $(\alpha h\upsilon)^{1/2}$ versus $h\upsilon$ as shown in Fig. 2. The inset in Fig. 2 shows the variation of Urbach energy (ΔE) and indirect allowed band gap with Tb^{3+} ions concentration. The band tailing parameters as well as the optical band gap for direct and indirect allowed transitions are tabulated in Table 2. From Table 2 it is conspicuous that, the optical band gap energy decreases while band tailing parameter increases with Tb^{3+} ions concentration in these glasses. The decreases in band gap (E_{opt}) values can be attributed to the variation of oxygen bonding within the glass network which further results in creating non-bridging oxygens (NBO). These NBO sites lie in the valence band maximum and increasing NBO shifts towards conduction band resulting decrease in E_{opt} values. The ΔE values which indicate disorderliness and formation of defects are increasing with Tb^{3+} ion concentration in these glasses. Relatively lower ΔE values obtained indicates that the defects and disorderliness are minimal in these

Accepted manuscript

ACCEPTED MANUSCRIPT

glasses under investigation. This may help in enhancing the optical properties of the as prepared glasses.

3.3 Analysis of emission spectra and evaluation of radiative properties

Excitation spectrum of 2 mol% Tb^{3+} ions doped LiPbAlB glasses recorded by fixing emission wavelength (λ_{em}) at 544nm is shown in Fig. 3. The spectrum displays different bands centered at 300, 316, 325, 337, 350, 366 and 377nm corresponding to the transitions $^7F_6 \rightarrow {}^5H_{5,6}$, ($^5H_7$, $^5D_1$), ($^5L_{7,8,}$ $^5G_3$), ($^5G_5$, $^5D_2$),$^5L_9$, $^5L_{10}$ and $^5G_6$ respectively. Among all, the band associated with $^7F_6 \rightarrow {}^5L_9$ transition (350 nm) is more intense and can be taken as an excitation wavelength (λ_{ex} = 350nm) to record emission spectra. This wavelength also matches well with the emission wavelength of commercial AlGaN LED [38]. The PL spectra of Tb^{3+} ions doped LiPbAlB glasses under 350nm excitation are shown in Fig. 4. It consists of four bands in weak red (623nm), weak yellow (586nm), strong green (544nm) and weak blue (498nm) regions associated with the transitions $^5D_4 \rightarrow {}^7F_J$, where J=3, 4, 5 and 6 respectively. The $^5D_4 \rightarrow {}^7F_6$ transition in blue region follows $\Delta J = \pm 1$ [39,40] which comes under magnetic dipole transition selection rule, while the $^5D_4 \rightarrow {}^7F_5$ transition observed in intense green region follows Laporte-forbidden selection rule [41]. The distortion effects produced by host network on Tb^{3+} ions produces a mild splitting in the peak centered at 544nm ($^5D_4 \rightarrow {}^7F_5$). This can be attributed to the stark splitting of energy levels. On the other hand, upon increasing Tb^{3+} ions concentration in the LiPbAlB glasses, intensity increases up to 2 mol% and beyond concentration quenching takes place and intensity deceases. This may be attributed to the cross-relaxation process through energy transfer mechanism. Fig. 5 shows the partial energy level diagram of glass D (2 mol%) explaining the excitation, emission and possible cross-relaxation channels for quenching. From Fig. 5 it is observed that the energy gap between $^7F_0$ to $^7F_6$ and $^5D_3$ to $^5D_4$ along with $^5D_3$ to $^7F_0$

Accepted manuscript

ACCEPTED MANUSCRIPT

and $^7F_6$ to $^5D_4$ matches quite well with each other. Emission from $^5D_3$ level is very feeble in intensity and not observed here due to the strong emission from $^5D_4$ level. Such weak intensity observed for $^5D_3$ transition supports the pronounced energy transfer via cross-relaxation to the $^5D_4$ level. However, at higher Tb^{3+} ions concentrations (>2 mol %) quenching of $^5D_4$ level takes place which may be due to energy migration or cooperative energy transfer mechanism as shown in Fig. 5. Fig. 6 represents the intensity variation of green to blue emission with Tb^{3+} ions concentration in LiPbAlB glasses. From Fig. 4 it is observed that 2 mol % of Tb^{3+} ions concentration in LiPbAlB glass is optimum for generating bright green emission.

In order to understand PL performance of Tb^{3+} doped LiPbAlB glasses, radiative parameters such as radiative transition probability (A_R), total transition probability (A_T), radiative branching ratio's (β_R), and radiative lifetimes (τ_R) were evaluated by coupling J-O parameters with the emission data and are given in Table 3. The suitable expressions needed for the estimation of the aforementioned radiative parameters are collected from literature [5,42-44]. The A_R and β_R are essential parameters for potential laser action because it is directly proportional to the stimulated emission cross section. Higher the branching ratios, greater will be stimulated emission cross-section (σ_{se}). Emission cross-section is another important parameter for laser action and is useful in identifying the potential laser transitions of Tb^{3+} ions in LiPbAlB host matrix. The σ_{se} parameter can be evaluated by the following equation [5, 9, 11, 12]

$$\sigma_{se}(a_j, b_{j'}) = \left[\frac{{\lambda_p}^4}{8\pi c n^2 \Delta\lambda_p}\right] A_R(a_j, b_{j'}) \qquad (3)$$

here, λ_P is emission peak wavelength, $\Delta\lambda_p$ is the line width (FWHM) of the transition. The values of σ_{se}, λ_P, $\Delta\lambda_P$, β_R & β_{exp} for the titled glasses were tabulated in Table 4. From Table 4 it can be observed, β_{exp} and β_R values are highest for glass D for $^5D_4 \rightarrow {}^7F_5$ (green) emission transition.

Accepted manuscript

ACCEPTED MANUSCRIPT

RE doped amorphous material can also act as a good optical fiber if gain band width (σ_{se} x $\Delta\lambda_p$) and optical gain parameter (σ_{se} x τ_R) are having higher values. From Table 4 it can be seen that, among all the LiPbAlB glasses under investigation, glass D is having highest values of σ_{se}, β_R & β_{exp}, σ_{se} x $\Delta\lambda_p$ and σ_{se} x τ_R for the $^5D_4 \rightarrow {}^7F_5$ (544nm) transition. This makes glass D to act as a potential candidate for green laser applications.

3.4 Photoluminescence decay spectral studies

The decay rates of the as-prepared glasses for $^5D_4$ fluorescent level were obtained by exciting the samples with 350nm ($^7F_6 \rightarrow {}^5L_9$) and monitoring the emission at 544nm ($^5D_4 \rightarrow {}^7F_5$). The decay curves are well fitted to the bi-exponential function for all the as-prepared glasses and are shown in Fig. 7. Though the PL decay curves at lower concentrations (up to 1.5mol% Tb^{3+} ions) show bi-exponential, they are predominantly single exponential in nature and beyond 1.5 mol% they are showing significant bi-exponential behavior. The average lifetime in case of bi-exponential fitting can be evaluated by using the following expression

$$\tau_{avg} = \frac{A_1\tau_1^2 + A_1\tau_1^2}{A_1\tau_1 + A_2\tau_2} \quad (4)$$

The decrease in experimental lifetime (τ_{exp}) with increasing concentration is observed which may be due to enhanced interactions between Tb^{3+}- Tb^{3+} at higher concentrations. The τ_{exp} values thus obtained are tabulated in Table 5. The predicted radiative lifetime (τ_R) values evaluated from J-O theory for $^5D_4$ excited state are given in Table 4. Considerable difference appearing between τ_{exp} and τ_R clearly indicates that the emissions from $^5D_4$ level are not totally radiative but contains some non-radiative decay contributions also. In general, non-radiative decay contribution (W_{NR}) arising due to energy transfer mechanism between Tb^{3+}- Tb^{3+} and can be evaluated by using the following formula

Accepted manuscript

ACCEPTED MANUSCRIPT

$$\frac{1}{\tau_{exp}} = \frac{1}{\tau_R} + W_{NR} \quad (5)$$

The W_{NR} values thus evaluated are presented in Table 5. Quantum efficiency η (%) is another important and most essential parameter which measures the luminescence efficiency of a material under investigation and is evaluated by taking the ratio between τ_{exp} and τ_R. From Table 5 it is observed that among all the as prepared glasses, η (%) value is highest for 2 mol% Tb^{3+} ion in LiPbAlB glass (glass D).

3.5 Inokuti-Hiryama (I-H) model analysis

In some cases, to understand the predominant energy transfer mechanism, the non-exponential decay profiles are fitted to I-H model [45]. Hence I-H model can be applicable for studying the interaction between donor-acceptor (Tb^{3+}- Tb^{3+}) at higher Tb^{3+} ions concentrations. The PL intensity decay in such a case is given by

$$I_t = I_0 \exp\{-\frac{t}{\tau_0} - Q(\frac{t}{\tau_0})^{\frac{3}{S}}\} \quad (6)$$

here, t is time after excitation and τ_0 is intrinsic decay time of donors without the presence of acceptors . The energy transfer parameter 'Q' can be evaluated as follows

$$Q = \frac{4\pi}{3} \Gamma(1 - \frac{3}{S}) N_0 R_0^3 \quad (7)$$

here, N_0 is the concentration of acceptor ions, R_0 is critical energy transfer distance, which is the distance between donor and acceptor when the rate of energy transfer is equal to intrinsic decay.

Depending on the type of interactions involved in the mechanism the values of "S" and gamma function Γ(X) are different such as dipole-dipole for S=6 & Γ(X)=1.77, dipole-quadrupole for

Accepted manuscript

ACCEPTED MANUSCRIPT

S=8 & Γ(X)=1.43) and quadrupole-quadrupole interactions for S=10 & Γ(X)=1.3. The energy transfer probability and donor acceptor interaction parameter can be expressed as

$$C_{DA} = R_0^{(S)} \tau_0^{-1} \text{ and } W_{ET} = C_{DA} R_0^{(S)} \quad (8)$$

In the present work, decay profiles observed for all the LiPbAlB glasses are fitted to I-H model by taking S=6 which indicates dipole-dipole interaction between Tb^{3+} ions as shown in Fig.7. The I-H fitting for all the glasses can be seen in Fig.7. It can be clearly seen from Fig. 7 that, I-H curves are well fitted for higher Tb^{3+} ions concertation (glass C to E) in these glasses. From Table 5 it is observed that as the concentration of Tb^{3+} increases, critical distance between donor and acceptors (R_0) and non-radiative decay rates (W_{NR}) decreases while energy transfer parameter (Q) increases. The variation of energy transfer parameter (Q) and τ_{exp} with Tb^{3+} ion concentration is shown in Fig. 8. From Fig. 8 it is conspicuous that, increase in Tb^{3+} ion concentration in LiPbAlB glasses can enhance the magnitude of Q while reduces τ_{exp}.

3.6 CIE chromaticity co-ordinates and color purity analysis

The PL spectra of Tb^{3+} doped LiPbAlB glasses under 350nm excitation were characterized by using their CIE chromaticity co-ordinates. The calculated values of CIE chromaticity co-ordinates of the as-prepared glasses under investigation are tabulated in Table 6. The color purity or color saturation is an important parameter in the colorimetric calculations and it can be defined as the separation of the color coordinate point of test source (x, y) to equal energy point (x_{ee}, y_{ee}) divided by separation of equal energy point to dominant wavelength point (x_d, y_d). The value of color purity can be estimated from the relation [46]

$$Color\ purity = \frac{\sqrt{(x-x_{ee})^2+(y-y_{ee})^2}}{\sqrt{(x_d-x_{ee})^2+(y_d-y_{ee})^2}} \quad (9)$$

Accepted manuscript

ACCEPTED MANUSCRIPT

The values of green color purity calculated for the as-prepared glasses under 350nm excitation for glasses A-E are 44.56, 47.23, 50.19, 53.45 and 52.14 respectively. Fig. 9 shows the CIE color coordinates of 2 mol% of Tb^{3+} doped LiPbAlB glass (glass D) under 350nm excitation. From the Fig.9 it is observed that the values of CIE co-ordinates (0.31, 0.62) of glass D are close to European Broadcasting Union illuminant green (0.29, 0.60).

Further, correlated color temperature (CCT) is another essential tool for studying key features of the illuminant and can be defined as temperature of Planckian black body whose color coordinates are near to the standard white light source. The CCT values can be calculated by using the following formula proposed by McCamy [47]

$$CCT = -449n^3 + 3525n^2 - 6823.2n + 5520.3 \quad (10)$$

here, $n = \frac{x-x_e}{y-y_e}$, $x_e = 0.332, y_e = 0.186$. The values of CCT for all the titled Tb^{3+} doped LiPbAlB glasses under 350nm excitation are presented in Table 6 and found to be in cool green light region (5700-6000K). The Higher the CCT better will be visual acuity along with higher brightness perception. From the aforementioned colorimetric parameters, it is observed that glass D under 350nm excitation is very efficient for the fabrication of tricolor w-LED as well as solid state green lasers.

Accepted manuscript

4. Conclusions

In summary, LiPbAlB glasses doped with Tb^{3+} ions at varying concentrations were prepared by using melt quench technique and their absorption, PL and PL decay spectral properties were discussed in detail. The J-O parameters evaluated from the absorption spectra are following the same trend ($\Omega_2 > \Omega_4 > \Omega_6$) in all the glasses under investigation and in turn used to estimate various radiative parameters. The PL spectra monitored for the as prepared glasses under 350nm

ACCEPTED MANUSCRIPT

excitation show four bands corresponding to $^5D_4 \rightarrow {}^7F_J$ (J=3-6) transitions. Among all the emission bands, the intense emission observed in green region ($^5D_4 \rightarrow {}^7F_5$) is centered at 544nm. The intensity of green and blue band increases up to 2 mol % of Tb^{3+} ion concentration and beyond concentration quenching took place due to non-radiative cross-relaxation processes. Stimulated emission cross-section, branching ratios, quantum efficiency and CIE chromaticity coordinates evaluated by using the emission spectral data suggests the utility of these glasses for green luminescence. The decay profiles show gradual change from single exponential to non-exponential resulting decrease in experimental lifetime (τ_{exp}) with increase in RE ion concentration. This has been attributed to the cross-relaxation processes and subsequent concentration quenching observed. The I-H model reveals the energy transfer mechanism between Tb^{3+}-Tb^{3+} ions as electric dipole-dipole in nature. The CCT values evaluated for all the titled glasses under 350nm excitation are found to be in cool green light region (5700-6000K). All the aforementioned results suggest the feasibility of using Tb^{3+} ions doped LiPbAlB glasses for visible green luminescent applications. Particularly glass D with 2 mol% of Tb^{3+} ions in LiPbAlB glass is most suitable for green lasers and tricolor w-LEDs.

Acknowledgement: The authors are very much thankful to Prof. G. Vijaya Prakash, IIT-Delhi and Dr. D. Haranath, Principal Scientist, CSIR-NPL, New Delhi for their experimental help in the present work.

Accepted manuscript

ACCEPTED MANUSCRIPT

References

[1] Y. Zheng, B. Chen, H. Zhong, J. Sun, L. Cheng, X. Li, J. Zhang, Y. Tian, W. Lu, J. Wan, T. Yu, L. Huang, H. Yu, H. Lin, Optical transition, excitation state Absorption, and energy transfer study of Er^{3+},Nd^{3+} single-doped, and Er^{3+}/Nd^{3+} codoped tellurite glasses for mid-infrared laser applications, J. Am. Ceram. Soc. 94 (2011) 1766–1772.

[2] C.S. Rao, C.K. Jayasankar, Spectroscopic and radiative properties of Sm^{3+}-doped K-Mg-Al phosphate glasses, Opt. Commun. 286 (2013) 204–210.

[3] F. Varsanyi, Surface Lasers, Appl. Phys. Lett. 19 (1971) 169–171.

[4] K. Jha, M. Jayasimhadri, Structural and emission properties of Eu^{3+}-doped alkaline earth zinc-phosphate glasses for white LED applications, J. Am. Ceram. Soc. (2017) 1–10.

[5] N. Deopa, A.S. Rao, Sk. Mahamuda, M. Gupta, M. Jayasimhadri, D. Haranath, G.Vijaya Prakash, Spectroscopic studies of Pr^{3+} doped lithium lead alumino borate glasses for visible reddish orange luminescent device applications, J. Alloys Compd. 708 (2017) 911–921.

[6] D. L. Griscon, Structure, Application, Ed: I. D. Pye, V. D. Frechette and N. J. Kreidl (Plenum, New York, 1978), Elsevier.

[7] B. Tian, B. Chen, Y. Tian, X. Li, J. Zhang, J. Sun, H. Zhong, L. Cheng, S. Fu, H. Zhong, Y. Wang, X. Zhang, H. Xia, R. Hua, Excitation pathway and temperature dependent luminescence in color tunable $Ba_5Gd_8Zn_4O_{21}$:Eu^{3+} phosphors, J. Mater. Chem. C. 1 (2013) 2338–2344.

Accepted manuscript

ACCEPTED MANUSCRIPT

[8] S. Kaur, M. Jayasimhadri, A.S. Rao, A novel red emitting Eu^{3+} doped calcium aluminozincate phosphor for applications in w-LEDs, J. Alloys Compd. 697 (2017) 367–373.

[9] N. Deopa, A.S. Rao, Photoluminescence and energy transfer studies of Dy^{3+} ions doped lithium lead alumino borate glasses for w-LED and laser applications, J. Lumin. 192 (2017) 832–841.

[10] K. Jha, M. Jayasimhadri, Spectroscopic investigation on thermally stable Dy^{3+} doped zinc phosphate glasses for white light emitting diodes, J. Alloys Compd. 688 (2016) 833–840.

[11] N. Deopa, A.S. Rao, Spectroscopic studies of Sm^{3+} ions activated lithium lead alumino borate glasses for visible luminescent device applications, Opt. Mater. 72 (2017) 31–39.

[12] Sk. Mahamuda, K. Swapna, M. Venkateswarlu, A.S. Rao, S. Shakya, G. Vijaya Prakash, Spectral characterisation of Sm^{3+} ions doped oxy-fluoroborate glasses for visible orange luminescent applications, J. Lumin. 154 (2014) 410–424.

[13] A.G.S. Filho, J.M. Filho, F.E.A. Melo, M.C.C. Custodio, R. Lebullenger, A.C. Hernandes, Optical properties of Sm^{3+} doped lead fluoroborate glasses, J. Phys. Chem. Solids. 61 (2000) 1535–1542.

[14] S. Arunkumar, K. Marimuthu, Concentration effect of Sm^{3+} ions in B_2O_3-PbO-PbF_2-Bi_2O_3-ZnO glasses-Structural and luminescence investigations, J. Alloys Compd. 565 (2013) 104–114.

Accepted manuscript

ACCEPTED MANUSCRIPT

[15] J.E. Shelby, Introduction to glass science and technology, the royal society of chemistry, Cambridge, 1997.

[16] L. V Wullen, W.M. Warmuth, ^{11}B MAS NMR spectroscopy for characterizing the structure of glasses, Solid State Nucl. Magn. Reson. 2 (1993) 279–284.

[17] M. Ganguli, K.J. Rao, Structure role of PbO in Li_2O– $PbO–B_2O_3$ glasses, J. Solid State Chem. 145 (1999) 65–76.

[18] L. Zur, M. Soltys, J. Pisarska, W.A. Pisarski, Absorption and luminescence properties of terbium ions in heavy metal glasses, J. Alloys Compd. 578 (2013) 512–516.

[19] B.C. Jamalaiah, J.S. Kumar, A.M. Babu, T. Sasikala, L.R. Moorthy, Study on spectroscopic and fluorescence properties of Tb^{3+}-doped LBTAF glasses, Phys. B. 404 (2009) 2020–2024.

[20] L. Fenga, L. Biana, W. Renc, X. Zhangb, H. Li, Cooperative upconversion of Tb^{3+}/Yb^{3+} codoped oxyfluoride glasses, Mater. Res. Bull. 89 (2017) 263-266.

[21] A. Bahadur, R.S. Yadav, R.V. Yadav S.B. Rai, Multimodal emissions from Tb^{3+}/Yb^{3+} co-doped lithium borate glass: Upconversion, downshifting and quantum cutting, J. Solid State Chem. 246 (2017) 81-86.

[22] G. Li, C. Zhang, P. Songa, P. Zhua, K. Zhu, J. He, Luminescence properties in Tb^{3+}/Yb^{3+} codoped phosphate glasses for solar cells, J. Alloys Compd. 662 (2016) 89-93.

Accepted manuscript

ACCEPTED MANUSCRIPT

[23] I.A.A.Terra, L.J. B. González, T.R. Figueredo, J.M.P. Almeidaa, A.C.Hernandes, L.A.O. Nunesa, O.L. Malta, J. Lumin. 132 (2012) 1678-1682.

[24] A. Vedda, M. Martini, M. Nikl, E. Mihokova, K. Nitsch, N. Solovieva, F. Karagulian, Optical absorption and thermoluminescence of Tb^{3+}-doped phosphate scintillating glasses, J. Phys. Condens. Matter. 14 (2002) 7417–7426.

[25] K. Swapna, Sk. Mahamuda, A.S. Rao, M. Jayasimhadri, S. Shakya, G.Vijaya Prakash, Tb^{3+} doped zinc alumino bismuth borate glasses for green emitting luminescent devices, J. Lumin. 156 (2014) 180–187.

[26] W.T. Carnall, P.R. Fields, K. Rajnak, Electronic energy levels of the trivalent lanthanide aquo ions . III . Tb^{3+}, J. Chem. Phys. 49 (1968) 4447–44450.

[27] G.S. Ofelt, Intensities of crystal spectra of rare earth ions, J. Chem. Phys. 37 (1962) 511–520.

[28] Sk. Mahamuda, K. Swapna, P. Packiyaraj, A.S. Rao, G. Vijaya Prakash, Visible red, NIR and Mid-IR emission studies of Ho^{3+} doped zinc alumino bismuth borate glasses, Opt. Mater. 36 (2013) 362–371.

[29] M. Srinivasulu, A.S. Rao, Absorption and emission spectra of Pr^{3+} -doped mixed alkali fluorophosphate optical glasses, J. Mater. Sci. Lett. 20 (2001) 737–740.

[30] M. Venkateswarlu, M.V.V.K.S. Prasad, K. Swapna, Sk. Mahamuda, A.S. Rao, A.M. Babu, D. Haranath, Pr^{3+} doped lead tungsten tellurite glasses for visible red lasers, Ceram. Int. 40 (2014) 6261–6269.

Accepted manuscript

ACCEPTED MANUSCRIPT

[31] S. Kaur, A.S. Rao, M. Jayasimhadri, Spectroscopic and photoluminescence characteristics of Sm^{3+} doped calcium aluminozincate phosphor for applications in w-LED, Ceram. Int. 43 (2017) 7401–7407.

[32] B.R. Judd, Optical absorption intensities of rare-earth ions, Phys. Rev. 127 (1962) 750–761.

[33] D.K. Sardar, K.L. Nash, R.M Yow, J.B. Gruber, U.V. Valiev, Absorption intensities and emission cross sections of Tb^{3+} ($4f^8$) in $TbAlO_3$, J. Appl. Phys. 100 (2006) 083108–5.

[34] L.B. Shaw, B. Cole, P.A. Thielen, J.S. Sanghera, I.D. Aggarwal, Mid-wave IR and long-wave IR laser potential of rare-earth doped chalcogenide glass fiber, IEEE J. Quantum Electron., 48 (2001) 1127-37.

[35] D. Umamaheswari, B.C. Jamalaiah, T. Sasikala, T. Chengaiah, G. Kim, L.R Moorthy, Photoluminescence and decay behavior of Tb^{3+} ions in sodium fluoro-borate glasses for display devices , J. Lumin. 132 (2012) 1166–70.s

[36] E.A. Davis, N.F. Mott, Conduction in non-crystalline systems V. Conductivity, optical absorption and photoconductivity in amorphous semiconductors, Philos. Mag. 22 (1970) 903–922.

[37] A. Agarwal, V.P. Seth, S. Sanghi, P. Gahlot, D.R. Goyal, Optical band gap studies and estimation of two photon absorption coefficient in alkali bismuth borate glasses, Radiat. Eff. Defects Solids. 158 (2013) 793–801.

[38] T. Nishida, T. Ban, N. Kobayashi, 340 –350 nm GaN-free UV-LEDs, Phys. Status Solidi A. 109 (2003) 106–109.

Accepted manuscript

ACCEPTED MANUSCRIPT

[39] V. Aruna, S. Buddhudu, Spectral properties of Tb^{3+} : B_2O_3 – P_2O_5 – R_2SO_4 glasses, Mater. Lett. 36 (1998) 24–28.

[40] H.X. Zhang, S. Buddhudu, C.H. Kam, Y. Zhou, Y.L. Lam, K.S. Wong, B.S. Ooi, S.L. Ng, W.X. Que, Luminescence of Eu^{3+} and Tb^{3+} doped Zn_2SiO_4 nanometer powder phosphors, Mater. Chem. Phys. 68 (2001) 31–35.

[41] C.H. Kam, S. Buddhudu, Photoluminescence properties of Eu^{3+} : ZrF_4 – BaF_2 – LaF_3 – YF_3 – AlF_3 – NaF glasses, Phys. B. 344 (2004) 182–189.

[42] R. Cases, M.A. Chamarro, R. Alcala, V.D. Rodriguez, Optical properties of Nd^{3+} and Dy^{3+}ions in ZnF_2-CdF_2 based glasses, J. Lumin. 48 (1991) 509–514.

[43] V. Venkatramu, P. Babu, C.K. Jayasankar, W. Sievers, G. Wortmann, Optical spectroscopy of Sm^{3+} ions in phosphate and fluorophosphate glasses, 29 (2007) 1429–1439.

[44] R. Praveena, V. Venkatramu, P. Babu, C.K. Jayasankar, Fluorescence spectroscopy of Sm^{3+} ions in P_2O_5 – PbO – Nb_2O_5 glasses, Phys. B. 403 (2008) 3527–3534.

[45] M. Inokuti, F. Hirayama, Influence of energy transfer by the exchange mechanism on donor luminescence, J. Chem. Phys. 43 (1965) 1978–1988.

[46] T.W. Kuo, W.R. Liu, T.M. Chen, High color rendering white light-emitting-diode illuminator using the red-emitting Eu^{3+} -activated CaZnOS phosphors excited by blue LED, Opt. Express. 18 (2010) 8187–8192.

[47] C.S. McCamy, Correlated color temperature as an explicit function of chromaticity coordinates, Color Res. Appl. 17 (1992) 142–144.

Accepted manuscript

ACCEPTED MANUSCRIPT

Figure captions

Fig. 1. Absorption Spectrum of 2.0 mol% of Tb^{3+} ions in LiPbAlB glass.

Fig. 2. Indirect bandgap plot of Tb^{3+} ions in LiPbAlB glasses [Inset shows the variation of Urbach energy and indirect band gaps with Tb^{3+} ion concentration in LiPbAlB glasses].

Fig. 3. Excitation spectrum of 2.0 mol% of Tb^{3+} ions in LiPbAlB glasses under 544nm emission.

Fig. 4. PL spectra of Tb^{3+} ions in LiPbAlB glasses under 350nm excitation.

Fig.5. Energy level diagram of 2.0 mol% of Tb^{3+} ions in LiPbAlB glass with excitation, emission and cross-relaxation channels.

Fig.6. Variation of blue ($^5D_4 \rightarrow {}^7F_6$) and green ($^5D_4 \rightarrow {}^7F_5$) luminescence intensity as a function of Tb^{3+} ion concentration in LiPbAlB glasses.

Fig.7. The decay spectral profiles of $^5D_4 \rightarrow {}^7F_5$ (544nm) emission transition of Tb^{3+} ions in LiPbAlB glasses under 350nm excitation along with I-H fitting curves .

Fig. 8. Variation of energy transfer parameter (Q) and experimental lifetime (τ_{exp}) with increase in Tb^{3+} ion concentration in LiPbAlB glasses.

Fig. 9. CIE chromaticity coordinates of 2 mol% Tb^{3+} ions in LiPbAlB glass.

Accepted manuscript

ACCEPTED MANUSCRIPT

Fig. 1.

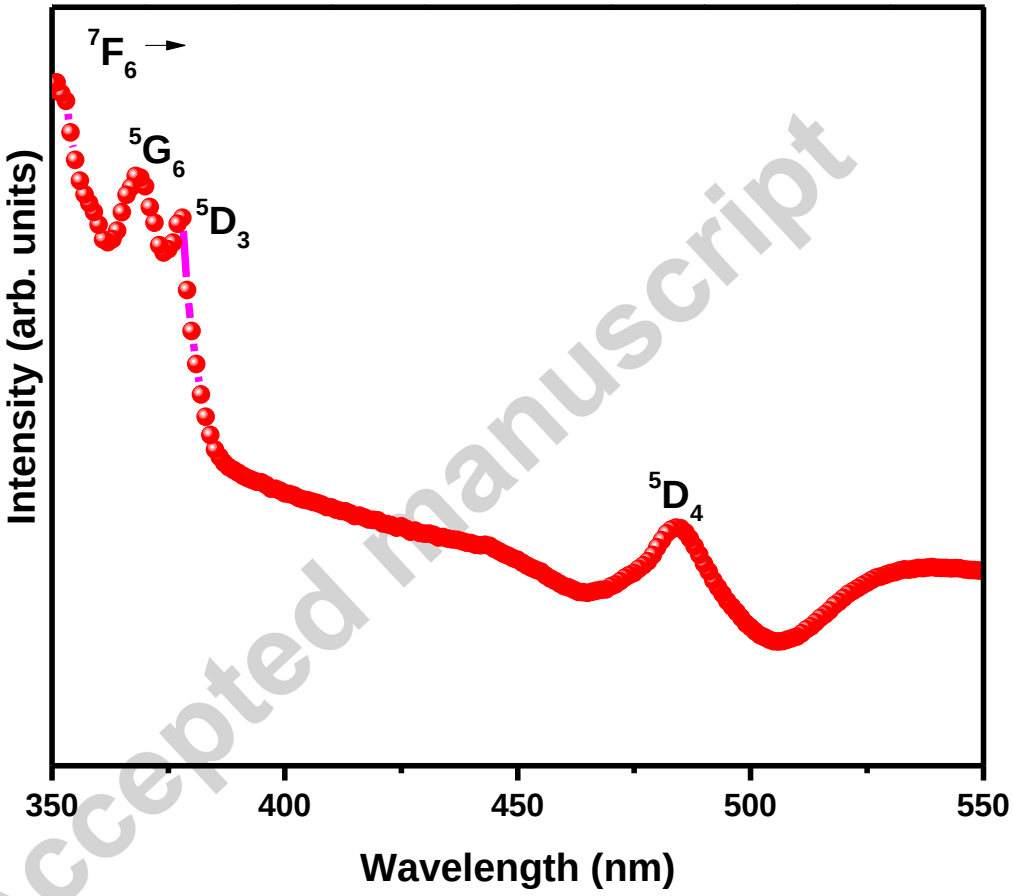

Accepted manuscript

ACCEPTED MANUSCRIPT

Fig. 2.

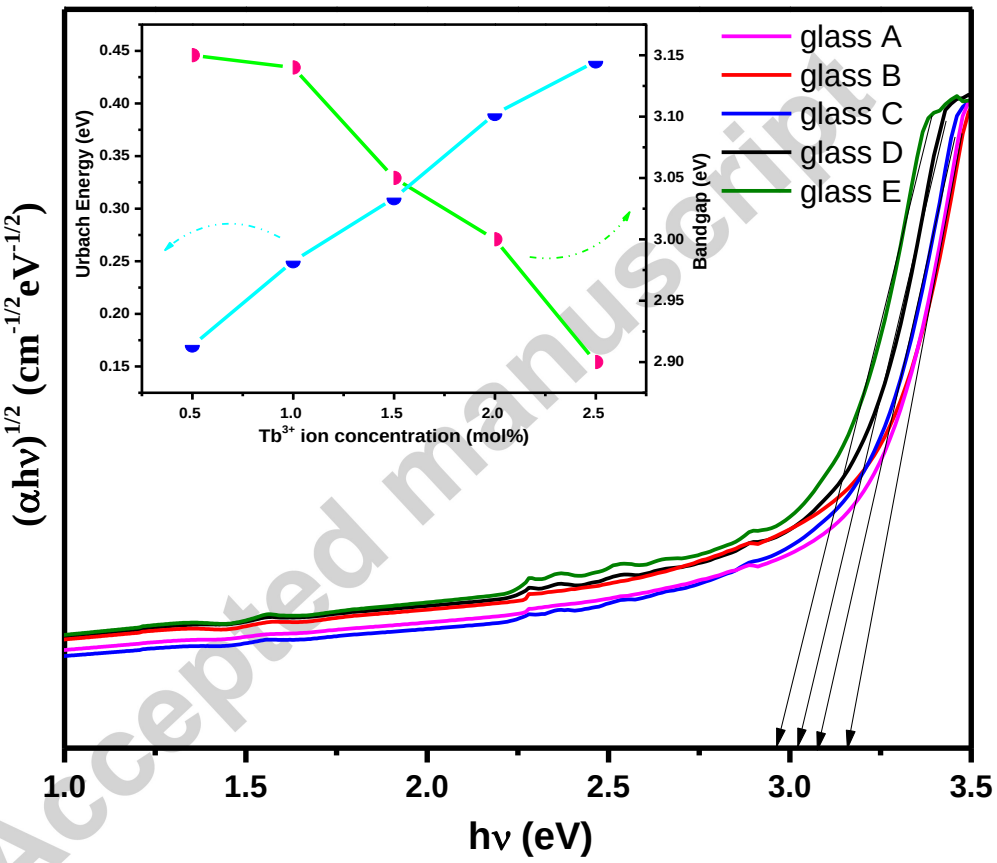

Accepted manuscript

ACCEPTED MANUSCRIPT

Fig. 3.

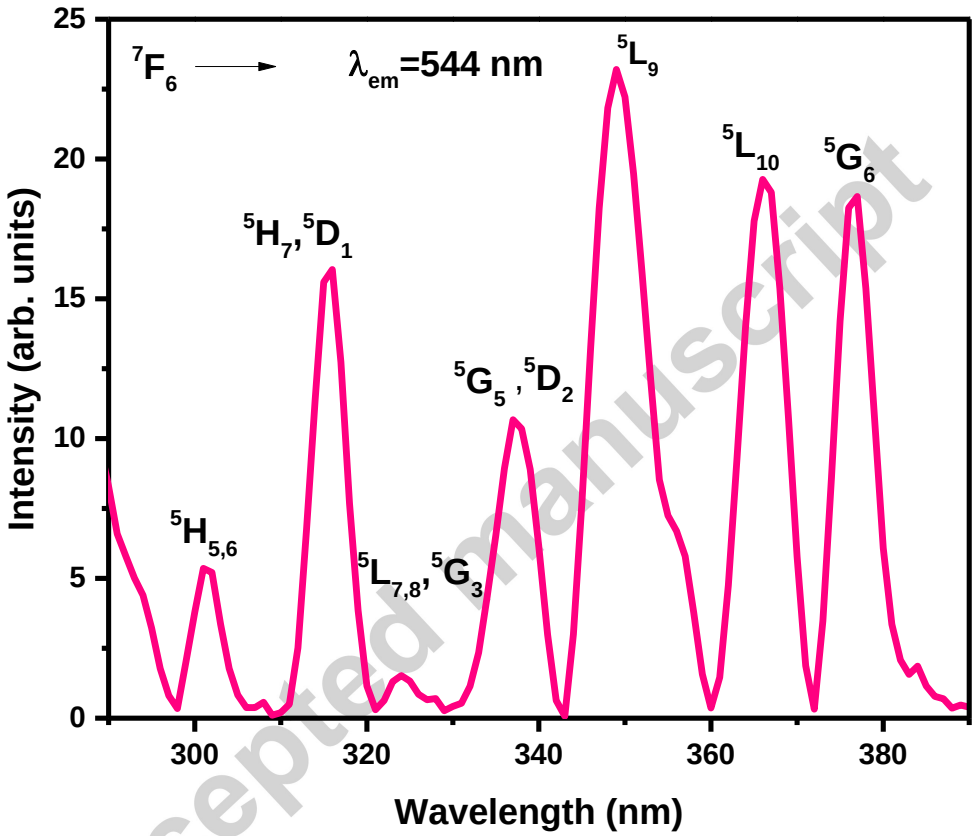

Accepted manuscript

ACCEPTED MANUSCRIPT

Fig. 4.

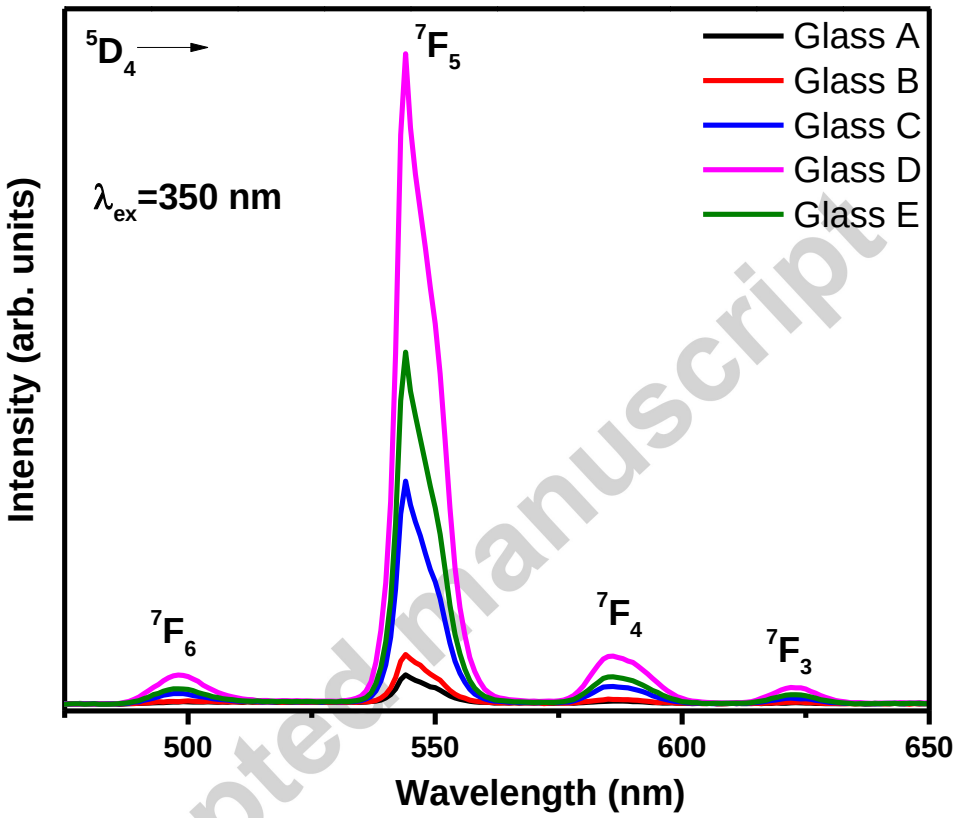

Accepted manuscript

ACCEPTED MANUSCRIPT

Fig. 5.

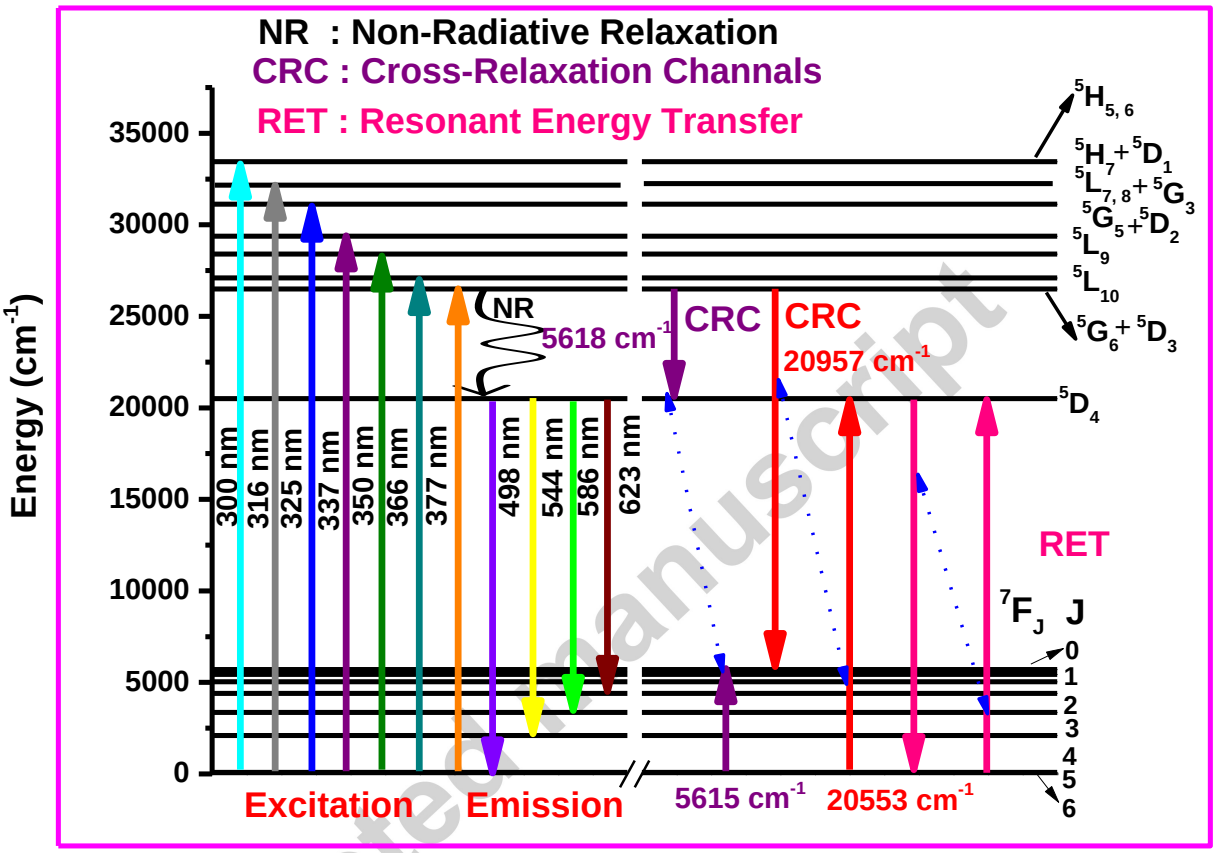

Accepted manuscript

ACCEPTED MANUSCRIPT

Fig. 6.

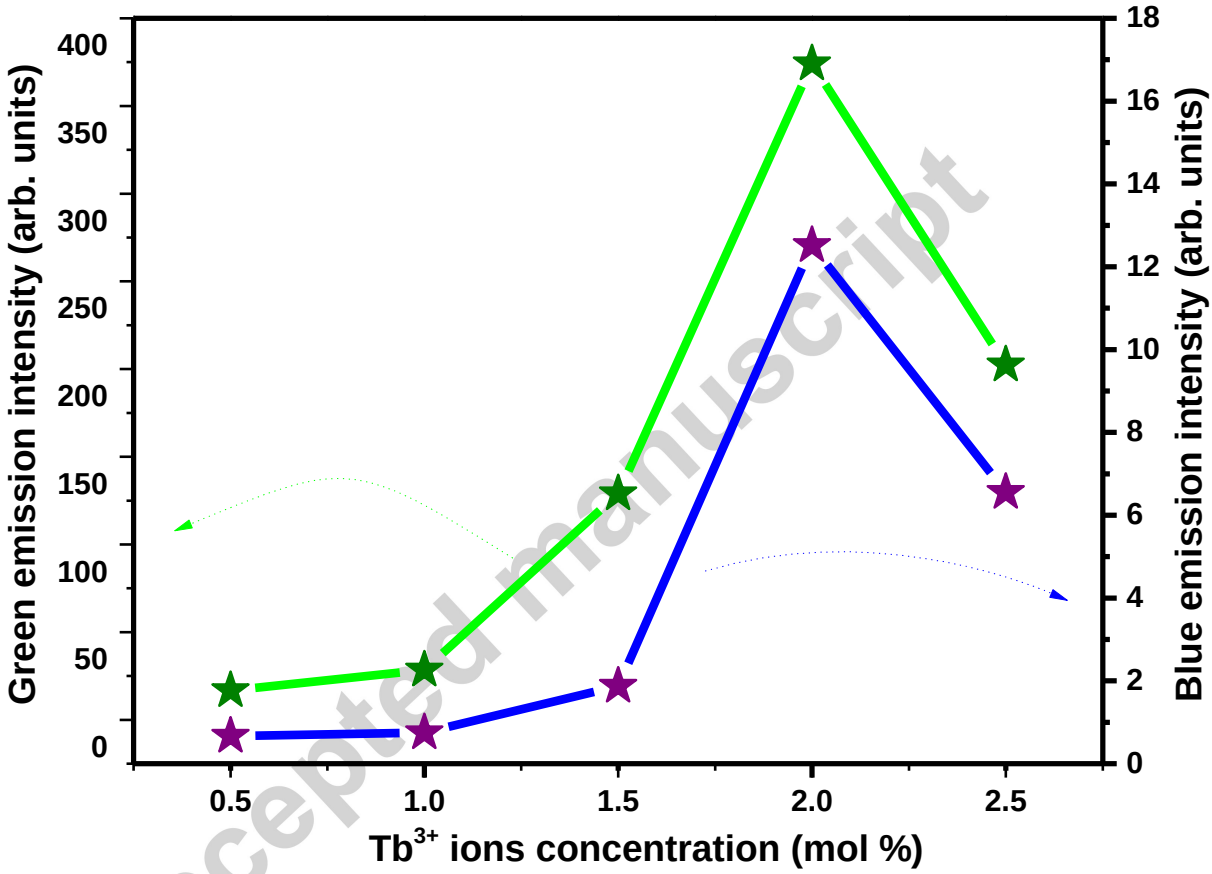

Accepted manuscript

ACCEPTED MANUSCRIPT

Fig. 7.

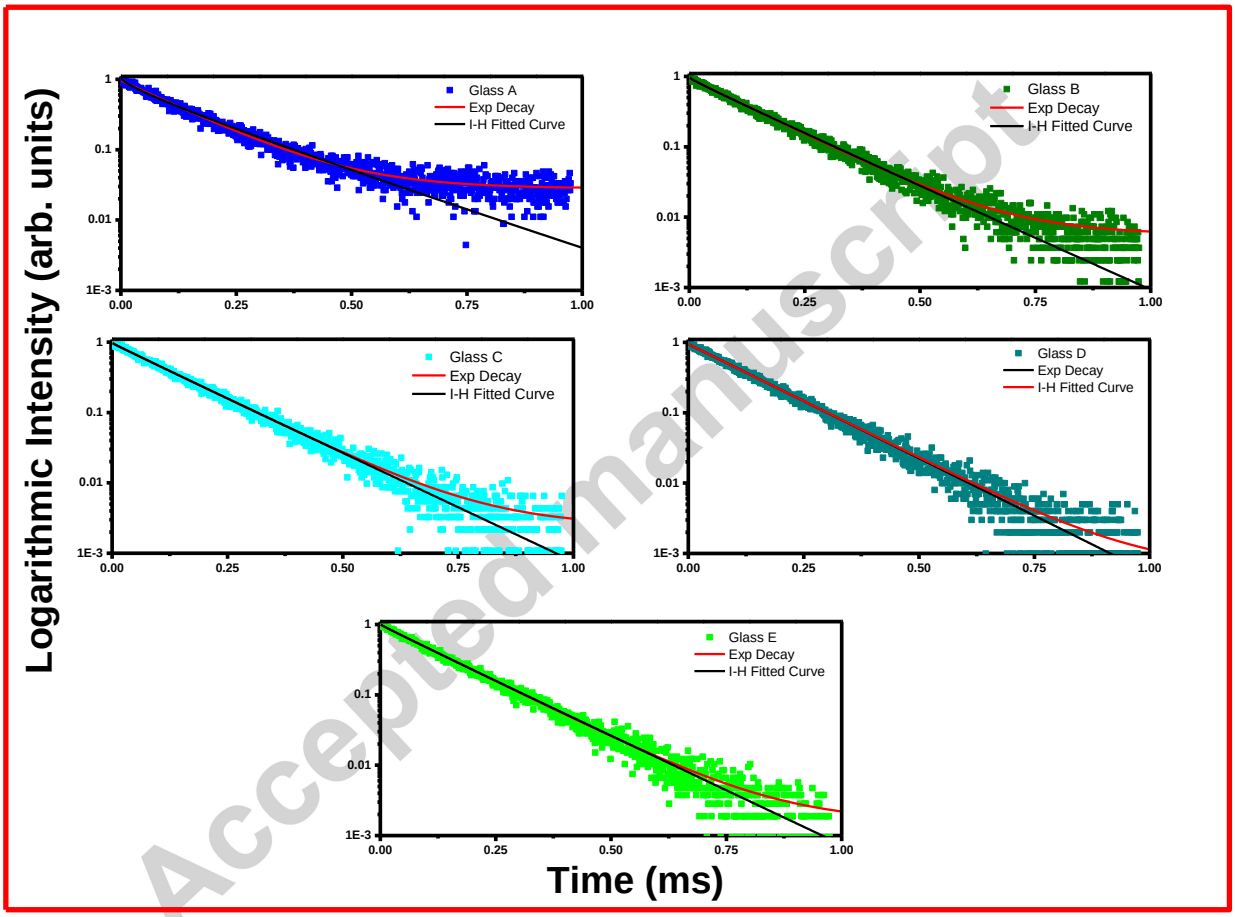

Accepted manuscript

ACCEPTED MANUSCRIPT

Fig. 8.

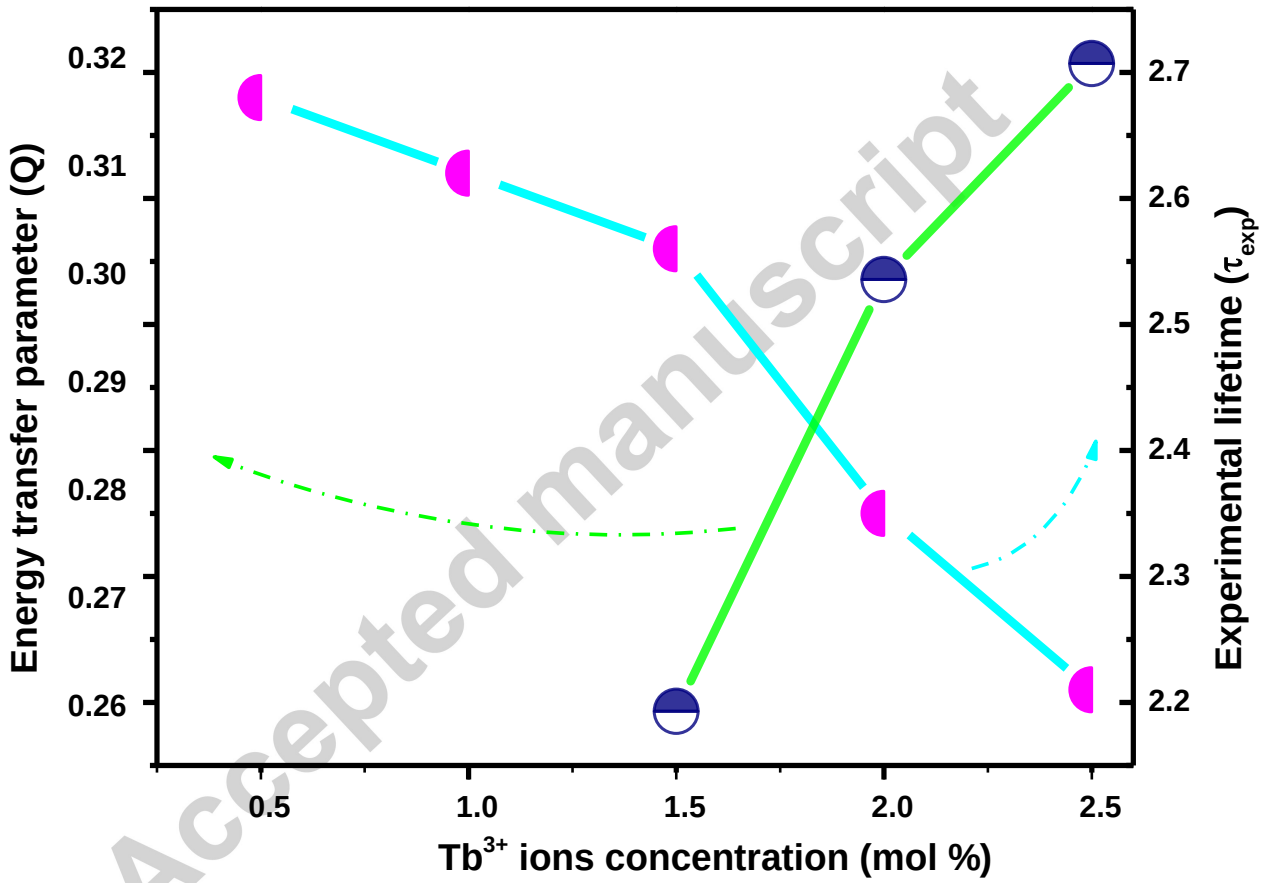

Accepted manuscript

ACCEPTED MANUSCRIPT

Fig. 9.

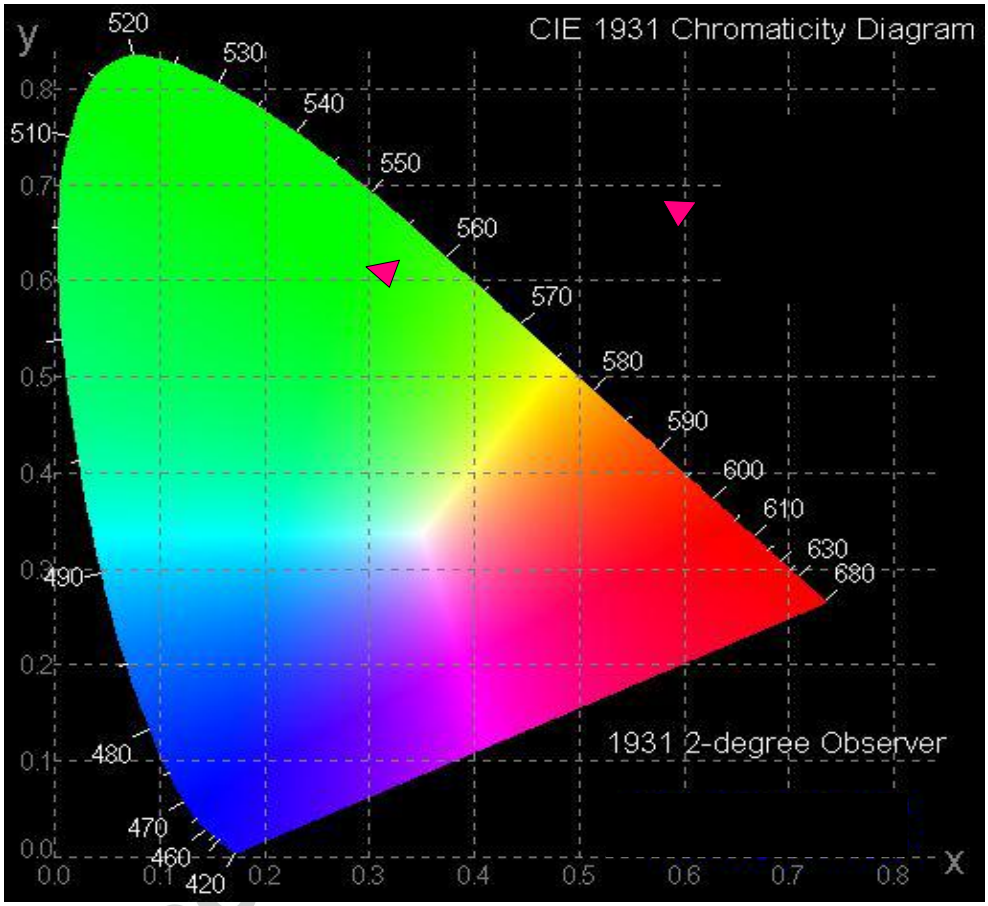

ACCEPTED MANUSCRIPT

Table 1

Judd-Ofelt Parameters ($\Omega_\lambda \times 10^{-20} cm^2$) of Tb^{3+} ions in LiPbAlB glasses along with other reported values.

Glass System	Ω_2	Ω_4	Ω_6	Trend	References
Glass A	1.37	0.95	0.19	$\Omega_2 > \Omega_4 > \Omega_6$	present work
Glass B	1.39	1.06	0.23	$\Omega_2 > \Omega_4 > \Omega_6$	present work
Glass C	1.41	1.21	0.28	$\Omega_2 > \Omega_4 > \Omega_6$	present work
Glass D	1.48	1.34	0.32	$\Omega_2 > \Omega_4 > \Omega_6$	present work
Glass E	0.84	0.64	0.22	$\Omega_2 > \Omega_4 > \Omega_6$	present work
ZnAlBiBTb1.0	7.60	16.7	2.69	$\Omega_4 > \Omega_2 > \Omega_6$	[21]
$TbAlO_3$	40.5	8.74	2.26	$\Omega_2 > \Omega_4 > \Omega_6$	[29]
TbGAGSe	7.50	4.40	2.40	$\Omega_2 > \Omega_4 > \Omega_6$	[30]
TbSFB	0.45	5.53	1.39	$\Omega_4 > \Omega_6 > \Omega_2$	[31]

Accepted manuscript

ACCEPTED MANUSCRIPT

Table 2

Optical band gap (E_{opt}), band tailing parameter (B) for indirect and direct allowed transitions along with Urbach energy (ΔE) of Tb^{3+} ions in LiPbAlB glasses.

Glass Samples	**n = 1/2 (Indirect allowed)**		**n = 2 (Direct allowed)**		**Urbach energy (ΔE) (eV)**
	E_{opt} (eV)	**B ($cm^{-1/2}$ eV)**	**E_{opt} (eV)**	**B ($cm^{-1/2}$ eV)**	**ΔE**
Glass A	3.10	2.58	3.39	88.53	0.17
Glass B	3.08	2.69	3.05	150.98	0.25
Glass C	3.06	3.27	2.89	205.34	0.31
Glass D	2.97	3.78	2.70	263.76	0.39
Glass E	2.95	3.95	2.63	308.32	0.44

Accepted manuscript

ACCEPTED MANUSCRIPT

Table 3

Transition probability (A_R) (s^{-1}), branching ratio (β_R), total transition probability (A_T) (s^{-1}) and radiative lifetime (τ_R) (μs) for the observed emission transitions of Tb^{3+} ions in LiPbAlB glasses.

Transition	A_R	β_R	A_T	τ_R
Glass A				
$^5D_4 \rightarrow {}^7H_6$	21.99	0.1117	196.79	5.08
$^5D_4 \rightarrow {}^7F_5$	47.90	0.2434		
$^5D_4 \rightarrow {}^7F_4$	37.65	0.2546		
$^5D_4 \rightarrow {}^7F_3$	27.34	0.1913		
Glass B				
$^5D_4 \rightarrow {}^7H_6$	13.04	0.1315	99.13	10.08
$^5D_4 \rightarrow {}^7F_5$	26.65	0.2688		
$^5D_4 \rightarrow {}^7F_4$	19.25	0.2685		
$^5D_4 \rightarrow {}^7F_3$	13.56	0.1941		
Glass C				
$^5D_4 \rightarrow {}^7H_6$	17.25	0.1155	149.25	6.70
$^5D_4 \rightarrow {}^7F_5$	36.83	0.2467		
$^5D_4 \rightarrow {}^7F_4$	37.99	0.2545		
$^5D_4 \rightarrow {}^7F_3$	28.18	0.1888		
Glass D				
$^5D_4 \rightarrow {}^7H_6$	33.08	0.1213	269.78	3.75
$^5D_4 \rightarrow {}^7F_5$	101.52	0.3646		
$^5D_4 \rightarrow {}^7F_4$	98.01	0.3518		
$^5D_4 \rightarrow {}^7F_3$	36.39	0.1305		
Glass E				
$^5D_4 \rightarrow {}^7H_6$	13.56	0.1016	133.36	7.49
$^5D_4 \rightarrow {}^7F_5$	28.73	0.2154		
$^5D_4 \rightarrow {}^7F_4$	31.82	0.2385		
$^5D_4 \rightarrow {}^7F_3$	27.63	0.2071		

Accepted manuscript

ACCEPTED MANUSCRIPT

Table 4

Emission peak wavelength (λ_P) (nm), effective band widths ($\Delta\lambda_P$) (nm), measured and experimental branching ratios (β_R & β_{exp}), stimulated emission cross-sections (σ_{se}) (cm^2), gain band width ($\sigma_{se} \times \Delta\lambda_P$) ($cm^3$) and optical gain parameter ($\sigma_{se} \times \tau_R$) ($cm^2$ s) for the emission transitions of Tb^{3+} ions in LiPbAlB glasses.

Spectral parameters	Glass A	Glass B	Glass C	Glass D	Glass E
$^5D_4 \rightarrow {}^7F_6$ (Blue)			**$\lambda_P = 498\ nm$**		
$\Delta\lambda_P$	12.64	12.78	12.85	12.92	12.53
β_R	0.11	0.13	0.11	0.12	0.10
β_{exp}	0.05	0.07	0.06	0.05	0.05
σ_{se} (x 10^{-23})	3.41	1.53	1.94	4.45	1.33
$\sigma_{se} \times \Delta\lambda_P$ (x 10^{-28})	0.44	0.19	0.24	0.57	0.16
$\sigma_{se} \times \tau_R$ (x 10^{-25})	1.77	1.53	1.28	1.24	0.97
$^5D_4 \rightarrow {}^7F_5$ (Green)			**$\lambda_P = 544\ nm$**		
$\Delta\lambda_P$	8.76	8.77	8.83	9.24	8.82
β_R	0.24	0.27	0.24	0.36	0.22
β_{exp}	0.62	0.73	0.79	0.82	0.80
σ_{se} (x 10^{-23})	15.6	6.43	8.42	26.5	5.63
$\sigma_{se} \times \Delta\lambda_P$ (x 10^{-28})	1.36	0.56	0.74	2.45	0.49
$\sigma_{se} \times \tau_R$ (x 10^{-25})	7.31	6.50	5.68	7.41	4.17
$^5D_4 \rightarrow {}^7F_4$ (Yellow)			**$\lambda_P = 586\ nm$**		
$\Delta\lambda_P$	12.34	12.83	12.85	13.55	13.05
β_R	0.25	0.27	0.25	0.35	0.24
β_{exp}	0.09	0.11	0.09	0.08	0.09
σ_{se} (x 10^{-23})	11.7	4.22	8.03	23.53	5.62
$\sigma_{se} \times \Delta\lambda_P$ (x 10^{-28})	1.44	0.55	1.04	3.18	0.74
$\sigma_{se} \times \tau_R$ (x 10^{-25})	5.94	4.32	5.42	6.57	4.21
$^5D_4 \rightarrow {}^7F_3$ (Red)			**$\lambda_P = 623\ nm$**		
$\Delta\lambda_P$	10.10	10.48	10.96	10.64	10.19
β_R	0.19	0.19	0.19	0.13	0.20
β_{exp}	0.04	0.04	0.05	0.02	0.05
σ_{se} (x 10^{-23})	13.3	4.71	8.92	14.2	8.04
$\sigma_{se} \times \Delta\lambda_P$ (x 10^{-28})	1.34	0.49	0.96	1.51	0.82
$\sigma_{se} \times \tau_R$ (x 10^{-25})	6.73	4.76	6.03	3.97	5.98

Accepted manuscript

ACCEPTED MANUSCRIPT

Table 5

Experimental lifetime (τ_{exp}) (ms), quantum efficiency (η), energy transfer parameter (Q), critical transfer distance (R_0) (Å) and non-radiative decay rates (W_{NR}) for $^5D_4 \rightarrow {}^7F_5$ (544nm) transition of Tb^{3+} ions in LiPbAlB glasses.

Name of sample	τ_{exp}	**η (%)**	**Q**	R_0	W_{NR}
Glass A	2.68	52.7	----	----	176.28
Glass B	2.62	25.9	----	----	282.47
Glass C	2.56	38.2	0.26	1.36	241.13
Glass D	2.35	66.6	0.30	1.32	158.8
Glass E	2.21	29.1	0.32	1.28	281.96

Accepted manuscript

ACCEPTED MANUSCRIPT

Table 6

Colorimetric parameters of Tb^{3+} ions in LiPbAlB glasses under 350nm excitation wavelength.

Glass Samples	x-coordinates	y-coordinates	CCT(K)
Glass A	0.3143	0.6462	5805
Glass B	0.3187	0.6420	5725
Glass C	0.3184	0.6278	5724
Glass D	0.3187	0.6213	5718
Glass E	0.3193	0.6316	5708

Accepted manuscript

ResearchGate

See discussions, stats, and author profiles for this publication at: https://www.researchgate.net/publication/319617865

Sportsmen's energy package Cordyceps sinensis: Medicinal importance and responsible phytochemical constituents

Article · March 2017

CITATIONS
0

READS
2

6 authors, including:

Mukesh C Joshi
University of Delhi (India), University of Cape Town (South Africa).
17 PUBLICATIONS **228** CITATIONS

SEE PROFILE

Some of the authors of this publication are also working on these related projects:

UGC-MHRD View project

All content following this page was uploaded by Mukesh C Joshi on 10 September 2017.

The user has requested enhancement of the downloaded file.

American Journal of Essential Oils and Natural Products

Available online at www.essencejournal.com

AJEONP American Journal of Essential Oils and Natural Products

AkiNik

ISSN: 2321-9114
AJEONP 2017; 5(2): 37-51
© 2017 AkiNik Publications
Received: 28-02-2017
Accepted: 30-03-2017

Yogesh Chandra Joshi
Research Scholar, Department of Physical Education & Sports Science, Swarnim Gujrat Sports University, Gujrat, India

Mukesh Chandra Joshi
Department of Chemistry, Motilal Nehru College, University of Delhi, Delhi, India

Vivek Chopra
Department of Biotechnology, Delhi Technological University Delhi, Delhi, India

Rakesh Kumar Joshi
Department of Education, Government of Uttrakhand, India

Rajni Kant Sharma
Department of Chemistry, Global Research Institute of Managment and Technology, Kurukshetra University, Haryana, India

Vikrant Kumar
Department of Chemistry, Acharya Narendra Dev College, University of Delhi, Delhi, India

Correspondence
Vikrant Kumar
Department of Chemistry, Acharya Narendra Dev College, University of Delhi, Delhi, India

Sportsmen's energy package *Cordyceps sinensis*: Medicinal importance and responsible phytochemical constituents

Yogesh Chandra Joshi, Mukesh Chandra Joshi, Vivek Chopra, Rakesh Kumar Joshi, Rajni Kant Sharma and Vikrant Kumar

Abstract
Yarsagumba (*Cordyceps sinensis*) is one of the world rarest fungal species that parasites on the body of a caterpillar of a moth and found underground of alpine grass at high altitude. The *Cordyceps sinensis* is known as "summer plant and winter insect" or "*half*-caterpillar-*half*-mushroom". This fungus used for various medicinal purposes, caring diseases and specially used as a food product in China and south Asian countries. It contains various biologically active pharmacophores which helps to maintain the health and body. Reports say that, the regular use of *Cordyceps*, is very useful for sportsperson to maintain their body balance, endurance, strength, and to make healthy body weight etc. On the basis of scientific and manmade facts, we tried to summarise, why *Cordyceps* is recommended to sport person as a physical booster. It contains various bioactive pharmacophores including essential oil, which are medicinally important. Thus body always looks for such type of dietary supplements.

Keywords: Yarssgumba, *Cordyceps*, Physical endurance, Physical booster, Stamina, Phytochemical constituents

1. Introduction
Yarsagumba is one of the world rarest fungal species that parasitizes the body of a caterpillar of a moth [1]. This herb is found underground of alpine grass at high altitude (3000-5000 m) between the Himalayas of Indian, Chinese, Nepal, Bhutan and Tibetan Plateau. It is also named as Caterpillar fungus known as *Cordyceps sinensis* which is hosted by Thitarodes insect during its asexual cycle. Recent study proposed that the botanical name of Yarsagumba changed from *Cordyceps sinensis* to *Ophiocordyceps sinensis* [2]. The latin name *Cordyceps sinensis* means "summer plant and winter insect" so called the mysterious "*half*-caterpillar-*half*-mushroom". Before the rainy season begins, spores of the *Cordyceps* mushroom settled on the heads of caterpillars that lives underground. The fungus gets so much into the body of the caterpillars that it grows out through its head and drains all the energy from the insect and ultimately it dies (Fig. 1, *www.youtube.com/ channel/ UCIl7KZhkaWBsVCEFKUMGDOg*). The fungus takes 5-7 years for complete its life cycle. It is dark brown fructification and yellowish white stalk having small spikes. The size of the fungus is about 4 to 12 cm in length and 0.14 to 0.4 cm in girth. *Cordyceps* is known by different names Yarsagumba, Buti, Jivanbuti, caterpillar mushroom and *Cordyceps* while in China it is known as Dong Chong Xia Cao and in Tibet it is known as winter (yarsa) and summer (gumba) grass. It is also called Keera Jhar (insect herb) by the local Nepalese.
It has been used since ancient in China as a traditional medicine and in south Asian content for more than 3000 years [3]. Caterpillar fungus specially been used for its medicinal importance [4-12]. It is also used as food product in China and south Asian countries. It has traditionally been used for backache, blood production, impotence, to increase sperm production, chronic cough, asthma, improve shortness of breath anemia, improves blood circulation and regulates blood pressure, production of bone marrow, to remove tiredness, soreness of loins and knees, dizziness, tinnitus, to strengthen the immune system of tumor patients who have received radiotherapy, chemotherapy, anticancerous [4, 11, 12], in the treatment of deficiency syndrome caused by overstrain, to strengthen the immune system by attacking on virus and bacteria, anti-allergic, reduce triglycerides and cholesterol level, increases vitality and stamina, enhancing physical endurance and mental stability, controls liver, lung and kidney dysfunction, reduces

pains of loins and knees [13-17]. It is also used as traditional healer such as erectile dysfunction, malignant tumors, diabetes, female aphrodisia, bronchitis, asthma, cough and cold, jaundice, alcoholic hepatitis, anti-tussive and expectorant effects etc. It is also used as a natural Viagra or also known as Himalayan Herbal Viagra.

Cordycep contains several biologically active pharmacophores such as sterols, alkaloids, polysaccharides, nucleosides, amino acids, inorganic elements, vitamins, fatty acids and other ketone, aldehydes, ether, and phenols etc. Thus human body always look for such type of dietary supplements which contains all the material in it. Thus, we can say *Cordyceps* must be responsible for its mode of action against human health hazards.

Fig 1: Caterpillar fungus

Scientific classification

Kingdom	:	Fungi
Subkingdom	:	Dikarya
Phylum	:	Ascomycota
Subphylum	:	Pezizomycotina
Class	:	Sordariomycetes
Subclass	:	Hypocreomycetidae
Order	:	Hypocreales
Family	:	Clavicipitaceae
Genus	:	*Cordyceps* Species

Spp. about 300 described species [18] some common are as follows:

C. bassiana (Bals.-Criv.)
C. gunnii
C. militaris
C. ophioglossoides
C. sinensis
C. subsessilis (Petch)
C. unilateralis

2. Habitat, Ecology and Economy

Cordyceps is generally found in the alpine region of the Himalayas at the elevation >3000 m. *Cordyceps* mostly found above the snowline in Jumla, Dolpa, Kalikot, Baglung, Mustang, Humla, Rasuwa and Manang districts of Nepal and Ganzi, Lithang and high Himalayas of India, Tibet and Bhutan [19]. The suitable conditions are high altitude, low oxygen level and low temperature for *Cordyceps* cultivation.

Most of Alpine rural population economically based on this cultivation in Nepal and Tibet. It has a very high trade value that is transacted at more than twice the cost of gold by weight. For last couple of years, the trade of Yarsagumba is increasing and it has been regarded as an expensive life saving tonic. Yarsagumba is a remedy for headache, toothache or any many other diseases. Thousands of villagers particularly from Nepal and Tibet are risking their own lives to collect Yarsagumba from high mountains during May and August for making money.

3. *Cordyceps* as a physical booster for sportsman

Cordyceps has been used to support good balance, strength, and a healthy body weight. It is also used widely and traditionally to increase the energy and enhance stamina in the human body. It has a positive effect on blood sugar and fat metabolism, which is important to boost the health, because fats and sugars are actively mobilized during activation of the stress response to supply the body with extra energy. Furthermore, the cell-protective and antioxidant activities of *Cordyceps* have been documented [6]. Traditional Chinese medicine practitioners also recommend the regular use of *Cordyceps* to strengthen the body [6, 20, 21].

Daily dietary supplements are the best known to reducing the risk of disease, to maintain good health and to improve homeostasis. Thus research for complete package energy food is high in demands, which can be effective, nontoxic, antioxidant and ergogenic properties has gained attention. During the training of sportsperson, the individual is looking for large amount of physical and psychic energy. During this time numerous energetic and other substances are consumed by the sportsperson to retain their physical energy and strength [22-26]. Thus the individuals are looking for the complete package of energy and we know that giving individuals a complete package of energy substances through food is not possible therefore; nutrition specialists are facing lot of problems regarding this. For strengthened the body it has been scientifically proved that various food supplements are helpful in solving this problem [27], and one of them is *Cordyceps*, which is gaining a lot of attention as a food supplement or a complete energy package for sportsmen's nutrition.

In 1993 World Championships in Athletics, the manager of a group of dominant Chinese female distance runners, announced that his athletes had been fed a soup of Yarsagumba and turtle blood. Daniel Winkler, an ecologist has done extensive research on this fungus, and explains in one of his articles that, "Among the wealthy and power in China," Yarsagumba, "has come to rival French champagne as a status symbol at dinner parties or as a prestigious gift." Researchers are working to raise the adaptive reserves of sportsmen functional system to ensure the positive result in the training outcome. Therefore, the important part is to investigations of the effects of *Cordyceps* (a food supplement used by sportsmen), on their blood haematological and biochemical indices of the individual sportsperson. Thus, it has been concluded that the effect of *Cordyceps* may contribute to improving the course of adaptation of elite sportsmen to physical loads, increasing the physical and functional capacity of their body, results in better sport results. Researchers studied the effect of *Cordyceps* in 28 sportsmen aged between 22–25 years. Members of the experimental group were administered *Codyceps* in capsules, each containing 500 mg of dry fermented powder of the *Cordyceps sinensis*. *Cordyceps* was administered for 14 days (according to the following scheme: one capsule with breakfast and one with lunch for 4 days, one capsule three

times a day for 6 days, and one capsule four times a day for 4 days) which shows that no significant change in red blood corpuscles, mean red corpuscle volume, red corpuscle distribution area, mean corpuscular haemoglobin and its concentration in the blood and also there is no positive effect of *Cordyceps* on haemopoiesis. However during this, the positive changes in number of leukocyte and leukocyte formula were observed. The number of lymphocytes increased, and the percentage ratio between granulocytes and agranulocytes was levelled in the leucogram. Creatinine concentration, which statistically significantly increased over the experimental period on the background of lowered creatinekinase, uric acid and urea levels in the blood of the studied individuals, indicates the ergogenic effect of *Cordyceps* on the energetic system, physical and functional performance of the sportsmen's body [28]. Related study has been done by Meena *et al*. [29] in rat and observed that no significant change in organ weight and serological parameters, however, there was a significant increase in food intake, body weight gain and haematological parameters such as RBC, WBC, Hb and lymphocytes in treated group.

The traditional uses of *Cordyceps* in Sikkim, India, found that most of local folk healers/traditional healers use *Cordyceps* for the treatment of 21 ailments. One research group from China have reported that *Cordyceps* helps in lactate clearance and improved lactate energy metabolism within the cell of mice and allowing athletes greater anaerobic physical performance [30]. There are few other reports have been published regarding the curative effect of *Cordyceps* involving various experimental model and some clinical trials in volunteer athletes [31]. Clinical research has shown that *Cordyceps* increased cellular bio-energy ATP [32] by increase in useful energy and improves internal mechanism, which results more and more efficient utilization of oxygen [33].

Rossi et. al. reported that a specific combination of fungal supplements can help to improve the performance of endurance in athletes. They studied the effects of a brief 3-month trial of two fungal supplements, *Ganoderma lucidum* and *Cordyceps sinensis* (3 capsules of *C. sinensis* and 2 capsules of *G. lucidum* per day), in ages between 30-40 years old, 7 healthy male volunteers, amateur cyclists participated in "Gran Fondo" cycling races. They reported the effects of fungal supplements on physical fitness of the athletes by monitoring and comparing the testosterone/cortisol ratio in the saliva and oxidative stress [DPPH (1, 1'-diphenyl-2-picrylhydrazyl) free radical scavenging activity] just before and after the physical activity [34, 35]. They observed a decrease of more than 30% in the testosterone/cortisol ratio after race compared to before race was considered as a risk factor for nonfunctional overreaching (NFO) or the overtraining syndrome (OTS). The results show that, after 3 months of supplementation, the testosterone/cortisol ratio changed in a statistically significant manner, thereby protecting the athletes from NFO and OTS. Antioxidant activity was also measured by quantifying the scavenging ability of the human serum on the synthetic free radical DPPH. After 3 months of fungal supplementation, the data demonstrate an increased scavenger capacity of free radicals in the athletes' serum after the race, thereby protecting the athletes from oxidative stress [36]. It also helps to reduce the lactic acid accumulation in the muscles. The reduction of lactic acid is the reason of reduction in exhaustion and stress, and thus improves physical performance and increases the stamina. By using swimming test the similar results were found in a rat study [37, 38].

Now, researchers believe that *Cordyceps* is the best known multimedicine or complete energy package (dietary supplements) or booster for increasing physical stamina. Thus, consumption of *Cordyceps* by human led individual to great physical enhancement, extra endurance and the anti-fatigue ability [39-41].

4. *Cordyceps* medicinal importance and phytochemical constituents

Cordyceps has various biological effects on the human organ systems viz., on the, central nervous system (sedative, anticonvulsant and cooling effects), respiratory system (relaxant role in the bronchi, it increases adrenaline secretion from the adrenal glands and important role in tracheal contraction caused by histamine, antitussive, expectorant and anti-asthmatic action and prevents pulmonary emphysema), endocrine system (it can increase plasma corticosterone levels thus affects male hormone), nourishing the kidney, renal, hyposexuality and hyperlipidemia etc. [42]. It also has been used as an antitumor and haemostatic, mycolytic, antiashmatic, and expectorant etc., few pharmacophore such as cordycepin and polysaccharides are mostly detected as cytotoxic, antibiotic, antitumor, antioxidation and boosting the immune system etc. [43-48].

Cordyceps contains multicomponent biologically active pharmacophores such as sterols [39] fatty acids, inorganic metals [49], polysaccharides, phenols, almost all the essential amino acids, few aliphatic and aromatic ketones, aldehydes, and essential oil etc. Biologically active pharmacophores are discussed one by one as follows:

4.1 Sterols

Sterols are one of the major constituent extracted from *Cordyceps*. The glycosylated form of ergosterol peroxide was found to be a greater inhibitor to the proliferation of K562, Jurkat, WM-1341, HL-60, and RPMI-8226 tumor cell lines [39, 43-48, 50-54]. Examples are, ergosterol (1), ergosteryl-3-*O*-*β*-D-glucopyranoside (2), ergosterol peroxide (3), *5α,*8*α*-epidioxy-24(*R*)-methylcholesta-6,22-dien-3*β*-D-glucopyranoside (4), 5*α*-ergosta-7,22-diene-3*β*,5*β*,6*β*-triol (cerevisterol) (5), ergosta-4,6,8(14),22-tetraen-3-one (6, ergone), 4,4-dimethyl-5*α*-ergosta-8,24(28)-dien-3*β*-ol (7), 3-*o*-ferulylcycloartenol (8), 5*α*,6*α*-epoxy-24(*R*)-methylcholesta-7,22-dien-3*β*-ol (9), 3*β*,15*β*-dihydroxy-(22*E*,24*R*)-ergosta-5,8(14),22-trien-7-one [H1-A] (10), 22, 23-dihydroergosteryl-3-*O*-*β*-D-glucopyranoside (11), *β*-sitosterol (12), *β*-sitosterol-3-*O*-acetate (13), daucosterol (14), stigmasterol (15), stigmasterol 3-*O*-acetate (16), cholesterol (17), campesterol (18), dihydrobrassicasterol [D5-ergosterol] (19); fungisterol [D7-ergosterol] (20), and (17*R*)-17-methylincisterol (21).

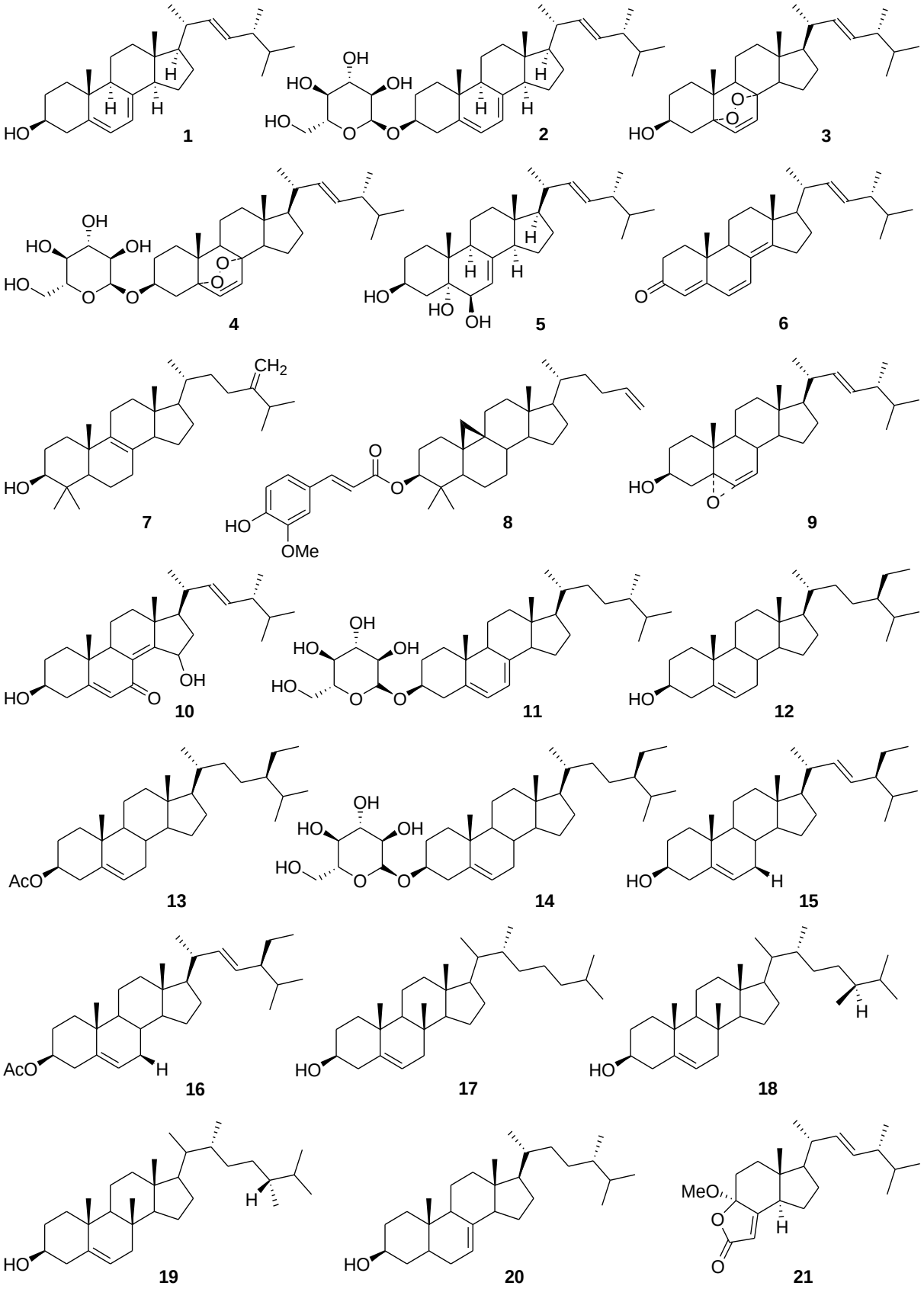

Ergosterol (1) and its derivatives have diverse medicinal value including cytotoxicity and antimicrobial activity [50, 52-54]. Ergosterol (1) is well known as diuretic bioactive compound with excellent efficacy [13]. Ergosterol derivative (2) have significant inhibition of superoxide anion generation and elastase release with IC_{50} values of 5.42 ± 0.50 and 5.62 ± 0.37 μM, respectively [53] and ergosterol peroxide (4) act as a greater inhibitor to the proliferation of K562, Jurkat, WM-1341, HL-60 and RPMI-8226 tumor cell lines and could be a potential anticancer property [43]. Sterol (5) improved kidney function in renal diseases, including IgA nephritis, autoimmune nephritis, and lupus nephritis by inhibiting IL-2 formation by monocyte and proliferation of mesangial cells and lymph node and also preventing and treating bronchial hyper responsiveness and acute asthma attack and improving pulmonary function. H1-A (10) can suppress the activated human mesangial cells HMC and alleviate IgAN (Berger's disease) with clinical and histological improvement [7].

4.2 Nitrogenous compounds

Another major constituent [55] extracted from *Cordyceps* are nitrogen containing compounds which includes nitrogenous bases, nucleosides and nucleosides etc. These are as follows:

Nitogenous base: Cytosine (22), uracil (23), thymine (24), adenine (25), guanine (26), hypoxanthine (27), 2-nicotinic acid (28), caffeine (29), cordysinin C (30), cordysinin D (31), and cordysinin E (32).

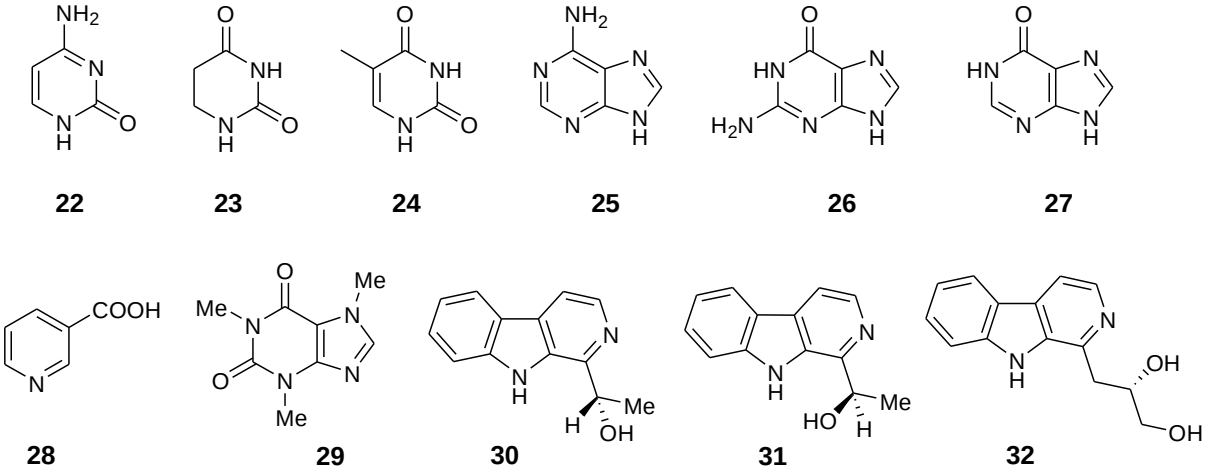

22 **23** **24** **25** **26** **27**

28 **29** **30** **31** **32**

Nucleosides [55]**:** Adenosine (33), cordycepin (34), guanosine (35), dideoxyadenosine (36), N6-(2-hydroxyethyl) adenosine (37), inosine (38), thymidine (39), uridine (40), dideoxyuridine (41), and cordysinin B (42). All nitrogenous bases and nucleosides can play a major role in the biological system. Adenosine (33) has anticonvulsant activity, inhibits cancer cell growth, anti-inflammatory and other effect [5, 9, 10, 16, 56-58, 60-62]. Cordycepin (34) has been well characterized [57, 58] and can have a role in DNA repair mechanism for antitumor response [31] and inhibit the phosphorylation of Akt and p38 in dose-dependent manners in LPS-activated macrophage. It also helps to decrease the expressions of cycloxygenase-2 (COX-2) and inducible nitric oxide synthase (*i*NOS) in RAW 264.7 cell and has good effect on diabetic osteopenia in diabetic rats [63]. The significant effect of Cordycepin (Cordymin) on diabetic osteopenia might be directly through weakening of ALP and TRAP activity and mediate through recovery of β-cells and lowering the concentration of serum glucose, which subsequently triggered a lower extent of oxidative stress in diabetic rats. Other uses of Cordycepin as an antitumor, antibacteria, antivirus, antinsecticidal, anti-inflammatory, analgesic effect, and can stimulates steroidogenesis and enhances immunity [64-67].

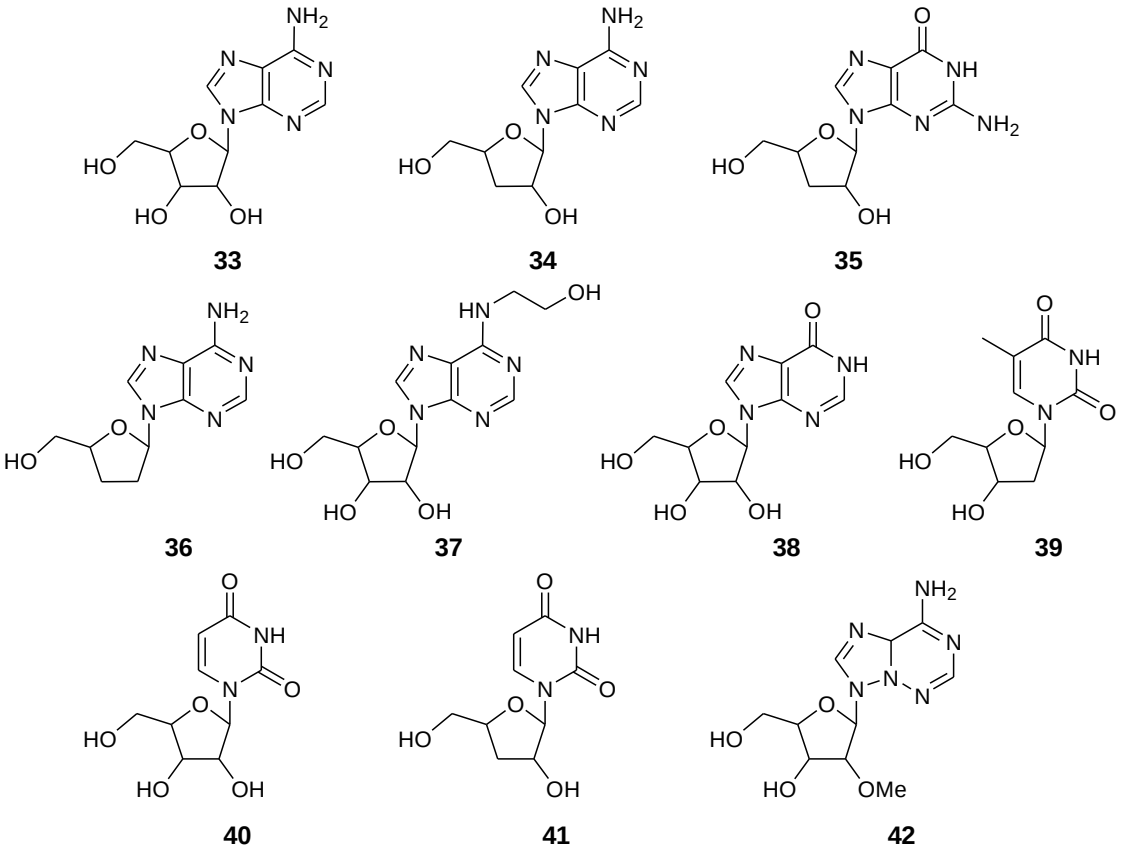

33 **34** **35**

36 **37** **38** **39**

40 **41** **42**

4.3. Proteins and amino acids and polypeptides

Cordyceps contains many amino acids (43-62) and polypeptides, which played an important role in clinical trials. *Cordyceps* contain crude protein which is made up of 18 amino acids such as aspartic acid, threonine, serine, glutamate, proline, glycine, valine, methionine, isoleucine, leucine, tyrosine, phenylalanine, lysine, histidine, cystine, cysteine and tryptophan and among these glutamate, arginine and aspartic acid have highest content.

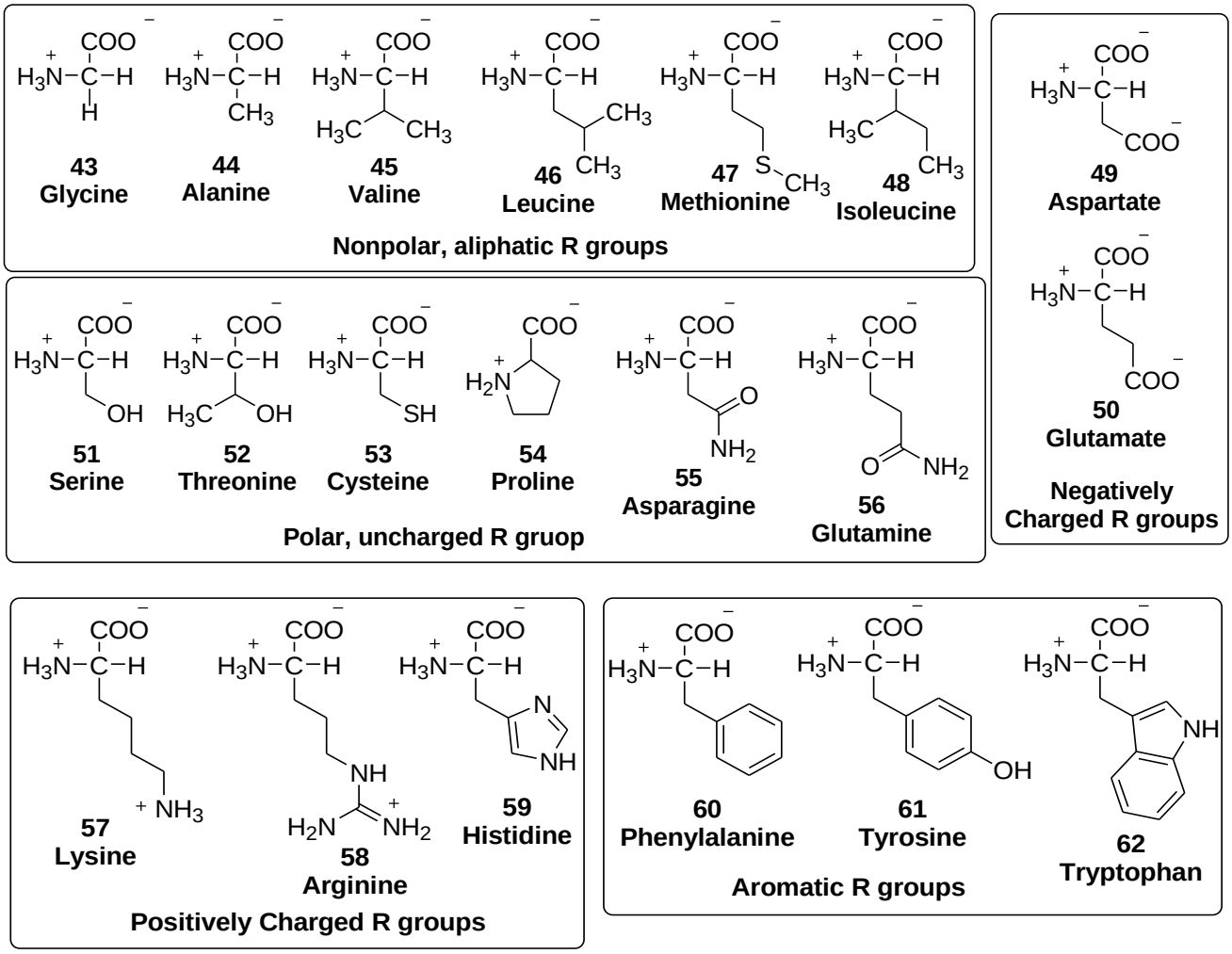

Peptides [53, 58]**:** Aurantiamide acetate (63), cordyceamides A (64), cordyceamides B (65), cordysinin A (66), cordycedipeptide A (3-acetamino-6-isobutyl-2,5-dioxopiperazine) (67), 3-isopropyl-6-isobutyl-2,5-dioxopiperazine (68), 3,6-di(4-hydroxy)benzyl-2,5-dioxo-piperazine (69), cyclo-(Gly-Pro) (70), cyclo-(Val-Pro) (71), cyclo-(Leu-Pro) (72), cyclo-(L-Pro-L-Val) (73), cyclo-(L-Phe-L-Pro) (74), cyclo-(L-Pro-L-Tyr) (75), cyclo-(Ala-Leu) (76), cyclo-(Ala-Val) (77), cyclo-(Thr-Leu) (78), and myriocin (79). cordyceamides A (64) and B (65) as well as cordycedipeptide A (67) act as cytotoxic against L-929, A375 and Hela cell lines. Cordycedipeptide A (67) showed significant IC_{50} value of 6.30 mg/mL (L-929), 9.16 mg/mL (A375). 64 showed better effect than 65 on L929 cell and A375 cell, but on Hela cell 65 showed better effect. Jia *et al*. [57] reported that Cordycedipeptide A (68) the cytotoxic activities of the constituent to L-929, A375, and Hela and its better effect on several tumor cell lines. Peptide 75 reported as good antifungal [68] as well as antimicrobial property [69]. Myriocin (79, antibiotic ISP1 or thermozymocidin) is a typical amino acid which is responsible for inhibit the upregulated expression of cyclin D1 induced by high concentrations of glucose, restoring the expression of cyclin D1 [70]. Some macromolecule polypeptides isolated from *C. sinensis* could be used for the treatment of hypertension.

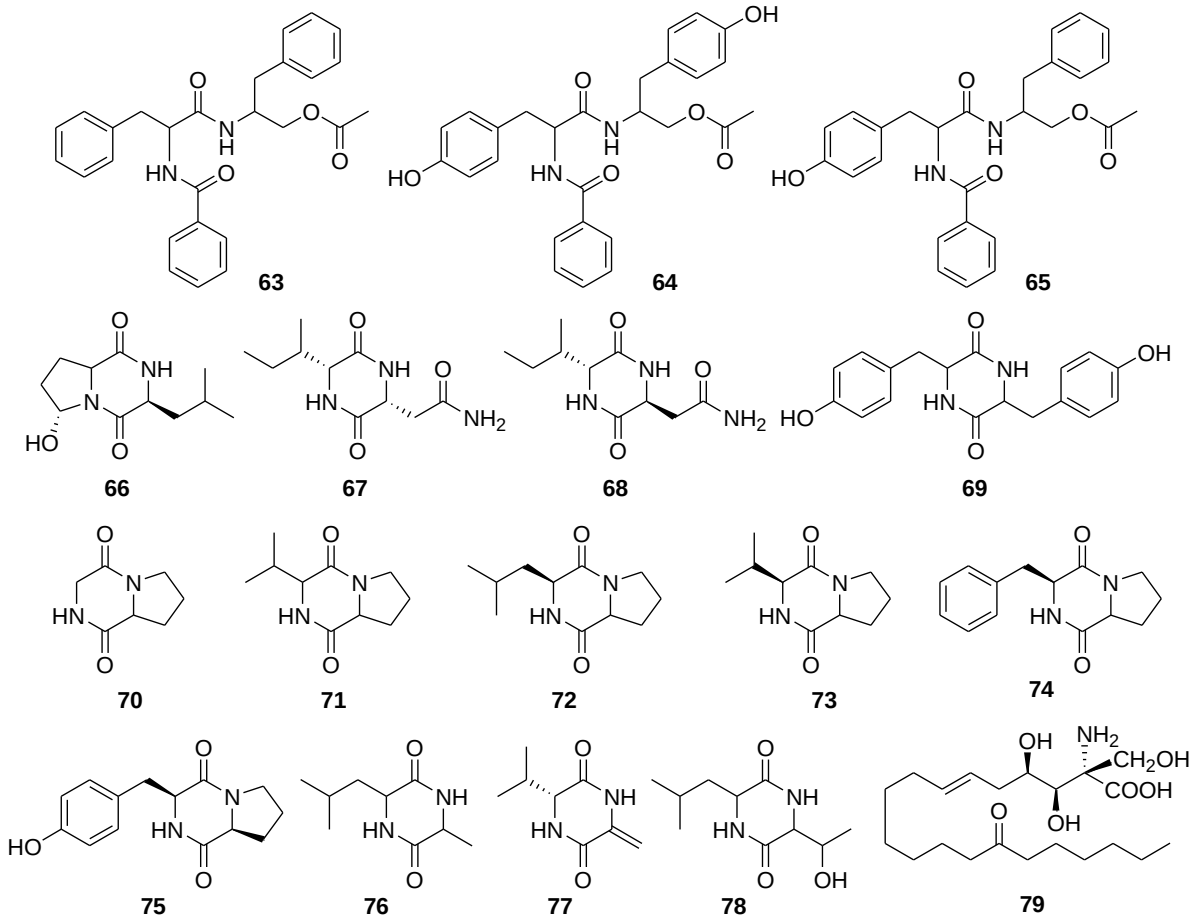

They significantly reduce the mean arterial pressure of rats and induce a direct endothelium dependent vasorelaxant effect by stimulating the production of nitric oxide and endothelium-derived hyperpolarizing factor [71].

Amines and polyamines [20, 53]**:** 1,3-Diamino propane (80), spermidine (81), spermine (82), putrescine (83), cadaverine (84), *N*-(2'-hydroxy-tetracosanoyl)-2-amino-1,3,4-trihydroxy-octadec-8*E*-ene(tetracosanamide) (85), 1-acetyl-a-carboline (86), perlolyrine (87), flazin (88) and including all nitrogenous compounds.

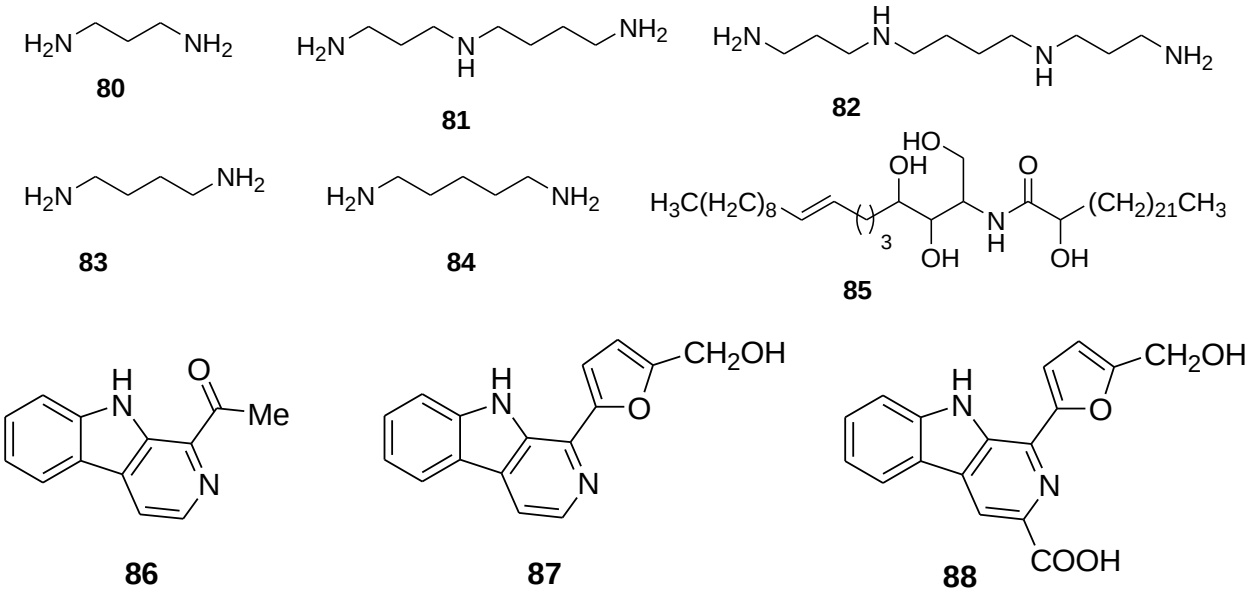

4.4 Fatty acids and other organic acids

Unsaturated fatty acids are the components [53, 72] which playing a major role in cells or in living host. These have a unique function of decreasing blood lipids and protecting against cardiovascular disease.

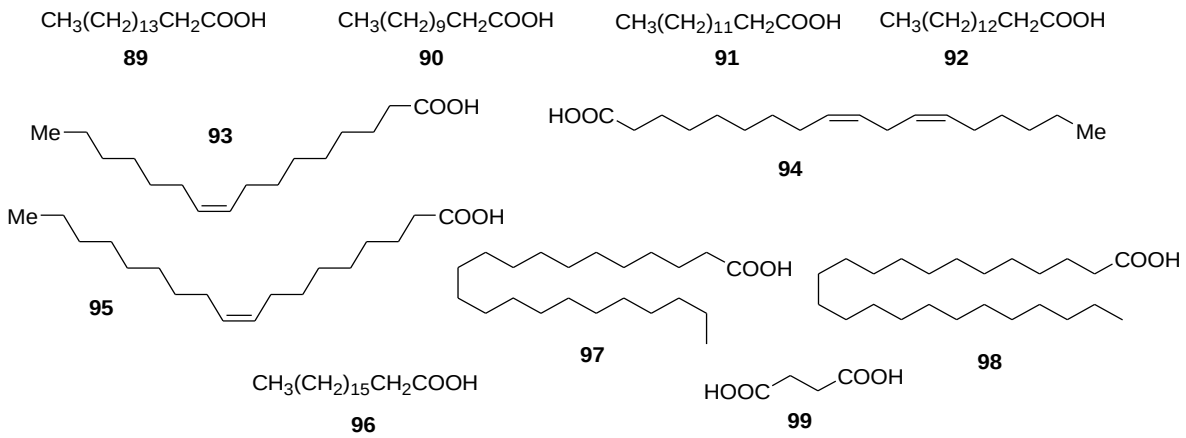

The content of unsaturated fatty acid is higher than that of saturated fatty acid in commercial preparations of *Cordyceps*. Examples are Palmitic acid (89), lauric acid (90), myristic acid (91), pentadecanoic acid (92), palmitoleic acid (93), linoleic acid (94), oleic acid (95), stearic acid (96), docosanoic acid (97, behenic acid), lignoceric acid (98, tetracosanoic acid), and succinic acid (99).

4.5 Phenolics and acids [53]

p-Hydroxybenzoic acid (100), vanillic acid (101), syringic acid (102), *p*-methoxybenzoic acid (103), *p*-hydroxyphenylacetic acid (104), 3,4-dihydroxyacetophenone (105), 4 hydroxyacetophenone (106), protocatechuic acid (107), 3, *p*-methoxyphenol (108), acetovanillone (109), salicylic acid (110), 3-hydroxy-2-methyl-4-pyrone (111), methyl *p*-hydroxyphenylacetate (112), 2-deoxy-D-ribono-1,4-lactone (113), and furancarboxylic acid (114).

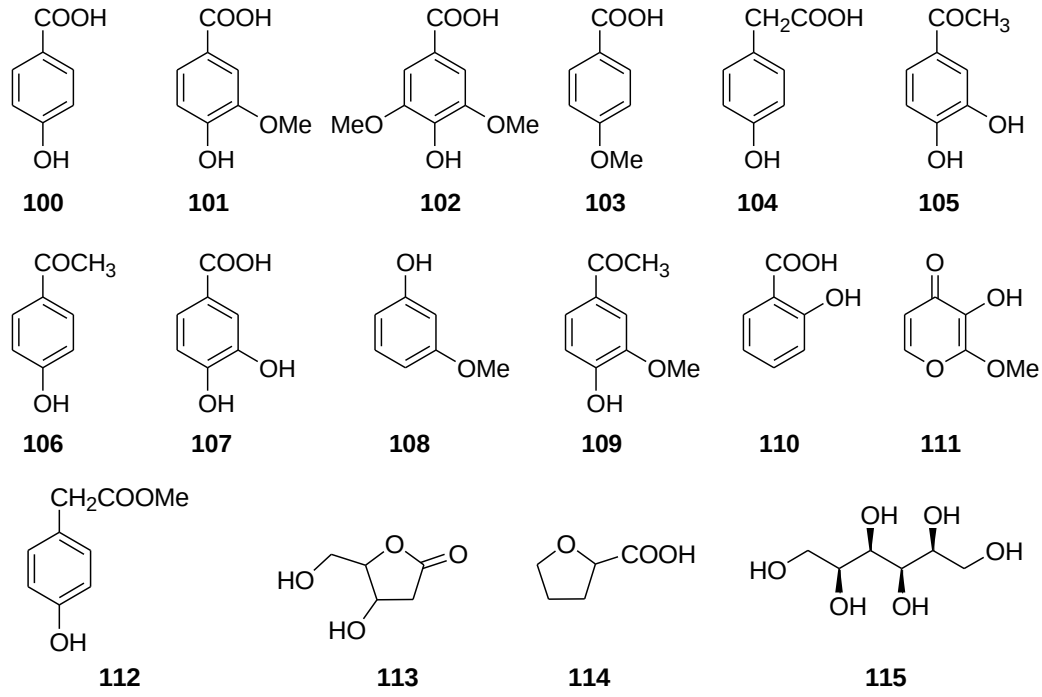

4.6 Isoflavones [53]

3,4,7-Trihydroxyisoflavone (116), glycitein (117), daidzein (118), orobol (119), and genistein (120). Compound 116 displayed significant scavenging of DPPH free radicals with IC_{50} values of 31.97 μM.

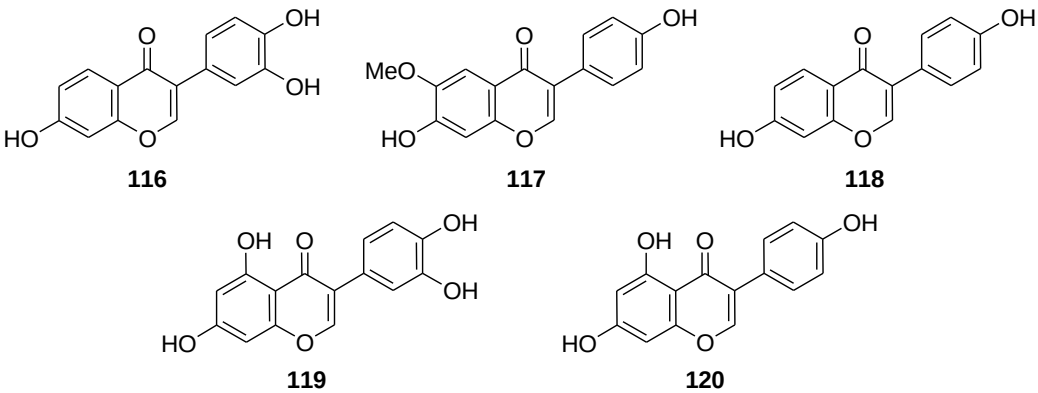

4.7 Sugar derivatives and polysaccharide [73-81]

Polysaccharides (PS) are the major bioactive constituents of *Cordyceps* which have proven anticancer and immunomodulation activities [83] and other notable health effects such as anti-oxidation etc. [76] Some glucose and polysaccharide derivatives were isolated from *Cordyceps* are D-mannitol (121), cordycepic acid (122), CS-F30 [Gal:Glc:Man = 62:28:10] (123), CS-F10 [Gal:Glc:Man = 43:33:24] (124), CT-4N [Man:Gal =3:5] (125), CS-81002 [Man:Gal:Glc = 10.3:3.6:6.1] (126), SCP-I [D-glucan] (127), CSP-1 [Glc:Man:Gal = 1:0.6:0.75] (128), CPS1 [Glc:Man:Gal = 2.8:2.9:1] (129), CPS2 (130), Cordysinocan [Glc:Man:Gal = 2.4:2.1] (131), PS-A [Glc:Gal:Man = 2:1:1] (132), CS-PS [Man:Rhm:Ara:Xyl:Glc:Gal = 38.37:2.51:2.21:5.22:27.44:24.45] (133), mannoglucan [Man:Glc = 1:9] (134).

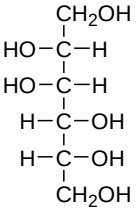

121

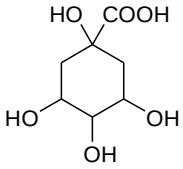

122

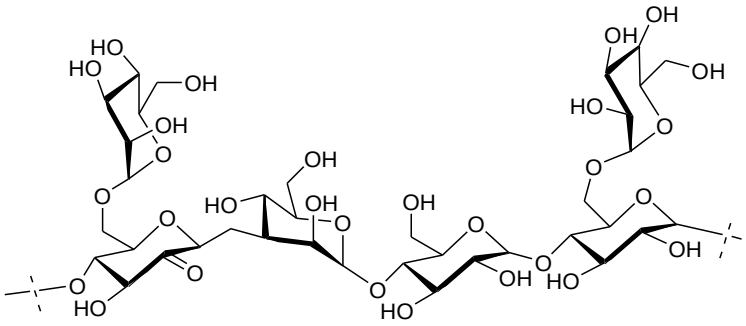

130, Predicted structure of CPS-2 isolated from the fruiting bodies of cultured *C. sinensis*

In *Cordyceps*, polysaccharides are well explored as a medicinally important pharmacophore [80, 82], such as D-Mannitol and Cordycepic acid. These polysaccharides are well explored as an effective in regulating blood sugar [73], antimetastatic, immunomodulating, antitumor effects [43, 77], antioxidants [45, 75], hypoglycmic [73, 74], antiinfluenza and hypo-cholesterolemic effects. Cordycepic acid is another very important medicinal components and used with variety of medicines [31, 81] and can be used in treating liver fibrosis diuretic, improving the plasma osmotic pressure, and anti-free radical [76].

Polygucans having high molecular weight tends to have greater water solubility and have more effective as an anti-tumour [79]. The crude exopolysaccharide (EPS) isolated from the mycelia liquid culture medium by ethanol precipitation contained 65–70% sugar and about 25% protein, suggesting that the EPS was composed of polysaccharide–protein complexes and showed moderate antioxidant activities with a Trolox equivalent antioxidant capacity of 35–40 μmol Trolox/g and a ferric reducing ability of plasma of 50–52 μmol Fe(II)/g. It also exhibited moderate radical scavenging and ferric reducing activities [84-90]. Shao, *et al*. first time reported that polysaccharide (glucose: mannose: galactose, 1:0.6:0.75) from *Cordyceps* can protects against the free radical-induced neuronal cell toxicity [72]. An acid polysaccharide (APS, 122) was isolated from cultivated *C. sinensis* mycelia contains mannose, glucose, and galactose in an approximate ratio of 1: 2: 1 [21]. APS possesses protective effects in $PC1_2$ cells against H_2O_2-induced injury [72]. Polysaccharide CS-F30 (123) increased the activities of hepatic glucokinase, hexokinase and glucose-6-phosphate dehydrogenase and decreased glycogen content in the liver [85] and CS-F10 (124) significantly increased the activity of hepatic glucokinase in streptozotocin (STZ)-induced diabetic mice leading to reduced hepatic glucose output [75]. CSP-1 (128) had strong antioxidant activities, which can be used to reduce the blood glucose level [6] and treat renal failure. CSP-1 (128) showed hypoglycemic properties which increased circulating insulin level in diabetic animals, due to stimulate pancreatic release of insulin and/or reduce insulin metabolism [6]. A water-soluble polysaccharide named CPS-1 (129) had been isolated from *C. sinensis* mycelium having composition of glucose, mannose, and galactose in approximate ratio of 2.8: 2.9: 1 and can be used as scavenge hydroxyl radicals and reduce power- and Fe^{2+} chelating. CPS-2 (130) contains mannose, glucose, and galactose in the approximate ratio of 4: 11: 1 [89]. Wang *et al*. found that 130 could reduce PDGF-BB-induced cell proliferation through the PDGF/ERK and TGFb1/Smad pathways [90] and fibrinolytic activity [88]. Cheung *et al.* reported that Cordysinocan (131) contains glucose, mannose and galactose in a ration approximate of 2.4: 2: 1 and used to induced the cell proliferation and the secretion of interleukin-2, interleukin-6 and interleukin-8 in cultured T-lymphocytes and triggering the immune responses [84]. The heteropolysaccharide PSA (132) composed of D-glucose, D-galactose, and D-mannose in approximate ration of 2: 1: 1 possess strong inhibitory activity against cholesterol esterase and may be a potential agent to control hypercholesterolemia [87].

4.8 Inorganic Metals ion and elements [49, 91]

Alkali Metals: K^+, Na^+, Ca^{2+}, Mg^{2+}, and Al^{3+}.

Metals: Fe^{2+}, $Cu^{2+/+}$, Mn^{2+}, Zn^{2+}, Ni^{2+}, Sr^{2+}, Ti^{3+}, Cr^{2+}, and V^{3+}.

Non Metal: $P^{3+/5+}$, Se^{2+}, Si^{4+}, and Ga^{3+}.

4.9 Vitamins [49, 91]

Vitamin B1 (thyamine hydrochloride, 135), vitamin B2 (riboflavin, 136), vitamin B12 (137), vitamin E (tocopherols (140), tocotrienols (141)), vitamin K1 (phylloquinone, 138), and vitamin K2 (Group of menaquinone, 139).

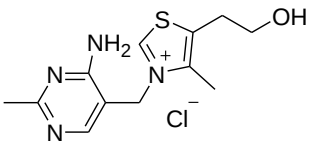

135

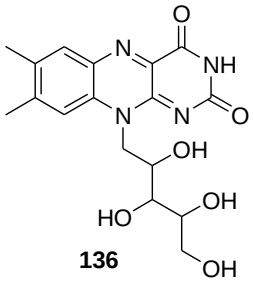

136

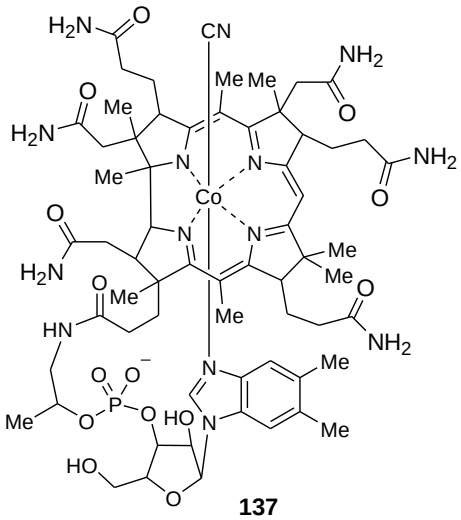

137

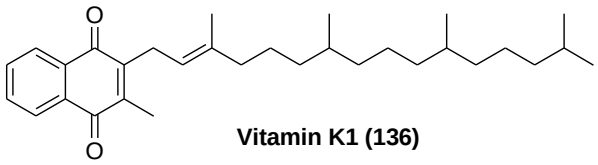

Vitamin K1 (136)

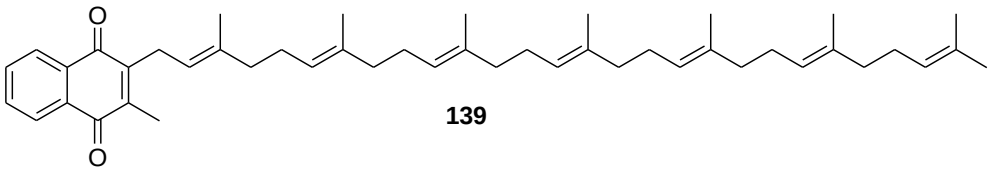

139

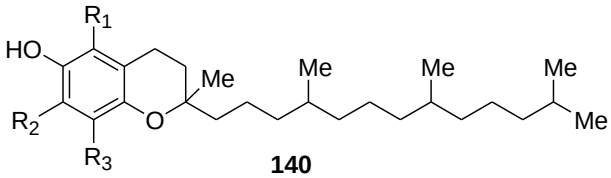

140

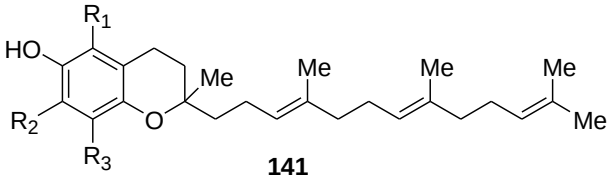

141

Forms of Vitamin E

α if, $R_1 = R_2 = R_3 = CH_3$

β if, $R_1 = R_3 = CH_3$, $R_2 = H$

γ if, $R_1 = H$, $R_2 = R_3 = CH_3$

δ if, $R_1 = R_2 = H$, $R_3 = CH_3$

4.10 Volatile compounds [49, 91]

Aldehydes: Benzaldehyde (142), benzeneacetaldehyde (143), 4-fluoro-3-hydroxy-benzaldehyde (144), (*E*)-2-nonenal (145), (*E*)-2-dodecenal (146), (*E*,*E*)-2,4-nonadienal (147), nonanal (148), and decanal (149).

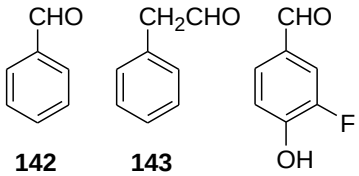

142 **143** **144**

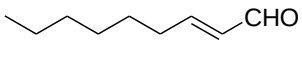

145

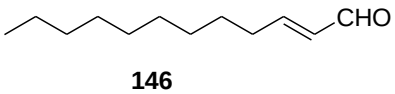

146

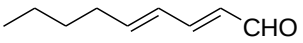

147

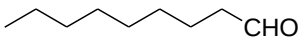

148

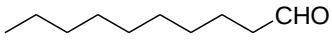

149

Alcohols and phenols: Phenylethyl alcohol (150), 2-(methylthio)-3-pyridinol (151), *p*-menth-4(E)-en-9-ol (152), 2-methyl-phenol (153), decahydro-2-naphthalenol (154), 2-butyl-2,7-octadien-1-ol (155), and 5-methyl-5-hexen-2-ol (156).

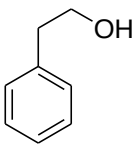

150

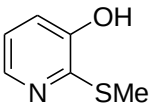

151

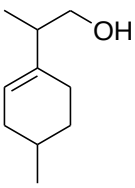

152

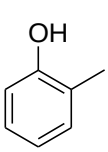

153

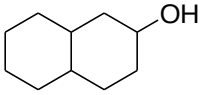

154

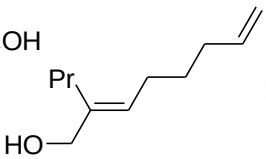

155

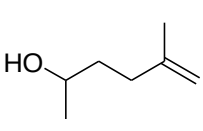

156

Ketones: 4-(2-Furanyl)-3-buten-2-one (157), 6-Ethenyldihydro-2,2, 6-trimethyl-2H-pyran-3(4H)-one (158), *trans*-3-Nonen-2-one (159), and 4-Butoxy-3-penten-2-one (160).

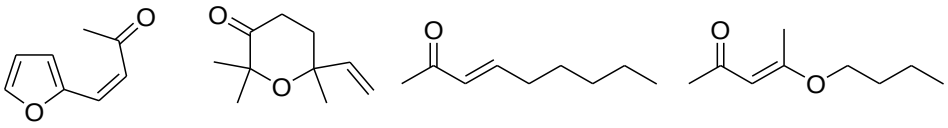

157 **158** **159** **160**

Esters: 1-Oxaspiro (4, 5)decan-2-one (161), (Z)-Dihydro-5-(2-octenyl)-2(3H)-furanone (162), 1,3-Cyclohexadiene-1,3-diol, 5,5-dimethyl-diacetate (163), 2-Butynedioic acid, di-2-propenyl ester (164), and Oxalic acid, isobutyl tetradecyl ester (165).

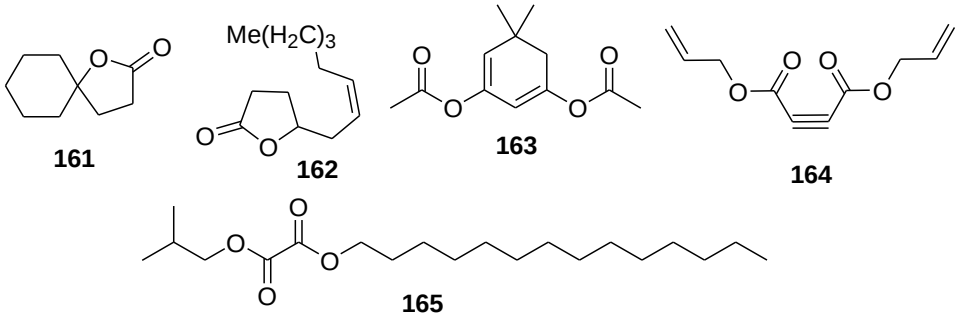

161 **162** **163** **164**

165

Aromatics: 2,6-Dimethylnaphthalene (166), 1,6-dimethyl-naphthalene (167), azulene (168), and 1-methylene-1H-indene (169).

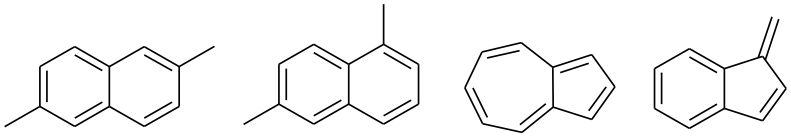

166 **167** **168** **169**

Alkanes: 2, 4-Diisopropyl-1,1-dimethyl-cyclohexane (170), 2-methyl-dodecane (171), 2,6,10,14-tetramethyl-hexadecane (172), 1,54-dibromo-tetrapentacontane (173), and 1-chloro-nonadecane (174).

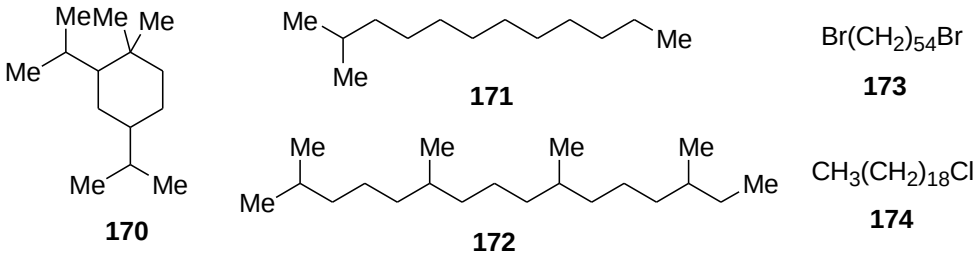

170 **171** **172** **173** **174**

Others: Indole (175), 1,2-benzisothiazole (176), 1,2-benzisothiazole, 3-(hexahydro-1H-azepin-1-yl)-1,1-dioxide (177), 2-pentyl-furan (178), 1-(chloromethyl)-3-methoxy-benzene (179), (E)-9-eicosene (180), ditert-dodecyl disulfide (181), phosphonic acid (182), 7-chloro-2,3-dihydro-3-(4-*N*,*N*-dimethylaminobenzylidene)-5-phenyl-1H-1,4-benzodiazepin 2-one (183), and 1,5-dihydro-1-methyl-2H-pyrrol-2-one (184).

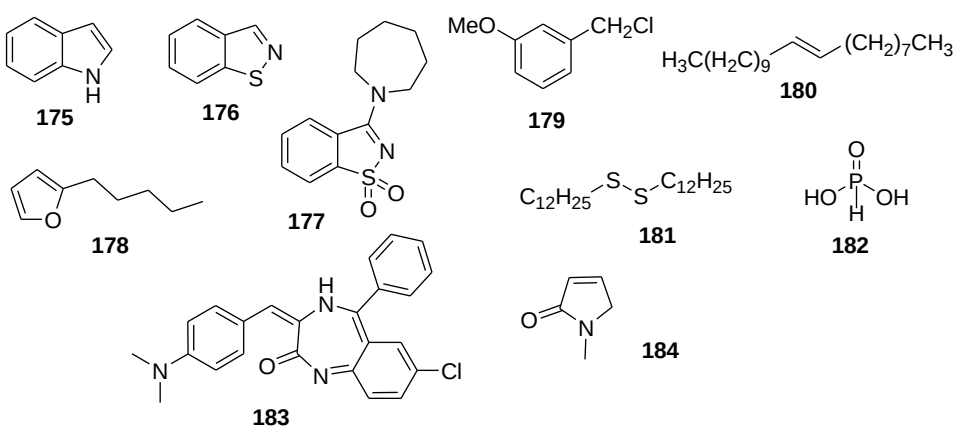

175 **176** **177** **178** **179** **180** **181** **182**

183 **184**

4.11 Essential oils

A number of essential oils has been identifies using gas chromatography (GC–MS). Verticiol (**185**) has been found in *C. sinensis* which indicates anti-tussive and expectorant effects of *C. sinensis* [92, 93].

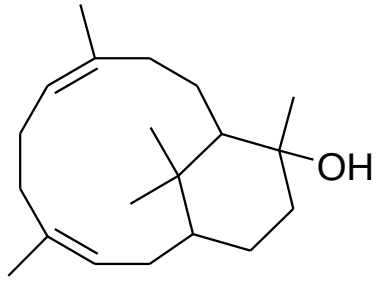

185

5. Conclusion

Yarsagumba is one of the world rarest fungal species known as "summer plant and winter insect" so called the mysterious "*half*-caterpillar-*half*-mushroom". This fungus specially used for food verbiage in China and south Asian countries, since ancient time and used as various medicinal purposes. Recent studies says that, Yarsagumba is a complete package or dietary supplements for sportsperson which results in increase body energy, stamina, endurance, strength, and caring body diseases. This is because the availability of variety of biologically active pharmacophores present in Yarsagumba. Thus, in this text we tried to summarize, the benefits of Yarsagumba specially for sportsperson due to biologically active pharmacophores present in Yarsagumba which are actually responsible for better efficacy of the body.

6. Acknowledgement

The authors would like to acknowledge DST Delhi, Swarnim Gujrat University, Delhi Technological University, and Delhi University of India for valuable literature support.

7. Conflicts of Interest

The authors have no conflicts of interest to declare.

8. References

1. Illana EC. *C. sinensis* - A fungi used in the Chinese traditional medicine. Revista Iberoamericana de Micologia, 2007; 24(4):259-262.
2. Sung GH, Hywel-Jones NL, Sung JM, Luangsa-ard JJ, Shrestha B, Spatafora JW. Phylogenetic classification of *Cordyceps* and the *Clavicipitaceous* fungi. Studies in Mycology, 2007; 57:5-59.
3. Committee of Pharmacopeia, Chinese Ministry of Health. The People's Medical, Beijing. 1964, Chinese pharmacopeia-I.
4. Chen J, Zhang W, Lu T, Li J, Zheng Y, Kong L. Morphological and genetic characterization of a cultivated *C. sinensis* fungus and its polysaccharide component possessing antioxidant property in H22 tumor-bearing mice. Life Sciences, 2006; 78:2742-2748.
5. Gessi S, Merighi S, Borea PA. Targeting adenosine receptors to prevent inflammatory skin diseases. Experimental Dermatology, 2014; 23(8):553-554.
6. Li SP, Zhang GH, Zeng Q, Huang ZG, Wang YT, Dong TT *et al*. Hypoglycemic activity of polysaccharide, with antioxidation, isolated from cultured *Cordyceps* mycelia. Phytomedicine, 2006; 13(6):428-433.
7. Lin CY, Lin CC, Chen CC, Kuo YC. The isolation of active fraction and active compound from *C. sinensis* can be used to improve bronchial hyper-responsiveness, Patent TW 582999 B 20040411, 2004.
8. Mei QB, Tao JY, Gao SB, Xu GC, Chen LM, Su JK. Antiarrhythmic effects of *C. sinensis* (Berk.) Sacc (in Chinese). China Journal of Chinese Materia Medica, 1989; 14(10):616-618.
9. Nakav S, Chaimovitz C, Sufaro Y, Lewis EC, Shaked G, Czeiger D *et al*. Anti-inflammatory preconditioning by agonists of adenosine A1 receptor. PLoS ONE, 2008; 3(5):e2107.
10. Tsai YJ, Lin LC, Tsai TH. Pharmacokinetics of adenosine and Cordycepin, a bioactive constituent of *C. sinensis* in rat. Journal of Agricultural and Food Chemistry, 2010; 58(8):4638-4643.
11. Wu JY, Zhang QX, Leung PH. Inhibitory effects of ethyl acetate extract of *C. sinensis* mycelium on various cancer cells in culture and B16 melanoma in C57BL/6 mice. Phytomedicine, 2007a; 14:43-49.
12. Yamaguchi N, Yoshida J, Ren LJ, Chen H, Miyazawa Y, Fujii Y *et al*. Augmentation of various immune reactivities of tumor-bearing hosts with extract of *C. sinensis*. Biotherapy, 1990; 2(3):199-205.
13. Lin CY. (24*R*)-Ergosta-7, 22-dien-3*β*,5*β*,6*β*-triol from *C. sinensis* for improving kidney function in renal diseases, Patent JP 2002053488 A 20020219, 2002.
14. Marchbank T, Ojobo E, Playford CJ, Playford RJ. Reparative properties of the traditional Chinese medicine *Cordyceps sinensis* (Chinese caterpillar mushroom) using HT29 cell culture and rat gastric damage models of injury. British Journal of Nutrition. 2011; 105(9):1303-1310.
15. Vestergaard P, Rejnmark L, Mosekilde L. Diabetes and its complications and their relationship with risk of fractures in type 1 & 2 diabetes. Calcified Tissue International, 2009; 84(1):45-55.
16. Yang D, Yaguchi T, Lim CR, Ishizawa Y, Nakano T, Nishizaki T. Tuning of apoptosis-mediator gene transcription in HepG2 human hepatoma cells through an adenosine signal. Cancer Letters, 2010; 291(2):225-229.
17. Tianzhu Z, Shihai Y, Juan D. Antidepressant-like effects of Cordycepin in a mice model of chronic unpredictable mild stress. Evidence-Based Complementary and Alternative Medicine, 2014; 2014:438-506.
18. Massee G. A revision of the genus *Cordyceps*. Annals of Botany, 1895; 9(1):1-44.
19. Chen SJ, Yin DH, Li L, Zha X, Shuen JH, Zhama C. Resources and distribution of *C. sinensis* in Naqu Tibet. Journal of Chinese medicinal materials, 2000; 23(11):673-675.
20. Holliday J, Cleaver M. Medicinal value of the caterpillar fungi species of the genus *Cordyceps* (Fr.) Link (Ascomycetes). International Journal of Medicinal Mushrooms, 2008; 10(3):219-234.
21. Shen WB, Song D, Wu JY, Zhang W. Protective effect of a polysaccharide isolated from a cultivated *Cordyceps* mycelia on hydrogen peroxide-induced oxidative damage in PC12 cells. Phytotherapy Research, 2011; 25(5):675-680.
22. Chen J, Lee S, Cao Y, Peng Y, Winkler D, Yang D. Ethnomycological use of medicinal Chinese caterpillar fungus, *O. sinensis* (Berk.) Sung GH, *et al*. (Ascomycetes) in Northern Yunnan Province, SW China.

International Journal of Medicinal Mushrooms, 2010; 12:427-434.
23. Hultman E, Greenhaff FP. Food stores and energy reserves. In: Shephard RJ, Astrand PO, eds. Endurance in Sport, New York, Blackwell Science Ltd, 1992, 127-135.
24. Milasius K, Peciukoniene M, Palaikiene Z. The use of biologically active substances for better adaptation of athletes to physical loads. Acta Medica Lituanica, 1996; 4:39-43.
25. Chen S, Li Z, Krochmal R, Abrazado M, Kim W, Cooper CB. Effect of Cs-4 (*Cordyceps sinensis*) on exercise performance in healthy older subjects: a double-blind, placebo-controlled trial. Journal of Alternative Complementary Medicine, 2010; 16(5):585-90.
26. Chen S, Li Z, Krochmal R, Abrazado M, Kim W, Cooper CB. Effect of Cs-4 (*Cordyceps sinensis*) on Exercise Performance in Healthy Older Subjects: A Double-Blind, Placebo-Controlled Trial. The Journal of Alternative and Complementary Medicine, 2010; 16(5):585-590.
27. Peciukoniene M, Stukas R, Kemeryte–Riaubiene E. Sportininkų mitybos ir energijos sunaudojimo ypatumai. Sporto mokslas, 2001; 1(23):69-74.
28. Milasius K, Dadeliene R, Peciukoniene M, Malickaite R. Effects of *Cordyceps* food supplement on the adaptation of physically active individuals to physical loads. Acta Medica Lituanica, 2007; 14(4):278-284.
29. Meena H, Singh KP, Negi PS, Ahmed Z. Sub-acute toxicity of cultured mycelia of Himalayan entomogenous fungus *C. sinensis* (Berk.) Sacc. in rats. Indian Journal of Experimental Biology. 2013; 51:381-387.
30. Wang ZX, Wang XM, Wang TZ. Current status of pharmacological studies on *Cordyceps sinensis* and *C. hyphae*. Chung-Kuo Chung His I Chieh Ho Tsa Chih, 1995; 15:255-256.
31. Zhu JS, Halpen GM, Jones K. The Scientific study of an ancient Chinese medicine: *C. sinensis*. Part 2: Journal of Alternative Complementary Medicine. 1998; 4:429-457.
32. Dai G, Bao T, Xu C, Cooper R, Zhu JS. CordyMax™ Cs-4 improves steady-state bioenergy status in mouse liver. Journal of Alternative Complementary Medicine, 2001; 7:231-240.
33. Zhu JS, James R. Presented at the American Physiological Society's (APS) annual scientific conference. Experiment Biology, in Washington, D.C, 2003-2004, 17-21.
34. Zou Y, Liu Y, Ruan M, Feng X, Wang J, Chu Z *et al*. *Cordyceps sinensis* oral liquid prolongs the lifespan of the fruit fly, *Drosophila melanogaster*, by inhibiting oxidative stressing. International Journal of Molecular Medicine. 2015; 36(4):939-946.
35. Ji DB, Ye J, Li CL, Wang YH, Zhao J, Cai SQ. Antiaging effect of *Cordyceps sinensis* extract. Phytotherapy Research. 2009; 23(1):116-22.
36. Rossi P, Buonocore D, Altobelli E, Brandalise F, Cesaroni V, Iozzi D *et al*. Improving training condition assessment in endurance cyclists: Effects of *G. lucidum* and *O. sinensis* dietary supplementation. Evidence Based Complementary Alternative Medicine, 2014; 97-96(13):1-11.
37. Kumar R, Negi PS, Singh B, Ilavazhagan G, Bhargava K, Sethy NK. Cordyceps sinensis promotes exercise endurance capacity of rats by activating skeletal muscle metabolic regulators. Journal of Ethnopharmacology. 2011; 136(1):260-266.
38. Koh JH, Kim KM, Kim JM, Song JC, Suh HJ. Antifatigue and antistress effect of the hot-water fraction from mycelia of *Cordyceps sinensis*. Biological and Pharmaceutical Bulletin, 2003; 26(5):691-4.
39. Zhu JS, Halpen GM, Jones K. The Scientific study of an ancient Chinese medicine: *C. sinensis*. Part 2: Journal of Alternative and Complementary Medicine, 1998; 4:429-457.
40. Dai G, Bao T, Xu C, Cooper R, Zhu JS. CordyMax Cs-4 improves steady-state bio-energy status in mouse liver. Journal of Alternative and Complementary Medicine, 2001; 7(3):231-240.
41. Manabe N, Azuma Y, Sugimoto M, Uchio K, Miyamoto M, Taketomo N *et al*. Effects of the mycelial extract of cultured *Cordyceps sinensis* on in *vivo* hepatic energy metabolism and blood flow in dietary hypoferric anaemic mice. British Journal of Nutrition. 2000; 83(2):197-204.
42. Zhang CK, Yuan SR. Recent advance in studies on immune pharmacological activities of *C. sinensis* and its submerge-cultured mycelia. Journal of Capital University of Medical Sciences, 1997; 18:37-38.
43. Bok JW, Lermer L, Chilton J, Klingeman HG, Towers GH. Antitumor sterols from the mycelia of *C sinesis*. Phytochemistry, 1999; 51:891-898.
44. Kunwar RM. Some threatened medicinal and aromatic plants: Status, trade and management practice in Dolpa, Midwestern, Nepal. Journal of Natural History Museum, 2002; 21:173-186.
45. Li SP, Li P, Dong TTX, Tsim KWK. Antioxidant activity of different types of natural *C. sinensis* and cultured *Cordyceps* mycelia. Phytomedicine, 2001; 8:207-212.
46. Liu C, Lu S, Ji MR. Affected of *C. sinensis* on *in vitro* natural killer cells. Chung-Kuo Chung His I Chieh Ho Tsa Chih, 1992; 12:267-269.
47. Wang SY, Shiao MS. Pharmacological functions of Chinese medicinal fungus *C. sinensis* and related species. Journal of Food and Drug Analysis, 2000; 8:248-257.
48. Wu JY, Zhang QX, Leung PO. Inhibitory effect of ethyl acetate extract of *C. sinensis* mycelium on various cancer cell growth. Phytomedicine, 2007; 10:53-58.
49. Zhu J, Wang ZG. Several metal tests in *C. sinensis* and its mycelium. Journal of Jining Medical College, 1993; 12:52-54.
50. Kitchawalit S, Kanokmedhakul K, Kanokmedhakul S, Soytong K. A new benzyl ester and Ergosterol derivatives from the fungus *G. Reessii*. Natural Product Research, 2014; 28(14):1045-1051.
51. Matsuda H, Akaki J, Nakamura S, Okazaki Y, Kojima H, Tamesada M *et al*. Apoptosis-inducing effects of sterols from the dried powder of cultured mycelium of *C. sinensis*. Chemical & Pharmaceutical Bulletin, 2009; 57(4):411-414.
52. Seitz LM. Ergosterol as a measure of fungal growth. Phytopathology, 1979; 69(11):1202-1206.
53. Yang ML, Kuo PC, Hwang TL, Wu TS. Anti-inflammatory principles from *C. sinensis*. Journal of Natural Product, 2011; 74:1996-2000.
54. Zheng J, Wang Y, Wang JF, Liu P, Li J, Zhu W. Antimicrobial Ergosteroids and Pyrrole derivatives from halotolerant *Aspergillus flocculosus* PT05-1 cultured in a hypersaline medium. Extremophiles, 2013; 17(6):963-971.
55. a) Liu Y, Xu F, Chen B, Zhang J, Yao S. CZE determination of nucleosides and nucleobases from natural *C. sinensis* and cultured *C. militaris*. Chinese Journal of Pharmaceutical Analysis, 2010; 30:24-29.
b) Xiao JH, Qi Y, Xiong Q. Nucleosides, a valuable

chemical marker for quality control in traditional Chinese medicine *Cordyceps*. Recent Patents Biotechnology, 2013; 7(2):153-166.
56. Coelho JE, Alves P, Canas PM, Valadas JS, Shmidt T, Batalha VL *et al*. Overexpression of adenosine A2A receptors in rats: effects on depression, locomotion, and anxiety. Frontiers in Psychiatry, 2014; 5(67):1-8.
57. Jia JM, Ma XC, Wu CF, Wu LJ, Hu GS. Cordycedipeptide-A, a new cyclodipeptide from the culture liquid of *C. sinensis* (Berk.) Sacc. Chemical and Pharmaceutical Bulletin, 2005; 53: 582-583.
58. Jia JM, Tao HH, Feng BM. Cordyceamides-A and B from the culture liquid of *C. sinensis* (Berk.) Sacc. Chemical and Pharmaceutical Bulletin, 2009; 57: 99-101.
59. Kitakaze M., Hori M. Adenosine therapy: a new approach to chronic heart failure. Expert Opinion on Investigational Drugs, 2000; 9(11): 2519–2535.
60. Ma YF, Zhang J, Zhang Q, Chen P, Song J, Yu S, Liu H, Liu F, Song C, Yang D, Liu J. Adenosine induces apoptosis in human liver cancer cells through ROS production and mitochondrial dysfunction. Biochemical and Biophysical Research Communications, 2014; 448(1): 8–14.
61. Ontyd J, Schrader J. Measurement of adenosine, inosine, and hypoxanthine in human plasma. Journal of Chromatography, 1984; 307(2): 404–409.
62. Yang D, Yaguchi T, Yamamoto H, Nishizaki T. Intracellularly transported adenosine induces apoptosis in HuH-7 human hepatoma cells by down regulating c-FLIP expression causing caspase-3/-8 activation. Biochemical Pharmacology, 2007; 73(10): 1665–1675.
63. Vestergaard P, Rejnmark L, Mosekilde L. Diabetes and its complications and their relationship with risk of fractures in type 1 & 2 diabetes. Calcified Tissue International, 2009; 84(1): 45–55.
64. Park ES, Kang DH, Yang MK, Kang JC, Jang YC, Park JS, Kim SK, Shin HS. Cordycepin, 3'-deoxyadenosine, prevents rat hearts fromischemia/reperfusion injury via activation of Akt/GSK-3*β*/p70S6K signalling pathway and HO-1 expression. Cardiovascular Toxicology, 2014; 14(1): 1–9.
65. Wang J, Liu YM, Cao W, Yao KW, Liu ZQ, Guo JY. Anti-inflammation and antioxidant effect of cordymin, a peptide purified from the medicinal mushroom *C. sinensis*, in middle cerebral artery occlusion-induced focal cerebral ischemia in rats. Metabolic Brain Disease, 2012; 27(2): 159–165.
66. Ying XZ, Peng L, Chen H, Shen Y, Yu K, Cheng S. Cordycepin prevented IL-*β*-induced expression of inflammatory mediators in human osteoarthritis chondrocytes. International Orthopaedics, 2014; 38(7): 1519–1526.
67. Zhou XX, Luo LP, Dressel WK, Shadier G, Krumbiegel D, Schmidtke P, Zepp F, Meyer CU. Cordycepin is an immunoregulatory active ingredient of *C. sinensis*. The American Journal of Chinese Medicine, 2008; 36(5): 967–980.
68. Cimmino A, Puopolo G, Perazzolli M, Andolfi A, Melck D, Pertot I, Evidente. Four hemisynthetic derivatives were prepared from maculosin (cyclo(L-Pro-L-Tyr)), isolated from *Lysobacter capsici* AZ78 and having anti-oomycete activity against some fungi pathogenic crop plants. A very strong antifungal activity was showed by the azido derivatives of maculosin, which could have pratical application in agriculture as safe fungicide. Chemistry of Heterocyclic Compounds, 2014; 50(2): 290-295.
69. Wattana-Amorn P, Charoenwongsa W, Williams C, Crump MP, Apichaisataienchote B. Antibacterial activity of cyclo(L-Pro-L-Tyr) and cyclo(D-Pro-L-Tyr) from *Streptomyces* sp. strain 22-4 against phytopathogenic bacteria. Natural Product Research, 2016; 30(17):1980-1983.
70. Xiao ZH, Zhou JH, Wu HS. Effect of myriocin on the expression of cyclin D1 in high glucose induced hypertrophy mesangial cells. Chinese Journal of Contemporary Paediatrics. 2011; 13:677-679.
71. Chiou WF, Chang PC, Chou CJ, Chen CF. Protein constituent contributes to the hypotensive and vasorelaxant of *C. sinensis*. Life Sciences, 2000; 66(14):1369-1376.
72. Shao PL, Kui JZ, Zhao NJ, Zong HS, Tina TXD, Chun KL *et al*. A polysaccharide isolated from *C. sinensis*, a traditional Chinese medicine, protects PCl2 cells against hydrogen peroxide-induced injury. Life Sciences, 2003; 73:2503-2513.
73. Kiho T, Hui J, Yamane A, Ukai S. Hypoglycemic activity and chemical properties of a polysaccharide from the cultural mycelium of *C. sinensis*. Biological and Pharmaceutical Bulletin, 1993; 16(12):1291-1293.
74. Kiho T, Ookubo K, Usui S, Ukai S, Hirano K. Structural features and hypoglycemic activity of a polysaccharide (CS- F10) from the cultured mycelium of *C. sinensis*. Biological and Pharmaceutical Bulletin, 1999; 22(9):966-970.
75. Li SP, Su ZR, Dong TTX, Tsim KWK. The fruiting body and its caterpillar host of *C. sinensis* show close resemblance in main constituents and anti-oxidation activity. Phytomedicine, 2002; 9(4):319-324.
76. Liu F, Ooi VEC, Chang ST. Free radical scavenging activities of mushroom polysaccharide extracts. Life Sciences, 1997; 60:763-771.
77. Nakamura K, Yamaguchi Y, Kagota S, Shinozuka K, Kunitomo M. Activation of *in-vivo* Kupffer cell function by oral administration of *C. sinensis* in rats. The Japanese Journal of Pharmacology. 1999; 79(4):505-508.
78. Wu Y, Hu N, Pan Y, Zhou L, Zhou X. Isolation and characterization of a mannoglucan from edible *C. sinensis* mycelium. Carbohydrate Research, 2007; 342:870-875.
79. Yalin W, Ishurd O, Cuirong S, Yuanjiang P. Structure analysis and antitumor activity of (1→3)-*β*-D-glucans (cordyglucans) from themycelia of *C. sinensis*. Planta Medica, 2005; 71(4):381-384.
80. Yuan JG, Cheng XH, Hou YQ. Studies on the components and pharmacological action of polysaccharide from *C. sinensis*. Food and Drugs, 2005; 7:45-48.
81. Zhan TR, Song JM. Progress in studies of Mannitol in medicinal application. Chinese Journal of Marine Drugs, 2003; 22:57-61.
82. Zhong S, Pan HJ, Fan LG, Lv GY, Wu YZ, Parmeswaran B *et al*. Advances in research of polysaccharides in *Cordycep* species. Food Technology and Biotechnology, 2009; 47:304-312.
83. Wasser SP. Medicinal mushrooms as a source of antitumor and immunomodulating polysaccharides. Applied Microbiology and Biotechnology, 2002; 60:258-274.
84. Cheung JK, Li J, Cheung AW, Zhu Y, Zheng KY, Bi CW

et al. Cordysinocan, a polysaccharide isolated from cultured *Cordyceps*, activates immune responses in cultured Tlymphocytes and macrophages: Signaling cascade and induction of cytokines. Journal of Ethnopharmacology, 2009; 124:61-68.
85. Kiho T, Yamane A, Hui J, Usui S, Ukai S. Polysaccharides in fungi, XXXVI. Hypoglycemic activity of a polysaccharide (CS-F30) from the cultural mycelium of *C. sinensis* and its effect on glucose metabolism in mouse liver. Biological and Pharmaceutical Bulletin, 1996; 19:294-296.
86. Kim SW, Xu CP, Hwang HJ, Choi JW, Kim CW, Yun JW. Production and characterization of exopolysaccharides from an enthomopathogenic fungus *C. militaris* NG3. Biotechnology Progress, 2003; 19:428-435.
87. Kim SD. Isolation, structure and cholesterol esterase inhibitory activity of a polysaccharide, PSA, from *C. Sinensis*. Journal of Applied Biological Chemistry. 2010; 53:784-789.
88. Li HP, Hu Z, Yuan JL, Fan HD, Chen W, Wang SJ *et al*. A novel extracellular protease with fibrinolytic activity from the culture supernatant of *C. sinensis* purification and characterization. Phytotherapy Research, 2007; 21(12):1234-1241.
89. Wang Y, Yin H, Lv X, Gao H, Wang M. Protection of chronic renal failure by a polysaccharide from *C. sinensis*. Fitoterapia, 2010; 81(5):397-402.
90. Wang Y, Liu D, Zhao H, Jiang H, Luo C, Wang M *et al*. *C. sinensis* polysaccharide CPS-2 protects human mesangial cells from PDGFBB-induced proliferation through the PDGF/ERK and TGF-β1/Smad pathways. Molecular and Cellular Endocrinology, 2014; 382(2):979-988.
91. Yu S, Zhang Z, Fan M. Analysis of volatile compounds of mycelia of *H. sinenis*, the anamorph of *O. sinensis*. Applied Mechanics and Material, 2012; 140:253-257.
92. Holliday JC, Cleaver P, Powers ML, Patel D. Analysis of quality and techniques for hybridization of medicinal fungus Cordyceps sinensis (Berk.) Sacc. (Ascomycetes). International Journal of Medicinal Mushrooms. 2004; 6:151-164.
93. Li SP, Yang FQ, Tsim KWK. Quality control of *Cordyceps sinensis*, a valued traditional Chinese medicine. Journal of Pharmaceutical and Biomedical Analysis. 2006; 41:1571-1584.

View publication stats

Available Online at http://www.journalajst.com

ASIAN JOURNAL OF SCIENCE AND TECHNOLOGY

ISSN: 0976-3376

Asian Journal of Science and Technology
Vol. 08, Issue, 09, pp.5783-5786, September, 2017

RESEARCH ARTICLE

STUDY OF MICROSTRUCTURE AND PHASE OF PLASMA SPRAYED HIGH MOLYBDENUM COMPOSITE COATING

***Shailesh Mani Pandey, R.S.Walia andQasim Murtaza**

Department of Mechanical Engineering, Delhi Technological University, New Delhi

ARTICLE INFO

Article History:
Received 25th June, 2017
Received in revised form
26th July, 2017
Accepted 22nd August, 2017
Published online 27th September, 2017

Key words:

Plasma spray coating,
Microstructure, SEM,
X-Ray Diffraction.

ABSTRACT

Automotive sectors now days are focused on improving the engine efficiency. To enhance the tribological properties of the engine, the thermal spray technique was used for depositing the coating on the cast iron substrate. To provide a reliable basis for the practical application in automotive industry, composite powder containing 60% high carbon molybdenum, 20% pure molybdenum, 10% CrC and 10% NiCr deposited on the cast iron substrate by atmospheric plasma spray method. In this paper, to investigate the microstructure and phases analysis of the deposited coating, scanning electron microscope and X-ray diffraction was performed. The results show that the obtained composite coating has a uniform, laminar and dense microstructure with good coating adhesion with the substrate. The thickness of the composite coating on the substrate is about 371µm.

Copyright©2017, Shailesh Mani Pandey et al. *This is an open access article distributed under the Creative Commons Attribution License, which permits unrestricted use, distribution, and reproduction in any medium, provided the original work is properly cited.*

INTRODUCTION

Manufacturers of the internal combustion(IC) engine facing the challenge to reduce fuel consumption and emissions by improving engine efficiency. Only 21.5% of the total fuel energy is available for car's motion (Holmberg *et al*., 2012; Tung and McMillan, 2004; Jost, 1990; Priest and Taylor, 2000; Andersson, 1991 and K and Jadhav, 2013). The major part of the fuel energy is consumed to overcome friction, only 28% (excluding rolling resistance) of the total fuel energy is used to overcome engine friction losses including piston skirt friction, piston rings, and bearings. Because of these losses, there is a requirement of considerable reduction in engine frictional losses. The components of the piston and cylinder system and crankshaft drive are at the centre of these development efforts. The piston ring pack has a significant potential for bringing down friction losses due to its impartially high (24%) share of mechanical frictional losses (Johansson *et al*., 2011; Quillen *et al*., 2006; He *et al*., 2016). When considering measures to optimise, the tribological system of the piston ring and cylinder surface, piston ring coatings play a progressively important role as they can directly influence the wear and friction behaviour and the resulting scuff resistance. Automotive manufacturers have specified hard chromium coating for piston rings for decades because of its wear and corrosion resistance, however hard chromium plating cause effects on human health because of the use Cr6+ ions in the galvanic process (Janka *et al*., 2016; Zhang *et al*., 2015; Ang *et al*., 2015 and Rastegar and Richardson, 1997). The improvements of the thermal spray process allow the chromium coating replacement with a comparable or superior surface and more environment-friendly coatings (Erdemir, 2005 and Hogmark *et al*., 2000). At present plasma, the sprayed coating has shown significant improvements in reducing wear and CoF in piston rings. Plasma spray processes utilise the energy contained in a thermally ionised gas to melt partially and propel fine powder particles on to a surface such that they adhered and agglomerated to produce coatings. Plasma itself consists of gaseous ions, free electrons, and neutral atoms. The functions of a plasma spray torch are to generate and sustain a captive high-temperature region so that powder particles introduced into that region can be heated and accelerated on to a workpiece (Ahn *et al*., 1997 and Gangopadhyay, 2017). In this study, a coating of 60% high iron carbon molybdenum powder blended with 20% pure molybdenum, 10% chromium carbide and 10% Nickel Chromium was sprayed using atmospheric plasma spraying technique on a cast iron substrate. The microstructure and phase of high iron carbon molybdenum based coating were studied in this paper, to provide a reliable basis for the practical application in automotive industry.

****Corresponding author:*** **Shailesh Mani Pandey**
Department of Mechanical Engineering, Delhi Technological University, New Delhi

EXPERIMENTAL PROCEDURE

Substrate Preparation: The substrate material is heated until it is in the liquid state. This melted material then poured into a mould containing the cavity having a shape similar to that of required for the experiment. Cope and drag used for the casting respectively. The after being poured, substrate melt is allowed to solidify. This solidified part is known as casting. This casting is then ejected from the mould and sent for further processing, i.e. grinding operation to obtain a clean and smooth surface with minimum possible irregularities. The experience of the designer and material's strength determines the soundness of casting (Blair *et al*., 2005). This entire substrate is prepared using stag casting all in one go to achieve maximum uniform composition. After solidification, the casting was ejected from the mould, by breaking the sand mould, and sand blasting operation performed. The powder of Carbon (C), Silicon (Si), Magnesium (Mg), Phosphorous (P), Sulphur (S), Chromium (Cr) and Copper (Cu) was used for the preparation of charge. The above charge used for Induction Arc Furnace at temperature 1540°C. The composition of the substrate material is shown in Table 1.

Coating preparation: Atmospheric Plasma Spray Coating

The substrate is made of cast iron similar to that piston ring material, with dimension 90x90x2 mm was plasma sprayed with a Sulzer-Metco PT-F4 torch in an isolated environment using a robot. The robot ensured controlled and reproducible trajectories and speed. Ar-H_2 were used as primary gas and secondary gas respectively. Before spraying, the surface of the substrate was sandblasted with 35-mesh al_2o_3 particles to a roughness value of 10μm to enhance the adherence while coating. During spraying, a cooling system applied that consisted of air jets and venturi nozzles. The dependency of microstructure and the power of the plasma jet (13-19.5 kW) were a primary concern during the process. The substrate prepared through casting, which was further cleaned by sand blasting, was used in plasma spray for coating purpose. The substrate fixed in the fixture of the Plasma Spray Machine. Table 3 shows the operating parameters of coating setup. The coating material used to spray was a composite powder of 60% wt. high iron carbon molybdenum blended with 20% wt. pure molybdenum, 10%wt chromium carbide, 10%wt nickle chromium.

Table 1. Substrate Composition

Element	C (%)	Si (%)	Mn (%)	P (%)	S (%)	Cr (%)	Cu (%)
Target	3.75±0.05	2.70±0.05	0.53±0.01	0.36±0.02	.06±0.005	0.04±0.01	0.035±0.03

Table 2. Powder Morphology

Sr. No	Name	Composition	Density/Uses/ Melting Point	SEM Micrographs
1	Metco (350NS)/ Iron molybdenum composite powder	Fe16Mo2C0.25Mn	2.8 g/cm^3- 3.4 g/cm^3 Wear and scuff resistance 1400 °C	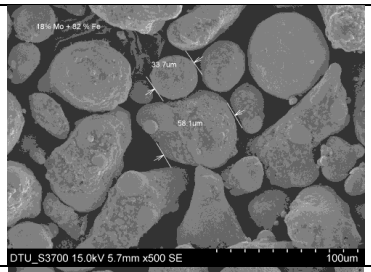
2	Amdry(313)/ molybdenum powder	99.5% (by wt.) of Molybdenum	2.5 g/cm^3 - 5.9 g/cm^3 Wear and scuff resistance 2620^{0}C	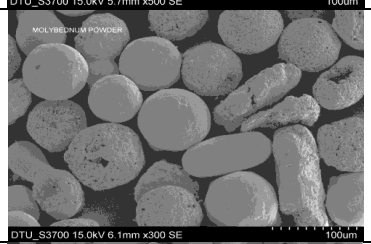
3	Metco(43) F-NS / nickel chromium alloy powder	Ni20Cr	3.1 g/cm^3 - 4.6 g/cm^3 Corrosion-resistant bond coat 1400 ^{0}C	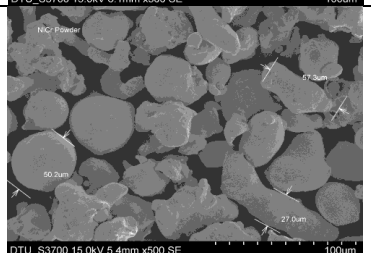
4	Metco(70) CNS / chromium carbide powder	Cr_3C_2	2.7 g/cm^3 - 3.0 g/cm^3 Wear resistance 1930 °C	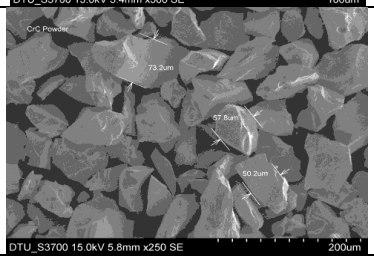

Whose chemical composition and SEM images are shown in Table 2. The powder particle size varied from 10 – 50 µm.

RESULT AND DISCUSSION

XRD Analysis

X-ray diffraction (XRD) is the most powerful and the least expensive technique for identifying coating crystallographic structures. In the as-deposited condition, the phase analysis of the coating is shown in Fig. 2, the main phase of the coating are Cr_2C_2, $Fe_{0.875}Mo_{0.125}$, $Cr_{0.5}Mo_{0.5}$. It can be inferred that Cr3C2 decomposed during plasma spraying, forming carbides of Cr element. These carbides are the hard phase, having a high hardness and a strong wear- resistance. These hard phases distribute uniformly, disperse in the coating and have a high strength with the matrix, which can heighten the coating's resistance to wear.

to form a disc, the detailed shape of which is determined by surface tension, density, viscosity and velocity of the liquid droplet. In most conditions solidification occurs as flattening of the liquid droplet proceeds, i.e. 'splat' type morphology. Therefore, within a limited size range, the particle morphology in the coating is dependent on the both the degree of superheat in the droplet and the velocity of the droplet as it impacts the substrate surface. The lower the degree of superheat and particle velocity, less flattening of the droplet will occur, i.e. the 'splat' is less elongated in the direction parallel to the surface. Oxides can also be formed during the time between the passes on the outer surface of the layer. This oxidation can be decreased by spraying in a vacuum or inert atmosphere. The microstructure of the coating, observed by the scanning electron microscope is shown in Figure 3. The micrograph of coating surface shows a typical lamellar structure. The interior coating body is composed of numerous flat particles, partially melted Mo, an irregular layer of coating, fully melted, disc

Table 3. Process Parameter of Plasma Spray Coating

Sr. No	Process Parameter	Specification
1	Powder Port Internal Diameter	2.2 (mm)
2	Water Flow Rate	4.0 (l/m)
3	Temperature Of Chiller	17 (ºC)
4	Distance Between Spray Gun & Mandrel (At gun angle 300º)	140 (mm)
5	Argon Flow Rate	1.87 (m^3/s)
6	Hydrogen Flow Rate	0.21 (m^3/s)
7	Argon Pressure	6.5 (bar)
8	Hydrogen Pressure	5.5 (bar)
9	Powder Flow Rate	50 (g/min)
10	Voltage	70 (V)
11	Current	460 (A)
12	Gun Feed	10 (mm/min)
13	Gun Angle During Spray	30 (º)
14	Cooling Air Pressure	46 (bar)
15	Powder Driving Temperature	120 (ºC)
16	Powder Mixing time in V-type mixer	5400 (s)

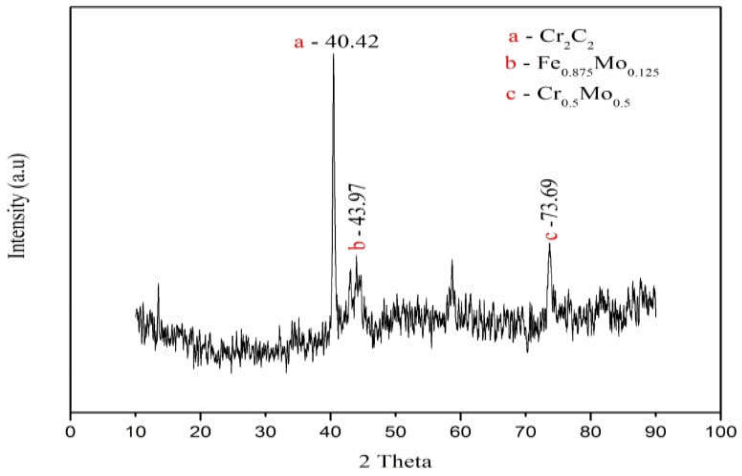

Figure 2. X-ray Diffraction Pattern of Coating

Coating Structure Analysis

Scanning electron micrographs of the thermally sprayed coating under investigation are shown in Fig 3. The sprayed coating progress as the spray gun repeatedly traverses over the surface and applies the coating in layers, with a typical layer thickness 371 µm as shown in Fig 4. Plasma spraying is a process where particles typically 10–100 mm in diameter are rapidly melted and accelerated to produce a stream of molten particles onto a substrate. On impact the liquid droplet flattens splat, partially melted region and unmelted Mo particle. The micrographs of the coating suggest that the splat of the sprayed material does not seem to form a continuous layer in figure 3(e), but at the cross section, it was observed that the coating was more homogeneous and regular in Fig.4. The microstructure seen in the present study is analogous with the findings reported in the studies of various researchers (Vicenzi *et al*., 2008; Lin *et al*., 2015; Pandey *et al*., 2017). Figure 4 shows a photomicrograph of x-section of the sprayed coatings. The coating thickness can be up to several microns shown in

Figure 4(a). Here the typical coating thickness is from 350 to 400μm. Figure 4 (b) recognizes the laminated structure and existing porosity (small black regions). The round black spot (Figure 3b) in micrographs is those that did not melt completely before re-solidifying.

Conclusion

Plasma sprayed composite coating (60% high carbon molybdenum, 20% pure molybdenum, 10% CrC and 10% NiCr) has been deposited on the piston ring is investigated by scanning electron microscope and X-ray diffraction. The following points are concluded from the experimental results are as follows:

- The grain size of the different powder varies from 30 - 70 μm
- The X-ray diffraction results of the coated sample show the sharp peaks of Cr_2C_2, $Fe_{0.875}Mo_{0.125}$ and $Cr_{0.5}Mo_{0.5}$; it can be inferred that Cr_3C_2 decomposed during plasma spraying, forming carbides of Cr element. This is the clear evidence for the formation of the different structure in the coating.
- The microstructure of plasma sprayed coating shows a uniformly dense and laminar structure with an excellent coating adhesion to the substrate. It also shows unmelted Mo, partially melted Mo particle, disc splat, and an irregular layer of the coating investigated by SEM results.
- The observed coating thickness of the coating was found to be about 371 μm, as observed by SEM.

REFERENCES

Ahn, H., Kim, J. and Limb, D. 1997. "Tribological behaviour of plasma-sprayed zirconia coatings", *Wear*, Vol. 4 No. 203–204, pp. 77–87.

Andersson, B.S. 1991. "Paper XVIII (iii) Company Perspectives in Vehicle Tribology - Volvo", *Tribology Series*, Vol. 18 No. C, pp. 503–506.

Ang, A.S.M., Howse, H., Wade, S.A. and Berndt, C.C. 2015. "Manufacturing of nickel based cermet coatings by HVOF process", Vol. 0 No. March, pp. 1–12.

Blair, M., Monroe, R., Beckermann, C., Hardin, R., Carlson, K. and Monroe, C. 2005. "Predicting the occurrence and effects of defects in castings", *JOM*, Springer-Verlag, Vol. 57 No. 5, pp. 29–34.

Erdemir, A. 2005. "Review of engineered tribological interfaces for improved boundary lubrication", Vol. 38, pp. 249–256.

Gangopadhyay, A. 2017. "A Review of Automotive Engine Friction Reduction Opportunities Through Technologies Related to Tribology", *Transactions of the Indian Institute of Metals*, Springer India, Vol. 70 No. 2, pp. 527–535.

He, P.F., Ma, G.Z., Wang, H.D., Yong, Q.S., Chen, S.Y. and Xu, B.S. 2016. "Tribological behaviors of internal plasma sprayed TiO2-based ceramic coating on engine cylinder under lubricated conditions", *Tribology International*, Elsevier, Vol. 102, pp. 407–418.

Hogmark, S., Jacobson, S. and Larsson, M. 2000. "Design and evaluation of tribological coatings", *Wear*, Vol. 246 No. 1–2, pp. 20–33.

Holmberg, K., Andersson, P. and Erdemir, A. 2012. "Global energy consumption due to friction in passenger cars", *Tribology International*, Elsevier, Vol. 47, pp. 221–234.

Janka, L., Norpoth, J., Trache, R. and Berger, L.M. 2016. "Influence of heat treatment on the abrasive wear resistance of a Cr3C2NiCr coating deposited by an ethene-fuelled HVOF spray process", *Surface and Coatings Technology*, Elsevier B.V., Vol. 291, pp. 444–451.

Johansson, S., Nilsson, P.H., Ohlsson, R. and Rosén, B.G. 2011. "Experimental friction evaluation of cylinder liner/piston ring contact", *Wear*, Vol. 271 No. 3–4, pp. 625–633.

Jost, H.P. 1990. "Tribology - Origin and future", *Wear*, Vol. 136 No. 1, pp. 1–17.

K, B.S. and Jadhav, N.P. 2013. "Friction Losses between Piston Ring-Liner Assembly of Internal Combustion Engine: A Review", *International Journal of Scientific and Research Publications*, Vol. 3 No. 6, pp. 2250–3153.

Lin, L., Li, G.-L., Wang, H.-D., Kang, J.-J., Xu, Z.-L. and Wang, H.-J. 2015. "Structure and wear behavior of NiCr–Cr 3 C 2 coatings sprayed by supersonic plasma spraying and high velocity oxy-fuel technologies", *Applied Surface Science*, Vol. 356, pp. 383–390.

Pandey, S.M., Murtaza, Q. and Walia, R.S. 2017. "Study of dry wear behavior and morphological characteristic of 60%Mo-20%NiCr-10%CrC-10%Mo+Fe based alloy coating by atmospheric plasma spray technique", *Advances in Materials and Processing Technologies*, pp. 1–14.

Priest, M. and Taylor, C.M. 2000. "Automobile engine tribology—approaching the surface", *Wear*, Vol. 241 No. 2, pp. 193–203.

Quillen, K., Moughon, L., Stanglmaier, R.H., Wong, V., Takata, R., Reinbold, E. and Donahue, R. 2006. "ICES2006-1327 Coefficient of Variance Net indicated Mean Effected Pressure", pp. 1–10.

Rastegar, F. and Richardson, D.E. 1997. "Alternative to chrome: HVOF cermet coatings for high horse power diesel engines", *Surface and Coatings Technology*, Vol. 90 No. 1–2, pp. 156–163.

Tung, S.C. and McMillan, M.L. 2004. "Automotive tribology overview of current advances and challenges for the future", *Tribology International*, Vol. 37 No. 7, pp. 517–536.

Vicenzi, J., Marques, C.M. and Bergmann, C.P. 2008. "Hot and cold erosive wear of thermal sprayed NiCr-based coatings: Influence of porosity and oxidation", *Surface and Coatings Technology*, Vol. 202 No. 15, pp. 3688–3697.

Zhang, W.C., Liu, L. Bin, Zhang, M.T., Huang, G.X., Liang, J.S., Li, X. and Zhang, L.G. 2015. "Comparison between WC-10Co-4Cr and Cr3C2-25NiCr coatings sprayed on H13 steel by HVOF", *Transactions of Nonferrous Metals Society of China (English Edition)*, The Nonferrous Metals Society of China, Vol. 25 No. 11, pp. 3700–3707.

****

Supplementary Material

Identification of a novel class of BRD4 inhibitors by computational screening and binding simulations

Bryce K. Allen[1,2] , Saurabh Mehta[3], Stuart W.J. Ember[4,‡], Jin-Yi Zhu[4,^], Ernst Schönbrunn[4], Nagi G. Ayad[5,6,7], Stephan C. Schürer[1,2,7,*]

1. Department of Molecular and Cellular Pharmacology, Miller School of Medicine, University of Miami, Miami, FL, US.
2. Center for Computational Science, University of Miami, Miami, FL, US.
3. Department of Applied Chemistry, Delhi Technological University, Delhi, India.
4. Drug Discovery Department, H. Lee Moffitt Cancer Center and Research Institute, Tampa, FL, US.
5. Center for Therapeutic Innovation Miller School of Medicine, University of Miami, Miami, FL, US.
6. Miami Project to Cure Paralysis, Department of Psychiatry and Behavioral Sciences, Miller School of Medicine, University of Miami, FL, US.
7. Sylvester Comprehensive Cancer Center, Miller School of Medicine, University of Miami, FL, US.
‡. Department of Research and Development, Reaction Biology Corporation, Malvern, PA 19355.
^. Current address: Dart Neuroscience, San Diego, CA 92131, United States.
*. To whom correspondence should be addressed: sschurer@miami.edu

1. **Supplementary Figure 1.** Crystal structures show similar binding conformation across all compounds.
2. **Supplementary Figure 2.** Interaction diagrams for co-crystal structures of sulfonamide compounds.
3. **Supplementary Figure 3.** Schematic demonstrating the use of molecular dynamics to improve docking pose prediction.
4. **Supplementary Table 1.** DSF results for experiments performed with sulfonamide compounds and recombinant BRD4, bromodomain 1.
5. **Supplementary Table 2.** RMSD calculations with respect to co-crystal binding conformation.
6. **Supplementary Figure 4.** ROC curves characterizing predictive performance of known active BRD4 compounds for docking models.
7. **Supplementary Figure 5.** Experimentally determined pIC50 values of sulfonamide compounds shown in relation to their ranking by docking score
8. **Supplementary Table 3.** ROC score and enrichment results for the initial BRD4 docking model and the docking model optimized by MD for the 908 prioritized compounds.
9. **Supplementary Figure 6.** Log-Enrichment curve for docking results before and after MD optimization.
10. **Supplementary Figure 7.** Histogram density distribution of ECFP4 Tanimoto similarities of novel BRD4 actives to all reported BRD4 compounds.
11. **Supplementary Figure 8.** Histogram density distribution for ROCS shape similarity results.
12. **Supplementary Figure 9.** Comparison of co-crystal binding conformation for known active BRD4 compound PFI-1.
13. **Supplementary Figure 10.** RMSD of BRD4(BD4) with ligand 8302 over the time course of a 500 ns MD simulation.
14. **Supplementary Table 4.** Crystallographic table.
15. **Compound Purity.** HPLC traces of the novel sulfonamide BRD4(BD1) inhibitors.

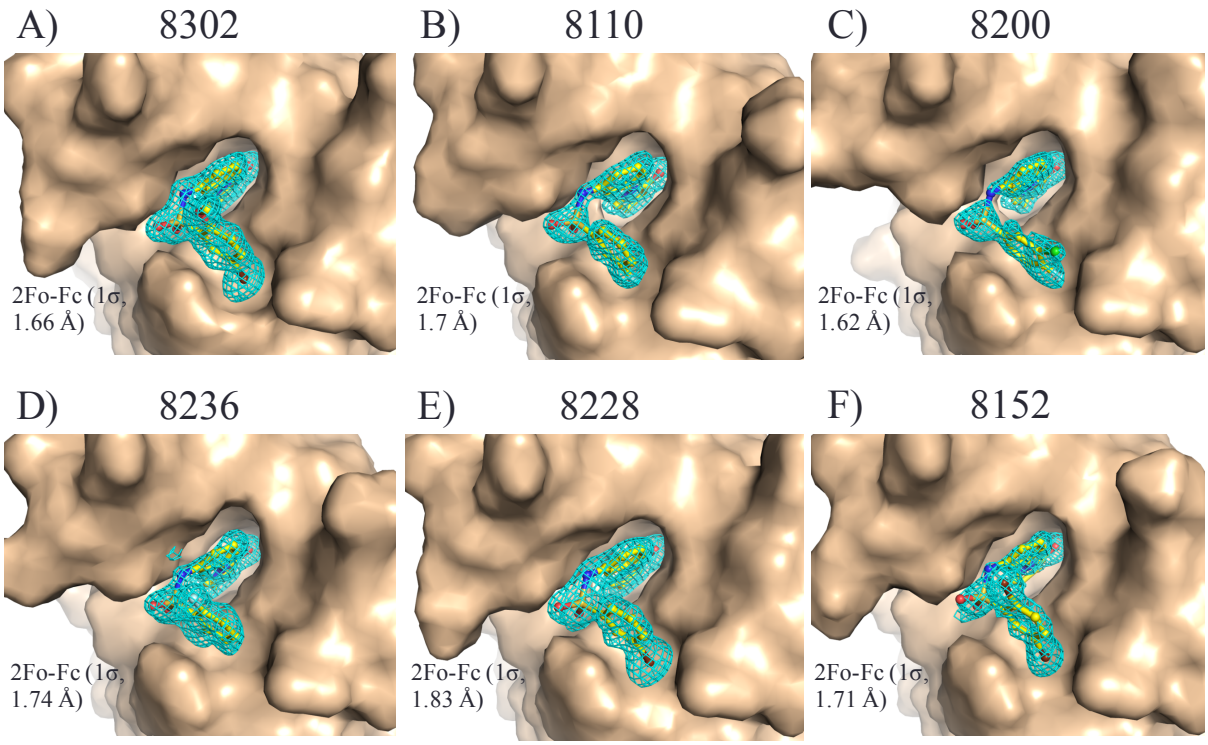

Supplementary Figure 1. Crystal structures show similar binding conformation across all compounds.

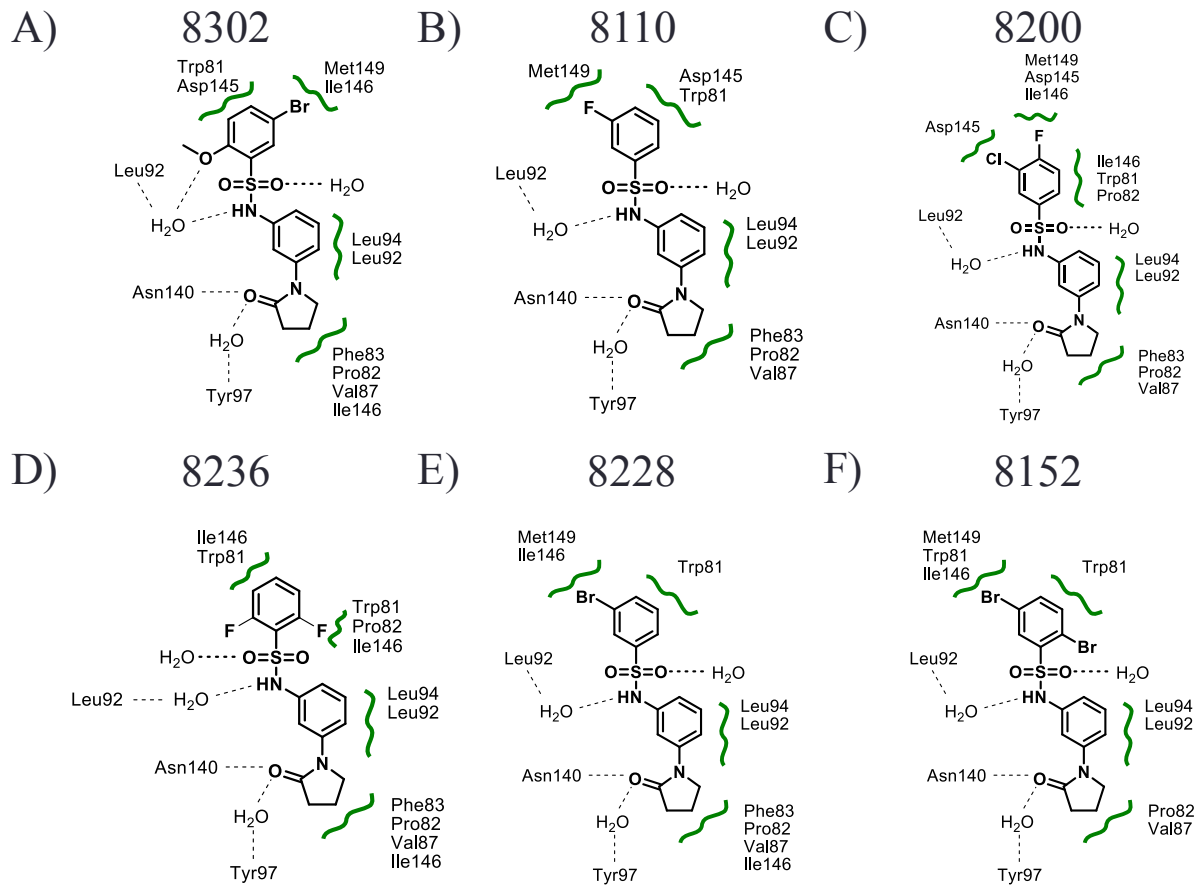

Supplementary Figure 2. Interaction diagrams for co-crystal structures of sulfonamide compounds. H-bonding (2.2 < d < 3.5 Å) and VDW (hydrophobic, 3.3 < d < 4.0 Å) interactions indicated in black and green lines, respectively.

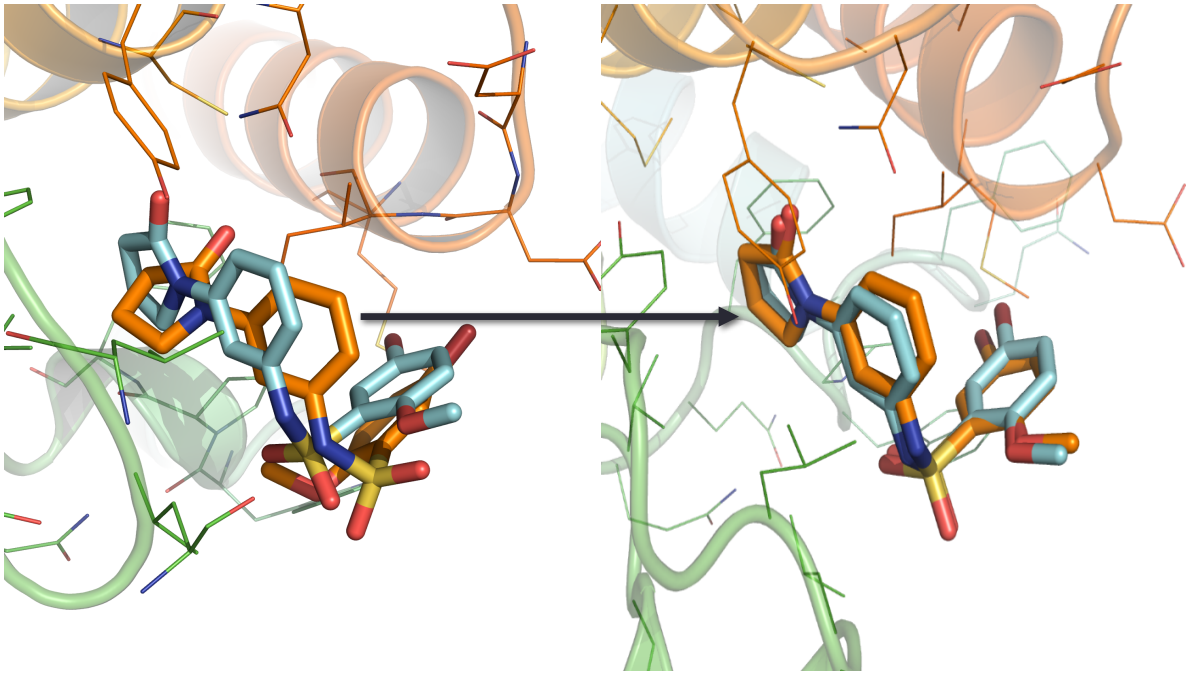

Supplementary Figure 3. Schematic demonstrating the use of molecular dynamics to improve docking pose prediction. Left diagram shows the original docking pose of 8302 (orange) as compared to co-crystal structure (teal). Right diagram shows binding conformation after molecular dynamics simulation.

Supplementary Table 1. DSF results for experiments performed with sulfonamide compounds and recombinant BRD4, bromodomain 1. JQ1 was used as a control.

Compound	ΔTm (°C)	ΔTm Std. Err. (°C)	Estimated IC_{50} (μM)
JQ1	9.37	0.07	0.02
8302	0.62	0.11	11.90
8236	0.04	0.19	21.07
8110	-0.12	0.16	23.83
8200	-0.21	0.10	25.56
8228	-0.84	0.14	41.49
8152	-0.91	0.24	43.71

Supplementary Table 2. RMSD calculations relative to the co-crystal binding conformation (heavy atom ligand RMDS).

Compound	Initial Docking RMSD	RMSD after MD	ΔRMSD
8302	1.864	0.0786	1.7854
8236	1.687	0.302	1.385
8110	2.354	0.124	2.23
8200	2.082	0.253	1.829
8228	1.573	0.464	1.109
8152	1.979	0.126	1.853

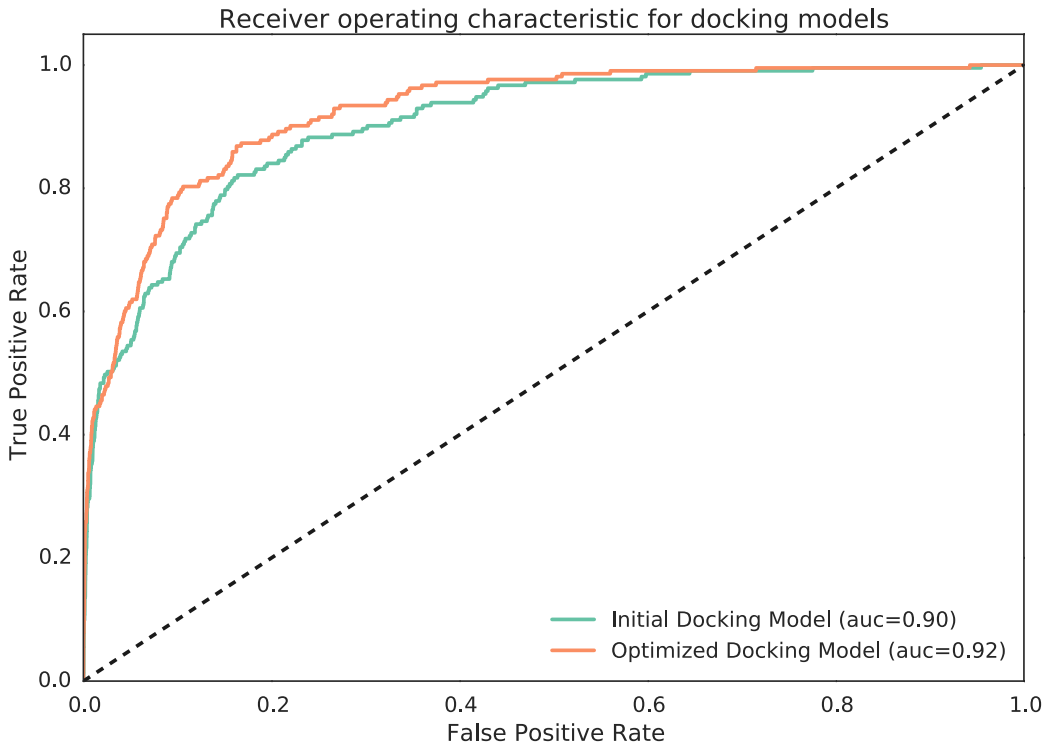

Supplementary Figure 4. ROC curves characterizing predictive performance of known active BRD4 compounds for docking models optimized by molecular dynamics (orange) as compared to the initial docking model (teal).

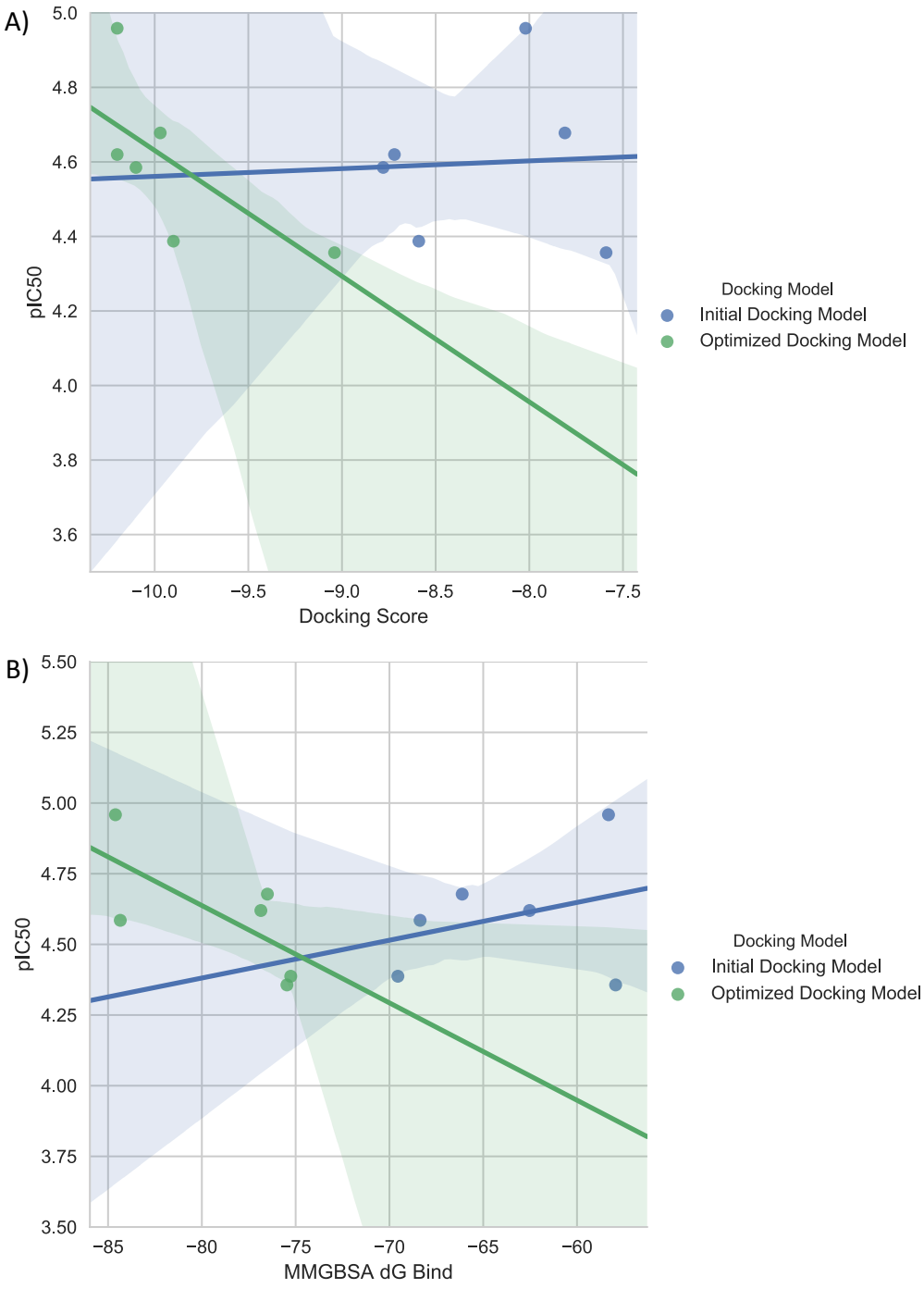

Supplementary Figure 5. Experimentally determined pIC50 values of sulfonamide compounds shown in relation to their ranking by A) docking score and B) MMGBSA dG of binding for the initial docking model (blue) and the optimized docking model after MD (green).

Supplementary Table 3. ROC score and enrichment results for the initial BRD4 docking model and the docking model optimized by MD for the 908 prioritized compounds.

	Initial Docking Model	Optimized Docking Model
ROC Score	0.953	0.967
Enrichment Factor 1%	32.5	50.6

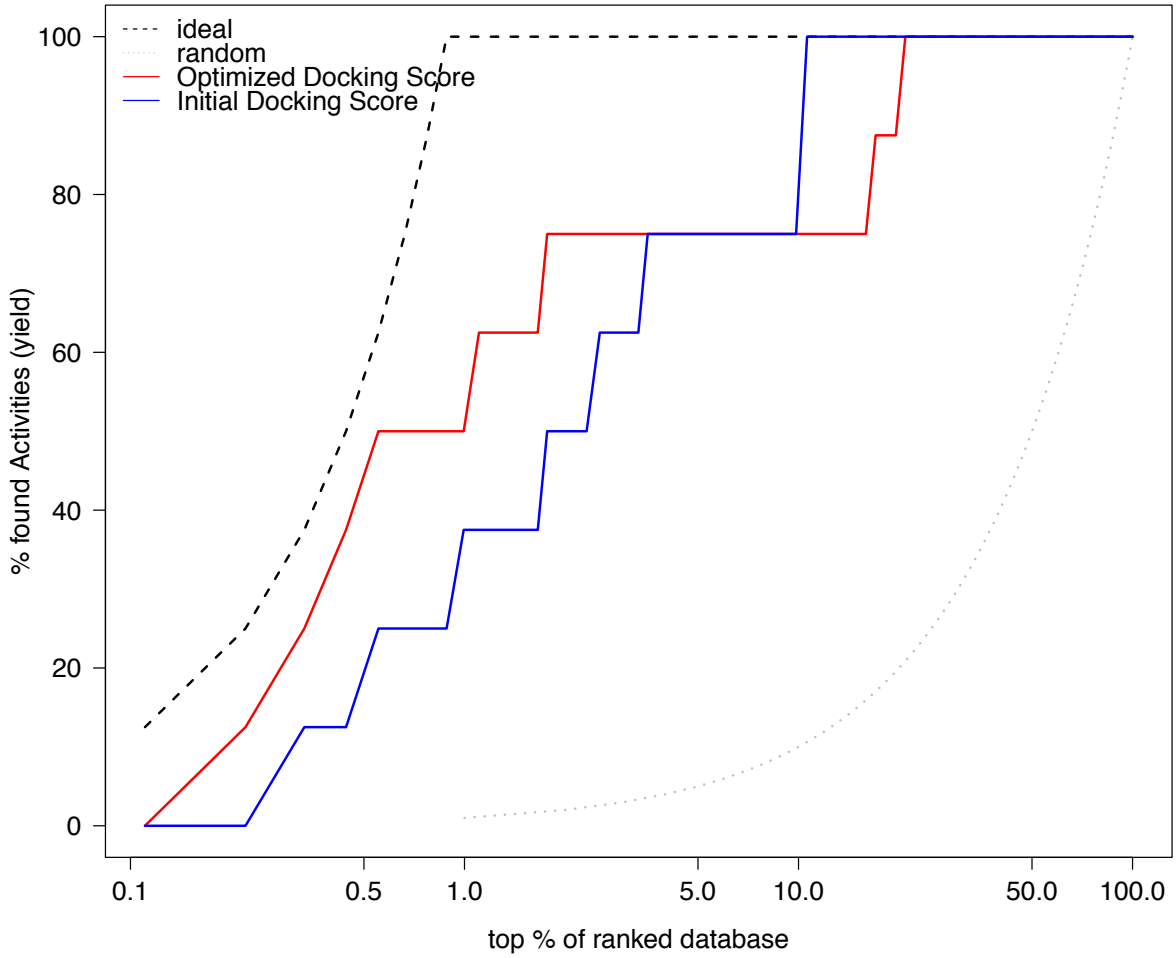

Supplementary Figure 6. Log-Enrichment curve for docking results before and after MD optimization; (blue and red respectively). The optimized docking model is better able to enrich active compounds in the top scoring 1% of the dataset. The x-axis corresponds to the % of data evaluated, ranked by the docking score. The y-axis displays the % of actives discovered as more data are evaluated.

A)

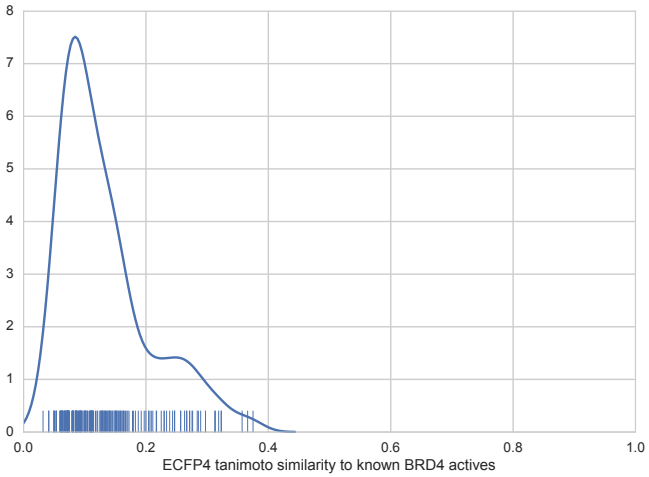

B)

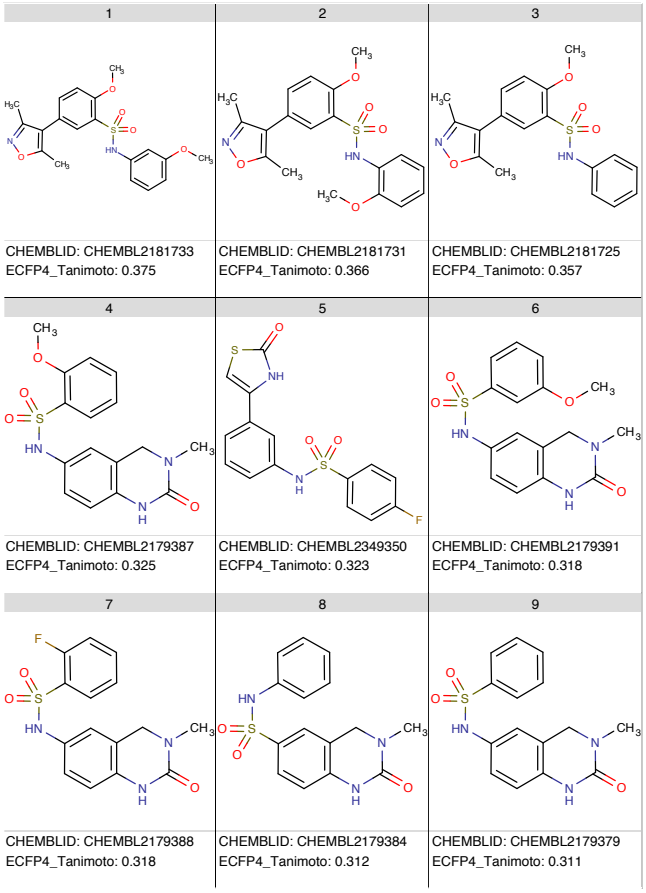

Supplementary Figure 7. A) Histogram density distribution of ECFP4 Tanimoto similarities of novel BRD4 actives to all reported BRD4 compounds obtained from ChEMBL release 18. B) The nine highest scoring compounds are shown.

A)

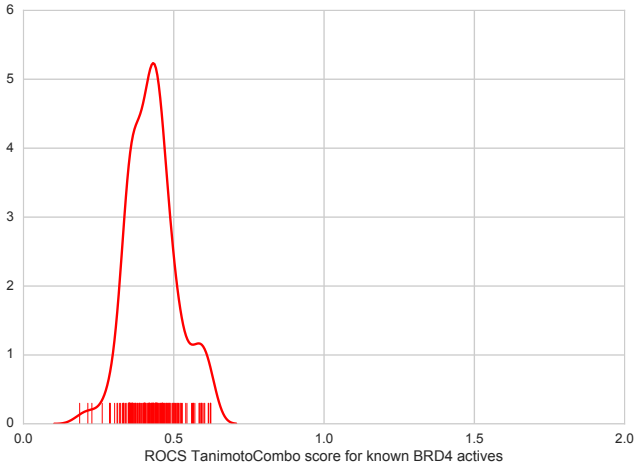

B)

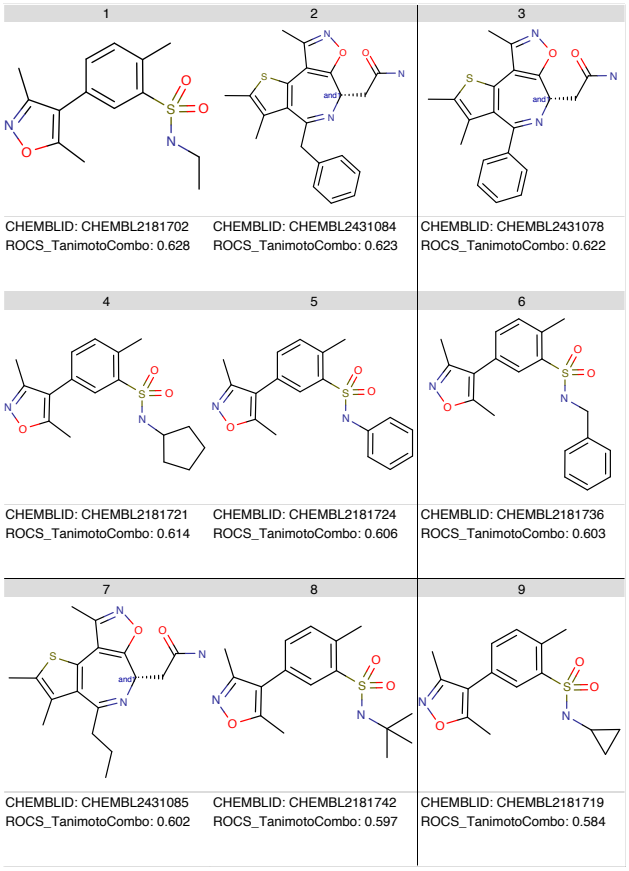

Supplementary Figure 8. A) Histogram density distribution for ROCS shape similarity results. The score corresponds to the TanimotoCombo metric, which is a combination of both TanimotoShape and TanimotoColor similarity metrics. Note that the score ranges from 0 – 2. B) The nine highest scoring ROCS TanimotoCombo compounds are shown.

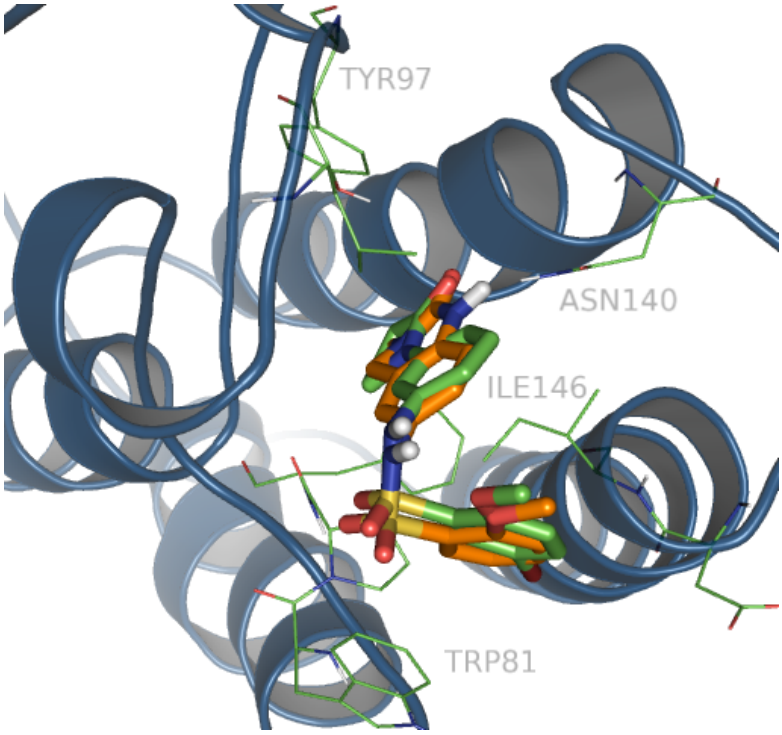

Supplementary Figure 9. Comparison of co-crystal binding conformation for known active BRD4 compound PFI-1 (orange) and the most active sulfonamide compound 8302 (green). Residues within 3Å of ligand are included.

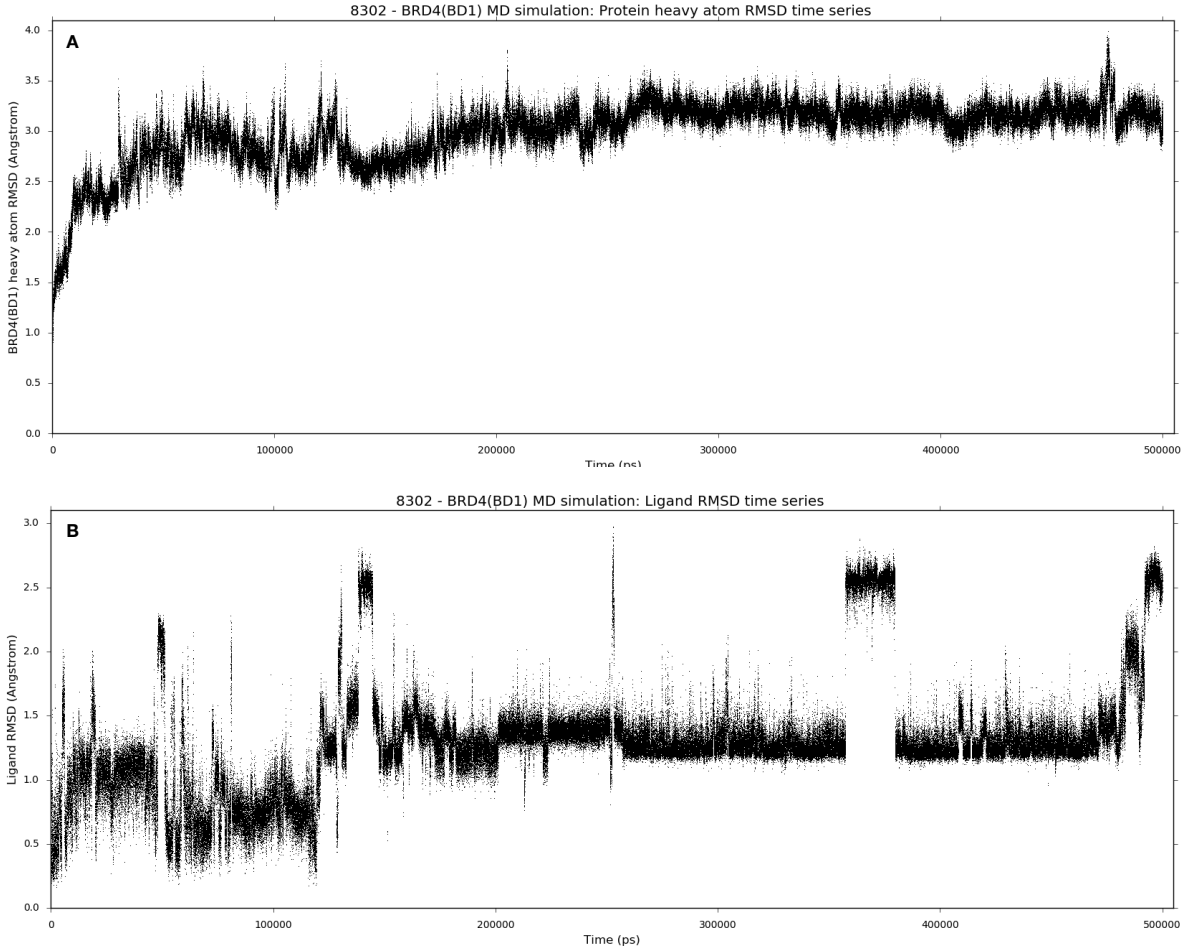

Supplementary Figure 10. RMSD of BRD4(BD4) with ligand 8302 over the time course of a 500 ns MD simulation. A (top) Protein heavy atom RMSD of 8320-BRD4(BD1) over the 500 ns. B (bottom) Ligand RMSD of 8302-BRD4(BD1) over the 500ns. The RMSD time course demonstrates a relatively stable protein back bone and ligand pose throughout an extended MD simulation. Visualizations were generated using the Desmond Simulation Event Analysis tool.

Supplementary Table S4. Crystallographic data collection and refinement statistics.

Ligand ID	1	2	3	4	5	6
Ligand name	7635936	17503468	8841871	8841880	8841881	17528462
PDB ID	5TI2	5TI3	5TI4	5TI5	5TI6	5TI7
Data Collection						
Space group	$P\ 2_12_12_1$	$P\ 2_12_12_1$	$P\ 2_12_12_1$	$P\ 2_12_12_1$	$P\ 2_12_12_1$	$P\ 2_12_12_1$
Unit cell dimensions						
a, b, c (Å)	37.2, 43.9, 78.7	37.1, 43.9, 78.5	37.0, 44.0, 78.7	35.1, 46.5, 77.8	37.3, 43.8, 78.7	36.2, 46.0, 77.7
α, β, γ (°)	90, 90, 90	90, 90, 90	90, 91.7, 90	90, 90, 90	90, 90, 90	90, 90, 90
Resolution range	1.65-100.0 (1.65-1.69)	1.70-100.0 (1.70-1.75)	1.62-100.0 (1.62-1.66)	1.83-100.0 (1.83-1.88)	1.70-100.0 (1.70-1.75)	1.65-100.0 (1.65-1.69)
Unique Reflections	15694 (1011)	14471 (950)	16730 (1059)	11742 (857)	14431 (943)	16009 (1013)
Rsym[a] (%)	2.3 (5.8)	10.0 (22.1)	4.1 (24.3)	8.1 (38.9)	10.3 (26.9)	3.3 (20.8)
Completeness (%)	97.5 (85.2)	99.0 (90.6)	98.8 (87.7)	99.7 (99.9)	98.4 (88.5)	98.8 (88.5)
I/σ I	42.8 (14.9)	13.9 (6.6)	22.0 (3.5)	14.9 (4.8)	13.4 (6.0)	25.9 (4.1)
Wilson B ($Å^2$)	11.2	11.5	12.3	19.4	10.1	14.8
Refinement						
Rcryst[b] (%)	12.5	14.7	13.1	16.4	13.2	13.9
Rfree[c] (%)	18.1	19.4	18.5	21.4	18.6	19.2
Ave. B all[d] ($Å^2$)	13.3	15.9	15.9	27.0	12.3	19.9
Ave. B protein ($Å^2$)	11.8	14.2	14.0	26.7	10.3	18.5
Ave. B ligand ($Å^2$)	22.4	28.9	26.2	23.7	16.4	14.7
Ave. B solvent ($Å^2$)	22.9	25.1	27.3	32.0	22.9	29.9
rmsd[e] bonds (Å)	0.011	0.011	0.009	0.007	0.010	0.008
rmsd angles (°)	1.30	1.29	1.20	1.10	1.30	1.20
Coordinate Error (Å)	0.16	0.13	0.12	0.23	0.14	0.15
Ramachadran favored (%)	99.21	99.20	99.21	98.40	99.20	99.20
Ramachadran allowed (%)	0.79	0.80	0.79	1.60	0.80	0.80

[a]Rsym = 100 xΣhΣi|Ihi-Ih|/ΣhiI where h are unique reflection indices

[b]Rcryst = 100 xΣ|Fobs-Fmodel|/F obs where Fobs and Fmodel are observed and calculated structure factor amplitudes respectively

[c]Rfree is Rcryst calculated for randomly chosen unique reflections

[d]Excluding hydrogen atoms

[e]rmsd = root-mean-square deviation from ideal values which were excluded from the refinement

COMPOUND PURITY

Z115668200

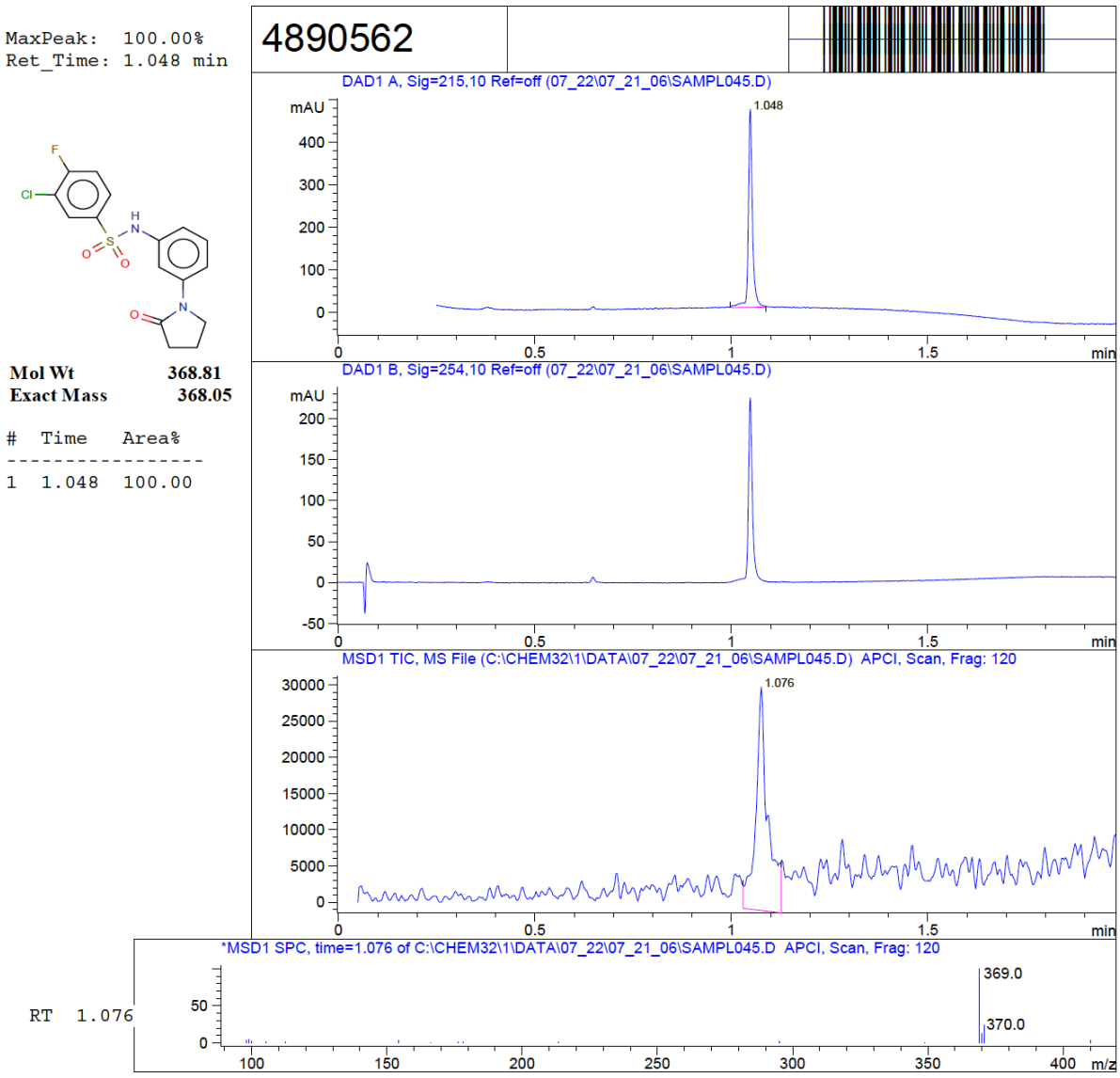

Z115668236

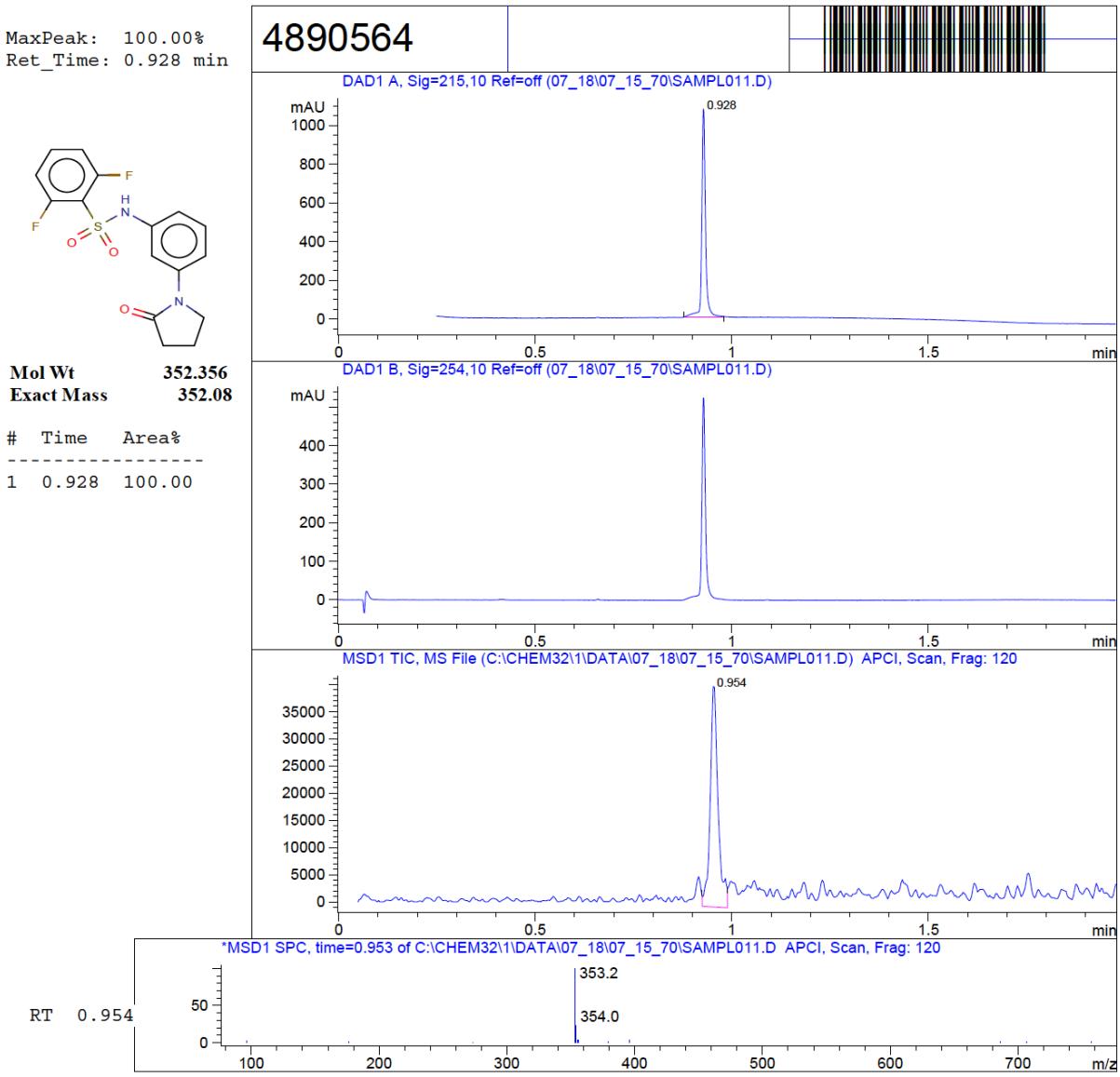
MaxPeak: 100.00%
Ret_Time: 0.928 min
4890564
DAD1 A, Sig=215,10 Ref=off (07_18\07_15_70\SAMPL011.D)
mAU
0.928
min
DAD1 B, Sig=254,10 Ref=off (07_18\07_15_70\SAMPL011.D)
MSD1 TIC, MS File (C:\CHEM32\1\DATA\07_18\07_15_70\SAMPL011.D) APCI, Scan, Frag: 120
0.954
*MSD1 SPC, time=0.953 of C:\CHEM32\1\DATA\07_18\07_15_70\SAMPL011.D APCI, Scan, Frag: 120
353.2
354.0
m/z
Mol Wt 352.356
Exact Mass 352.08
Time Area%
1 0.928 100.00
RT 0.954

Z115668302

MaxPeak: 100.00%
Ret_Time: 1.356 min

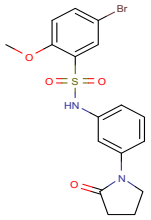

Mol Wt **425.3**
Exact Mass **426.02**

#	Time	Area%
1	1.356	100.00

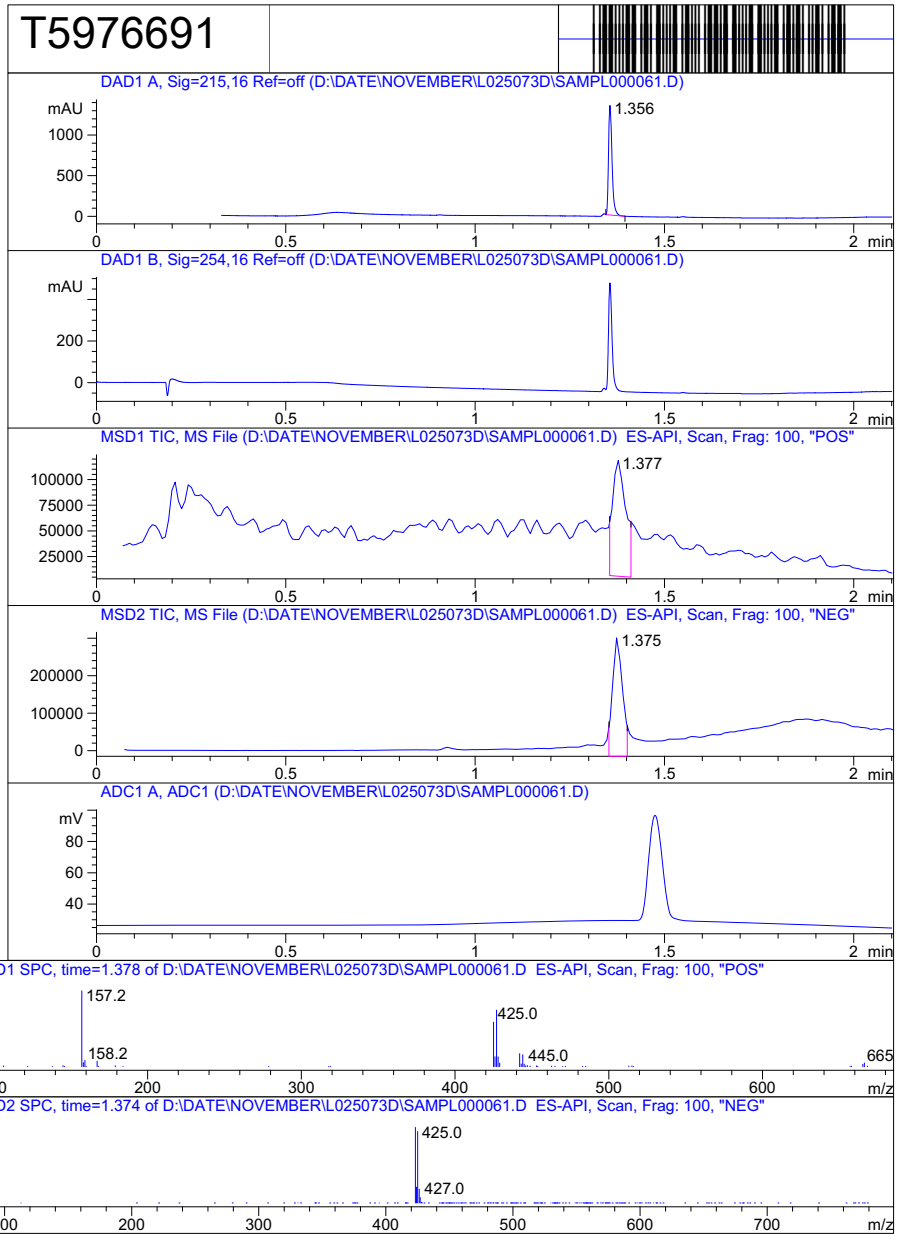

RT 1.377

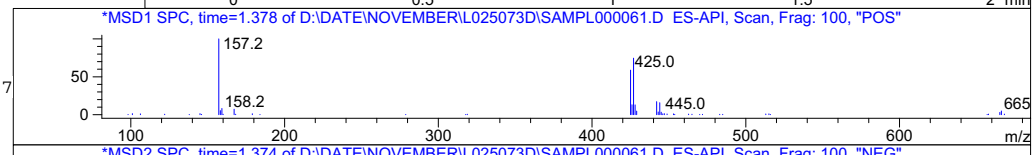

RT 1.375

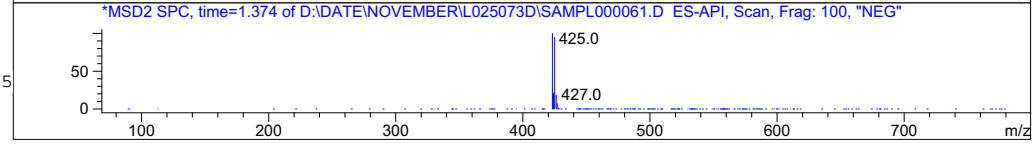

Z115668110

MaxPeak: 100.00%
Ret_Time: 1.275 min

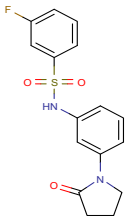

Mol Wt **334.36**
Exact Mass **334.09**

#	Time	Area%
1	1.275	100.00

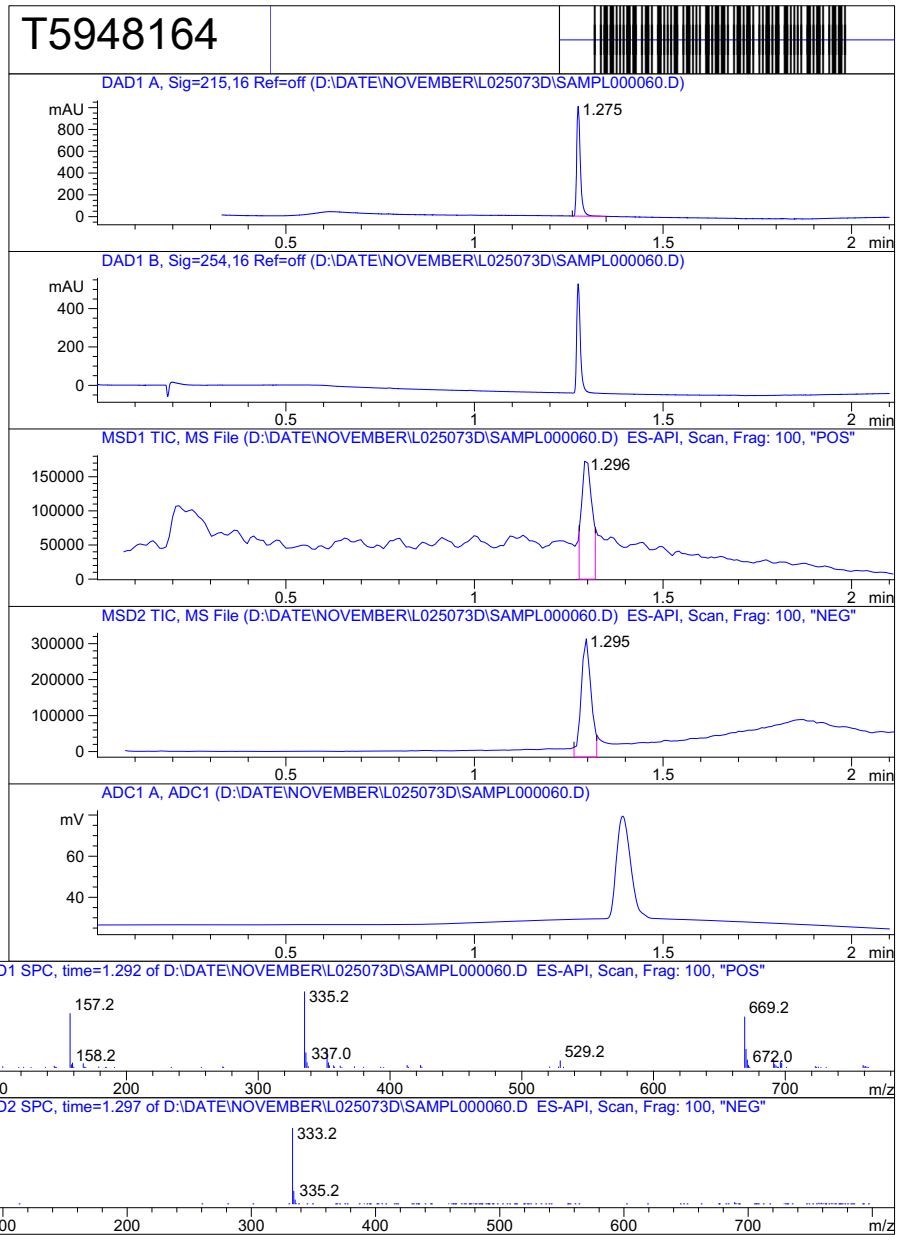

RT 1.296

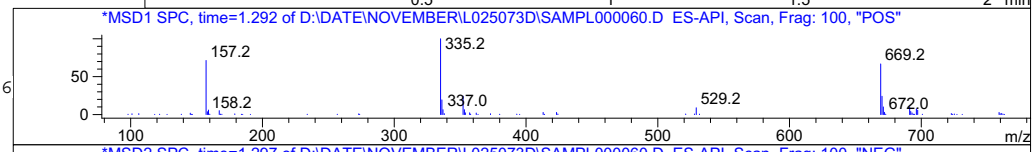

RT 1.295

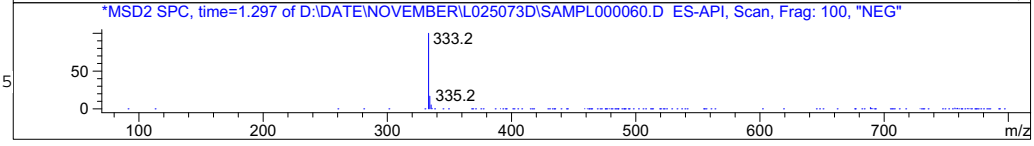

Z115668152

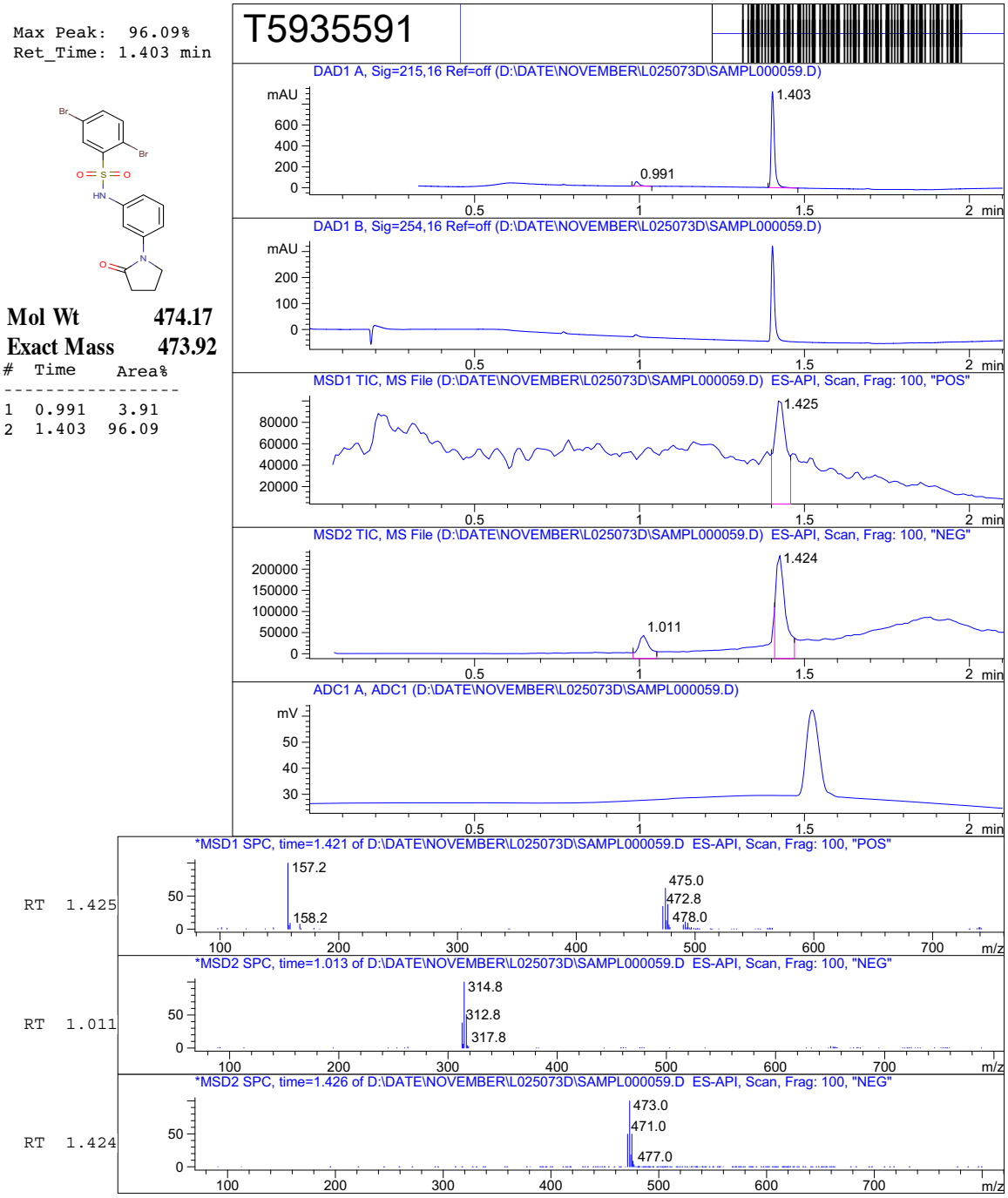
Max Peak: 96.09%
Ret_Time: 1.403 min
T5935591
Mol Wt 474.17
Exact Mass 473.92
Time Area%
1 0.991 3.91
2 1.403 96.09
DAD1 A, Sig=215,16 Ref=off (D:\DATE\NOVEMBER\L025073D\SAMPL000059.D)
DAD1 B, Sig=254,16 Ref=off (D:\DATE\NOVEMBER\L025073D\SAMPL000059.D)
MSD1 TIC, MS File (D:\DATE\NOVEMBER\L025073D\SAMPL000059.D) ES-API, Scan, Frag: 100, "POS"
MSD2 TIC, MS File (D:\DATE\NOVEMBER\L025073D\SAMPL000059.D) ES-API, Scan, Frag: 100, "NEG"
ADC1 A, ADC1 (D:\DATE\NOVEMBER\L025073D\SAMPL000059.D)
*MSD1 SPC, time=1.421 of D:\DATE\NOVEMBER\L025073D\SAMPL000059.D ES-API, Scan, Frag: 100, "POS"
RT 1.425
*MSD2 SPC, time=1.013 of D:\DATE\NOVEMBER\L025073D\SAMPL000059.D ES-API, Scan, Frag: 100, "NEG"
RT 1.011
*MSD2 SPC, time=1.426 of D:\DATE\NOVEMBER\L025073D\SAMPL000059.D ES-API, Scan, Frag: 100, "NEG"
RT 1.424

Z115668228

MaxPeak: 100.00%
Ret_Time: 1.347 min

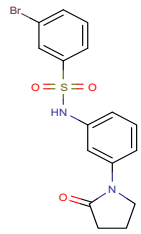

Mol Wt **395.27**
Exact Mass **396.01**

#	Time	Area%
1	1.347	100.00

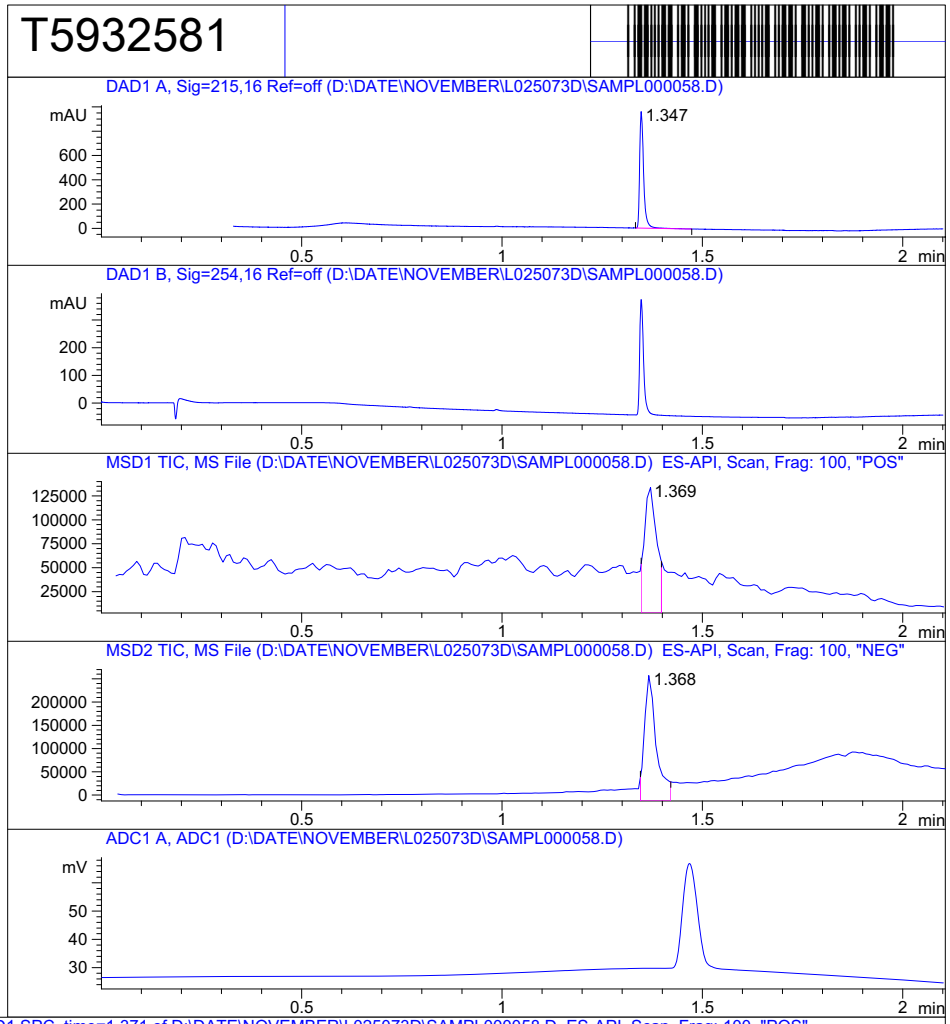

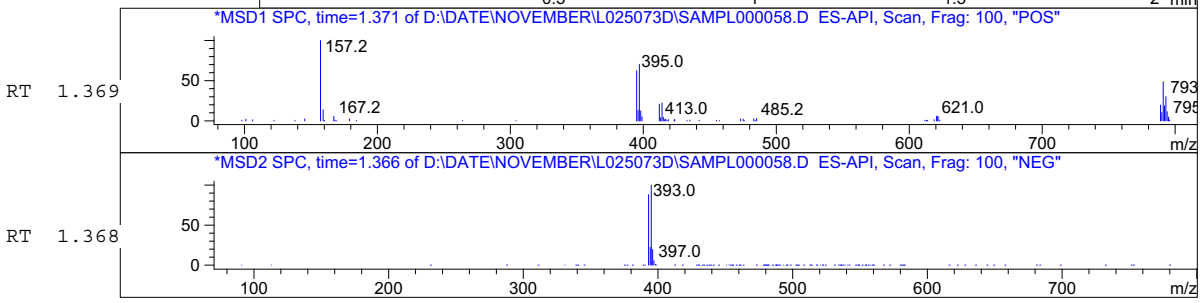

International Journal of Research in Engineering and Innovation (IJREI)
journal home page: http://www.ijrei.com
ISSN (Online): 2456-6934

Thermodynamic (Energy-Exergy) analysis of combined cycle gas turbine power plant (CCGT) for improving its thermal performances

Dr. R.S Mishra, Amit Singh

Department of Mechanical, Production & Industrial and Automobile Engineering, Delhi Technological University, delhi-110042

Abstract

The objective of the presented work is to develop a Thermodynamic optimization method in order to optimize the efficiency of a combined cycle gas turbine (CCGT) power plant and suggest ways of improving the efficiency.
The Thermodynamic analysis provides a complete diagnosis of the performance of the combined cycle power plant, both in energetic and in exergetic terms. The system considered in this thesis is a combined cycle power plant which couples the two power cycles, Brayton cycle (gas turbine), Rankine cycle (steam turbine). There are various ways in which the efficiency of both cycle individually can be improved. But when couple together optimization is different thing because improving efficiency of one cycle can adversely affect the efficiency of other cycle and of combined cycle gas turbine. By using thermodynamic analysis, parametric study is done in this work to find the optimum parameter at which efficiency of system is maximum. A program of numerical code is established using EES (Engineering Equation Solver) software to perform the calculations required for the thermodynamic analysis considering real variation ranges of the main operating parameters such as pressure, temperature, pressure ratio. The effects of theses parameters on the system performances are investigated. Parametric study has been performed using combined first and second law approach to investigate the effects of compressor air inlet temperature and pressure of steam on first and second law efficiency, exergy destruction in the system components.
© 2017 ijrei.com. All rights reserved
Keywords: Combined Cycle Gas Turbine, Energy-Exergy Analysis, First and second law analysis, Performance improvement

1. Introduction

The drastic change in living standards of people in the last sixty years, has resulted in huge demand for electricity (power). Though there is high growth in power output, but there is always a gap in the demand and supply. Optimization of energy conversion systems becomes more important due to limits of fossil fuels and the environmental impact during their use. To achieve above we need an innovative technology which has higher efficiency than the present one and also environment friendly. Conventional power engines have lower efficiencies. To improve the efficiency, one innovative technology "combined cycle gas turbine" is used nowadays.

1.1 Combined Cycle Gas Turbine Technology

The continuous effort to increase thermal efficiencies of power plants have resulted in innovative modification to existed power plants. One such modification is combined gas-vapor cycle. A combined cycle power plant unites 2 power cycles such that the heat rejected (waste energy) by heat transfer from top cycle can be utilize as the input source for the bottom cycle. This discharged energy is utilized in many ways such as cogeneration, organic Rankine cycle, kalian cycle etc. Popular combined cycle system is gas-vapor power cycle.
Brayton cycle typically works at high temperatures than Rankine cycle. The steam temperature at turbine entry can be about 600˚C for steam turbine but it is over 1450˚C for gas turbine. Due to recent advance technologies such as recent innovation in cooling turbine blades and high temperature resistant coating of the blades. To obtain higher thermal efficiency, heat is supplied at high temperature. However, gas turbine cycle has one drawback: the exhaust gas has high temperature usually above 520˚C, which is a waste energy for gas turbine power plant. It makes engineering sense to utilize this energy as the input source for steam cycle. The energy is

Corresponding Author: R.S. Mishra
Email Id: rsmishra@dce.ac.in

utilized from flue gases to generate steam in HRSG which serve as boiler.

1.2 Combined-Cycle Gas Turbine Features [1]

The gas turbine uses high temperature gas at entry and discharges thermal energy at sufficient high temperature which is generally used as the input source for the bottom steam Cycle. Combined cycle systems is used in practical application because of

1. High first law efficiency
2. Heat rejection from topping cycle at a sufficient high temperature
3. Working fluids are easily available.

Combined cycle systems have attractive features such as,

1.2.1 High Thermal Efficiency

Thermal efficiency of combined cycle system is higher than any other existing power systems

1.2.2 Low installation cost

Combined cycle equipment are available in market. So installation time and cost are low comparatively.

1.2.3 Environmental compatibility- Innovation

In combustion process also means that the harmful effect of exhaust gases can be controlled effectively. Carbon dioxide and nitric oxide discharge can be minimized when plants are fired with methane.

1.2.4 Fuel flexibility

A wide variety of fuel such as natural gas, methane, distillate oil fuel can be utilized efficiently in combined cycle power plants.

1.2.5 Rapid start-up

It allows rapid start-up, short shut-down time, and fast and efficient adjustment to varying load condition.

1.2.6 Short construction time

The top cycle (gas turbine) allows combined cycle power plant to be compact, which minimizes the construction period about two- years.

1.2.7 Less staff and space requirement

Combined cycle gas turbine plants are developed on a modular basis, which requires comparatively lesser staff.

1.2.8 High Reliability/Availability

High reliability operation results are possible due to innovative design and development of components of power plants.

1.3 Thermodynamic description

A combined cycle system couples 2 power cycles, gas turbine and steam turbine. It has three main parts.

a. Brayton cycle (topping cycle)
b. HRSG (heat exchanger)
c. Rankine cycle (bottoming cycle)

1.3.1 Brayton cycle (Topping Cycle) [2]

Brayton cycle is used in gas turbine.

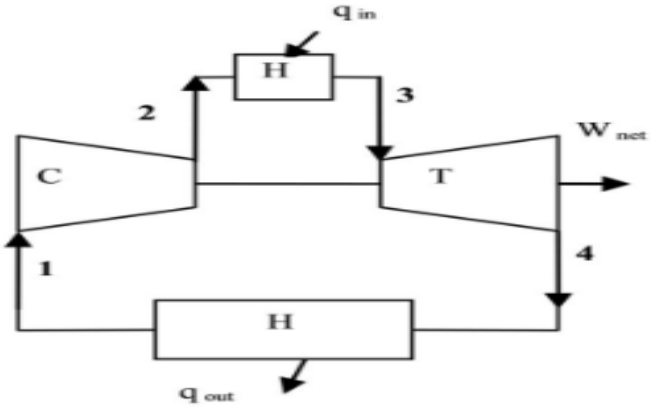

Figure 1. A closed cycle gas turbine [2]

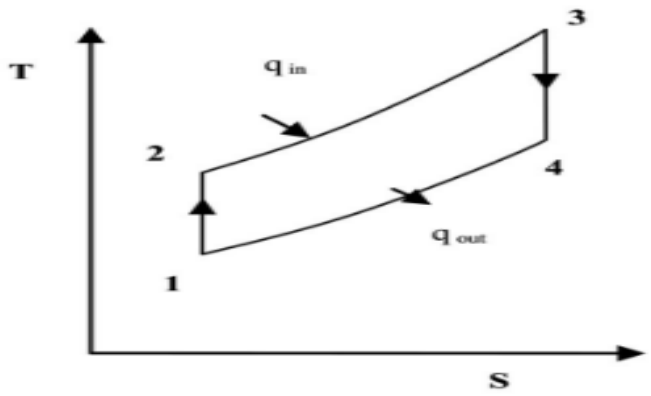

Figure 2: T-s diagram of Brayton cycle [2]

The following efforts are made to improve the Brayton cycle efficiency

1.3.1.1 Increasing the turbine inlet temperature

This method is in practice to improve efficiency. But we can only increase temperature to a certain point. The turbine inlet temperature has increased from 500 ˚C (in 1940's) to 1400 ˚C. This increase was possible by innovative techniques and new material (high temperature resistant). Steam injection method allowed an increase in TIT by 100 ˚C.

1.3.1.2 Increasing the efficiency of component

The improved efficiency of turbine and compressor resulted in increase in the first law efficiency.

1.3.1.3 Improvise to the basic cycle

Simple cycle efficiency can be practically increase (doubled) by incorporating modification such as intercooling, regeneration and reheating.
The work output of can be improved (increase) by decreasing the work consumed by compressor. By using multistage compressor with intercooler, compressor work can be decreased. Work output of gas turbine can be improved (increase) by reheating. This idea is based on simple principal that the work in flow process is proportional to specific volume of gas so this should be minimum as possible in case of compressor and high as in case of turbine.

1.3.2 Rankine Cycle (Bottoming Cycle) [2]

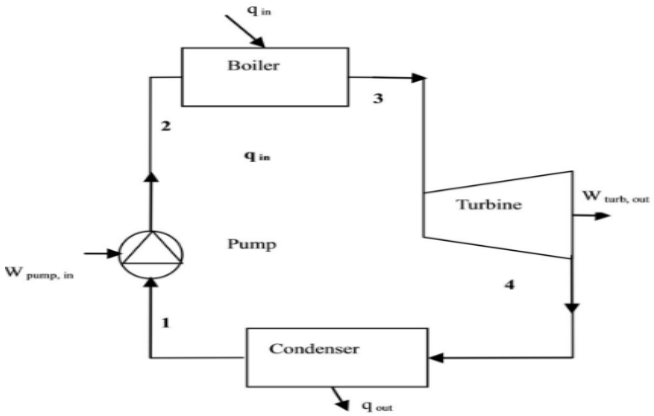

Figure 3: Simple Rankine cycle [2]

Steam power plants (Rankine cycle) generate the huge power in India even a minute improvement in plant efficiency can be beneficial (less fuel consumption).
The following methods are used to improve the Rankine cycle efficiency

1. Lowering the condenser pressure: Before entering the condenser, working fluid is in mix state (steam and water). By lowering the condenser pressure automatically decreases temperature for heat rejection.
2. Superheating the steam (constant pressure) to high temperature: mean temperature of heat addition is increased by this method without increasing the boiler pressure.
3. Increasing pressure (in boiler): by increasing the working pressure of steam, average temperature of heat addition can be increased.
4. Regenerative Rankine cycle: ideal regeneration is not practical. A practical process is achieved in plants by extracting working fluid from turbine at various points. By regeneration average temperature of heat addition can be increased.

1.3.3 Heat recovery steam generator (HRSG)

HRSG provides thermodynamic bridge between topping (gas turbine) and bottoming (steam turbine) in combined cycle gas turbine. Exhaust gases of gas turbine carry huge energy. HRSG is used to utilize this energy. HRSG is heat exchanger and used to generate steam.

2. Literature Review

Combined cycle Gas turbine cogeneration is an extensive area of research, in which several researchers have already made some mark and several others are indulging themselves in this direction. Furthermore, the optimization can be analyzed from a thermodynamic point of view, according to the first and/or second law analysis (Ahmadi and Dincer [3], Boyano et al [4] and Petrakopoulou et al [5]). From the point of view of optimization methodology, there are many types of analyses. In this work, the review will highlight most common methodology: the exergy destruction method. Literature survey for the project is enlisted below.

2.1. Review of Analysis of Gas turbine

2.1.1 Thermodynamic Analysis and Optimization

The gas turbine operating parameters which influence the combined cycle gas turbine performance are; ambient conditions, compressor pressure ratio, and turbine inlet temperature.
One of the factors that affect gas turbine performance is the ambient conditions, mainly ambient temperature, atmospheric pressure, and the relative humidity of air. These parameters affect the generated electric power and the heat-rate during operation. The location of power plant plays a major role on its performance. The atmospheric air, which enters the compressor, becomes hotter after compression and it is directed to a combustion chamber. Several authors reported the effect of ambient temperature: Arora and Rai [6], Ibrahim et al [7], Ameri and Hejazi [8], Boonnasa et al [9] and Hosseini et al [10].
Arora and Rai [6] shows the plant consists of a compressor, combustor, gas turbine, waste heat recovery boiler, steam turbine, and generator(s). The input temperature to a steam turbine is about 540°C and the exhaust can be maintained at the atmospheric pressure, due to design consideration the input temperature is limited and the efficiency of the about 40%. The input temperature of the gas turbine can be as high as 1100°C but the exhaust temperature can be lowered to about 500-600°C, the efficiency of a gas turbine is about 33%. It can be seen that to obtain higher efficiencies the exhaust of the gas turbine can used to drive the steam turbine giving efficiency up to 60%.

Ameri and Hejazi [8] observed that the variation in the ambient temperature causes a loss of 20% of the rated capacity of the 170 gas turbine units in Iran. They studied five gas turbines, where the difference between the ambient temperature and the ISO conditions was on average 11.8 °C. They found that for each 1 °C increase in ambient temperature, the power output was decreased by 0.74%, and they suggested cooling the compressor's intake-air temperature to improve the gas turbine cycle efficiency.
Hosseini et al [10] indicated that the gas turbine compressor is designed for constant air volume flow, which makes the electric power output dependent on the ambient temperature through the specific mass flow rate. They added that the increase in the ambient temperature also decreases the compressor's output pressure, which reduces the gas turbine cycle efficiency, while the increase in the air density reduces the gas turbine's heat rate and increases its specific fuel consumption. They stated that for each 1°C increase in the ambient air temperature, the electric power output of the gas turbine decreases by 0.5% to 0.9%, and by 0.27% for a combined cycle.

2.1.2 Effect of Compressor Pressure Ratio

The properties of air entering combustion chamber depend upon the compressor pressure ratio studied by: Ibrahim et al [7], Ibrahim and Rahman [11], and Khaliq and Kaushik [12].
Ibrahim and Rahman [11] performed a parametric thermodynamic analysis of a combined cycle gas turbine. They investigated the effect of operating parameters, compression ratio, gas-turbine peak temperature ratio, isentropic compressor and efficiency and air fuel ratio on the overall plant performance. Their results show that the compression ratios, air to fuel ratio as well as the isentropic efficiencies are strongly influenced by the overall thermal efficiency of the combined cycle gas turbine power plant. The overall thermal efficiency increases with compression ratio. However, the variation of overall thermal efficiency is minor at the lower compression ratio while it is very significant at the higher compression ratio for both isentropic compressor and turbine efficiency. The overall efficiencies for combined cycle gas turbine are much higher than the efficiencies of gas turbine plants. Efficiency quoted range is about 61%. In addition, the overall thermal efficiency increases and total power output decreases linearly with the increase of the compression ratio with constant turbine inlet temperature. The peak overall efficiency occurs at the higher compression ratio with the higher cycle peak temperature ratio as well as higher isentropic compressor and turbine efficiencies.

2.1.3 Effect of Turbine Inlet Temperature

The turbine inlet temperature (TIT) plays an important role on the performance of combined cycle. The maximum value of TIT is fixed due to the metallurgical problem of turbine blade cooling. Research in this area was done by:

Sanjay [13] observed that the parameter that affects cycle performance most is the turbine inlet temperature (TIT). The TIT should be kept on the higher side, because at lower values, the exergy destruction is higher.
Khaliq and Kaushik [12] and Khaliq [14] reported in their detailed analyses that the exergy destruction in the combustion chamber increases with the cycle temperature ratio, and the second-law efficiency of the primary combustor behaves in reverse from the second-law analysis. Increasing the maximum cycle temperature gives a significant improvement in both efficiency and specific work-output. The study also concludes that the efficiency reduces rapidly with a reduction in the TIT.

2.2 Review of Analysis and Optimization of Bottoming Cycle

2.2.1 Thermodynamic Analysis and Optimization

The efficiency of steam power plants can be improved by increasing the live steam and reheat-steam parameters, and by introducing high-efficiency, low-loss turbine blade geometries. The first goal, to increase the steam parameters, is primarily achieved by choosing appropriate materials for the components operating under live-steam and reheat-steam conditions while retaining the proven designs. Collaborative European programs have led to the development and qualification of steels with much improved creep properties at temperatures of up to 600 °C, appropriate for the manufacture of key components. At the same time, optimization of the blade profiles and geometries allowed further major improvements in operating efficiency. The achievable improvements in efficiency is about 0.5% per 10 °C live steam and reheat (RH) temperature increase, and 0.2 % per 10 bar pressure increase. Second important part of the bottoming cycle is the heat recovery steam turbine (HRSG), its design and optimization affects to a large extent influence the efficiency and the cost of the whole plant.
Mohagheghi and Shayegan [16], performed the thermodynamic optimization of design variables and heat exchangers layout in a heat recovery steam generator HRSG for combined cycle gas turbine CCGT using a genetic algorithm. Their method was introduced for modelling the steam cycle in advanced combined cycles by organizing the non-linear equations and their simultaneous used solutions with numerical methods. In addition to the optimization of design variables of the recovery boiler, they performed the distribution of heat exchangers among different sections and optimized their layouts in HRSGs. A standard gas turbine was assumed, and then outlet gas stream conditions (mass flow rate, temperature, and chemical composition of gas stream) were considered as the inlet parameters for the recovery boiler model. From the optimization process maximum output power from a steam cycle for different HRSGs was then analyzed.
Bracco and Silvia [17] studied a combined cycle power plant with a single level heat recovery steam generator HRSG. They developed a mathematical model to determine the optimal steam pressure values in the HRSG according to different objective functions (in the HRSG for a given gas turbine).

Their work reports numerical results for the combined cycle power plant considering four different gas turbines. The optimization approach was focused on the study of the heat transfer between the steam and the exhaust gas in the HRSG, based on an exergetic analysis. They present the comparison among different objective functions that refer to the HRSG specifically or to the whole bottoming cycle. In their mathematical model, they considered the presence of specific constraints for the operating parameters of the power plant, the most important constraints that were considered refer to the steam quality at the turbine outlet, the HRSG outlet exhaust gas temperature and the steam turbine blade height. In their work, a parametric analysis was also performed to evaluate the influence of the gas temperature at the HRSG inlet and the pinch point temperature difference on the considered objective functions.

Woudstra et al [18] performed the thermodynamic evaluation of combined cycle plants with the same gas turbine and different steam bottoming cycles. The evaluation showed that the increasing the number of pressure levels of steam generation will reduce the losses due to heat transfer in the HRSG, but also the exergy loss due to the exhaust of flue gas to the stack. Among the investigated configurations for bottoming cycle, triple pressure reheat was the best option from exergy point of view.

Mansouri et al [19] investigated the effect of pressure levels of steam generation at heat recovery steam generator HRSG on the energetic and exergetic efficiency of HRSG, bottoming cycle and combined cycle power plants, as well as the effect of HRSG (heat recovery steam generator) pressure levels on exergy destruction at HRSG and other main components of the bottoming cycle. Their result show that an increase in pressure levels of steam generation at HRSG leads to an increase in the exergy efficiency of HRSG and CCPP increase respectively. In addition, an increase in pressure levels at HRSG decreases the exergy destruction due to heat transfer in HRSG: the exergetic efficiency of HRSG increases with an increase in pressure levels of steam generation and adding reheat to the cycle.

Tyagi and Khan [20] studied the effects of gas turbine exhaust temperature, stack temperature and ambient temperature on the overall efficiency of combine cycle power plant keeping the gas turbine efficiency as well as steam turbine efficiency constant. They concluded that the stack temperature should be minimum and gas turbine exhaust temperature should be maximum. Out of these three variables i.e. turbine exhaust temperature, stack temperature and ambient temperature, the dominating factor of increasing the overall efficiency of the combine cycle power plant is the stack temperature. *Valdés et al [21]* showed a possible way to achieve a thermo economic optimization of combined cycle gas turbine power plants. The optimization was done by using a genetic algorithm, tuned by applying it to a single pressure CCGT power plant. Once tuned, the optimization algorithm was used to evaluate more complex plants, with two and three pressure levels in the heat recovery steam generator. The variables considered for the optimization were the thermodynamic parameters that established the configuration of the HRSG. Two different objective functions were proposed: one minimizes the cost of production per unit of output and the other maximizes the annual cash flow. The results obtained with both functions were compared in order to find the better optimization strategy. The results show that it is possible to find an optimum for each design parameter. This optimum depends on the selected optimization strategy.

Bassily[22] presented the effects of varying the inlet temperature of the gas turbine and PP on the performance of a dual pressure reheat combined cycle. He also modeled some feasible techniques to reduce the irreversibility of the HRSG of both cycles, and showed that optimizing or reducing the irreversibility of these cycles could increase their efficiencies by 2–3%. Applying gas reheat increases the generated power and average temperature at which heat is supplied, whereas applying gas recuperation takes advantage of the increased gas temperature at the outlet of the GT to enhance cycle efficiency. For gas-reheat gas-recuperated combined cycles, recuperated heat exchangers fabricated from stainless steel have to be used to withstand these conditions. He compared the optimized results with the regularly designed triple pressure reheat combined cycle.

Boonnasa et al [23] studied the performance improvement of an existing combined cycle power plant located in Bangkok that consisted of two gas turbines (110.76MW each), and one 115.14MW steam turbine in ISO conditions. The plant used an absorption chiller to cool one of the two gas turbine's intake-air to 15°C, in addition to having a thermal energy storage tank that stored the sensible heat of the chilled water to meet the varying daily cooling load. Low-pressure steam from a heat recovery steam generator was used to drive the absorption chiller needed to meet a maximum load of 7049.58kW with the help of the thermal heat storage. As a result, the power output of the cooled gas turbine increased by 10%, improving the CCPP total power output by 6.24%. Economically, the study found that due to the low initial investment cost of retrofitting the absorption chiller the internal rate of return was 40%, and the payback period was just 3.81 years. However, the authors also reported a reduction by 2.85% in the steam turbine power output, which was due to powering the absorption chiller directly from the HRSG unit steam that was powering the steam turbine. This reduction in the steam turbine power output could have been avoided if they had used a boiler that utilized the waste heat energy from the stack after the HRSG unit.

Ahmet Cihan et al [24] studied the energy and exergy fluxes at the inlet and the exit of the devices in one of the power plant main units and calculate the energy and exergy losses. He found out that highest energy loss occurs at chimney. In addition, energy losses of 18.94 and 18.98% take place at the condenser and the cooling tower, respectively.

2.3 Conclusions of Literature Review

The researchers in the field of combined cycle gas turbine system have already delivered a vast variety of work. However, the possibility of improving the domain of work is still there by combining different methods and methodologies

for enhancing the performance of the system. The main conclusions from the Literature review are pointed below-

- Exergy analysis of combined cycle gas turbine system has been performed by various researchers based on first and second law of thermodynamics in which exergy destruction in each and every component of the system has been calculated when it is operated at part and full load conditions. Opportunities are available to analyze different combined cycle gas turbine system viz. simple cycle, combined cycle gas turbine system with alternative bottoming cycle, and combined cycle gas turbine system with VARS based on the same input parameters, to analyze the superiority of any particular method in power generation, economy and environmental issues.
- Simulation and dynamic modelling of combined cycle gas turbine-based plants consisting of a gas turbine, heat recovery steam generator and steam turbine has been worked out.
- The concept of reheat has been applied in evaluating thermodynamic performance of combustion gas turbine cogeneration system.
- Individual effect of reheat and intercooling after system modification has been studied by the simulation of the power generation system.
- First and Second law analysis have been performed by various researcher.

2.4 Objectives of the Present Research Work

- To analyze and design combined cycle gas turbine system integrated with reheat and intercooling in topping cycle and reheat in bottom cycle.
- To develop formulation of various components of combined cycle gas turbine system by combined first and second law analysis.
- To develop a computer based design methodology for a modified combined cycle gas turbine system.
- To perform a parametric study for wide range of variables such as compressor air inlet temperature, compressor pressure ratio, turbine inlet temperature, regenerator effectiveness etc.

The effect of these parameters on first law efficiency or fuel utilization efficiency, second law efficiency or exergetic efficiency, specific fuel consumption, power to heat ratio etc. has been studied. Exergy destruction in each and every component of gas turbine and steam turbine system has been calculated.

3. Thermodynamic analysis and formulation of combined cycle gas turbine

3.1 Combined Cycle Gas Turbine System Description

A simple combined cycle gas turbine is shown. This consist all basic components. Air at atmospheric condition is passed through compressor where the air is compressed to high pressure. After compressor it enters to combustor where the fuel is supplied and combustion starts. Due to combustion temperature of the mixture increases. Hot gases from combustion chamber is then passed through gas turbine where energy from hot gases is extracted by turbine. Flue gases from gas turbine is then passed through heat exchanger where energy from hot gases is supplied to water. Generated steam is passed through steam turbine where they expand and produce the work output (alternator to generate electricity). After steam turbine steam is passed through condenser where steam loses its heat and gets converted into water.

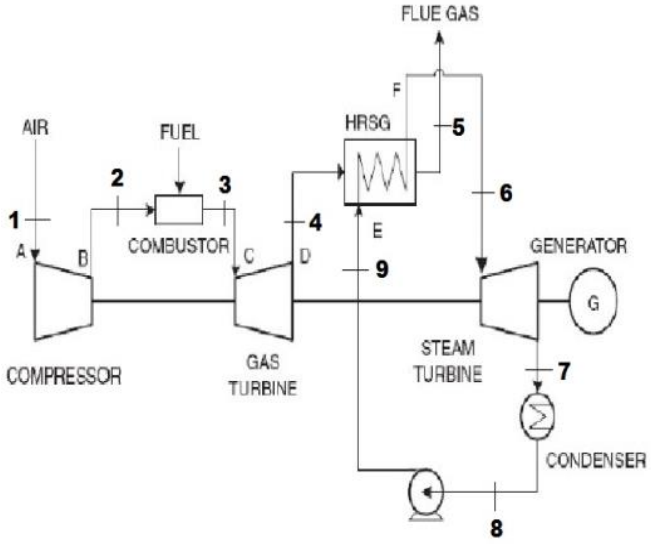

Figure 4: Simple combined cycle gas turbine

Table 1 Description of different states corresponding to fig-4.

Points	Description
1	Entry to compressor
2	Compressor exit
3	gas turbine inlet
4	gas turbine outlet or inlet HRSG
5	HRSG outlet(mixture)
6	HRSG outlet(steam) or steam turbine inlet
7	steam turbine exit
8	condenser outlet or pump inlet
9	pump inlet or inlet HRSG(water)

In this research work, modified combined cycle gas turbine is analyzed which is shown in figure. System consist intercooled and reheat gas turbine with dual pressure HRSG and reheat steam turbine.

Table 2 description of points corresponding to fig.4

State points	Description
	Gas turbine
1	Compressor(A) entry
2	Compressor(A) exit
3	Compressor(B) inlet or intercooler outlet

4	Compressor(B) outlet or combustion chamber inlet
5	Gas turbine(A) inlet or combustion chamber outlet
6	Gas turbine(A) outlet or reheater inlet
7	Gas turbine(B) inlet or reheater outlet
8	Gas turbine(B) outlet or HRSG inlet
9	HRSG outlet
	Steam turbine
10	Steam turbine(A) inlet
11	Steam turbine(A) outlet
12	Steam turbine(B) inlet
13	Condenser inlet
14	Pump inlet
15	HRSG inlet

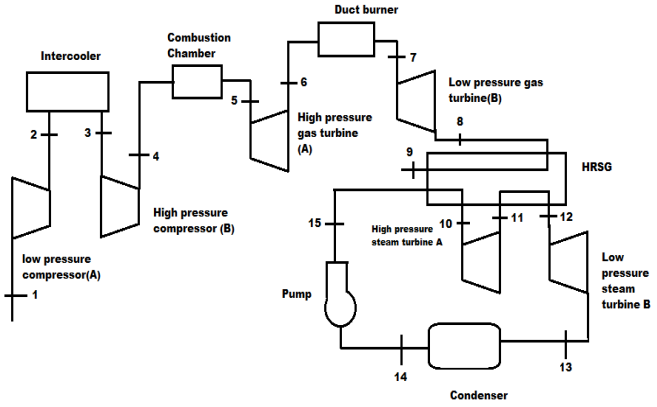

Figure 5: Combined cycle gas turbine (in present analysis)

3.2 Mathematical Formulation

The mathematical formulation of present analysis of CCGT is based on following assumptions.

1. Combined cycle gas turbine operates at steady state.
2. Ideal gas laws are applied to the air and the combustion products.
3. The fuel is taken as methane and taken as an ideal gas.
4. The combustion process in the CC (combustion chamber) is complete and N2 is assumed as inert gas.
5. Pressure drop in various component is neglected.
6. HRSG taken is dual pressure.

The thermodynamic analysis of the proposed combined cycle system has been carried out using equation of mass energy and exergy balance.
For a particular component, a set of governing equations are as follows
Mass rate balance

$$\sum_k \dot{m}_{i,k} = \sum_e \dot{m}_{e,k}$$

Energy rate balance

$$\dot{Q}_{cv,k} - \dot{W}_{cv,k} = \sum_e \dot{m}_{e,k} h_{e,k} + \sum_i \dot{m}_{i,k} h_{i,k}$$

Exergy rate balance

$$\dot{E}_{D,k} = \sum \dot{E}_{q,k} - \dot{W}_{cv,k} + \sum_i \dot{E}_{i,k} - \sum_e \dot{E}_{e,k}$$

3.2.1 Thermodynamic Analysis of Low Pressure Compressor A

Air enters the compressor at point 1. Point 1represents inlet of compressor A. In compressor air is compressed to point 2. Work done in compressor is given by,
$\dot{W}_{c,A} = \dot{m}_a(h_2-h_1)$
Where $\dot{m}_a$ is mass flow rate of air and (h_2-h_1) specific enthalpy difference between states 1 and 2. The value of specific enthalpy h_2 can be evaluated using the compression isentropic efficiency. Solving the expression for compression for compressor isentropic efficiency

$$\eta_c = \frac{h_{2s}-h_1}{h_2-h_1}$$

Where η_c isentropic efficiency of compressor, $h_1$and h_2 is are enthalpies of air at state 1 and 2 is the isentropic enthalpy at compressor exit.

Physical Exergy at point 1

$\dot{E}_{x,1} = \dot{m}_a*((h_1-h_0)-T_0*(s_1-s_0))$

Physical Exergy at point 2

$\dot{E}_{x,2} = \dot{m}_a*((h_2-h_0)-T_0*(s_2-s_0))$

Exergy destruction rate in low pressure compressor can be given by

$\dot{E}_{D,\text{ compressor A}} = (\dot{E}_{x,1} - \dot{E}_{x,2}) + \dot{W}_{c,A}$

Where $\dot{E}_{D,k}$ represents the exergy destruction rate in k component.

3.2.2 Thermodynamic analysis of Intercooler

Intercooler is type of heat exchanger. Purpose of intercooler is to cool the hot compressed air from low pressure compressor before sending it to high pressure compressor. So that work consumed by high pressure compressor can be reduced. Heat is transferred from hot compressed air to cooling water.
Hot compressed air from compressor A is cooled to point 3 in intercooler.
From energy balance

$\dot{m}_a*(h_2-h_3) = \dot{m}_{w,ic}*(h_{w,out}-h_{w,in})$

Where $\dot{m}_{w,ic}$ represents the mass flow rate and $h_{w,out}$ and $h_{w,in}$ represents the specific enthalpy.
Exergy at point 3,
$\dot{E}_{x,3} = \dot{m}_a*((h_3-h_0)-T_0*(s_3-s_0))$
Exergy at cooling water inlet,
$\dot{E}_{x,w,in} = \dot{m}_{w,ic}*((h_{w,in}-h_0)-T_0*(s_{w,in}-s_0))$

Exergy rate at cooling water outlet,
$\dot{E}_{x,w,out} = \dot{m}_{w,ic}*((h_{w,out}-h_0)-T_0*(s_{w,out}-s_0))$

3.2.3 *Thermodynamic analysis of high pressure Compressor B*

High pressure compressor is used to increase the overall pressure ratio. Work done in high pressure compressor is given by
$\dot{W}_{c,B} = \dot{m}_{a*}(h_4-h_3)$
value of h_4 can be evaluated from isentropic formula. Isentropic efficiency of compressor
$\eta_c=\frac{h_{4s}-h_3}{h_4-h_3}$
Physical exergy at point 4,
$\dot{E}_{x,4} = \dot{m}_a*((h_4-h_0)-T_0*(s_4-s_0))$
Exergy destruction in high pressure compressor is given by,
$\dot{E}_{D,compressorB} = (\dot{E}_{x,3}- \dot{E}_{x,4})+ \dot{W}_{c,B}$

3.2.4 *Thermodynamic analysis of Combustion chamber*

Compressed air from compressor B (at point 4) enters into combustion chamber. Fuel is added into chamber and after combustion, temperature and enthalpy of air-fuel mixture rises. From energy balance

$\dot{m}_a*h_4+ \dot{m}_{fcc}*LHV*\eta_{cc}= (\dot{m}_{a+}\dot{m}_{fcc}) *h_5$

where $\dot{m}_{fcc}$ represents the mass flow rate of fuelin cc, LHV represents the lower heating value of fuel and η_{cc}represents the efficiency of combustion chamber.
Exergy at point 5,

$\dot{E}_{x,5}= (\dot{m}_{a+}\dot{m}_{fcc})*((h_5-h_0)-T_0*(s_5-s_0))$

For gaseous fuel with composition CxHy, the following correlation is used for calculating exergy of fuel,

$\zeta = \frac{\dot{E}x,f}{LHV}$ and $\zeta = 1.033+ 0.0169\frac{y}{x} - \frac{0.0698}{x}$

Where $\dot{E}_{x,f}$ represent the exergy of fuel, Exergy destruction is given by,

$\dot{E}_{D, combustion\ chamber}= (\dot{E}_{x,4}- \dot{E}_{x,5})+ \dot{E}_{x,fcc}$

3.2.5 *Thermodynamic analysis of high pressure Gas Turbine A*

Hot compressed air from combustion chamber is expanded in high pressure gas turbine. Turbine extracts the energy from hot gases and converts it to mechanical energy. Work done by gas turbine is given by,

$\dot{W}_{GT,A} = (\dot{m}_{a+}\dot{m}_{fcc})*(h_5-h_6)$
Isentropic efficiency of turbine,

$\eta_T=\frac{h_5-h_6}{h_5-h_{6s}}$
Physical exergy at point 6,
$\dot{E}_{x,6}= (\dot{m}_{a+}\dot{m}_{fcc})*((h_6-h_0)-T_0*(s_6-s_0))$
Exergy destruction in high pressure gas turbine is given by,
$\dot{E}_{D,gasturbineA} = (\dot{E}_{x,5}- \dot{E}_{x,6})- \dot{W}_{GT,A}$

3.2.6 *Thermodynamic analysis of Duct Burner*

After expansion from high pressure gas turbine A, low temperature combustion gases enter into reheater (duct burner) where fuel is added into chamber and after combustion hot combustion gases exit at point 7.
From energy balance,
$(\dot{m}_{a+}\dot{m}_{fcc})*h_6+ \dot{m}_{fdb}*LHV*\eta_{rh}= (\dot{m}_{a+}\dot{m}_{fcc}+ \dot{m}_{fdb})*h_7$
Where $\dot{m}_{fdb}$ represents the mass flow rate in duct burner.
Physical exergy at point 7,
$\dot{E}_{x,7}= (\dot{m}_{a+}\dot{m}_{fcc}+ \dot{m}_{fdb})*((h_7-h_0)-T_0*(s_7-s_0))$
Exergy destruction in duct burner is given by,
$\dot{E}_{D,ductburner}= (\dot{E}_{x,6}- \dot{E}_{x,7})+ \dot{E}_{x,fdb}$

3.2.7 *Thermodynamic analysis of low pressure Gas turbine B*

After duct burner (point 7), hot flue gases expand through gas turbine B where energy is extracted by turbine and flue gases exit at point 8. Work done by gas turbine is given by

$\dot{W}_{GT,B} = (\dot{m}_{a+}\dot{m}_{fcc}+ \dot{m}_{frh})*(h_7-h_8)$

Isentropic efficiency of turbine,

$\eta_T=\frac{h_7-h_8}{h_7-h_{8s}}$

Physical Exergy at point 8,

$\dot{E}_{x,8}= (\dot{m}_{a+}\dot{m}_{fcc}+ \dot{m}_{frh})*((h_8-h_0)-T_0*(s_8-s_0))$

Where $\dot{m}_{frh}$represent the mass flow rate of fuel in duct burner.
Exergy destruction in low pressure gas turbine B,
$\dot{E}_{D,gasturbineB} = (\dot{E}_{x,7}- \dot{E}_{x,8})- \dot{W}_{GT,B}$

3.2.8 *Heat Recovery Steam Generator*

.
From energy balance,
$(\dot{m}_{a+}\dot{m}_{fcc}+ \dot{m}_{frh})*(h_8-h_9)= \dot{m}_v*(h_{10}-h_{15}+h_{12}-h_{11})$
Where $\dot{m}_v$ represents the mass flow rate of steam.
Physical Exergy at point 9,

$\dot{E}_{x,9}= (\dot{m}_{a+}\dot{m}_{fcc}+ \dot{m}_{frh})*((h_9-h_0)-T_0*(s_9-s_0))$

Exergy destruction in heat recovery steam generator is given by,
$\dot{E}_{D,HRSG} = \dot{E}_{x,8} + \dot{E}_{x,15} + \dot{E}_{x,11}- \dot{E}_{x,9}- \dot{E}_{x,10}- \dot{E}_{x,12}$

3.2.9 *Thermodynamic analysis of high pressure Steam Turbine A*

High pressure and pressure steam is expanded through high pressure steam turbine A where turbine extracts the energy from steam and produces mechanical work. Work done by turbine is given by,

$\dot{W}_{ST,A} = (\dot{m}_v)*(h_{10}-h_{11})$

Isentropic efficiency of turbine is given by,

$\eta_T=\frac{h_{10}-h_{11}}{h_{10}-h_{11s}}$

Physical exergy at point 10,

$\dot{E}_{x,10}= (\dot{m}_v)*((h_{10}-h_0)-T_0*(s_{10}-s_0))$

Physical exergy at point 11,

$\dot{E}_{x,11}= (\dot{m}_v)*((h_{11}-h_0)-T_0*(s_{11}-s_0))$

Exergy destruction in high pressure turbine is given by,

$\dot{E}_{D,steamturbineA} = (\dot{E}_{x,10}- \dot{E}_{x,11})- \dot{W}_{ST,A}$

3.2.10 Thermodynamic analysis of low pressure Steam Turbine B

Low temperature steam from exhaust of high pressure steam turbine is reheated in heat recovery steam generator to high temperature. This high temperature steam is expanded in low pressure steam turbine. Work done in steam turbine is given by,

$\dot{W}_{ST,B} = (\dot{m}_v)*(h_{12}-h_{13})$

Isentropic efficiency of turbine is given by,

$\eta_T=\frac{h_{12}-h_{13}}{h_{12}-h_{13s}}$

Physical exergy at point 12,

$\dot{E}_{x,12}= (\dot{m}_v)*((h_{12}-h_0)-T_0*(s_{12}-s_0))$

Physical exergy at point 13,

$\dot{E}_{x,13}= (\dot{m}_v)*((h_{13}-h_0)-T_0*(s_{13}-s_0))$

Exergy destruction in low pressure steam turbine,

$\dot{E}_{D,steamturbineB} = (\dot{E}_{x,12}- \dot{E}_{x,13})- \dot{W}_{ST,B}$

3.2.11 Thermodynamic analysis of Condenser

Condenser is a type of heat exchanger. After expansion, steam is passed through condenser where heat is transferred from steam to cooling water which flows around condenser and steam is condensed to water.

From energy balance.

$(\dot{m}_v)*(h_{13}-h_{14})= \dot{m}_{w,cond}*(h_{w,out}-h_{w,in})$

Where $\dot{m}_{w,cond}$ represents the mass flow rate of cooling water around condenser.

Physical exergy at point 14,

$\dot{E}_{x,14}= (\dot{m}_v)*((h_{14}-h_0)-T_0*(s_{14}-s_0))$

Physical exergy at point of cooling water in,

$\dot{E}_{x,w,in}= \dot{m}_{w,cond}*((h_{w,in}-h_0)-T_0*(s_{w,in}-s_0))$

Physical exergy at point cooling water out,

$\dot{E}_{x,w,out}= \dot{m}_{w,cond}*((h_{w,out}-h_0)-T_0*(s_{w,out}-s_0))$

Exergy destruction in condenser,

$\dot{E}_{D,condenser} = (\dot{E}_{x,13}- \dot{E}_{x,14})+(\dot{E}_{x,w,in} -\dot{E}_{x,w,out})$

3.2.12 Thermodynamic analysis of pump

Pump is used to pump condensed water from condenser.to operating pressure. Work done in pump is given by,

$\dot{W}_P = \dot{m}_{v*}(h_{15}-h_{14})$

Value of h_{15} can be evaluated from isentropic formula.

Isentropic efficiency of pump

$\eta_p=\frac{h_{15s}-h_{14}}{h_{15}-h_{14}}$

Physical exergy at point 15,

$\dot{E}_{x,15}= (\dot{m}_v)*((h_{15}-h_0)-T_0*(s_{15}-s_0))$

Exergy destruction in pump is given by,

$\dot{E}_{D,pump} = (\dot{E}_{x,14}- \dot{E}_{x,15})+ \dot{W}_P$

Net work output of combined cycle gas turbine is given by,

$\dot{W}_{net}= \dot{W}_{GT,A}+ \dot{W}_{GT,B}+ \dot{W}_{ST,A}+ \dot{W}_{ST,B}- \dot{W}_{C,A}- \dot{W}_{C,B}- \dot{W}_P$

3.3 Performance Parameters

The relevant parameters required for the thermodynamic analysis of COMBINED CYCLE gas turbine cogeneration system are summarized below:

By first law efficiency,

$$\eta_I= \frac{\dot{W}net}{(Total\ Heat\ Supplied\ By\ Fuel)}$$

Second law efficiency

It is also called exergetic efficiency (effectiveness or rational efficiency). By definition,

$$\eta_{II}= \frac{\dot{W}net}{(Total\ Exergy\ Supplied\ By\ Fuel)}$$

4. Simulation Studies and Results

This chapter describes the formulation of combined cycle gas turbine system. Based upon this formulation, solution methodology, model validation, comparison of results and discussions are given below.

4.1 Solution Methodology

The structure of computer program consists of different equations written in EES (Engineering Equation Solver) software to calculate wide range of output parameters required. These parameters have been used to perform energy and exergy analysis of different components of the system. Different properties (fuel, air, combustion products etc.) are inbuilt in EES software which has been used directly in calculation. One of the most interesting features of EES is that it can solve the problem iteratively in less time and the solution of required output parameters appears in the solution window. The main condition of solving any problem is that the number of equations should be equal to number of unknowns.

4.2 Model Validation

Initially, the computer program developed for cogeneration system has been validated with the system given in ref. The various components of the combined cycle gas turbine system are shown. In this system, there is no modification of in any of both cycle.

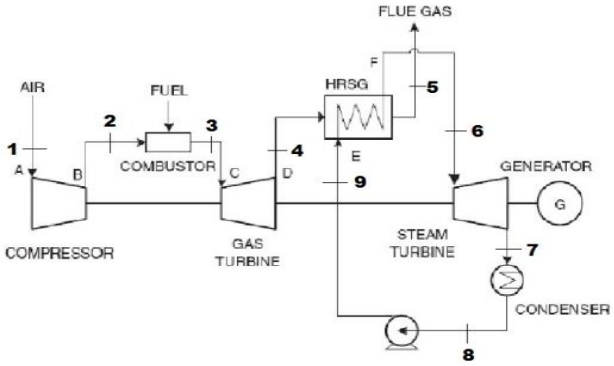

Figure 6: Simple Combined Cycle Gas Turbine System

Table 3: Input data for analysis of simple combined cycle gas turbine system

Air inlet pressure to compressor, in bar	1.013
Air inlet temperature to compressor, (T_1) in K	300
Pressure ratio of compressor (r_p)	12:1
Isentropic efficiency of compressor (η_{SC}), in %	85
Exhaust pressure of combustion prod after HRSG (P_5), in bar	1.013
Pressure of steam at turbine inlet(P_9) in bar	60
Lower heating value of fuel (LHV), in kJ/kg	47140
Net power output of the plant (W_{net}), in MW	45
Steam turbine inlet temperature in K	673
Condenser pressure in kPa	8

Table 4 Results obtained from analysis of simple combined cycle system

Compressor work in kJ	37706
Gas turbine work in kJ	65908
Steam turbine work in kJ	16930
Pump work in kJ	132.8
Mass flow rate of air(in kg/s)	103.5
Mass flow rate of steam(in kg/s)	17.61
Mass flow rate of fuel(in kg/s)	1.898
First law efficiency in (%)	50.28

To improve the efficiency of above system, some modifications are done, reheat and intercooling are introduced in topping cycle while reheat also introduced in bottom cycle. Above system is shown in figure.

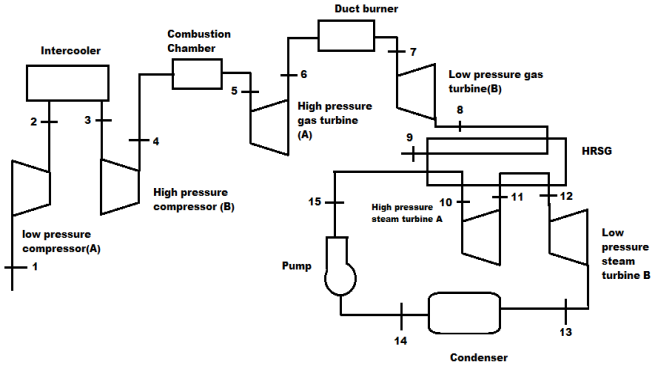

Figure 7: Modified combined cycle system

Initially a computer is developed to get starting result and later on parametric study is done to optimize the overall system

Table 5 Input data for analysis of modified combined cycle system

Air temperature at compressor(A) inlet in K	300
Pressure at compressor A inlet in bar	1.03
Pressure ratio in compressor (A)	8:1
Overall pressure ratio	60:1
Gas turbine inlet temperature in K (TIT)	1400
Gas reheat temperature in K	1400
Pressure ratio in gas turbine A	10:1
Pressure at exit of HRSG	1.03
Temperature of gas at exit of HRSG in K	370
Pressure of steam generated in HRSG in bar	120
Temperature of steam at steam turbine inlet in K	700
Steam reheat temperature in K	700
Pressure ratio in steam turbine A	10:1
Condenser pressure in bar	0.08

Table 6 Results obtained from modified combined cycle system

First law efficiency in %	55.51
Second law efficiency in %	52.85
Mass flow rate of air in kg/s	46.85
Mass flow rate of steam in kg/s	8.37
Mass flow rate of fuel in combustion chamber in kg/s	1.005

Table 7: Exergy analysis of different components of modified combined cycle system

Component	Work in kJ/s	Exergy Destruction In kJ/s	% exergy destruction	Second law efficiency in %
Compressor A	13720	1202	2.763	91.24
Compressor B	14421	1205	2.771	91.65
Gas turbine A	33979	639.4	1.47	98.15
Gas turbine B	28243	342.2	0.6878	98.8
Steam turbine A	3728	425.2	0.97	89.76
Steam turbine B	7296	1219	2.84	85.68
Pump	105.3	0.64	0.01	95.27
Intercooler		4055	9.325	98.2
Combustion chamber		18302	42.09	77.15
Duct burner		11650	26.79	81.96
HRSG		2889	6.644	88.21
Condenser		934.8	2.15	98.5
Exhaust gas		407.8	0.9378	

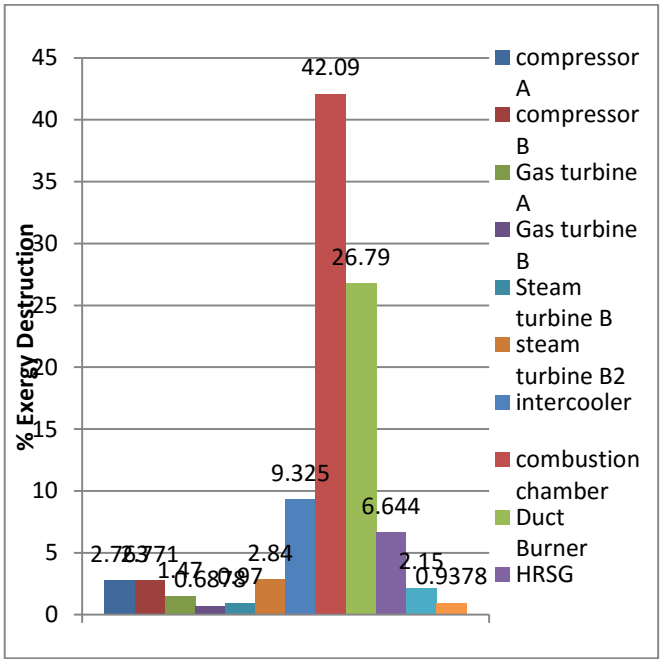

Figure 8: % Exergy destruction of total Exergy destruction in different components of simple Combined Cycle Gas Turbine System

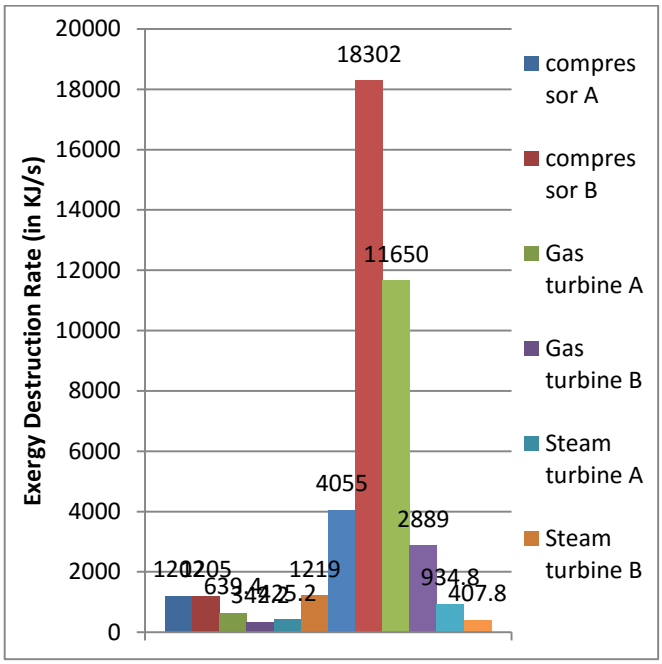

Figure 9: Exergy destruction rate in different components of Modified combined cycle system

4.3 Parametric Studies

Parametric studies are done to optimize the system in this case combined cycle gas turbine. Main purpose of this work is to improve thermal efficiency of combined cycle gas turbine system. The exergy destruction in each components of system are shown in Fig-8 and Fig-9 respectively. The effects of various parameters on the thermal efficiency are described below

4.3.1 Effect of overall pressure ratio in gas turbine (r_p) on first and second law efficiency

Fig.10 and Fig-11 illustrates the efficiency of combined cycle gas turbine power plant as the function of overall pressure ratio at various gas turbine inlet temperature (TIT). Pressure ratio is varied from 60 to 100 in step of 5 while TIT is varied from 1600 K to 1800K. It is observed that as the overall pressure ratio increases both first and second law efficiency increase. But for particular value of pressure ratio both first and second law efficiency increases with increase in TIT. Because at higher pressure ratio work done by gas turbine increases more rapidly than work consumed by compressor.

4.3.2 Effect of pressure ratio (r_{p1}) of low pressure compressor A on first and second law efficiency

Fig.12 and Fig-13 shows the effect of pressure ratio of low pressure compressor on the first and second law efficiency at various gas turbine inlet temperature (TIT). Pressure ratio is varied from 2 to 50 while TIT is varied from 1600 K to 1800. It is observed from the figures that at constant TIT as pressure ratio increases both first and second law efficiency first increase attains maximum value and then decrease. This is because at high pressure ratio, work consumed by low pressure compressor increases rapidly while work done by gas turbine is constant. Both first and second law efficiency increases with the increase in TIT at constant pressure ratio.

4.3.3 Effect of pressure ratio (r_{p3}) of high pressure Gas Turbine A on first and second law efficiency

Fig. 14 and Fig-15 illustrate the effect of pressure ratio of high pressure gas turbine on the first and second law efficiency at various gas turbine inlet temperature (TIT). Pressure ratio is varied from 2 to 50 while TIT is varied from 1600 K to 1800. It is observed from the figures that at constant TIT as pressure ratio increases both first and second law efficiency first increase then attain maximum value and then decrease. This is because as pressure ratio in high pressure gas turbine increases the temperature of exhaust gas decreases and more fuel is required in duct burner to raise the temperature of gas. Though work done by high pressure gas turbine increases but energy consumption is more and work done in low pressure gas turbine also decreases hence the efficiencies decrease.

4.3.4 Effect of Gas Turbine Inlet Temperature (TIT) on First and Second Law Efficiency

Fig. 16 and Fig.17 describe the effect of gas turbine inlet temperature (TIT) on the first and second law efficiency at various overall gas turbine pressure ratio. TIT is varied from 1500 K to 1800 K in step of 10 while pressure ratio is varied from 60 to 100. Both first and second law efficiency increase

with the increase in TIT at constant pressure ratio. As the TIT increases, more fuel is required to raise the temperature of the compressed air but the work done by both high and low pressure gas turbines also increase and at the same time temperature of exhaust gases also increase so more steam is generated and work done by steam turbines also increase. At constant TIT, both first and second law efficiency increase with increase in overall pressure ratio.

4.3.5 Effect of Steam Turbine Pressure on First and second Law Efficiency

Fig.18 and Fig-19 demonstrate the effect of steam turbine pressure on the first and second law efficiency at various gas turbine inlet temperature (TIT). Steam turbine pressure is varied from 120 bar to 180 bar in steps of 10 while TIT is varied from 1600 K to 1800 K. It is observed from figures that both first and second law efficiency increase with increase in steam turbine pressure at constant TIT. As the steam pressure increases, work done by both high pressure and low pressure steam turbine also increases but this increase, fuel consumption also decreases and at the same time work done by both high and low pressure gas turbines also decreases hence this has very little effect on the first and second law efficiency. At constant steam pressure, both first and second law efficiency increase with increase in TIT.

4.3.6 Effect of Pressure Ratio of high pressure Steam Turbine on First and Second Law Efficiency

Fig.20 and Fig-21 describe the effect of pressure ratio of high pressure steam turbine on first and second law efficiency at various gas turbine inlet (TIT) temperatures. Pressure ratio is varied from 2 to 50 in step of 2 while TIT is varied from 1600 K to 1800 K. it is observed from the figure that, as the pressure ratio increases, both first and second law efficiency first increase then attains maximum value and decrease. This is because at high pressure ratio work done by high pressure steam turbine increases but work done by low pressure steam turbine decreases rapidly and fuel consumption also increases. At constant pressure ratio both first and second law efficiency increase with increase in TIT.

4.3.7 Effect of steam turbine inlet temperature on First and second Law Efficiency

Fig.22 and Fig.-23 describe effect of steam turbine inlet temperature on first and second law efficiency of combined cycle gas turbine at various gas turbine inlet (TIT) temperature. Steam turbine inlet temperature is varied from 600 K to 800 K in step of 10 units while TIT is varied from 1600 K to 1800K. Both first and second law efficiency increase with the increase in steam turbine inlet temperature. This is because, work done by both high pressure and low pressure gas turbines increases and fuel consumption decreases with increases in steam turbine inlet temperature. At constant steam turbine inlet temperature both first and second law efficiency increase with increase in TIT

4.3.8 Effect of Temperature of Air at low pressure Compressor Inlet on First and second Law Efficiency

Fig.10 and Fig-11 tell the effect of inlet air temperature on first and second law effiiency of combined cycle gas turbine at various gas turbine inlet temperatures. Temperature of inlet air is varied from 285 K to 305 K while TIT is varied from 1600 K to 1800 K. from figures it can be seen that both first and second law efficiency decrease with increase in inlet air temperature at constant TIT. As inlet air temperature increases work done by both high and low pressure gas turbine increases but work consumed in both high pressure and low pressure compressor increas rapidly and fuel consumption also increases.at constant inlet air temperature both first and second law efficiency increase with increase in TIT.

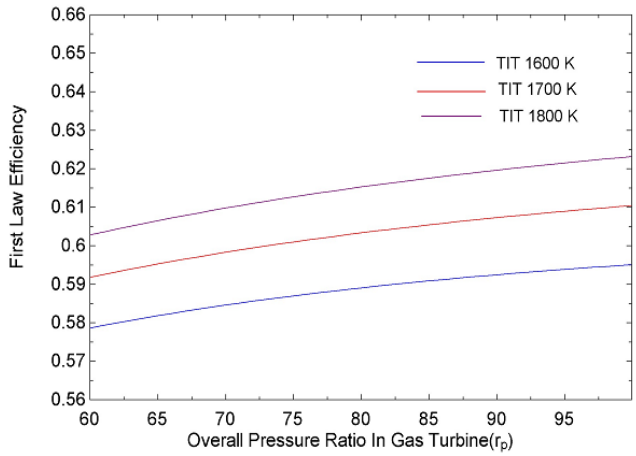

Figure 10: Variation of first law efficiency with overall pressure ratio in gas turbine

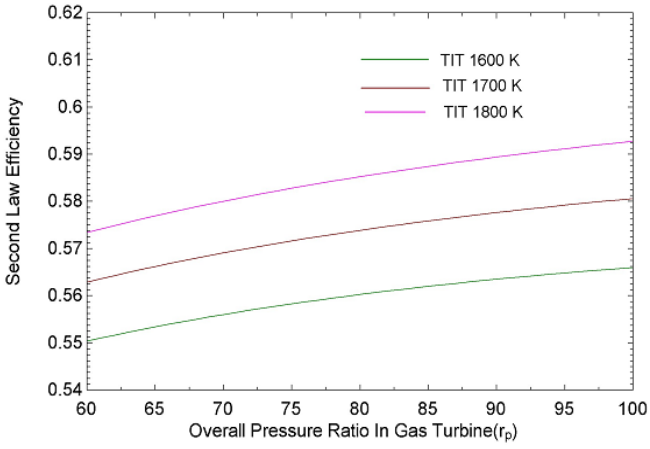

Figure 11: Variation of second law efficiency with overall pressure ratio in gas turbine

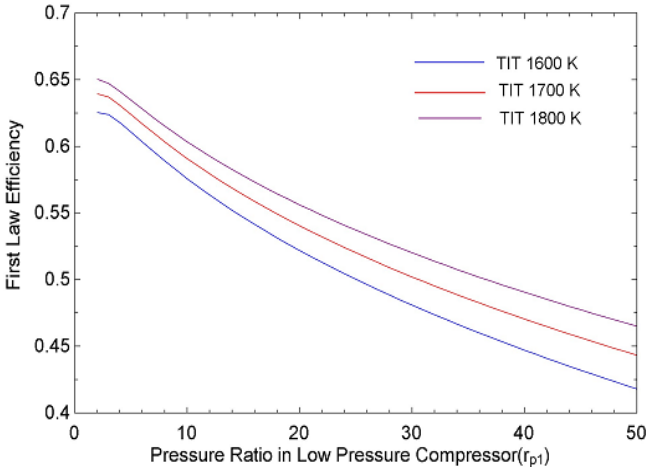

Figure 12: Effect of pressure ratio in low pressure compressor on first law efficiency

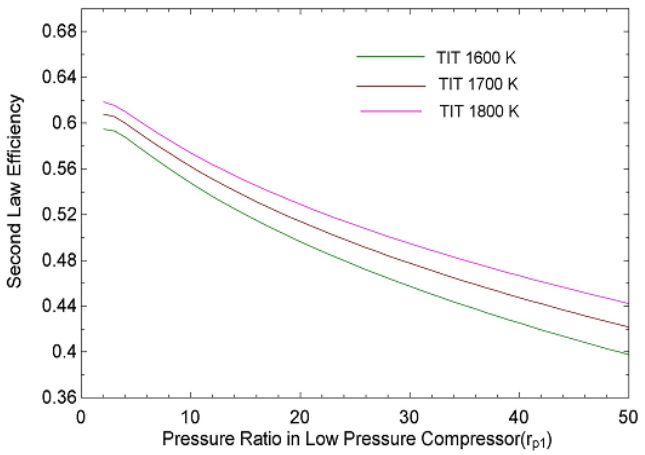

Figure 13: Effect of pressure ratio in low pressure compressor on second law efficiency

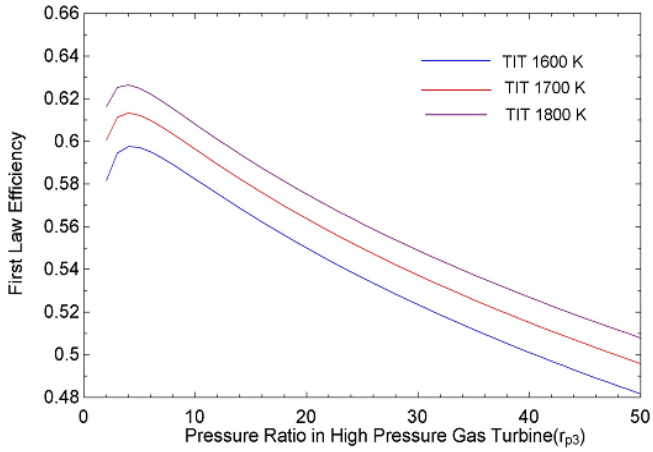

Figure 14: Effect of pressure ratio in high pressure gas turbine on first law efficiency

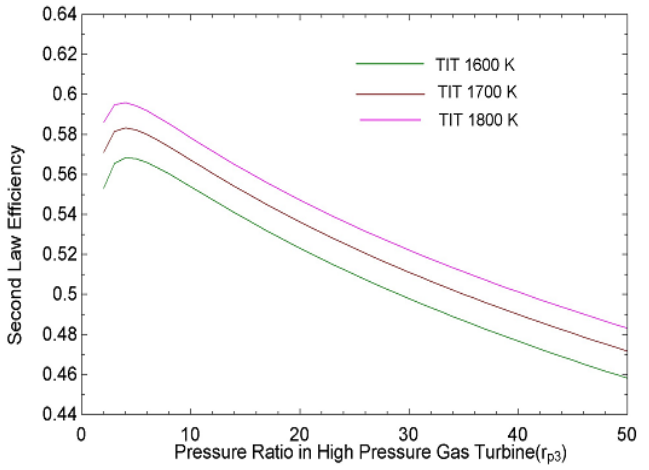

Figure 15: Effect of pressure ratio in high pressure gas turbine on second law efficiency

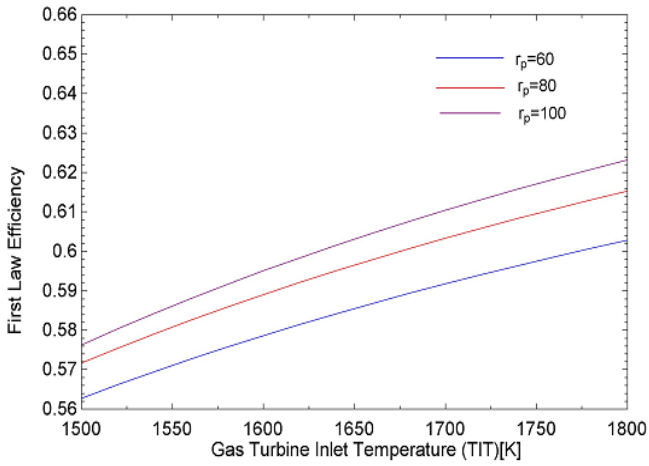

Figure 16: Effect of gas turbine inlet temperature on first law efficiency

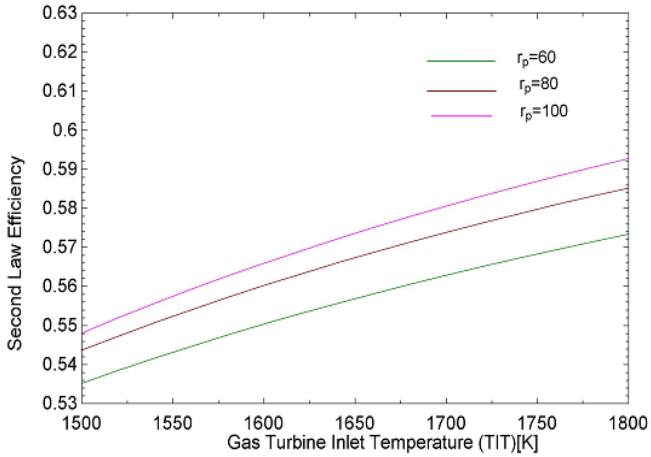

Figure 17: Effect of gas turbine inlet temperature on second law efficiency

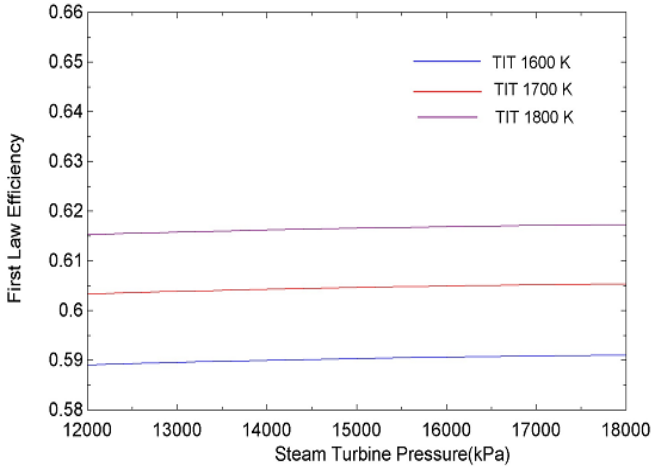

Figure 18: Effect of steam turbine pressure on first law efficiency

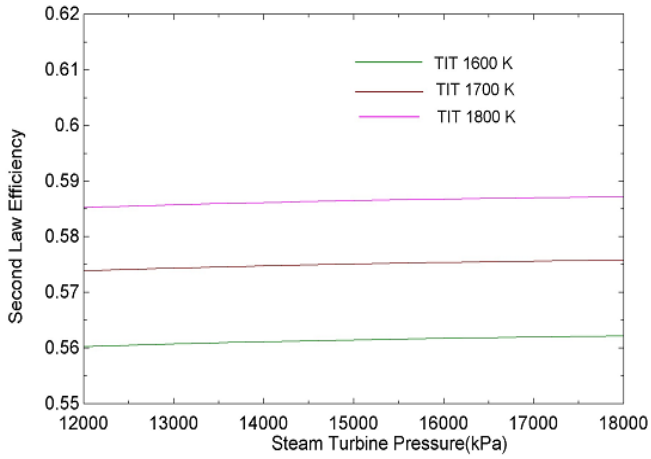

Figure 19: Effect of steam turbine pressure on second law efficiency

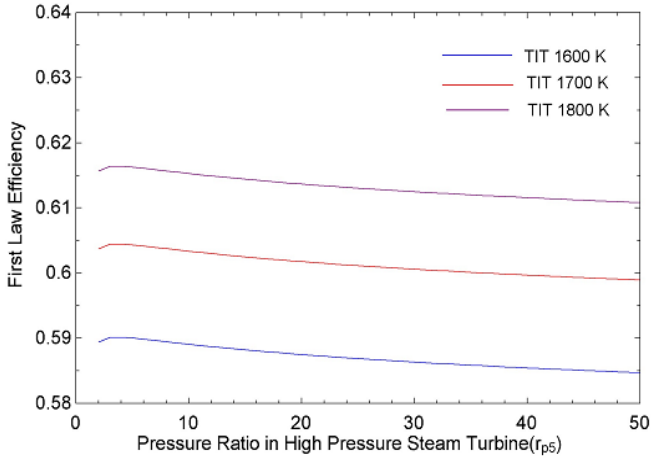

Figure 20: Effect of pressure ratio of high pressure steam turbine on first law efficiency

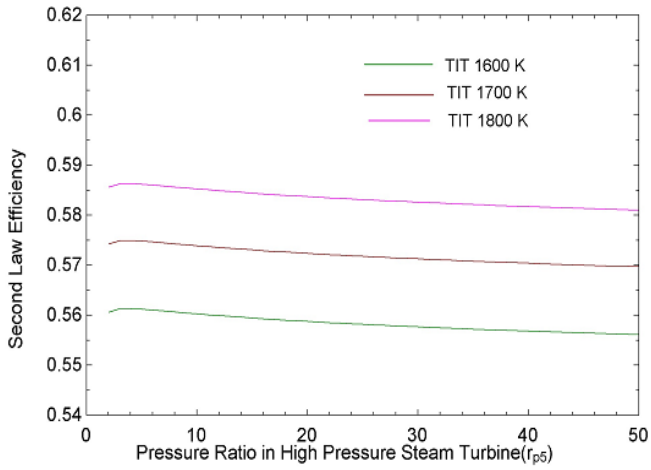

Figure 21: Effect of pressure ratio of high pressure steam turbine on second law efficiency

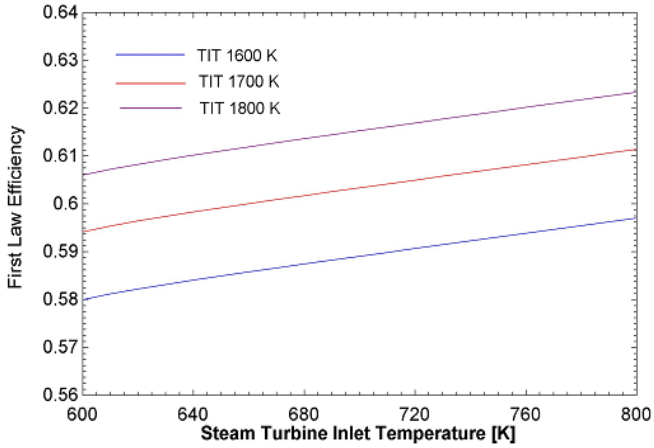

Figure 22: Effect of steam turbine inlet temperature on first law efficiency

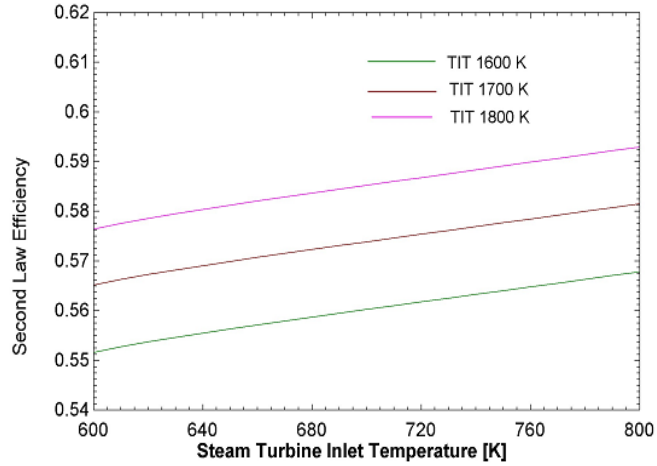

Figure 23: Effect of steam turbine inlet temperature on second law efficiency

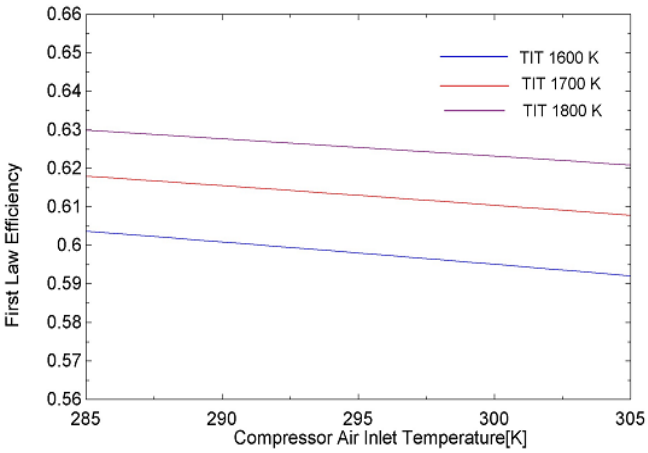

Figure 24: Effect of compressor inlet air temperature on first law efficiency

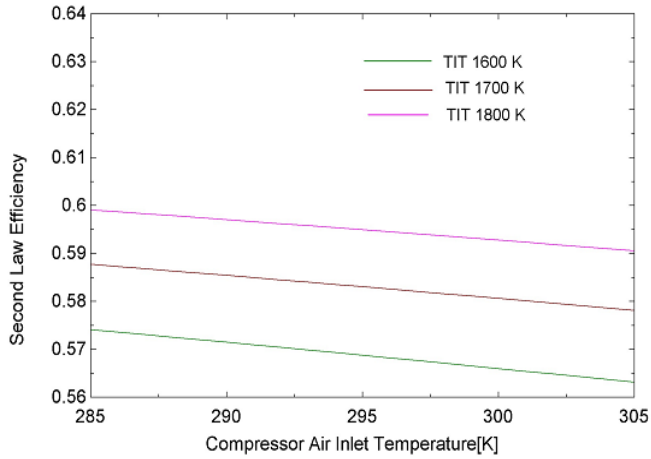

Figure 25: Effect of compressor inlet air temperature on second law efficiency

5. Conclusion and Recommendation

In this work, thermodynamic analysis of combined cycle gas turbine is done. Energetic and Exergetic analysis is done find ways to improve plant's efficiency and reduce the exergy destruction rate of components.

For given plant's requirement, when analyzed with simple combined cycle gas turbine, the first law efficiency obtained is 50.28%, and when analyzed with modified combined cycle gas turbine, the improved efficiency obtained is 55.51%. By exergy analysis it is found out that combustion chamber and duct burner have the highest exergy destruction rate.

From parametric study, it is found out that first law efficiency can be improved up to or more than 60% by choosing optimize parameter.

5.1 Conclusions

From this study following conclusion can be drawn:

1. By increasing the overall pressure ratio in topping cycle, first and second law efficiency can be increased.
2. To obtain high efficiency, pressure ratio in low pressure compressor should be low and high for high pressure compressor.
3. To achieve high efficiency, pressure ratio in high pressure gas turbine should be low and high for low pressure turbine.
4. By increasing the Gas Turbine Inlet Temperature, efficiency of turbine can be improved so TIT should be as high as possible.
5. Increase in steam turbine pressure has very minute effect (increase) on the efficiency of combined cycle.
6. As the value of steam turbine inlet temperature increases, the efficiency of cycle also increases. There is certain value of temperature, above that temperature there is sudden increase in efficiency. So steam turbine should work above that temperature.
7. Effect of pressure ratio in high pressure steam turbine on efficiency is minute but it should be low in high pressure steam turbine and high for low pressure steam turbine.
8. As the temperature of inlet air decreases, efficiency of cycle increases, because decrease in compressor work.
9. Exergy destruction rate is high for combustion chamber and duct burner.

5.2 Recommendations

The recommendations for future research are as follows:

1. In this study steam turbine is used in bottom cycle. Other cycles such as Organic Rankine Cycle and Kalina cycle can also be analyzed.
2. As the efficiency depends on compressor inlet air temperature, solar powered VARS can be employed to cool the inlet air in summer.
3. Steam injection system can be used for cooling of gas turbine blade, so that TIT can be increased.
4. Use more innovative combustion process in combustion chamber.
5. Optimization of HRSG.
6. The emissions from the CCPP system can be reduced by, for example, using a more efficient Stack after HRSG or switch to the biomass fuel. However, by considering the carbon natural cycle, the CO2 emissions from the biomass fuel could be considered having lesser environmental impact.

References

[1] Chase D.L. and Kehoe P.T. GE Power Systems Schenectady, NY GE Combined-Cycle Product Line and Performance.

[2] YunusCengel and Micheal Boles, Thermodynamics: An Engineering Approach.

[3] Ahmadi P., Dincer I., Exergoenvironmental Analysis and Optimization of a Cogeneration Plant System using Multimodal Genetic Algorithm (MGA). Energy, 35(2010), pp. 5161-72.

[4] Boyano A., Blanco-Marigorta A. M., Morosuk T., Tsatsaronis G., Exergoenvironmental Analysis of a Steam Methane Reforming Process for Hydrogen Production. Energy, 36(2011), pp. 2202-2214.
[5] Petrakopoulou F., Boyano A., Cabrera M., Tsatsaronis G., Exergoeconomic and Exergoenvironmental Analyses of a Combined Cycle Power Plant with Chemical Looping Technology. International Journal of Greenhouse Gas Control, 5(2011), pp. 475-482.
[6] Hasan Naimul, Rai JitendraNath and Arora B. B.2014 Optimization of CCGT power plant and performance analysis using MATLAB/Simulink with actual operational data. SpringerPlus 2014, 3:275, 1-9.
[7] Ibrahim K. T., Rahman M. M., Abdalla N. A., Optimum Gas Turbine Configuration for Improving the Performance of Combined Cycle Power Plant. Procedia Engineering,15(2011), pp.4216-4223.
[8] Ameri M., Hejazi H. S., The Study of Capacity Enhancement of the Chabahar Gas Turbine Installation using an Absorption Chiller. Applied Thermal Engineering, 24(2004), pp.59–68.
[9] Boonnasa S., Namprakai P., Muangnapoh T., Performance Improvement of the Combined Cycle Power Plant by Intake Air Cooling using an Absorption Chiller, Energy,31(2006), pp. 2036–2046.
[10] Hosseini R., BeshkanI. A., Soltani M., Performance Improvement of Gas Turbines of Fars (Iran) Combined Cycle Power Plant by Intake Air Cooling using a Media Evaporative Cooler. Energy Conversion and Management, 48(2007), pp. 1055–1064.
[11] Ibrahim T. K., Rahman M. M., Effect of Compression Ratio on Performance of Combined Cycle Gas Turbine. International Journal of Energy Engineering,2(2012)1, pp. 9-14.
[12] Khaliq A., Kaushik S., Thermodynamic Performance Evaluation of Combustion Gas Turbine Cogeneration System with Reheat. Applied Thermal Engineering, 24(2004), pp. 1785–1795.
[13] Sanjay, Investigation of Effect of Variation of Cycle Parameters on Thermodynamic Performance of Gas-Steam Combined Cycle. Energy, 36(2011), pp. 157-167.
[14] Khaliq A., Exergy Analysis of Gas Turbine Trigeneration System for Combined Production of Power Heat and Refrigeration. International Journal of Refrigeration, 32(2009), pp. 534-545.
[15] Kaviri A. G., Jaafar M. N., Lazim, T. M., Modeling and Multi-Objective Exergy Based Optimization of a Combined Cycle Power Plant using a Genetic Algorithm. Energy Convers Manage, 58(2012), pp. 94-103.
[16] Mohagheghi M., Shayegan J., Thermodynamic Optimization of Design Variables and Heat Exchangers Layout in HRSGs for CCGT, using Genetic Algorithm. Applied Thermal Engineering, 29(2009), pp. 290–299.
[17] Bracco S., Silvia S., Exergetic Optimization of Single Level Combined Gas Steam Power Plants Considering Different Objective Functions. Energy, 35(2010), pp. 5365-5373.
[18] Woudstra N., Woudstra T., Pirone A., Van der Stelt T., Thermodynamic Evaluation of Combined Cycle Plants. Energy Conversion and Management, 51(2010)5, pp. 1099–1110.
[19] Mansouri M. T., Ahmadi P., Kaviri A. G., Exergetic and Economic Evaluation of the Effect of HRSG Configurations on the Performance of Combined Cycle Power Plants. Energy Conversion and Management, 58(2012), pp. 47–58.
[20] Tyagi K. P., Khan M. N., Effect of Gas Turbine Exhaust Temperature, Stack Temperature and Ambient Temperature on Overall Efficiency of Combine Cycle Power Plant. International Journal of Engineering and Technology, 2(2010)6, pp. 427-429.
[21] Valdés M., Durán D. M., Antonio R., Thermoeconomic Optimization of Combined Cycle Gas Turbine Power Plants using Genetic Algorithms. Applied Thermal Engineering, 23(2003)17, pp. 2169-2182.
[22] Bassily A., Modeling and Numerical Optimizations, and Irreversibility Reduction of a Dual Pressure Reheat Combined Cycle. Applied Energy, 81(2005), pp. 127-151.
[23] Boonnasa S., Namprakai P., Muangnapoh T., Performance Improvement of the Combined Cycle Power Plant by Intake Air Cooling using an Absorption Chiller, Energy,31(2006), pp. 2036–2046.
[24] Cihan A., Hacıhafızoglu O., Kahveci K., Energy–exergy analysis and modernization suggestions for a combined-cycle power plant, Int. J. Energy Res. 2006; 30:115–126.

International Journal of Research in Engineering and Innovation (IJREI)
journal home page: http://www.ijrei.com
ISSN (Online): 2456-6934

Thermodynamic (energy-exergy) analysis of pre-cooled linde system

R. S. Mishra, Devendra Kumar

Department of Mechanical, Production & Industrial and Automobiles Engineering, Delhi Technological University, Delhi, India

Abstract

The present studies concern on detailed thermodynamic (energy and exergy analyses) of Pre cooled Linde cryogenic system up to their sub component level. This parametric study is conducted to investigate the effects of variation of various system input parameters such as pressure ratio, expander mass flow ratio, compressor output temperature on different performance parameters like COP , work input ,liquefaction rate ,specific heat and exergy. The numerical computations have been carried out for Claude system are study with six different gases for liquefaction like oxygen, argon, methane, fluorine, air and nitrogen respectively. It was observed that methane has better thermal performances (first law performance i.e. COP) and exergetic efficiency (second law performance) as compared to other gases. The total net work done decreasing. © 2017 ijrei.com. All rights reserved

Keywords: Thermodynamics Analysis, Collin Cryonic System, Energy-Exergy Analysis, First and second Law Analysis

1. Introduction

The term “cryogenic” is derived from the Greek word Kryos which means cold or frost. It is frequently applied to very low temperature refrigeration applications such as in the liquefaction of gases and in the study of physical phenomenon at temperature approaching absolute zero.

The first low temperature refrigeration system was primarily developed for the solidification of carbon dioxide and the liquefaction and subsequent fractional distillation of gases such as air, oxygen, nitrogen, hydrogen and helium. Cryogenic process to liquefy air which is further extent to extract various particular gas like oxygen, nitrogen, feron etc. Always various analyses is done to identify the loop hole of process and to rectify it to their upper level. electro caloric cooling is a transiting to new cooling principle’s is critical and one of the most promising alternatives may be [1].Various particular part are taken under study to increase overall performance of cryogenic system e.g. A good exergetic design of a heat exchanger would allow for an increase in the global efficiency of the process, by defining a thermodynamic cycle in which the exergetic losses would be limited [2] apart from this other parts like expander, mass ratio and input variables are considered to improve cryo systems.

Pre-cooled Linde Hampson system is advanced stage old simple Linde Hampson system .In this system vapour compression evaporator having R134 a refrigerant is taken as additional equipment to fill the gap of simple Linde system. In Fig.1 (a&b) shows the detail block diagram and T-S diagram of Pre-cooled Linde system. Vapor compression system lower down the temperature of gases coming through the compressor which is desirable for better performance of system. The method of cooling the gas after the compression or before the entrance to the heat exchanger is called as precooling. The precooling limit of the precooling cycle is governed by the boiling point of refrigerant at its suction pressure this increment in the yield is dependent on the The change in enthalpy values from $(h_d - h_a)$of the refrigerant. Refrigerant flow rate (m_r). the heat of compression Q_R can be obtained by using 2nd Law for an isothermal compression.

Corresponding author: R.S. Mishra
Email Id:rsmishradtu@gmail.com

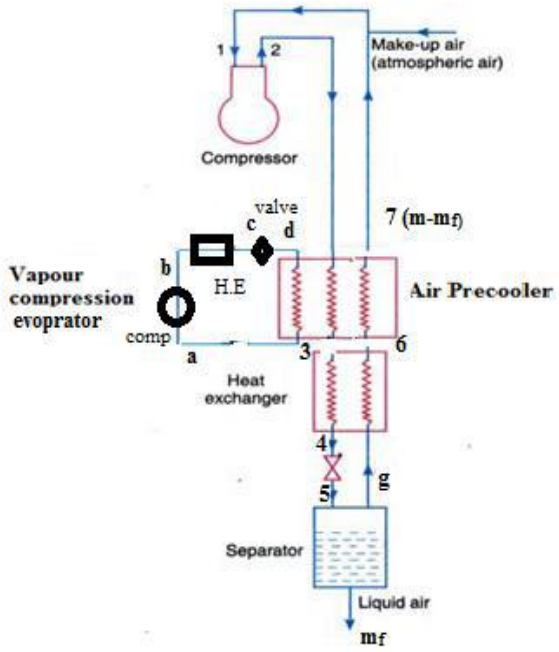

Figure 1(a): Schematic of Pre-cooled linde system

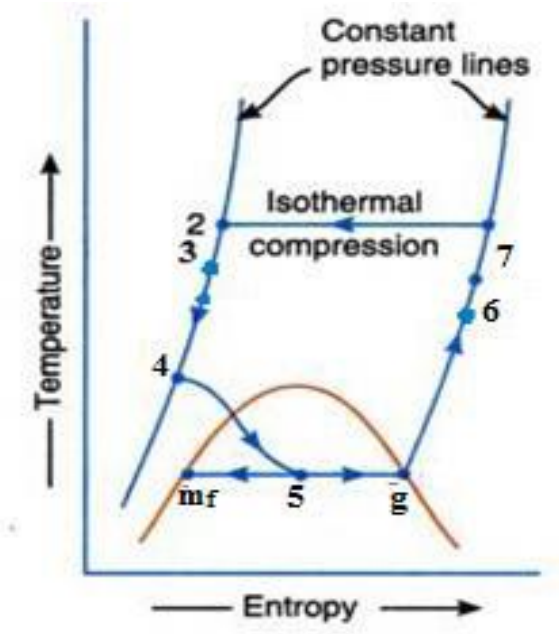

Figure 1(b: T-S diagram of Pre-cooled linde system

2. Mathematic Modelling of "Pre-Cooled Linde Hampson Cycle

Working Fluid Properties

$R\$ = 'oxygen'$
$P_1 = 1.013, T_1 = 298, T_1 = T_0, P_2 = 100, T_2 = T_1$
$P_f = P_1, x_0 = 0, x_1 = 1, T_f = T_g,$

Refrigerant Properties R134 a

$P_a = 1.013$
$P_b = 10.013$ Adiabatic Compression
$P_c = P_b, T_a = 300, T_b = 373, T_c = 300, h_a = 278, h_b = 334.9, h_c = 89.07$
"Boiling Temperature of Refrigerant"
$T_d = 247.1$

Control Vol having 2 HT, J-T, Separator

"Energy Balance by First Law"
$\frac{m_r}{m} = r, r = 0.08$
$m_r * h_d + m * h_2 = m_r * h_a + (m - m_f) * h_1 + m_f * h_f$
$y = \frac{m_f}{m}$
Control Vol having HT,J-T,Seperator

$m * h_3 = m_f * h_f + (m - m_f) * h_6$
$y_{max} = \frac{h_6 - h_3}{h_6 - h_f}$
$W_{total} = W_{c1} + W_{c2}$

Compressor work per liquefaction of system

$E_{in} = E_{out}$
$E_{in} = m * h_1 - W_{c1}$
$E_{out} = m * h_2 - Q_R$
$Q_R = m * T_1 * (s_2 - s_1)$

Compressor work of ref system

$m_r * h_a - W_{c2} = m_r * h_b$
$-\frac{W_{total}}{m_f} = Z$
$-\frac{W_{total}}{m} = abs\left(\begin{matrix} T_1 * (s_1 - s_2) - \\ (h_1 - h_2) + r * (h_b - h_a) \end{matrix}\right)$
$-\frac{W_i}{m} = T_1 * (s_1 - s_f) - (h_1 - h_f)$
$-\frac{W_i}{m_f} = K$
$FOM = \frac{Z}{K}$
$COP = \left(\frac{h_1 - h_f}{W_{total}}\right)$
$Eta_{2nd\%} = abs\left(\left(\frac{(h_f - h_1) - T_0 * (s_f - s_1)}{W_{total}} * m_f\right) * 100\right)$

First Heat Exchanger (HX_1) analysis

$TypeHX_{1\$} = 'counterflow'$
$epsilon_{HX1} = 0.85$
$T_{c_o} = 292, T_{h_i} = T_1, T_{10} = T_{c_o}$
$m_{h_{HX1}} = m, m_{c_{HX1}} = m - m_f$
$T_{h_o} = T_3, T_{c_i} = T_9$
$C_{h_{HX1}} = m_{h_{HX1}} * cp_{fluid_{HX1}}$
$C_{c_{HX1}} = m_{c_{HX1}} * cp_{fluid_{HX1}}$
$q_{HX1} = C_{h_{HX1}} * (T_{h_i} - T_{h_o})$
$q_{HX1} = C_{c_{HX1}} *$

$q_max_HX1 = C_min_HX1 * (T_h_i - T_c_i)$
$epsilon_HX1 = q_HX1 / q\max_{HX1}$
$Ntu_{HX1} = HX(TypeHX_{1\$}, epsilon_{HX1}, C_{h_{HX1}}, C_{c_{HX1}}, 'Ntu')$
$Ntu_HX1 = (G_HX1) / C\min_{HX1}$
$Ed_{HX1} = \left(T_0 * ((s_2 + s_9) - (s_3 + s_{10}))\right)$

Second Heat Exchanger (HX_3) analysis

$TypeHX_{3\$} = '\text{ counterflow}'$
$epsilon_{HX3} = 0.85$
$m_{h_{HX3}} = m$
$m_{c_{HX3}} = m - m_f$
$C_{h_{HX3}} = mh_{HX3} * cp_{hot_{fluid_{HX3}}}$
$C_{c_{HX3}} = m_{c_{HX3}} * cp_{cold_{fluid_{HX3}}}$
$q_{HX3} = C_{h_{HX3}} * (T_4 - T_5)$
$q_{HX3} = C_{c_{HX3}} * (T_9 - T_g)$
$q_max_HX3 = C_min_HX3$
$(T_4 - T_g)$
$epsilon_HX3 = q_HX3 / q\max_{HX3}$
$Ntu_{HX3} = HX(TypeHX_{3\$}, epsilon_{HX3}, C_{h_{HX3}}, C_{c_{HX3}}, 'Ntu')$
$Ntu_HX3 = (G_HX3) / C\min_{HX3}$
$Ed_{HX3} = \left(T_0 * \left(\begin{matrix}(s_4 + s_g) - \\ (s_5 + s_9)\end{matrix}\right)\right)$

In Non-ideal gas any variable can be defined by two other dependent variable on them

$$a_{non-ideal\ gas} = fx(b, c)$$

Table: 1 Variable Table (Pre-cooled Linde system)

Variable (a)	Gas	Variable (b)	Variable (c)
h_0	R$	T_0	P_1
h_1	R$	T_1	P_1
h_2	R$	T_2	P_2
s_0	R$	T_0	P_1
s_1	R$	T_1	P_1
s_2	R$	h_2	P_2
s_f	R$	x_f	T_f
T_f	R$	x_0	P_1
h_f	R$	x_f	T_f
s_g	R$	x_1	P_1
h_g	R$	x_1	T_g
s_3	R$	T_3	P_2
h_3	R$	T_d	P_2
s_9	R$	T_9	P_1
s_{10}	R$	T_{10}	P_1
$cp(fluid)_{HX1}$	R$	T_2	P_2
$cp(cf)_{HX1}$	R$	T_8	P_1
C_{min}	-	C_{hot_HX1}	C_{cold_HX1}
$cp(hf)_{HX3}$	R$	T_3	P_2
$cp(cf)_{HX3}$	R$	$T_g + 1$	P_1
C_{min}	-	C_{hot_HX3}	C_{cold_HX3}
h_6	R$	h_d	P_1
s_4	R$	T_4	P_2
s_5	R$	T_5	P_2

3. Result and Discussion

Fig.2 illustrates the variations in COP and second law efficiency with compressor pressure. It has been observed that methane has the highest COP and second law efficiency among the other gases, i.e. 1.615 at 40bar and 47.27% at 220 bar. Fig.3 illustrates the variations in liquefaction mass flow rate with the compressor pressure from 40 to 220bar. It has been noticed that methane has the highest liquefaction mass flow rate, i.e. 0.07248kg/s to 0.3444kg/s followed by other considered gases

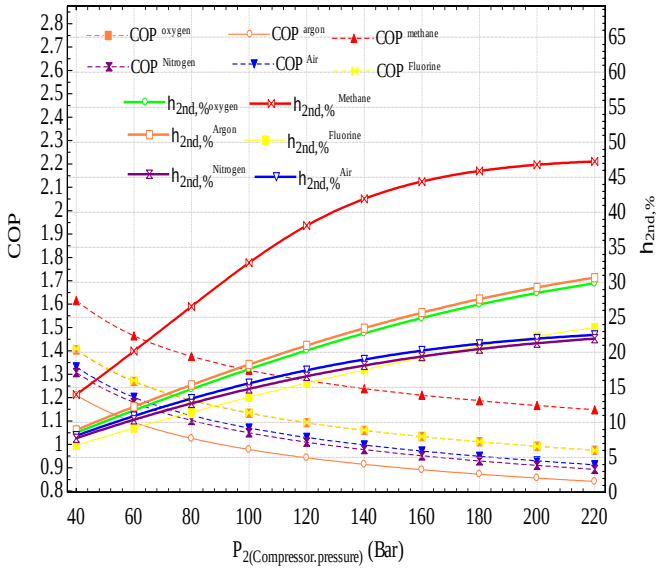

Figure 2: Variation in COP and second law efficiency with the compressor pressure

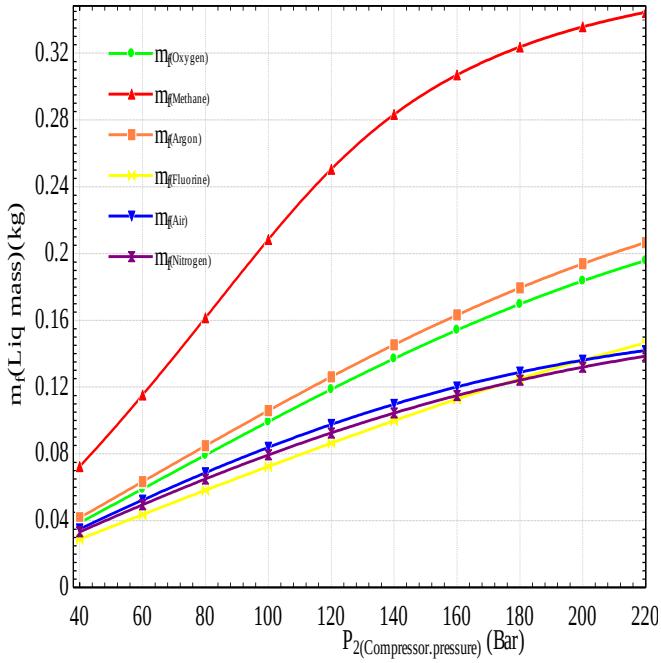

Figure 3: Variation in liquefaction mass flow with compressor pressure

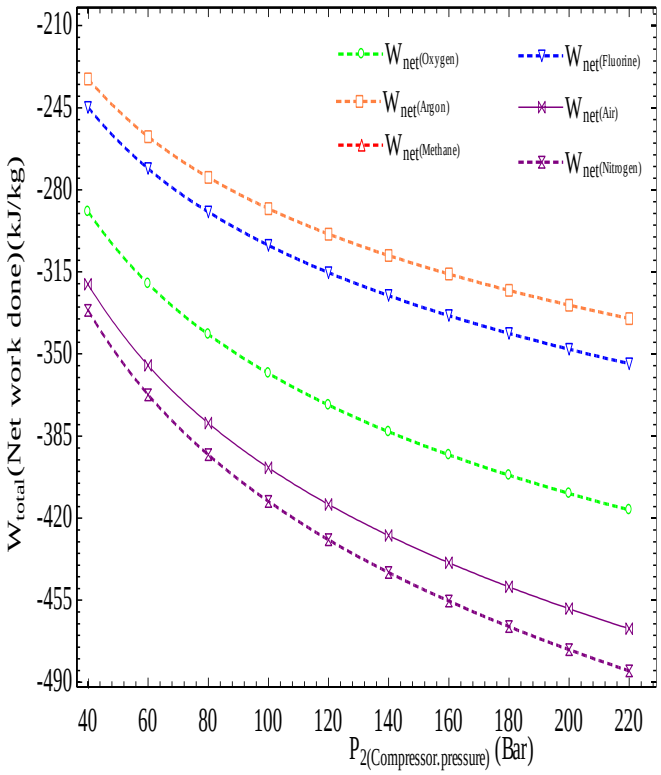

Figure 4: Variation in total net work done with compressor pressure

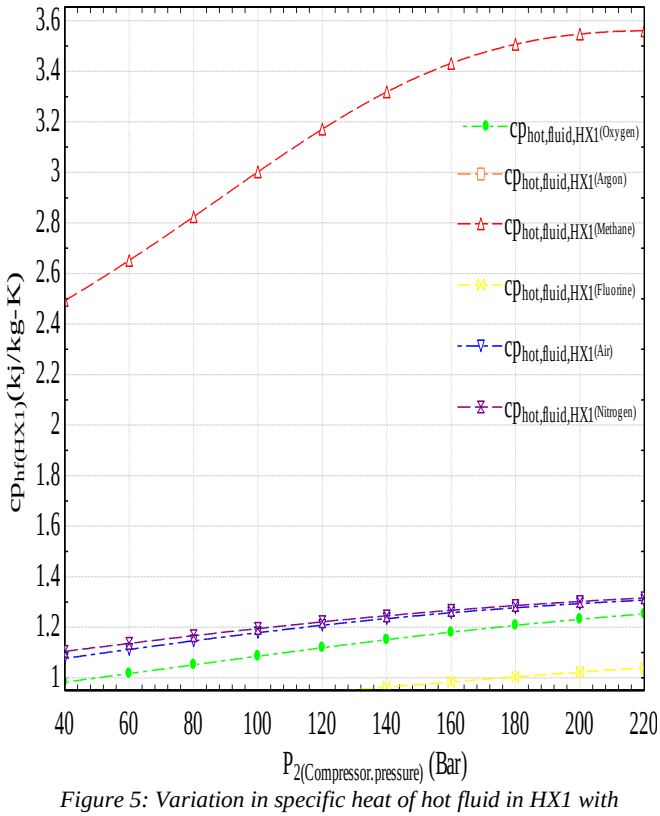

Figure 5: Variation in specific heat of hot fluid in HX1 with compressor pressure

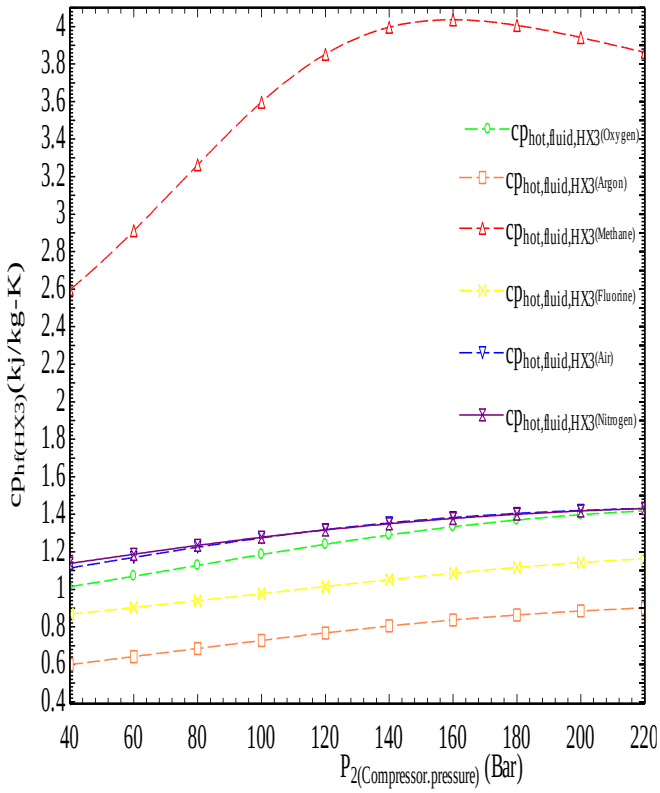

Figure 6: Variation in specific heat of hot fluid in HX3 with compressor pressure

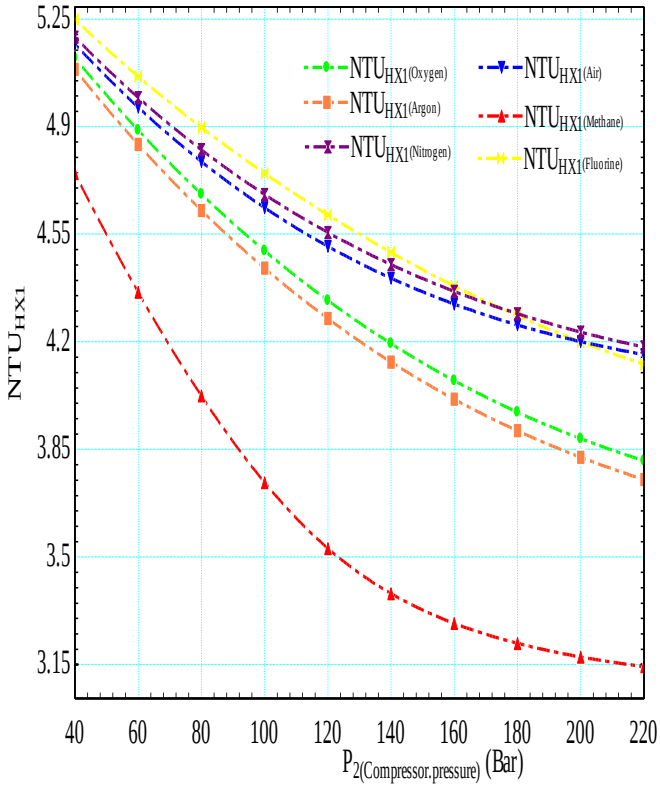

Figure 7: Variation in NTU in HX1 with compressor pressure

Table 2(a) Various performance parameters on optimum Temperature (300K) and P_2 (100 bar)

Gases	COP	Eff. η2nd %	Edest (HX1) (kj/kg)	Edest (HX3) (kj/kg)
Oxygen	1.136	17.54	2.38	39.48
Argon	0.9814	18.21	2.424	31.58
Methane	1.321	32.65	9.414	87.63
Fluorine	1.139	13.54	1.296	49.8
Air	1.072	15.52	2.368	190
Nitrogen	1.051	14.73	2.086	9.818

Table 2(b) Various performance parameters on optimum Temperature (300K) and P_2 (100 bar)

Gases	COP	Efficiency η2nd %	m_f kg/s	FOM
Oxygen	1.136	17.54	0.09928	0.566
Argon	0.9814	18.21	0.1059	0.5814
Methane	1.321	32.65	0.2084	0.2084
Fluorine	1.139	13.54	0.07244	0.5349
Air	1.072	15.52	0.0839	0.5405
Nitrogen	1.051	14.73	0.07938	0.5387

Table 2(c) Various performance parameters on optimum Temperature (300K) and P_2 (100 bar)

Gases	COP	Efficiency η2nd %	NTU (HX1)	NTU (HX3)
Oxygen	1.136	17.54	4.496	3.518
Argon	0.9814	18.21	4.439	3.387
Methane	1.321	32.65	3.742	2.718
Fluorine	1.139	13.54	4.748	3.757
Air	1.072	15.52	4.636	3.956
Nitrogen	1.051	14.73	4.679	3.911

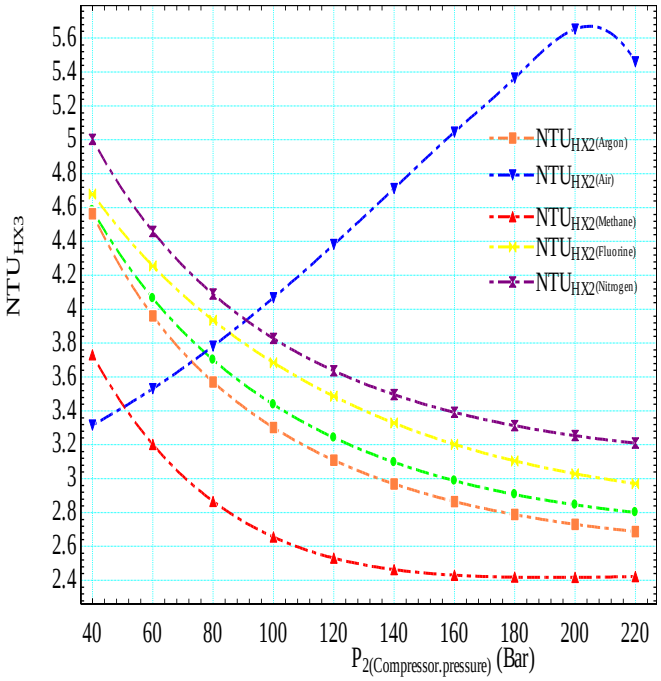

Figure 8: Variation in NTU in HX3 with compressor pressure

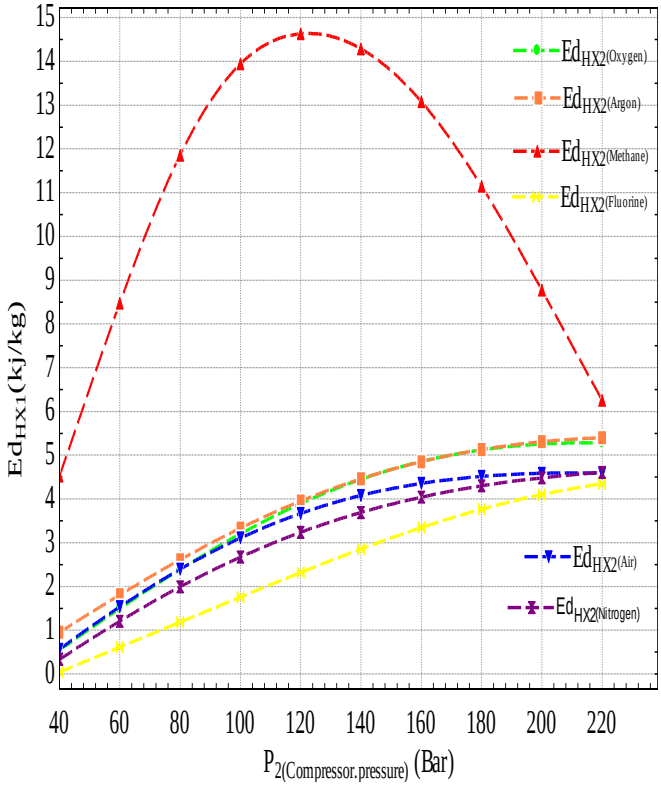

Figure 9: Variations in exergy destruction in HX1 with compressor pressure

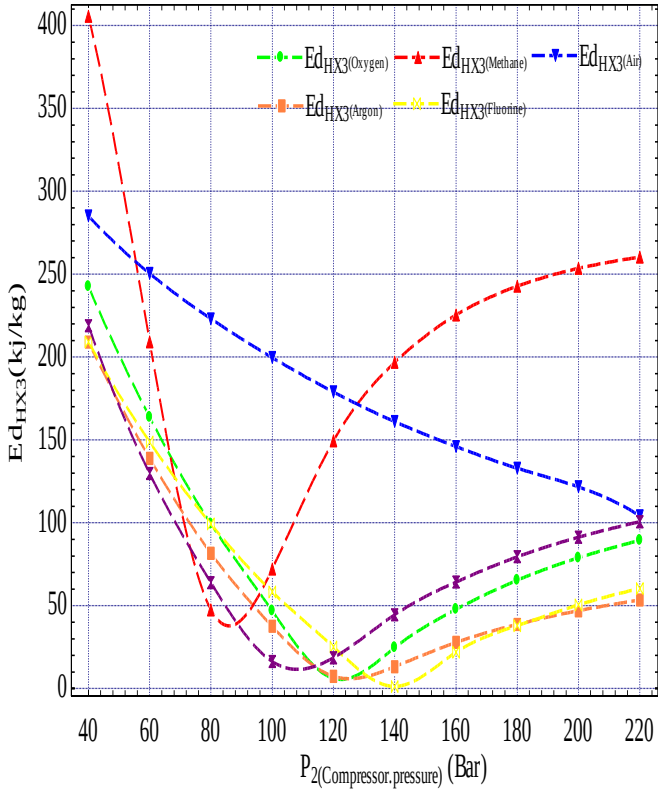

Figure 10: Variation in exergy destruction in HX3 with compressor pressure

The optimum performance parameters at optimum temperature at optimum pressure are shown in Table-2 respectively.

Fig.4 shows the variation in net work done with the compressor pressure and it has been observed that total net work done decreases with the compressor pressure, and argon has the highest value among other gases. Fig.5 illustrates the specific heat of hot fluid in HX1 and methane has the largest value of specific heat among the other gases i.e. 3.561kJ/kg-K at 220bar. Fig.6 demonstrates that methane has the highest value of specific heat of hot fluid in HX3 among the other considered gases, i.e. 4.036Kj/kg-K at 160bar. Fig.7 shows that NTU in HX1 continuously decreasing and fluorine has the highest value of NTU among the other gases, i.e. 4.747 at 40bar. Fig.8 shows the NTU in HX3 and it has been seen that all the gases has the decreasing trend except air between the prescribed the temperature range of 40bar to 220bar. Fig.9 illustrates the exergy destruction rate in HX1 and it has been seen that methane shows the highest value of exergy destruction rate, and its graph first increasing then shows the decreasing trend. Alternatively, all the other gases shows the increasing trend. Fig.10 shows the exergy destruction rate in HX3 and it has been seen that methane has the highest value, and it is decreasing first up to a certain pressure and then increasing followed by other considered gases

4. Conclusions

- Methane has the highest first law efficiency (i.e. COP) and second law efficiency (i.e. exergetic Efficiency) among the other gases.
- Methane has the highest liquefaction mass flow rate, followed by other considered gases.
- The total net work done decreases with the compressor pressure, and argon has the highest value among other gases.
- NTU in the third heat exchanger (HX3) for all gases has the decreasing order.
- Methane shows the highest value of Exergy destruction rate in first heat exchanger (HX1).
- Methane has the highest value of specific heat of hot fluid in HX3 among the other considered gases.
- Exergy destruction rate of methane in the third heat exchanger (HX3) has the highest value, and it is decreasing first up to a certain pressure and then increasing followed by other considered gases.
- Total net work done decreases with the compressor pressure, and argon has the highest value among other gases.

References

[1] Yu. V. Sinyavskii, Electro caloric refrigerators: A promising alternative to current low-temperature Apparatus, Chemical and Petroleum Engineering, 31(6), 1995, 295-306.

[2] R. Agrawal, D. W. Woodward, Efficient cryogenic nitrogen generators: An exergy analysis, Gas Separation & Purification, 5(3), 1991, 139-150.

International Journal of Research in Engineering and Innovation (IJREI)
journal home page: http://www.ijrei.com
ISSN (Online): 2456-6934

Thermodynamic performance analysis of claude cryogenic system

R. S. Mishra, Devendra Kumar

Department of Mechanical, Production & Industrial and Automobiles Engineering, Delhi Technological University, Delhi, India

Abstract

The present investigation is concern on Thermal (energy and exergy analyses) of various cryogenic system up to their sub component level. A parametric study is conducted to investigate the effects of variation of various system input parameters such as pressure ratio, expander mass flow ratio, compressor output temperature on different performance parameters like COP , work input ,liquefaction rate ,specific heat and exergy. The numerical computations have been carried out for Claude system are study with six different gases for liquefaction like oxygen, argon, methane, fluorine, air and nitrogen respectively. Effect of different input gas also studies carefully and behavior of different gases in different system is concluded i.e. first law efficiency (COP) and second law efficiency (exergetic efficiency) of claude system decrease with increase in pressure ratio. For Methane gas COP decreases.

© 2017 ijrei.com. All rights reserved

Keywords: Claude Cryogenic system, Thermodynamic Analysis, Energy-Exergy Analysis, Irreversibility Optimization

1. Introduction

In the year 1920, Claude developed an air liquefaction system and established Air Liquide. Claude system consists of compressor, expander, three heat exchangers with throttle valve and separator. The fluid which has to liquefy first fed to compressor in its gaseous form at atmospheric pressure, it is compressed isothermally in compressor after that the high pressure gas is partially cooled by passing through the first heat exchanger, at the exits of first heat exchanger a portion if air is bled and called by expansion in expander ,the remaining portion of air passes through the second and third heat exchanger ,the gas from third heat exchanger is throttled irreversibly at atmospheric pressure. The liquid gas is collected in separator after throttling. The low temperature gas from expander is mixed with the gaseous part from the separator, producing an effect of increased mass flow rate at feed system. In the Claude system, energy is removed from the gas stream by allowing it to do some work in an expansion engine or expander. An expansion valve is still necessary in the Claude system because much liquid cannot be tolerated in the expander in the actual system. The liquid has much compressibility than the gas, therefore, if the liquid were formed in the cylinder of an expansion engine (positive displacement type), high momentary stress would result. Some rotary turbine expanders (axial-flow type) have developed that can tolerate as much as 15% liquid by weight without damage to the turbine blade. In some Claude systems, the energy output of the expander is used to help compress the gas to be liquefied. In small scale system, the energy is dissipated in the brake or in an external air blower. This energy is wasted or not it does not affect the liquid yield; however, it increases the compression work requirement when the expander work is not used. A schematic diagram is shown in below figure. Cryogenic process to liquefy air which is further extent to extract various particular gas like oxygen, nitrogen, feron etc. Always various analyses is done to identify the loop hole of process and to rectify it to their upper level. electro caloric cooling is a transiting to new cooling principle's is critical and one of the most promising alternatives may be [1].Various particular part are taken under study to increase overall performance of cryogenic system e.g. A good exergetic design of a heat exchanger would allow for an increase in the global efficiency of the process, by defining a thermodynamic cycle in which the exergetic losses would be limited [2] apart from this other parts like expander, mass ratio and input variables are considered to improve cryo-systems.

Corresponding author: R.S. Mishra
Email Id:rsmishradtu@gmail.com

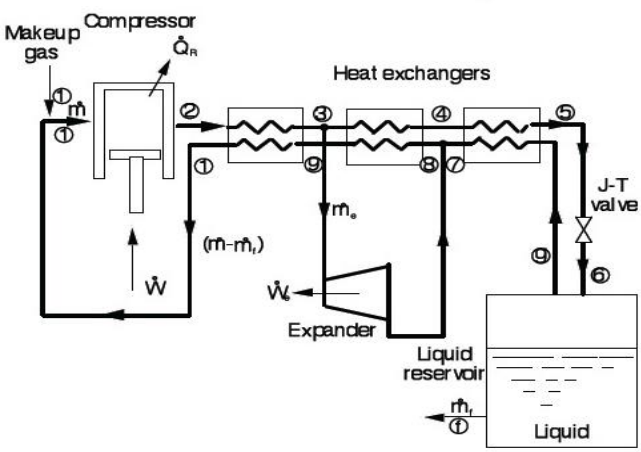

Figure 1(a): Schematic diagram of Claude system

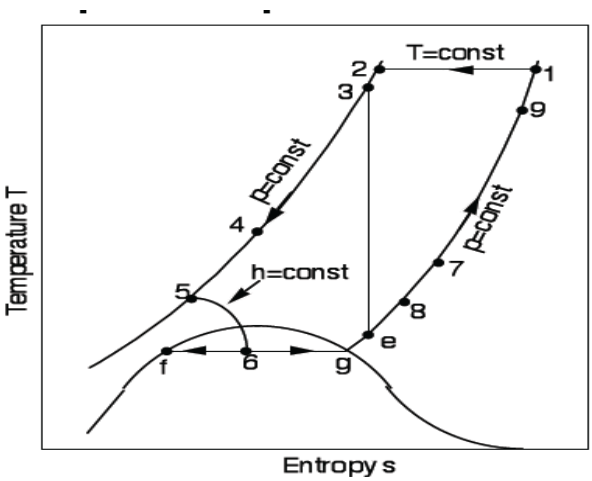

Figure 1(b): T-S diagram of Claude system

In non ideal gas any variable can be defined by two other dependent variables on them:

$a_{non-ideal\ gas} = fx(b, c)$

Following study is carried out to study the behavior of various considered gases in Claude liquefaction system. Exergy analysis help in determining the optimum working parameters of system with different gases.

Table 1: Variable Table

Variable (a)	Gas	Variable (b)	Variable (c)
h_0	$R\$$	T_0	P_1
h_1	$R\$$	T_1	P_1
h_2	$R\$$	T_2	P_2
s_0	$R\$$	T_0	P_1
s_1	$R\$$	T_1	P_1
s_2	$R\$$	h_2	P_2
T_e	$R\$$	h_e	P_1
h_e	$R\$$	s_3	P_1
s_e	$R\$$	h_e	P_1
s_f	$R\$$	x_f	T_f
T_f	$R\$$	x_0	P_1
h_f	$R\$$	x_f	T_f
T_g	$R\$$	x_1	P_1
s_g	$R\$$	x_1	T_g
h_g	$R\$$	x_1	T_g
s_3	$R\$$	T_3	P_2
h_3	$R\$$	T_3	P_2
s_4	$R\$$	T_4	P_2
h_4	$R\$$	T_4	P_2
s_8	$R\$$	T_8	P_1
h_8	$R\$$	T_8	P_1
s_9	$R\$$	T_9	P_1
h_9	$R\$$	T_9	P_1
s_{10}	$R\$$	T_{10}	P_1
h_{10}	$R\$$	T_{10}	P_1
$cp(hf)_{HX1}$	$R\$$	T_2	P_2
$cp(cf)_{HX1}$	$R\$$	T_8	P_1
C_{min}	-	C_{hot_HX1}	C_{cold_HX1}
$cp(hf)_{HX2}$	$R\$$	T_2	P_2
$cp(cf)_{HX2}$	$R\$$	T_8	P_1
C_{min}	-	C_{hot_HX2}	C_{cold_HX2}
$cp(hf)_{HX3}$	$R\$$	T_2	P_2
$cp(cf)_{HX3}$	$R\$$	$T_g - 1$	P_1
C_{min}	-	C_{hot_HX3}	C_{cold_HX3}
h_7	$R\$$	T_7	P_1
s_7	$R\$$	T_7	P_1
X_6	$R\$$	h_6	P_1
s_6	$R\$$	h_6	P_1
s_5	$R\$$	h_5	P_1
h_5	$R\$$	T_5	P_2

$R\$ = ' Gas'$

$m_2 = 1, m = m_2, \frac{m_f}{m} = y,\ \frac{m_e}{m} = r, r = 0.2,\ T_0 = 298,$

$T_1 = 300,\ T_2 = T_1, P_1 = 1, P_2 = 40, c_{p_{fluid}} = 1.004\ \left[\frac{kj}{kgK}\right]$

$c_{v_{fluid}} = 0.718\ \left[\frac{kj}{kgK}\right]$

Analysis of Compressor

$W_c = \left(m_2 * \left((h_2 - h_1)\right) - T_2 * (s_2 - s_1)\right),$

$Q_c = m_2 * (h_2 - h_1)$

$Ed_{comp} = \left(m_2 * T_1 * (s_1 - s_2) - \left(Q_c * \left(\frac{T_0}{T_1}\right)\right)\right)$

$COP = \frac{(h_1 - h_f)}{W_c + W_e}$

$W_{net} = (W_c + W_e)$

$Eta_{2nd\%} = \left(\frac{m_f * \left((h_f - h_1) - T_0 * (s_f - s_1)\right)}{W_{net}}\right) * 100$

Expander

$$W_e = m_e * \left((h_3 - h_e) - T_0 * (s_3 - s_e)\right)$$
"Heat Exchanger HX1"
$$TypeHX1\$ =' counterflow'$$
$$m_h = m, m_c = m - m_f$$
$$C_h = m_h * c_{p_{HX1}}\ , C_c = m_c * c_{p_{cold_{HX1}}}$$
$$q = C_h * (T_2 - T_3)$$
$$q = C_c * (T_{10} - T_9)$$
$$C_{max} = C_{\min} * (T_2 - T_9)$$
$$epsilon = q/q_max$$
$$epsilon = 0.85$$
$$Ntu_HX1 =$$
$$HX(TypeHX1\$, epsilon, C_dot_h, C_dot_c, 'Ntu')$$
$$Ntu_HX1 = (G_HX1)/C_min$$
$$Ex_{in_{HX1}} = m * \left((h_2 - h_3) - \left(T_0 * (s_2 - s_3)\right)\right)$$
$$Ex_{out_{HX1}} = (m - m_f) * \left((h_9 - h_{10}) - \left(T_0 * (s_9 - s_{10})\right)\right)$$
$$Ed_{HX1} = \left(\left(Ex_{in_{HX1}}\right) - \left(Ex_{out_{HX1}}\right)\right)$$

Heat Exchanger HX2

$$TypeHX_{2\$} =' counterflow'$$
$$epsilon_{HX2} = 0.85$$
$$m_{h_{HX2}} = m - m_e, m_{c_{HX2}} = m - m_f$$
$$C_{h_{HX2}} = m_{h_{HX2}} * cp_{hot_{fluid_{HX2}}}$$
$$C_{c_{HX2}} = m_{c_{HX2}} * cp_{cold_{fluid_{HX2}}}$$
$$q_{HX2} = C_{h_{HX2}} * (T_3 - T_4)$$
$$q_{HX2} = C_{c_{HX2}} * (T_9 - T_8)$$
$$C_\min_HX2 = \min(C_h_HX2, C_c_HX2)$$
$$q_{\max_{HX2}} = C_{\min_{HX2}} * (T_3 - T_8)$$
$$epsilon_HX2 = q_HX2/q\ \max_HX2 \qquad (47) Ntu_{HX2} =$$
$$HX\left(TypeHX_{2\$}, epsilon_{HX2}, C_{dot_{h_{HX2}}}, C_{dot_{c_{HX2}}}, 'Ntu'\right)$$
$$Ntu_HX2 = (G_HX2)/C\ \min_HX2$$
$$Ex_{in_{HX2}} = (m - m_e) * \left((h_3 - h_4) - \left(T_0 * (s_3 - s_4)\right)\right)$$
$$Ex_{out_{HX2}} = (m - m_f) * \left((h_8 - h_9) - \left(T_0 * (s_8 - s_9)\right)\right)$$
$$Ed_{HX2} = \left(\left(Ex_{in_{HX2}}\right) - \left(Ex_{out_{HX2}}\right)\right)$$

Heat Exchanger HX3

$$TypeHX_{3\$} =' counterflow'$$
$$T_7 = T_8$$
$$epsilon_{HX3} = 0.85$$
$$m_{h_{HX3}} = m - m_e\ , m_{c_{HX3}} = m - m_f$$
$$C_{h_{HX3}} = m_{h_{HX3}} * cp_{hot_{fluid_{HX3}}}$$
$$C_{c_{HX3}} = m_{c_{HX3}} * cp_{cold_{fluid_{HX3}}}$$
$$q_{HX3} = C_{h_{HX3}} * (T_4 - T_5)$$
$$q_{HX3} = C_{c_{HX3}} * (T_7 - T_g)$$
$$q_\max_HX3 = C_\min_HX3 * (T_4 - T_g)$$
$$epsilon_HX3 = q_HX3/q_\max_HX3$$
$$Ntu_{HX3} = HX\left(TypeHX_{3\$}, epsilon_{HX3}, C_{h_{HX3}}, C_{c_{HX3}}, 'Ntu'\right)$$
$$Ntu_HX3 = (G_HX3)/C \min_{HX3}$$
$$Ex_{in_{HX3}} = (m - m_e) * \left((h_4 - h_5) - \left(T_0 * (s_4 - s_5)\right)\right)$$
$$Ex_{out_{HX3}} = (m - m_f) * \left((h_g - h_7) - \left(T_0 * (s_g - s_7)\right)\right)$$
$$Ed_{HX3} = \left(\left(Ex_{in_{HX3}}\right) - \left(Ex_{out_{HX3}}\right)\right)$$

Analysis of Valve

$$h_5 = h_6$$
$$Ex_{in_{Val}} = (h_5 - h_0) - T_0 * (s_5 - s_0)$$
$$Ex_{out_{val}} = (h_6 - h_0) - T_0 * (s_6 - s_0)$$
$$Ed_{val} = Ex_{in_{Val}} - Ex_{out_{val}}$$

Analysis of seperator

$$(m - m_e) * h_6 = \left(\left(m_f * h_f\right) + \left(m_g * h_g\right)\right)$$
$$m_g = \left(m - m_e - m_f\right)$$
$$Ed_{sep} = \left(T_0 * \begin{pmatrix} \left(m_g * s_g - \left(m_g + m_f\right) * s_6\right) + \\ \left(\frac{m_g * h_g - m_f * h_f}{T_0}\right) \end{pmatrix}\right)$$
$$Ed_{comp_{\%}} = \left(\frac{Ed_{comp}}{Ed_{Claude}}\right) * 100$$
$$Ed_{HX1_{\%}} = \left(\frac{Ed_{HX1}}{Ed_{Claude}}\right) * 100$$
$$Ed_{HX3_{\%}} = \left(\frac{Ed_{HX3}}{Ed_{Claude}}\right) * 100$$
$$Ed_{HX2_{\%}} = \left(\frac{Ed_{HX2}}{Ed_{Claude}}\right) * 100$$
$$Ed_{val_{\%}} = \left(\frac{Ed_{val}}{Ed_{Claude}}\right) * 100$$
$$Ed_{sep_{\%}} = \left(\frac{Ed_{sep}}{Ed_{Claude}}\right) * 100$$
$$Ed_{Claude} = Ed_{comp} + Ed_{HX1} + Ed_{HX2} +$$
$$Ed_{HX3} + Ed_{val} + Ed_{sep}$$

2. Result and Discussion

Fig.2 show the COP and second law efficiency variation with different pressure ratio from analysis, it is noticed that in Claude liquefaction system COP and second law efficiency decrease with increase in pressure ratio. Methane gas COP decreases from 1.35 to 0.95 for the PR range of 40- 220. While other gases like fluorine, oxygen, air, nitrogen and argon COP decreases from 1.15 to 0.75. For all gases 40 bar PR is optimum pressure point. Second law efficiency of system is highest for fluorine gas i.e. 85% followed by nitrogen, air oxygen respectively which has 80-83% second law efficiency. Methane gas show least second law efficiency 67% which continuously decreases from 67% to 45 % for PR range 40 - 220. Liquefaction rate of different gases at different pressure ratio is shown in fig.3. Gases such as argon, oxygen and methane show sharp decrease in liquefaction rate with increase in PR while gases fluorine, nitrogen and air show slight decrease as compared to above gases with increase in PR .The

liquefaction decrement rate of air is lowest i.e. 45% to 42.5% for entire PR range in among all six gases while argon show highest liquefaction rate of 48% which decreases with increase in PR from 48% to 42.5%. Again 40 PR is the ideal pressure for highest liquefaction rate for all gases.Fig.4 show variation in work requirement for gases at different pressure ratio of Claude system. All gases work requirementincreases with increase in pressure ratio of system. Methane gas show highest work requirement 725 kJ/kg to 950 kJ/kg for PR range while Argon show lowest work requirement 275 kJ/kg which increases up to 350 kJ/kg on highest PR 220 in gases. Specific heat of gas in very important factor while energy is transferred between cold and hot fluid. Specific heat of gas is very much influenced by the temperature change during heat exchange in heat exchanger. Fig. 5 show change in specific heat of gases during first heat exchanger with variation in PR. It notice that specific heat for all gases increases during heat exchange with increases in PR of compressor. Methane gas show large change in specific heat 2.4 kJ/kg-K to 3.6 kJ/kg-K compare to other gases with increase in PR 40 to 220. Other gases such as nitrogen, air, and oxygen of first heat exchanger (HX1) show very slight change in specific heat 1.1 kJ/kg-K to 1.3 kJ/kg-K. Fluorine show lowest specific heat 0.8 kJ/kg-K at 40 PR. Change in NTU of first heat exchanger for considered gases with variation in PR as shown in fig.6. At 40 PR, nitrogen and air show equal value of NTU 2.75 but as the pressure ratio increases nitrogen NTU value vary from 2.75 to 2.62 whereas air in same PR range vary from 2.75 to 2.51. Methane gas show lowest value of NTU 2.6 to 2.37 at PR range (40-220). Other gases NTU value decrease with increase in pressure ratio.As the temperature decreases the trend of decrease in NTU for gases also get change. NTU variation with PR in second heat exchanger shown in fig.7. The highest NTU value for air and nitrogen are 5.6 and 5.5 at 80 and 100 PR respectively. The trend of NTU for air and nitrogen with PR show that NTU value first increasesup to said PR then they start decreasing again. Gases like oxygen, fluorine argon and methane show decreasing trend with increasing PR. Methane has lowest NTU value which varies from 4.6 to 3.4 for PR range. In third heat exchanger of claude system the NTU variation with respect to pressure ratio is shown in fig.8. In this Methane gas show highest value of NTU among all gases and it varies from 3.2 to 4.1. From analysis, it is noticed that after 180 PR the change in NTU of methane get constant and show very less variation. All other gases NTU varies from 2.2 to 3 in which argon gas shows least NTU value. Fig.9 shows variation in exergy destruction rate in compressor with increasing pressure ratio. The highest destruction rate is notice for methane gas which ranges from 600 kJ/kg to 1150 kJ/kg for PR range while other gases also show increase in exergy destruction rate with increase in PR. Argon and Fluorine show almost same trend of exergy destruction ranging from 250 kJ/kg to 325 kJ/kg. Exergy destruction in first, second and third heat exchanger is shown in figs [10-12]. In first and second heat exchanger, there is decrease in exergy destruction with increase in PR while in third heat exchanger this variation is reverse, in the low temperature heat exchanger exergy destruction rate increases with increases in PR. In first heat exchanger gas nitrogen and air show sharp variation in exergy destruction rate up to 80 PR but after this PR the slope of decrement of two gases reduces. Fluorine gas exergy destruction variation over PR is very less as compared to other gases, it vary from 1.8 to 1.6 over entire PR range. Argon show least exergy destruction rate among all six gases. In third heat exchanger the rate of exergy destruction of gases air and nitrogen show unusual behavior, in both gas there is slight dip in exergy destruction rate up to 80 PR then it rise up again up to 160 PR and then become almost constant up to 220 PR. The range of variation in exergy destruction in both gas are 119 to 121 which almost constant. Fig.13 show variation in exergy rate in valve with pressure ratio. The slope of increasing exergy destruction rate for methane and nitrogen is high as compared to other gases. Nitrogen gas destruction rate varies from 30 kJ/kg to 140 kJ/kg between PR of (40-220). In valve, air has least exergy destruction rate and almost constant for considered PR range. Fig.14 show exergy destruction trend for gases with pressure ratio. Oxygen, argon, air, nitrogen exergy destruction range is 675 kJ/kg to 600 kJ/kg, 500 kJ/kg to 450 kJ/kg and 350 kJ/kg to 325 kJ/kg respectively. Outlet temperature of expander also get affected by the PR. Fig.15 show variation in outlet temperature of expander with increasing PR with all six gases. Gases outlet temperature decrease in the range of 65-80 PR from 100 K to 88 k (fluorine), 95K -92 K (oxygen), 94K - 83 K(air) and 95K-76 K(nitrogen) respectively. Argon and Nitrogen show almost constant value of outlet temperature that 87 K and 113 K respectively on entire PR range. Fig.16 show the variation in COP and second law efficiency keeping constant optimum PR 40 with variation in expander mass flow ratio or ratio of compressor flow through expander (r). For all gases except methane second law efficiency decreases from 80 % to 40 % when flow ratio through expander increases from 0.5 to 0.8.In methane gas case the system show lowest efficiency range 70 % to 15% over expander flow ratio range. Moreover, COP of system first decreases marginally up to 0.6 PR then it start increasing with increase in flow ratio of expander. The highest COP is exhibit by methane 1.25 followed by other gases. Argon gas show least COP 1 and it is almost entire flow ratio range. Fig.17 show effect on liquefaction rate when there is increase in flow ratio of expander .From graph it is concluded that the liquefaction rate drop from 0.45 kg/s to 0.2 kg/s an average for all gases over increasing flow ratio. Net Work done also affected by expander flow ratio. Fig.18 show methane require 750 kW energy when the expander flow ratio is 0.5 and it almost same up to 0.8. Other gases follow the same trend of decrement over expander flow ratio range from 0.5-0.8. Compressor outlet temperature effect the performance of system. In fig.19, the variation in COP and second law efficiency of system is measured with the increase in compressor outlet temperature of all considered gas as a working fluid. Highest COP of system show at 280 K for all six gases which start decreasing gradually over increase in compressor temperature. The argon gas show lowest COP 1.02 and methane show highest. Same decreasing trend is followed by second law efficiency also and have highest second law

efficiency of methane 90 % to 75% over compressor temperature range while argon show lowest second law efficiency among all gases which range from 55% to 15% over increasing temperature of compressor. Rest of four gases show same decreasing trend for COP and second law efficiency. Fig.20 shows the effect of compressor temperature variation over outlet temperature of expander. In this graph study, it analyses that the for methane gas the variation in outlet temperature (110K) is constantup to 300 K then it start increasing with increase in temperature of compressor. All other gases except argon show increasing trend in outlet temperature with increase in compressor temperature. Argon has the least outlet temperature and remain constant over the compressor temperature range of 280 K to 420K.After 420 K there is small increase in outlet temperature of expander. Fig. 21-23 show variation in specific heat of first, second and third heat exchanger with respect to outlet temperature of compressor. In all three graph same trend of variation in specific heat of gases is notice. The methane gas show highest specific heat ranging from 2.5 kJ/kg-K to 2.9 kJ/kg-K for compressor temperature range 280 K -460 K, while other gases show average specific heat of nitrogen, air, oxygen, fluorine and argon 1.1 kJ/kg-K,1.12 kJ/kg-K, 1 kJ/kg-K, 0.9 kJ/kg-K and 0.6 kJ/kg-K respectively at 280 K. The variation in gases except methane is not notice much and almost seem constant over increasing outlet temperature of compressor. Fig.24 show effect of compressor outlet temperature on liquefaction rate of gases .it observed that argon have highest liquefaction rate 0.474 kg/s and air is least 0.455 kg/s at 280 K. All gases have same liquefaction rate 0.4 kg/s at temperature 280K. All gases liquefaction rate is decreasing with increase in compressor outlet temperature. Variation in work requirement of system with increases in outlet temperature of compressor is shown in fig.25 .The methane gas show highest requirement of work 700 kW at 280 K and argon required least 250 kW at 280K .The trend of gases work requirement is progressing with increase in compressor temperature. .Exergy destruction rate in compressor is also showing same trend of increasing in nature for all gases shown fig.26.The methane range of exergy destruction is 600 kJ/kg -900kJ/kg whereas other gases such as nitrogen, air, oxygen, fluorine and argon range from 320 kJ/kg-500kJ/g, 310kJ/kg- 480 kJ/kg, 290 kJ/kg - 440kJ/kg, 230 kJ/kg-370kJ/kg and 210kJ/kg - 350 kJ/kg respectively. The exergy destruction rate in first heat exchanger is very low at low temperature. Most of the gases first show decreases in exergy destruction up to 320 K and then start increasing at very fast rate if compressor temperature is further increased. Methane gas show highest destruction rate ranging from 8 kJ/kg to 42 kJ/kg. The trend of exergy destruction is shown in fig.27. In second heat exchanger the variation in exergy destruction rate of methane and fluorine gas is first increases up to 300 K then start decreasing on increasing compressor temperature. Gases such as oxygen, air and argon are not much affected up to 340 K but beyond this compressor temperature exergy destruction rate start decreasing.

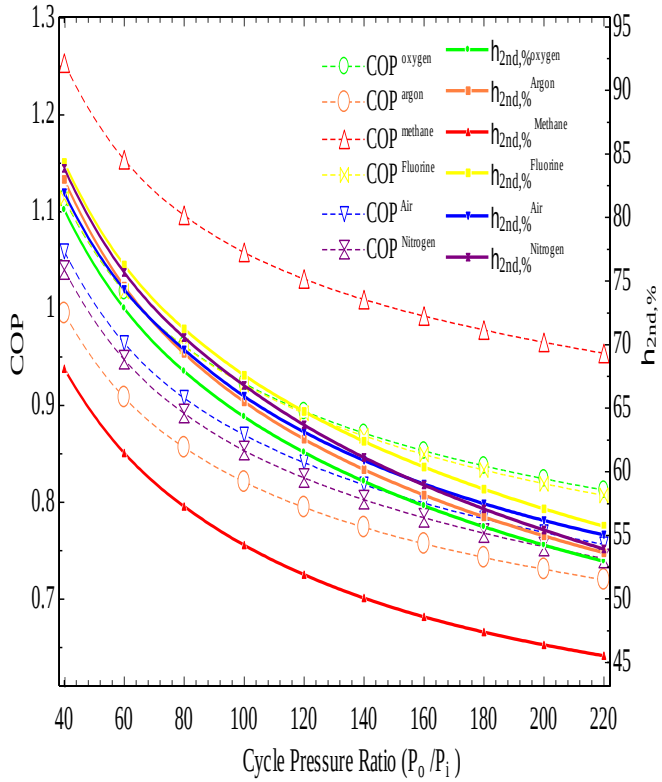

Figure 2: Variations in COP and second law efficiency with respect to cycle pressure ratio

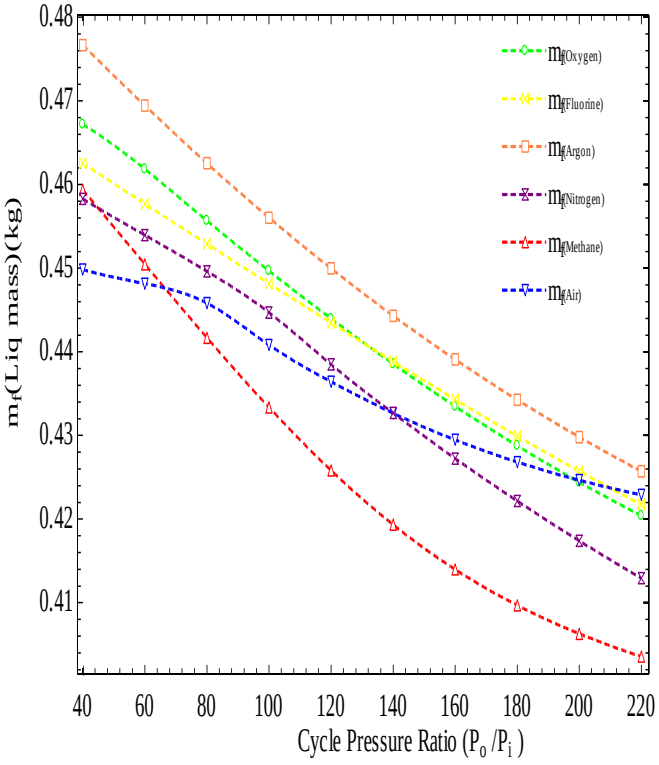

Figure 3: variations in the mass liquefaction rate with respect to cycle pressure ratio

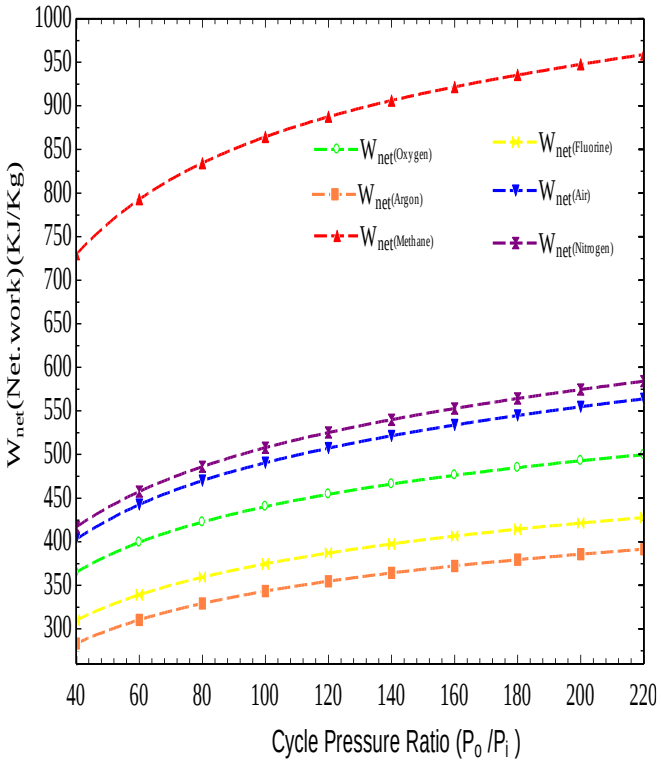

Figure 4: Variations in net work done with respect to cycle pressure ratio

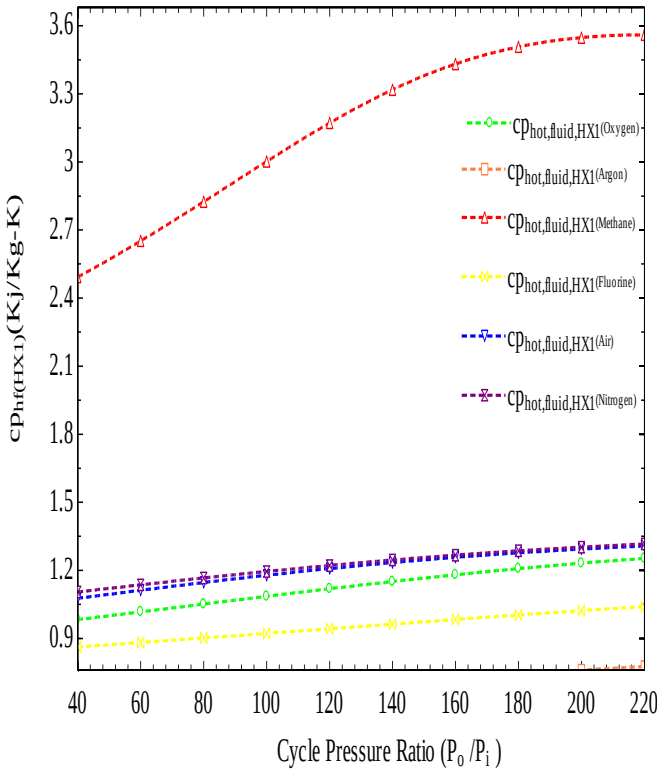

Figure 5: Variations in specific heat of hot fluid in HX1 with cycle pressure ratio

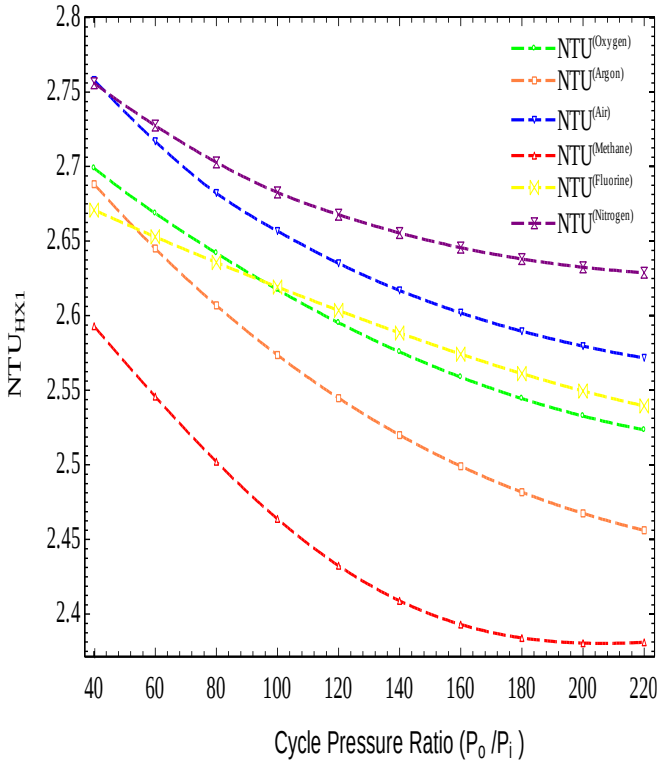

Figure 6: Variations in NTU in HX1 with respect to cycle pressure ratio

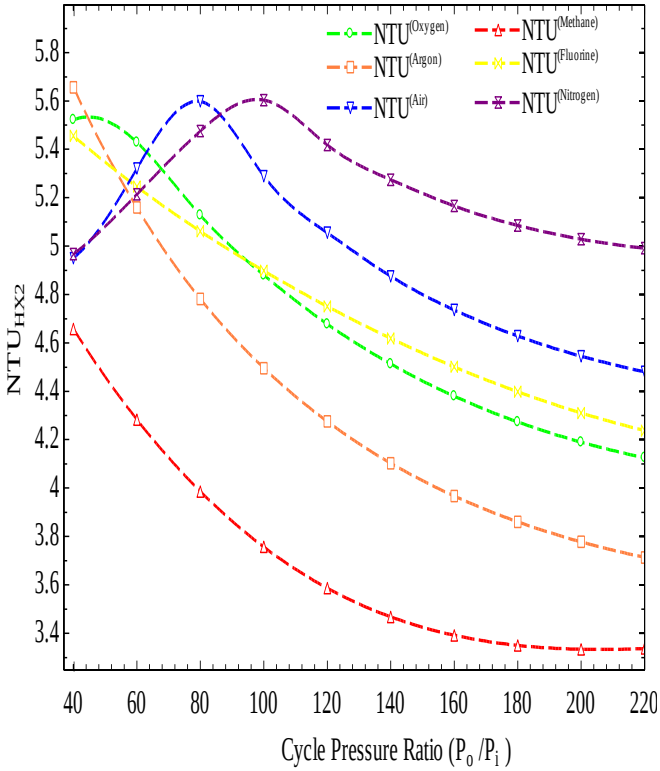

Figure 7: Variations in NTU in HX2 with cycle pressure ratio

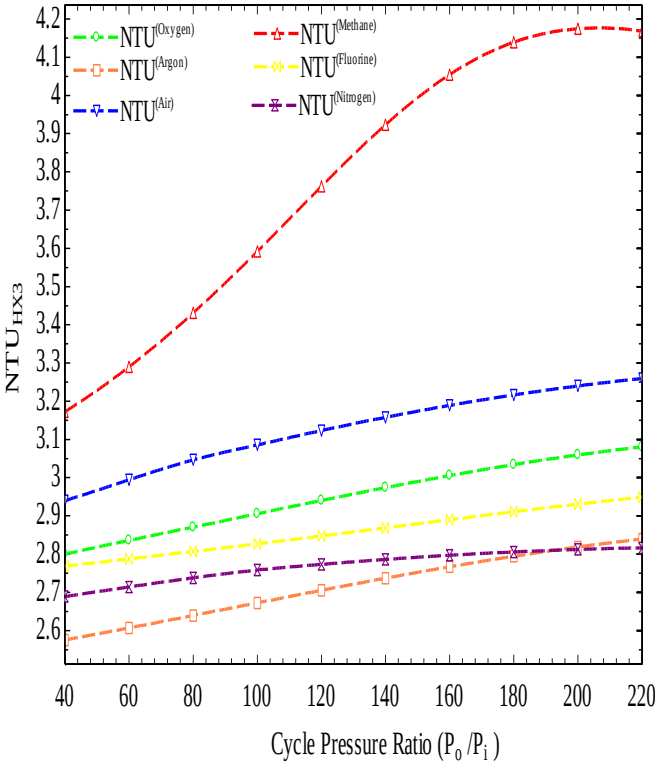

Figure 8: Variations in NTU in HX3 with the cycle pressure

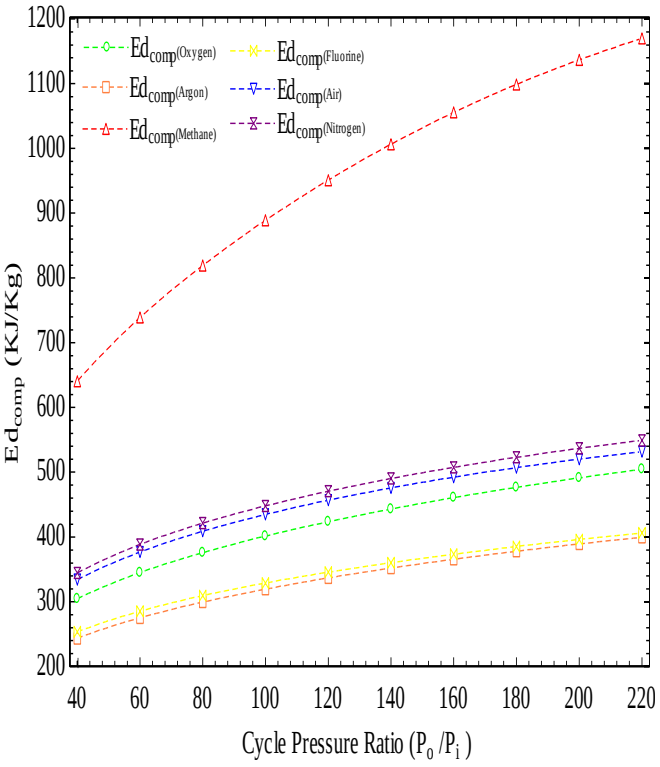

Figure 9: Variations in exergy destruction of compressor with cycle pressure ratio

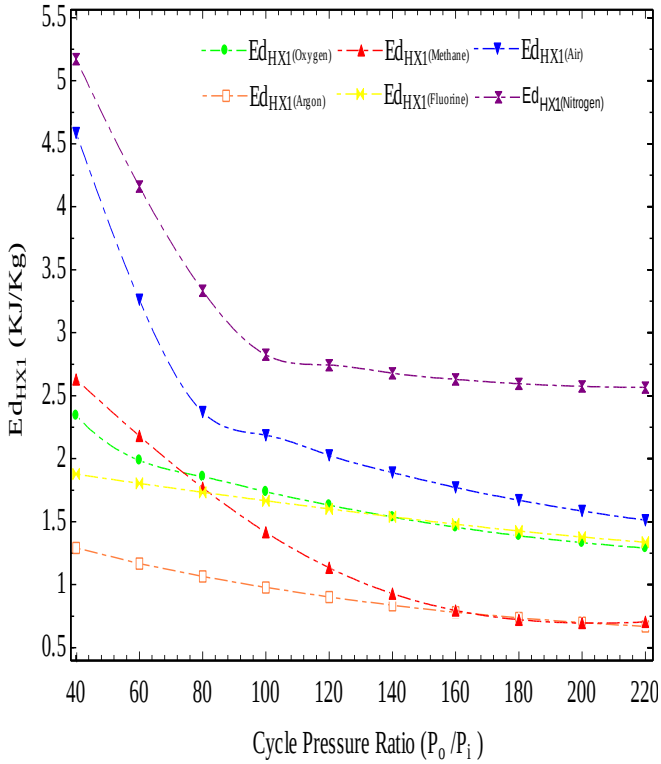

Figure 10: Variations in exergy destruction in HX1with respect to cycle pressure ratio

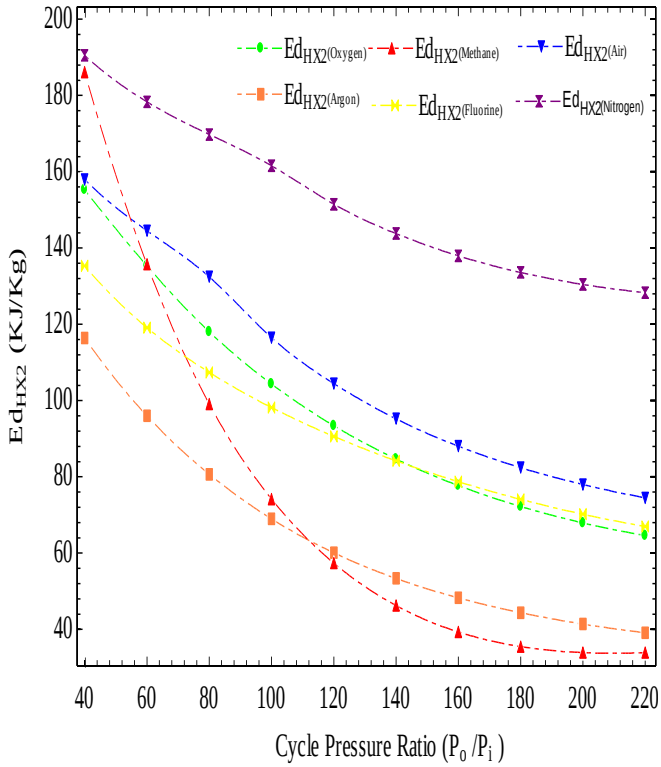

Figure 11: Variations in exergy destruction in HX2 with Cycle pressure ratio

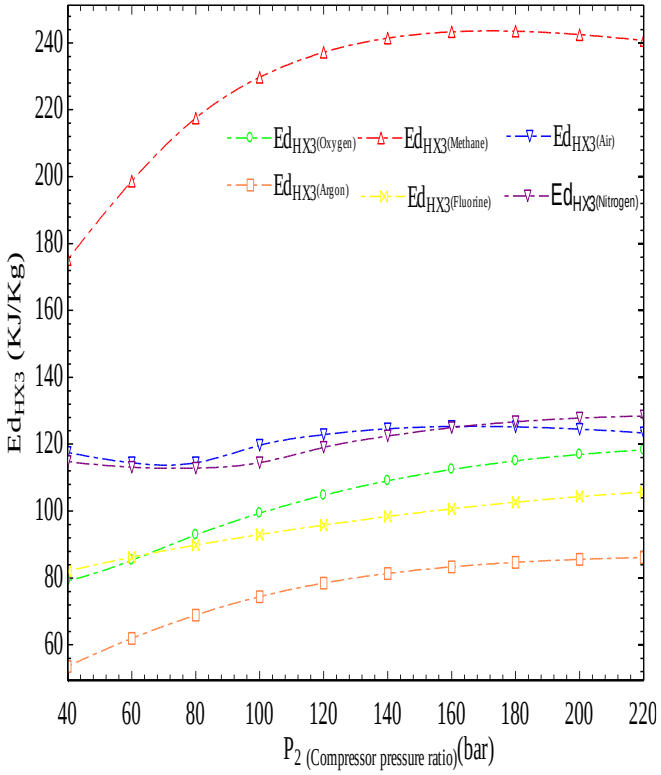

Figure 12: Variations in exergy destruction in HX3 with cycle pressure ratio

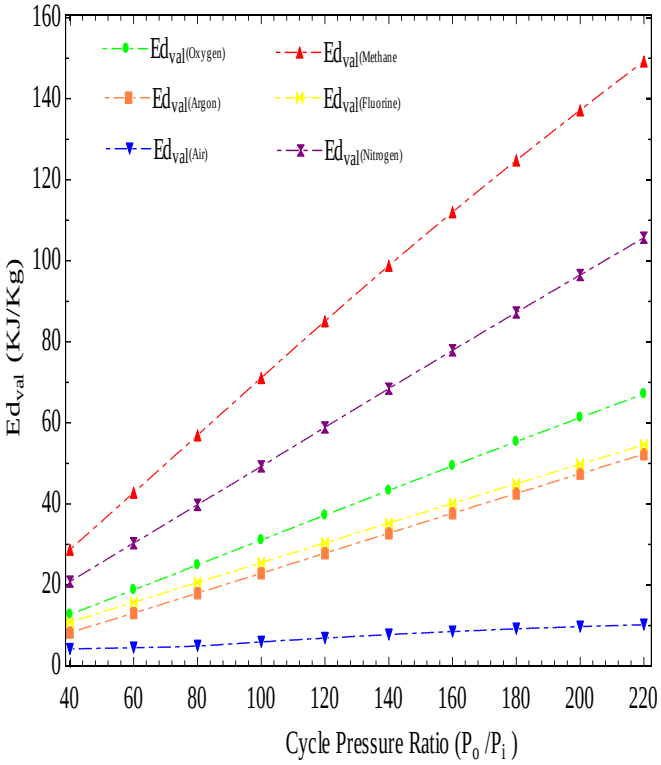

Figure 13: Variations in exergy destruction in valve with cycle pressure ratio

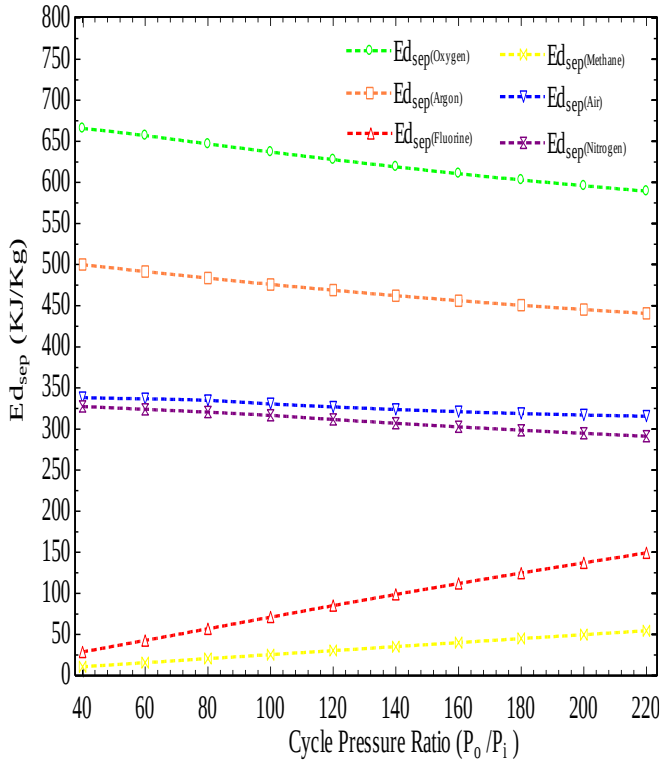

Figure 14: Variations in exergy destruction in separator with respect to cycle pressure ratio

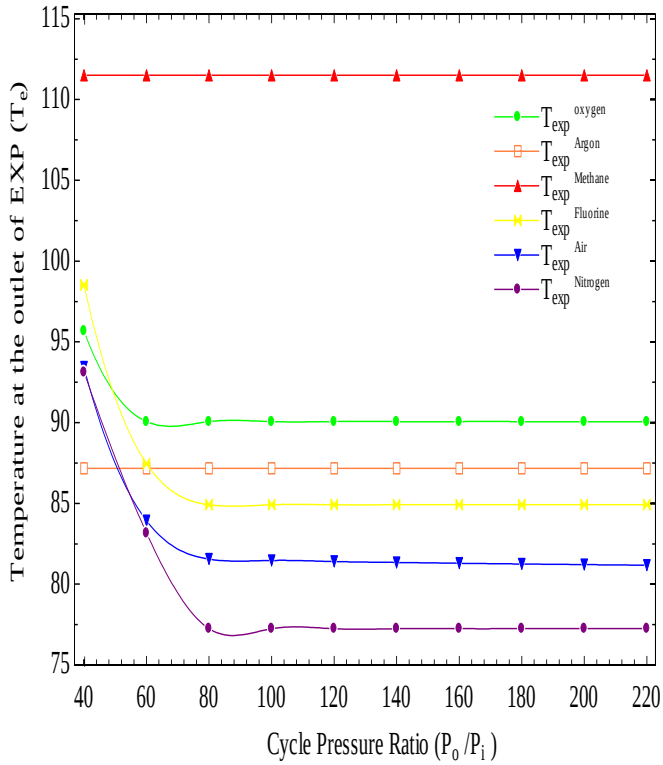

Figure 15: Variations in temperature at the outlet of expander with respect to cycle pressure ratio

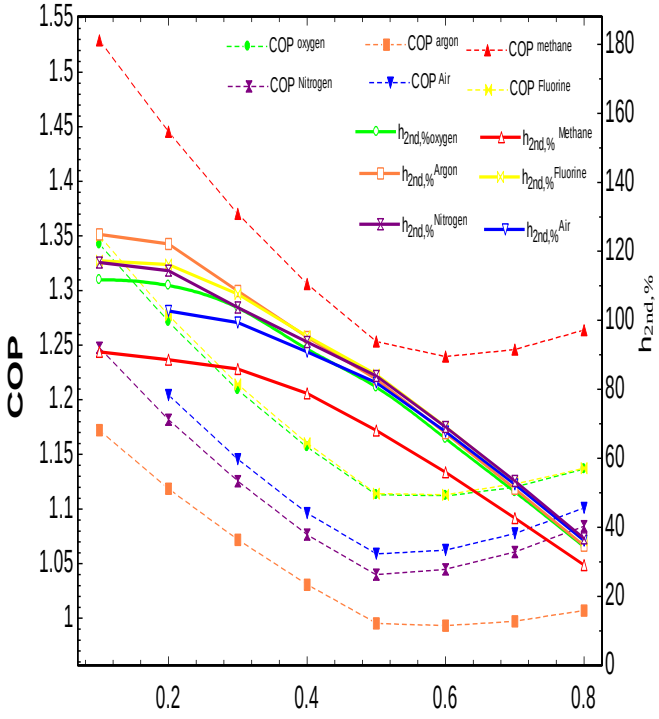

Figure 16: Variations in COP and second law efficiency with respect to ratio of compressor flow through expander

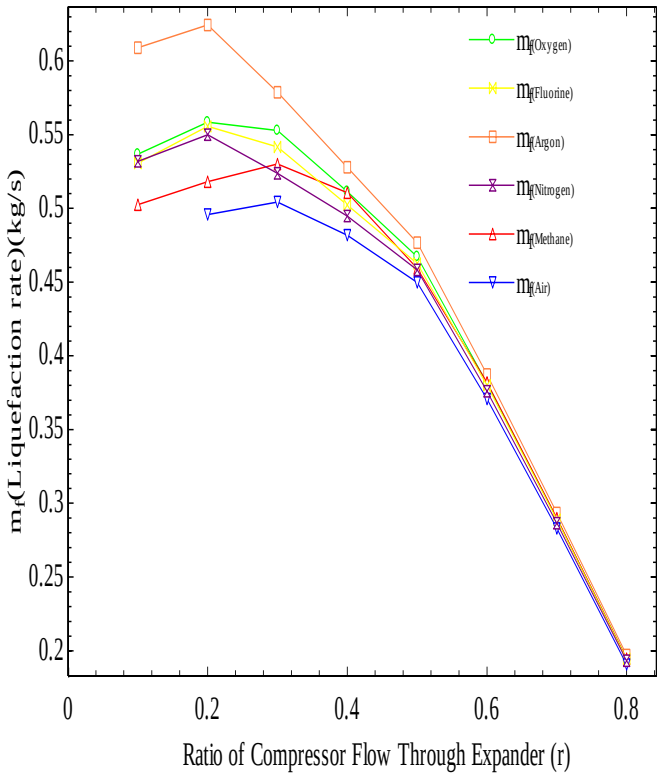

Figure 17: Variations in mass liquefaction rate with respect to ratio of compressor flow through expander

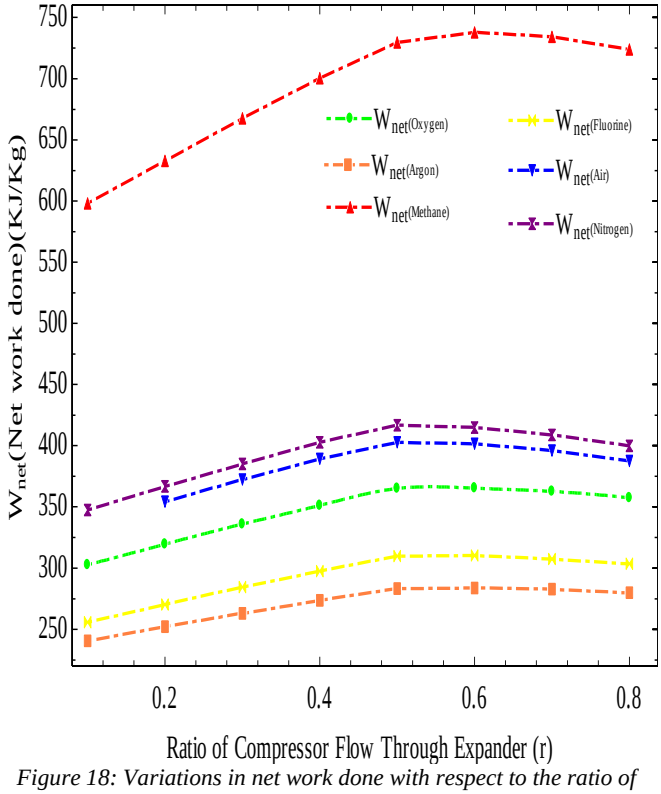

Figure 18: Variations in net work done with respect to the ratio of compressor flow through expander

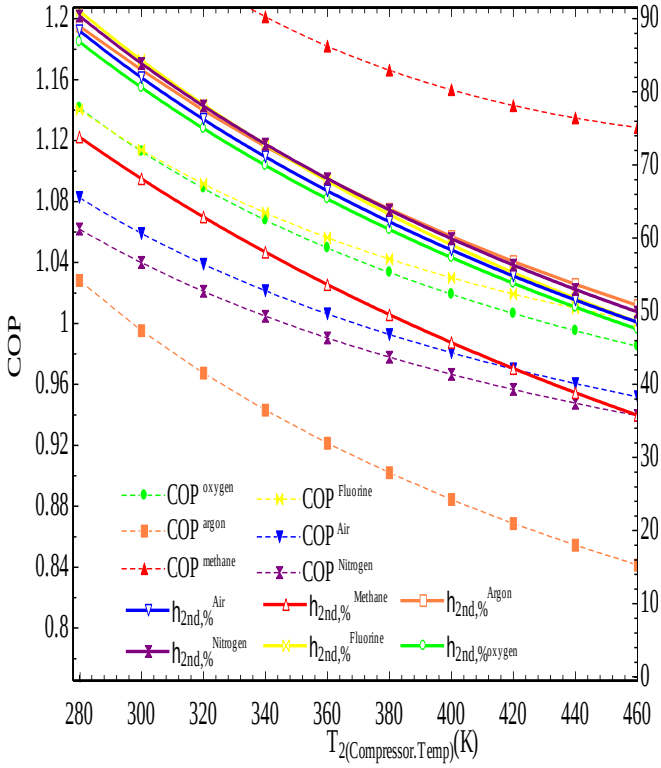

Figure 19: Variations in COP with respect to compressor temperature

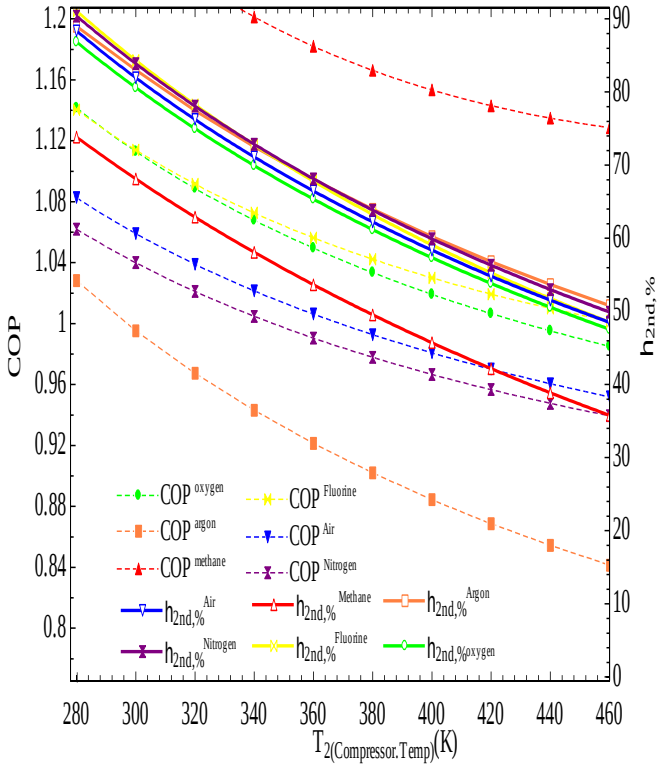

Figure 20: Variations in COP with respect to compressor temperature

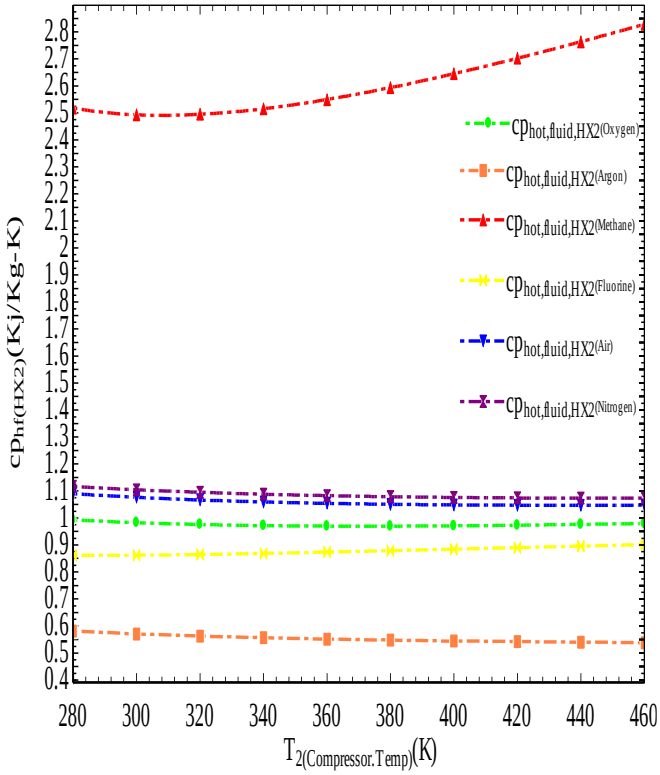

Figure 22: Variations in specific heat in HX2 with respect to compressor temperature

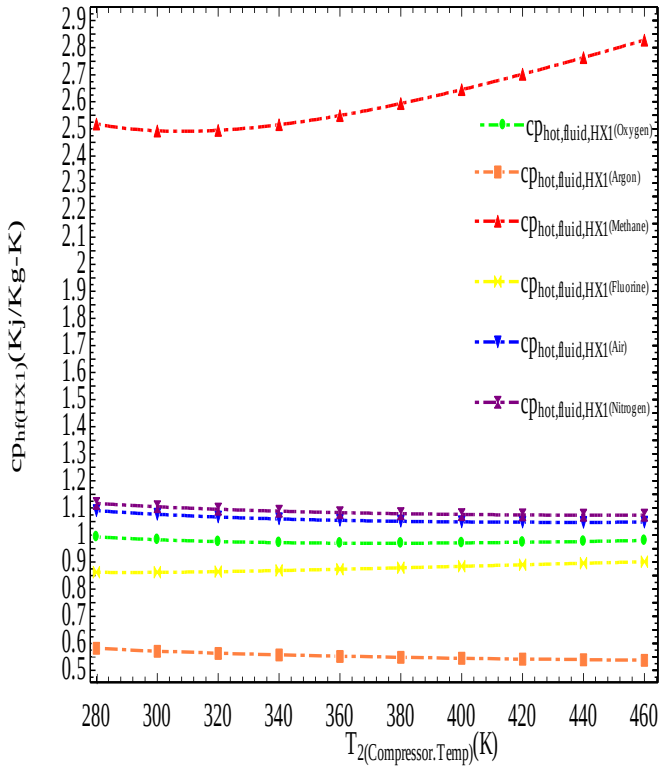

Figure 21: Variations in specific heat in HX1 with respect to compressor temperature

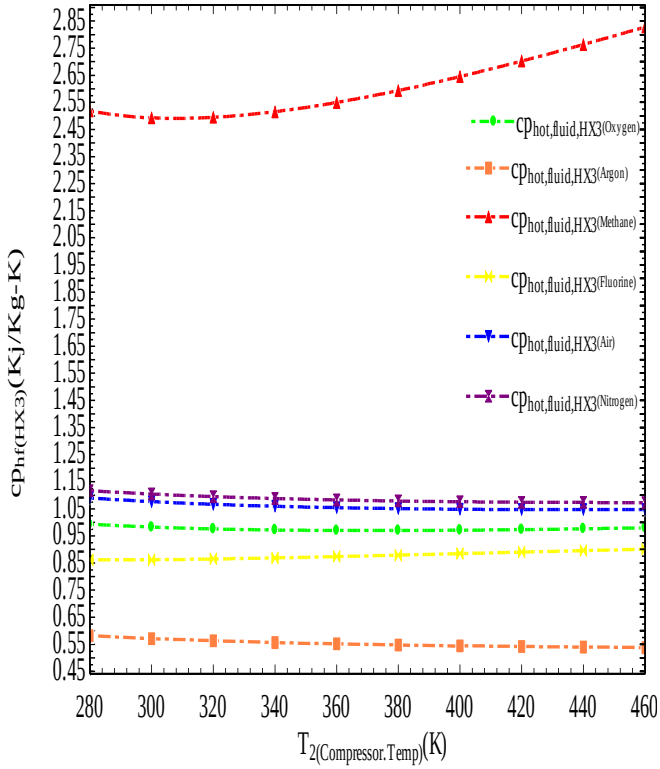

Figure 23: Variations in specific heat in HX3 with respect to compressor temperature

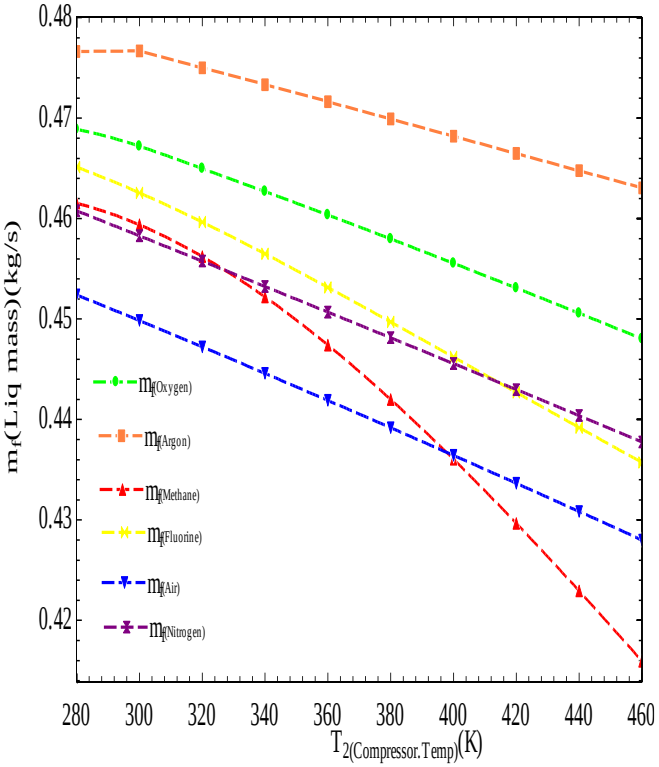

Figure 24: Variations in liquefaction mass flow rate with respect to compressor temperature

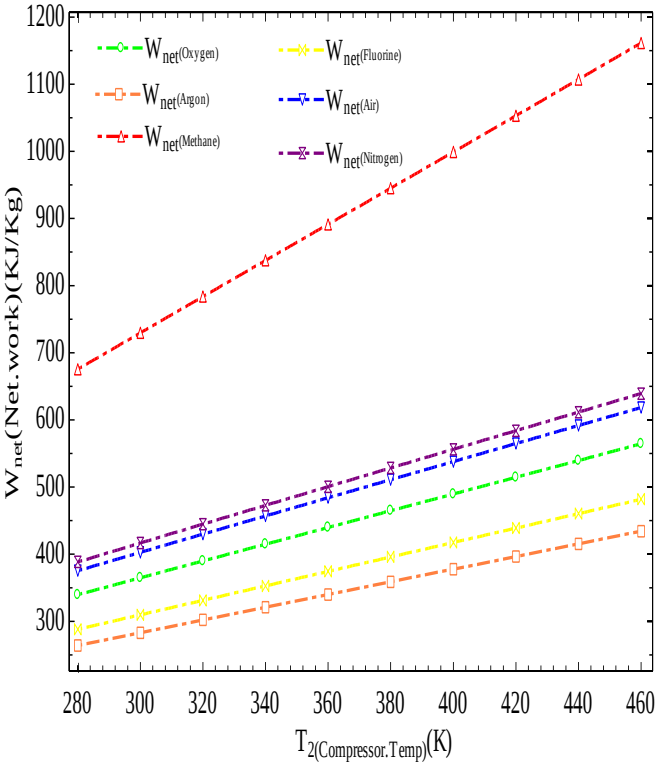

Figure 25: Variations in net work done with respect to compressor temperature

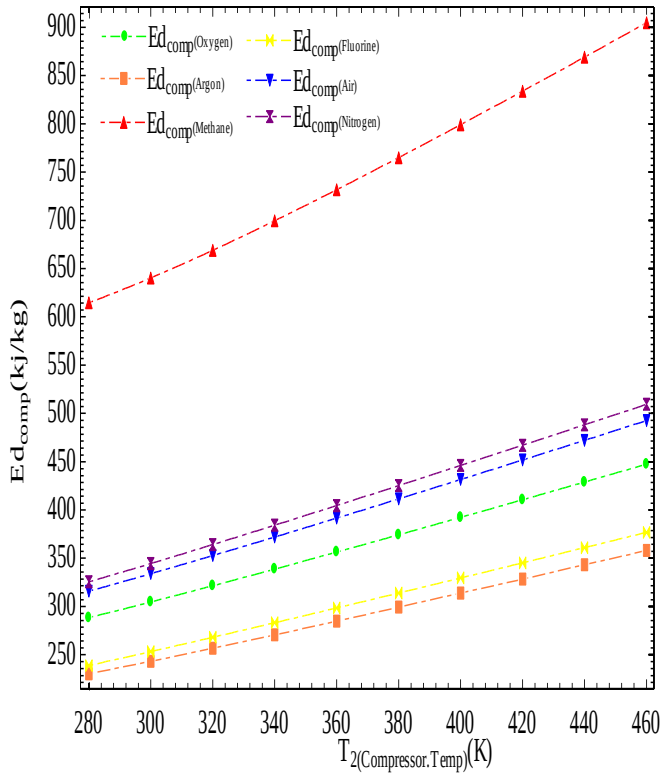

Figure 26: Variations in exergy destruction in Compressor with respect to compressor Temperature

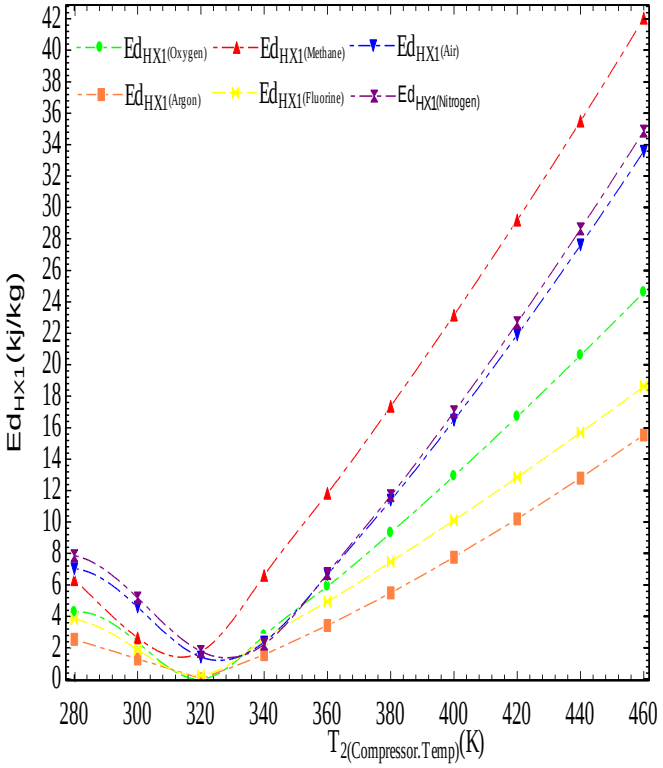

Figure 27: Variations in exergy destruction in HX1 with respect to compressor temperature

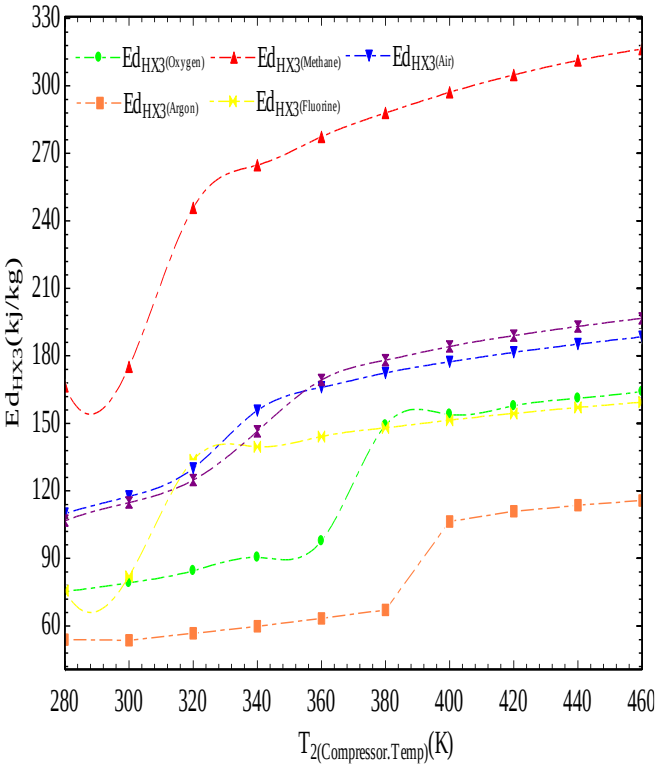

Figure 28: Variations in exergy destruction in HX2 with respect to compressor temperature

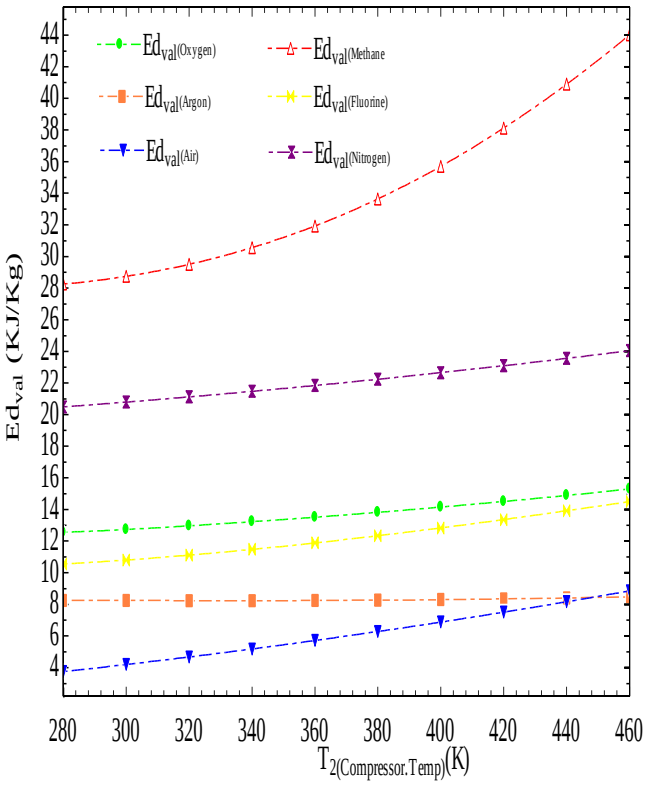

Figure 29: Variations in exergy destruction in HX3 with compressor temperature

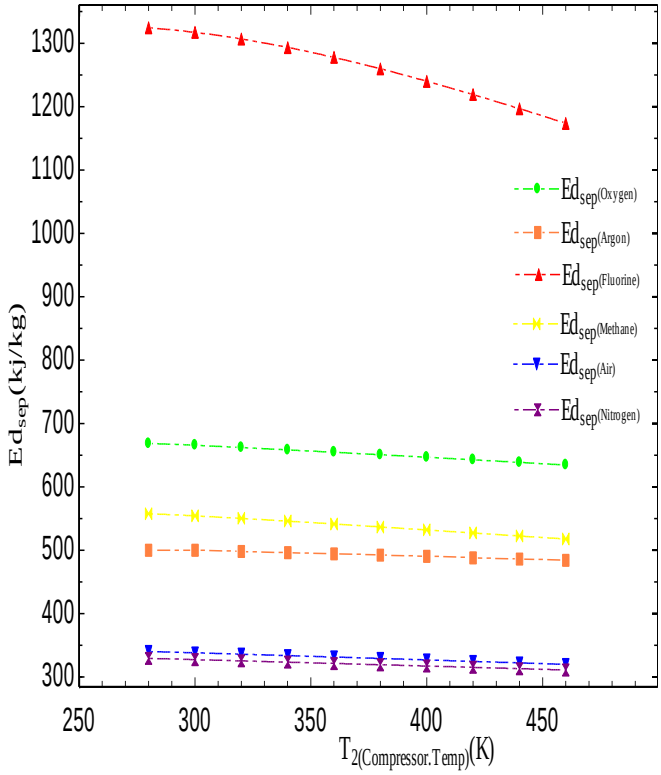

Figure 30: Variations in exergy destruction in compressor with compressor temperature

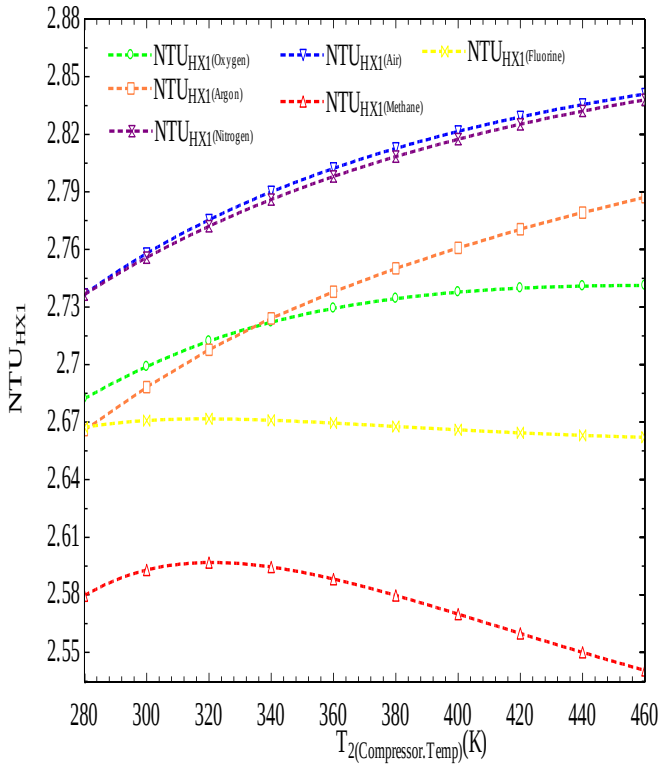

Figure 31: Variations in NTU in HX1 with compressor temperature

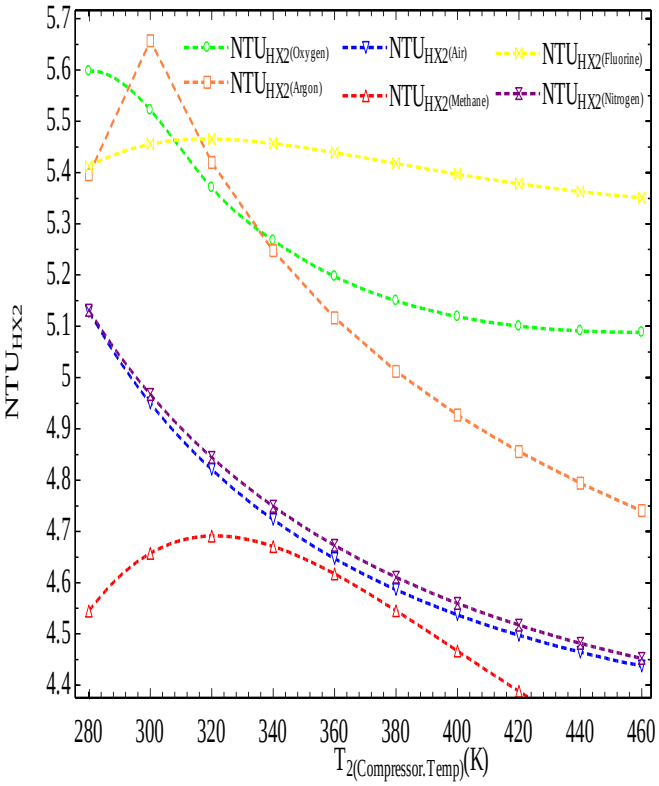

Figure 32: Variations in NTU in HX2 with compressor temperature

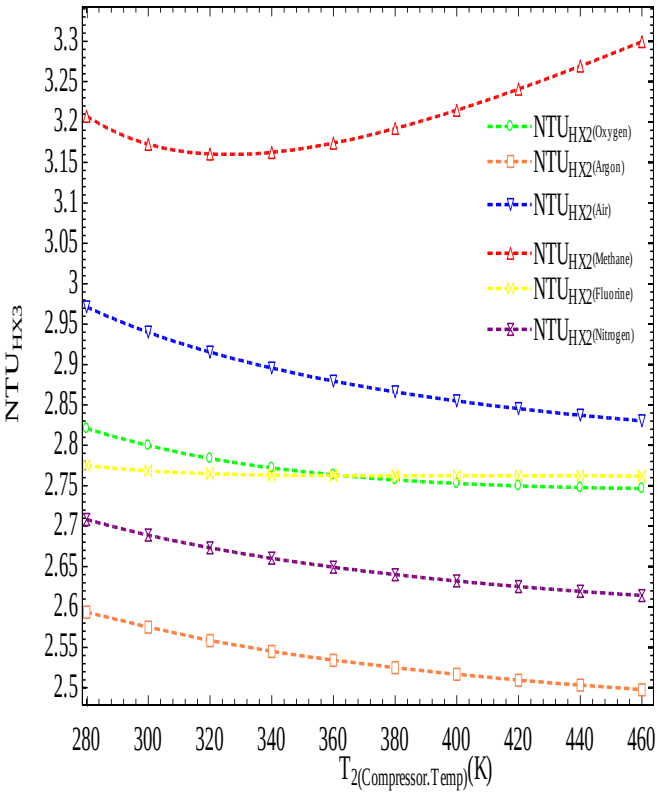

Figure 33: Variations in NTU in HX3 with compressor temperature

Figure 29 show exergy destruction rate in third heat exchanger with respect to compressor outlet temperature. In third heat exchanger the methane and fluorine gas show same trend of exergy destruction, both gas exergy destruction rate first decreases and then start increasing up to 460 K. Other remaining four gases shows increase in exergy destruction rate with increases in outlet compressor temperature. Exergy destruction rate in valve with respect to compressor outlet temperature is explained in fig.31. At 280 K, methane show 28 kJ/kg exergy destruction which increases up to 42 kJ/kg at 460 K. Gases like nitrogen show almost pressure range 280 K - 460 K. In fig.32, all gases exergy destruction rate in separator decreases with increase in compressor temperature. Fig.33 shows the variations in NTU in HX3 with compressor temperature.

3. Conclusions and Recommendations

(1) COP and second law efficiency decrease with increase in pressure ratio. For Methane gas COP decreases.

(2) Second law efficiency of system is highest for fluorine gas followed by nitrogen, air oxygen respectively which has 80-83% and methane gas shows lowest second law efficiency is which continuously decreases.

(3) Gases such as argon, oxygen and methane show sharp decrease in liquefaction rate with increase in PR while gases fluorine, nitrogen and air show slight decrease as compared to above gases with increase in pressure ratio (PR) .The liquefaction decrement rate of air is lowest.

(4) The methane gas show highest requirement of work and argon required lowest. The trend of gases work requirement is progressing with increase in compressor temperature.

(5) Specific heat for all gases increases during heat exchange with increases in pressure ratio (PR) of compressor. Methane gas show large change in specific heat 2 as compare to other gases with increase in PR. Other gases such as nitrogen, air, and oxygen of first heat exchanger (HX1) show very slight change in specific heat while the fluorine show lowest specific heat.

(6) Methane gas show highest value of NTU among all gases and it varies with pressure ratio.

(7) The exergy destruction rate in first heat exchanger is very low at low temperature. Most of the gases first show decreases in exergy destruction up to 320 K and then start increasing at very fast rate if compressor temperature is further increased. Methane gas show highest destruction rate.

(8) In third heat exchanger the methane and fluorine gas show same trend of exergy destruction, both gas exergy destruction rate first decreases and then start increasing.

(9) For all gases exergy destruction rate in separator decreases with increase in compressor temperature.

(10) In second heat exchanger the variation in exergy destruction rate of methane and fluorine gas is first increases up to 300 K and then start decreasing on increasing compressor temperature. Gases such as

oxygen, air and argon are not much affected

References

[1] Yu. V. Sinyavskii, Electrocaloric refrigerators: A promising alternative to current low-temperatureApparatus, Chemical and Petroleum Engineering, 31(6), 1995, 295-306

[2] R. Agrawal, D. W. Woodward, Efficient cryogenic nitrogen generators: An exergy analysis, Gas Separation & Purification, 5(3), 1991, 139-150.

Bull Environ Contam Toxicol
DOI 10.1007/s00128-017-2183-6

Uptake of Heavy Metals from Industrial Wastewater Using In Vitro Plant Cultures

Nupur Jauhari[1] · Sanjay Menon[1] · Neelam Sharma[2] · Navneeta Bharadvaja[1]

Received: 7 April 2017 / Accepted: 22 September 2017
© Springer Science+Business Media, LLC 2017

Abstract The plant species *Bacopa monnieri* has been observed to reduce the heavy metal concentrations in its vicinity. The present study is a comparison of in vitro culture and soil-grown plants of *B. monnieri* to remove Cr and Cd, from synthetic solution and effluent obtained from industrial area. Results were obtained at every half hour interval upto 180 min. Samples were observed for light absorption using UV–Visible spectrophotometer. Statistically, both systems reclaimed Cr and Cd from polluted water. In vitro cultures showed 67% and 93% removal of Cr and Cd from industrial wastewater whereas soil-grown plants showed 64% and 83% Cr and Cd removal. However, reduction rate was significantly higher for in vitro culture as compared to soil-grown plants. Besides other advantages, in vitro plant cultures proved to be more potent to detoxify pollutants in less time. This approach can be used for the removal of heavy metals at large scale.

Keywords *Bacopa monnieri* · Bioactive compound · Ecology · Phytoremediation · Water pollution

Industrial development, especially in developing countries deals with new challenges to the biosphere. Among the available resources, water is a precious commodity that requires special attention. Majority of water near industrial areas is highly polluted thereby not suitable for human consumption and agriculture (Hettick et al. 2016). The world is heading towards water crisis (Rosegrant and Cai 2001) due to the burgeoning population which is exhausting the available fresh water resources. Improvement of living conditions often comes at the cost of the environment. Heavy metal contaminated water from industries is added to rivers making it unfit for human consumption. Hazardous heavy metals found in industrial wastewater are Cr, Cd, Cu, Ni, Pb, As and Zn. A density of more than 5 g per cubic centimeter is generally considered as heavy metal determining factor. Ingestion of heavy metals beyond the permitted concentration, can adversely affect the human health (Chang et al. 1996; Wang and Shi 2001; Beyersmann and Hartwig 2008). One of the toxic heavy metal present in the contaminated water is chromium (Cr) which exists in two forms—trivalent [Cr (III)] or hexavalent [Cr (VI)]. Hexavalent Cr occurs in the form of chromate (CrO_4^{2-}) and dichromate ($Cr_2O_7^{2-}$) which has more toxicity than other valency states. Trivalent chromium is non-toxic and absorbed less readily than hexavalent chromium (Sharma and Forster 1995). High exposure to Cr (VI) can lead to cancer in the digestive tract and lungs, gastric pain, nausea, vomiting, severe diarrhea, fatigue, irritability, hemorrhage, and damage to nervous system (Rosegrant and Cai 2001; Singh et al. 2011). Cd is commonly used in industrial practices as an anticorrosive agent, a stabilizer in polyvinyl chloride products, as a color pigment and in the fabrication of Ni–Cd batteries (Godt et al. 2006). Continued consumption of food or water, containing even low levels of Cd may result in renal failure (CSEM 2008).

Conventional methods for removing heavy metal ions from industrial wastewater demands high investments and operational costs (Rich and Cherry 1987) and therefore, not suitable for small scale industries. On the contrary, in vitro technique like adsorption through activated carbon (AC) is an effective and economical substitute to remediate

✉ Navneeta Bharadvaja
navneetab@dtu.co.in

[1] Department of Biotechnology, Delhi Technological University, New Delhi, India

[2] ICAR-National Bureau of Plant Genetic Resources, Pusa Campus, New Delhi, India

Published online: 30 September 2017

wastewater from toxic heavy metals. Used contaminated biomaterial can be disposed off or processed for further use without harming the environment depending on the contaminant characteristics (Kim and Qi 1995; Wilbur et al. 2012). Environment friendly technique of utilizing in vitro plant cultures for the uptake of heavy metals has an advantage in metabolic studies like the ease of adding inhibitors and inducers in the culture medium (Doran 2009), which can be helpful to enhance the remediation efficiency of in vitro plant cultures. However, not much has been explored so far about the metabolic pathways associated in the transformation of xenobiotic compounds and capacity of certain plants to bear, detoxify and gather a significant amount of heavy metals (Couselo et al.2012), moreover dissimilarity in xenobiotic metabolism between in vitro culture and soil-grown plants was noticed (Doran 2009). In a greenhouse pot experiment, a biomaterial biochar decreased the bioavailability of Cd, Cr and Zn with the promotion in the growth of *Machilus pauhai* plant (Guo et al. 2017). As the in vitro cultures are maintained in microbial free environment, they can be exploited to distinguish the responses and metabolic capabilities of tissue-culture plants from those encountered with microorganisms in their natural environment (Chaudhry et al. 2005; Lebeau et al. 2008). In vitro technique namely hairy root culture was found to be particularly noteworthy in understanding the enzymatic process involved in phytoremediation of phenols and thereby exploring a cost effective system to remediate the polluted environments (Paola et al. 2006). Waoo et al. (2013) standardized an in vitro technique to propagate large number of *Lantana camera* for the removal of heavy metals from the environment. The small amount of biomaterial generated by the plant species that have inherent competence to accumulate or metabolize various pollutants could be enhanced by in vitro culture material without sacrificing the natural habitat. In addition, soil-grown plants have a limited lifespan whereas in vitro plant cultures can be supplied on demand without disturbing the natural habitat. Therefore, use of plant tissue culture has tremendous scope in phytoremediation research as model plant system to discover the biochemical response of plant cells to environmental pollutants. The plant species *Bacopa monnieri* (Brahmi), family Scrophulariaceae, is a weak wetland plant known as memory enhancer in *Ayurvedic* systems of medicine. Various studies on uptake of single or mixed metal removal by *B. monnieri* through in vitro techniques have been successfully done by various scientists till date (Sinha et al. 1996; Sinha 1999; Shukla et al. 2007). Acknowledging above facts, the present study is focused on removal of heavy metals like Cr (VI) and Cd by in vitro plant cultures and soil-grown plants of *B. monnieri* from synthetic solution as well as industrial wastewater with respect to time. Multilinear regression (MLR) has been used for statistical analysis.

Materials and Methods

Plant samples of *B. monnieri* obtained from National Bureau of Plant Genetic Resources (ICAR-NBPGR, Delhi)- were maintained at Delhi Technological University, Delhi. Green parts of the plants were air-dried and crushed using mortar and pestle. AC was prepared by the method used by Singanan and Singana (2007). To the powdered samples, concentrated sulphuric acid was added in the ratio of 1:1.8. Samples were then heated in a hot-air oven at 160°C for 6 h, to release black, coarse AC. After cooling, the AC was washed with double distilled water by repeated centrifugation at 5000 rpm (Medline Scientific). Once pH 7.0–7.5 was attained, the samples were dried in the hot air oven at 105°C for 2–3 h until moisture was completely removed. The dried samples were sieved through 90 µm sieve to obtain only fine AC particles. The prepared biomaterial i.e. AC samples were weighed, characterized and stored at room temperature. The characteristics of AC derived from in vitro propagated and agro net grown plant of *B. monnieri* is represented in Table 1.

Synthetic wastewater containing Cr and Cd was prepared by using analytical grade $K_2Cr_2O_7$ and $CdCl_2$ (Sigma-Aldrich), at concentration of 100–500 and of 1000–5000-ppm respectively. Wastewater containing effluents from metal industries in the Bawana Industrial Area, Delhi, India, was collected from the Western Yamuna Canal, which flows through that area. Wastewater was diluted with double distilled water to a dilution factor of 10 for the study. Samples of Cr and Cd were observed for light absorption using spectrophotometer (UV/Vis PerkinElmer LEMBDA 950) at absorption maxima 350 and 283 nm respectively. Characteristics of industrial wastewater used in the experiment are shown in Table 2. Batch mode adsorption experiment was carried out by taking 60 mL of each test solution with 1 mg/mL AC in 150 ml conical flask. The conical flasks were then agitated at 100 rpm using a mechanical shaker (REMI

Table 1 Characteristics of AC prepared in vitro culture and soil-grown plants of *B. monnieri*

Serial no.	Parameters	Value	
		In vitro	Soil-grown
1	Moisture (%)	0.18	0.15
2	Ash (%)	0.37	0.41
3	pH	7.2	7.4
4	Particle size	≤90 µm	≤90 µm
5	Iodine number	720 mg/g	690 mg/g

Table 2 Characteristics of industrial wastewater

Sl. no	Parameters	Value
1	pH	7.9
2	Electrical conductivity	368 µS/cm
3	Total dissolved solids	328-ppm
4	Cr concentration	225-ppm
5	Cd concentration	1950-ppm

Orbital Shaker). Periodic observation was taken from 30 to 180 min until there was little or negligible decrease in concentration of Cr and Cd. Percent removal of Cr and Cd on the adsorbents was calculated as:

Removal $\% = 100 \times (C - C_f)/C_o$, where C_o is the initial concentration and C_f is the final concentration in ppm.

Before starting the experiment, the instrument was calibrated with optimum wavelength. Presence of any target metal in the blank solution was checked for the accuracy of the results. Limit of detection and limit of quantification for Cr was 20 and 60 ppm whereas for Cd it was 1000 and 3000 ppm respectively. Detection of Cr and Cd was performed by the method used by Parks et al. (2004) and Gavris et al. (2013) respectively.

Results and Discussion

Two standard curves corresponding to the concentration for Cr and Cd in the synthetic water sample have been shown in the Fig. 1a and b respectively.

In vitro plant cultures adsorbed significantly higher amount of metal ion as compared to soil-grown plants. Noticeable effect of in vitro culture and soil-grown plants on synthetic Cr and Cd removal with respect to time was observed (Table 3). Soil grown plants showed 55%–100% removal whereas in vitro plant cultures removed 86%–100% of Cr. Cd removal from in vitro plant cultures and soil grown plants was 54% and 55% respectivelyIncrease in the concentrations of metal ions adversely affects the adsorption. Maximum amount of Cr and Cd removal was noticed up to 120 min. Rate of removal was significantly higher up to 90 min, which reduced afterwards. Equilibrium was attained at 180 min for all the concentrations studied. According to statistical analysis (MLR) of synthetic Cr, percentage removal of Cr is highly correlated with time and concentration as R-Sq(adj) is 87.2% and 93.5% for in vitro plant cultures and soil-grown plants respectively. Significant differences in the removal of Cr using in vitro plant cultures and soil-grown plants could be justified by the value of F being greater than $F_{critical}$ (ANOVA). Further AC obtained from in vitro plant cultures removes higher amount of Cr as compared to soil-grown plants. For synthetic Cd, percentage removal is highly correlated with time and concentration as R-Sq(adj) is 92.9% and 92.2% for in vitro plant cultures and soil-grown plants respectively. Since $F < F_{critical}$, it can be concluded that the removal of synthetic Cd using in vitro and soil-grown plants is almost equal. Similar study was conducted by Singanan and Singanan (2007) using AC from *Tridax procumbens* to remove Cr (95%–97%) from the tannery water after 180 min of treatment. Absorption of hexavalent Cr by AC prepared from bamboo waste (*Oxytenanthera*

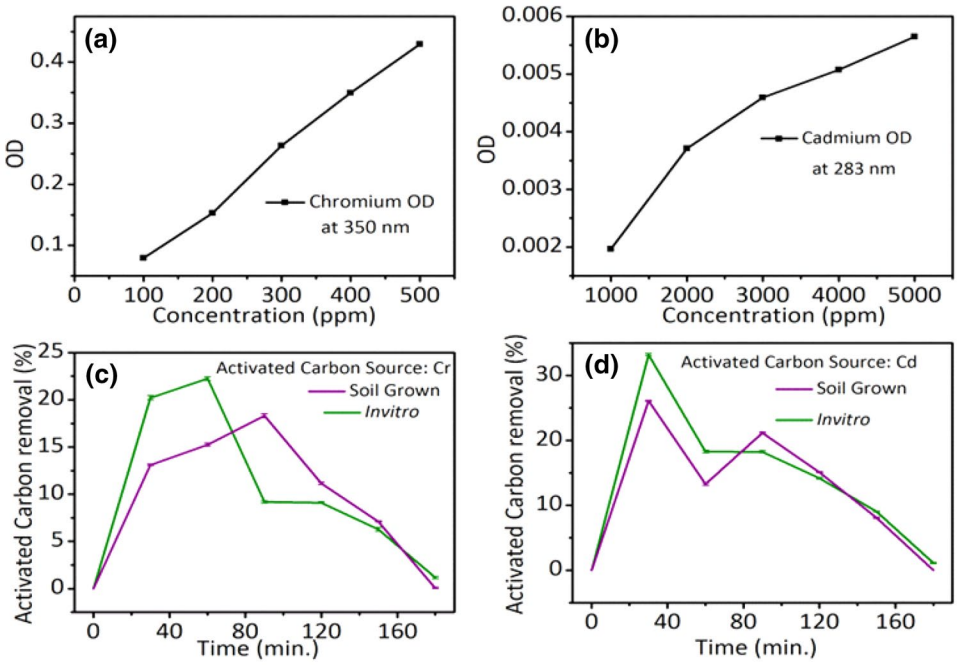

Fig. 1 Standard curve **a** Cr and **b** Cd. Comparison of rate of removal **c** Cr **d** Cd with in vitro culture and soil-grown plants in industrial wastewater

Table 3 Effect of in vitro culture and soil-grown plants on the removal of synthetic Cr and Cd with respect to time

Time (min)	Concentration of Cr and Cd (ppm)																			
	IV		SG		IV		SG		IV		SG		IV		SG		IV		SG	
	100	1000	100	1000	200	2000	200	2000	300	3000	300	3000	400	4000	400	4000	500	5000	500	5000
	Cr	Cd	Cr	Cd	Cr	Cd	Cr	Cd	Cr	Cd	Cr	Cd	Cr	Cd	Cr	Cd	Cr	Cd	Cr	Cd
0	100	1000	100	1000	200	2000	200	2000	300	3000	300	3000	400	4000	400	4000	500	5000	500	5000
30	70	300	90	400	80	1400	150	1200	130	2300	265	2200	200	3750	340	2900	250	4500	430	4100
60	30	200	65	100	60	1100	95	1050	85	1850	230	1650	145	2950	285	2400	210	3900	370	3800
90	10	50	30	50	20	600	65	500	50	1250	70	1400	100	2500	210	2000	130	3300	300	3150
120	0	0	0	0	0	400	40	200	18	930	163	1750	64	2060	200	1660	85	2800	250	2650
150	0	0	0	0	0	280	24	100	0	620	85	1120	40	1790	195	1460	70	2400	225	2300
180	0	0	0	0	0	280	16	100	0	590	59	1120	40	1770	195	1460	70	2300	225	2250

abyssinica) was reported by Dula et al. (2014). AC from eucalyptus seeds exhibited toxic metal ion (zinc) adsorption from the contaminated water (Senthil et al. 2016). Khoramnejadian and Saeb (2017) reported metal (Cr, Cd Cu and Ni) quenching ability of *Amaranthus retroflexus* from contaminated soil after 120 days of cultivation.

After attaining equilibrium at 180 min, metal ion was removed from industrial wastewater. However, in vitro culture rapidly removes toxic metals as compared to soil-grown plants. Effect of in vitro culture and soil-grown plants on industrial wastewater is shown in Table 4. According to statistical analysis, $F < F_{critical}$, it can be concluded that there was not much difference in the removal of Cr and Cd from industrial wastewater using in vitro and soil-grown plants.

Comparison of rate of removal of Cr and Cd with in vitro culture and soil-grown plants in industrial wastewater is shown in Fig. 1c and d respectively. Rate of reduction in metal ion concentration was higher with in vitro plant cultures as compared to soil-grown plants.

Many researchers have proved that in vitro cultures are reliable source for toxicity and tolerant studies (Mumma and Davidonis 1983; Azevedo et al. 2005). Singh et al. (2017) reported the potential of in vitro cultured *Vetiveria zizanoids* for Arsenic removal. In vitro cultures are also appropriate for applying inhibitors and chemical effectors as several metabolic inhibitors and agents helped in revealing this mechanism (Doran 2009). In vitro cultures are suitable to meet the maximum contaminant level (MCL) standard 0.005 mg/L (Agency for Toxic Substances and Disease 1999) and 0.1 mg/L (EPA 2008) for Cd and Cr respectively. In addition, in vitro plant cultures own the exact genomic information of their soil-grown parent plant and could be used in –omic research aimed at uptake of heavy metals like genomic, transcriptomic, proteomic and metabolic (Doran 2009). Application of this methodology need preliminary treatment, like suspended solid removal from polluted water but it can be applied for industrial wastewater treatment.

Present study concludes that in vitro plant cultures of *B. monnieri* are more competent over soil-grown plants for reclamation of polluted water containing Cr and Cd and for large-scale remediation process for the betterment of mankind, agriculture and environment. It has been proven statistically also that both reclaimed Cr and Cd from synthetic solutions as well as from industrial wastewater. However, rate of reduction was significantly higher with in vitro plant cultures as compared to soil-grown plants. In vitro plant

Table 4 Effect of in vitro culture and soil-grown plants on Cr and Cd concentration in industrial wastewater

Time (min)	Activated carbon source			
	In vitro grown plants against Cr	Soil-grown plants against Cr	In vitro grown plants against Cd	Soil-grown plants against Cd
0	225	225	1950	1950
30	180	195	1300	1450
60	130	160	950	1200
90	110	120	600	800
120	89	96	325	515
150	76	81	156	360
180	74	81	136	351

cultures offer microbial free environment with no translocation barrier to determine intrinsic capacity of plant cells for remediation of contaminants. Technical applicability like cost-effectiveness, easily manageable biomaterial, rapid and eco-friendly set up are the key factors that play an important role in the selection of in vitro cultures for detoxification of pollutants from the wastewater.

Acknowledgements The authors wish to express thanks to the Vice Chancellor of Delhi Technological University and Head of Department of Biotechnology for providing the facility and support to conduct the research work.

References

Agency for Toxic Substances and Disease Registry (1999) US Department of Health and Human Services, Environment health and Medicine Education. https://www.atsdr.cdc.gov/csem/csem.asp?csem=6&po=7

Azevedo H, Pinto CGG, Santos C (2005) Cadmium effects in sunflower. Membrane permeability and changes in catalase and peroxidase activity in leaves and calluses. J Plant Nutr 28:2233–2241

Beyersmann D, Hartwig A (2008) Carcinogenic metal compounds: recent insight into molecular and cellular mechanisms. Arch Toxicol 82:493–512. doi:10.1007/s00204-008-0313-y

Case Studies in Environmental Medicine (CSEM) (2008) Cadmium Toxicity Agency for Toxic Substances and Disease Registry (ATSDR). US Department of Health and Human Services, Public Health Service, Atlanta. http://www.atsdr.cdc.gov/csem/cadmium/docs/cadmium.pdf. Accessed 18 March 2016

Chang LW, Magos L, Suzuki T (1996) Toxicology of metals. CRC Press, Boca Raton

Chaudhry Q, Blom-Zandstra M, Gupta S, Joner EJ (2005) Utilising the synergy between plants and rhizosphere microorganisms to enhance breakdown of organic pollutants in the environment. Environ Sci Pollution Res. doi:10.1065/espr2004.08.213

Couselo JL, Corredoira E, Vieitez AM, Ballester A (2012) Plant tissue culture of fast-growing trees for phytoremediation research. Plant Cell Cult Protoc. doi:10.1007/978-1-61779-818-4_19

Doran P (2009) Application of plant tissue cultures in phytoremediation research: incentives and limitations. Biotechnol Bioeng 103:60–76. doi:10.1002/bit.22280

Dula T, Siraj K, Kitte SA (2014) Adsorption of hexavalent chromium from aqueous solution using chemically activated carbon prepared from locally available waste of Bamboo (*Oxytenanthera abyssinica*). ISRN Environ Chem. doi:10.1155/2014/438245

Environmental Protection Agency (2008) United States. https://www.epa.gov/dwstandardsregulations/chromium-drinking-water

Gavriş G, Caraban A, Stanasel O, Badea GE (2013) Cadmium ions recovery by chemical precipitation method from rezidual solutions of galvanic plating. J Sustain Energy 4(1):1–5

Godt J, Scheidig F, Christian GS, Esche V, Brandenburg P, Reich A, Groneberg DA (2006) The toxicity of cadmium and resulting hazards for human health. J Occup Med Toxicol. doi:10.1186/1745-6673-1-22

Guo X, Li H, Chen H (2017) The effects of biochar and intercropping on the Cd, Cr and Zn speciation in soils and plant uptake by *Machilus pauhoi*. Bull Environ Contam Toxicol. doi:10.1007/s00128-016-2013-2

Hettick BE, Cañas-Carrell JE, Martin K, French AD, Klein DM (2016) Arsenic uptake by muskmelon (cucumismelo) plants from contaminated water. Bull Environ Contam Toxicol. doi:10.1007/s00128-016-1893-5

Khoramnejadian S, Saeb K (2017) Accumulation and translocation of heavy metals by *Amaranthus retroflexus*. J Earth Environ Health Sci 1:58–60

Kim BJ, Qi S (1995) Hazardous waste treatment technologies. Water Environ Res 67:560–570

Lebeau T, Braud A, Je´Ze´Quel K (2008) Performance of bioaugmentation-assisted phytoextraction applied to metal contaminated soils. Environ Pollut. doi:10.1016/j.envpol.2007.09.015

Mumma RO, Davidonis GH (1983) Plant tissue culture and pesticide metabolism. In: Hutson DH, Roberts TR (eds) Progress in pesticide biochemistry and toxicology, vol 3. Wiley, Chichester, pp 255–278

Nomanbhay SM, Palanisamy K (2005) Removal of heavy metal from industrial wastewater using chitosan coated oil palm shell charcoal. Electron J Biotechnol 8:43–53. doi: 10.2225/vol8-issue1-fulltext-7

Paola SG, Cristian EC, Horacio AT, Silvia RM, Elizabeth A (2006) Phytoremediation of phenols from wastewater, by peroxidises of tomato hairy root cultures. Enzyme Microbial Technol 59:647–653. doi:10.1016/j.enzmictec.2005.11.014

Parks JL, McNeill L, Frey M, Eaton AD, Haghani A, Ramirez L, Edwards M (2004) Determination of total chromium in environmental water samples. Water Res 38:2827–2838

Rich G, Cherry K (1987) Hazardous waste treatment technologies. Pudvan Publishers, Co. Inc., Northbrook, IL, p 182

Rosegrant MW, Cai X (2001) Water scarcity and food security: alternative futures for the 21st century. Water Sci Technol 43:61–70

Senthil Kumar P, Saravanan A, Anish Kumar K, Yashwanth R, Visvesh S (2016) Removal of toxic zinc from water/wastewater using eucalyptus seeds activated carbon: non-linear regression analysis. IET Nanobiotechnol 10:244–253. doi:10.1049/iet-nbt.2015.0087

Sharma DC, Forster CF (1995) Chromium studies into the adsorption of chromium (VI) using sphagnum moss peat. Bioresource Technol 52:261–267

Shukla OP, Dubey S, Rai UN (2007) Preferential accumulation of cadmium and chromium: toxicity in *Bacopa monnieri* L. under mixed metal treatments. Bull Environ Contam Toxicol 78:252–257

Singanan M, Singanan AAV (2007) Studies on the removal of hexavalent chromium from industrial waste water by using biomaterials. Electron J Environ Agric Food Chem 6:2557–2564

Singh R, Gautam N, Mishra A, Gupta R (2011) Heavy metals and living systems: an overview. Indian J Pharmacol 43:246–253. doi:10.4103/0253-7613.81505

Singh S, Sounderajan S, Kumar K, Fulzele DP (2017) Investigation of arsenic accumulation and biochemical response of in vitro developed *Vetiveria zizanoides* plants. Ecotoxicol Environ Saf 145:50–56. doi:10.1016/j.ecoenv.2017.07.013

Sinha S (1999) Accumulation of Cu, Cd, Cr, Mn and Pb from syntheticly contaminated soil by *Bacopa monnieri*. Environ Monit Assess 53:253–264. doi:10.1023/A:1006091215529

Sinha S, Gupta M, Chandra P (1996) Bioaccumulation and biochemical effect of mercury in the plant *Bacopa monneri* (L.). Environ Toxicol. doi:10.1002/(SICI)1098-2256(1996)11:2<105::AID-TOX5>3.0.CO;2-D

Wang S, Shi X (2001) Molecular mechanisms of metal toxicity and carcinogenesis. Mol Cell Biochem. doi:10.1023/A:1017918013293

Waoo A, Khare S, Ganguly S (2013) In vitro culture of *Lantana camera* from nodal and shoot tip explants in phytoremediation studies. Curr Trends Technol Sci 11:183–186

Wilbur S, Abadin H, Fay M, Yu D, Tencza B, Ingerman L, Klotzbach J, James S (2012) Toxicological profile for chromium Atlanta (GA): Agency for Toxic Substances and Disease Registry (US). https://www.ncbi.nlm.nih.gov/books/NBK158855/. Accessed Sept 2008

International Journal of Research in Engineering and Innovation (IJREI)
journal home page: http://www.ijrei.com
ISSN (Online): 2456-6934

Utility of thermodynamic (exergy-exergy) analysis in cryogenic systems for liquefaction of gases: A Review

Dr. R.S Mishra & Devendra Kumar

Department of Mechanical, Production & Industrial and Automobile Engineering, Delhi Technological University, Delhi-110042

Abstract

The exergy efficiency depend upon mainly upon the inlet condition of the system because inlet condition best suit for a particular type of the system except to increase the whole system efficiency stresses are done on particular parts of system and research are done on that systems. It was observed that that every part of system has its own and equal importance because ones effect on another whether it is small or big create a lot of difference in proper thermodynamic analysis of system. Ignoring one small system due less effect can put gap in complete thermodynamic research analysis of system that why it quite important take all parts of system as one and finding out the every part impact on another to calculate right equation for high output. Due to Air separation unit and compressor, condenser and evaporator of cryo system are the center of research because most of exergy destruction takes place in these parts. Heat exchanger and expansion valve, expander and other addition parts should also properly analyze
The main objectives of present investigations are Exergy analysis of considered cryogenics systems and finding exergy destruction in each and there individuals components Suggestion for reducing exergy destruction losses in whole systems and there components

© 2017 ijrei.com. All rights reserved

Keywords: Cryogenics, Thermodynamic Analysis, Energy-Exergy Analysis, First and second law efficiencies

1. Introduction

Cryogenics has been an important area of refrigeration because of its application in industrial and commercial utilization, and many scientific and engineering researches are going on by using low temperature liquefied gases. Cryogenics isa branch of physics which deals with the achieving very low temperatures (below the 173 K.) and study their effects on matter .Cryogenic study presents broad goals for cryogenic support for various gas liquefaction systems. Due to industrial revolution, various issues like cost, efficiency and reliability are the challenges factors in employment of cryogenic support technology. In field of mechanical engineering we try to refine or improve the ability or quality of material to get in maximum use at maximum level at a reduce cost. In past many fantasticclaim have been made as to the degree of improve performance achieved by employing cryogenics technology. Cryogenic engineering is the application of low temperatures that cannot be observed on Earth or in the atmosphere around earth under natural conditions to practical problems .In refrigeration, the temperature from -100 0C to -2730C (Or absolute Zero) are treated as low temperatures and Cryogenics is the science connected with reaching and applying temperatures below 120K (-1530C) [1].

1.1 Cryogenics Fluids

Today for achieving cryostat we uses many fluid but in due course some fluid considered as the main fluid to achieve cryostat and the temperature range of cryostat mostly depend upon the fluid we uses in apparatus .The chief fluids to achieve very low temperature are methane, oxygen, nitrogen, neon, hydrogen and helium. The characteristics of the most widely used cryogenic liquids are collected in Table 1. Table 1 gives the normal (1 bar) boiling temperature TN, the critical temperature TC and pressure PC, the temperature T3 and pressure p3 at triple point and the volume ratio VV/VL describing the increase in the fluid volume due to the process of vaporization and heating to the atmospheric temperature.

Corresponding Author: R.S. Mishra
Email Id: rsmishra@dce.ac.in

Table: 1 Properties of Cryogenics Liquids [2].

Cryogenics	TN	TC	Pc	T3	P3	VV/V L
Liquid	K	K	MPa	K	kPa	
Methane	111.6	190.7	4.63	88.7	10.1	590
Oxygen	90.2	154.6	5.04	54.4	0.15	797
Nitrogen	77.3	126.2	3.39	63.2	12.53	646
Neon	27.1	44.4	2.71	24.6	43.0	1341
Hydrogen	20.3	32.9	1.29	13.8	7.04	788
Helium	4.2	5.2	.227	-----	-----	701

As seen from the table helium can achieve a very low temperature of 4.2 K but initially when helium is evaporated from its liquid state under high vacuum , the temperature as low as 1.1 K (-271.90C) was obtained but now a days , the lowest temperature achieved is 0.001 K very close to absolute temperature) [1].

1.2 Applications of Cryogenics

- Cryogenic Technology is used for production of Gases for industrial and commercial applications. In this process liquefaction and purification of Helium, Nitrogen gases are done. Also using this technique production of inert gases is done.
- Cryogenics is very crucial for aerospace application. This technology is very critical for wind tunnel testing application. High performance wind tunnel required rapid movement of nitrogen gas around the aerodynamic circuit.
- Cryogenic is required for Frozen Food Industries for preservation of food item depending upon type of food item and whether they are cooked or not before freezing.
- Cryogenic has got lot of application in medical field. It is wildly used in MRI equipment for diagnosis of diseases.
- Cryogenic has got a great role in chilled water storage system.

2. Literature Review

Walther Nernst (1906) [1]: Implies the impossibility of attaining absolute zero and introduce third law thermodynamics but modern science has reached temperatures only one-millionth of a degree above absolute zero, but absolute zero itself cannot be attained

Ref No	Author	Journal	Year	Work Done	Future Scope
2	Thomas et al	Cryogenics	2011	Lowest temp. of high liquid system can be improved by increasing the pressure ratio, mass imbalance gets compensated by the specific heat imbalance, optimum expander flow is found to be 80% of the total flow through the cycle.	Optimization of every system can be done to analyze to improve efficiency
3	Thomas et al	International journal of refrigeration	2012	In He system when two Brayton stages are combined to make one modified Brayton stages, the performance deteriorates. When one Brayton stage is split into two modified Brayton stages without changine show improvement without changine HX area.	More alternate arrangement s of cycle can be explore to enhance efficiency
4	Thomas et al	Energy	2012	Done exergy analysis to system so the result can be applicable on large He liquefier to get right parameters for geometric design. . Compressor pressure, expander flow rates, heat exchanger surface area are some of the parameters optimized considering both presence and absence of pressure drop in the heat exchangers.	At Different pressure values the system is analysied and again to find best pressure ration for optimum number of stages for liquefaction system
5	Thomas et al	International journal of refrigeration	2013	It has been demonstrated that four refrigeration stages is the best option for large helium liquefiers when all expanders operate between the entire available pressure differences when some of the expanders are operated at intermediate pressure, a more number of stages gives a higher thermodynamic efficiency. The intermediate pressure that gives the maximum exergy efficiency for the plant increases	More analysis can be done adopting more intermediate expander to increase overall efficiency
6	Cammarata et al	Applied energy	2001	This paper presents an optimization methodology for liquefaction/refrigeration systems in the cryogenic field. An optimization methodology based on genetic algorithms has been defined on helium liquefaction system	More different methodology can be put to get better results like Applied mathematics dealing critical variables

7	Thomas et al	Cryogenics	2012	Time consuming simulation are demerit in computational technique. The simulation time of the flow-sheet with PR and MBWR EOS(s) is also found to be 45 times faster than the real time, while the flow sheet with MBWR is found to be only 39 times faster than the real time.	More advance technology and more good simulation tool like HYSYS can done simulation more better and use of them can
8	Berstad et al	International Journal of Hydrogen Energy	2009	A methodology for hydrogen liquefaction that compensate non –uniformity in feed specification has been developed and applied three liquid liquefier. The process in consideration has been modified to have equal hydrogen feed pressure, resulting in more consistent comparison. Decrease in feed pressure resulting in more power consumption but have high energy vice versa. The approach can be adapted in boundary condition that the liquefaction process will be subjected to a real energy system.	How much pre-compression will best suit at variable compression pressure
9	Valenti et al	International Journal of Hydrogen Energy	2008	Refrigeration is via four helium recuperative Joule–Brayton cycles arranged so that the refrigerant follows the cooling curve of hydrogen and the volume flow rates in compression and expansion processes are typical of axial-flow high-efficiency turbomachines, compressionis accomplished in 15 intercooled 8-stage devices derived from gas turbine technology. the predicted work of approximately 18 MJ kg^{-1} is half as much as the requirement of those liquefiers and corresponds to a second-law efficiency of almost 48%.	48% efficiency is predicted not achieved ,different arrangement with Bryton cycle and stages are still research of point to achieve high efficiency
10	Krasaein et al	International Journal of Hydrogen Energy	2010	A proposed liquid hydrogen plant using a multi-component refrigerant (MR) refrigeration system is explained in this paper. , it could represent a plant with the lowest construction cost with respect to the amount of liquid hydrogen produced in comparison to today's plant	Cost cutting in Cryo technology still a challenge in research.
11	Valenti et al	International Journal of Hydrogen Energy	2012	The work focuses specifically on the third issue by assessing the influence of the thermodynamic modeling of the fluid on the simulation outcomes. Numerical approaches to compute the heat capacities as well as the equations of state of hydrogen forms (ortho hydrogen and Para hydrogen) and their mixtures (equilibrium-hydrogen and normal-hydrogen) are described here. The attention is on equilibrium-hydrogen because it is highly exothermic and makes liquefaction process slow.	Work on heat losses over components not properly asses by computational work, experimental work to be done to get accurate results
12	David O. Berstad	International Journal of Hydrogen Energy	2010	An innovative large-scale, high-efficiency hydrogen liquefier based on mixed-refrigerant (MR) pre-cooling has been developed, the resulting figures for specific liquefaction power are 6.48 and 6.15kWh/kgLH2, respectively. Based on current models, a reduction in the range of 45–48% from that of state-of-the art may be obtainable.	Cost still a point of research because low cryo-technology still a challenge,
13	Nakano et al	International Journal of Hydrogen Energy	2010	To manufacture a small scale hydrogen liquefier a simple estimation method for the liquefaction rate and confirmed that the estimation method well explained the experimental result	Small scale and low cost hydrogen liquefier can be improve using more mathematical and statically tool.

14	Yongliang Li et al	International Journal of Hydrogen Energy	2010	In this paper an optimization methodology for thermodynamic design of large scale gas liquefaction Systems proposed. The methodology has been applied to the design of expander cycle based liquefaction processes. High exergy efficiencies (52% for hydrogen and 58% for methane and nitrogen) are achievable based on very general consumptions.	Low exergy still the problem in all system of cryogenics .Various research methodology like computational ,experimental can be done to improve the efficiency
15	Mahabadipour H. et al	Applied Thermal Engineering	2013	In this paper, two typical types of low temperature expander cycles for cold section of olefin plant are designed and simulated. . The results conclude that the expander cycle with one cooling stage surpasses the expander cycle with two cooling stages. The main irreversibility exists in the expander due to its large pressure difference. The net power of the expander cycle with one cooling stage is 3549 kW, the flow rate is 47.35 kg/s and the overall exergy efficiency is 50.18% for the considered cycle in this research.	
16	Hoseyn Sayyaadi	International journal of refrigeration	2010	An optimization of the LNG-BOG re-liquefaction system was presented, it was found that increasing of the pressure ratio for nitrogen compressors, leads to decreasing of the total product cost. However, increasing of the pressure ratio for the BOG compressor leads to increasing in the total product cost	LNG is auto fuel widely used as clean fuel but its cost still a problem, low cost production and installation of fast filling plant still a concerned to researchers
17	Mehmet Kanoglu	Applied Thermal Engineering	2004	A procedure is developed for the energy and exergy analyses of open cycle desiccant cooling systems. The analysis shows that an exergy analysis can provide some useful information with respect to the theoretical upper limit of the system performance, which cannot be obtained from an energy analysis alone. The analysis allows the determination of the sites with the losses of exergy, and therefore showing the direction for the minimization of exergy losses to approach the reversible COP.	Exergy analysis can be applied on other system for optimization
18	Abdullah Alabdulkarem	Applied Thermal Engineering	2012	In this open CO2 liquefaction cycle model was developed and its performance was investigated. An improvement was made on the conventional open CO2 liquefaction cycle that resulted in a 10.61% power savings over the conventional open CO2 liquefaction cycle.	Further research using single and 3 cascade system is power consumption can further be reduced
19	Dincer et. al.	Exergy (Second Edition) Energy	2013	In this a comprehensive exergy analysis is presented of a multistage cascade refrigeration cycle used for natural gas liquefaction, which is a cryogenic process. The multistage cascade cryogenic system is described and an exergy analysis of the cycle components and the minimum work required for liquefaction are provided.	Exergy analysis is power full tool of optimization. Cascade refrigeration analysis show very low exergy efficiency.
20	Cornelissen et. al	Energy Conversion and Manage ment	1998	More than half of the exergy loss takes place in the liquefaction unit and almost one-third in the air compression unit. The major cause of exergy loss is the use of compressors and to a lesser extent the use of turbines In this research is done on air separation unit.	Compressor and air separation unit show more exergy losses more research will be done for avoid losses in these unit.
21	Wood et. al	Cryogenics	1985	In this refrigeration optimization is presented based on the concept that the most appropriate and meaningful measure of the level of refrigeration is the product of entropy absorbed by the refrigerant at the cycle cold temperature, ΔS_c, and the temperature span, ΔT, over which it is pumped.	Optimization using other temperature measuring scale and use of various other term like para and fero magnetic unveil the new optimization methods.

22	Sorin Gherghinescu	U.P.B. Sci. Bull, Series D	2010	In this paper thermodynamic analysis of the two cycles reveals that the hydrogen cycle obtains a higher degree of reversibility, as well as a higher cryogenic efficiency. The Carnot efficiency of cryogenic cycle with hydrogen is higher than the Carnot efficiency of helium cycle, this it explicable by the fact that the minimum temperature of liquid helium is less than the one of hydrogen	Hyderogen and helium liquefaction still a challenge in front of researcher .Thermodynamic analysis provide useful information but thermodynamic analysis of component wise and whole plant involve high research data and future work still need of it
23	Yumrutaş et. al	Exergy	2002	It is found that the evaporating and condensing temperatures have strong effects on the exergy losses in the evaporator and condenser and on the second law of efficiency and COP of the cycle but little effects on the exergy losses in the compressor. The second law efficiency and the COP increases, and the total exergy loss decreases with decreasing temperature difference between the evaporator and refrigerated space and between the condenser and outside air.	Condenser and evaporator unit show effect on exergy efficiency of system ,proper research will be done to completely understand the multi stage condenser evaporator unit
24	Ahamed J.U.	Renewable and Sustainable Energy Reviews	2011	Among the components of the vapor compression system, much research showed that major part of exergy losses is occurred in the compressor. Nano fluid and Nano lubricant cause to reduce the exergy losses in the compressor indirectly, Other than it is found that exergy depends on evaporating temperature, condensing temperature, sub-cooling and compressor pressure. Different refrigerant used and exergy efficiency is analyzed on the basis of these.	Nano fluid used in cryogenics is completely new area of research ,use of Nano-fluid take cryo-technology to new heights
25	Kansha et al.	Separation and Purification Technology	2011	In this paper, a novel cryogenic air separation process that reduces energy consumption by self-heat recuperation is proposed. A simulation demonstrated that the energy consumption of the proposed cryogenic air separation process with self-heat recuperation decreased by more than 36% compared with the conventional cryogenic air separation process, when producing 99.99 mol% oxygen from air	Air separation unit in cryogenic system show high power consumption, new technology can be used to reduce losses.
26	Ham et al.	Energy	2010	Two process designs of a cryogenic ASU (air separation unit) have been evaluated using exergy analysis. The two process designs separate the same feed into products with the same specifications. They differ in the number of distillation columns that are used; either two or three. The three-column design destroyed 12% less exergy than the two-column design. Almost half of the exergy destruction is located in compressor after-coolers	Research on ASU and ther column design still a area of research in exergy losses, by further simulation technique on separation unit can lead to more reliable and cost effective results
27	Rizk J.	Energy	2012	Paper on Distillation columns research is done. Their inconvenient is their high energy consumption. A comparative exergy analysis between the distillation columns considered for cryogenic air separation shows that the exergy efficiency of a double diabatic column, with heat transfer all through the length of the column, is 23% higher than that of the conventional adiabatic double columns. In a simple adiabatic distillation column, most of the exergy losses occur in the column itself (57%)	In ASU high exergy losses occur, more research are to be done to reduce further losses of exergy by using advance technology like ceramic.

28	Syed et. al.	International Journal of Hydrogen Energy	1998	Solar hydrogen system get light in research. Economic analysis of three hydrogen liquefaction systems with an associated cost comparison. The analysis showed that the cost of liquefying hydrogen is lowest for an optimized large-scale type liquid hydrogen plant and is highest for a simple conceptual liquid hydrogen plant.	Solar technology merge with cryogenic technology open new era of technology .One time cost of solar system lead to overall less cost of system in operation
29	Agrawal et al	Gas Separation & Purification	1991	Through exergy analysis, inefficiencies were identified in the distillation system. Two solutions using two vaporizer/condensers in the bottom section of the low pressure (LP) column were suggested, which reduce the exergy loss of the cryogenic part of the plant by 8–9.5%. A process in which nitrogen is condensed in both the vaporizer/condensers located in the bottom section of the LP column yielded the lowest exergy losses for the distillation system.	Use of liquid nitrogen I n condenser side put positive result in system .Advance design in stages lead to high efficiency.so research on this part lead to more efficient design
30	Agrawal et al.	Encyclopedia of Separation Science, Academic Press, Oxford	2000	In this a brief history of air distillation process is discussed with continuous advancement in them over the age. Various columns here to describe the air distillation processes	Brief history helps us in understanding the current present work of ASU. Considering this more efficient system can be developed
31	Gaelle Gosselin	KTH industrial engineering and management	2012	Oxygen separation from air, preference is given to polymeric membranes and from a few years also to ceramic-based membranes. The diffusion of some gas compounds through polymeric membranes is driven by pressure difference between the two sides of the membrane.	Selection and research on polymeric membrane in cryogenic system can be apply to for multi gas separation ASU.
32	Sun et al.	Advances in Cryogenic Engineering	1996	In this loss mechanisms of an Oxford Stirling cryo-cooler are examined using a new simulation model together with second law analysis. The simulation employs a new correlation for heat transfer and friction in oscillating flow. The significant exergy destructions in the cryo-cooler, due to viscous dissipation, heat transfer, mixing processes, shuttle heat transfer and heat conduction in the solid members, are evaluated independently	Proper Heat dissipation in cryogenics system result in improve efficiency, Research should be done on the thermal analysis of system
33	Ray Radebaugh	Low Temperature and Cryogenic Refrigeration ,NATO Science Series	2003	This paper presents a review of the pulse tube refrigerator from its inception in the mid-1960s up to the present. . Efficiencies as high as 24% of Carnot at 80 K and temperatures as low as 2 K have been achieved in pulse tube refrigerators. Pulse tube refrigerators operate with oscillating pressures and mass flows and have no moving parts in the cold end.	Pulse tube refrigerators are used in space so more research on these cryo system improve the space technology.
34	Sinyavski Yu. V.	Chemical and Petroleum Engineering	1995	Compressor alternatives may be electrocaloric cooling. But The numerical value of the integral electrocaloric effect at temperature T= 10-300 K for a change in the external field in the interval 0-25 kV/cm generally are no greater than tenths of a degree and only in some materials do the maximum values of delta T reach one degree .This has been the main reason why the electrocaloric effect for a long time was not considered as an alternative for realization of the cooling process T > 10 k	More research need to be done to overcome the limitation of electro caloric technology in cryogenic field
35	Minta et al	Advances in Cryogenic Engineering	1984	An Entropy Flow Optimization Technique for Helium Liquefaction Cycles is discusses. The intensity of the effort to design efficient cycles is reflected in the numerous discussions of optimization techniques in the literature	Optimization is tool to reduce cost and get economical design of system .Entropy generation that cause of irreversibility

36	Shen et al	Frontiers in Energy	2012	In this paper, the utilization of LNG cold energy in seawater desalination system is proposed and analyzed. A simplified model of the direct-contact heat transfer in this desalination system is proposed and theoretical analyses are conducted. The calculated results are in reasonable agreement with the available experimental data of the R114/water system	Bye changing the refrigerant with more effective and environmental friendly refrigerant lead to get more better result of sea water distillation
37	Gadhiraju Venkatarathnam	International Cryogenics Monograph Series	2008	Process simulation is a widely used technique in the design, analysis, and optimization of process plants. Simulators are computer programs that simulate the behavior of the process plants using appropriate mathematical models. Simulators are used for a variety of purposes	Different simulation tool used to get better and better result of a system that are practically very costly to check performance so more research in field of optimization using simulation technique.
38	Wouagfak et al.	Energy Systems	2011	In this paper thermo-ecological optimization criterion (ECOP) for three-heat-source refrigerators with linear phenomenological heat transfer law is done. The results show that the three-heat-source refrigeration cycle working at maximum ECOP conditions has a significant advantage in terms of entropy production rate and coefficient of performance over the maximum E and maximum R conditions.	Ecological optimization criteria is a complete new technique of optimization, more research by using different cryo system evolve to method to improve efficiency of system
39	. Erdt et al	Advances in Cryogenic Engineering	1994	The LINDE helium refrigeration plant combines an extremely compact construction with remarkably good cycle efficiency. It was in part achieved by arranging 3 expansion turbines in the temperature region below 20 K, one of which expands to roughly saturated liquid. The paper describes the system, the results of performance measurements.	
40	Belnov et al	Theoretical Foundations of Chemical Engineering	2007	The relationship between the plant efficiency and the duration of each of the operating cycle stages is studied using an ad hoc computer program for numerically solving the model equations. It is shown that optimization of the durations of cycle stages increases the thermodynamic efficiency of the plant to 20–22% in comparison to industrial plants.	Research can be proceed by knowing accurate timing of each stage and data can be utilized to get more useful result to increase any other cryo-plant efficiency
41	Brodyanski V. M.	Thermal Engineering	2006	In this It is shown that replacing water, which is traditionally used as a working medium for the thermal power cycle, by an ammonia-water mixture (the Kalina's cycle) or another substance that does not freeze at condensation temperatures ranging from −30 to −40°C allows the capacity of both nuclear and geothermal power stations to be increased substantially during most of the year.	Research on choosing right medium to get high efficiency of any nuclear and geo thermal plant
42	Manzagol et al.	Academic Journal	2002	Cryogenic expanders with work production have a predominant influence on refrigerator/liquefier reliability and efficiency. This paper presents a new cryogenic expander technology. This expander has been tested on a Brayton cycle refrigerator and reached an isentropic efficiency of 50 to 60% for inlet gas conditions of 35 K and 0.7 MPa.	Expander in different cryo with different pressure ratio still the area of concern due to great influence on optimization of a system
43	Elcock et al.	*Argonne National Laboratory*	2007	They found that TiO_2 nanoparticles can be used as additives to enhance the solubility of the mineral oil with the hydro fluorocarbon (HFC) refrigerant. Refrigeration systems using a mixture of HFC134a and mineral oil with TiO_2 nanoparticles appear to give better.	TiO_2 nanoparticles can be potentially used in refrigeration system.

44	Hindawi	Hindawi	2009	It has been carried out by experimental study on boiling heat transfer characteristics of R22 refrigerant with Al_2O_3 nanoparticles and found that the nanoparticles enhanced the refrigerant heat transfer characteristics by reducing bubble sizes	Nanoparticles can be used to enhance heat transfer capabilities
45	Eastman et al.	Mater Res Soc Symp Proc	1996	They investigated the pool boiling heat transfer characteristics of R11 refrigerant with TiO_2 nanoparticles and showed that the heat transfer enhancement reached by 20% at a particle loading of 0.01 g/L.	TiO_2 nano particles can be used to enhance the heat transfer capability of R11 refrigerants.
46	Liu et al.	Chemical Engineering and Technology	2006	They investigated the effects of carbon nanotubes (CNTs) on the nucleate boiling heat transfer of R123 and HFC134a refrigerants. Authors reported that CNTs increase the nucleate boiling heat transfer coefficients for these refrigerants.	CNT have an potential to increase the nucleate boiling heat transfer coefficient of the refrigerants.
47	Jiang et al.	International Journal of Thermal Sciences	2009	The experimental results showed that the thermal conductivity of carbon nanotubes (CNT) nanorefrigerants are much higher than those of CNT–water nanofluids or spherical nanoparticle–R113 nanorefrigerants. Authors reported that the smaller the diameter of CNT larger the thermal conductivity enhancement of CNT nanorefrigerant.	CNT with smaller diameter can be used to enhance the thermal conductivity of the refrigerants
48	Hwang et al.	Current Applied Physics	2006	They suggested that thermal conductivity enhancement of nanofluids is greatly influenced by thermal conductivity of nanoparticles and base fluid. For instance, thermal conductivity of water based nanofluid with multiwall carbon nanotubes has noticeably higher thermal conductivity fluid.	Multiwalled carbon nanotubes has the higher thermal conductivity among the other nano particles.
49	Yoo et al.	Thermochimica Acta	2007	They argued that surface to volume ratio of nanoparticles is a dominant factor. Surface to volume ratio is increased with smaller sizes of nanoparticles. Choi et al.[8] reported that 150% thermal conductivity enhancement was observed in poly (a-olefin) oil by addition of multiwalled carbon nanotubes (MWCNT) at 1% volume fraction.	Surface to volume ratio is an dominant factor to enhance the thermal properties of Nano fluid
50	Yang	University of Kentucky	2006	He reported, a 200% thermal conductivity enhancement for poly (a-olefin) oil containing 0.35% (v/v) MWCNT. It is important to note that this thermal conductivity enhancement was accompanied by a three order of magnitude increase in viscosity.	MWCNT nanoparticles can increase the thermal conductivity as well as viscosity
51	Eastman	Applied Physics Letters	2001	He observed 40% thermal conductivity enhancement for ethylene glycol with 0.3% (v/v) copper nanoparticles (10 nm diameter), although the authors also added that about 1% (v/v) thioglycolic acid helpful for dispersion of nanoparticles in base fluid. The addition of this dispersant yielded a greater thermal conductivity than the same concentration of nanoparticles in the ethylene glycol without the dispersant.	Dispersant can be used to enhance the conductivity.
52	Kang et al.	Experimental Heat Transfer	2006	They reported a 75% thermal conductivity enhancement for ethylene glycol with 1.2% (v/v) diamond nanoparticles between 30 and 50 nm diameter. Despite of these remarkable results, some researchers also measured the thermal conductivity of nanofluids and found no anomalous results.	Diamond nanoparticles can be used to enhance the thermal conductivity of ethylene glycol.

53	Lee et al.	International Journal of Heat and Mass Transfer	2008	They revealed that optimum combination of pH level and surfactant leads to 10.7% thermal conductivity enhancement of 0.1% Cu/H2O nanofluid. They also concluded that during nanofluid preparation stage thermal conductivity of nanofluid is affected by pH level and addition of surfactant.	PH level and surfactant potentially used to enhance the thermos-physical properties.
54	Jiang et al.	International Journal of Thermal Sciences	2009	They added that thermal conductivity of nanofluids also depend on the nanoparticles size and temperature	Size and temperature can be affected to the thermal properties of nano-particles.
55	Wu et al.	Journal of Engineering Thermophysics	2008	They observed that the pool boiling heat transfer was enhanced at low TiO_2 nanoparticles concentration in R11 but deteriorated under high nanoparticles concentration.	Low concentration of TiO_2 in R11 can affectively enhanced the pool boiling heat transfer.
56	Trisaksri and Wongwises	International Journal of Heat and Mass Transfer	2009	They investigated TiO_2 in HCFC 141b in a cylindrical copper tube and found that the nucleate pool boiling heat transfer deteriorated with increasing nanoparticle concentrations especially at higher heat fluxes.	Increasing concentration nd heat flux can badly affect to the thermal properties of nano particles.
57	Hao et al.	International Journal of Refrigeration	2009	They investigated flow boiling inside a smooth tube at different nanoparticles concentration, mass fluxes, heat fluxes, and inlet vapor qualities in order to analyze the influence of nanoparticles on the heat transfer characteristics of refrigerant-based nanofluid. Authors observed that the heat transfer coefficient of refrigerant-based nanofluid in flow boiling is larger than that of pure refrigerant and the maximum enhancement is about 29.7% when observed with a mass fraction of 0–0.5 wt%.	Nanoparticle can enhance the heat exchange capability of refrigerants.
58	Hao et al.	International Journal of refrigeration	2010	They studied experimentally the nucleate pool boiling heat transfer characteristics of refrigerant/oil mixture with diamond nanoparticles. The results indicate that the nucleate pool boiling heat transfer coefficient of R113/VG68 oil mixture with diamond nanoparticles is larger than that of R113/oil mixture by 63.4%. Enhancement in same factor increases with the increase of nanoparticles concentration in the nanoparticles/oil suspension and decreases with the increase of lubricating oil.	Refrigerant/oil mixture with diamond nanoparticles can be used to enhance the thermal conductivity.
59	Wang et al.	Proceedings of the 4th symposium on refrigeration and air condition	2006	They carried out an experimental study of boiling heat transfer characteristics of R22 with Al_2O_3 nanoparticles and found that nanoparticles enhanced the refrigerant heat transfer characteristics by reduction of bubble sizes that moved quickly near the heat transfer surface.	R22 with Al_2O_3 nanoparticles showed the better thermal properties
60	Li et al.	Proceedings of the 12th symposium on engineering thermo physics	2006	They investigated the pool boiling heat transfer characteristics of R-11 with TiO_2 nanoparticles and showed that the heat transfer enhancement reached by 20% at a particle loading of 0.01 g/L.	R-11 with TiO_2 nanoparticles and showed the pool boiling heat transfer characteristics.
61	Peng et al.	International Journal of Refrigeration	2009	They investigated the influence of CuO nanoparticles on the heat transfer characteristics of R-113 refrigerant-based nanofluids and presented a correlation for prediction of heat transfer performance of refrigerant based nanofluids. Authors reported that the heat transfer coefficient of refrigerant-based nanofluids is higher than that of pure refrigerant, and the maximum enhancement of heat transfer coefficient found to be about 29.7%.	CuO in 113 refrigerant-based nanofluids can enhanced the heat transfer characteristics.

62	Kumar and Elansezhian	J Front Mech Engg	2014	They experimentally investigated the effect of varying concentration of ZnO nanoparticles on various performance parameters like COP, suction temperature, input power and pressure ratio with 152a as working fluid in vapour compression refrigeration system. They found that 0.5% v ZnO nanoparticles with R152a gives maximum COP of 3.56 and 21% reduction in power input. Pressure ratio decreases with increase in ZnO concentration.	
63	Mahbubul et al.	International Journal of Heat and Mass Transfer	2013	They measured thermo physical properties, pressure drop and heat transfer performance of Al_2O_3 nanoparticles and R-134a mixture. Thermal conductivity of Al_2O_3/R-134a nano refrigerant increased with temperature and augmentation of particle concentration. It was also observed that pumping power, viscosity, pressure drop, and heat transfer coefficients of the Nano refrigerants show significant increment with the increase of volume fractions. The frictional pressure drop also shows rapid increment with 3 vol. % particle fraction.	The pumping power, viscosity, pressure drop, and heat transfer coefficients of the nano refrigerants shows significant increment with the increase of volume fractions.

3. Conclusion and Recommendation

From the literature review it is found that various research and different method are employed to increase efficiency of cryo system. Second law efficiency are very low in all above said cryogenic systems like hydrogen ,helium liquefaction etc. and its value ranging from 3% to 23 % for most of systems. Advance technology like different cryo fluid include Nano one (Nano fluid and Nano lubricants) are also tried to reduces the losses. Ceramic technology is also used in separator to increase the high output with less losses. Low increase in exergy efficiency is noticed in various different systems. Exergy efficiency are mainly depend upon the inlet condition of system and in most of cases the inlet conditions are NTP (normal temperature pressure) conditions that is 298 K temperature and one atmosphere pressure.

3.1. Conclusions

Exergy analysis of cryogenics systems in which first six system with different gases and rest systems such as hydrogen, Collin, improved Collin system are evaluated on the basis of pressure ratio, compressor outlet temperature, and expander mass flow ratio. Experiment has been done on the vapour compression system to give valuable suggestion for increasing efficiency of cryogenics systems. Following results are concluded from study.

(1) During off design condition, performance of cycle does not hamper within the specific range of cyclic pressure ratio, for particular considered system there is always appropriate operating pressure ratio range for each working gas on which system work better
(2) All six system are compared on the basis of performance parameters at different pressure ratio, form the data observation it observed that simple Claude cycle is most suitable system because the three heat exchanger help in achieving more refrigerant effect which is in turn optimize the performance of the system.
(3) During PR increase, there is an imbalance in mass flow of forward and return stream of heat exchanger HX. Second law efficiency with the help of increasing pressure ratio which variate and create specific heat imbalance to overcome the mass imbalance.
(4) Variation in expander mass flow has highly influence the refrigeration effect of expander and overall performance of system. Optimum range of EXP flow fraction (r) producing refrigeration effect is 0.55 to 0.7. Liquid production rate is highly influenced by refrigeration effect of expander.
(5) Inlet temperature of expander also plays an important factor to determine the refrigeration effect while other parameters in the system are constant. As the mass flow fraction increases through EXP, the output temperature of expander T_e also decreases which in turn lower the inlet temperature of input temperature of$T_{\text{in EXP}}$.
(6) In all gases methane gas show highest performance parameters in most of system while argon show lowest.
(7) The performance of hydrogen liquefaction cycle does not much deteriorate during off design condition when it is operated in selected operated range of PR 20-52 bar (the compressor suction pressure is atmospheric).
(8) Exergetic efficiency of the heat exchanger (HXD) at the lowest temperature of a hydrogen liquefier can be improved by increasing the pressure ratio because the mass imbalance gets compensated by the specific heat imbalance.
(9) While designing the hydrogen liquefaction cycle, owing to their lower exergetic efficiencies, additional care should be taken for ensuring superior heat transfer performance by the high temperature heat exchanger HXA and the lowest temperature heat exchanger HXD.
(10) Initial feasible range of pressure ratio in hydrogen liquefaction system is 20 to 87 bar, COP of the system decrease at very rapid rate but after that the rate of

reduction in COP with increase PR start becoming constant with very less change while the second law efficiency show a constant reduction with increase in PR.

(11) Design parameter NTU for HX is carefully study for best performance of system. NTU term continuously decrease in hydrogen liquefaction system upto 70 bar for the J-T heat exchanger HXD and minimum at 70 bar while the variation in NTU term for HXA and HXB is quite different due to the different cold stream temperature of exchangers

(12) Improved Collin system show high efficiency as compared to Collin system, the nitrogen chamber and extra expander gives extra refrigerant effect which enhance liquefaction rate in the system and increasing the performance parameters of systems.

(13) The improved Collin system at PR 11 bars show highest exergtic efficiency of 54.19% keeping the expander ratio of all three expander is 70%,10%,10% respectively while simple Collin helium liquefaction system show 3.54% exergtic efficiency keeping the both expander flow ratio 35% and 50% respectively

(14) Experiment is done to give valuable suggestion for increasing efficiency of cryogenics systems.. Test results show that the parameters such as exergy efficiency, heating capacity of the considered system improved in the range of 1.9-5.96% and 26-82% respectively by using 0.06 Vol% silver Nano fluid compared to water as cold based fluid for considerable range of cold base fluid flow rate.

(15) Exergy destruction decreases in the range of 29-31.28%, 65.77-70.01%, 14.31-16.03%, 17-23% in compressor, condenser, evaporator and expansion valve respectively. whereas 0.015 Vol% silver Nano fluid shows very less effect on performance parameters of system for different base fluid mass flow rates.

References

[1] Robert C. Clauss “Cryogenic Refrigeration Systems” Chapter - 4, pages 159-193.

[2] Rijo Jacob Thomas, Parthasarathi Ghosh, Kanchan Chowdhury, Exergy analysis of helium liquefaction systems based on modified Claude cycle with two-expanders, Cryogenics, Volume 51, Issue 6, June 2011, Pages 287-294.

[3] Rijo Jacob Thomas, Parthasarathi Ghosh and Kanchan Chowdhury, “ Exergy based analysis on different expander arrangements in helium liquefiers” international journal of refrigeration 35 (2012).

[4] Rijo Jacob Thomas, Parthasarathi Ghosh and Kanchan Chowdhury, “Application of exergy analysis in designing helium liquefiers” 7th Biennial International Workshop “Advances in Energy Studies” Volume 37, Issue 1, January 2012, Pages 207–219.

[5] Rijo Jacob Thomas, Parthasarathi Ghosh and Kanchan Chowdhury, “Optimum number of stages and intermediate pressure level for highest exergy efficiency in large helium liquefiers” International Journal of Refrigeration, June 2013.

[6] G. Cammarata, A. Fichera and D. Guglielmino, “Optimization of a liquefaction plant using genetic algorithms”, Applied Energy 68 (2001),Pages 19-29.

[7] Rijo Jacob Thomas, Parthasarathi Ghosh and Kanchan Chowdhury, “ Applicability of equations of state for modeling helium systems” Cryogenics 52 (2012) , pages 375–381.

[8] David O. Berstad,Jacob H. Stangand Petter Neksa, “Comparison criteria for large-scale hydrogen liquefaction processes” International Journal of Hydrogen Energy, Volume 34, Issue 3, February 2009, Pages 1560–1568.

[9] Gianluca Valenti andEnnio Macchi, “Proposal of an innovative, high-efficiency, large-scale hydrogen liquefier” International Journal of Hydrogen Energy, Volume 33, Issue 12, June 2008, Pages 3116–3121.

[10] Songwut Krasae-in,Jacob H. Stangand Petter Neksa, “Simulation on a proposed large-scale liquid hydrogen plant using a multi-component refrigerant refrigeration system” International Journal of Hydrogen Energy, Volume 35, Issue 22, November 2010, Pages 12531–12544.

[11] Gianluca Valenti,Ennio Macchi and Samuele Brioschi, “The influence of the thermodynamic model of equilibrium-hydrogen on the simulation of its liquefaction” International Journal of Hydrogen Energy, Volume 37, Issue 14, July 2012, Pages 10779–10788.

[12] David O. Berstad, Jacob H. Stangand Petter Neksa, “Large-scale hydrogen liquefier utilising mixed-refrigerant pre-cooling”, International Journal of Hydrogen Energy, Volume 35, Issue 10, May 2010, Pages 4512–4523.

[13] Akihiro Nakano, Tetsuhiko Maeda, Hiroshi Ito,Masao Masuda, Yoshiaki Kawakami, Atsushi Kato, Manabu Tange,Toru Takahashiand Masahiro Matsuo, “Small-scale hydrogen liquefaction with a two-stage Gifford–McMahon cycle refrigerator” , International Journal of Hydrogen Energy, Volume 35, Issue 17, September 2010, Pages 9088–9094.

[14] Yongliang Li, Xiang Wang and Yulong Ding, “An optimal design methodology for large-scale gas liquefaction” , Applied Energy 99 (2012) , Pages 484–490.

[15] H. Mahabadipour and H. Ghaebi, “Development and comparison of two expander cycles used in refrigeration system of olefin plant based on exergy analysis”, Applied Thermal Engineering 50 (2013) , Pages 771-780.

[16] Hoseyn Sayyaadi and M. Babaelahi, “Thermoeconomic optimization of a cryogenic refrigeration cycle for re-liquefaction of the LNG boil-off gas”, international journal of refrigeration 33 (2010) , Pages 1197-1207.

[17] Mehmet Kanoglu, Melda Ozdinc,Carpınlıoglu and Murtaza Yıldırım, “Energy and exergy analyses of an experimental open-cycle desiccant cooling system”, Applied Thermal Engineering 24 (2004) , Pages 919–932.

[18] Abdullah Alabdulkarem, Yunho Hwang and Reinhard Radermacher, “Development of CO2 liquefaction cycles for CO2 sequestration”, Applied Thermal Engineering 33-34 (2012) , Pages 144-156.

[19] Ibrahim Dincer and Marc A. Rosen “Exergy Analysis of Cryogenic and Liquefaction Systems” Exergy (Second Edition) Energy, Environment and Sustainable Development, 2013, Pages 319–334.

[20] R.L. Cornelissen, G.G. Hirs, Exergy analysis of cryogenic air separation, Energy Conversion and Management, Volume 39, Issues 16–18, November–December 1998, Pages 1821-1826.

[21] M.E. Wood, W.H. Potter, General analysis of magnetic refrigeration and its optimization using a new concept: maximization of refrigerant capacity, Cryogenics, Volume 25, Issue 12, December 1985, Pages 667-683.

[22] Sorin Gherghinescu “Energetic and exergetic analysis of cryogenic systems used in a detritiation pilot plant” U.P.B. Sci. Bull., Series D, Vol. 72, Issue. 4, 2010.

[23] Recep Yumrutaş, Mehmet Kunduz, Mehmet Kanoğlu, Exergy analysis of vapor compression refrigeration systems, Exergy, An International Journal, Volume 2, Issue 4, 2002, Pages 266-272.

[24] J.U. Ahamed, R. Saidur, H.H. Masjuki, A review on exergy analysis of vapor compression refrigeration system, Renewable and Sustainable Energy Reviews, Volume 15, Issue 3, April 2011, Pages 1593-1600.

[25] Yasuki Kansha, Akira Kishimoto, Tsuguhiko Nakagawa, Atsushi Tsutsumi, A novel cryogenic air separation process based on self-heat recuperation, Separation and Purification Technology, Volume 77, Issue 3, 4 March 2011, Pages 389-396.

[26] L.V. van der Ham, S. Kjelstrup, Exergy analysis of two cryogenic air separation processes, Energy, Volume 35, Issue 12, December 2010, Pages 4731-4739.

[27] J. Rizk, M. Nemer, D. Clodic, A real column design exergy optimization of a cryogenic air separation unit, Energy, Volume 37, Issue 1, January 2012, Pages 417-429.

[28] M.T. Syed, S.A. Sherif, T.N. Veziroğlu, J.W. Sheffield, An economic analysis of three hydrogen liquefaction systems, International Journal of Hydrogen Energy, Volume 23, Issue 7, July 1998, Pages 565-576.

[29] R. Agrawal, D.W. Woodward, Efficient cryogenic nitrogen generators: An exergy analysis, Gas Separation & Purification, Volume 5, Issue 3, September 1991, Pages 139-150.

[30] R. Agrawal, D.M. Herron, Air liquefaction: distillation, In: Editor-in-Chief: Ian D. Wilson, Editor(s)-in-Chief, Encyclopedia of Separation Science, Academic Press, Oxford, 2000, Pages 1895-1910.

[31] Gaëlle Gosselin "Thermodynamic study of oxygen-enhanced combustion: analysis of different techniques of oxidant production" KTH industrial engineering and management, Master of Science Thesis EGI 2012.

[32] Z. F. Sun, C. G. Carrington "Simulation and Second Law Analysis of a Miniature Stirling Cycle Cryocooler" , Advances in Cryogenic Engineering , 1996 ,pages 1551-1560.

[33] Ray Radebaugh "Pulse Tube Cryocoolers" , Low Temperature and Cryogenic Refrigeration ,NATO Science Series, Volume 99, 2003, , Pages 415-434.

[34] Yu. V. Sinyavskii, "Electrocaloric refrigerators: A promising alternative to current low-temperature apparatus" Chemical and Petroleum Engineering ,June 1995, Volume 31, Issue 6, Pages 295-306.

[35] Moses Minta, Joseph L. Smith Jr. , "An Entropy Flow Optimization Technique for Helium Liquefaction Cycles" Advances in Cryogenic Engineering ,1984,Pages 469-478.

[36] Qingqing Shen, Wensheng Llin, Anzhong Gu and Yonglin Ju , "A simplified model of direct-contact heat transfer in desalination system utilizing LNG cold energy", Frontiers in Energy ,June 2012, Volume 6, Issue 2, Pages 122-128.

[37] Gadhiraju Venkatarathnam , "Simulation of cryogenic processes" , Cryogenic Mixed Refrigerant Processes ,International Cryogenics Monograph Series 2008, , Pages 51-63.

[38] Paiguy Armand Ngouateu Wouagfack and Réné Tchinda, "Irreversible three-heat-source refrigerator with heat transfer law of $Q\alpha\Delta(T^{-1})$ and its performance optimization based on *ECOP* criterion" , Energy Systems ,November 2011, Volume 2, Issue 3-4, Pages 359-376.

[39] W. K. Erdt, P. Frandsen, D. Güsewell, K. Kurtcuoglu, K. LÖhlein, A.-E. Senn, N. O. Solheim, U. Wagner, G. Winkler and B. Ziegler, "Performance of an Efficient 6 Kw Helium Refrigerator for the LEP 200 Project at CERN" ,Advances in Cryogenic Engineering, Volume 39, 1994, Pages 553-561.

[40] V. K. Bel'nov, N. M. Voskresenskii, D. M. Predtechenskaya, M. S. Safonov and L. I. Kheifets, "Increasing the efficiency of an air separation plant by varying the cycle stage durations" , Theoretical Foundations of Chemical Engineering , April 2007, Volume 41, Issue 2, pp 143-149.

[41] V. M. Brodyanskii "Improving the efficiency of nuclear and geothermal power stations by using low environment temperatures", Thermal Engineering ,March 2006, Volume 53, Issue 3, pp 201-207.

[42] Manzagol, Jean, D Harboulle , Philippe; Claudet, Gerard; Baguer, Guy Gistau, "Cryogenic scroll expander for claude cycle with cooling power of 10 to 100 Watts at 4.2 K" , Academic Journa, AIP Conference Proceedings;2002, Vol. 613, Issue 1, , Page 267

[43] Elcock D. Potential, Impacts of nanotechnology on energy transmission applications and needs, Environmental Science Division, Argonne National Laboratory (2007).

[44] Hindawi, Special issue on heat transfer in nanofluids (2009.

[45] Eastman JA, Choi US, Thompson LJ and Lee S, Enhanced thermal conductivity through the development of nanofluids, Mater Res Soc Symp Proc, 457 (1996) 3–11.

[46] Liu MS, Lin MCC, Huang IT and Wang CC, Enhancement of thermal conductivity with CuO for Nanofluids, Chemical Engineering and Technology 29(1) (2006) 72–77.

[47] Jiang W, Ding G and Peng H, Measurement and model on thermal conductivities of carbon nanotube nanorefrigerants, International Journal of Thermal Sciences 48 (2009) 1108–1115

[48] Hwang YJ, Ahn YC, Shin HS, Lee CG, Kim GT and Park HS, Investigation on characteristics of thermal conductivity enhancement of nanofluids, Current Applied Physics 6(6) (2006) 1068–1071.

[49] Yoo DH, Hong KS and Yang HS, Study of thermal conductivity of nanofluids for the application of heat transfer fluids, Thermochimica Acta 2007;455(1–2):66–69.

[50] Yang Y. Carbon nanofluids for lubricant application. University of Kentucky (2006).

[51] Eastman JA, Choi SUS, Li S, Yu W, and Thompson LJ, Anomalously increased effective thermal conductivities of ethylene glycol-based nanofluids containing copper nanoparticles. Applied Physics Letters 78(6) (2001) 718–720.

[52] Kang H.U, Kim S.H and Oh J.M., Estimation of thermal conductivity of nanofluid using experimental effective particle, Experimental Heat Transfer 19(3) (2006) 181–191.

[53] Lee J.H, Hwang K.S, Jang S.P, Lee B.H, Kim J.H and Choi SUS, Effective viscosities and thermal conductivities of aqueous nanofluids containing low volume concentrations of Al2O3 nanoparticles. International Journal of Heat and Mass Transfer 51 (2008) 2651–2656.

[54] Jiang W, Ding G and Peng H., Measurement and model on thermal conductivities of carbon nanotube nanorefrigerants. International Journal of Thermal Sciences 48 (2009) 1108–1115.

[55] Wu X.M, Li P, Li H and Wang W.C, Investigation of pool boiling heat transfer of R11 with TiO_2 nano-particles. Journal of Engineering Thermophysics 29(1) (2008) 124–126.

[56] Trisaksri V and Wongwises S, Nucleate pool boiling heat transfer of TiO_2–R141b nanofluids, International Journal of Heat and Mass Transfer 52 (2009) 1582–1588.

[57] Hao P, Guoliang D, Weiting J, Haitao H and Yifeng G, Heat transfer characteristics of refrigerant-based nanofluid flow boiling inside a horizontal smooth tube. International Journal of Refrigeration 32 (2009) 1259–1270.

[58] Hao P, Guoliang D, Haitao H, Weiting J, Dawei Z and Kaijiang W. Nucleate pool boiling heat transfer characteristics of refrigerant/oil mixture with diamond nanoparticles. International Journal of refrigeration 33 (2010) 347–358.

[59] Wang K.J, Ding G.L and Jiang WT, Nano-scale thermal transporting and its use in engineering, Proceedings of the 4th symposium on refrigeration and air condition (2006) 66–75.
[60] Li P, Wu XM and Li H, Pool boiling heat transfer experiments of refrigerants with nanoparticles TiO_2, Proceedings of the 12th symposium on engineering thermo physics, (2006) 325–333.
[61] Peng H, Ding G, Jiang W, Hu H and Gao Y, Heat transfer characteristics of refrigerant-based nanofluid flow boiling inside a horizontal smooth tube. International Journal of Refrigeration 32 (2009):1259–1270.
[62] D.Sendil Kumar and R. Elansezhian, ZnO nanorefrigerant in R152a refrigeration system for energy conservation and green environment, J Front Mech Engg (2014) 1-6.
[63] I.M. Mahbubul,S.A. Fadhilah, R. Saidur, K.Y. Leong and M.A. Amalina, Thermophysical properties and heat transfer performance of Al_2O_3/R-134a nanorefrigerants, International Journal of Heat and Mass Transfer 57 (2013) 100–108.